Numerical simulations of aeronautical engine ignitions under realistic high altitude conditions

Antoine Pestre

THÈSE

En vue de l'obtention du

DOCTORAT DE L'UNIVERSITÉ DE TOULOUSE

Délivré par :

Institut National Polytechnique de Toulouse (Toulouse INP)

Discipline ou spécialité :

Dynamique des fluides

Présentée et soutenue par :

M. ANTOINE PESTRE

le jeudi 12 janvier 2023

Titre :

Simulations numériques d'allumages des moteurs aéronautiques en conditions réalistes de hautes altitudes

---

Ecole doctorale :

Mécanique, Energétique, Génie civil, Procédés (MEGeP)

Unité de recherche :

Centre Européen de Recherche et Formation Avancées en Calcul Scientifique (CERFACS)

Directeur(s) de Thèse :

MME BÉNÉDICTE CUENOT

MME ELEONORE RIBER

Rapporteurs :

M. EPAMINONDAS MASTORAKOS, UNIVERSITE DE CAMBRIDGE

M. STEPHANE JAY, IFPEN

Membre(s) du jury :

M. RONAN VICQUELIN, CENTRALESUPELEC GIF SUR YVETTE, Président

M. FÉLIX COLLIN-BASTIANI, GROUPE SAFRAN, Invité(e)

M. MARC BELLENOUE, ENSMA POITIERS, Membre

MME BÉNÉDICTE CUENOT, CERFACS, Membre

MME ELEONORE RIBER, CERFACS, Invité(e)

M. NICOLAS BERTIER, ONERA, Membre

Abstract

The relight capability is a critical aspect of the aeronautical engine design and safety standards require the ignition of the engine under high altitude conditions (low pressure: $P = 0.3\,bar$ and low temperature: $T = 233\,K$). Therefore the influence of low pressure and low temperature conditions on the ignition processes must be better understood. For this purpose, the effect of these conditions on the chemical phenomena has been first evaluated with purely gaseous configurations. The results have shown the detrimental effect of sub-atmospheric conditions via a slowing down of the chemical reactivity and thus a reduction of the power released. In addition, direct numerical simulations performed using a multi-component ARC chemistry enable to compare the kernel developments depending on the pressure and temperature conditions and indicate that low pressure kernels are less robust to extinction phenomena. On the other hand, the influences of high altitude conditions on the two-phase flow have also been evaluated. Firstly, at the fuel injection, the available experimental measurements have shown that low pressure reduces the atomization phenomenon resulting in a spray with larger and fewer droplets. Two-phase ignition simulations have thus been performed taking into account the different droplet distribution due to the high altitude conditions. A complete modification of the combustion regime has then been observed compared to the gaseous case. Finally, this work enables to develop new numerical methods which have been used to simulate the ignition under realistic high altitude conditions in the MERCATO configuration. This computation highlighted the critical role of the two-phase phenomena in the formation and development of the kernel. Furthermore, the detrimental effect of low pressure and low temperature on the ignition has been recovered once again.

Keywords:
Low Pressure, Low Temperature, Computational Fluid Dynamic, Direct Numerical Simulation, Analytically Reduced Chemistry, flame kernel formation, two-phase flow, evaporation, multi-component.

Résumé

La capacité de rallumage est un aspect critique de la conception des moteurs aéronautiques et les normes de sureté exigent l'allumage du moteur en conditions de haute altitude (basse pression : $P = 0.3\,bar$ et basse température : $T = 233\,K$). Ainsi, l'influence des conditions de basse pression et de basse temperature doit être mieux comprise. Pour cela, l'effet de ces conditions sur les phenomènes chimiques a tout d'abord été étudié en configurations purement gazeuses. Les résultats ont alors montré que les conditions sub-atmosphériques étaient désavantageuses à cause d'un ralentissement de la réactivité chimique et donc d'une réduction de la puissance dégagée. De plus, des simulations numériques directes ont été réalisées en utilisant une chimie ARC multi-composante ce qui a permis de comparer le développement des noyaux de flamme en fonction des conditions de pression et de température. Les résultats indiquent alors que les noyaux formés en condition de basse pression sont moins robustes aux phénomènes d'extinctions. D'autre part, l'influence des conditions de haute altitude sur le diphasique a aussi été évaluée. Premièrement, au niveau de l'injection de carburant, les données expérimentales disponibles ont montré que les basses pressions réduisent les processus d'atomisation ce qui conduit à la formation d'un spray composé de gouttes plus larges et moins nombreuses. Des simulations d'allumage diphasique ont alors été réalisées en prenant en compte la modification de la distribution de goutte induite par les conditions de haute altitude. Un changement complet du régime de combustion a alors été observé par rapport au cas gazeux. Pour finir, ce travail a permis de développer de nouvelles méthodes numériques qui ont pu être utilisées pour simuler l'allumage en condition réaliste de haute altitude dans le banc MERCATO. Ce calcul a mis en évidence le rôle critique des phénomènes diphasiques dans la formation et le développement du noyau. De plus, l'effet néfaste des basses pressions et des basses températures sur l'allumage a été retrouvé.

Mots clefs:
Basse Pression, Basse Température, simulation de la dynamique des fluide, Simulation Numérique Directe, chimie analytiquement réduite, formation du noyau de flamme, diphasique, évaporation, multi-composant.

Acknowledgments

Avant tout je souhaite remercier les différents membres du jury, Epaminondas Mastorakos, Stéphane Jay, Ronan Vicquelin, Marc Bellenoue, et Nicolas Bertier pour avoir évalué mon travail ainsi que pour les échanges très enrichissants qui ont suivi la soutenance.

Je remercie ensuite les encadrants de cette thèse. Bénédicte et Eleonore, pour les conseils scientifiques que vous m'avez apportés mais aussi pour la bonne humeur toujours présente. Bénédicte, je souhaitais aussi te remercier d'avoir partagé avec moi ton bébé NTMIX. Travailler sur ce code m'a apporté beaucoup de crise de rage entrecoupées de "Je suis un génie !!", mais m'a sourtout permis d'acquérir de nombreuses compétences sur le développement d'un code CFD dans son ensemble et de découvrir une affinité sur les aspects développement. Merci également à toi Félix. J'espère ne pas avoir été trop compliqué comme premier doctorant ! Personnellement j'ai vraiment apprécié nos échanges, tes conseils et les apports du point de vue industriel qui m'ont permis d'avoir une meilleure compréhension de mon sujet et des problématiques sous-jacentes.

Je souhaite maintenant remercier le personnel du CERFACS. Tout d'abord l'équipe CSG. En particulier Isabelle qui fait des miracles en résolvant n'importe quel problème en 2 minutes, Gérard sûrement la personne la plus gentille du labo, Fabrice qui nous envoie régulièrement des petits messages perso pour les mises à jour du Mac mais sourtout grâce à qui la soutenance s'est déroulée sans aucun problème. De même, je remercie Michelle, Marie, Brigitte, Lydia, Amandine et toute l'équipe admin qui fait un travail impressionnant et nous permet de nous soucier uniquement de notre travail de recherche. Et surtout **Chantal** pour son rire que l'on peut entendre à l'autre bout du CERFACS.

Ces années au CERFACS n'auraient pas été aussi plaisantes sans les doctorants (et post-doctorants !) du labo que je remercie également. Jon, mon ~~allemand~~ ~~alsasien~~ lorrain préféré (j'ai quand même verifié sur une carte) pour le temps passé au tableau à essayer de comprendre mes problèmes. Nico, le plasma guy, grand seigneur du magret séché. Clovis le révolutionnaire, tes soirées jeu jusqu'à 2h du matin vont me manquer. Thomas (Laroche), premier co-bureau et grand guide qui m'a montré le chemin (je t'autorise encore à m'appeler "mon ptit"). Thomas (Lesaffre) le co-bureau qui m'a accueilli et supporté sur la fin de la rédaction, à quand le prochain voyage ? Marchal, bientôt la fin pour toi aussi, on va pouvoir repartir à Bayonne ! Quentin, le grand maître chimiste, et Gersois en plus ! Etienne, pense à rédiger plutôt que faire de l'alpi, surtout maintenant que t'es à Pau. Théo, avec tes 50 pages par jour tu dois approcher les 20000 maintenant, passe à la conclusion. Anto, faudra que tu m'expliques comment tu as réussi à faire des allumages. Arthur, c'est bizarre depuis que t'es de retour mon tableau est de nouveau rempli de trucs inutiles. Mais aussi Lionel, Benjamin, Victor, Camille, Minh, Thomas (Lafarge), Aurélien, Guillaume, Alex, Mouze, et tout ceux que j'oublie. Petite mention spéciale : Jon, Thomas, Nico et Anto merci pour la relecture du manuscrit.

Je remercie aussi mes parents pour avoir fait naître en moi depuis tout petit le goût des sciences et la curiosité qui m'ont conduit jusqu'ici. Mais aussi plus globalement ma famille qui n'a pas toujours compris pourquoi j'avais choisi de faire une thèse mais qui m'a toujours soutenu dans ce choix et motivé pour arriver au bout.

Je termine par le plus important à mes yeux. Marine. Tout d'abord pour la relecture, peu de personnes l'auraient fait. Mais surtout pour m'avoir encouragé, motivé, supporté, et accompagné dans les meilleurs moments comme les plus durs au cours de ces 4 dernières années (particulièrement sur la fin !). Un grand merci !

A ma mère.

Contents

Nomenclature

Roman Symbols

$[A_k]$	Molar concentration of species k	mol/m^3
$\dot{\mathcal{Q}}$	Energy source term	$J/m^3/s$
$\dot{A}_f$	Liquid film surface creation rate	m^2/s
$\dot{E}_{c,f}$	Liquid kinetic energy rate	J/s
$\dot{E}_{s,f}$	Liquid surface energy rate	J/s
$\dot{m}_p$	Droplet evaporation rate	kg/s
$\dot{m}$	Mass flow rate crossing the kernel boundary	kg/s
$\dot{S}_E$	Energy rate source term	J/s
$\mathcal{A}$	Flame surface	m^2
$\mathcal{A}$	Rate constant	s^{-1}
$\mathcal{A}_{A\rightarrow B}$	Atom $\mathcal{A}$ flux from species A to B	$mol/m^3/s$
$\mathcal{F}_f$	Flammability factor	-
$\mathcal{F}_{\Delta t}$	Time-step reduction factor	–
$\mathcal{F}_{def}$	Film deformation factor	–
$\mathcal{G}_\Delta$	Convolution filter	m^{-1}
$\mathcal{I}$	Inter-droplet distance	m
$\mathcal{P}_{bd}$	Breakdown probability	-
$\mathcal{P}_{igni}$	Ignition probability	-
$\mathcal{P}_{loss}$	Kernel power associated to the conductive thermal losses	J/s
$\mathcal{P}_{prod}$	Kernel power associated to the heat release	J/s
$\mathcal{Q}_j$	Rate of progress of reaction j	$mol/m^3/s$
$\mathcal{R}$	Perfect gas constant	$J/mol/K$
$\mathcal{R}_p$	R-parcel parameter	–
$\mathcal{S}$	Information entropy	bit
$\overrightarrow{n}$	Normal unity vector	–
$\overrightarrow{w}$	Local flame front velocity	m/s
A	Area	m^2
a	Strain rate	s^{-1}

A_j	Pre-exponential constant of reaction j	$mol^{1-order_j}/m^{3(1-order_j)}/s/K^{\beta_j}$
A_p	Area of the fuel slots in the swirl chamber	m^2
c	Progress variable	–
c	Sound speed	m/s
C_A	Molar consumption term of species A	$mol/m^3/s$
C_D	Discharge coefficient	–
c_k	Mass concentration of species k	kg/m^3
$C_{\mathcal{D}}$	Drag coefficient	–
$C_{chem,k}$	Chemical number associated to species k	–
$C_{p,k}$	Massic heat capacity of species k at constant pressure	$J/K/kg$
C_p	Massic heat capacity of the mixture at constant pressure	$J/K/kg$
$C_{v,k}$	Massic heat capacity of species k at constant volume	$J/K/kg$
C_v	Massic heat capacity of the mixture at constant volume	$J/K/kg$
d_0	Diameter of the swirl chamber nozzle	m
D_k	Diffusion coefficient of species k	m^2/s
D_p	Diameter of the swirl chamber slots	m
d_p	Droplet diameter	m
D_s	Diameter of the swirl chamber	m
$d_{p,10}$	Linear mean droplet diameter	m
$d_{p,20}$	Surface mean droplet diameter	m
$d_{p,30}$	Volume mean droplet diameter	m
$d_{p,32}$	Sauter mean droplet diameter	m
D_{th}	Thermal diffusion coefficient	m^2/s
$dn_{\mathcal{A}}$	Excess of atom $\mathcal{A}$ between two explicit iterations	mol
E	Total energy (massic)	J/kg
E_f	Error factor coefficient	–
E_i	Deposed energy	J
e_s	Sensible energy	J/kg
e_t	Total chemical energy	J/kg
E_{aj}	Activation energy of reaction j	J/mol
E_{turb}	Turbulent kinetic energy	m^2/s^2
f	Frequency	Hz
F_p^{ext}	External forces applying on the droplet	N
G	Gibbs free energy	J
h_k	Massic enthalpy of species k	J/kg
H_t	Film instability amplitude	m

$h_{s,k}$	Sensible enthalpy of species k	J/kg
hr	Mass heat release	J/kg
J_{ij}	Jacobian matrix coefficient	s^{-1}
k	Wave number	m^{-1}
K_{fj}	Forward reaction rate of reaction j	$mol^{1-order_j}/m^{3(1-order_j)}/s$
K_{rj}	Backward reaction rate of reaction j	$mol^{1-order_j}/m^{3(1-order_j)}/s$
L	Characteristic length	m
l_0	Length of the swirl chamber nozzle	m
L_b	Film break-up length	m
L_c	Length of the swirl chamber convergent	m
L_s	Length of the swirl chamber	m
L_t	Integral turbulent scale	m
L_v	Latent heat of evaporation	J/kg
m_k	Mass of species k	kg
M_{SC}	Maximum number of chemical sub-cycles	–
n	Current iteration	
N_c	Number of child droplets	–
n_k	Number of mole of species k	mol
N_s	Number of fuel slots in the swirl chamber	–
$n_{\mathcal{A},B}$	Number of atom $\mathcal{A}$ in species B	–
$N_{\mathcal{A},j}$	Number of atom $\mathcal{A}$ in reaction j	–
N_{elem}	Number of atomic elements	–
N_{react}	Number of reaction j	–
N_{SC}	Number of chemical sub-cycles	–
N_{spec}	Number of species k	–
P	Pressure	Pa
P_A	Molar production term of species A	$mol/m^3/s$
q	Shapte factor of the Rosin-Rammler distribution	–
q_j	j^{th} component of the heat diffusion flux	$J/m^2/s$
R	Radius	m
r	Modified perfect gas constant	$J/kg/K$
R_0	Radius of the nozzle exit	m
R_a	Air core radius at the nozzle exit	m
R_b	Burst radius	m
r_p	Droplet radius	m
R_s	Swirl radius	m

$r_{AB,path}$	Error propagation coefficient between species A and B	–
r_{AB}	Interaction coefficient between species A and B	–
S	Section	m^2
S_a	Absolute flame speed	m/s
S_c	Consumption flame speed	m/s
S_d	Displacement flame speed	m/s
S_L	Laminar flame speed	m/s
S_T	Turbulent flame speed	m/s
s_X	Molar stoichiometric ratio	–
s_Y	Mass stoichiometric ratio	–
$S_{\mathcal{Y}_{u,j}}$	Sensitivity coefficient associated to the quantity $\mathcal{Y}_{u,j}$ and reaction j	–
S_{ij}	Strain rate tensor	s^{-1}
T	Temperature	K
t	Time	s
t_f	Liquid film thickness	m
t_{arc}	Characteristic time of the arc phase	s
t_{bd}	Characteristic time of the breakdown phase	s
t_{glow}	Characteristic time of the glow phase	s
U	Internal energy	J
U	Velocity magnitude difference between gas and liquid phase	m/s
u	Film velocity	m/s
u_j	Gas velocity associated to j direction	m/s
U_l	Liquid film velocity magnitude	m/s
V	Velocity	m/s
V	Volume	m^3
$V_{j,k}$	Diffusion velocity of species k in direction j	m/s
W	Mean molecular weight	kg/mol
W_k	Molecular weight of species k	kg/mol
X	Dimension factor of the Rosin-Rammler distribution	m
x_f	Distance travelled in the liquid film	m
x_j	j^{th} component of the position	m
X_k	Mole fraction	–
$X_{p,i}$	i^{th} component of the droplet position	m
Y_k	Mass fraction	–
z	Mixture fraction	–

Greek Symbols

α	Angle of the swirl chamber convergent	$^\circ$
α_l	Liquid fraction	$-$
β	Film instability growth rate	s^{-1}
β_j	Temperature exponent of reaction j	$-$
χ	Scalar dissipation rate	s^{-1}
$\Delta h^0_{f,k}$	Formation enthalpy of species k	J/kg
$\Delta m^*_{\mathcal{A}}$	Normalized atomic variations of atom $\mathcal{A}$	$-$
ΔP	Pressure difference between liquid injection and combustion chamber	Pa
δ	Diffusive flame thickness	m
Δ_s	Characteristic radius of the energy deposit	m
Δ_t	Characteristic half-duration of the energy deposit	s
Δ_t	Numerical time-step	s
Δ_x	Numerical space discretization	m
Δ_{ff}	Inter-front length	m
δ_{ij}	Kronecker symbol	$-$
δ_{th}	Thermal flame thickness	m
$\dot{\omega}_k$	Production rate of species k	$kg/m^3/s$
$\dot{\omega}_T$	Heat release rate	$J/m^3/s$
$\dot{\Phi}_p$	Droplet heat flux	J/s
ϵ	Turbulent dissipation rate	m^2/s^3
η_K	Kolmogorov scale	m
γ	Euler–Mascheroni constant	$-$
κ	Flame stretch	s^{-1}
λ	Heat conduction coefficient	$J/m^2/s$
λ	Wave length	m
λ_{opt}	Film instability wavelength	m
μ	Dynamic viscosity	$kg/m/s$
μ_k	Chemical potential of species k	J
ν'_{kj}	Forward stoichiometric coefficient of species k in reaction j	$-$
ν''_{kj}	Backward stoichiometric coefficient of species k in reaction j	$-$
ϕ	Equivalence ratio	$-$
ρ	Gas density	kg/m^3
σ	Liquid surface tension	N/m
σ	Liquid surface tension	N/m
σ_s	Gaussian characteristic size of the energy deposit	m
σ_t	Gaussian characteristic duration of the energy deposit	s

σ_{ij}	Stress tensor	$kg/m/s^2$
τ_c	Characteristic combustion time	s
τ_g	Characteristic convection gaseous time	s
τ_k	Chemical characteristic time of species k	s
τ_{chem}	Characteristic chemical time	s
τ_{cond}	Characteristic conduction time	s
τ_{dis}	Film disintegration characteristic time	s
τ_{evap}	Characteristic evaporation time	s
τ_{ig}	Characteristic auto-ignition time	s
τ_{ij}	Viscosity momentum tensor flux	$kg/m/s^2$
τ_K	Characteristic Kolmogorov turbulent time	s
$\tau_{p,\mathcal{D}}$	Characteristic drag droplet time	s
τ_{turb}	Characteristic turbulent time	s
θ	Half liquid cone angle	$\circ$
ε_i	Amount of energy deposited	$J/m^{(3-n)}$
ε_κ	mass fraction of the component κ in the evaporation flux	$-$
Ξ	Kernel deformation	$-$
ξ	Angle of the swirl chamber slots	$\circ$

Other symbols

$\Gamma(x)$	Standard gamma function
∇	Nabla operator
$\overline{}$	Temporal mean part of the field
$\sim$	Favre filtering
$E(m)$	Complete elliptic integral of the second kind

Superscripts

$'$	Temporal fluctuation part of the field
cond	Relative to conductive fluxes
conv	Relative to convective fluxes
n	Number of space dimension
oxi	Refers to the oxidation processes
pyr	Refers to the pyrolysis processes
sgs	Sub-grid scale term
t	Relative to turbulence
tp	Relative to two-phase flow

Subscripts

0	Refers to the initial position / time at the nozzle exit

∞	Relative to the infinity far field
κ	Refers to the liquid fuel species
θ	Refers to the tangential direction
ζ	Relative to the droplet surface
a	Refers to the air
$adia$	Relative to the adiabatic condition
b	Relative to the burnt gases
$boil$	Relative to the boiling condition
$conv$	Refers to convective effects
ED	Relative to the energy deposit
eq	Relative to the equilibrium
ev	Relative to evaporation
exp	Refers to the experimental measurements
$expo$	Refers to the exponential chemistry integration
ext	Refers to the external liquid film surface
F	Relative to the fuel
f	Relative to the fresh gases
g	Relative to the gas phase
gas	Relative to the gas phase
i	Refers to the initial state
inj	Refers to the liquid injection
int	Refers to the internal liquid film surface
j	Relative to the reaction
k	Relative to the species
ker	Relative to the kernel
l	Relative to the liquid phase
liq	Relative to the liquid phase
$lump$	Refers to the lumping reduction step
num	Refers to the numerical probability density function
$order_j$	Order of reaction j
p	Relative to the droplet
r	Refers to the radial direction component
$reac$	Refers to the reactions
sat	Relative to saturation condition
$spark$	Refers to the spark
$spec$	Refers to the species

st Relative to the stoichiometric proportions

$swirl$ Refers to the injection swirl

t Refers to the tangential direction component

t Relative to turbulence

vol Refers to the volumic probability density function

wb Relative to the wet-bulb condition

x Refers to the axial direction component

Dimensionless numbers

B_M Mass Spalding transfer number

B_T Heat Spalding transfer number

CFL Courant-Friedrichs-Lewy number

Da Damköhler number

FN Flow number

FO Fourier number

K Geometrical parameter

Ka Karlovitz number

Le_k Lewis number of species k

Nu Nusselt number

Oh Ohnesorge Number

Pr Prandtl number

Re Reynolds number

Sc_k Schmidt number of species k

Sh Sherwood number

We Weber number

Acronyms / Abbreviations

pdf Probability density function

ACARE Advisory Council for Aviation Research and Innovation in Europe

APLAREP Augmentation du PLafond d'Allumage - REduction des Particules fines

ARC Analytically Reduced Chemistry

AV Artificial viscosity

BPR ByPass Ratio

CAEP Committee on Aviation Environmental Protection

CFD Computational Fluid Dynamic

CPU Central Process Units

CRZ Corner Recirculation Zones

CSP Computational Singular Perturbation

CTRZ Center Toroidal Recirculation Zone

DCN Derived Centane Number

DIC Direct Interaction Coefficient

DNS Direct Numerical Simulation

DRG Direct Relation Graph

DRGEP Direct Relation Graph with Error Propagation

EE Euler-Euler formalism

EL Euler-Lagrange formalism

F-TACLES Filtered Tabulated Chemistry for Large Eddy Simulation

FAR Fuel-Air Ratio

FAST Secondary break-up model Fast Atomization Stochastic Treatment

FPI Flame Prolongation of Intrinsic Low Dimensional Manifold

HIT Homogeneous Isotropic Turbulence

HPC High Performance Computing

ICAO International Civil Aviation Organisation

IPCC Intergovernmental Panel on Climate Change

IRZ Inner Recirculation Zones

LDA Laser Doppler Anemometry

LDSC Local and Dynamical Sub-Cycling

LES Large Eddy Simulation

LHV Lower Heating Value

LOI Level of Importance

LP Low Pressure

LPLT Low Pressure and Low Temperature conditions

LT Low Temperature

LTC Low Temperature Chemistry

LW Lax-Wendroff numerical scheme

MERCATO Moyen d'Etude et de Recherche en Combustion Aérobie par Techniques Optiques

MIE Minimum Ignition Energy

NRP Nanosecond Repetitively Pulsed

NSCBC Navier-Stokes Characteristic Boundary Condition

NTC Negative Temperature Coefficient

ODE Ordinary Differential Equation

ORZ Outer Recirculation Zone

PBM Particle Bursting Method

PDA Particle Doppler Analyser

PDF Probability Density Function

PEA Pre-Exponential Adjustment

PFA Path Flux Analysis

POLIMI Politecnico di Milano

PTatmo Reference atmospheric pressure and temperature conditions

PVC Precessing Vortex Core

QSS Quasi-Steady-State

RANS Reynolds Average Navier-Stokes

RGE Regeneration after Global Extinction

RMS Root Mean Square

RPKs Revenue Passenger Kilometers

RQL Rich burn - quick Quench - Lean burn

RR Rosin-Rammler distribution

RtoS Reactions to Species analysis tool

SAE Safran Aircraft Engines

SAF Sustainable Aviation Fuels

SHE Safran Helicopter Engines

SMD Sauter Mean Diameter

StoRtoS Species to Reactions to Species analysis tool

StoS Species to Species analysis tool

SWJ SWirled Jet

TI Takeno index

TTGC Two step Taylor-Galerkin 'C' numerical scheme

Introduction

Contents

0.1 Environmental and aeronautical challenges

0.1.1 Global warming and environmental challenges

"It is unequivocal that human influence has warmed the atmosphere, ocean and land. Widespread and rapid changes in the atmosphere, ocean, cryosphere and biosphere have occurred" [IPCC 2021][1].

Stopping the progression of global warming is maybe the biggest challenge of the human civilisation for the current century. As shown in Fig. 0.1.1, the $1.1° C$ temperature increase observed since the pre-industrial period was achieved with an unprecedented rate within the last millennia. Extreme weather events, sea level increase, loss of biodiversity, famines, and population displacements are part of the global warming consequences.

The origin of this global warming has been clearly identified and is linked to the human activities with the emissions of greenhouse gases in the atmosphere. In particular CO_2 emissions due to the combustion of fossil fuels are the main contributors to the global warming [IPCC 2021]. Figure 0.1.2 shows the near-linear relationship between the cumulative CO_2 emissions and the global surface temperature increase. In order to respect the COP21 Paris agreements and limit the global warming to $1.5° C$, only 500 additional Gigatons of CO_2 can be released in the atmosphere (starting from 2020), which corresponds approximately (based on the current worldwide emissions) to 5% reduction of CO_2 emissions each year until reaching 0-net emissions in 2050[2].

In this context, the aeronautical sector has a non-negligible influence on the CO_2 emissions. Based on pre-COVID data from 2018, the civil aviation is responsible for approximately 2.4% of total anthropogenic emissions [IPCC 2022].

[1] The Intergovernmental Panel on Climate Change (IPCC) is the United Nation body for assessing the science related to climate change.

[2] For instance, the reduction of the world economic activity during the COVID pandemic in 2020 led to 5% reduction of CO_2 emissions

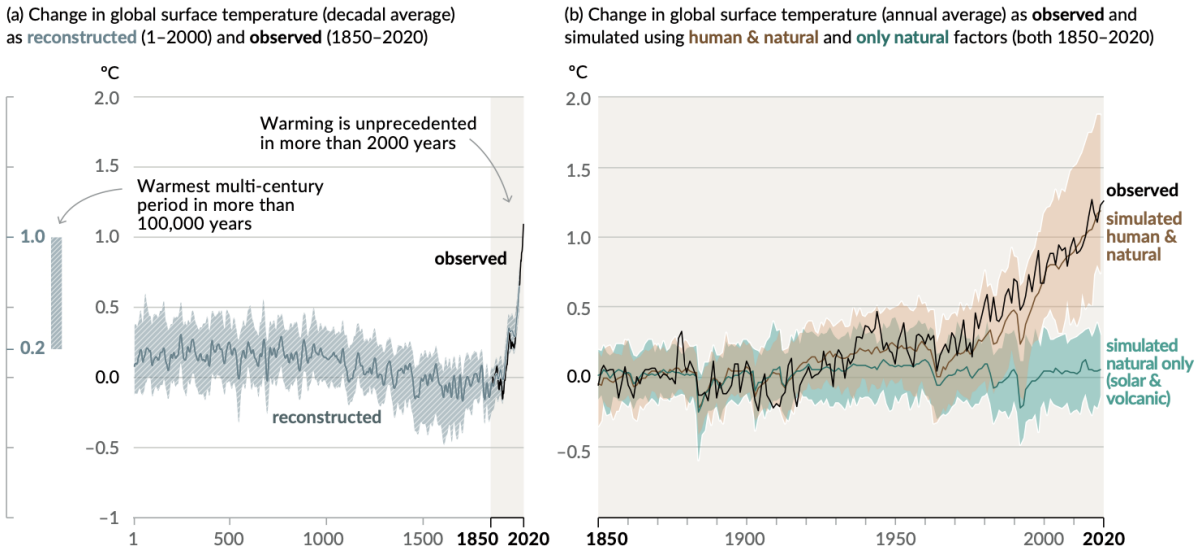

Figure 0.1.1: History of global temperature change and causes of recent warming (extracted from [IPCC 2021]).

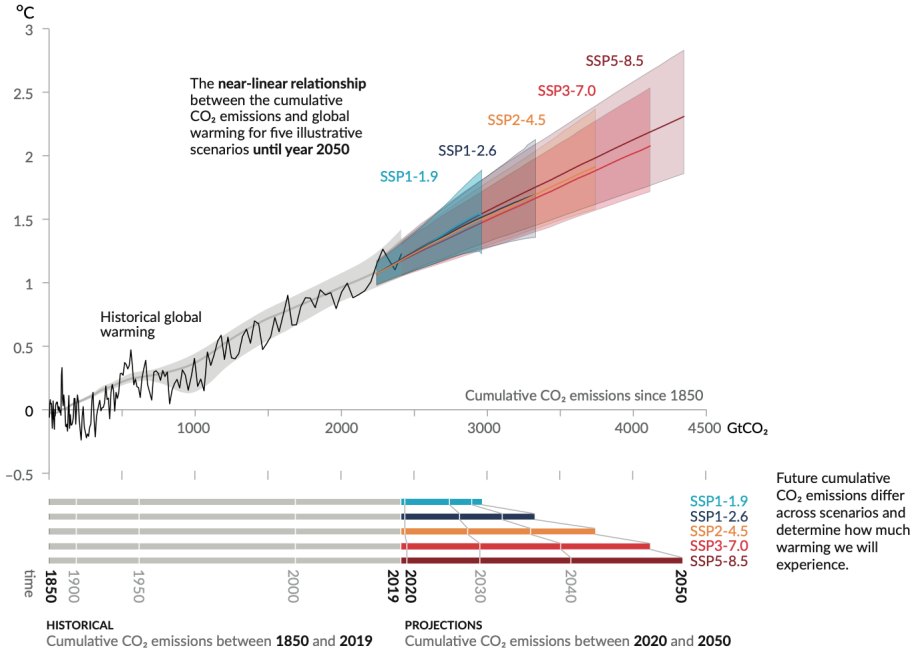

Figure 0.1.2: Near-linear relationship between cumulative CO_2 emissions and the increase in global surface temperature (extracted from [IPCC 2021]).

0.1.2 Aeronautical traffic

The 2022 Environmental Report from the International Civil Aviation Organisation[3] (ICAO) presents past air traffic evolution and forecast until 2050. Figure 0.1.3 clearly shows an increase of the air traffic[4] for all scenarios including the unprecedented COVID crisis.

The increase of the air traffic has large consequences on the CO_2 and other pollutant emissions. Indeed, as shown on Fig. 0.1.4, a typical airplane with 150 passengers consumes 2.7 tons of kerosene for one hour flight and releases 8.5 tons of CO_2 plus other pollutants such as nitrogen oxides (NOx), sulphur dioxide

[3]Agency attached to the United Nations

[4]RPKs (Revenue Passenger Kilometers) per year is an air traffic metric corresponding to the number of passengers multiplied by the travelled distance.

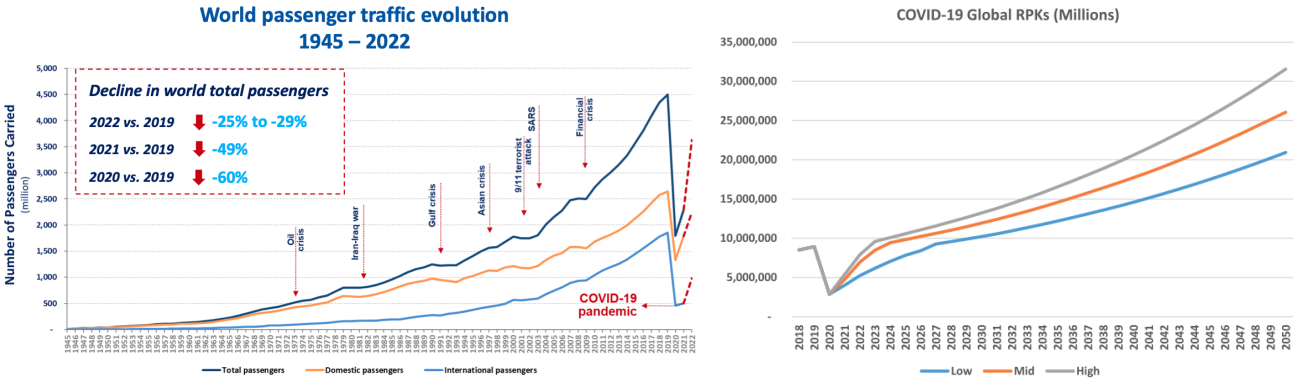

Figure 0.1.3: Left: historical world passenger traffic evolution. Right: air traffic forecast (extracted from [ICAO 2022]).

(SO_2), unburnt compounds and soot. In addition, noise levels must also be considered as pollution, especially around airports for take-off and landings.

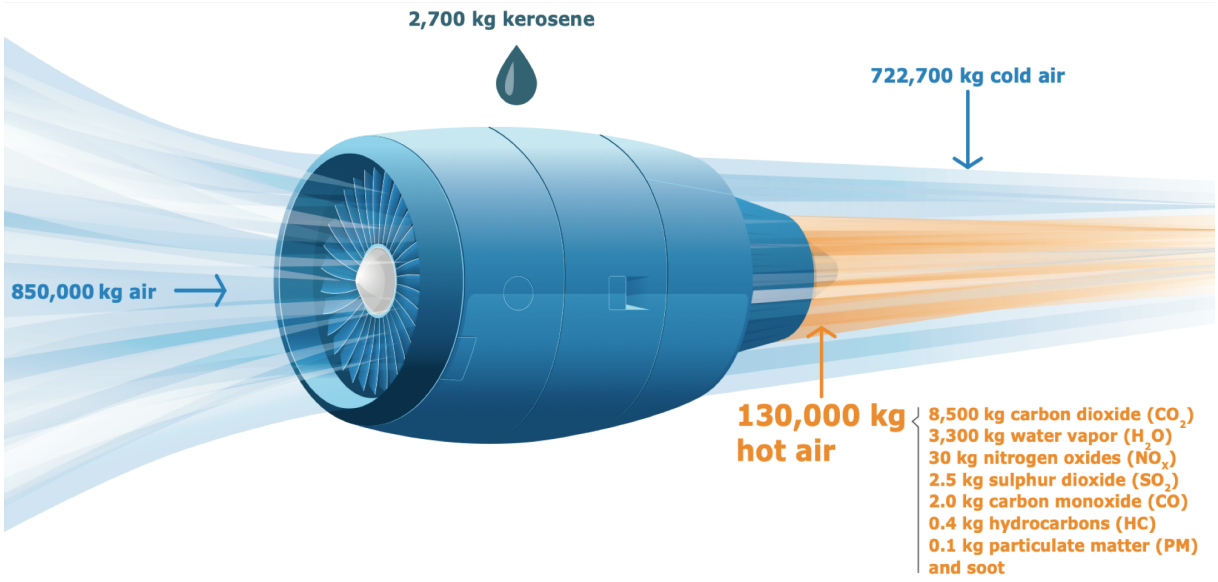

Figure 0.1.4: Emissions from a typical two-engine jet aircraft during 1-hour flight with 150 passengers (adapted from [EEA et al. 2019]).

In order to conciliate the constant air traffic increase with the environmental challenges presented above, very strict regulations are progressively settled on engine certifications. Objectives for 2050 are given by the Committee on Aviation Environmental Protection[5] (CAEP) and the Advisory Council for Aviation Research and Innovation in Europe (ACARE) [ACARE 2022]:

- net-zero CO_2 emissions,
- 90% reduction in NOx emissions relative to 2000,
- 90% reduction in non-volatile particle matter relative to 2000,
- 90% reduction in warming contrail cirrus relative to 2000,
- reduction of the perceived noise emission of flying aircraft by 65% relative to 2000.

To achieve these objectives, the aeronautical engine manufacturers need to continuously improve the engine performances and develop new disruptive concepts.

[5] Member of the ICAO.

0.1.3 Brief description of propulsive system technologies

The aircraft engine is used to create a thrust force enabling the plane to move forward, which then generates lift with the air flow around the wings. Conventional aircraft double-flux engine design is described in Fig. 0.1.5. The air enters the primary flux by the fan and is first compressed with low and high pressure compressor before arriving in the combustion chamber to optimize the thermodynamic cycle. Then, the air and kerosene are mixed and burn in the combustion chamber, which accelerates the flow. The flow kinetic energy is finally transferred to the high and low pressure turbines and the burnt gases are then released through the nozzle. The turbine rotation drives the fan and the compressors, which is actually the main purpose of the primary flux. As shown in Fig. 0.1.4, the total air mass going through the secondary flux is much larger. The major part of the thrust is given by this secondary flux based on the law of action-reaction: the air from the secondary flux is ejected at a much higher velocity than at intake thanks to the energy transfer from the fan.

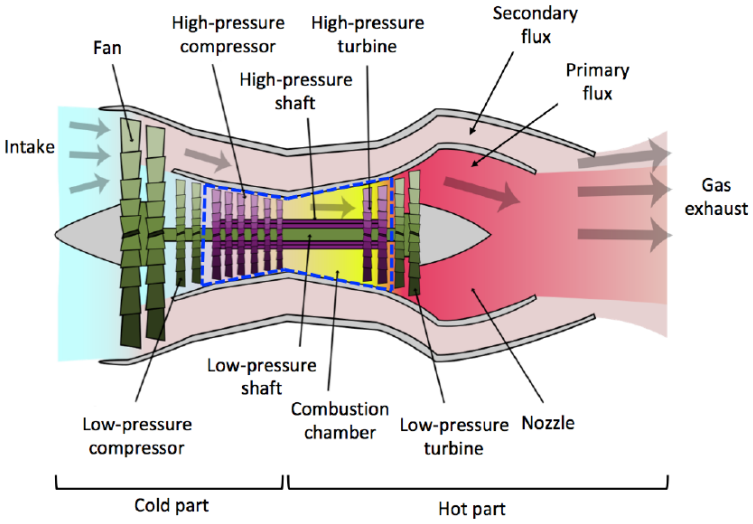

Figure 0.1.5: Sketch of a conventional double-flux gas turbine engine (extracted from [Collin-Bastiani 2019]).

The combustion chamber is the heart of the engine where combustion reactions of fuel with air release a large amount of energy which drives the engine. The design of a combustion chamber is complex because it must enable to stabilise and contain the flame. Indeed, the flow velocity downstream the compressor is around $150\,m.s^{-1}$ which prevents the flame stabilization. A typical design of a combustion chamber is represented in Fig. 0.1.6 (left) which corresponds to an axial cut of one combustion chamber sector with one injection system.. The air coming from the compressor enters the plenum through the diffuser which smoothly reduces the incoming gas velocity. Then, the air is distributed between the injection system (around 30 %) and the cooling of the combustion tube. The injection system is composed of two main parts: the liquid fuel injector and the air swirler. The induced swirled air motion enables the formation of recirculation zones which act as strong mechanisms to stabilize the flame [Syred and Beér 1974]. Furthermore the induced turbulence enables a better mixing of the fuel with air. Such combustion chamber technologies are called Rich burn - quick Quench - Lean burn (RQL) due to 3 main zones. The primary zone (coloured in red) corresponds to an overall rich (fuel excess) zone where the flame is stabilized. Then, the cooling air fluxes enter the chamber through the dilution holes (blue region), quench the flame and mix with the unburnt products. Finally, these products are oxidized in the third (brown) zone under lean conditions (oxidizer excess). Such design enables a complete combustion and a reduction of the NOx emissions limiting the maximum temperature in rich and lean regimes.

The integration of the combustion chamber in the engine is displayed in Fig. 0.1.6 (right). The global structure has an annular shape composed of several connected sectors.

To reach the ACARE and CAEP objectives, several evolutions of propulsive system technology are evaluated:

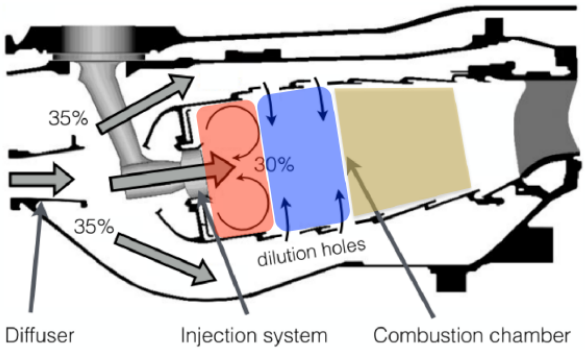

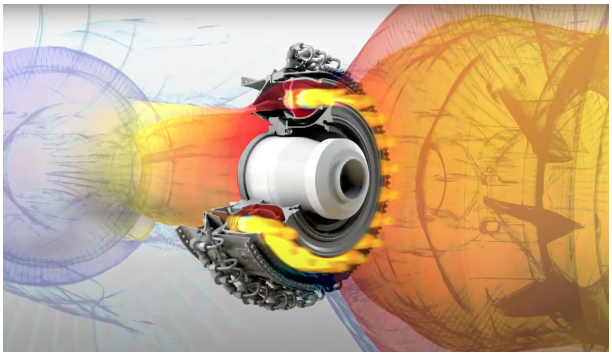

Figure 0.1.6: Left: typical design of a conventional RQL combustion chamber (Extracted from [Collin-Bastiani 2019]). Right: visualization of the annular combustion chamber sectors integration in the engine (Courtesy of Safran Aircraft Engines).

- **Sustainable Fuels:**
  The use of Sustainable Aviation Fuels (SAF) is one of the most promising solutions to reduce the CO_2 emissions. Such fuels are characterised by a near zero CO_2 emissions on the life-cycle assessment. The main families are:

  1) The bio-fuels which are derived from biomass products (plants, agriculture or wastes) and the electrofuels (or e-fuels) which are drop-in replacement fuels that are manufactured using captured carbon dioxide or carbon monoxide together with hydrogen (obtained from sustainable electricity sources). However, the manufacturing of SAF is more costly, the production infrastructure is not ready for the world needs yet and their uses require slight engine design modifications.

  2) The zero-carbon fuels such as hydrogen and ammonia do not involve carbon reactions during the combustion process. They are not categorized as SAF in the literature because they cannot directly replace classical jet fuels. Indeed, they require complete engine design modifications and specific aircraft architectures for storage and safety precautions.

- **Disruptive concepts:**
  The reduction of the fuel consumption can be achieved by an increase of the engine efficiency. For an aeronautical engine, the propulsive efficiency is mainly controlled by the ByPass Ratio (BPR) which is the ratio of the mass flow rates going through the secondary and the primary fluxes. On current engine architectures, the optimal BPR of 10:1 to 15:1 is limited by the nacelle weight and the drag effects. To overcome this issue, the Open Rotor concept illustrated on Fig. 0.1.7 has been developed and may lead to a potential BPR over 30:1 (compared to BPR 11:1 currently used on LEAP engines operated since 2013). The Open Rotor project is expected to be commercialized by 2035 but requires also aircraft modifications because the engine cannot be placed under the wings due to the large blades and passenger safety must be ensured in case of blade rupture.

- **Combustion chamber designs:**
  Finally, the combustion chamber design can also be improved. Especially, low-Nox combustor technologies are currently evaluated. The main strategies rely on leaner combustion regimes with a higher air mass flow rate at the injection and a reduction of the residence time with shorter combustion chambers. However, such modifications induce less stable flames prone to thermo-acoustic instabilities, temperature heterogeneities which can persist until the turbine and difficulties to ignite the chamber.

These propulsive system technology evolutions have large influences on the engine performances. For instance, geometrical or fuel modifications can trigger instabilities, increase the noise levels, increase the pollutant emissions or reduce the engine operability in terms of ignition and lean blow out. Therefore, these processes must be well understood and require dedicated studies. As presented in the following section, this work focuses on ignition phenomena.

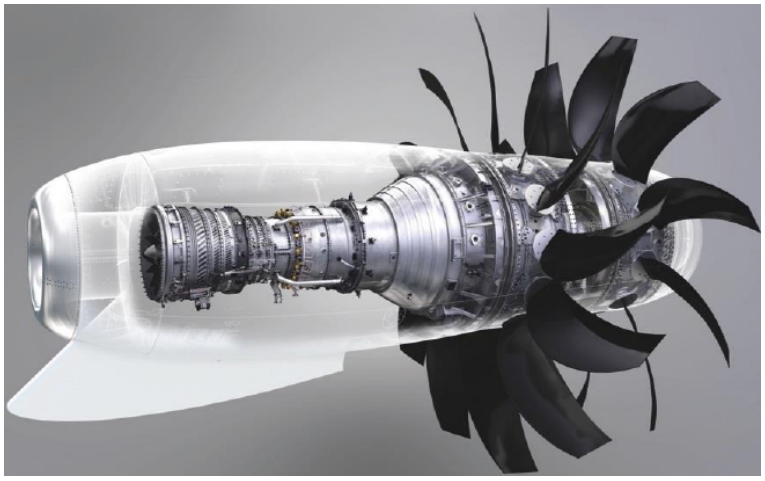

Figure 0.1.7: Illustration of the Open Rotor engine concept (Courtesy of Safran Aircraft Engines).

0.2 Engine ignition under high altitude conditions

0.2.1 Safety constraints

The technological evolutions and combustion chamber design modifications must be certified before the engine is released for sale. Even if the engine resistance is tested against water, ice, sand, or bird ingestion, engine failure may happen and extinction events must be considered. Therefore, the high altitude relight capability is mandatory[6] and is the starting point of this work. The high altitude conditions, also referred as sub-atmospheric conditions, correspond to the temperatures and pressures encountered by the engine during the flight at the altitude of $10\,km$: $P = 0.3\,bar$ and $T = -40°\,C$ $(233\,K)$. These Low Pressure and Low Temperature (LPLT) conditions[7] are detrimental for ignition due to several reasons which are introduced in the following sections.

0.2.2 Ignition of an aeronautical engine

Overview of the ignition process

The ignition phenomenon is complex and includes small time/space-scales with the spark (microsecond to millisecond and millimeters) as well as large scales with the flame propagation to the fuel injectors of the chamber (hundred microseconds and about ten centimeters). Three main phases are identified during ignition [Lefebvre 1998] and are summarized in Fig. 0.2.1:

- **Phase 1: Kernel formation**
  The first phase corresponds to the formation of a hot and large enough flame kernel to enable its propagation and self-development. The formation of the flame kernel is triggered by specific devices that are detailed hereafter.

- **Phase 2: Kernel propagation**
  Once the kernel is formed, it has to propagate towards the closest injector. This phase can be divided in two steps [Mastorakos 2009]: first the expansion of the flame kernel, and then the ignition and stabilisation at the first injector.

- **Phase 3: Light-around**
  The last phase of the engine ignition is the flame propagation towards all injectors/sectors of the combustion chamber.

[6] The high altitude relight is not a legal certification but rather a specification on the engine performances during the design. The main certifications are related to pollutants emissions. The modifications of combustion chambers to reduce such emissions degrade ignition performances which manufacturers want to avoid for safety reasons.

[7] These conditions are more critical than those encountered in the case of engine failure because the engine is still hot and the compressor residual rotation ensures a small gas compression. However, regarding the safety regulations, "he who can do the most can also do the least" is generally a good motto to follow.

In this work, only the initiation (phase 1) and kernel expansion (phase 2, first part) are focused on.

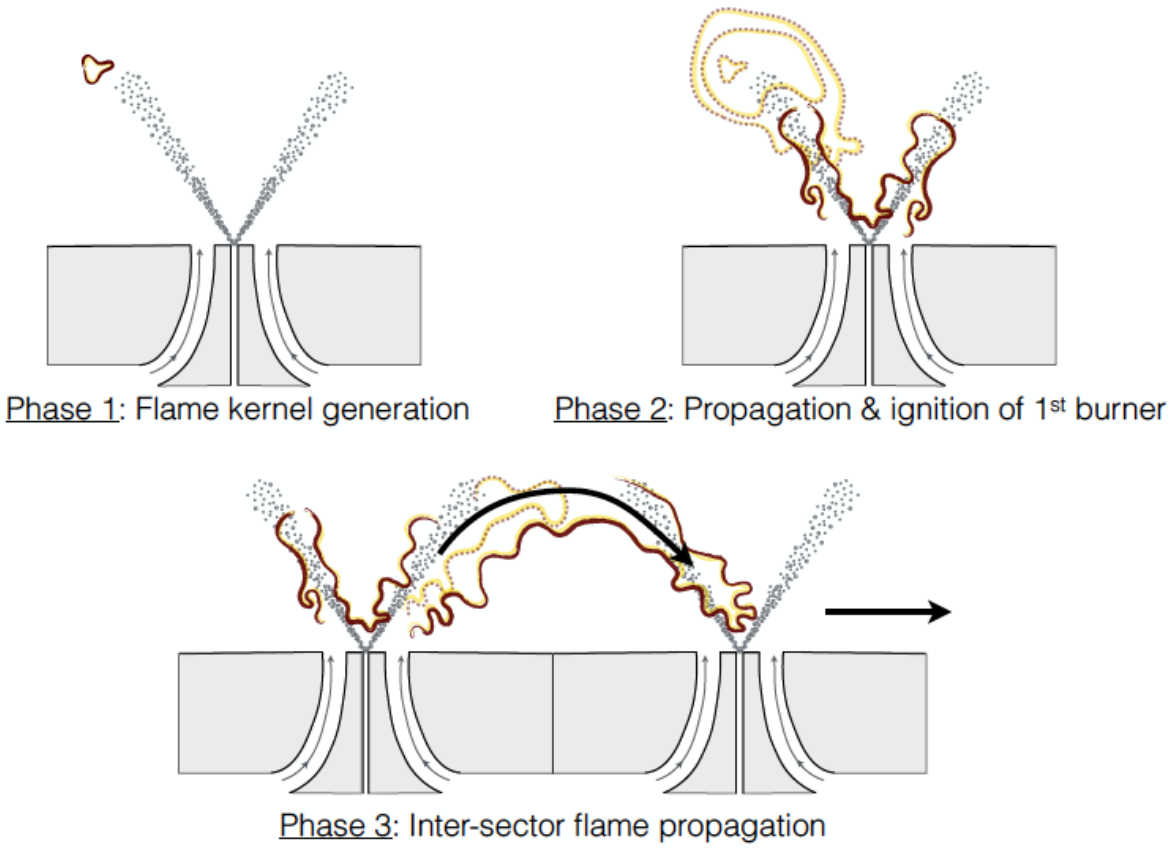

Figure 0.2.1: Illustration of the three ignition phases (extracted from Lefebvre [1998])

Ignition devices

In aeronautical engines, ignition is triggered by an energy deposit in the primary zone of the combustion chamber to ensure a reliable presence of kerosene and a favourable gaseous flow. The location of the energy deposit must be carefully chosen to maximize the ignition success but is also constrained by engineering design considerations. The ignition device enables to convert and transmit an external energy source (electrical or chemical) to the surrounding gas in the combustion chamber. Thus, their designs have an influence on the first ignition phase. The main technologies used in the aeronautical burners are the followings:

- **Spark plug:**
  These ignition systems are generally composed of a first central electrode surrounded by a second one, both being separated by an insulating ceramic [Lefebvre 1998]. The device is then powered with an electrical circuit delivering a high voltage and current. The gas between the electrodes is first ionized, and then an intense electric arc is formed delivering a part of the energy to the gas. It has been estimated that only 10 to 30 % of the energy is transmitted to the gas [Teets and Seel 1988, Maly and Vogel 1978] because of losses in the electric circuit, the creation of a shock wave, radiative phenomena, and thermal conduction in the electrodes.

- **Laser:**
  In this case, the flame kernel results from a laser focus where photons emissions accelerate the electrons at the focal point. Then, the highly energetic electrons cause surrounding molecule ionizations. In the first 10 nanoseconds, the resulting plasma can reach 100000 kelvins and 1000 bar [Phuoc and White 1999]. As a consequence, a strong shock wave is created [Phuoc and White 2002]. This relatively recent technology has been evaluated in experimental studies [Bradley et al.

2004]. Contrary to the spark plug technology, the laser ignition enables to control the position of the energy deposit. However, lasers are very sensible to the high temperatures which limit their uses in combustion chambers.

- **Torch igniter:**
  This ignition device is the combination of a spark plug associated with an additional fuel jet injection [Lefebvre 1998]. It ensures the presence of a flammable mixture at the spark location. This technology is often used in cryogenic rocket engines but can be also found in specific aeronautical engines. The main issue is the large size required by the system integration which prevents its use in most of the aeronautical combustion chambers.

- **Plasma jet igniter:**
  This ignition system is also close to the spark plug. In this case, two successive sparks are used [Mittinti and Dabora 1984]. The first one is localized in a small cavity at the tip of the electrode, and is used to ionize the gas. The second one creates an over-pressure producing a plasma jet. As a consequence, this plasma is convected far from the wall which reduces the thermal losses and promotes the flame kernel development. However, this technology suffers from fast erosion of the spark cavity.

Most of the aeronautical engines use the spark plug technology because this ignition device is relatively small and its integration in the combustion chamber reduces the maintenance cost. However, the deposed energy must be large enough to overcome the thermal losses at the walls. An illustration of this ignition device is presented on Fig. 0.2.2.

Figure 0.2.2: Illustration of an aeronautical spark plug ignition system

Flame kernel formation

The first phase of ignition corresponds to the formation of a flame kernel using the ignition devices presented in the previous section. These devices are used to transfer energy to the gas phase. However, the capability to create a sustainable and stable flame kernel relies on several parameters and has been studied by several authors [Ballal and Lefebvre 1975, Rao and Lefebvre 1976, Ballal and Lefebvre 1977].

The kernel formation can be simplified for theoretical studies of the phenomenon: the ignition of the kernel is triggered if the deposed energy and the heat release rate due to chemical reactions is higher than the losses due to diffusion and turbulence [Zeldovich et al. 1980, Dehaies and Joulin 1984, Champion et al. 1986, Vasquez-Espi and Linan 2002]. Once the flame kernel is formed, the energy from the ignition device is no more considered. Indeed, to be able growth, the kernel heat release rate alone must be higher

than the thermal losses.

Experimental and theoretical researches have introduced the Minimum Ignition Energy (MIE) concept as the minimal energy required to initiate a flame kernel [Joulin 1985, Lewis and von Elbe 1987]. Studies have shown that the MIE primarily depends on the injector geometry [Lewis and von Elbe 1987, Kono et al. 1984, Ko et al. 1991], the gas composition [Lewis and von Elbe 1987, Ziegler et al. 1985] and the turbulent intensity [Beduneau and Kim 2003, Shy et al. 2010, Cardin 2013]. Because of the intrinsic variability of these phenomena, the first phase of ignition is a stochastic process. Thus, the MIE is statistically defined as the energy required to get a 50% probability of ignition success [Kono et al. 1984].

Flame kernel propagation

When the deposited energy is sufficient to trigger the chemical reactions, and the kernel size enables a heat release larger than the thermal losses, the kernel is able to develop, to interact with the turbulent flow, and then to propagate to the injector.

The kernel survival primarily depends on the turbulent intensity and especially the interaction between the flame front and the turbulent motions. Indeed, the turbulence may induce a kernel deformation which eventually leads to its splitting, a wrinkling or a stretch of the flame front, and a global increase of the diffusion phenomena. Hence, the turbulence can promote the kernel development by increasing the flame surface and thus the heat release rate, but it can also cause its extinction in the case of too large turbulent intensities.

The expansion of a spherical kernel in laminar or turbulent flows has been largely studied experimentally because it is a canonical configuration to measure the flame speed [Abdel-Gayed et al. 1984, Weiß et al. 2008, Galmiche et al. 2012]. In the general case, the kernel propagation starts laminar due to the small kernel size and the increased viscosity along with the high temperature deposit. The expansion then switches towards a turbulent flame.

Two-phase ignition

In aeronautical engines the kerosene is injected in the combustion chamber under a liquid form and a resulting droplet mist is observed around the spark device. This liquid phase has a large influence on the ignition phenomenon. Droplet ignition can be found under two main states: isolated droplet ignition or dilute spray ignition depending on the two-phase flow parameters (temperature, droplet density, evaporation rate, etc.). The first ignition mode is characterized by a flame envelop around the droplet [Paulhiac 2015] having a size of the order of the droplet, while the second one corresponds to the presence of a global flame surrounding the spray [Annamalai and Ryan 1992]. Determining the ignition mode is of great importance as it influences the kernel development and the transitory propagation phase, but also the pollutant emissions, the flame stability and structure, and the MIE. However, recent high quality experimental diagnostics and Direct Numerical Simulation (DNS) studies [De Oliveira et al. 2019, Neophytou et al. 2012] have shown that both modes can coexist as highlighted on Fig. 0.2.3 where individual droplets burn while the flame front is propagating in the inter-droplet space.

0.2.3 High altitude conditions

In the previous work of Collin-Bastiani [2019] the ignition phenomena and the flame kernel propagation until the complete combustion chamber ignition have been largely studied. However, the two-phase ignitions have been performed in hot ($T = 416\,K$) and atmospheric ($P = 1\,bar$) conditions favourable for ignition. The influence of the LPLT conditions on the ignition process remains to be evaluated.

The high altitude conditions encountered by the aeronautical engine have a large impact on the combustion processes. Especially, low pressure ($P = 0.3\,bar$) and low temperature ($T = 233K$) conditions have shown to be detrimental for the engine relight. For example Fig. 0.2.4 clearly indicates the reduction of the ignition probability with the reduced pressure. However, experiments under realistic conditions of an altitude relight are scarce [Mosbach et al. 2010, Read 2010, Denton et al. 2018]. Hence, it is necessary to

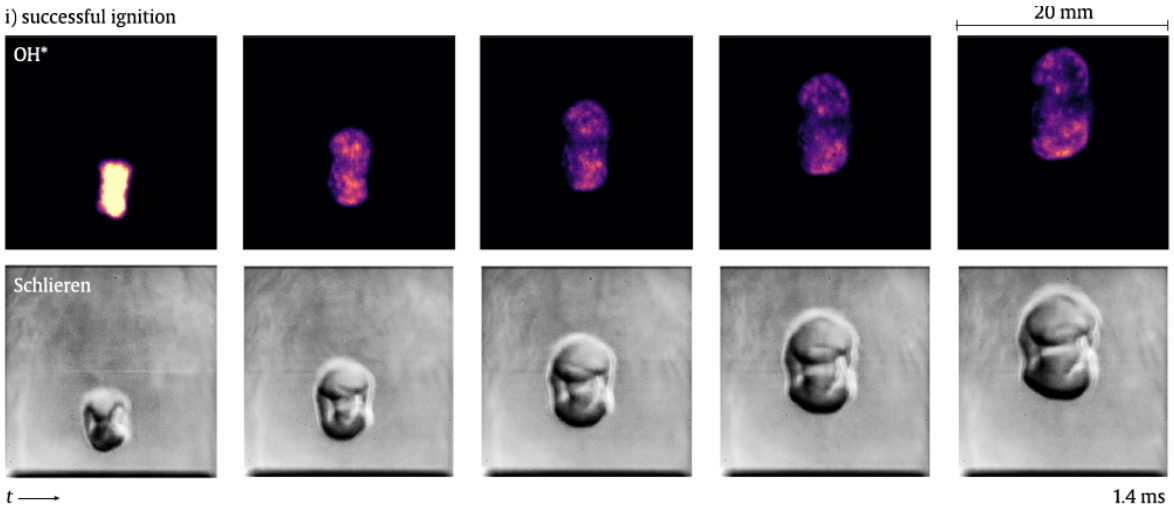

Figure 0.2.3: Droplet mist ignition visualized with OH∗ and Schlieren images (extracted from [De Oliveira et al. 2019]).

better understand the effects of low pressure and low temperature on the combustion behavior.

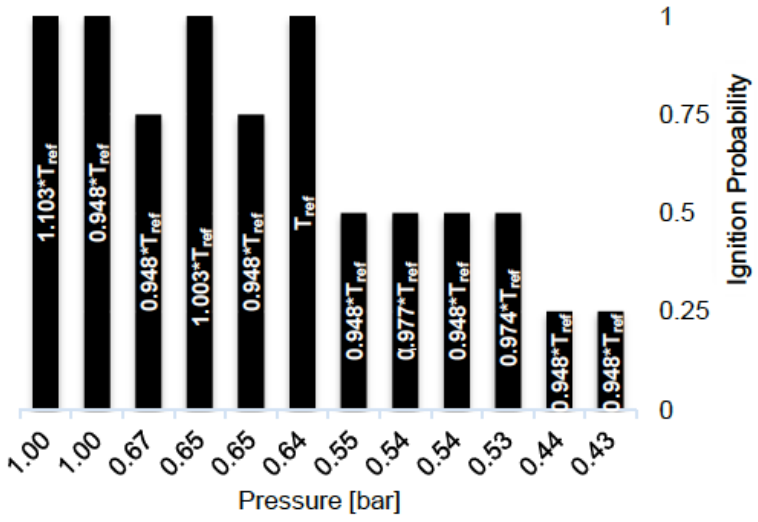

Figure 0.2.4: Ignition probability with respect to pressure (extracted from Martinos et al. [2020])

Influence on the chemical reactions

The influence of high altitude conditions have been observed on chemical reactions via the effect of low pressure. For example, Li et al. [2018] have shown a reduction of the chemical reactivity leading to longer auto-ignition times for low pressure butane mixtures. Another study from Burrell et al. [2018] has shown a modification of the chemical pathways at low pressure modifying the flame speed. However, the effect of low pressure and low temperature is globally poorly described in the literature and the influence of LPLT conditions on the chemical combustion processes deserves further analyses. For instance, one may ask if the chemical mechanisms derived at atmospheric conditions remain valid under LPLT conditions.

Influence on the two-phase related phenomena

The high altitude conditions not only influence the gaseous combustion chemistry but also the two-phase flow processes such as fuel injection and atomization. Indeed, at low pressure, the air density, and thus

the mass flow rate, are reduced which modifies the interaction between the liquid and gaseous phases. One of the main effects is the deterioration of fuel atomization performances. For instance, Fig. 0.2.5 shows that, for low air mass flow rates (similar at low pressure), the characteristic droplet size is increased and the resulting spray is more heterogeneous.

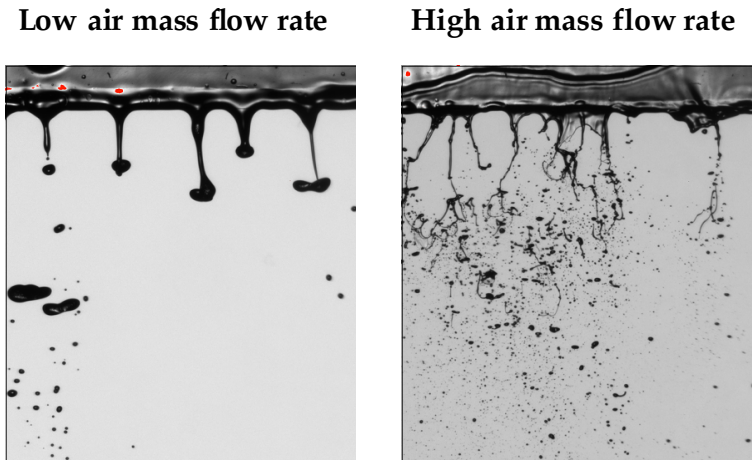

Figure 0.2.5: Photographs illustrating the effect of air mass flow rate in air-blast atomization (adapted from [Chaussonnet et al. 2020]).

Secondly, the evaporation processes are also highly dependent on the pressure and temperature conditions. For example, Fig. 0.2.6 shows the characteristic evaporation delays of isolated droplets at $P = 0.37\,bar$ depending on their sizes and the gaseous temperature. For low temperatures, these evaporation delays are higher than one second which is at least one order magnitude higher than the characteristic residence time of the droplet in the combustion chamber. Therefore, the pre-evaporation phenomenon that may promote the ignition at atmospheric conditions is negligible under LPLT conditions.

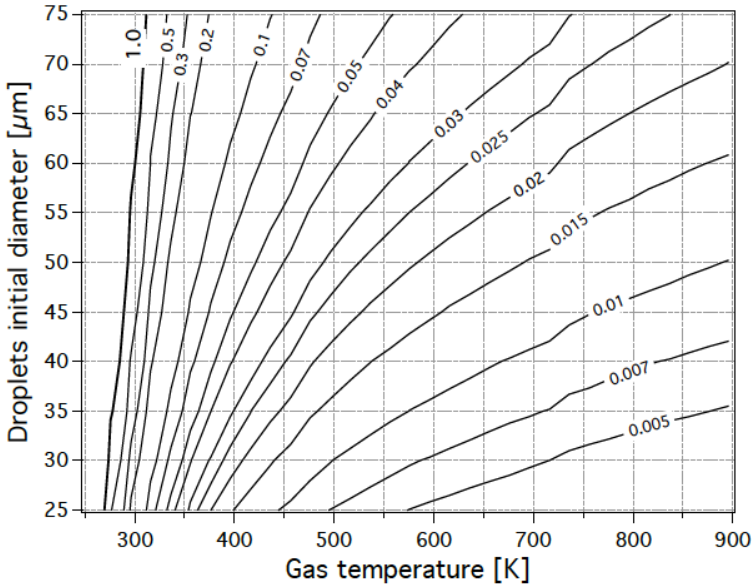

Figure 0.2.6: Evaporation delays [s] of an isolated droplet in quiescent atmosphere at $P = 0.37\,bar$ (extracted from [Esclapez 2014]).

These processes are not directly related to combustion but seem to indicate a large influence of high altitude conditions on the two-phase ignitions in combustion chamber. Hence, dedicated studies are required.

0.3 About numerical simulations

The engine relight certification is necessary at the end of the engine manufacturing, but these relight capabilities must be taken into account from the first conception steps to reduce the costs. Indeed, if the engine re-ignition fails during the test phase, the whole engine architecture may require to be redesigned which generates large extra costs and delays in the engine conception.

Nowadays, the Computational Fluid Dynamic (CFD) is largely used in the industry thanks to the technological and computing progresses but also the constant increase of the computing power. The growing computational resources enable more and more accurate simulations including multi-physics. Numerical simulations are then used in the industry as analysis tools and to reduce the engine experimental tests which are very expensive. However, the numerical simulations cannot replace the engine tests for the certification. The engine relight capabilities must be evaluated in-fine.

In the research framework, numerical simulation is used to solve the theoretical equations of the fluid dynamic on different configurations to better understand physical phenomena. Compared to the experimental measurements the simulation produces results more or less close to the reality depending on the numerical method and physical phenomena taken into account. However, the numerical simulation has several benefits compared to the experiments:

- A complete results overview is accessible whereas experimental measurement tools (sometimes intrusive) are required and provide a limited scope of the physical phenomena.
- Experimental measurements are sometimes not possible in confined regions or with complex geometries.
- The simulation gives access simultaneously to several quantities (temperature, pressure, density, species composition, etc.) and at several positions which is hardly reachable with measurement tools.
- The simulation enables relatively easily to isolate physical phenomena by adding or removing them from the computation. For example, liquid phase, radiation, wall heat transfers, chemical modeling, turbulence, etc.

Both approaches are complementary. Indeed, to get a reliable numerical simulation tool, a development phase from theoretical models and experimental measurements is required to ensure the validity and results representativeness. Beside, the numerical simulations enable to explain and understand the physical phenomena observed experimentally.

Concerning this work, numerical simulation is mainly used to better understand the ignition phenomenon in aeronautical engines and the influences of LPLT conditions. The results should also help to identify the main paths improving the ignition performance for the engine conception.

0.4 Objectives and organisation of the PhD

This PhD has been funded within the APLAREP (Augmentation du PLafond d'Allumage - REduction des Particules fines) project. This project gathers industrial entities such as Safran Aircraft Engines (SAE) and Safran Helicopter Engines (SHE) but also research laboratories as ONERA, CORIA and CERFACS. The general objective of APLAREP is to provide experimental and numerical tools enabling the conception of aeronautical engines with a reduced level of particle matter emissions without compromising, and on the contrary, improving the engine operating. This work is focused on the package A3 which aims to develop numerical methods able to simulate ignition phenomena in aeronautical engines including the effect of the high altitude conditions.

To answer this objective, this PhD manuscript is divided in four main parts:

- **Part I: Theoretical background:**
  This first part introduces the theoretical notions required for the following parts of the manuscript.

Chapter 1 presents the system of equations which is solved and the numerical approaches or modeling used. Chapter 2 focuses on the chemistry related notions. Chapter 3 introduces basic combustion concepts. Finally, chapter 4 is a literature review on ignition phenomena.

- **Part II: Chemical and gaseous aspects:**
  In the second part, the influence of low pressure and low temperature conditions is evaluated on the chemistry and on gaseous ignition configurations. In the first place, the LPLT conditions effect is studied on canonical 0-dimensional and 1-dimensional cases from a macroscopic point of view in chapter 5. Then, in chapter 6, chemical analysis tools are developed to evaluate the LPLT influence on the chemical reactions. After that, an Analytically Reduced Chemistry (ARC) is derived in chapter 7 to reproduce the LPLT effects in 3-dimensional simulation. In order to reduce the computational cost arising from the ARC mechanism and the ignition intrinsic stiffness, new numerical methods are presented in chapter 8 for the integration of the chemistry in explicit solvers. Finally, a DNS of gaseous flame kernel ignitions are performed and analysed in chapter 9.

- **Part III: Two-phase flow aspects:**
  After evaluating the ignition in gaseous configurations, the two-phase flow related phenomena are added to the modeling. The third part is first tackled, in chapter 11, with the effect of LPLT conditions on the fuel injection. A literature review on the spray injection is presented with the influence of high altitude conditions and is followed by a primary atomization modeling strategy. Chapter 12 is dedicated to the evaporation processes. Fuel droplet multi-component evaporations are performed and the LPLT conditions effect is evaluated. Finally, two-phase ignition simulations are computed and analysed in chapter 13. Several cases are evaluated varying the droplet distribution and the pressure/temperature conditions.

- **Part IV: Applications:**
  The last part of this work corresponds to the application of the numerical models developed in the previous chapters. Hence, in chapter 14, the simulation of a realistic two-phase ignition under high altitude conditions is performed in the academical configuration MERCATO from ONERA and compared to the experimental results available.

Part I

Theoretical background

Ignorance more frequently begets confidence than does knowledge:
it is those who know little, not those who know much, who so positively assert that this
or that problem will never be solved by science.
Charles Darwin, 1809-1882

Chapter 1

Conservation equations for the numerical simulation of reacting flows

Contents

This chapter aims at presenting the Navier-Stokes equations and the multi-species formalism used to describe the gaseous turbulent reactive flows (Sec. 1.1). In the second part of this chapter (Sec. 1.2), the numerical concepts required for the simulations are introduced: numerical schemes, used solvers, turbulence modeling with a particular focus on the LES formalism, and boundary conditions. Finally, the liquid phase modeling is presented in Sec. 1.3.

1.1 System equations for gaseous reacting flows

The mathematical description of fluid dynamic started in 1757 with Euler's equations describing inviscid flows. Then, Claude-Louis Navier introduced the viscosity notion in 1822, and finally, George Stokes wrote the complete set of equations describing the viscous fluid dynamic in 1845. These non-linear partial differential equations cannot be solved analytically (except in simplified cases). The Navier-Stokes equations are part of the Millennium Prize Problems: the mathematician who demonstrates the existence and smoothness of solutions to the incompressible form of Navier-Stokes equations will receive a one million dollar prize. In the context of combustion, a multi-species formulation is required with additional conservation equations and the computation of species diffusion.

1.1.1 Navier-Stokes

The Navier-Stokes equations used for compressible flows arise from conservation laws of mass, momentum and energy. They are presented in their conservative form using Einstein summation convention [Kuo 2005, Poinsot and Veynante 2012]:

- **Mass conservation:**

$$\frac{\partial \rho}{\partial t} + \frac{\partial \rho u_j}{\partial x_j} = 0 \tag{1.1}$$

with ρ the density, and u_j the j^{th} velocity component.

- **Momentum conservation:**

$$\frac{\partial \rho u_i}{\partial t} + \frac{\partial \rho u_i u_j}{\partial x_j} = -\frac{\partial P\delta_{ij}}{\partial x_j} + \frac{\partial \tau_{ij}}{\partial x_j} \qquad \text{for } i = 1,3 \tag{1.2}$$

with $P\delta_{ij}$ the pressure tensor flux, and τ_{ij} the viscosity momentum tensor flux. δ_{ij} corresponds to the Kronecker symbol equals to 1 if $i = j$ and 0 otherwise. In the case of Newtonian fluids, the viscosity momentum tensor flux writes:

$$\tau_{ij} = 2\,\mu \left(S_{ij} - \frac{1}{3}\delta_{ij} S_{ll} \right) \tag{1.3}$$

with μ the fluid dynamic viscosity, and S_{ij} the strain rate tensor:

$$S_{ij} = \frac{1}{2}\left(\frac{\partial u_i}{\partial x_j} + \frac{\partial u_j}{\partial x_i} \right) \tag{1.4}$$

$\sigma_{ij} = \tau_{ij} - P\delta_{ij}$ is the stress tensor.

- **Energy conservation:**

$$\frac{\partial \rho E}{\partial t} + \frac{\partial \rho E u_j}{\partial x_j} = -\frac{\partial q_j}{\partial x_j} - \frac{\partial u_i P\delta_{ij}}{\partial x_j} + \frac{\partial u_i \tau_{ij}}{\partial x_j} + \dot{\mathcal{Q}} \tag{1.5}$$

with $E = e_s + 1/2 \times u_j u_j$, the total energy, q_j the j^{th} component of the energy flux, and $\dot{\mathcal{Q}}$ the external energy source term. $e_s = \int_{T_0}^{T} C_v dT - \mathcal{R}T_0/W$ is the sensible energy. The energy flux corresponds to the heat diffusion and writes:

$$q_j = -\lambda \frac{\partial T}{\partial x_j} \tag{1.6}$$

with T the fluid temperature, and λ the heat conduction coefficient.

- **Perfect gas law:**
The Navier-Stokes set of equations requires an additional equation to close the system. In this work, the perfect gas law is used since it is adapted for gaseous flow at sub-critical conditions.

$$P = \rho r T \tag{1.7}$$

with $r = \mathcal{R}/W$. $\mathcal{R} = 8.314\,J.mol^{-1}.K^{-1}$ is the molar perfect gas constant, and W the mean molecular weight.

1.1.2 Multi-species formulation

Species quantities

The combustion phenomenon requires the simulation of several species, and therefore a multi-species formalism. Hence, each species is characterized by the following quantities:

- **Mole fraction:**

$$X_k = \frac{n_k}{n_{tot}} \tag{1.8}$$

with n_k the number of moles of species k and n_{tot} the total number of mole in the mixture.

$$n_{tot} = \sum_{k=1}^{N_{spec}} n_k \tag{1.9}$$

with N_{spec} the number of species. By definition:

$$\sum_{k=1}^{N_{spec}} X_k = 1 \tag{1.10}$$

- **Mass fraction:**

$$Y_k = \frac{m_k}{m_{tot}} \tag{1.11}$$

with m_k the mass of species k and m_{tot} the total mass of the mixture.

$$m_{tot} = \sum_{k=1}^{N_{spec}} m_k \tag{1.12}$$

$$m_k = n_k W_k \tag{1.13}$$

with W_k the molecular weight of species k
By definition:

$$\sum_{k=1}^{N_{spec}} Y_k = 1 \tag{1.14}$$

Furthermore:

$$Y_k = X_k \frac{W_k}{W} \tag{1.15}$$

W the mean molecular weight of the mixture writes:

$$W = \sum_{k=1}^{N_{spec}} X_k W_k = \left(\sum_{k=1}^{N_{spec}} \frac{Y_k}{W_k} \right)^{-1} \tag{1.16}$$

- **Density - Mass concentration:**

$$\rho_k = c_k = \rho Y_k \tag{1.17}$$

$$\rho = \sum_{k=1}^{N_{spec}} \rho_k = \sum_{k=1}^{N_{spec}} \rho Y_k \tag{1.18}$$

with ρ the mixture density.

- **Molar concentration:**

$$[A_k] = \rho \frac{X_k}{W} = \rho \frac{Y_k}{W_k} \tag{1.19}$$

- **Partial pressure:**
In this work, the Perfect gas law is used to link pressure, density and temperature. In the context of multi-species, the pressure of the domain becomes:

$$P = \sum_{k=1}^{N_{spec}} P_k = \sum_{k=1}^{N_{spec}} \rho_k \frac{\mathcal{R}}{W_k} T = \rho \frac{\mathcal{R}}{W} T \tag{1.20}$$

with P_k the partial pressure of species k.

- **Massic heat capacities:**

$$C_p = \sum_{k=1}^{N_{spec}} C_{p,k} Y_k \tag{1.21}$$

with C_p the massic heat capacity of the mixture at constant pressure, and $C_{p,k}$ the massic heat capacity of the species k at constant pressure.

$$C_v = \sum_{k=1}^{N_{spec}} C_{v,k} Y_k \tag{1.22}$$

with C_v the massic heat capacity of the mixture at constant volume, and $C_{v,k}$ the massic heat capacity of the species k at constant volume.
Massic heat capacities are linked by the following relation:

$$C_{v,k} = C_{p,k} - \frac{\mathcal{R}}{W_k} \tag{1.23}$$

- **Massic enthalpy:**

$$h_k = h_{s,k} + \Delta h^0_{f,k} \tag{1.24}$$

with $h_{s,k} = \int_{T_0}^{T} C_{p,k} dT$ the sensible enthalpy of species k, and $\Delta h^0_{f,k}$ its formation enthalpy.

Modification of the system equations

The simulation of several species also requires additional conservation equations (one per species) and new terms in the energy equation to take into account the effect of chemical reactions and species diffusion:

- **Species conservation:**

$$\frac{\partial \rho Y_k}{\partial t} + \frac{\partial \rho (u_j + V_{j,k}) Y_k}{\partial x_j} = \dot{\omega}_k \quad \text{for } k = 1, N_{spec} \tag{1.25}$$

with $\dot{\omega}_k$ the species source terms, its computation is detailed in Chap. 2. $V_{j,k}$ is the j^{th} component of the diffusion velocity of species k and its computation is detailed in Sec. 1.1.3. Based on Eq. (1.18), the mass conservation equation Eq. (1.1) becomes redundant and is not necessarily computed.

- **Energy conservation:**

$$\frac{\partial \rho E}{\partial t} + \frac{\partial \rho E u_j}{\partial x_j} = -\frac{\partial q_j}{\partial x_j} - \frac{\partial u_i P \delta_{ij}}{\partial x_j} + \frac{\partial u_i \tau_{ij}}{\partial x_j} + \dot{\mathcal{Q}} + \dot{\omega}_T \tag{1.26}$$

with the additional term $\dot{\omega}_T$ corresponding to the energy source terms coming from chemical reactions, the expression is detailed in Chap. 2. The energy flux is also modified due to the diffusion of the species:

$$q_j = -\lambda \frac{\partial T}{\partial x_j} + \rho \sum_{k=1}^{N_{spec}} V_{j,k} Y_k h_{s,k} \tag{1.27}$$

In this work, the Dufour effect corresponding to the temperature rise due to species diffusion is neglected because it has a weak influence on the total heat flux [Garcia-Ybarra et al. 1984].
The energy conservation can also be written by conserving the total chemical energy: $e_t = E + \sum_{k=1}^{N_{spec}} \Delta h^0_{f,k} Y_k$. In this case, the energy source term coming from chemical reactions is already taken into account and removed from Eq. (1.26). The energy flux must also be modified replacing, in its expression (Eq. (1.27)), the sensible enthalpy by the species enthalpy (Eq. (1.24)).

1.1.3 Transport modelling

The resolution of the system of equations still requires the computation of unknown quantities such as mixture viscosity, mixture conductivity, and diffusion velocities. These transport properties are often complex and expensive to compute and several strategies can be used in CFD solvers.

Multi-component transport

The exact diffusion velocities $V_{j,k}$ are obtained by solving the following system [Williams 1985]:

$$\frac{\partial X_p}{\partial x_j} = \sum_{k=1}^{N_{spec}} \frac{X_p X_k}{D_{pk}}(V_{j,k} - V_{j,p}) \qquad p = 1, N_{spec}\,;\, j = 1,3 \tag{1.28}$$

with $D_{pk} = D_{kp}$ the binary mass diffusion coefficient of species p into species k which are derived from the kinetic gases theory. The pressure force is neglected because they are only relevant for compressible effect dominated flows, as well as the volumic forces (gravity, electro-magnetism). The Soret effect (diffusion of mass due to temperature gradient) is also neglected in this work because, according to Giovangigli [2015], it is only relevant for light species combustion (H, H_2). The system Eq. (1.28) is a linear system of size N_{spec}^2 to solve for the three directions, at each node, and each iteration. Thus, it is too costly for numerical integration of explicit CFD solvers.

Mixture-averaged transport model

In most numerical codes, the multi-component transport is often replaced by the Hirschfelder and Curtiss approximation [Hirschfelder et al. 1969] which is the best first order approximation of the exact solution of system Eq. (1.28) [Giovangigli 1999]:

$$V_{j,k} = -\frac{1}{X_k} D_k \frac{\partial X_k}{\partial x_j} \tag{1.29}$$

with D_k the diffusion coefficient of species k into the mixture computed from binary coefficients:

$$D_k = \frac{1 - Y_k}{\sum\limits_{p=1, p\neq k}^{N_{spec}} \frac{X_p}{D_{pk}}} \tag{1.30}$$

However, this first order approximation is not conservative, thus a correction velocity V_j^c is added to ensure mass conservation:

$$\sum_{k=1}^{N_{spec}} Y_k \times (V_{j,k} + V_j^c) = 1 \quad \Leftrightarrow \quad V_j^c = \frac{1}{W} \sum_{k=1}^{N_{spec}} W_k D_k \frac{\partial X_k}{x_j} \tag{1.31}$$

Then, the corrected diffusion velocity writes: $V_{j,k}^{corr} = V_{j,k} + V_j^c$. This corrected quantity will be simply labeled $V_{j,k}$ in the following.

The dynamic viscosity of the mixture can be expressed using the Wilke formula [Wilke 1950] modified by Mathur and Saxena [1966]:

$$\mu = \sum_{k=1}^{N_{spec}} \frac{\mu_k X_k}{\sum\limits_{p=1}^{N_{spec}} X_p \Phi_{kp}} \tag{1.32}$$

where

$$\Phi_{kp} = \frac{1}{\sqrt{8}} \left(1 + \frac{W_k}{W_p}\right)^{-\frac{1}{2}} \left[1 + \left(\frac{\mu_k}{\mu_p}\right)^{\frac{1}{2}} \left(\frac{W_k}{W_p}\right)^{-\frac{1}{4}}\right]^2 \tag{1.33}$$

Finally, the mixture thermal conductivity is expressed as mixture-average [Mathur and Saxena 1967, Mathur et al. 1967]:

$$\lambda = \frac{1}{2}\left(\sum_{k=1}^{N_{spec}} X_k\lambda_k + \frac{1}{\sum_{p=1}^{N_{spec}} X_k\lambda_k^{-1}}\right) \tag{1.34}$$

Simplified transport

The computation of diffusion coefficients, viscosity, and thermal conductivity in the mixture-average transport model can still be expensive for a LES solver. In the case of hydrocarbon/air combustion, the viscosity is considered independent from the mixture and close to the one for pure air. Then, it can be expressed either with a Sutherland law:

$$\mu = \alpha_1 \frac{T_{3/2}}{T+\alpha_2}\frac{T_{ref}+\alpha_2}{T_{ref}^{3/2}} \tag{1.35}$$

or with a power law:

$$\mu = \alpha_1 \left(\frac{T}{T_{ref}}\right)^{\beta} \tag{1.36}$$

where α_1, α_2, and β are parameters to calibrate depending on T_{ref}.

Then, several non-dimensional numbers are introduced to compute the diffusion coefficients and the thermal conductivity:

- Schmidt number Sc_k:
  It corresponds to the ratio between momentum diffusivity and species diffusivity:

$$Sc_k = \frac{\mu}{\rho D_k} \tag{1.37}$$

- Prandtl number Pr:
  It corresponds to the ratio between momentum diffusivity and thermal diffusivity:

$$Pr = \frac{\nu}{D_{th}} = \frac{\mu C_p}{\lambda} \tag{1.38}$$

  with $D_{th} = \lambda/(\rho C_p)$ the thermal diffusion coefficient of the mixture.

- Lewis number Le_k:
  It corresponds to the ratio between thermal diffusivity and species diffusivity:

$$Le_k = \frac{\lambda}{\rho C_p D_k} = \frac{Sc_k}{Pr} \tag{1.39}$$

Assuming constant Lewis numbers across a flame [Poinsot and Veynante 2012], the thermal conductivity and diffusion coefficients can simply be computed from viscosity, Prandtl, and Schmidt numbers:

$$\lambda = \frac{\mu c_p}{Pr} \tag{1.40}$$

$$D_k = \frac{\mu}{\rho Sc_k} \tag{1.41}$$

Prandtl and Schmidt numbers are optimized before the computation on a specific range of conditions (equivalence ratio, pressure, fresh gases temperature) to recover macroscopic quantities such as the laminar flame speed.

Then, the Hirschfelder and Curtiss approximation is used to compute the diffusion velocities.

1.2 Numerical simulations

Since there are no general analytical and continuous solutions to the Navier-Stokes equations, these equations need to be discretized using numerical schemes. For this purpose, the computational domain is divided in multiple points (or elementary volumes) separated by a distance Δ_x. The conservation equations are computed at each individual points and the temporal evolution of the system is evaluated at several instant separated by a time-step Δ_t. The numerical schemes and models used during the simulation are integrated to the numerical solver. Starting from an initial state at each point and with boundary conditions, the solver is able to compute the system evolution until the final time.

In this work, two different solvers are mainly used: AVBP [Schönfeld and Rudgyard 1999] and NTMIX [Baum 1994]. The first one is designed for academical and industrial simulations using complex geometries, for example, aeronautical combustion chambers. This solver is co-developed by CERFACS and IFPEN. The second one has been developed for very accurate DNS (see Sec. 1.2.2) computations using simplified geometries, for example, turbulence-combustion interaction. This code is co-developed by CERFACS and University of Melbourne.

1.2.1 Numerical schemes

There are several methods to discretize the Navier-Stokes equations: finite differences, finite volumes, or finite elements which can be associated to an implicit or explicit time integration. These approaches lead to many different numerical schemes that differ by their precision order, stability limits, and diffusive and dispersive properties. The precision order corresponds to the rate at which the numerical error is reduced when the spatial and temporal discretization are reduced. In the case of explicit integration, there is a stability limit which gives a relationship between the temporal and spatial discretizations. It is expressed through a Courant-Friedrichs-Lewy (CFL) number for convection terms Eq. (1.42), and Fourier (FO) numbers for diffusion terms Eq. (1.43). A diffusive (or dissipative) numerical scheme adds extra numerical diffusion to the physical one. It helps to stabilise the computation of strong gradients, however the results are smoothed and less precise. The dispersive error corresponds to a wrong computation of wave speeds leading to the wiggles phenomenon (numerical propagation of oscillations in the solution) that may crash the computation. In the simple example of a pure sinusoidal wave propagation, a diffusive scheme will damp the wave amplitude, and a dispersive scheme will propagate the wave at the wrong speed.

$$CFL = \frac{(|u| + c)\Delta_t}{\Delta_x} \tag{1.42}$$

with $c = \sqrt{C_p/C_v \times P/\rho}$ the sound speed required in compressible solvers.

$$FO_{qdm} = \frac{\nu\Delta_t}{{\Delta_x}^2} \quad ; \quad FO_{th} = \frac{D_{th}\Delta_t}{{\Delta_x}^2} \quad ; \quad FO_{spec} = \frac{D_k\Delta_t}{{\Delta_x}^2} \tag{1.43}$$

Numerical schemes in AVBP

The AVBP solver is based on a Cell-Vertex formulation [Rudgyard 1993]: the variables are stored at the mesh nodes, but the numerical integration and the fluxes computations are performed at the center of the cells. The residual are then re-distributed to the nodes to update the solution. This operation is called "gather-scatter". AVBP uses non-structured grids with tetrahedral or hexahedral cell shapes.

A complete review of numerical schemes implemented in AVBP is available in the PhD thesis of Lamarque [2007]. The two main schemes used in this work are:

- **Lax-Wendroff (LW)**:
  This scheme is a central finite volume developed by Lax and Wendroff [1960] and uses an explicit time integration with a one step Runge-Kutta. It is a time and space second order precision scheme. The main advantage is that it includes a diffusive term that increases the robustness. Therefore, this scheme is often used for initialisation of non-reactive simulations and to reach faster convergence in stabilized flame computations.

- **Two step Taylor-Galerkin 'C' (TTGC)**:
  The Cell-Vertex formulation being close to finite element methods with residuals pondering, Colin and Rudgyard [2000] developed a finite element scheme of the continuous Taylor-Galerkin family [Donea and Huerta 2003]. This scheme is a time and space third order, and can reach a fourth order precision on cartesian regular meshes [Moureau et al. 2005]. The TTGC scheme presents very good dispersion and dissipation properties which made it a good candidate for Large Eddy Simulation (LES, see Sec. 1.2.2) computations. However, this numerical scheme is less robust than LW and the CPU cost[1] can be multiplied by a factor 2.5.

Due to their centered construction, these schemes have low dissipation properties. Then, the AVBP schemes (especially TTGC) are more prone to dispersion errors that appear at strong gradients. Hence, to limit the apparition of spurious modes or wiggles, artificial viscosity (AV) is often added where it is needed. The AV model [Colin 2000] is based on the combination of a choc capture term (second order AV), and a backward dissipation term (fourth order AV or hyper-viscosity). The second order AV acts like the physical viscosity by adding an artificial viscosity which smoothens the local strong gradients ($\nu_{tot} = \nu + \nu_{artif}$). The fourth order AV, is used to control high frequency wiggles. When the AV is activated, a sensor based on the flow is first computed, then, the AV is locally applied depending on the value of this sensor.

For both schemes in AVBP, the stability criteria applied in this work are: $CFL = 0.7$ and $FO = 0.1$.

Numerical schemes in NTMIX

The NTMIX solver [Baum 1994] uses a vertex formulation where conservative variables and fluxes are saved and computed at nodes. The energy equation is based on the conservation of the total chemical energy e_t (while the total non chemical E is used in AVBP). Contrarily to AVBP that is able to manage complex geometries, only rectangular domains can be computed with NTMIX. It enables to use simpler Cartesian structured grids without connectivity tables which provides better performances and allows the implementation of high order schemes with large stencils.

The numerical schemes used in NTMIX are the centered finite differences of order 6 or 8, and a three step Runge-Kutta for the explicit temporal integration. The finite differences write under the general form:

$$\frac{\partial f_j}{\partial x} = \frac{1}{\Delta_x} \sum_{l=-N}^{N} \alpha_l \times f_{j+l} \tag{1.44}$$

$$\frac{\partial^2 f_j}{\partial x^2} = \frac{1}{{\Delta_x}^2} \sum_{l=-N}^{N} \beta_l \times f_{j+l} \tag{1.45}$$

with f_j the variable to derive at the node j, N the scheme stencil, α_l and β_l the pondering coefficients which can be found in the work of Fornberg [1988]. In the case of centered finite differences, the scheme order is $2N$.

Using wave number analyses, one can show that the centered finite difference scheme is perfectly not dissipative but has dispersion errors [Pestre 2018]. Fig. 1.2.1 shows the evolution of the numerical wave number k_{num} (left) and the associated error depending on the resolution p (right) for the first order derivative (Eq. (1.44)) and with both schemes. The right picture clearly shows that for the same number of points per wavelength, the eight order scheme provides less errors. Thus, this scheme is able to better capture high frequency phenomena. However, it requires a larger stencil, and therefore, the CPU-cost increases.

$$k\Delta_x = \frac{2\pi}{\lambda}\Delta_x = \frac{2\pi}{p} \tag{1.46}$$

with λ the wavelength and p the number of points used to discretize this wavelength.

[1] The CPU cost is the time required by the computation multiplied by the number of CPU (Central Process Units) used. This quantity is often expressed in CPU-hours (hCPU). It corresponds to the time in hours needed to perform the simulation using only one core, and may vary depending on the CPU performances.

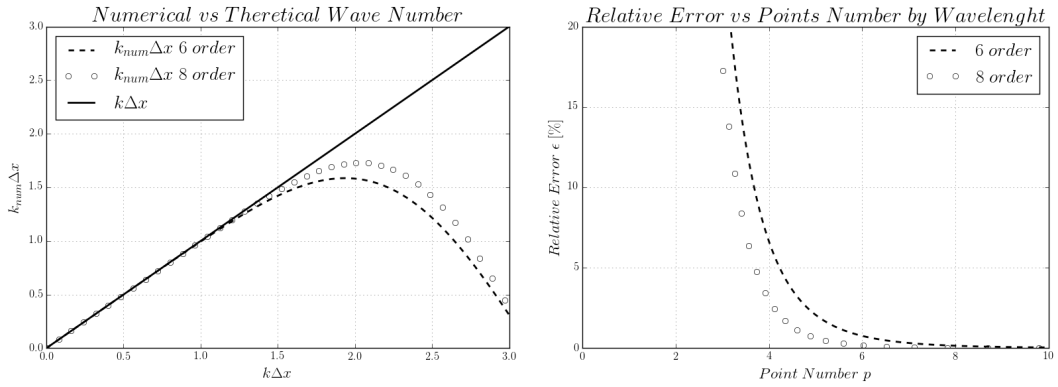

Figure 1.2.1: Wave number analysis of centered finite difference schemes of order 6 and 8

Because of the low dissipation property and high order schemes, NTMIX is a very accurate solver. However, the dispersive properties of its numerical schemes make it very unstable, wiggles appear and amplify as soon as the gradients are not well discretized. To avoid those phenomena, a high frequency filter of order 6 to 10 [Kennedy and Carpenter 1997] can be applied. This filter is able to damp only the high frequency oscillations that are not resolved by the numerical scheme. However, it increases the CPU-cost of the computation.

For both schemes in NTMIX, the stability criteria applied in this work are: $CFL = 0.5$ and $FO = 0.5$.

1.2.2 Turbulence modelling

Fundamental notions of turbulence

The transition between laminar and turbulent flow is characterized by the Reynolds number which compares the inertia to the viscous forces:

$$Re = \frac{\rho u L}{\mu} \tag{1.47}$$

with L a characteristic length of the problem studied and u the velocity magnitude.

In turbulent conditions, the flow can be divided into a mean part and a fluctuating part:

$$u = \overline{u} + u' \tag{1.48}$$

The turbulence is characterized by the turbulent Reynolds number:

$$Re_t = \frac{u'\, L_t\, \rho}{\mu} = \frac{u'\, L_t}{\nu} \tag{1.49}$$

where L_t is the integral turbulent scale which is derived from the mean correlation length L^l_{ik} in the direction l and between the velocity components i and k: $L_t = 2 \times L^i_{ii}$.

The turbulent kinetic energy E_{turb} and the dissipation rate ϵ write for a Homogeneous Isotropic Turbulence (HIT):

$$E_{turb} = \frac{1}{2} u'_i u'_i = n \frac{u'^2}{2} \tag{1.50}$$

with $n = 3$ the dimension of the flow,

$$\epsilon = 2\nu S_{ij} S_{ij} \approx -\frac{dE_{turb}}{dt} \approx \frac{u'^2(r)}{r/u'(r)} \approx \frac{u'^3}{L_t} \tag{1.51}$$

The Root Mean Square (RMS) of velocity fluctuations is also often used to characterise the level of turbulence:

$$u'_{RMS} = \sqrt{\overline{u'^2}} = \sqrt{\overline{u^2} - \overline{u}^2} \tag{1.52}$$

When the Reynolds number is high, the inertial forces dominate and the flow is characterized by vortexes of multiple sizes and intensities which cause spatial and temporal fluctuations of the flow velocity field. These vortexes (or eddies) strongly interact through a phenomenon called the Kolmogorov cascade (or energy cascade) where they break into smaller structures. As consequence, the energy is transmitted from the largest scales towards the smallest ones. Moreover, the variation of the turbulent kinetic energy corresponds to the dissipation rate at the small scales:

$$\overline{\epsilon} \approx -\frac{d\overline{E_{turb}}}{dt} \tag{1.53}$$

Fig. 1.2.2 shows a characteristic energy spectrum for an homogeneous isotropic turbulent flow (HIT). This spectrum can be divided in three parts from the largest scale to the smallest [Pope 2000]:

- **Integral zone:**
  This zone is centered on the wave number k_t corresponding to the integral scale L_t. This zone contains the largest and most energetic eddies. It is where the turbulent energy is produced. The characteristic size of the eddies is of the same order of magnitude as the geometry. These scales are mainly controlled by inertial effects and not affected by the viscosity.

- **Inertial zone:**
  In this zone, the eddies interact, become unstable, and break up via the energy cascade phenomenon. There is no dissipation but an energy transfer from the integral zone to the dissipation zone. This transfer is constant and follows a $k^{-5/3}$ law in the case of a HIT [Kolmogorov 1941].

- **Dissipation zone:**
  This zone corresponds to the Kolmogorov scale η_K where the viscous forces dominate the inertial ones. Then, the turbulent energy is dissipated into heat by viscous friction. The Kolmogorov scale and the velocity fluctuation associated (u'_K) can be estimated in the case of a HIT by [Tennekes and Lumley 1973]:

  $$\eta_K = L_t \times {Re_t}^{-\frac{3}{4}} = \left(\frac{\nu^3}{\epsilon}\right)^{1/4} \quad \text{and} \quad u'_K = (\nu\epsilon)^{1/4} \tag{1.54}$$

  Hence, this length decreases when the velocity fluctuation and the mixture density increase. On the contrary, the Kolmogorov scale rises with an increase of the viscosity and also the integral length scale to a lesser extent.

Several turbulent times-scales can be defined. The first one is based on the dissipation rate and the turbulent kinetic energy, and corresponds to the large scales:

$$\tau_{eps} = \frac{E_{turb}}{\epsilon} = \frac{L_t}{u'} \tag{1.55}$$

For HIT however, the direct use of the auto-correlation length is more accurate:

$$\tau_{turb} = \frac{L^i_{ii}}{u'} = \frac{L_t}{2u'} = \frac{\tau_{eps}}{2} \tag{1.56}$$

A characteristic time can be also defined for the Kolmogorov scale:

$$\tau_K = \sqrt{\frac{\nu}{\epsilon}} = \frac{\eta_K}{u'_K} \tag{1.57}$$

Turbulence has a great importance in the flow structure and for the physical behaviors. Indeed, it improves the mass, momentum, and energy transfers through convective motions. Hence, it has a large influence on the combustion processes.

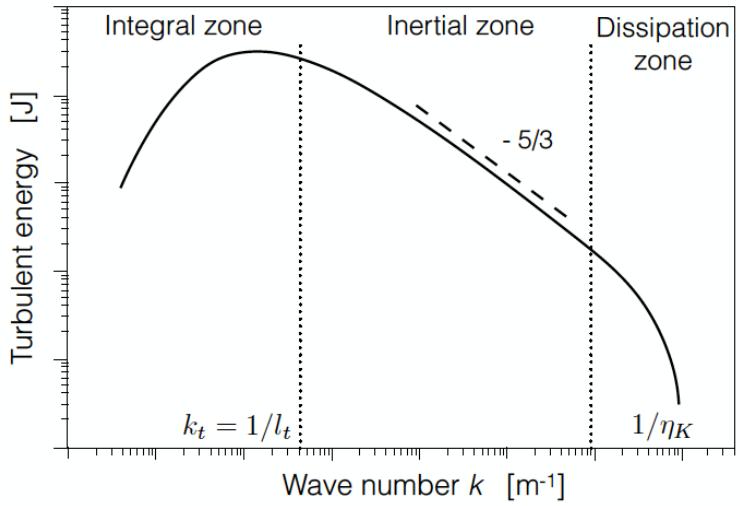

Figure 1.2.2: Energy spectrum in an homogeneous isotropic turbulent flow (HIT) (extracted from [Richardson 1922])

Numerical approaches

The resolution of Navier-Stokes equations and species conservation equations in turbulent flows is complex and remains today a challenge. Indeed, between the largest and most energetic eddies (L_t), and the smallest ones (η_K), there may be several order of magnitude depending on the Reynolds flow number [Kolmogorov 1941]:

$$\frac{L_t}{\eta_K} = Re^{3/4} \tag{1.58}$$

Considering a discretization of the order $\Delta_x = \eta_K$ to compute all the turbulent structures, the Eq. (1.59) gives an estimation of the number of points required in the numerical simulation:

$$N_{pts} = (Re^{3/4})^D \tag{1.59}$$

where D is the dimension of the simulation. In the case of an aeronautical engine, the Reynolds number ranges from one hundred thousand to one million. Thus, the number of points required range from one hundred billion to thirty thousand billion which largely exceeds the available numerical resources[2].

There are three methods to solve the Navier-Stokes equations in the context of turbulent flows. These approaches are illustrated on Fig. 1.2.3 and vary depending on their modelling of the turbulent spectrum:

- **Reynolds Average Navier-Stokes (RANS):**
  In the RANS formalism, only the mean temporal quantities are solved. The RANS equations are obtained by applying a Favre averaging (detailed in Sec. 1.2.3) on the Navier-Stokes equations. In this process, new terms appear and have to be modeled to ensure equations closure. These models account for the effect of the whole turbulent spectrum on the mean fields. Even though this method has been the first to be used and is still used because of its reasonable CPU-cost, it lacks universality and representability because the largest turbulent structures mainly rely on geometrical effects and cannot be modeled in the same way as the smallest ones.
  In this work, the RANS formalism is not used, because it is not adapted to the study of unsteady configurations such as ignition.

- **Large Eddy Simulation (LES):**
  This method introduces a separation between the large and the small scales of the turbulence. Since the first ones are supposed to rely on the geometry, they are computed, whereas the second ones are modeled. This modeling requires less assumptions than the RANS one because the small turbulent eddies have similar and universal shape and behavior (except near boundary conditions). The

[2]Nowadays, the largest numerical simulations reaches one billion points, but the majority of combustion chamber simulations lie between one to one hundred million points

LES equations are obtained applying a spatial filter on the Navier-Stokes equations. This method enables to study unsteady effects which made it a good candidate for the numerical combustion [Esclapez 2015, Collin-Bastiani 2019].
In this work, the LES formalism is used for the simulations of combustion chamber in Chap. 14 with the AVBP solver. More details on the LES implementation in AVBP are given in Sec. 1.2.3.

- **Direct Numerical Simulation (DNS):**
The DNS consists in solving directly the Navier-Stokes equations including the whole turbulent spectrum. Thus, no additional models are used. In this sense, the DNS is the best approach in terms of result accuracy. However, as explained above, this method requires large CPU resources. Today, using DNS on complete and realistic engine configurations is not affordable, but some academical configurations at moderate Reynolds number can be computed with this approach [Chen et al. 2009, Moureau et al. 2011b]. Furthermore, the DNS formalism has been used to analyse and better understand the combustion-turbulence interaction [Colin et al. 2000], which enables to develop new models for LES and RANS computations.
In this work, the DNS approach is used for the simulations of kernel ignition in turbulent flows in Chap. 9 with the NTMIX solver.

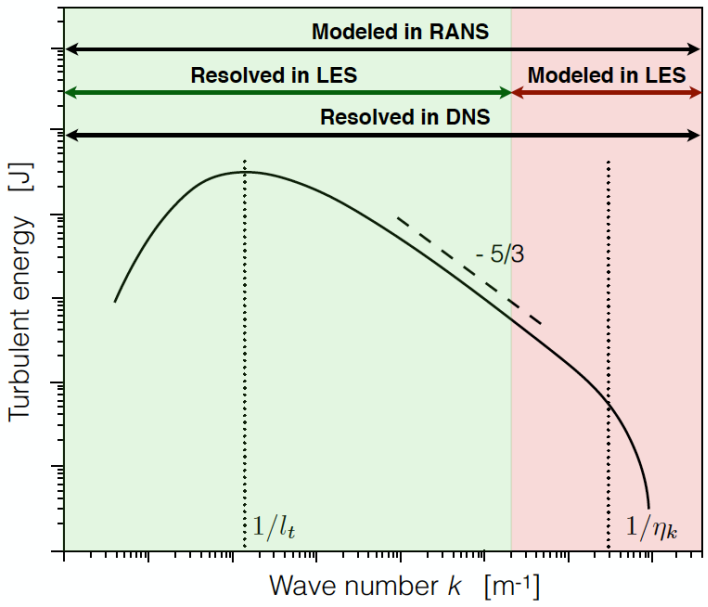

Figure 1.2.3: Numerical approaches for turbulence modelling: DNS, LES, RANS (extracted from [Esclapez 2015])

1.2.3 Large Eddy Simulations

In the LES formalism, the filtered quantities are obtained by convolution of a filter $\mathcal{G}_\Delta$:

$$\overline{f}(\vec{x},t) = \int f(\vec{\xi},t)\mathcal{G}_\Delta(\vec{x}-\vec{\xi})d\xi \tag{1.60}$$

Using directly this expression in the compressible conservation equations leads to additional source terms due to the correlation with density [Poinsot and Veynante 2012]. To avoid this issue, the Favre filtering is often used [Favre 1992]:

$$\widetilde{f}\overline{\rho} = \overline{\rho f} = \int \rho f(\vec{\xi},t)\mathcal{G}_\Delta(\vec{x}-\vec{\xi})d\xi \tag{1.61}$$

There are two families of LES depending on the filtering method. With the explicit LES, the filter is directly applied on the Navier-Stokes equations which are then numerically solved. The second method is called implicit LES and consists in using the mesh as a filter. An under-resolved mesh corresponds to a filter with a size equal to the non resolved scales ($\Delta \approx \Delta x$). In this work, only the explicit LES will be used, modified equations are presented below.

Filtered equations

Applying the filtering procedure Eq. (1.61) on the conservation equations (Eq. (1.1) (1.2), (1.25), and (1.26)) the following filtered equations are obtained[3]:

- **Mass conservation:**

$$\frac{\partial \overline{\rho}}{\partial t} + \frac{\partial \overline{\rho}\widetilde{u_j}}{\partial x_j} = 0 \tag{1.62}$$

- **Momentum conservation:**

$$\frac{\partial \overline{\rho}\widetilde{u_i}}{\partial t} + \frac{\partial \overline{\rho}\widetilde{u_i}\widetilde{u_j}}{\partial x_j} = -\frac{\partial \overline{P\delta_{ij}}}{\partial x_j} + \frac{\partial}{\partial x_j}\left(\overline{\tau_{ij}} + \overline{\tau_{ij}^{sgs}}\right) \quad \text{for} \quad i = 1,3 \tag{1.63}$$

- **Energy conservation:**

$$\frac{\partial \overline{\rho}\widetilde{E}}{\partial t} + \frac{\partial \overline{\rho}\widetilde{E}\widetilde{u_j}}{\partial x_j} = -\frac{\partial}{\partial x_j}\left(\overline{q_j} + \overline{q_j^{sgs}}\right) - \frac{\partial \overline{u_i P\delta_{ij}}}{\partial x_j} + \frac{\partial \overline{u_i \tau_{ij}}}{\partial x_j} + \overline{\dot{\omega}_T} + \overline{\dot{\mathcal{Q}}} \tag{1.64}$$

- **Species conservation:**

$$\frac{\partial \overline{\rho}\widetilde{Y_k}}{\partial t} + \frac{\partial \overline{\rho}\widetilde{Y_k}\widetilde{u_j}}{\partial x_j} = -\frac{\partial}{\partial x_j}\left(\overline{J_{j,k}} + \overline{J_{j,k}^{sgs}}\right) + \overline{\dot{\omega}_k} \quad \text{for} \quad k = 1, N_{spec} \tag{1.65}$$

Viscous fluxes

The previous set of equations Eq. (1.62) - (1.65) shows on the right hand side filtered fluxes that are computed as follow:

- **Filtered viscosity momentum flux tensor:**

$$\overline{\tau_{ij}} = \overline{2\mu\left(S_{ij} - \frac{1}{3}\delta_{ij}S_{kk}\right)} \approx 2\overline{\mu}\left(\widetilde{S_{ij}} - \frac{1}{3}\delta_{ij}\widetilde{S_{kk}}\right) \tag{1.66}$$

with

$$\widetilde{S_{ij}} = \frac{1}{2}\left(\frac{\partial \widetilde{u_j}}{\partial x_i} + \frac{\partial \widetilde{u_i}}{\partial x_j}\right) \quad \text{and} \quad \overline{\mu} \approx \mu(\widetilde{T}) \tag{1.67}$$

- **Filtered diffusive species flux vector:**

$$\overline{J_{j,k}} = -\overline{\rho\left(D_k \frac{W_k}{W}\frac{\partial X_k}{\partial x_j} - Y_k V_j^c\right)} \approx -\overline{\rho}\left(\overline{D_k}\frac{W_k}{\overline{W}}\frac{\partial \widetilde{X_k}}{\partial x_j} - \widetilde{Y_k}\widetilde{V_j^c}\right) \tag{1.68}$$

with

$$\widetilde{V_j^c} = \sum_{k=1}^{N_{spec}} \overline{D_k}\frac{W_k}{\overline{W}}\frac{\partial \widetilde{X_k}}{\partial x_j} \quad \text{and} \quad \overline{D_k} \approx \frac{\overline{\mu}}{\overline{\rho} Sc_k} \tag{1.69}$$

- **Filtered heat flux vector:**

$$\overline{q_j} = -\overline{\lambda\frac{\partial T}{\partial x_j}} + \overline{\rho\sum_{k=1}^{N_{spec}} V_{j,k}Y_k h_{s,k}} \approx -\overline{\lambda}\frac{\partial \widetilde{T}}{\partial x_j} + \sum_{k=1}^{N_{spec}} \overline{J_{j,k}}\widetilde{h_{s,k}} \tag{1.70}$$

with

$$\overline{\lambda} \approx \frac{\overline{\mu}\overline{C_p(\widetilde{T})}}{Pr} \tag{1.71}$$

[3] High order cross terms are neglected

Sub-grid scale closure

The previous set of equations Eq. (1.62) - (1.65) also shows unresolved sub-grid scale (SGS) terms due to the smallest turbulent fluctuations. Since turbulence has dissipative properties, these terms are modelled by a diffusion effect. Hence, the SGS terms are computed as follow:

- **SGS Reynolds stress tensor:**

$$\overline{\tau_{ij}^{sgs}} = -\overline{\rho}(\widetilde{u_i u_j} - \widetilde{u}_i\widetilde{u}_j) \equiv 2\mu_t\left(\widetilde{S_{ij}} - \frac{1}{3}\delta_{ij}\widetilde{S_{kk}}\right) \tag{1.72}$$

  with μ_t the turbulent viscosity. Turbulent viscosity models available in AVBP are presented below.

- **SGS species flux vector:**

$$\overline{J_{j,k}^{sgs}} = \overline{\rho}(\widetilde{u_j Y_k} - \widetilde{u}_j\widetilde{Y_k}) \equiv -\overline{\rho}\left(D_k^t\frac{W_k}{\overline{W}}\frac{\partial\widetilde{X_k}}{\partial x_j} - \widetilde{Y_k}\widetilde{V_j^{c,t}}\right) \tag{1.73}$$

  with

$$\widetilde{V_j^{c,t}} = \sum_{k=1}^{N_{spec}} D_k^t\frac{W_k}{\overline{W}}\frac{\partial\widetilde{X_k}}{\partial x_j} \quad \text{and} \quad D_k^t = \frac{\mu_t}{\overline{\rho}Sc_k^t} \tag{1.74}$$

  where Sc_k^t is the turbulent Schmidt number of species k. In this work, $Sc_k^t = Sc^t = 0.6$.

- **SGS heat flux vector:**

$$\overline{q_i^{sgs}} = \overline{\rho}(\widetilde{u_j E} - \widetilde{u}_j\widetilde{E}) \equiv -\lambda_t\frac{\partial\widetilde{T}}{\partial x_j} + \sum_{k=1}^{N}\overline{J_{j,k}}\widetilde{h_{s,k}} \tag{1.75}$$

  with

$$\lambda_t = \frac{\mu_t\overline{C_p}}{Pr^t} \tag{1.76}$$

  where Pr^t is the turbulent Prandtl number. In this work, $Pr^t = 0.6$.

Sub-grid turbulence modeling

The SGS closures presented above, rely on a viscosity term to model the sub-grid turbulence (Boussinesq assumption [Boussinesq 1877]). This approach assumes that the SGS effects are purely dissipative. The LES models differ with the estimation of the turbulent viscosity ν_t. Several are available in AVBP:

- **Smagorinsky model:**

$$\nu_t = (C_s\Delta)^2\sqrt{2\widetilde{S_{ij}}\widetilde{S_{ij}}} \tag{1.77}$$

  with $\Delta = {V_{cell}}^{1/3}$ the filter characteristic length, and $C_s = 0.18$ a model constant that may vary between 0.1 to 0.8 depending on the flow configuration. The Smagorinski model [Smagorinsky 1963] has been largely used on multiple configurations. This model has the good property to deliver the correct kinetic energy dissipation rate in the case of a HIT. However, it is too dissipative in the general case and it has been shown that it is not adapted for the study of laminar-turbulence transition [Sagaut 2006]. Furthermore, this formulation does not take into account the wall influences.

- **WALE (Wall Adapting Local Eddy-viscosity) model:**

$$\nu_t = (C_w\Delta)^2\frac{(s_{ij}^d s_{ij}^d)^{3/2}}{(\widetilde{S_{ij}}\widetilde{S_{ij}})^{5/2} + (s_{ij}^d s_{ij}^d)^{5/4}} \quad \text{with} \quad s_{ij}^d = \frac{1}{2}(\widetilde{g_{ij}}^2 - \widetilde{g_{ji}}^2) - \frac{1}{3}\widetilde{g_{kk}}^2\delta_{ij} \tag{1.78}$$

  with $\widetilde{g_{ij}}^2 = \widetilde{g_{ik}}\widetilde{g_{kj}}$ where $\widetilde{g_{ik}} = \partial\widetilde{u}_i/\partial x_k$ is the resolved velocity gradient, and $C_w = 0.4929$ the model constant. This model has been developed by Nicoud and Ducros [1999] for near wall flows, and aims to recover the wall laws.

- **SIGMA model:**

$$\nu_t = (C_\sigma \Delta)^2 \frac{\sigma_3(\sigma_1 - \sigma_2)(\sigma_2 - \sigma_3)}{\sigma_1^2} \tag{1.79}$$

with σ_i the eigenvalues of the tensor built from resolved velocity gradients, and $C_\sigma = 1.35$ the model constant. This model is an improvement of the WALE model for rotating flows [Nicoud et al. 2011]. This model is then adapted for aeronautical engine which are confined and where swirling flows are generated.

1.2.4 Boundary conditions

Accurate boundary conditions are required for the simulation of reacting flows especially in the context of LES and high order DNS.

In order to control the acoustic perturbations during the computation, the residuals of convective and diffusive fluxes need to be corrected at the boundaries. For this purpose, the conservation equations are re-formulated as characteristic propagating waves. The acoustic waves propagating at the sound speed are then isolated from the entropic waves propagating at the flow speed. Then, depending on the boundary condition required, these waves are processed differently. For example, for non-reflecting inlet boundary conditions, the incoming acoustic waves are removed. In the general case, relaxation coefficients are used to smoothly reduce the wave influence. This method is called Navier-Stokes Characteristic Boundary Condition (NSCBC) and has been developed by [Poinsot and Lelef 1992] and extended to the multi-species formalism [Baum et al. 1995]. More information on this method can be found in [Poinsot and Veynante 2012].

The previous method applies for inlet, outlet and walls. In NTMIX, NSCBC conditions has been corrected and validated during this PhD. Due to higher stencil used for the numerical schemes, the gradient computations cannot be evaluated with the classical centered finite differences. Instead, the code uses non-centered finite differences of order 3 and 4. However, this is not the case for periodic and symmetric (normal components to the boundary condition equal to zero) conditions. In the first case, the stencil points are recovered from MPI communications, in the second one, points are symmetrically duplicated from the domain. Therefore, in both cases, centered finite difference high order schemes can be used.

1.3 Numerical modeling of the liquid phase

This section aims at presenting the modeling and the associated equations of the liquid phase in AVBP. The equations for the gaseous phase have already been detailed in the previous sections. In this work, the two-phase flow numerical simulations computed with AVBP focus onon dilute sprays. The dense liquid phase which may be encountered in fuel injectors or at the injector nozzle is not considered.

1.3.1 Euler and Lagrangian approaches

The fuel spray can be described with two main methodologies:

- **Euler-Euler (EE):**
  In the Eulerian formalism, the liquid phase is considered as a continuous phase. Hence, the liquid phase is resolved using the same formalism as the gaseous phase. Indeed, the liquid fraction $\alpha_l = V_{liq}/V_{gas}$ is transported on the same grid than the gaseous phase. The main advantage of the EE formalism is to be very scalable in a parallel solver since the liquid and gaseous phases are solved on the same grid. Therefore, this method is often used in many applications including LES of aeronautical combustion chambers [Eyssartier 2012]. However, EE simulations are generally mono-dispersed[4] and do not enable an easy implementation of the multi-component evaporation.

[4] The spray poly-dispersion can be recovered using sectional methods but implies to resolve multiple liquid phases with a large CPU-cost.

For those reasons, the EE formalism was not retained in this work and will not be detailed.

- **Euler-Lagrange (EL):**
  In the Lagrangian formalism, the dispersed liquid phase is viewed as a discrete phase composed of an ensemble of droplets. Each droplet is seen as a simple material point also called particle with its individual properties (size, mass, temperature, composition). Thus, the particles are tracked following point mechanics equations and the poly-dispersion of the spray is naturally taken into account. Considering the small droplet sizes ($1\mu m < d_p < 100\mu m$) and the high surface tension they are also considered perfectly spherical. The EL formalism does not require a grid for the tracking, but the droplets must be located in the Euler grid for the coupling with the gaseous phase, boundary conditions and processor exchanges. In this work, the EL formalism implemented in the AVBP code [Senoner 2010, Paulhiac 2015, Collin-Bastiani 2019] is retained.

1.3.2 Equations for the particles in the Lagrangian formalism

With the EL formulation, the droplets are seen as individual material points. The particle trajectories as well as mass and temperature variations are computed using the following set of equations:

$$\frac{DX_{p,i}}{Dt} = u_{p,i} \qquad \text{for } i = 1,3 \tag{1.80}$$

$$\frac{Dm_p u_{p,i}}{Dt} = F^{ext}_{p,i} \qquad \text{for } i = 1,3 \tag{1.81}$$

$$\frac{Dm_p}{Dt} = \dot{m}_p \tag{1.82}$$

$$\frac{Dm_p h_{s,p}}{Dt} = \dot{\Phi}_p \tag{1.83}$$

where $X_{p,i}$ is the particle position, m_p its mass and $u_{p,i}$ its velocity. $F^{ext}_{p,i}$ are the external forces applied to the particle and are detailed in Sec. 1.3.3. $\dot{m}_p$ and $\dot{\Phi}_p$ are respectively the evaporation rate and the heat flux described in Sec. 1.3.4. D/Dt is the total or particular derivative introduced in Eq. (9.5).

In this work, the two-phase wall boundary conditions are simple elastic rebound. Particles leaving the numerical domain are removed and injection conditions are detailed in Chap. 11.

1.3.3 External forces

Several forces apply on the droplets and can be taken into account in the term $F^{ext}_{p,i}$ of Eq. (1.81).

Gravity and Buoyancy

Gravity and buoyancy forces can be combined and write:

$$\overrightarrow{F}_{\mathcal{G},\mathcal{A}} = \rho_l V_p \overrightarrow{g} \left(1 - \frac{\rho_g}{\rho_l}\right) \tag{1.84}$$

with ρ_l and ρ_g respectively the liquid and gaseous densities, $V_p = 4/3\pi {r_p}^3$ the particle volume where r_p is the particle radius, and $\overrightarrow{g}$ the gravity.

Considering the ratio of densities between air ($\rho_g \approx 1\, kg.m^{-3}$) and fuel ($\rho_F \approx 800\, kg.m^{-3}$), the buoyancy force can be neglected. The unsteady virtual mass effect and Basset force (also called historical force) due to the acceleration of the particle in the fluid is also neglected for the same reasons [Crowe et al. 2011]. Finally gravity is also neglected in comparison of the strong convective transport in the target applications of this work.

Drag

Due to the small droplet size and thus mass, the most important force is the drag force $\overrightarrow{F}_{\mathcal{D}}$ which writes:

$$\overrightarrow{F}_{\mathcal{D}} = \frac{1}{2}\rho_g C_{\mathcal{D}} A_p ||\overrightarrow{u}_g - \overrightarrow{u}_p||(\overrightarrow{u}_g - \overrightarrow{u}_p) \tag{1.85}$$

with $\overrightarrow{u}_g$ and $\overrightarrow{u}_p$ respectively the gaseous and particle velocities, $A_p = \pi {d_p}^2/4$ the projected area of the spherical particle where d_p is the particle diameter, and $C_{\mathcal{D}}$ the drag coefficient.

As shown on Fig. 1.3.1, the drag coefficient is a function of the particle Reynolds number defined as:

$$Re_p = \frac{\rho_g d_p ||\overrightarrow{u}_g - \overrightarrow{u}_p||}{\mu_g} \tag{1.86}$$

with μ_g the gaseous dynamic viscosity.

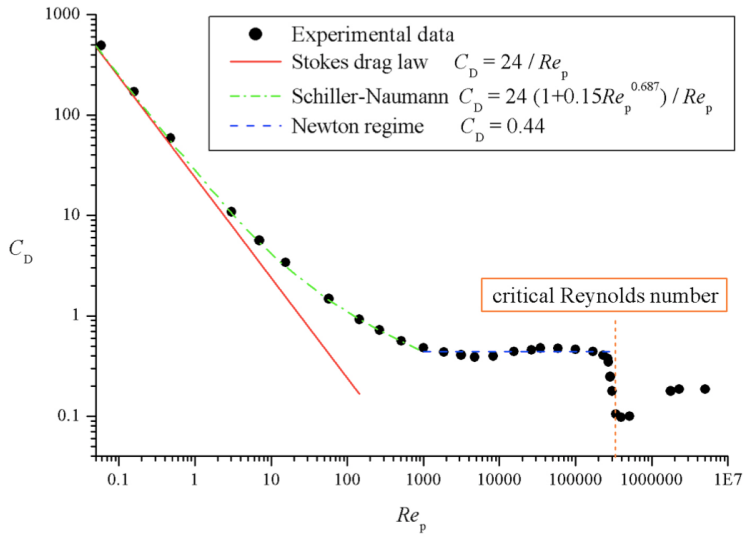

Figure 1.3.1: Drag coefficient as function of the particle Reynolds number for an isolated rigid sphere (extracted from [Wörner 2003])

In typical spray aeronautical applications, Re_p stays under 500. Thus, the Schiller & Naumann empirical correlation [Schiller and Naumann 1935] is used in this work. The correlation remains valid for $Re_p < 800$ and writes:

$$C_{\mathcal{D}}(Re_p) = \frac{24}{Re_p}(1 + 0.15 {Re_p}^{0.687}) \tag{1.87}$$

The droplet velocity response to the drag force can be described with a characteristic drag droplet time $\tau_{p,\mathcal{D}}$:

$$\tau_{p,\mathcal{D}} = \frac{\rho_l {d_p}^2}{18\mu_g(1 + 0.15 {Re_p}^{0.687})} \tag{1.88}$$

This characteristic time can be compared to a flow time $\tau_g = L_c/u_g$ via a Stokes number $St = \tau_{p,\mathcal{D}}/\tau_g$ where L_c is the characteristic length of the considered flow. For low St numbers, the droplet behaves like a tracer and the droplet velocity follows the gaseous one. On the contrary, for high St numbers, the particle trajectory is driven by its inertia and is weakly affected by the gaseous flow.

1.3.4 Mono-component droplet evaporation

Evaporation is responsible for the exchange terms $\dot{m}_p$ and $\dot{\Phi}_p$. The computation of these terms in AVBP is based on the classical Spalding model [Spalding 1953] presented here.

Spalding model

The equations describing the droplet evaporation can be solved analytically under several hypothesis:

- The droplet is spherical.
- The droplet is isolated, thus interaction with other droplets is neglected.
- The droplet heat conductivity is infinite. Thus, the droplet temperature is uniform. Indeed, the liquid heat conductivity is generally one order of magnitude higher than the gaseous one. Hence, the temperature homogenization characteristic time is faster than gaseous adaptation and internal droplet resolution is not needed.
- The gas mixture is supposed to be at rest.
- The evolution of the gaseous phase is quasi-static and follows a succession of equilibrium states.

Using these assumptions, only the radial variations in the spherical reference frame are considered as shown on Fig. 1.3.2. The conservation equation of mass, momentum, and energy are written between the droplet surface ($_\zeta$ subscript) and the infinite far field ($_\infty$ subscript):

$$\rho_g u_g r^2 = \text{ constant } = \frac{\dot{m}_F}{4\pi} \tag{1.89}$$

$$\rho_g u_g r^2 \frac{dY_F}{dr} = \frac{d}{dr}\left(r^2 \rho_g D_F \frac{dY_F}{dr}\right) \tag{1.90}$$

$$\rho_g u_g r^2 C_p(T) \frac{dT}{dr} = \frac{d}{dr}\left(r^2 \lambda \frac{dT}{dr}\right) \tag{1.91}$$

with r the radial coordinate, $\dot{m}_F$ the fuel vapor flux at the droplet surface (mass source term from the mixture point of view), Y_F the gaseous fuel mixture fraction and D_F its diffusivity.

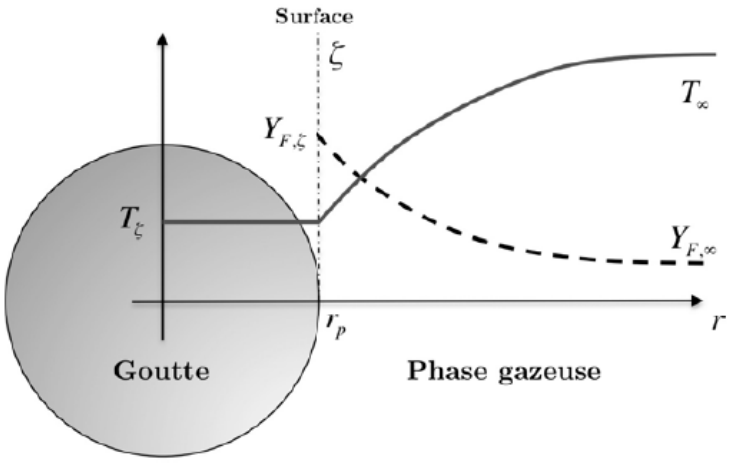

Figure 1.3.2: Sketch of the temperature and fuel mass fraction radial profiles around an evaporation droplet (extracted from [Paulhiac 2015])

Thermal and species diffusivities are supposed constant along the radial profile and are evaluated at a reference temperature using a $1/3 - 2/3$ law [Miller et al. 1998]:

$$D_F = \frac{\mu(T_{ref})}{\rho_g Sc_F^{ev}} \tag{1.92}$$

$$\lambda = \frac{\mu(T_{ref}) C_p(T_{ref}, Y_{ref})}{Pr^{ev}} \tag{1.93}$$

with

$$T_{ref} = T_\zeta + \frac{1}{3}(T_\infty - T_\zeta) \tag{1.94}$$

$$Y_{F,ref} = Y_{F,\zeta} + \frac{1}{3}(Y_{F,\infty} - Y_{F,\zeta}) \tag{1.95}$$

The dynamic viscosity can be computed using either a power law, the Sutherland law or the Wilke formula for more accuracy (see Sec. 1.1.3). Sc_F^{ev} and Pr^{ev} are specific evaporation Schmidt and Prandtl numbers used to account for complex transport effects [Sierra Sànchez 2012]. Finally, the infinite droplet heat conduction assumption translates into $T_p = T_\zeta$.

Mass transfer

Since the liquid/gas interface does not store mass, the fuel vapor flux is directly linked to the droplet evaporation rate:

$$\dot{m}_F = -\dot{m}_p \tag{1.96}$$

Hence, integrating twice Eq. (1.90) between the droplet surface and the far field, the following expression of the evaporation rate is obtained:

$$\dot{m}_p = -2\pi\, d_p\, \rho_g\, D_F\, ln(B_M + 1) \tag{1.97}$$

with B_M the mass Spalding transfer number:

$$B_M = \frac{Y_{F,\zeta} - Y_{F,\infty}}{1 - Y_{F,\zeta}} \tag{1.98}$$

The surface fuel mass fraction $Y_{F,\zeta}$ is obtained assuming liquid-vapor equilibrium and using the mono-component Raoult's law[5]:

$$Y_{F,\zeta} = \frac{W_F}{W}\frac{P_{sat}(T_p)}{P} \tag{1.99}$$

where P_{sat} is the saturating vapor pressure which is tabulated from experimental measurements or using approximations of the Clausius-Clapeyron relation. In this work the Ambrose-Walton corresponding states method is used [Poling et al. 2001].

Equations (1.97), (1.98) and (1.99) indicate that the evaporation rate relies on the droplet temperature, the droplet size and the surrounding fuel vapor concentration.

The temporal evolution of the droplet diameter is obtained by applying mass conservation on the droplet:

$$\dot{m}_p = \frac{d\,\rho_p V_p(t)}{dt} \tag{1.100}$$

Thus integrating Eq. (1.97), and assuming the droplet temperature T_p, and thus B_M, constant, the classical d^2 law is obtained:

$${d_p}^2 = {d_{p,0}}^2 - \frac{8\rho_g D_F}{\rho_p}\ln(B_M + 1) \times t \tag{1.101}$$

with $d_{p,0}$ the initial droplet diameter. Then, a characteristic evaporation time can be obtained:

$$\tau_{evap} = \frac{\rho_p d_{p,0}^2}{8\rho_g D_F ln(B_M + 1)} \tag{1.102}$$

In reality the droplet temperature and the mass Spalding transfer number vary in time, leading to some deviation from the d^2 law. Especially, B_M can diverge towards infinity when saturation is reached at the interface.

[5] Demonstrated for ideal mixture where molecule interactions are identical: the enthalpy of mixing is zero as is the volume change on mixing.

Heat transfer

The evolution of the droplet temperature is found starting with the enthalpy balance on the droplet at rest[6][7] Eq. (1.83):

$$\frac{D}{Dt}\left(m_p h_{s,p}(T_p)\right) = \frac{d}{dt}\left(m_p h_{s,l}(T_p)\right) = \dot{\Phi}_p = \dot{\Phi}_l^{cond} + \dot{\Phi}_l^{conv} \tag{1.103}$$

$\dot{\Phi}_l^{cond}$ and $\dot{\Phi}_l^{conv}$ are respectively the conductive and convective energy fluxes at the droplet surface. Then, developing the derivative and using the definition of enthalpy:

$$\frac{dT_p}{dt} = \frac{1}{m_p C_{p,l}}\left(\dot{\Phi}_l^{cond} + \dot{\Phi}_l^{conv} - \dot{m}_p h_{s,l}(T_p)\right) \tag{1.104}$$

But $\dot{\Phi}_l^{cond}$ is not defined because of the infinite heat conductivity assumption inside the droplet.

Yet, as the liquid/gas interface does not store energy, there is a balance between the liquid and gaseous energy fluxes:

$$\dot{\Phi}_l^{cond} + \dot{\Phi}_l^{conv} + \dot{\Phi}_g^{cond} + \dot{\Phi}_g^{conv} = 0 \tag{1.105}$$

The convective fluxes correspond to the enthalpy transfers due to the phase change and write:

$$\dot{\Phi}_l^{conv} = \dot{m}_p h_{s,l}(T_p) \tag{1.106}$$

$$\dot{\Phi}_g^{conv} = \dot{m}_F h_{s,g}(T_\zeta) \tag{1.107}$$

Then, using Eq. (1.96) and since $T_p = T_\zeta$:

$$\dot{\Phi}_l^{conv} + \dot{\Phi}_g^{conv} = -\dot{m}_p L_v(T_p) \tag{1.108}$$

Where $L_v(T) = h_{s,g}(T) - h_{s,l}(T)$ is the latent heat of evaporation.

Hence, Eq. (1.104) becomes:

$$\frac{dT_p}{dt} = \frac{1}{m_p C_{p,l}}\left(-\dot{\Phi}_g^{cond} + \dot{m}_p L_v(T_p)\right) \tag{1.109}$$

Where the gaseous conductive flux is defined on the gaseous side of the interface as:

$$\dot{\Phi}_g^{cond} = 4\pi r_p^2 \lambda \left.\frac{dT}{dr}\right|_{\zeta,g} \tag{1.110}$$

The analytical expression of $\dot{\Phi}_g^{cond}$ can be obtained integrating Eq. (1.91). A first integration leads to:

$$\dot{m}_F C_p(T_{ref})(T - T_\zeta) = 4\pi r^2 \lambda \frac{dT}{dr} - 4\pi {r_p}^2 \lambda \left.\frac{dT}{dr}\right|_{\zeta,g} \tag{1.111}$$

where the gaseous conductive flux can be identified on the right term.

The second integration of Eq. (1.111) gives the following expression:

$$\dot{m}_F = 4\pi r_p \frac{\lambda}{C_p(T_{ref})} \ln\left(B_T + 1\right) \tag{1.112}$$

with B_T the heat Spalding transfer number which writes:

$$B_T = \frac{\dot{m}_F C_p(T_{ref})(T_\infty - T_\zeta)}{-\dot{\Phi}_g^{cond}} \tag{1.113}$$

Combining Eq. (1.112) and (1.113) give the expression of $\dot{\Phi}_g^{cond}$:

$$-\dot{\Phi}_g^{cond} = 4\pi r_p \lambda (T_\infty - T_\zeta) \frac{\ln\left(B_T + 1\right)}{B_T} \tag{1.114}$$

[6] The total derivative is equal to the simple derivative because there is no flow velocity.
[7] In the case of a fuel droplet the enthalpy of the particle is equal to the liquid enthalpy.

In the above expression, B_T is obtained combining Eq. (1.96), (1.97) and (1.112):

$$B_T = (B_M + 1)^{1/Le_F^{ev}} - 1 \tag{1.115}$$

where $Le_F^{ev} = \lambda/(C_p(T_{ref})\rho_g D_F) = Sc_F^{ev}/Pr^{ev}$ is the evaporation Lewis fuel number.

Finally, replacing the expression of the gaseous conductive flux Eq. (1.114) in Eq. (1.109) the droplet temperature evolution is obtained:

$$\frac{dT_p}{dt} = \frac{1}{m_p C_{p,l}} \left(4\pi r_p \lambda (T_\infty - T_\zeta) \frac{ln(B_T + 1)}{B_T} + \dot{m}_p L_v(T_p) \right) \tag{1.116}$$

And the droplet heat flux required in Eq. (1.83) writes:

$$\dot{\Phi}_p = 4\pi r_p \lambda (T_\infty - T_\zeta) \frac{\ln(B_T + 1)}{B_T} + \dot{m}_p L_v(T_p) + \dot{m}_p h_{s,l}(T_p) \tag{1.117}$$

and can be also computed from the gaseous heat flux:

$$\dot{\Phi}_p = -\dot{\Phi}_g = 4\pi r_p \lambda (T_\infty - T_\zeta) \frac{\ln(B_T + 1)}{B_T} - \dot{m}_F h_{s,g}(T_\zeta) \tag{1.118}$$

Saturation

As explained previously, when the droplet approaches the saturation[8], the mass Spalding number diverges towards infinity as well as the evaporation rate. However, as shown in Eq. (1.116), the evaporation rate cools down the droplet which prevents the droplet from reaching the saturation condition and boiling.

An equilibrium state is reached when the heat brought to the droplet from the mixture fully contributes to the phase change i.e. is equal to the heat lost by the evaporation. At this stage, the droplet temperature stabilizes at a singular value T_{wb} called wet-bulb temperature (lower than the boiling temperature T_{boil}[9]).

However, the saturation condition must be handled in numerical solvers. Indeed, because of the time discretization, the mixture state can change from one iteration to the other. Pressure variations due to instabilities can trigger the saturation condition, or strong temperature increases during ignition can heat the droplets above the boiling temperature[10]. In such cases ($P_{sat}(T_p) \geq P$), the droplet temperature is fixed and the evaporation rate is directly computed from the heat flux:

$$\frac{dT_p}{dt} = 0 \quad \Leftrightarrow \quad \dot{m}_p = 4\pi r_p \lambda \frac{T_p - T_\infty}{L_v(T_p)} \frac{\ln(B_T + 1)}{B_T} \tag{1.119}$$

Abramzon and Sirignano correction

One of the assumptions of the Spalding evaporation model is that the flow is at rest. However, in practical applications, an important relative velocity between the gas and the droplet can be encountered. This flow enhances the evaporation process via the formation of a boundary layer around the droplet which increases heat and mass transfers because of mixing effects. Thus, the relative flow must be included to better model the evaporation.

Ranz and Marshall Jr. [1952] have introduced a Sherwood and a Nusselt numbers to take into account Re_p:

$$Sh = 2 + 0.55 {Re_p}^{1/2} {Sc_F}^{1/3} \tag{1.120}$$

$$Nu = 2 + 0.55 {Re_p}^{1/2} Pr^{1/3} \tag{1.121}$$

[8] Here the saturation term characterizes the droplet surface condition and should not be confused with the saturation of the gaseous mixture around the droplet which would lead to the condensation phenomenon, not taken into account in this work.

[9] The boiling temperature is the temperature at which $P_{sat}(T) = P$.

[10] This remains possible because the evaporation rate is evaluated before the heat flux.

Eq. (1.97) and (1.117) are then modified as follows:

$$\dot{m}_p = -Sh\pi\, d_p\, \rho_g\, D_F\, ln(B_M + 1) \tag{1.122}$$

$$\dot{\Phi}_p = 2Nu\pi r_p \lambda (T_\infty - T_\zeta) \frac{ln(B_T + 1)}{B_T} + \dot{m}_p L_v(T_p) + \dot{m}_p h_{s,l}(T_p) \tag{1.123}$$

And the droplet temperature evolution Eq. (1.116) writes:

$$\frac{d\,T_p}{dt} = \frac{1}{m_p C_{p,l}} \left(2Nu\pi r_p \lambda (T_\infty - T_\zeta) \frac{ln(B_T + 1)}{B_T} + \dot{m}_p L_v(T_p) \right) \tag{1.124}$$

Finally Abramzon and Sirignano [1989] have proposed to modify the Nusselt and Sherwood numbers according to the film theory [Bird et al. 2006] to estimate more accurately mass and thermal fluxes:

$$Sh^* = 2 + \frac{Sh - 2}{F_M} \tag{1.125}$$

$$Nu^* = 2 + \frac{Nu - 2}{F_T} \tag{1.126}$$

with

$$F_{M,T} = (1 + B_{M,T})^{0.7} \times \frac{\ln(1 + B_{M,T})}{B_{M,T}} \tag{1.127}$$

1.3.5 Coupling with the gaseous phase

In the EL formalism, there are several levels of coupling between the gaseous and liquid phases depending on the dispersed phase density:

- **Very dilute sprays ($\alpha_l < 1e^{-6}$):**
  The liquid phase is not dense enough to have any impact on the gaseous phase. However, the droplet dynamics and evaporation processes (droplet velocity, mass and temperature variations) are influenced by the gas. This is called a one-way coupling.

- **Dilute to moderately dense sprays ($1e^{-6} < \alpha_l < 1e^{-3}$):**
  The liquid phase acts on the gas dynamics by a retro-coupling effect. The effects of drag force, evaporation rate and heat fluxes are taken into account using source terms in the gaseous conservation equations. Thus, it corresponds to a two-way coupling.

- **Very dense sprays ($1e^{-3} < \alpha_l$):**
  In this case, the droplets are close enough from each other to interact. This level of coupling is called four-way coupling.

In this work, the two-way coupling strategy is retained because it corresponds to typical aeronautical applications.

Coupling

As detailed in the introduction, the coupling of the liquid phase on the gaseous phase is simply done by transferring conservatively $F_{p,i}^{ext}$, $\dot{m}_p$ and $\dot{\Phi}_p$ for all droplets to the gaseous phase thanks to source terms:

- **Mass:**

$$S_{m,j}^{l \to g} = \frac{-1}{\Delta V_j} \sum_{p=1}^{N_{ptcl,el}} \Psi_{p,j} \dot{m}_p \tag{1.128}$$

- **Species:**

$$S_{k,j}^{l\to g} = \frac{-1}{\Delta V_j} \sum_{p=1}^{N_{ptcl,el}} \Psi_{p,j} \dot{m}_p Y_{k,p}^{ev} \tag{1.129}$$

with $Y_{k,p}^{ev}$ the species evaporation mass fraction. In the mono-component case $Y_{k,p}^{ev} = Y_{F,p}^{ev} = 1$

- **Momentum:**

$$\overrightarrow{S_{qdm,j}^{l\to g}} = \frac{-1}{\Delta V_j} \sum_{p=1}^{N_{ptcl,el}} \Psi_{p,j} \left(m_p \overrightarrow{F_p^{ext}} + \dot{m}_p \overrightarrow{u_p} \right) \tag{1.130}$$

- **Energy:**

$$S_{e,j}^{l\to g} = \frac{-1}{\Delta V_j} \sum_{p=1}^{N_{ptcl,el}} \Psi_{p,j} \left(m_p \overrightarrow{F_p^{ext}}.\overrightarrow{u_p} + \frac{1}{2}\dot{m}_p ||\overrightarrow{u_p}||^2 + \dot{\Phi}_p \right) \tag{1.131}$$

In the above expressions, $_j$ subscript refers to the vertex/node on which the source terms are interpolated. ΔV_j is the control volume of the node j, $N_{ptcl,el}$ is the number of particles in the element/cell. $\Psi_{p,j}$ is the interpolation function. In this work an inverse distance interpolation illustrated Fig. 1.3.3 is used:

$$\Psi_{p,j} = \frac{1/d_j}{\sum_{q=1}^{N_{vert}} 1/d_q} \tag{1.132}$$

where d_j is the distance between the particle and the vertex j and N_{vert} is the number of vertices in each element.

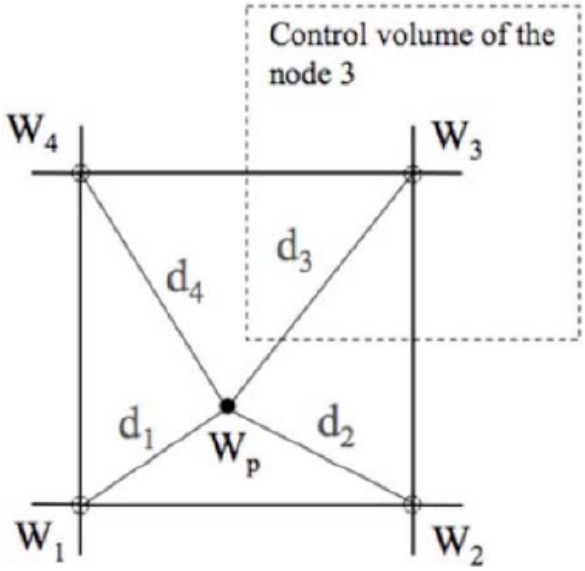

Figure 1.3.3: Particle source term projection on the nodes of the gaseous grid (extracted from [Paulhiac 2015])

The same inverse distance interpolation is used to get the gaseous properties at the particle position which is supposed to correspond to the infinite condition in the evaporation model.

Point source assumption

In the EL formalism, the droplets are seen as isolated points and the gaseous conditions used to compute drag, evaporation and heat conduction are evaluated at the particle position. These conditions are supposed to represent the state at an infinite distance i.e. not influenced by the droplet. However, due

to the two-way coupling, the local conditions are modified by the droplet presence.

In the case of large grid cell sizes ($\Delta_x >> d_p$), the droplet influence through the exchange source terms is negligible. Thus, the evaluation of drag, evaporation and heat flux are correct. On the contrary, when the droplet and cell sizes become comparable, large errors arise as shown on Fig. 1.3.4 which indicates that more than 20% error is done on the evaporation rate if $\Delta_x < 4d_p$ [Rangel and Sirignano 1989, Sontheimer et al. 2021].

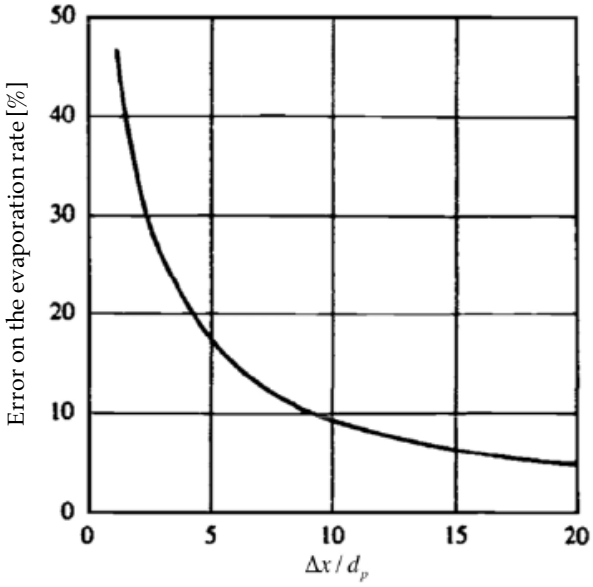

Figure 1.3.4: Evolution of the error on the evaporation rate of an isolated droplet depending the cell size over droplet diameter ratio (extracted from [Sirignano 2010])

To reduce the error, a local correction method can be applied [Paulhiac 2015]. The coupling source terms are distributed to a larger number of nodes in a target volume depending on the droplet size as shown on Fig. 1.3.5. Hence, the droplet coupling is diluted, reducing its influence at its position. The result is equivalent to the use of a coarser grid which follows the point source assumption.

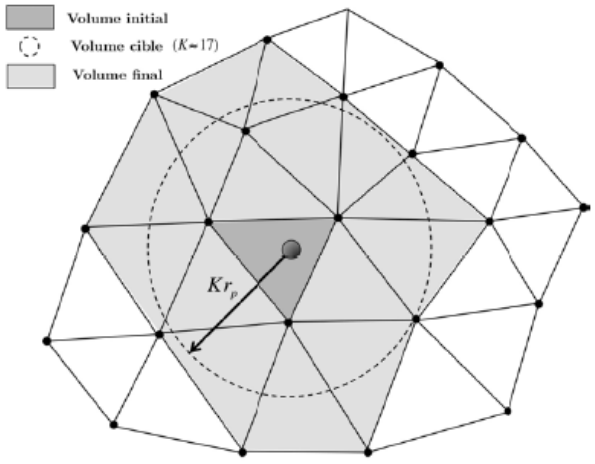

Figure 1.3.5: Source term spreading procedure to reduce the point source error (extracted from [Paulhiac 2015])

The use of this correction is discussed in Chap. 13.

R-parcel method

In classical aeronautical configuration, several million particles must be tracked. To reduce the CPU-cost of the Lagrangian solver, the R-parcel method can be used [Paulhiac 2015], which consists in using numerical particles with a R-parcel parameter $\mathcal{R}_p$ instead of $\mathcal{R}_p$ physical ones.

The numerical particles are initialized with the same mass m_p, temperature T_p and diameter d_p than the physical ones, and the computation of external forces, evaporation and heat flux is identical. However, the physical mass represented by a numerical particle is weighted by $\mathcal{R}_p$ as well as the coupling with the gaseous phase:

$$S^{l\to g} = S^{l\to g}_{num} \times \mathcal{R}_p \tag{1.133}$$

For example, the injection of one numerical particle with $\mathcal{R}_p = N$ and $m_{p,num} = m$ is equivalent to inject N physical particles of mass $m_p = m$ at the same position[11].

[11] The R-parcel method should be used only when the statistical convergence is reached.

Chapter 2

Theoretical concepts of chemistry

Contents

Combustion results in the exothermic oxidation process of a fuel molecule into oxides (CO_2 and H_2O in the case of hydrocarbon combustion). The heat released by this reaction enables to trigger other fuel oxidations in a chain reaction process. Therefore, a chemical modeling is required to determine how and at which rate this process is occurring. Concretely, the chemistry modeling enables to compute the heat and species production terms $\dot{\omega}_T$ and $\dot{\omega}_k$ required to solve the energy conservation equation Eq. (1.26) and the species conservation equation Eq. (1.25).

This chapter first introduces the theoretical concepts of kinetic chemistry in Sec. 2.1. Then several strategies for the implementation and modeling of the chemistry in numerical simulation are presented Sec. 2.2. Finally, Sec. 2.3 focuses on the hydrocarbon chemistry features, and gives the reference chemistries used in this work for methane and kerosene combustion.

2.1 Chemical kinetics

Chemical kinetics is the branch of physical chemistry that is concerned with understanding the rates of chemical reactions. Chemical kinetics includes investigations of how experimental conditions influence the speed of chemical reactions and yield to the construction of mathematical models that can describe the characteristics of a chemical reaction.

2.1.1 Elementary reactions

The combustion processes rely on a large number of species collisions (elementary reactions) leading to the formation of new species, before reaching a stable macroscopic equilibrium. This state is dependent

on the temperature, the pressure and the initial composition. A kinetic mechanism (or chemical scheme) corresponds to a collection of elementary reactions. This set of reactions enables to describe with more or less accuracy (depending on the number of reactions, species and chemical processes taken into account) the evolution of the reactive system in all possible configurations.

General form

There are three main classes of elementary reactions depending on the number of species colliding:

- Uni-molecular reactions:
  For these reactions, there are no species collisions. It describes the dissociation of a molecule A to form new products P. These reactions are encountered in pyrolysis or high temperature dissociation phenomena. The rate of progress of the reaction ($\mathcal{Q}_j$) is generally a first order law[1][2], which means that the rate at which the reaction occurs is linear to the concentration of the molecule A: $\mathcal{Q}_j = f([A])$

$$\mathrm{A} \rightarrow P \tag{2.1}$$

- Bi-molecular reactions:
  These reactions occur during the collision of two molecules A and B[3]. These reactions are the most common and follow a second order law: $\mathcal{Q}_j = f([A] \times [B])$

$$\mathrm{A} + \mathrm{B} \rightarrow P \tag{2.2}$$

- Tri-molecular reactions:
  These reactions require the collision of three molecules. It corresponds generally to recombination reactions to form the final combustion products. The reaction rate of progress obeys to a third order law: $\mathcal{Q}_j = f([A] \times [B] \times [C])$

$$\mathrm{A} + \mathrm{B} + \mathrm{C} \rightarrow P \tag{2.3}$$

  These reactions are often expressed under the form of third body reactions with one of the three molecules acting like a support of the reaction without being transformed.

Examples and Classification

Since the global combustion transformation is expressed using several elementary reactions, the presence of intermediate products is required. These radical species are compounds with unfilled outer electron configurations which makes them unstable and highly reactive. These species such as $\mathrm{O}\cdot$, $\mathrm{OH}\cdot$ or $\mathrm{H}\cdot$ are of great importance in combustion as they react with the relatively stable fuel species to start the reaction processes.

Several types of reactions can be found in chemical mechanisms [Gardiner Jr. 2000]:

- Homolysis:
  The homolysis corresponds to a dissociation reaction where a stable molecule breaks in two or more radical fragments, for example Eq. (2.4). In the case of heavy fuels with long carbon chains and in the presence of high temperature, this reaction is called pyrolysis, for exemple Eq. (2.5)[4] . When the result of the dissociation is an unsaturated compound and a free radical, this reaction is called β-scission, for example Eq. (2.6):

$$\mathrm{H_2O} \rightarrow \mathrm{H}\cdot + \mathrm{OH}\cdot \tag{2.4}$$

$$\mathrm{nC_{12}H_{26}} \rightarrow 0.35\,\mathrm{C_2H_4} + 0.75\,\mathrm{nC_5H_{10}} + 0.25\,\mathrm{nC_5H_{11}}\cdot + 0.15\,\mathrm{nC_7H_{14}}\cdot + 0.75\,\mathrm{nC_7H_{15}} \tag{2.5}$$

[1] Different from the species evolution order (more detailed in Chap. 8)

[2] In this PhD, as in many combustion kinetics, the principle of mass action law is used [Waage and Gulberg 1986]. It states that for ideal conditions the reaction order depends only on its concentration with no consideration about its size or functionality.

[3] B can be the same molecule as A

[4] n letter indicates the linear structure of the species

$$C_2H_5\cdot \rightarrow C_2H_4 + H\cdot \tag{2.6}$$

- H abstraction:
  It corresponds to a reaction in which a molecule (often an oxidizer species) removes a hydrogen atom from another one, for example in Eq. (2.7). When the "attacking" molecule is a free radical and the reaction produces an another free radical, the reaction is called metathesis, for example Eq. (2.8):

$$H_2 + O_2 \rightarrow HO_2\cdot + H\cdot \tag{2.7}$$

$$H_2 + O\cdot \rightarrow H\cdot + OH\cdot \tag{2.8}$$

- Addition:
  When two species combine to form one, it corresponds to an addition reaction. Generally the two species are radicals. In this case, the reaction is a combination (or recombination), for example Eq. (2.9):

$$CO\cdot + O\cdot \rightarrow CO_2 \tag{2.9}$$

- Izomerisation:
  It corresponds to a reaction where the atoms inside a molecule rearrange to form an isomer (same chemical formula but different thermodynamic properties), for example Eq. (2.10)[5]:

$$nC_4H_{10} \rightarrow iC_4H_{10} \tag{2.10}$$

- Disproportionation:
  A disproportionation or dismutation is a reaction between two radicals to stabilize the system (often hydrogen exchange) as in Eq. (2.11)

$$HO_2\cdot + O\cdot \rightarrow O_2 + OH\cdot \tag{2.11}$$

The ionisation reactions will not be considered in this PhD because the activation energies/temperatures required are far higher than those encountered in classical combustion. As well, electromagnetism effects will not be considered. However, the consideration of the plasma chemistry during the ignition phase will be discussed in Chap. 4.

2.1.2 Mathematical formalism

A chemical system can be represented under the following mathematical form [Poinsot and Veynante 2012]:

$$\sum_{k=1}^{N_{spec}} \nu'_{kj} A_k \leftrightarrow \sum_{k=1}^{N_{spec}} \nu''_{kj} A_k \tag{2.12}$$

with A_k the name of the species k, ν'_{kj} and ν''_{kj} are the stoichiometric coefficients of the reaction j.

The species production rates $\dot{\omega}_k$ ($[kg.m^{-3}.s^{-1}]$) are computed from the reaction rates of progress $\mathcal{Q}_j$ ($[mol.m^{-3}.s^{-1}]$):

$$\dot{\omega}_k = \sum_{j=1}^{N_{react}} \dot{\omega}_{kj} = W_k \sum_{j=1}^{N_{react}} \nu_{kj} \mathcal{Q}_j \quad \text{with} \quad \nu_{kj} = \nu''_{kj} - \nu'_{kj} \tag{2.13}$$

with $\dot{\omega}_{kj}$ the production rate of species k associated to the reaction j. The progress rates depend on the kinetic reaction and the species concentrations involved in the reaction:

$$\mathcal{Q}_j = K_{fj} \prod_{k=1}^{N_{spec}} [A_k]^{\nu'_{kj}} - K_{rj} \prod_{k=1}^{N_{spec}} [A_k]^{\nu''_{kj}} \tag{2.14}$$

with K_{fj} and K_{rj} that are respectively the forward and backward reaction rates of reaction j, and $[A_k]$ the molar concentration of the species k.

The expressions Eq. (2.12) and (2.14) correspond to the general form of reversible reactions. For the

[5] i letter indicates the branching structure of the species

specific case of irreversible reactions, the backward reaction rate is zero. A system of reversible reactions can be transformed to an irreversible system by duplicating the reversible reactions respectively into a forward component and a backward one with a negative sign added to the backward reaction rate. With this transformation the progress rates $\mathcal{Q}_j$ are separated in forward progress rates $\mathcal{Q}_{j,f}$ and reverse ones $\mathcal{Q}_{j,r}$. At the end, the production rate obtained with Eq. (2.13) remains the same in both formalisms. The vast majority of kinetic mechanisms are expressed using reversible and irreversible reactions at the same time. In this work, when the reversible nomenclature is used or specified, the number of reactions corresponds to reversible and irreversible reactions as they are presented in the kinetic mechanism. If the irreversible nomenclature is used, the number of reactions corresponds to irreversible reactions only.

2.1.3 Reaction rate computation

The computation of the species production rate $\dot{\omega}_k$ in Eq. (2.13) and the reaction rate of progress $\mathcal{Q}_j$ in Eq. (2.14) require to know the value of the reaction rates K_{fj} and K_{rj}. There are several reaction models that are found in the kinetic mechanisms, only those used in this work are detailed here.

Modified Arrhenius form

The forward reaction rates of elementary reactions are generally written as temperature dependant empirical laws known as modified Arrhenius equations[6]:

$$K_{fj}(T) = A_j \times T^{\beta_j} \times exp\left(-\frac{E_{aj}}{\mathcal{R}T}\right) \tag{2.15}$$

with A_j the pre-exponential constant, β_j the temperature exponent and E_{aj} the activation energy. These constants are provided with the reactions in the kinetic mechanism. The other following models are all based on the basic Arrhenius equation.

Third body

The third body reactions are specific reactions (often tri-molecular) requiring a collision partner to happen. These reactions are represented as follow:

$$A + B + M \rightarrow P + M \tag{2.16}$$

with M symbolizing the collision partner which can correspond to several species. The molar concentration of the collision partner is defined as:

$$[M] = \sum_{k=1}^{N_{spec}} \mathcal{Z}_k \times [k] \tag{2.17}$$

with $\mathcal{Z}_k$ the catalytic efficiency associated to the species k and provided in the kinetic mechanism.

In this case, the reaction rate is computed with a simple Arrhenius law, but the concentration of the collision partner has to be taken into account in Eq. (2.14).

Fall-off

The Fall-off reaction is a pressure dependent reaction which exhibits a third body behavior at low pressure, but an elementary reaction behavior at high pressure [Peters 1992]. These reactions are represented as follow:

$$A + B\,(+M) \rightarrow P\,(+M) \tag{2.18}$$

with M the collision partner like in third body reactions. This behavior is due to the variation of the concentration of the collision partners when the pressure changes. At high pressure, the reaction does

[6] The classical Arrhenius form does not include the temperature dependency ($\beta_j = 0$).

not depend on the collision partner because the species concentrations are high enough. On the contrary, at low pressure, the presence of collision partners is critical and changes significantly the reaction rate. Between those pressure limits yields the fall-off regime as represented on Fig. 2.1.1.

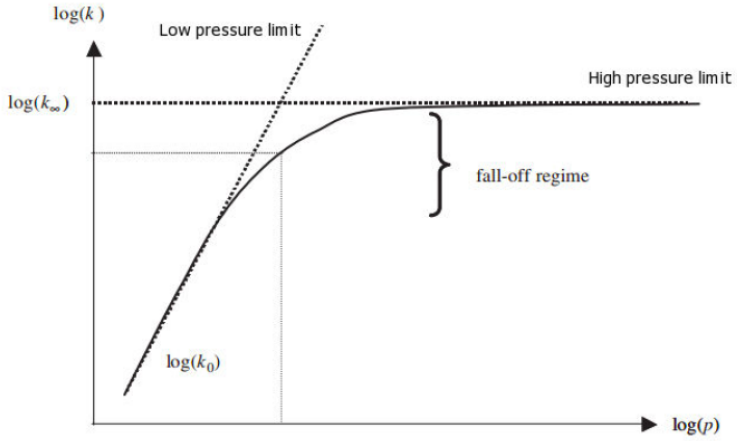

Figure 2.1.1: Reaction rate behavior depending on the pressure for fall-off reactions (extracted from [Felden 2017]).

For this type of reactions, two sets of Arrhenius constants are defined resulting in two reaction rates K_0 and K_∞ respectively for the low pressure and the high pressure limit. The final reaction rate for the fall-off reaction is defined as:

$$K_{fj}(T) = K_\infty \left(\frac{P_r}{P_r + 1} \right) \times F(P_r, T) \tag{2.19}$$

with P_r the reduced pressure expressed as:

$$P_r = \frac{K_0 \times [M]}{K_\infty} \tag{2.20}$$

Note that the pressure dependency is here taken into account through the concentration of the collision partner. The function $F(P_r, T)$ is described with the Troe formulation [Gilbert et al. 1983] or the SRI formulation [Stewart et al. 1989]. If not specified, the unitary function is used and the fall-off reaction is called Lindemann [Lindemann et al. 1922].

P-log

The P-log reaction is another way to take into account the pressure influence. In this case, the Arrhenius coefficients are defined for specific pressures. Then, to get the reaction rate at an intermediate pressure, the latter is logarithmically interpolated between Arrhenius rate expressions at various pressures. For example, given two rate expressions at two specific pressures P_1 and P_2:

$$K_{fj,1}(P_1, T) = A_{j,1} T^{\beta_{j,1}} \exp\left(-\frac{E_{aj,1}}{\mathcal{R}T} \right) \tag{2.21}$$

$$K_{fj,2}(P_2, T) = A_{j,2} T^{\beta_{j,2}} \exp\left(-\frac{E_{aj,2}}{\mathcal{R}T} \right) \tag{2.22}$$

The rate at an intermediate pressure $P_1 < P < P_2$ is computed as:

$$\ln(K_{fj}) = \ln(K_{fj,1}) + (\ln(K_{fj,2}) - \ln(K_{fj,1})) \times \frac{\ln(P) - \ln(P_1)}{\ln(P_2) - \ln(P_1)} \tag{2.23}$$

In this work, when used in CFD solvers, the P-log reactions are converted to simple Arrhenius using the closest set of Arrhenius constants to the pressure operating point. Indeed, the logarithmic interpolations, required at each iteration, add a non-negligible overcost. This modification is done only during the reduction of the ARC schemes (see Chap. 7) and tested a-posteriori.

Duplicated reactions

The duplicated reactions are not a specific type of reaction but rather a mathematical trick to complexify the temperature dependency of the reaction rate that is not possible with a simple Arrhenius form. Hence, using the same reaction with two (or more) different sets of Arrhenius constants provides more degrees of freedom to express the reaction rate. For more simplicity, in this PhD, these reactions will be considered as two (or more) separate entities.

Backward rates

In the case of reversible reactions, the backward reaction rate is computed from a thermodynamic equilibrium. The equilibrium constant $K_{eq,j}$ writes:

$$K_{eq,j} = \left(\frac{P_{atm}}{\mathcal{R}T}\right)^{\sum_{k=1}^{N_{spec}} \nu_{kj}} \times \exp\left(\sum_{k=1}^{N_{spec}} \nu_{kj} \frac{G_k}{\mathcal{R}T}\right) \tag{2.24}$$

with $P_{atm} = 101325\,Pa$ the atmospheric pressure. G_k is the Gibbs free energy of species k and defined as $G_k = H_k - S_k T$, H_k being species k standard enthalpy and S_k its standard entropy. Then the backward reaction rate writes:

$$K_{rj} = \frac{K_{fj}}{K_{eq,j}} \tag{2.25}$$

2.1.4 Thermochemistry and heat release

Combustion is characterized by highly exothermic reactions. Indeed, the global oxidation process of species containing carbon and hydrogen atoms to form CO_2 and H_2O, is known to release a lot of heat. Equations describing the energy source term or heat release rate ($\dot{\omega}_T$) issued from the chemical reactions is required in the energy conservation equation Eq. (1.26).

The energy is initially stored under a chemical form within the electronic bond. During the reaction, the chemical system aims at achieving chemical equilibrium by rearranging the molecular bonds and creating a less energetic mixture. Due to energy conservation, part of the chemical energy is released during the reaction into the mixture, which increases the gas temperature. This exothermic phenomenon applies for the global combustion reaction but also for the majority of the elementary reactions. However, some reactions called endothermic ones absorb the thermal energy of the mixture to store it under a chemical form, leading to a "negative" heat release and a reduction of the temperature. This is the case, for example, with pyrolysis and dissociation processes. These energy variations can be represented with the diagrams on Fig. 2.1.2.

The heat release rate can be expressed with respect to a species ($\dot{\omega}_{T,k}$) computed with Eq. (2.26), or with respect to a reaction ($\dot{\omega}_{T,j}$) computed with Eq. (2.27)

$$\dot{\omega}_{T,k} = -\Delta h^0_{f,k} \times \dot{\omega}_k \tag{2.26}$$

where $\Delta h^0_{f,k}$ is the mass formation enthalpy of species k. The mass formation enthalpy is defined as the heat released from the creation of one kilogram of molecule from its constituting elements at the reference temperature $T_0 = 298\,K$.

$$\dot{\omega}_{T,j} = -\sum_{k=1}^{N_{spec}} \Delta h^0_{f,k} \times \dot{\omega}_{k,j} = -\sum_{k=1}^{N_{spec}} \Delta h^0_{f,k} \times W_k \nu_{k,j} \mathcal{Q}_j \tag{2.27}$$

These quantities are directly related to the total heat release rate $\dot{\omega}_T$ ($[J.m^{-3}.s^{-1}]$) that writes:

$$\dot{\omega}_T = -\sum_{k=1}^{N_{spec}} \Delta h^0_{f,k} \times \dot{\omega}_k = \sum_{k=1}^{N_{spec}} \dot{\omega}_{T,k} = \sum_{j=1}^{N_{reac}} \dot{\omega}_{T,j} \tag{2.28}$$

The partial heat release form (per reaction or per species) is particularly useful in detailed mechanisms to identify dominant reaction pathways as it will be done in Chap. 6.

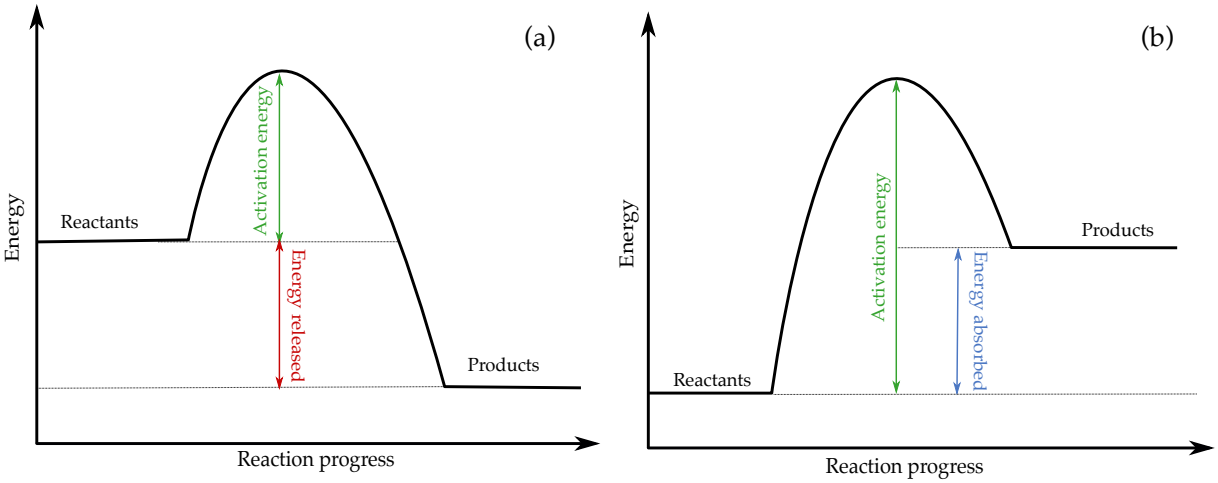

Figure 2.1.2: Energy profile of an exothermic (a) and an endothermic (b) reaction (extracted from [Cazères 2021]).

With CANTERA (and thus with ARCANE)[7], an equation for temperature is used instead of an energy conservation equation. In this case, the heat release rate term is slightly different:

$$\dot{\omega}'_T = -\sum_{k=1}^{N_{spec}} h_k \times \dot{\omega}_k = \sum_{k=1}^{N_{spec}} \dot{\omega}'_{T,k} = \sum_{j=1}^{N_{reac}} \dot{\omega}'_{T,j} \tag{2.29}$$

$$\dot{\omega}'_{T,k} = -h_k \times \dot{\omega}_k \tag{2.30}$$

$$\dot{\omega}'_{T,j} = -\sum_{k=1}^{N_{spec}} h_k \times \dot{\omega}_{k,j} = -\sum_{k=1}^{N_{spec}} h_k \times W_k \nu_{k,j} \mathcal{Q}_j \tag{2.31}$$

with h_k the enthalpy of species k that writes:

$$h_k = h_{s,k} + \Delta h^0_{f,k} = \int_{T_0}^{T} C_{p,k} dT + \Delta h^0_{f,k} \tag{2.32}$$

where $h_{s,k}$ is the sensible enthalpy.

The differences between $\dot{\omega}_T$ and $\dot{\omega}'_T$ are relatively low and the use of the one or the other term for chemical analyses will lead to the same conclusions. However, the correct term is required in the corresponding CFD solvers. Considering the assumption of equal heat capacities of all species, then both expressions are perfectly equals because $\sum_{k=1}^{N_{spec}} \dot{\omega}_k = 0$ (due to the mass conservation). In the following, the nomenclature $\dot{\omega}_T$ will be used for both expressions.

2.1.5 Stoichiometry

As already mentioned, the combustion is an oxidation process of fuel species that produces heat and burnt products. Then, the relative amount of fuel and oxidizer species is an important parameter that characterizes the whole process. The global balanced combustion reaction of hydrocarbon (and di-hydrogen) species is:

$$C_x H_y + s_X (O_2 + n_{N_2/O_2} N_2) = x CO_2 + \frac{y}{2} H_2O + s_X n_{N_2/O_2} N_2 \tag{2.33}$$

with x and y respectively the numbers of carbon and hydrogen atoms in the fuel, s_X is called the molar stoichiometric ratio, and n_{N_2/O_2} is the molar ratio between nitrogen and oxygen ($n_{N_2/O_2} = 3.76$ for classical air composition, made of 21% of di-oxygen and 79% of di-nitrogen). The molar stoichiometric

[7] These codes used for chemical studies are presented in Chap. 3 and 7

ratio corresponds to the molar ratio of air over fuel required for a complete combustion of both fuel and oxidizer. It writes:

$$s_X = x + \frac{y}{4} = \left(\frac{X_{oxidizer}}{X_{fuel}}\right)_{st} \tag{2.34}$$

In this case, the mixture is at stoichiometric proportions represented with the $_{st}$ index. With air, the oxidizer molar fraction is defined as $X_{oxidizer} = X_{O_2} + X_{N_2}$. For multi-component fuel, the fuel molar fraction is defined as $X_{fuel} = \sum_{k=1}^{N_{fuel}} X_k$, and x and y are respectively the number of carbon and hydrogen atoms in the fuel mean formula (weighted by the mole fraction).

The equivalence ratio ϕ is introduced to represent the excess of fuel also called rich regime ($\phi > 1$), or the excess of oxidant also called lean regime ($\phi < 1$):

$$\phi = \frac{X_{fuel}}{X_{oxidizer}} \times \left(\frac{X_{oxidizer}}{X_{fuel}}\right)_{st} = s_X \times \frac{X_{fuel}}{X_{oxidizer}} \tag{2.35}$$

The equivalence ratio can also be expressed in mass:

$$\phi = \frac{Y_{fuel}}{Y_{oxidizer}} \times \left(\frac{Y_{oxidizer}}{Y_{fuel}}\right)_{st} = s_Y \times \frac{Y_{fuel}}{Y_{oxidizer}} = s_Y \times \frac{m_{fuel}}{m_{oxidizer}} \tag{2.36}$$

with s_Y the mass stoichiometric ratio that writes:

$$s_Y = \frac{s_X W_{oxidizer}}{W_{fuel}} \tag{2.37}$$

where $W_{oxidizer} = W_{O_2} + n_{N_2/O_2} W_{N_2} = 137.28\, kg.mol^{-1}$, and $W_{fuel} = \sum_{k=1}^{N_{fuel}} W_k X_k$.

Other definitions of stoichiometric ratios consider the oxidizer to be only the di-oxygen [Poinsot and Veynante 2012]. In this case, the mass stoichiometric ratio writes:

$$s_{Y,O_2} = \left(\frac{Y_{O_2}}{Y_{fuel}}\right)_{st} = \frac{s_X W_{O_2}}{W_{fuel}} \tag{2.38}$$

and the equivalence ratio:

$$\phi = \frac{Y_{fuel}}{Y_{O_2}} \times \left(\frac{Y_{O_2}}{Y_{fuel}}\right)_{st} = s_{Y,O_2} \times \frac{Y_{fuel}}{Y_{O_2}} = s_{Y,O_2} \times \frac{m_{fuel}}{m_{O_2}} \tag{2.39}$$

Finally, the local equivalence ratio can also be based on an atomic budget as done in Cazères [2021]:

$$\phi_{loc} = \frac{2n_C + 0.5n_H}{n_O} \tag{2.40}$$

where n_C, n_H and n_O are respectively the number of carbon, hydrogen and oxygen atoms locally in the mixture. This expression is more convenient and general as it can be applied to the whole mixture even if fuel and oxidant species are not present (fresh gases, core flame front and burnt gases), and enables easily to assess fuel composition variations encountered with multi-component fuel evaporation. In the following, this definition will be used and directly labeled ϕ.

2.2 Implementation strategies for numerical simulations

The elementary reactions presented in the previous section and the associated Arrhenius rate constants are gathered in detailed kinetic mechanisms. Such chemical mechanisms are developed by the chemical scientific community based on accurate experimental measurements and complex quantum computations. From the point of view of the numerical combustion community, the detailed chemistries are considered as reference chemical processes that describe with the highest accuracy the evolution of a reactive system in all possible configurations.

However, the objective being to be the most accurate possible, always more species and reactions are taken into account. For example, Fig. 2.2.1 shows the evolution of the number of species and reactions in detailed chemical mechanisms. Recent chemical schemes developed by the CRECK modeling group from Politecnico di Milano (POLIMI)[8] reach more than 500 species and 27000 reactions.

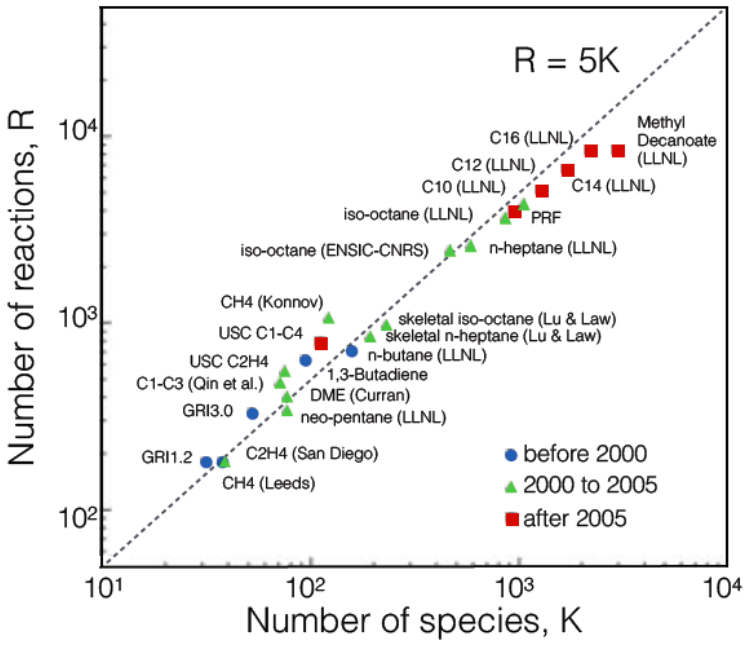

Figure 2.2.1: Exponential increase of mechanism size for hydrocarbon applications (extracted from [Lu and Law 2009]).

This large number of species and reactions is an issue for numerical simulations. Indeed, for explicit solvers, each new species requires an additional transport equation with the corresponding transport properties, and each reaction requires the computation of the corresponding rates. At the end, the memory and CPU costs for the use of detailed chemistries is prohibitive. Such kinetic mechanisms are restricted to simple 0/1-dimensional configurations. To overcome this issue, several implementation strategies are available and presented in the following sections.

2.2.1 Global Chemistry

At the opposite of the detailed chemistry lies the global chemistry. Contrary to the detailed schemes, the objective of the global chemistry approach, introduced by Westbrook and Dryer [1981], is to reproduce macroscopic quantities such as flame speed or adiabatic flame temperature keeping the number of reactions and species as small as possible.

Generally, these schemes consist in two reactions allowing an easy and fast implementation in combustion codes. The first R1 drives the fuel consumption and so the laminar flame speed while the second R2, corresponds to the CO/CO_2 equilibrium enabling to reach the correct adiabatic flame temperature.

$$C_xH_y + \left(\frac{x}{2} + \frac{y}{4}\right) O_2 \rightarrow xCO + \frac{y}{2}H_2O \tag{R1}$$

$$CO + 0.5O_2 \leftrightarrow CO_2 \tag{R2}$$

Furthermore, to be able to recover the correct laminar flame speed in the whole range of equivalence ratio, a Pre-Exponential Adjustment (PEA) function [Franzelli et al. 2010] is added to compute the reaction rate of the first reaction.

[8] http://creckmodeling.chem.polimi.it/

Due to its reduced cost, the global chemistry is a powerful approach to evaluate the combustion performances in complex 3-dimensional LES simulations of combustion chambers. However, when dealing with specific complex phenomena such as ignition, extinction, or pollutant emissions, this approach is not accurate enough.

2.2.2 Analytically Reduced Chemistry

An in-between solution is the Analytically Reduced Chemistry (ARC). The objective is to develop a chemistry accurate enough to target specific combustion phenomena while conserving a limited number of species and reactions to be used in 3-dimensional simulations with explicit solvers.

The chemical reduction is proceeded in two steps. Firstly, a skeletal reduction is computed. The species and reactions with low importance with respect to the combustion phenomena to study are discarded. Such information can be obtained with graph methods [Pepiot-Desjardins and Pitsch 2008b]. Then, with the Quasi-Steady-State Approximation (QSSA) [Lu and Law 2006], algebraic relations are used to model the effect of some species corresponding to this approximation. These QSS species are no more transported which reduces the CPU-cost. Indeed, less transport equations are solved and the numerical stiffness associated to these species is removed which enables to use large time-steps.

This strategy has been chosen in this work to reproduce accurately ignition processes, to study the effect of the high altitude conditions and to take into account a multi-species fuel formulation. Furthermore, ARC schemes conserve the structure of the reference detailed schemes. Hence, the chemical behavior for conditions or processes close to the targeted ones should remain valid. In that sense, the ARC formalism is more robust and adapted to the 3-dimensional combustion chamber simulations that include a large panel of local conditions and combustion processes. Finally, since the main chemical processes are conserved, the chemical analysis are facilitated and the species concentrations measured are close to those observed with the detailed approach or to the experimental measurements.

More information on the reduction methods and the developments of ARC schemes for methane and kerosene fuels are presented Chap. 7.

2.2.3 Tabulated Chemistry

The tabulated chemistry is a totally different approach where kinetic reactions are not resolved by CFD solvers. Instead, in the tabulated chemistry formalism, the species are assumed to be linked by a reduced number of variables/coordinates. For example, Maas and Pope [1992] have shown a flame structure may only be described by the progress variable ($c = \mathcal{F}(T)$) and the mixture fraction ($z = \mathcal{F}(\phi)$)[9]. Hence, using a reference flame database, each value c and z can be associated to a specific mixture composition and the associated heat release or temperature.

From an algorithmic point of view, this method requires a pre-processing phase where the flame database is constructed and reduced to a multi-dimensional thermochemical table with a limited number of coordinates. Then, the CFD code solves additional transport equations for the coordinates. Finally, thermochemical information are obtained through interpolations of the table.

This formalism, first introduced by Peters [1984], was developed in the FPI (Flame Prolongation of Intrinsic Low Dimensional Manifold) model [Gicquel et al. 2000] and more recently in the F-TACLES (Filtered Tabulated Chemistry for Large Eddy Simulation) model [Fiorina et al. 2010].

Interested readers are referred to Fiorina [2012] where the implementation of the tabulated chemistry formalism is more detailed with the correct choice of the coordinates depending on the physical phenomenon studied, as well as the modeling of the turbulence-combustion interaction.

In this work, this approach has not been chosen for several reasons. Firstly, the choice of the reduced variables has a large impact on the results. Indeed, if they are not well defined, some chemical processes

[9] More accurate definitions are given in Chap. 3

can be missed. Secondly, since the kinetic reactions are not conserved, and only the flame database is used to build the table, then, only the information included to the flame database can be used. For example, using the flamelet assumption stating that a reaction zone locally behaves as a laminar flame, the ignition phenomena may not be well reproduced. To take into account a large number of combustion phenomena, the table dimension must be increased as well as the diversity of the initial flame database which increases the cost of the method. Finally, it also requires to know apriori the combustion processes to integrate to the table. As consequences, the tabulated chemistry formalism seems more adapted for academical configurations with well defined operating points, and where the combustion processes are known.

2.2.4 Virtual Chemistry

The virtual chemistry formalism developed by Cailler et al. [2017] uses virtual species and reactions to model a behavior close to the detailed chemistry. The scheme development consists in an optimization, via genetic or machine learning algorithms, of the reactions constants and the virtual species properties. After the combustion simulation, a post-processing step must be applied to convert the virtual species field in a physical field.

Similarly to the tabulated or global methods, the chemical structure of the detailed scheme is not conserved. Then, it is not possible to perform a fine analysis of the chemical pathways leading to the final results, especially with the virtual species which do not correspond to physical chemical entities. Furthermore, the complex optimization procedure can lead to either a lack of accuracy, or an over-fitting of the optimization points reducing the robustness of the virtual scheme for extended operating conditions.

2.3 Carbonated chemistry

This PhD is focused on the hydrocarbon combustion and thus the carbonated chemistry. The hydrocarbon molecules are composed of carbon and hydrogen atoms (C_xH_y). The general characteristics of this chemistry are presented in Sec. 2.3.1 while Sec. 2.3.2 and Sec. 2.3.3 respectively introduce the reference detailed chemical schemes and fuel modeling used in this work.

2.3.1 General characteristics

The kinetic mechanisms for hydrocarbon combustion are often hierarchically structured. The combustion of heavy fuel is basically decomposed in a first pyrolysis phase. This phase produces light species composed of one to three carbon atoms. The second step corresponds to the oxidation of the light species into combustion products. Hence, in detailed mechanisms such as the one developed by the CRECK modelling group [Ranzi et al. 2012], the reactions are hierarchized in different families: hydrogen oxidation, methane oxidation, C2 species oxidation, and so on until the kerosene pyrolysis.

Radical species have a major influence in the oxidation processes of hydrocarbon species. As introduced in Sec. 2.1.1, a radical is a component with its outer electron layer unfilled. Thus, these species are very reactive and good reaction intermediates. Due to their reactivity, the radical concentrations are generally low. These species are directly consumed as soon as they are produced. However, they are needed in the elementary reaction formalism. Therefore, the reactions can be sorted depending on their radical behavior [Warnatz et al. 2006]:

- **Chain-initiation:**
  These reactions are characterized by the formation of a radical species from stable initial ones. These reactions are generally the first reaction steps: reactions between fuel and oxidizer as with (R1), or pyrolysis reactions.
  $$H_2 + O_2 \rightarrow 2\,OH\cdot \tag{R1}$$
- **Chain-propagation:**
  This second category corresponds to reactions between a radical species and a stable species to form another radical. For example, the H abstraction (R2):
  $$H_2 + OH\cdot \rightarrow H_2O + H\cdot \tag{R2}$$

- **Chain-branching:**
  These reactions are similar to the chain-propagation ones, however, in this case, the number of radical species increases at the end of the reaction, as in (R3). These reactions are critical in combustion processes, especially for the chemical runaway occurring during the ignition.

$$\mathrm{H}\cdot + \mathrm{O_2} \rightarrow \mathrm{OH}\cdot + \mathrm{O}\cdot \tag{R3}$$

- **Chain-termination:**
  These reactions are characterized by the reformation of stable species, often the combustion products as with (R4).

$$\mathrm{H}\cdot + \mathrm{OH}\cdot + \mathrm{M} \rightarrow \mathrm{H_2O} + \mathrm{M} \tag{R4}$$

In the following chapters, the dot symbol used to indicate a radical species will not be written for simplicity and readability reasons. A radical species can be implicitly determined with the number of chemical bonds between atoms.

2.3.2 Methane combustion

Methane (CH_4) is the simplest alkane because composed of a single carbon atom. It is the major component of natural gas, and generally used in gas turbines or furnaces. Hence, it has been largely experimentally and numerically studied as testify the reviews from Felden [2017] and the paper from Ranzi et al. [2012]. Furthermore, this species is often used as a first step to study the ignition processes (see the review in Chap. 4). Indeed, the methane chemistry, especially the methyl decomposition (CH_3), is a fundamental mechanism involved in all hydrocarbon combustion processes.

The main combustion mechanism of methane follows the decomposition presented on Fig. 2.3.1. Firstly the methane decomposes into methyl. Then, the latter is successively converted into formaldehyde (CH_2O), formyl (HCO) and carbon monoxide (CO). The last step is the formation of carbon dioxide (CO_2) in the post-flame region.

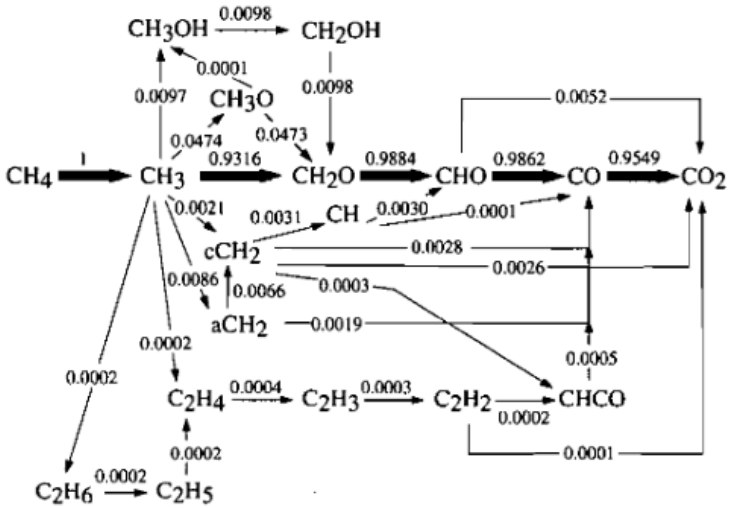

Figure 2.3.1: Decomposition pathways of methane oxidation in lean condition (extracted from [Frouzakis and Boulouchos 2000]).

In this work, the methane chemistry is used to develop the chemical analysis tools (see Chap. 6) and to test the new reduction methods on simplified cases (see Chap. 7).

Several detailed chemical schemes are available to model the methane combustion. Among them, the GRI3.0 [Smith et al. 2000] and the USC Mech II [Wang et al. 2007] are the most widespread in the literature. However, these mechanisms are not anymore up to date with the recent studies. Hence, for this work, a more recent scheme has been chosen from the CRECK Modeling group[10] [Ranzi et al. 2012;

[10] http://creckmodeling.chem.polimi.it/

2014; 2015][11]. The latter presents a good agreement with experimental measurements for the whole range of flammability limits as shown on Fig. 2.3.2. Moreover, it enables to test proper functioning of the analysis and reduction algorithms on the latest kinetic schemes versions. It is composed of 151 species and 2335 reactions allowing an accurate description of C1 to C3 alkanes combustion including NOx. This mechanism is labelled S151R2335 in the following.

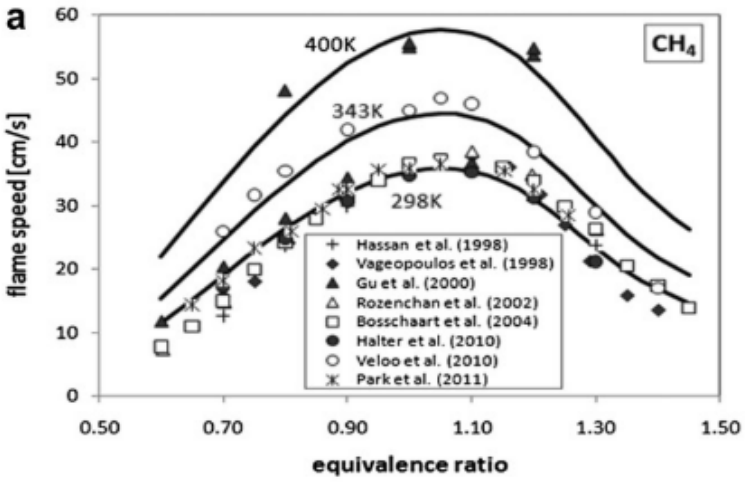

Figure 2.3.2: Laminar flame speed for methane-air combustion at atmospheric pressure (extracted from [Ranzi et al. 2012]).

2.3.3 Kerosene combustion

This PhD is mainly focused on kerosene ignition. A suited fuel modeling and a reference chemical mechanism are then required.

Fuel modeling

Contrarily to natural gas which is mainly composed of methane, kerosene fuels are actually a blend of multiple hydrocarbons with different properties. The Jet-A1 is the reference kerosene fuel for aeronautical applications (defined by the Aviation Fuel Quality Requirements for Jointly Operated Systems) and its composition[12] has been measured in the context of the JETSCREEN project[13]. Fig. 2.3.3 provides the mass distribution of each hydrocarbon family depending on the species number of carbon atoms. In the context of CFD computations, taking into account the real fuel composition is not feasible due to the large number of species and chemical pathways associated. Then, modeling strategies are required.

The simplest strategy is to model the fuel by a single species. In this way, kerosene fuels are often modeled with n-decane or n-dodecane since alkanes are the most abundant family and are close to the average chemical formula : $C_{10.52}H_{17.78}$. Such surrogates have been largely used in the literature [Dagaut and Gaïl 2007, Luche 2003, Jaravel 2016]. In a recent study, Hajiw-Riberaud and Alves-Fortunato [2020] used 1,2,3,4-tetramethylcyclohexane as a possible equivalent molecule. However, single species surrogates often lack representativity. Indeed, it is not possible to get at the same time similar reactivity, transport, thermodynamic, and two phase-flow properties.

To overcome this issue, a multi-component approach can be used. In this case, the fuel surrogate is a blend of several representative species. The species and proportions used are chosen with an optimization step to satisfy different key targets such as Derived Centane Number (DCN), H/C ratio, distribution of masses within the different hydrocarbon families, average molecular weight, sooting index, liquid density, liquid viscosity, distillation curves, etc. Hence, the multi-component approach allows to account for

[11] Mechanism version corresponds to May 2018
[12] The general Jet-A1 composition is not fixed and may vary depending on the refinement process and origin.
[13] https://cordis.europa.eu/project/id/723525

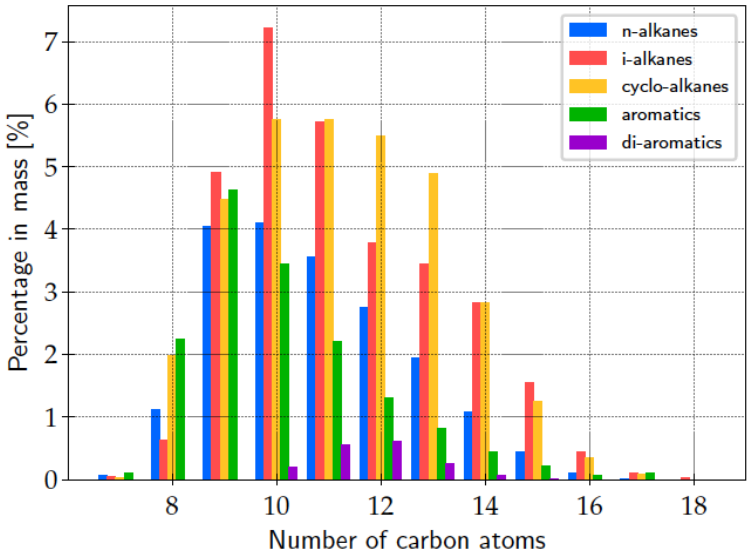

Figure 2.3.3: Mass distribution (in percentage of total mass) according to the number of carbon atoms in the species and its hydrocarbon family (extracted from Cazères [2021])

varied kinetic pathways more representative of pyrolysis mechanisms and auto-ignition. Furthermore, the multi-component strategy enables to take into account the preferential evaporation (i.e the delayed evaporation of the fuel components depending on their volatility) that plays a key role in spray flame propagation and ignition [Stagni et al. 2017, Shastry et al. 2020]. One possible issue is the multiplication of chemical pathways corresponding to each fuel species of the blends. It has been the case in Felden [2017] where the multi-component approach leads to a reduced mechanism composed of 136 species and 1148 reactions.

Another approach is to model the fuel decomposition into a reduced set of reactions to get the pyrolysis products that will be then oxidized. This methodology called HyChem has been developed by Wang et al. [2018]. It is based on the observation that for kerosene blends composed of several species, the pyrolysis step leads to a reduced number of key pyrolysed species. Furthermore, a punctual modification of fuel species or proportion in the blend has a negligible effect due to the reduced influence of each species independently. Then, the kerosene combustion modeling relies on the correct prediction of pyrolysed products. In the case of HyChem, the pyrolysis scheme is fitted on experimental data. This methodology has been successfully used in LES of industrial combustion chamber by Felden et al. [2018a]. Good results in terms of accuracy and computational cost have been obtained due to the reduction of a large number of species and chemical pathways in the pyrolysis step. However, this approach does not describe preferential evaporation allowed in the multi-component formulation, and prevents the study from the high altitude condition effects on the fuel pyrolysis step during the ignition.

In this work, only the multi-component approach is used. The issue concerning the large number of species and reactions is solved in this case thanks to the new reduction tool ARCANE (see Chap. 7) and shared decomposition pathways (see Chap. 6). The surrogate composition has been proposed by the CRECK modeling Team from Politechnico Di Milano from [Humer et al. 2011]. It consists in mole fraction of 60% of n-dodecane, 20% of methylcyclohexane, and 20% of xylene (molecular structure shown on Fig. 2.3.4). This blend has been already used in different proportions [Narayanaswamy and Pepiot 2018]. N-dodecane is a linear alkane representative of the paraffin behavior. Methylcyclohexane is representative of cyclic species. Xylene represents the aromatic components composed of double chemical bonds and is a lumped species corresponding to the three xylene isomers (ortho-, metha- and para-). From analyses done by IFPEN (in the context of JETSCREEN) [Hajiw-Riberaud and Alves-Fortunato 2020], Jet A1 fuel exhibits a H/C ratio of 1.94, and a liquid density of 789.7 $kg.m^{-3}$ (at ambient conditions). For the surrogate and using simple mixing law, we obtain close properties with a H/C ratio of 2 and a liquid density of 775 $kg.m^{-3}$.

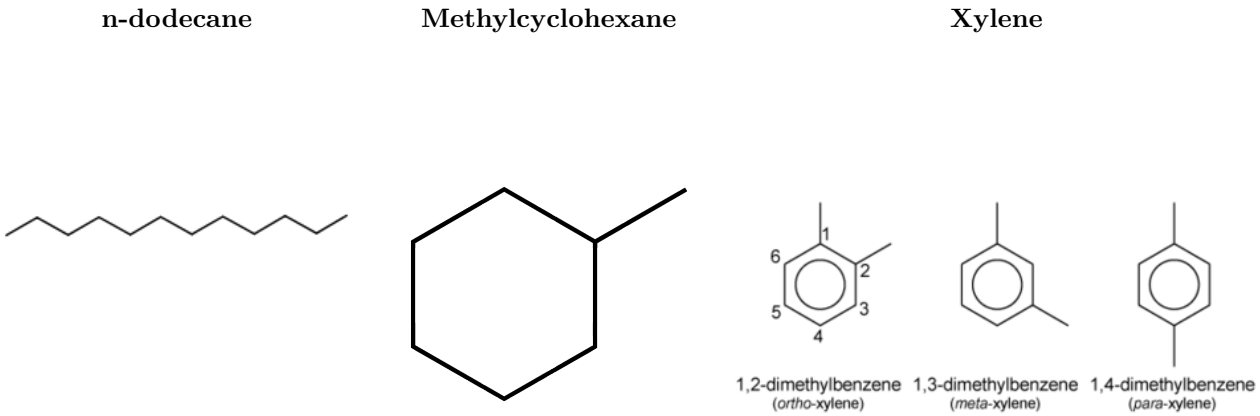

Figure 2.3.4: Three-component surrogate.

Reference mechanism

In this work, the studies of kerosene ignition are performed using the chemistry developed by the CRECK Modeling Group [Ranzi et al. 2012]. This hierarchical mechanism[14] composed of 491 species and 15276 reactions allows an accurate description of C1 to C16 carbonated species including high and low temperature chemical pathways Ranzi et al. [2015]. This mechanism incorporates most of the species involved in jet fuel combustion and is suited for multi-component surrogates. This chemistry has been validated with experimental measurements [Ranzi et al. 2014] and will be considered as reference. This mechanism is labelled S491R15276 in the following parts. Chemistries developed by the CRECK Modeling Group have been already successfully used for reductions, for multi-component surrogate modelings, to study two-phase flow flames, and in the context of alternative fuels [Shastry et al. 2020, Cazères 2021, Wirtz et al. 2021].

[14] Mechanism version corresponds to September 2019

Chapter 3

Theoretical concepts of combustion

Contents

This chapter aims to introduce general concepts of combustion. This chapter does not pretend to be extensive but only to provide the necessary knowledge on combustion for the comprehension of this work. These theoretical notions can be found in combustion textbooks [Kuo 2005, Poinsot and Veynante 2012, Peters 2000]. The classical laminar flame structures are first introduced with their general characteristics. Secondly, canonical combustion cases used for the numerical study of elementary combustion processes are detailed. Then, the effect of the turbulence on the combustion is presented. Finally two-phase flow combustion phenomena are discussed in the last section. A more detailed literature review dedicated to the ignition processes is presented in Chap. 4.

3.1 Laminar flame structure

The study of laminar flames is important because these flames are observed in several combustion processes, for example, at the first stages of ignition. Their description and understanding is at the basis of more complex phenomena such as turbulent combustion.

3.1.1 Premixed flames

Premixed combustion occurs when fuel and oxidizer are mixed before reaching the flame front and start reacting.
The structure of a premixed flame is presented on Fig. 3.1.1 and is composed of several distinct zones:

- **Preheat zone:**
  In this zone located before the flame front, the fresh gases are heated by the reactive zone via thermal diffusion, which explains the importance of the transport properties. For heavy hydrocarbon combustion, the fuel pyrolysis also starts in the preheat zone when the temperature is high enough.

- **Inner reaction zone:**
  Once the fresh gases are hot enough, exothermic reactions can start and fuel or pyrolysis products are oxidised. This zone is characterised by a large temperature gradient and the heat release rate peak. The reaction zone also concentrates all the transitory radical species. Hence, the major part of the species is located in this thin zone.

- **Post-flame region:**
  The post-flame region corresponds to the end of the final products formation like the conversion of CO to CO_2, the pollutant formation (soots, NOx,...), and where the mixture reaches the equilibrium.

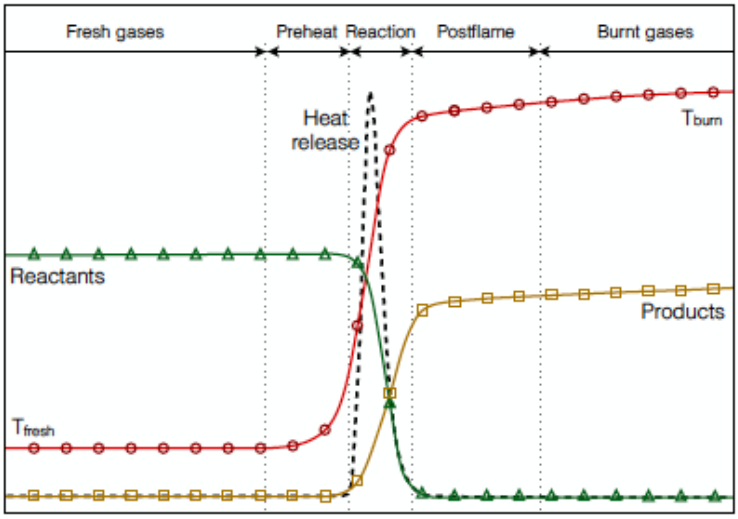

Figure 3.1.1: Schematic description of the laminar premixed flame structure (extracted from Esclapez [2015])

3.1.2 Diffusion flames

In several applications and for safety reasons, fuel and oxidizer are stored and injected separately in the combustion chamber. This configuration without mixing the combustion reactants leads to diffusion flames.

If fuel and oxidizer are not mixed, an interface can be defined, corresponding to the position where the reactants are in stoichiometric proportions. This interface is called the stoichiometric line. On one side (rich side), there is a fuel excess, while on the other side (lean side), there is an oxidizer excess. The diffusion flame structure is presented on Fig. 3.1.2.

Because the optimal combustion and maximum consumption speed are reached at stoichiometry, the flame is stabilized at the stoichiometric line as well as the temperature and heat release peaks. Hence,

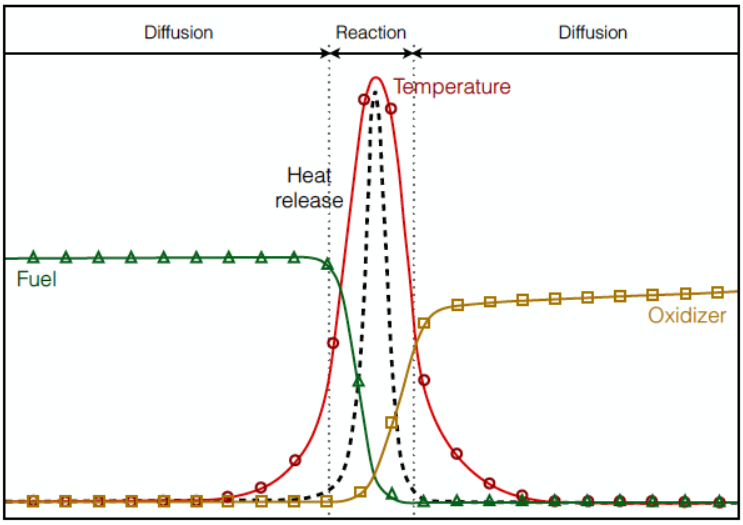

Figure 3.1.2: Schematic description of the laminar diffusion flame structure (extracted from Esclapez [2015])

the diffusion flame differs from the premixed flame by the absence of propagation. The flame displacement is driven by the stoichiometric line motion induced by the flow. The combustion is maintained by the diffusion of fuel and oxidizer towards the flame. Thus, this flame is totally driven by species diffusion effects which give its name.

3.1.3 Partially premixed flames

In real aeronautical systems, combustion occurs in a partially premixed regime. As explained previously, the fuel and oxidizer are injected separately for safety reasons. However, a better combustion efficiency is obtained with a premixed fuel-air mixture. Therefore, the mixing is done when entering in the combustion chamber using swirlers and advanced injection systems. Such systems are presented and studied in Chap. 11. Still, due to liquid fuels and large evaporation characteristic times, there is an incomplete mixing leading to equivalence ratio inhomogeneities and possible diffusion flame structures. More information on two-phase flames are given in Sec. 3.5.

To distinguish premixed from diffusion combustion regimes, the Takeno index [Yamashita et al. 1996] is generally used:

$$TI = \frac{\nabla Y_{fuel} \cdot \nabla Y_{oxidizer}}{|\nabla Y_{fuel} \cdot \nabla Y_{oxidizer}|} \tag{3.1}$$

For a premixed case, the gradients of fuel and oxidizer have the same sign, thus the resulting Takeno index is positive. On the contrary, for diffusion flames structures, the gradients are opposed resulting in a negative Takeno index.

In the case of ARC chemistries and differential evaporation of multi-component surrogate fuels, fuel species are not produced at the same time and in the same proportions. Thus, the species specified as fuel in Eq. (3.1) must be carefully chosen. Furthermore, mixed combustion regimes can be observed where the fuel decomposition is premixed while there is not enough oxidizer to unsure a complete combustion of the intermediate products. In this case, the oxidation of the pyrolysis products can adopt a diffusion structure. Such structures can be studied using a combination of several pyrolysis products as fuel in Eq. (3.1).

3.2 General flame characteristics

The premixed and diffusion flames can be characterised using several properties such as propagation velocity, fuel consumption speed, thickness or stretch. These properties are important because they en-

able to describe the flame behavior. Moreover, these properties are often used to study the interaction between the flame and the turbulent flow.

3.2.1 Combustion and mixture characterization

Progress variable

As shown on Fig. 3.1.1, for a premixed flame, the mixture evolves from a fresh gases state to a burnt gases state. The progress variable c is introduced to capture this transition as used in [Fiorina 2012]. This variable is generally defined by a species combination to get a monotonic evolution. If this condition is satisfied, then, there is a unique temperature and gas composition associated to the progress variable value:

$$T, Y_k = f(c) \tag{3.2}$$

The progress variable is generally normalised such that $c = 0$ in the fresh gases and $c = 1$ in the burnt gases:

$$c = \frac{Y_c - Y_{c,f}}{Y_{c,b} - Y_{c,f}} \tag{3.3}$$

with Y_c the progress variable mass fraction, and b and f subscripts referring respectively to the burnt gases and fresh gases. With this normalization, the progress variable is a passive scalar that can be used in a transport equation to track the flame front displacement (see Sec. 3.2.2).

The choice of the chemical species defining the progress variable mass fraction depends on the phenomena to study. For example, using CO and CO_2 species, the position of the flame front is well described [Fiorina 2012]:

$$Y_c = Y_{\mathrm{CO}} + Y_{\mathrm{CO_2}} \tag{3.4}$$

However, the prediction of NOx pollutants is incorrect because their formation via thermal pathway is much longer than the CO_2 formation. To solve this, NOx fractions can be added to the definition [Fiorina 2012]:

$$Y_c = Y_{\mathrm{CO}} + Y_{\mathrm{CO_2}} + Y_{\mathrm{NO}} \tag{3.5}$$

There is a similar issue for the fast phenomena such as the ignition processes. Indeed, the main combustion products are not created at the first instants. In this case, the fuel mass fraction is generally added to the definition of the progress variable [Fiorina 2012]:

$$Y_c = Y_{\mathrm{CO}} + Y_{\mathrm{CO_2}} - Y_{fuel} + Y_{fuel,f} \tag{3.6}$$

Finally, for simple cases or simplified chemistries, the temperature evolution is generally monotonic, then it can be used to define the progress variable[1]:

$$c = \frac{T - T_f}{T_b - T_f} \tag{3.7}$$

Mixture fraction

Similarly to the progress variable, the mixture fraction z is a passive scalar that enables to quantify, for diffusion flames structures, the mixing between the fuel and the oxidizer [Poinsot and Veynante 2012]. In pure fuel mixture $z = 1$, whereas for pure oxidizer mixture $z = 0$.

The mixture fraction is generally computed using the definition proposed by Bilger [1989]:

$$z = \frac{\beta - \beta_{oxidizer}}{\beta_{fuel} - \beta_{oxidizer}} \tag{3.8}$$

[1] Does not work for complex ARC mechanisms where pyrolysis and dissociation phenomena can reduce the temperature and create non monotonic variations. Dilution and wall thermal losses effects may also induce non monotonic variations. Finally, for spark ignitions, the temperature field is modified by the energy deposit and does not characterise the combustion state.

where β is defined with the mass fraction of atomic elements:

$$\beta = \sum_{\mathcal{A}}^{N_{elem}} \gamma_{\mathcal{A}} Y_{\mathcal{A}} = \sum_{\mathcal{A}}^{N_{elem}} \gamma_{\mathcal{A}} \sum_{k=1}^{N_{spec}} \frac{n_{\mathcal{A},k} W_{\mathcal{A}} Y_k}{W_k} \tag{3.9}$$

with $n_{\mathcal{A},k}$ the number of atoms $\mathcal{A}$ in species k, $Y_{\mathcal{A}}$ the mass fraction of atom $\mathcal{A}$, and $W_{\mathcal{A}}$ and W_k are respectively the molar weight of atom $\mathcal{A}$ and species k. $\gamma_{\mathcal{A}}$ is the weighting parameter corresponding to atom $\mathcal{A}$ and writes:

$$\gamma_{\mathrm{C}} = \frac{2}{W_{\mathrm{C}}} \quad \gamma_{\mathrm{H}} = \frac{1}{2W_{\mathrm{C}}} \quad \gamma_{\mathrm{O}} = \frac{-1}{W_{\mathrm{O}}} \quad \gamma_{\mathrm{N}} = 0 \tag{3.10}$$

Using a unity Lewis number assumption ($\lambda/(\rho C_p D_k) = 1$) the mixture fraction is solution of the following transport equation:

$$\frac{\partial \rho z}{\partial t} + \frac{\partial \rho u_j z}{\partial x_j} = \frac{\partial}{\partial x_j}\left(\rho D_z \frac{\partial z}{\partial x_j}\right) \tag{3.11}$$

with $D_z = \lambda/(\rho C_p)$ the diffusion coefficient of the mixture fraction.

Finally, the local equivalence ratio of the mixture is linked to the mixture fraction with the following relationship:

$$\phi = \frac{z(1 - z_{st})}{z_{st}(1 - z)} \tag{3.12}$$

where z_{st} is the mixture fraction corresponding to a stoichiometric mixture and is computed with Eq. (3.8) and $\beta_{st} = 0$.

3.2.2 Flame speed

To determine the flame speed, the flame front and its normal have to be defined which can be done using the progress variable. The flame front is represented with a progress variable iso-surface and the normal with its gradient:

$$c(\vec{x}, t) = c^* \qquad \vec{n} = -\left.\frac{\vec{\nabla} c}{|\vec{\nabla} c|}\right|_{c=c^*} \tag{3.13}$$

Using this definition, the normal is directed towards the fresh gases.

There are several definitions that can be used for the flame speed depending on the reference frame or the physical phenomena studied. These definitions are represented on Fig. 3.2.1:

- **Local flame front velocity $\vec{w}$:**
  This definition derived from the differentiation of the Eq. (3.13) [Peters 2000]:

$$\frac{\partial c}{\partial t} + \vec{\nabla} c \cdot \left.\frac{\partial \vec{x}}{\partial t}\right|_{c=c^*} = \frac{\partial c}{\partial t} + \vec{\nabla} c \cdot \vec{w} = 0 \tag{3.14}$$

- **Absolute speed S_a:**
  This speed corresponds to the projection of $\vec{w}$ on the flame front normal:

$$S_a = \vec{w} \cdot \vec{n} = \frac{1}{|\vec{\nabla} c|} \frac{\partial c}{\partial t} \tag{3.15}$$

- **Displacement speed S_d:**
  This speed correspond to the flame front displacement in the gaseous flow reference frame. Hence, this speed relies on the flow velocity and the front velocity:

$$S_d = S_a - \vec{u} \cdot \vec{n} = \frac{1}{|\vec{\nabla} c|} \frac{\partial c}{\partial t} + \vec{u} \cdot \frac{\vec{\nabla} c}{|\vec{\nabla} c|} \tag{3.16}$$

  If c is a passive scalar, i.e. the unity Lewis assumption is used, this speed can be also computed using its conservation equation [Gibson 1968, Peters 2000]:

$$S_d = \left.\frac{\vec{\nabla} \cdot (\rho D_c \vec{\nabla} c) + \dot{\omega}_c}{\rho |\vec{\nabla} c|}\right|_{c=c^*} \tag{3.17}$$

with $\dot{\omega}_c$ the chemical source terms of the species defining c and D_c the diffusion coefficient equal for all species since the unity Lewis assumption is used.

The Eq. (3.17) can be divided in three main components [Gran et al. 1996, Echekki and Chen 1999, Peters et al. 1998]:

$$S_d = \underbrace{\frac{\vec{n} \cdot \overrightarrow{\nabla(\rho D_c \vec{n} \cdot \vec{\nabla} c)}}{\rho |\vec{\nabla} c|}}_{\text{Normal diffusion}} - \underbrace{D_c \vec{\nabla} \cdot \vec{n}}_{\text{Tangential diffusion}} + \underbrace{\frac{\dot{\omega}_c}{\rho |\vec{\nabla} c|}}_{\text{Reaction}} \tag{3.18}$$

As for the previous definitions, the value of S_d changes across the flame front and depends on the value c^* chosen as reference. Furthermore, this speed is often weighted by the density to account for the gas expansion effect:

$$S_d^* = \frac{\rho(c = c^*)}{\rho_f} \times S_d \tag{3.19}$$

- **Consumption speed S_c:**
  This last speed is defined using the mass conservation across the flame front, hence it is expressed with the fuel consumption rate:

$$S_c = -\frac{1}{\rho_f Y_{F,f}} \int_{\text{fresh}}^{\text{burnt}} \dot{\omega}_F d\vec{n} \tag{3.20}$$

  This speed compared to the others above is a global quantity which explains why it is often preferred to analyse the reactive flows.

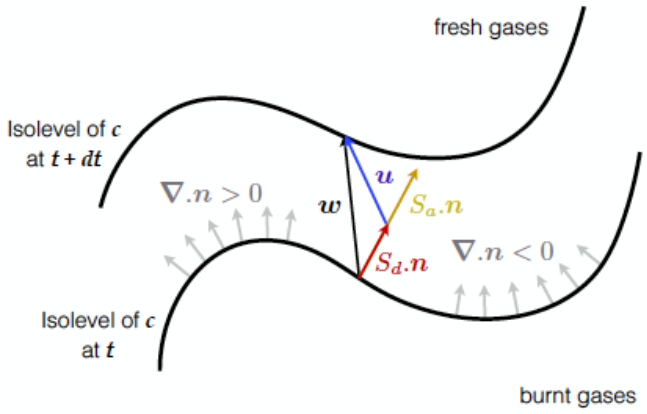

Figure 3.2.1: Representation of the different flame speed definitions (extracted from Esclapez [2015]).

For a non-stretched laminar premixed flame, the flame speed writes:

$$S_d^* = S_c = S_L \tag{3.21}$$

where S_L is called the laminar flame speed.

The previous definitions apply only for premixed flames. Indeed, for diffusion flames there is no propagation since the flame remains at the stoichiometric line. Hence the local flame front velocity is only driven by the flow velocity and $S_d = 0$. However, the consumption speed still can be defined with the fuel consumption rate.

3.2.3 Flame thickness

The flame thickness is an important parameter for the simulations because it enables to define the mesh resolution required for the combustion processes. Since the reaction zone concentrates the major part of the radical species and combustion mechanisms, it must be carefully resolved. Moreover, the flame thickness plays an important role in the flame turbulence interaction as it will be detailed in Sec. 3.4.

Premixed thicknesses

As for the flame speed, several characteristic thicknesses can be used depending on the physical phenomena studied:

- **Thermal thickness δ_{th}:**
  This thickness is based on the temperature gradient in the flame front. This thickness is the most used and enables to estimate grid resolution for DNS or LES.

$$\delta_{th} = \frac{T_b - T_f}{\max\left(|\nabla T|\right)} \tag{3.22}$$

- **Diffusive thickness δ:**
  This definition is based on the thermal diffusion and derived from the ZFK asymptotic theory. This thickness is less accurate than the thermal thickness. However, it enables to link flame thickness to flame speed.

$$\delta = \frac{\lambda_f}{\rho_f C_{p,f} S_L} = \frac{D_{th,f}}{S_L} \tag{3.23}$$

  The accuracy of the diffusion can be improved using the Blint correction [Blint 1986]:

$$\delta_b = 2\delta \frac{\lambda_b}{C_{p,b}} \frac{C_{p,f}}{\lambda_f} = \frac{2\lambda_b}{\rho_f C_{p,b} S_L} \tag{3.24}$$

- **Reaction thickness δ_r:**
  The thickness can also be defined based on the heat release rate profile. In this case, the reaction thickness is smaller than the thermal thickness and corresponds to the chemically exothermic reactive zone. If a one step reaction mechanism is used, this thickness writes:

$$\delta_r = \frac{\delta_{th} \mathcal{R} {T_b}^2}{E_a (T_b - T_f)} \tag{3.25}$$

  with E_a the activation energy of the global reaction.

  For ARC mechanism, similar thicknesses can be defined based on a radical production rate profiles.

Diffusion thicknesses

Contrarily to premixed thicknesses which are driven by the thermodynamics and transport properties, the thicknesses of diffusion flames are mainly driven by the flow properties and the strain rate. Two length scales are mainly used for diffusion flames [Bilger 1989]:

- **Diffusion thickness l_d:**
  This thickness corresponds to the region where the mixture fraction goes from 0 to 1, i.e. where the oxidizer and fuel mix and are diluted into the burnt products. This thickness can be estimated using the scalar dissipation rate which is linked to the mixture fraction:

$$\chi = 2D(\overrightarrow{\nabla z})^2 \tag{3.26}$$

  and writes:

$$l_d = \sqrt{\frac{D}{\chi_{st}}} \tag{3.27}$$

- **Reaction thickness l_r:**
  This thickness is similar to δ_r in the premixed case and thus corresponds to the region where combustion reactions occur. In the reaction thickness, the mixture fraction is close to the stoichiometric value z_{st}.

3.2.4 Stretch effects

The total flame stretch κ is defined as the temporal derivative of a flame surface element [Williams 1985]:

$$\kappa = \frac{1}{A}\frac{dA}{dt} \tag{3.28}$$

The stretch can be also decomposed in a first tangential component also called strain rate which is related to the flow non-uniformity, and a second part corresponding to the flame curvature [Chung and Law 1984]:

$$\kappa = \underbrace{\overrightarrow{\nabla_t} \cdot \overrightarrow{u}}_{\text{Strain rate}} + \underbrace{S_d \overrightarrow{\nabla_t} \cdot \overrightarrow{n}}_{\text{Curvature}} \tag{3.29}$$

In the above expression, $\overrightarrow{\nabla_t}$ is the tangential component of the nabla operator and writes:

$$\overrightarrow{\nabla_t} \cdot \overrightarrow{u} = -\overrightarrow{n}\,\overrightarrow{n} : \overrightarrow{\nabla}\,\overrightarrow{u} + \overrightarrow{\nabla} \cdot \overrightarrow{u} \tag{3.30}$$

with $(\overrightarrow{n}\,\overrightarrow{n} : \overrightarrow{\nabla})$ the gradient operator normal to the flame surface which writes in index notation:

$$\overrightarrow{n}\,\overrightarrow{n} : \overrightarrow{\nabla}\,\overrightarrow{u} = n_i n_j \frac{\partial u_i}{\partial x_j} \tag{3.31}$$

Hence, using index notation, the Eq. 3.29 becomes [Poinsot and Veynante 2012]:

$$\kappa = (\delta_{ij} - n_i n_j)\frac{\partial u_i}{\partial x_j} + S_d \frac{\partial n_i}{\partial x_i} \tag{3.32}$$

The flame front curvature can be expressed using the radii of curvature[2]:

$$\overrightarrow{\nabla} \cdot \overrightarrow{n} = -\left(\frac{1}{\mathcal{R}_1} + \frac{1}{\mathcal{R}_2}\right) \tag{3.33}$$

$1/\mathcal{R}_1$ and $1/\mathcal{R}_2$ are the main curvatures of the flame surface. These curvatures measure respectively the highest surface curvature and the surface curvature in the perpendicular direction.

Finally the stretch can be also computed using the local flame front velocity $\overrightarrow{w}$ [Candel and Poinsot 1990]:

$$\kappa = -\overrightarrow{n}\,\overrightarrow{n} : \overrightarrow{\nabla}\,\overrightarrow{w} + \overrightarrow{\nabla} \cdot \overrightarrow{w} \tag{3.34}$$

Several studies based on asymptotic theories have enable to characterise the flame response to stretch depending on the fuel Lewis number [Bush and Fendell 1970, Clavin 1985, Williams 1985]. It has been determined that displacement and consumption speeds have linear but different responses to the stretch:

$$\frac{S_d}{S_L} = 1 - M_a^d \frac{\kappa \delta_{th}}{S_L} \qquad \text{and} \qquad \frac{S_c}{S_L} = 1 - M_a^c \frac{\kappa \delta_{th}}{S_L} \tag{3.35}$$

where M_a^d and M_a^c are Markstein numbers respectively for displacement and consumption speeds.

These numbers are proportional to the fuel Lewis number and various expressions can be found in the literature [Clavin and Joulin 1983]. Hence, the flame speed response to stretch can be sumarized depending on the Lewis number as on Fig. 3.2.2:

- $Le_F = 1$:
  The temperature and species gradient increase in the same proportion when the stretch increases. Hence, the flame is thinned but the consumption speed doesn't change.

- $Le_F < 1$:
  The Markstein number is negative, thus the consumption speed increases linearly with the stretch. This behaviour can be observed with lean hydrogen flames.

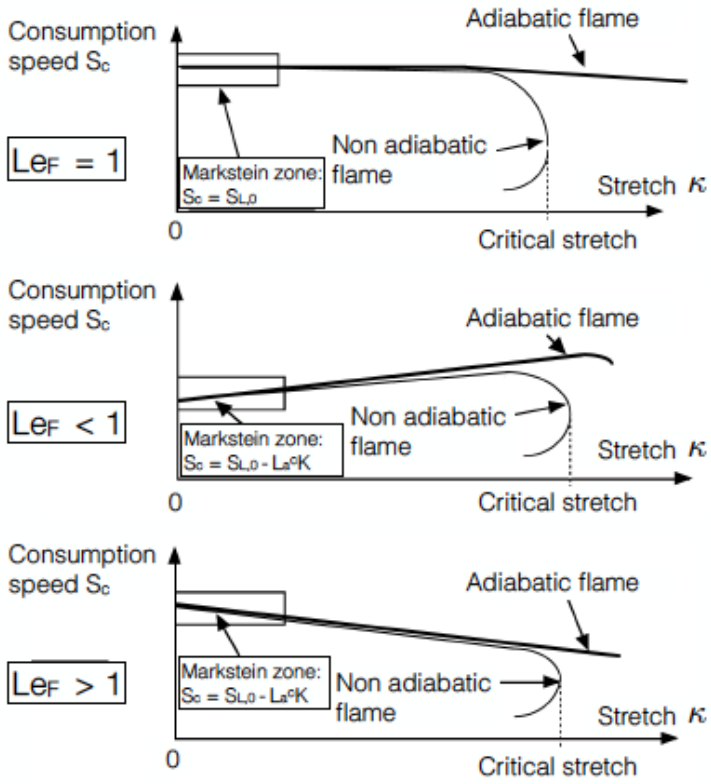

Figure 3.2.2: Flame speed responses to stretch depending on the fuel Lewis number (extracted from Poinsot and Veynante [2012]).

- $Le_F > 1$:
  On the contrary, for larger than unity fuel Lewis numbers, the consumption speed decreases when the stretch increases. This effect is often observed for heavy fuels as kerosene for instance.

These results are true only for low stretch values. When the stretch becomes too large, the asymptotic theories are no more valid and extinction phenomena arise.

3.3 Canonical 0D and 1D cases

The combustion processes can be analysed using simplified 0/1-dimensional canonical configurations with the code CANTERA [Goodwin et al. 2018]. This open source code enables to study chemical reactive systems with accurate transport and thermo-chemical properties. Furthermore, since the code is restricted to 0-dimensional and 1-dimensional configurations, detailed mechanisms with a large number of species and reactions can be used to get results as accurate as possible. The main canonical cases computed in this work are presented in the following sections.

3.3.1 Equilibrium computations

The equilibrium computation gives the equilibrium state of a mixture starting from initial composition, pressure, and temperature conditions [Wong 2001]. The equilibrium state is that corresponding to a minimum of a property called the energy function or Gibbs free energy (at constant pressure and temperature in this work):

$$dG = \sum_{k=1}^{N_{spec}} \mu_k dn_k = 0 \quad \text{and} \quad \mu_k = \frac{\partial U}{\partial n_k} \tag{3.36}$$

[2]Only in 3-dimensional cases

With μ_k the chemical potential, n_k the mole number of species k, and U the internal energy.

Adding the molar atom conservation, it yields to an optimisation problem under constraints which can be solved with the Lagrange multiplier method. The mixture composition corresponding to this equilibrium state can be then computed. Assuming constant pressure, the enthalpy of the transformation is constant. Thus, the adiabatic temperature can be computed based on the enthalpy definition:

$$h = \int_{T_0}^{T} C_p dT + \sum_{k=1}^{N_{spec}} Y_k \Delta h^0_{f,k} \quad \text{and} \quad \Delta h = 0 \tag{3.37}$$

With C_p the constant pressure heat capacity of the mixture, Y_k the mass fraction, and $\Delta h^0_{f,k}$ the formation enthalpies.

The constant volume assumption can also be used, which leads to a constant internal energy transformation. More information on equilibrium computations can be found in the book of Smith and Missen [1982].

An interesting property is that the equilibrium is only based on thermochemical properties of the species. Therefore, the result of the equilibrium does not depend on the kinetic reactions but only on the initial state and species thermochemical properties.

3.3.2 Isobaric OD reactors

In the case of the 0D reactor, the temporal evolution of an homogeneous mixture can be studied starting from an initial state. The mixture evolution is computed through the equation energy written under the temperature form with the ideal gas assumption:

$$\rho C_p \frac{dT}{dt} = \dot{\omega}'_T \tag{3.38}$$

with C_p the constant pressure heat capacity of the mixture and $\dot{\omega}'_T$ the heat release rate computed with Eq. (2.29).

This conservation equation corresponds to a constant pressure reactor. This reactor type is used in this work to compare auto-ignition time, chemical runaways and species decomposition at different pressures. However, for comparison with experimental measurements with shock tube [Herzler and Naumann 2009], the isochoric formulation using the internal energy should be used since the volume is fixed and the pressure can vary. The auto-ignition delay time τ_{ig} is defined here as the time when the heat release rate reaches its maximum value.

Since the 0D reactor only follows the time evolution of an homogeneous and isotropic mixture, the transport properties are not taken into account. Chemical schemes with a large number of species and reactions can then be studied at a reduced cost. Furthermore, this kind of reactor enables to isolate kinetic from transport effects.

CANTERA uses the CVODES solver from the SUNDIALS package to integrate the stiff ODE (Ordinary Differential Equation) of reacting systems. The time step of the computation is internally computed in order to satisfy predefined tolerances.

3.3.3 1D laminar premixed flames

Spatial premixed flame profiles and transport effects can be studied on simple one-dimensional configurations. In this steady case, the temporal evolution is not described. These simplifications enable to study detailed chemistries at a reasonable cost (less than a minute to several hours for the largest schemes).

The left side of the numerical domain corresponds to the inlet where a premixed mixture of oxidizer and fuel is injected. The mixing proportion is described with the equivalence ratio ϕ defined Sec. 2.1.5, the fresh gas temperature is T_f, the injection velocity corresponds to the laminar flame speed such that the

system is solved in the flame reference frame $u_0 = S_L$. The right side corresponds to the burnt gases exit. The pressure P is set constant on the whole domain.

Since the flame front concentrates all the transitory radical species and the major part of the species are located in the thin reaction zone, it must be carefully resolved. With CANTERA, the number of points is automatically adapted based on the temperature and species gradients.

Finally, CANTERA uses the system of equations described in section 6.2 of Kee et al. [2017] corresponding to a steady axisymmetric stagnation flow. The system is then solved using an iterative Newton solver damped with a time converging stabilization. The transport properties are computed with the multi-component formulation presented Sec. 1.1.3.

3.3.4 1D diffusion flames

For the 1-dimensional diffusion flame configuration, the fuel and oxidizer are injected separately. The resolution of the equations are similar to the premixed case except that inlet fuel and oxidizer are facing each other to form a counter-flow flame. Contrary to the 1D premixed flame, the radial component must be taken into account with an additional conservation equation for the radial momentum and an additional term in the continuity equation [Goodwin et al. 2018].

As explained previously, the flame front is located at the stoichiometric line where the mixing of fuel and oxidizer occurs. For this counter-flow set-up, the scalar dissipation rate at the stoichiometric line χ_{st}, introduced to characterize the mixing, can be computed as follow [Poinsot and Veynante 2012]:

$$\chi_{st} = \frac{a}{\pi} \exp\left(-2\left[erf^{-1}\left(\frac{\Phi - 1}{\Phi + 1}\right)\right]^2\right) \tag{3.39}$$

Φ is a different equivalence ratio from Eq. (2.36) and is defined for counter-flow diffusion flame as:

$$\Phi = s_{Y,\mathrm{O_2}} \frac{Y_{fuel,1}}{Y_{\mathrm{O_2},2}} \tag{3.40}$$

with $s_{Y,\mathrm{O_2}}$ the mass stoichiometric coefficient as defined in Sec. 2.1.5, and $Y_{fuel,1}$ and $Y_{\mathrm{O_2},2}$ the mass fractions of fuel and oxidizer in their respective inlet streams. Note that for counter-flow diffusion flames, since mass flow rate can be different at the inlets, this definition is not equivalent to the global equivalence ratio $\phi_g = \Phi \times \dot{m}_1/\dot{m}_2$ (index $_1$ refers to the fuel inlet, and index $_2$ to the oxidizer inlet).

a is the strain rate and can be roughly estimated from the global strain rate a_{global}:

$$a \approx a_{global} = \frac{|u_1| + |u_2|}{L} \tag{3.41}$$

with u_1 and u_2 respectively the fuel and oxidizer injection velocities. L is the distance between the two injectors.

Diffusion flames are generally represented and resolved in the mixture fraction space z. In this case, the scalar dissipation rate can be expressed under the following general form on the whole domain [Poinsot and Veynante 2012]:

$$\chi = \frac{a}{\pi} \exp\left(-2\left[erf^{-1}\left(1 - 2z\right)\right]^2\right) \tag{3.42}$$

The interesting value at the stoichiometric line is recovered from Eq. (3.39):

$$z_{st} = \frac{1}{1 + \Phi} \tag{3.43}$$

With a low scalar dissipation rate, the mixing between fuel and oxidizer is not sufficient to sustain a stable flame, as well as for too high values where the flame is quenched. This case is of interest because it enables to study in a simplified way the combustion behaviour in the diffusion flame regime, and to analyse the response of the flame to stretch which was not possible with the 1D premixed flame setup.

3.4 Turbulent combustion

Turbulence has a large influence on the combustion processes and flame structure. Basic notions of turbulence have been already presented in Sec. 1.2.2 so, this current section focuses on the interaction between the combustion processes and the turbulence.

3.4.1 Characterisation of the combustion-turbulence interaction

For premixed combustion regimes, the flame-turbulence interaction is characterized on one hand by the combustion characteristic time:

$$\tau_c = \frac{\delta_{th}}{S_L} \tag{3.44}$$

This combustion characteristic time corresponds to the duration required for the flame front to propagate on a distance equal to its own thickness.

On the other hand, the turbulence can also be characterized by two times scales. The first one, τ_{turb}, corresponds to the large scales and is defined in Eq. (1.56). The second one, τ_K, corresponds to the Kolmogorov scale and is defined in Eq. (1.57).

Two non-dimensional numbers can be created to describe the flame-turbulence interaction combining these characteristic times:

- **Damköhler** Da**:**
  This number is defined as the ratio of the integral turbulent characteristic time over the combustion time:
  $$Da = \frac{2 \times \tau_{turb}}{\tau_c} = \frac{L_t \, S_L}{u' \, \delta_{th}} \tag{3.45}$$
  For large Damköhler numbers, the turbulent characteristic time is larger than the combustion time. Therefore, the flame front structure is weakly perturbed by the turbulence. On the contrary, for low Da numbers, reactants and products are mixed by the turbulence before reacting with slower chemical reactions. Hence, the combustion processes are modified compared to a premixed laminar flame.

- **Karlovitz** Ka**:**
  This number enables to identify the interaction between the smallest turbulent scales and the flame:
  $$Ka = \frac{\tau_c}{\tau_K} = \frac{\delta_{th} \, u'_K}{\eta_K \, S_L} \approx \left(\frac{u'}{S_L}\right)^{3/2} \times \left(\frac{L_t}{\delta_{th}}\right)^{-1/2} \tag{3.46}$$
  The second part of the above expression is derived from relations Eq. (1.51) and (1.54), using the diffusion thickness instead of the thermal thickness and assuming a unity Prandtl number to write: $\delta = \nu / S_L$. This last expression is also refered as unity flame Reynolds number.
  The Karlovitz number is equivalent to the inverse of the Damköhler number applied at the Kolmogorov scale.

3.4.2 Interaction regimes

The transition between the combustion-turbulence interaction regimes can be determined using the previous non-dimensional numbers or with velocity and lenght ratios as for the turbulent combustion diagram from Peters [2000] presented on Fig. 3.4.1.

Several interaction regimes can be identified (other than the laminar flame corresponding to $Re_t < 1$) [Poinsot and Veynante 2012]:

- $Ka < 1$ and $Da > 1$:
  In this regime, the chemical time scale is shorter than any turbulent time scale. The flame front is thin, has an inner structure close to a laminar flame and is wrinkled by the turbulence motion. This

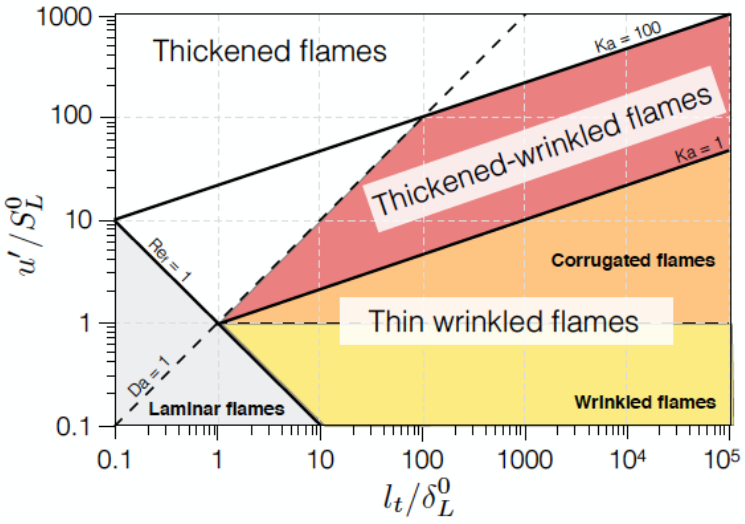

Figure 3.4.1: Diagram of the combustion-turbulence interaction regimes for premixed flames (extracted from Peters [2000]).

interaction regime is referred as "thin flame regime" or "flamelet regime" and can be divided in two sub-regions. If the flame speed is larger than the turbulent velocity fluctuation ($u'/S_L < 1$), the turbulent motion is only able to wrinkle the flame and this regime is identified as "wrinkled flame regime". This regime is illustrated on picture (a) of Fig. 3.4.2. On the contrary, the turbulence is able to wrinkled the flame up to the formation of flame-flame interaction structures which form pockets of fresh or burnt gases. This regime is identified as "thin flame regime with pockets" or "corrugated flame regime".

- $Ka > 1$ and $Da > 1$:
  In this case, the integral turbulent time scale is still larger than the chemical one, but at the smallest turbulent scales, the turbulence is able to modify the inner flame structure. The flame can no longer be identified as a laminar flame front but is still wrinkled. This regime is known as "thickened-wrinkled flame". This regime is illustrated on picture (b) of Fig. 3.4.2. Only the preheated zone is modified while the reaction zone remains close to a wrinkled laminar front.

- $Da < 1$:
  For the small Damköler numbers, the turbulent mixing is fast enough to modify the chemical processes in the flame front. The latter is then thickened by the turbulent structures which gives its name: "Thickened flame regime". This regime tends towards the "well stirred reactor" limit ($Da << 1$).

Similar approaches can be used to characterize the non-premixed combustion-turbulence interaction [Cuenot and Poinsot 1994] but will no be developed here.

3.4.3 Turbulence effects on the combustion processes

Turbulent flame speed

A consequence of the flame wrinkling in the flamelet regime is the increase of the turbulent flame surface $\mathcal{A}_T$ which increases the fuel consumption and speed-up the combustion process. Following the definitions on Fig. 3.4.3, the turbulent flame speed S_T depends on the ratio of the turbulent flame surface $\mathcal{A}_T$ and the non-wrinkled flame surface $\mathcal{A}_L$ [Driscoll 2008]:

$$\frac{S_T}{S_L} = \frac{\mathcal{A}_T \overline{S_c}}{\mathcal{A}_L S_L} \tag{3.47}$$

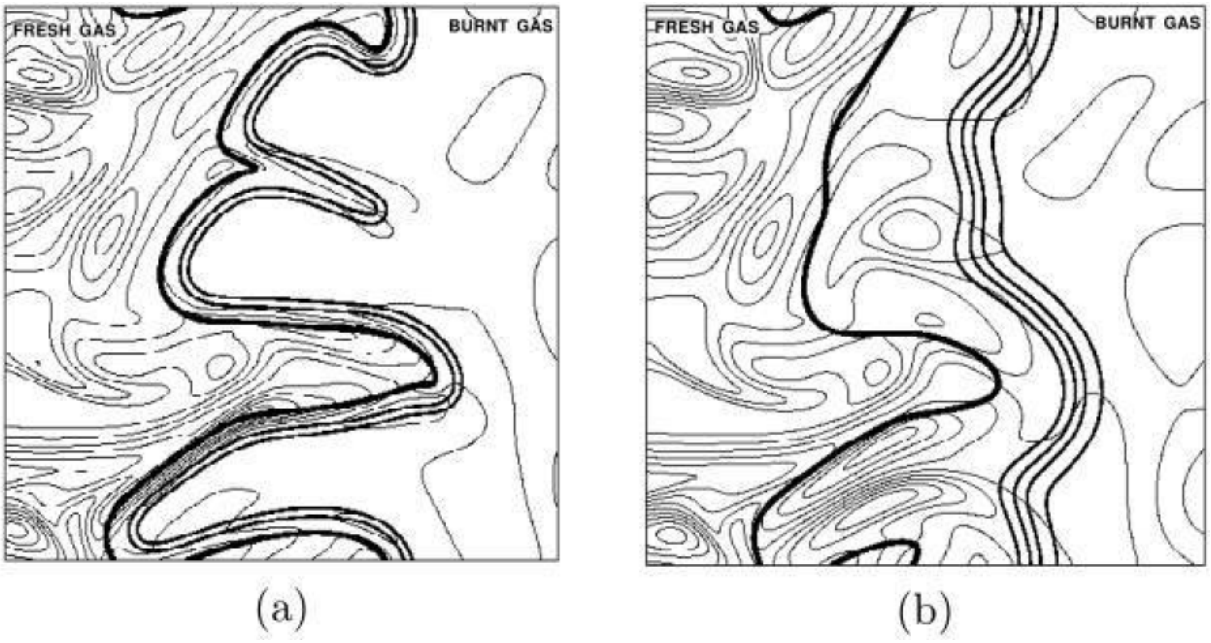

Figure 3.4.2: DNS of (a) a wrinkled flamelet regime and (b) a thickened-wrinkled flame regime. Vorticity field (thin lines) and reaction rate (bold lines). The very thick line denotes the fresh gases boundary of the preheat zone (extracted from Poinsot and Veynante [2012]).

Where the ratio $\overline{S_c}/S_L$ corresponds to the stretch factor and enables to account for stretch effects on the flamelet speed [Bray and Cant 1991] and $\overline{S_c}$ is the overall consumption speed of the turbulent flame.

Hence, following this expression, the turbulent flame speed increases with the turbulent fluctuation velocity as it enables to increase the flame surface. However, when the turbulent intensity becomes too large extinction phenomena start to appear. Several relations have been established to link the turbulent flame speed to u', Eq. (3.48) for instance [Abdel-Gayed et al. 1984], but experimental studies have shown non-negligible discrepancies with such models.

$$\frac{S_T}{S_L} \propto 1 + \frac{u'}{S_L} \tag{3.48}$$

Extinction phenomena

The extinction phenomena[3] arise when the flame stretch becomes too strong and locally reduces or prevents the combustion processes from occurring. For the turbulent flames, the stretch comes from the interaction of the flame with the flow vortexes. The studies of flame-vortex interactions using DNS [Poinsot 1991] or experimentally [Roberts et al. 1993] are similar to the flame-turbulence interaction in the flamelet regime. This interaction depends on two main parameters [Poinsot and Veynante 2012]: The ratio between the vortex velocity and the flame speed, and the ratio between the vortex size over the flame thickness. Then, the interaction can be classified as in the diagram on Fig. 3.4.4.

Following this diagram, if the vortexes have a low velocity compared to the flame speed, or if they are too small, they cannot influence the flame front. It corresponds to the cut-off limit. When the vortex size and velocity increase, the flame is firstly wrinkled, then fresh gases pockets are formed in the flame front, and finally the flame can extinct when the "quench" limit is reached.

3.4.4 Numerical combustion modeling

As shown previously, the turbulence has a wrinkling and/or a thickening effect on the flame front due to the flow vortexes. If the grid resolution is not fine enough, the wrinkled flame surface (red curve on

[3] related to the turbulence-combustion interaction

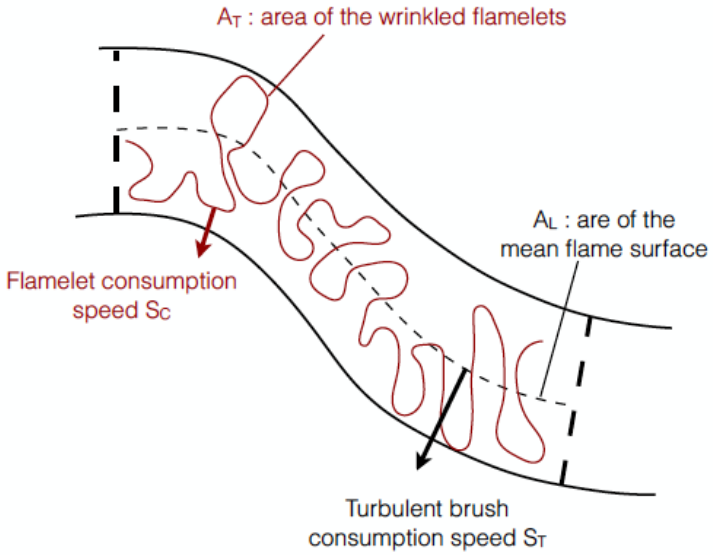

Figure 3.4.3: Scheme and definitions associated to the turbulent flame front in the flamelet regime (extracted from Driscoll [2008]).

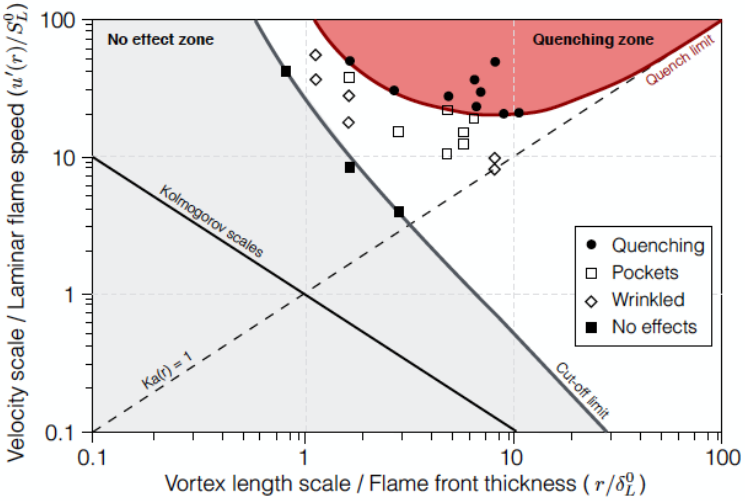

Figure 3.4.4: Flame-vortex interaction diagram obtained using DNS (extracted from Poinsot [1991]).

Fig. 3.4.3) cannot be fully resolved and only the mean flame front (black dashed curve on Fig. 3.4.3) is represented. Hence, the flame area, the consumption speed, the stretch, the curvature, and the mixing effects are under-predicted. Furthermore, from a chemical point of view and independently from the turbulent flow, the flame front must be discretized on several points (5-15 depending on the chemical modeling) to get a correct representation of the chemical processes and to resolve all the species profiles across the flame [Wirtz 2022].

This level of discretization is possible for DNS but hardly feasible for LES. Therefore, the mean species and heat production rates need to be modeled as function of the resolved fields. Several models can be found in literature textbooks [Poinsot and Veynante 2012]. For premixed combustion, the most used approaches are the Bray-Moss-Libby model [Bray and Moss 1977], the G-equation model [Moureau et al. 2009], the F-TACLES model [Fiorina et al. 2010] and the Thickened Flame model [Colin et al. 2000]. For non-premixed combustion, Probability Density Function methods coupled with external flamelet library [Cook and Riley 1994] are generally used.

In this work, we focus on the ignition phase of the combustion and the flame is always fully resolved at

the spark location. Hence, no combustion models are required in the computations.

3.5 Spray flames

The dispersed phase has a non negligible influence on the combustion processes. Large differences can be observed compared to the equivalent gaseous configurations. In the current section, the effect of the fuel droplets on the flame propagation is presented.

3.5.1 Equivalence ratio

In two-phase flow configurations, fuel species can be encountered under both liquid and gaseous phases. The local combustion and chemical processes are only affected by the gaseous phase, however, the global combustion performances and the flame structure evolution rely on both phases since the liquid fuel can evaporate and add gaseous fuel species to the mixture. Hence, global, gaseous and liquid equivalence ratios are introduced[4]:

$$\phi_{tot} = \phi_l + \phi_g \tag{3.49}$$

and can be computed using Eq. (2.40):

$$\phi_{tot} = \frac{2n_{\mathrm{C}}^{l+g} + 0.5n_{\mathrm{H}}^{l+g}}{n_{\mathrm{O}}^{g}} \qquad \phi_l = \frac{2n_{\mathrm{C}}^{l} + 0.5n_{\mathrm{H}}^{l}}{n_{\mathrm{O}}^{g}} \qquad \phi_g = \frac{2n_{\mathrm{C}}^{g} + 0.5n_{\mathrm{H}}^{g}}{n_{\mathrm{O}}^{g}} \tag{3.50}$$

with $n_{\mathcal{A}}^{p}$ the number of atoms $\mathcal{A}$ in the phase p. The index l+g corresponds to the sum of the atoms in the gaseous and the liquid phase.

3.5.2 Laminar two-phase flame structure

In addition to gaseous and chemical properties, the evaporation process is an important parameter which needs to be considered when dealing with two-phase flames. This process can be estimated using the evaporation characteristic time τ_{evap} given by Eq. (1.102)[5]. When this time is compared with the droplet residence time $\tau_{res} = L_c/u_p$, three combustion regimes can be observed. These cases are presented on Fig. 3.5.1 for a 1-dimensional two-phase laminar flame. For such a configuration, L_c is the distance between the flame front and the droplet injection position.

- $\tau_{evap}/\tau_{res} < 1$ (Case A):
  In the first case, the droplets are fully evaporated before reaching the flame front. Hence, the flame is similar to a gaseous flame with $\phi = \phi_{tot}$ and the fresh gas temperature corresponds to the gas temperature after evaporation which is lower than the initial temperature due to latent heat of evaporation.
  In multi-dimensional cases, the mixing processes must also be taken into account. If the mixing characteristic time between gaseous fuel and air is small enough, the flame is premixed. On the contrary, diffusion structures can be found.

- $\tau_{evap}/\tau_{res} \approx 1$ (Case B):
  In the second case, the droplets evaporate mainly in the preheated zone of the flame but are not able to cross the flame front. Still, in addition to pre-vaporized fuel, the reactive zone sees fuel droplets that change the flame structure: the flame thickness starts to increase and the endothermic droplet evaporation cools the flame front.

- $\tau_{evap}/\tau_{res} > 1$ (Case C):
  In the last case, if droplets are large or fast enough, they can cross the flame front and continue to

[4] Works only if the oxidant species is purely gaseous and no oxygen atoms are in the fuel species
[5] This expression works only for a fixed droplet temperature

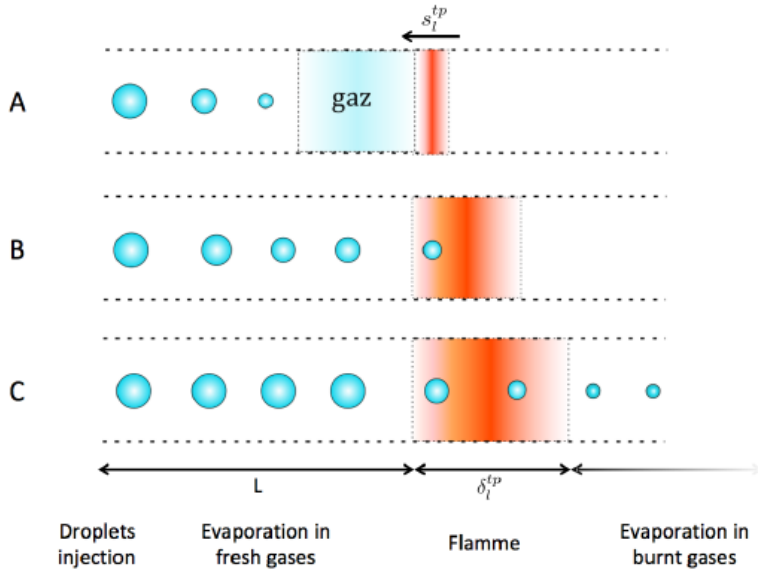

Figure 3.5.1: Two-phase laminar flame topology depending on τ_{evap}/τ_{res} (extracted from [Collin-Bastiani 2019])

evaporate in the burnt gases. If oxidizer species are available, combustion processes are possible in the burnt gases zone leading to a much thicker flame compared to the gaseous one.

3.5.3 Two-phase flame properties

As illustrated on Fig. 3.5.1, the two-phase flame properties δ_L^{tp} and S_L^{tp} can be very different than the gaseous one δ_{th} and S_L. Several studies have tried to model the two-phase flame speed from the gaseous one and the liquid properties. Ballal and Lefebvre [1981b] have proposed the following correlations:

$$S_L^{tp} = \left(\frac{\tau_{evap}}{D_{th}} + \frac{1}{{S_L}^2} \right)^{-\frac{1}{2}} \tag{3.51}$$

Although this correlation predicts the correct flame speed for overall lean mixtures ($\phi_{tot} < 1$), Neophytou and Mastorakos [2009] have shown that this formula was not able to catch effects occurring in rich conditions. This study has also demonstrated that spray flames can exist over the rich gaseous flammability limit ($\phi_{tot} > \phi_{rich}$), and that the two-phase flame speed could become higher than the gaseous one $S_L^{tp}(\phi_{tot}) > S_L(\phi_{tot})$ in rich cases.

These behaviors have been explained in [Rochette et al. 2019] where 1-dimensional spray flames have been numerically investigated, varying the droplet size, the droplet relative velocity, and the gaseous and liquid equivalence ratios. Two main topologies have been identified and are shown on Fig. 3.5.2:

- **Weakly evaporation controlled flames:**
  This regime is found if the gaseous mixture is already flammable, or if the evaporation enables to reach a flammable mixture before the flame front. In this case, the evaporation rate peak is located before the fuel consumption peak. The flame thickness and consumption speed are the one of the equivalent gaseous flame at an effective equivalence ratio ϕ_{eff}:

$$\phi_{eff} = \left(\frac{\delta_{th}}{\max\left(\delta_{evap}, \delta_{th}\right)} \right)^{\frac{2}{3}} \times \phi_l + \phi_g \leq \phi_{tot} \tag{3.52}$$

  with $\delta_{evap} = u_p \tau_{evap}$ the evaporation thickness.
  Therefore, for globally rich flames, ϕ_{eff} can be closer to stoichiometry than ϕ_{tot} which explains the observations from Neophytou and Mastorakos [2009]:

$$S_L^{tp}(\phi_{tot}) = S_L(\phi_{eff}) > S_L(\phi_{tot}) \quad \text{if} \quad |1 - \phi_{eff}| < |1 - \phi_{tot}| \tag{3.53}$$

- **Evaporation controlled flames:**
  In the evaporation controlled regime, the fuel consumption is limited by the evaporation rate. The fuel is directly consumed as soon as it evaporates resulting in a perfect superposition of the fuel evaporation and consumption profiles. This corresponds to the situation where $\tau_c < \tau_{evap}$ with $\tau_c = \delta_{th}/S_L$ a combustion characteristic time. In this case, the flame is much thicker and the two-phase flame speed can be estimated using τ_{evap}:

$$S_L^{tp} = \frac{\delta_{th}(\phi = \max(\phi_{tot}, 1))}{\tau_{evap}} \tag{3.54}$$

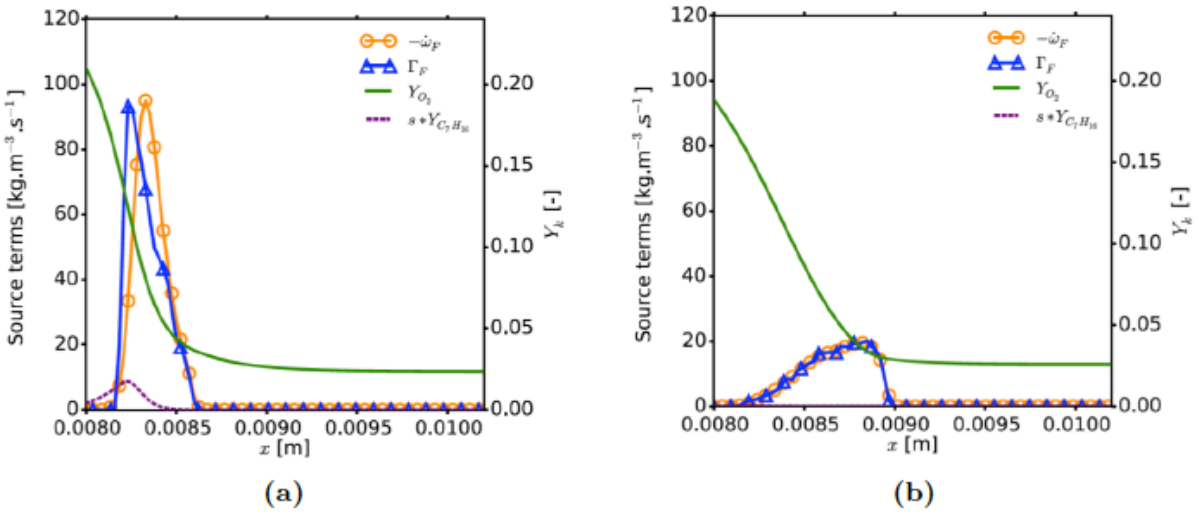

Figure 3.5.2: Two archetypes of spray flame structures. (a): Flame weakly controlled by evaporation. (b): Flame controlled by evaporation (extracted from [Rochette et al. 2019])

The effects of preferential evaporation can also have a large influence on the two-phase combustion processes especially with kerosene fuels that are composed of several components with different volatilities. These effects are discussed in Chap. 13 and require to account for multi-component fuel evaporation which is presented in Chap. 12.

3.5.4 Turbulent two-phase flames

In realistic 3-dimensional flows, the turbulence has a non negligible effect on the dispersed phase which in return can significantly modify the two-phase combustion regime. This interaction can be characterized by the Stokes number introduced Sec. 1.3.3.

The small droplets trajectories are driven by the turbulent flow which may lead to preferential segregation effects as shown on Fig. 3.5.3. The droplets are trapped by the turbulent structures in low vorticity regions. As a consequence, strong inhomogeneities of droplet size distribution are created.

These inhomogeneities have an influence on the evaporation rate. More gaseous fuel is formed in small droplets regions leading to stratified combustion. Moreover, as shown above, the droplet size influences the two-phase combustion regime. If a globally dilute homogeneous spray of small droplets reaches the flame front, an homogeneous reaction zone is preferentially found as shown on the left picture of Fig. 3.5.4. On the contrary, if a large range of droplet size is encountered, the flame may be bent by the dispersed phase and droplets can individually burn in the post-flame region leading to diffusion flame structure. This regime called heterogeneous combustion can be encountered in laminar flows with large poly-disperse distributions but is promoted in turbulent flows due to the segregation effect.

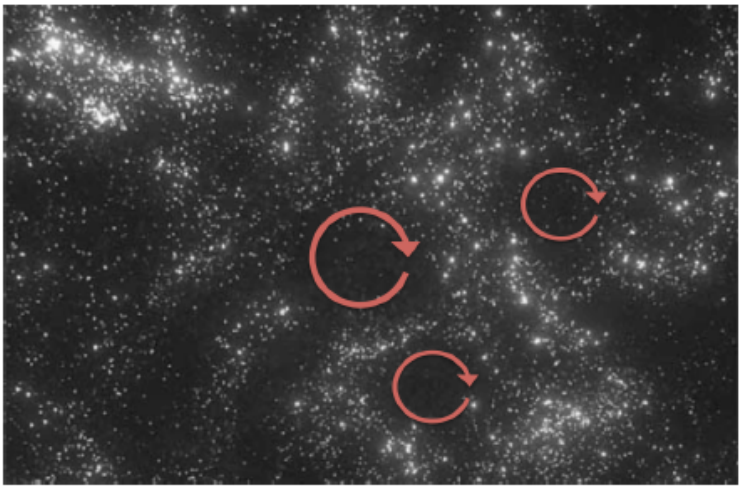

Figure 3.5.3: Preferential segregation of droplet in HIT (extracted from [Wood et al. 2005])

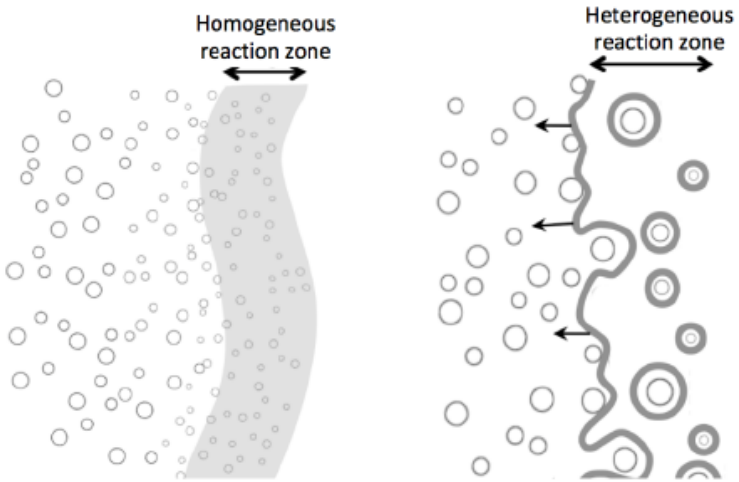

Figure 3.5.4: Homogeneous (left) and Heterogeneous (right) combustion regimes (adapted from [Paulhiac 2015])

Chapter 4

Literature review on ignition

Contents

Flame extinction in aeronautical engines can be caused by a rapid modification of the air flow inside the combustion chamber occurring during plane operations or after the ingestion of a large quantity of ice or water. Even though these events are scarce, the capability to re-ignite in flight conditions is mandatory and one of the most strict criteria for the combustion chamber design.

The literature review presented in this chapter only focuses on the first phases of the ignition. Sec. 4.1 is dedicated to the formation of the flame kernel resulting from the spark and Sec. 4.2 corresponds to the kernel development and propagation. The attachment to the first burner and the light-around phase are not presented in this work, but a review is available in [Collin-Bastiani 2019].

4.1 Flame kernel formation

The first step of the ignition is associated to the creation of a stable flame kernel. Such kernel formation results from an energy transfer to the gas phase using ignition devices that have been described in the introduction chapter. However, the ability to form a sustainable and stable flame kernel relies on many parameters that have been studied by several authors and are presented in the following sections.

4.1.1 Laminar ignition

At the early stages of the ignition, the mass fraction variations of the reactants are considered negligible compared to the temperature variation. Indeed, the ignition time is firstly controlled by the temperature and secondly by the reactant concentrations [Gorbachev 1981]. Hence, the study of ignition can be view as a thermal balance: the chemical runaway occurs if the heat release rate from the chemical reactions exceeds the surrounding thermal losses [Semenov 1928]. This balance can be expressed using characteristic times:

- **Conduction characteristic time:** τ_{cond}

$$\tau_{cond}(T) \propto \frac{{R_{ED}}^2}{D_{th}(T)} \tag{4.1}$$

with R_{ED} the characteristic radius of the energy deposit, and D_{th} the thermal diffusion coefficient.

- **Chemical characteristic time:** τ_{chem}

$$\tau_{chem}(T) \propto \left(\rho \times A \times exp\left(\frac{-E_a}{\mathcal{R}T}\right)\right)^{-1} \tag{4.2}$$

This chemical characteristic time is derived from an empirical Arrhenius law modeling the global behavior of the chemistry.
The chemical characteristic time can be also associated to the ignition time:

$$\tau_{chem}(T) \approx \tau_{ig}(T) \tag{4.3}$$

Based on these expressions, a critical radius is computed:

$$R_{ED,runaway} = \sqrt{\frac{D_{th}}{\tau_{ig}}} \tag{4.4}$$

For deposit sizes lower than this critical value, the conduction effects are too strong and the energy deposited is diffused before the chemical runaway occurs.

Vasquez-Espi and Linan [2002] studied the influence of these effects using a Damkhöler number $Da_{igni} = \tau_{cond}/\tau_{chem}$. Fig. 4.1.1 firstly shows that the energy deposit size must be several times larger than the theoretical critical radius $R_{ED,runways}$ to observe an ignition. Then, the required deposit size increases with the dimension because the diffusion effects are more important.

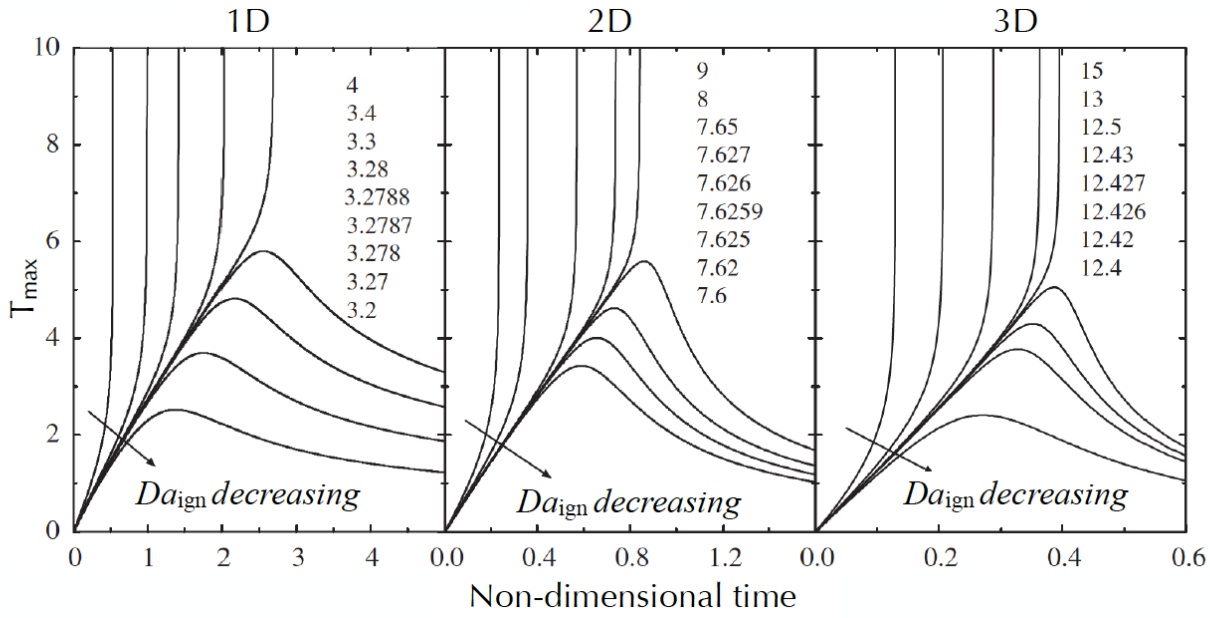

Figure 4.1.1: Temporal evolution of the temperature at the energy deposit center for several Da_{igni} (extracted from Vasquez-Espi and Linan [2002]).

Once the chemical runaway starts, the reduction of the chemical reactants can no longer be neglected. The heat release rate depends on the diffusion rate of the reactants towards the kernel. Zeldovich et al. [1980] demonstrated the existence of an unstable solution to the conservation equations applied to a spherical flame of radius R_c. In this configuration, the reactants diffusion towards the flame front enables

a heat release rate that compensates the conduction thermal losses. In the case of a spark ignition, the temperature reached after the energy deposit T_{ED} is largely greater than the adiabatic temperature T_{adia} [Joulin 1985]. Hence, $R_{ED,runaways} < R_c$ because $R_{ED,runaways}$ decreases considerably when T_{ED} increases. Therefore, the deposit radius can be large enough to enable the chemical runaway but too small to maintain the flame kernel.

The critical radius R_c is then strongly dependent on the limiting reactant Lewis number. Therefore Champion et al. [1986] derived an expression for R_c depending on the limiting reactant Lewis number Le_A:

$$R_c = \frac{\lambda(T_{adia})}{C_p(T_{adia})\rho_f S_L}\frac{T_{adia}}{T_b Le_A} exp\left(\frac{E_a}{2\mathcal{R}T_{adia}}\frac{T_{adia}-T_b}{T_b}\right) \tag{4.5}$$

T_b is here the burnt gas temperature observed due to non unity Lewis number which writes:

$$T_b = T_f + \frac{1}{Le_A}(T_{adia} - T_f) \tag{4.6}$$

Thus, the kernel development requires larger initial radius with heavy fuels ($Le_A > 1$) which is confirmed in experimental measurements [Lewis and von Elbe 1987].

Other studies show that the critical radius is of the order of the laminar flame thickness [Glassman and Yetter 2008]. It is consistent with the following observation: the expression Eq. (4.5) taken with unity Lewis number is equivalent to an expression of the diffusion laminar flame thickness Eq. (3.23) evaluated at the adiabatic temperature for the conductivity and heat capacity.

The critical energy deposited is then defined as the energy required to heat a gas mixture in a spherical volume of radius R_c up to T_{adia}:

$$E_i = \frac{4}{3}\pi R_c^3 \rho_f C_p(T_f)(T_{adia} - T_f) \tag{4.7}$$

This critical energy, corresponding to the MIE, highly depends on the equivalence ratio and decreases for rich mixtures [Ballal and Lefebvre 1977]. A convective effect has also been observed experimentally [Ballal and Lefebvre 1975, Kono et al. 1984] and numerically [Baum et al. 1995] with an increase of the MIE along with the rise of the mean flow velocity.

The results presented correspond to a premixed combustion regime, but are still valid for diffusion regimes. However, the spark position relative to the mixture fraction iso-contours must be taken into account. If the energy deposit occurs at a non flammable location, the gas temperature can decrease below the critical temperature before reaching a flammable mixture causing an ignition failure. The counter-flow laminar flame is often used to study the non-premixed ignition and the stretch effects. For example, [Richardson 2007] used such configuration with a complex chemistry modeling to evidence a stretch limit preventing the ignition.

4.1.2 Effect of turbulence

An efficient way to consider the effect of the turbulence is to introduce the concept of turbulent diffusivity [Akindele et al. 1982]:

$$D_{th} = \frac{\lambda}{\rho C_p} + D_{turb} \tag{4.8}$$

with

$$D_{turb} = 0.44 \times u' \times L_t \times \left(1 - \exp\left(-\frac{u' \times t}{0.44 \times L_t}\right)\right) \tag{4.9}$$

where D_{turb} is the extra thermal diffusivity due to the turbulent structures built under HIT assumptions. u' and L_t are respectively the turbulent velocity fluctuation and the integral turbulent length. This expression is time dependent with initially only the laminar thermal diffusion taken into account. In this approach, the turbulence is modeled with a diffusion term. The increase of the latter causes an increase of the critical radius R_c as well as the MIE.

This modification of the MIE is visible on Fig. 4.1.2 with an increase of the MIE with the normalized turbulence intensity. Furthermore, the study from Shy et al. [2010] demonstrated the presence of a MIE transition. For low turbulent intensities, the MIE slowly increases with the turbulence, whereas after the transition, the MIE rises faster. They explain the transition can be due to a modification of the turbulent combustion regime. At low turbulence intensity, the combustion is in the wrinkled flamelet regime, and it changes to the thin-reaction regime for higher turbulent intensities. Then, it modifies the flame structure and the thermal equilibrium which favours the diffusion processes and causes the strong MIE increase. Based on a recent DNS study, Turquand d'Auzay et al. [2019] argue that the MIE transition is due to a modification of the flame wrinkling response to turbulence. For low turbulent intensity, the flame wrinkling evolves almost linearly with the turbulent intensity. Hence, the increase of flame surface and the associated heat release rate compensate the thermal losses resulting in a low increase of the MIE with the turbulence intensity. However, at the MIE transition, the wrinkling factor becomes less sensitive to the turbulence, but the thermal diffusion continues to increase. Thus, the MIE becomes strongly dependent to the turbulence.

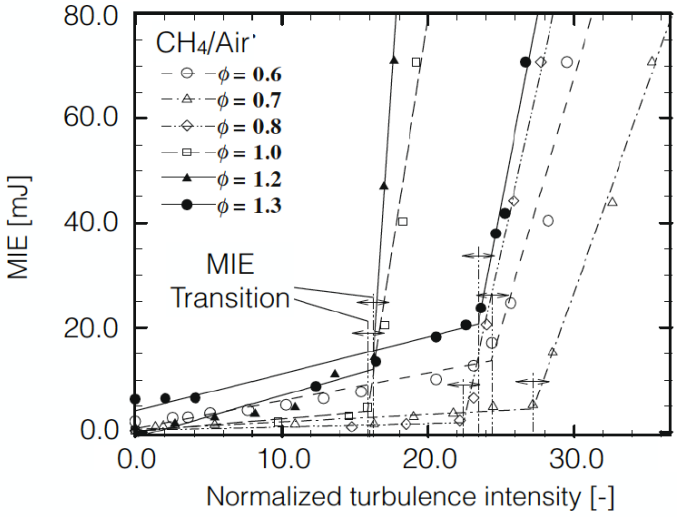

Figure 4.1.2: Evolution of the MIE in methane-air mixtures depending on the ratio u'/S_L for several equivalence ratios (extracted from Shy et al. [2010])

In the case of non-premixed regimes, the velocity and equivalence ratio variations control the kernel formation. The stochastic dimension of mixture fraction due to the turbulence can be taken into account with a Probability Density Function (PDF) of the mixture fraction $P(z)$. Birch et al. [1981], Smith et al. [1988] introduced the flammability factor that enables to evaluate the probability to encounter a flammable mixture at a given location.

$$\mathcal{F}_f = \int_{z_{lean}}^{z_{rich}} P(z)dz \tag{4.10}$$

Cardin [2013] has shown that the ignition probability is strongly correlated to the flammability factor. However, Ahmed and Mastorakos [2006] have found this probability could be much lower than the flammability factor in large stretch regions. Hence, both the transport and mixing effects must be taken into account to compute the ignition probability. On the contrary, they also have shown that it is possible to ignite a mixture in regions where $\mathcal{F}_f = 0$, which confirms the possibility to ignite through heat convection from a non flammable location.

4.1.3 Ignition in two-phase flows

In the following paragraphs, the main features associated to two-phase ignition are summarized. Complementary information can be found in the reviews of Aggarwal [1998] and Mastorakos [2017].

Two-phase kernel formation

When considering ignition in a droplet mist, the conclusions associated to gaseous ignition presented Chap. 4 remain globally unchanged but can be significantly impacted. For example, the pressure influence on the MIE in a two-phase flow is $MIE \propto P^{-0.5}$ while $MIE \propto P^{-2}$ has been observed for purely gaseous mixtures [Lefebvre 1998]. Ballal and Lefebvre [1977] have experimentally investigated ignition in lean two-phase mixtures at sub-atmospheric conditions that can be encountered in aeronautical gas turbines for instance. The authors have concluded that the ignition processes are controlled by the evaporation rate instead of the chemical kinetic. As shown on Fig. 4.1.3, the MIE is found to increase along with the spray Sauter Mean Diameter[1] (SMD), showing the importance of the atomization processes in combustion chambers. Moreover, fuel volatility is also found to promote easier ignition.

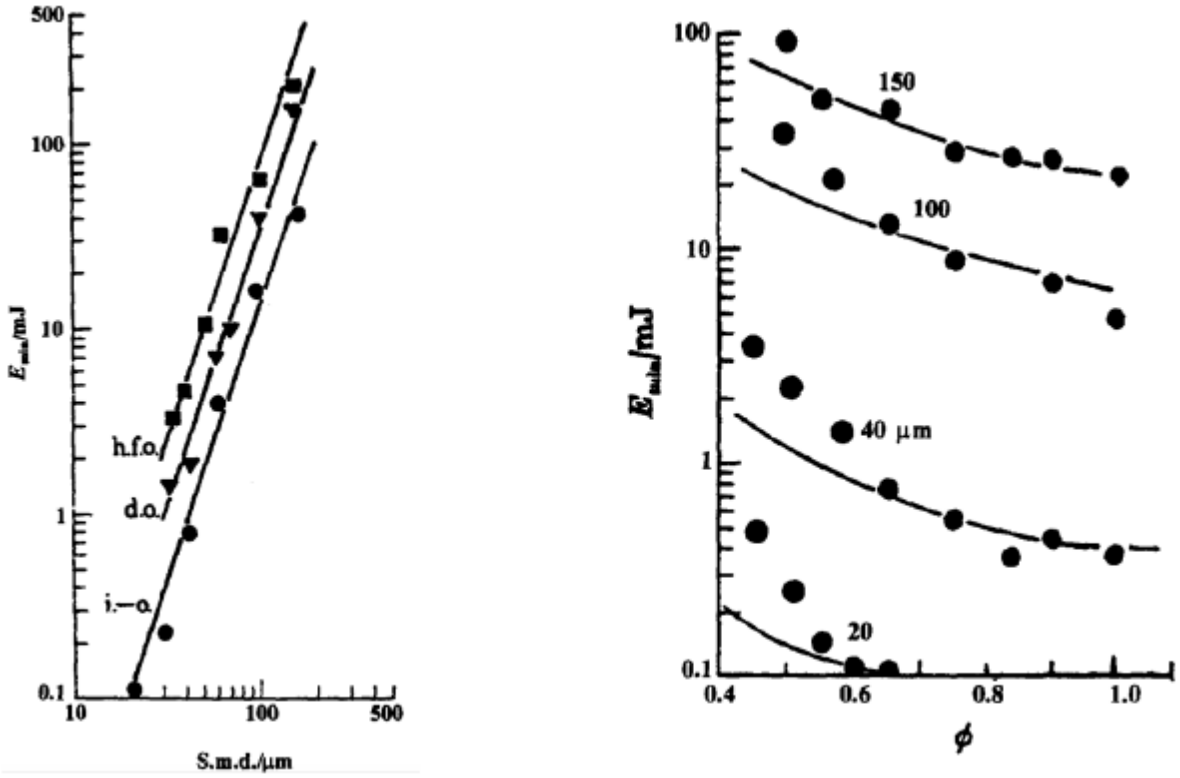

Figure 4.1.3: Left: MIE versus SMD for iso-octane, diesel-oil, and heavy-fuel-oil at $\phi_{tot} = 0.65$. Right: MIE versus total equivalence ratio for iso-octane and several SMD. (extracted from [Ballal and Lefebvre 1977])

The following expressions have been proposed for the critical kernel radius and MIE [Ballal and Lefebvre 1977]:

$$R_c^{tp} = \overline{D_p} \sqrt{\frac{\rho_p}{\rho_g \, \phi_{tot} \, ln(1 + B_M)}} \tag{4.11}$$

$$MIE^{tp} = \frac{\pi \, C_p (T_{adia} - T_f) \overline{D_p}^3}{6\sqrt{\rho_g}} \times \left(\frac{\rho_p}{\phi_{tot} \, ln(1 + B_M)} \right)^{3/2} \tag{4.12}$$

with $\overline{D_p}$ the droplet mean diameter. Note that this analytical model is built using infinitely fast chemistry and the pre-evaporation is not considered.

Pre-evaporation effects

However, in a latter study, Ballal and Lefebvre [1981a] demonstrated the importance of pre-evaporation on ignition as well as the competition between evaporation and chemical processes. The effect of pre-

[1] Defined in Chap. 11

evaporation has also been studied by De Oliveira et al. [2019], who have compared the probability of mixture breakdown ($\mathcal{P}_{bd}$) and ignition probability ($\mathcal{P}_{igni}$). With pre-heated mixture (i.e. fuel pre-evaporation), the ignition probability is increased due to the presence of flammable mixture (see Fig. 4.1.4). In this case, the mixture breakdown always leads to ignition ($\mathcal{P}_{igni} = \mathcal{P}_{bd}$). On the contrary, for low gaseous temperatures the pre-evaporation is reduced and the mixture breakdown does not imply ignition ($\mathcal{P}_{igni} < \mathcal{P}_{bd}$). A cool-down effect has been observed and explained by the droplet evaporation in the kernel resulting in a long extinction mode [Wandel et al. 2009]. It differs from the short extinction mode which corresponds to the lack of energy required to start the combustion reactions. This work also highlights stochastic dimension of the two-phase ignition.

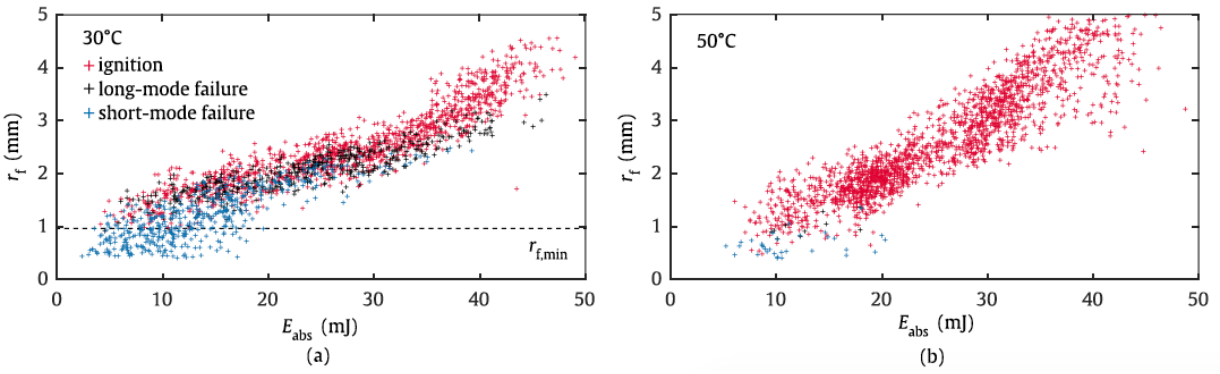

Figure 4.1.4: Evaluation of ignition success or failure depending on deposed energy and initial kernel size for (a) no pre-heating ($T_f = 303K$) and (b) pre-heating ($T_f = 323K$) (extracted from [De Oliveira et al. 2019]).

Detailed numerical analysis of the transient ignition phenomenon in two-phase flow has been completed by Aggarwal and Sirignano [1985] and Aggarwal and Nguyen [1990] for a large range of equivalence ratio and compared to premixed gaseous cases. As shown on Fig. 4.1.5, the existence of an optimal total equivalence ratio minimizing the MIE for a fixed droplet size has been demonstrated.

Interaction spark-droplets

A lot of open questions remain concerning the early stage of the ignition process and the interaction of the spark with the droplets. A realistic two-phase ignition DNS of a pin-pin configuration using high temperature energy deposition and plasma kinetic has been performed in [Collin-Bastiani 2019]. The result on Fig. 4.1.6 indicates that the shock wave resulting from the spark pushes away the droplets, leading to their accumulation ahead of the flame front and to the pre-evaporation of the mixture by the shock-induced thermal elevation. The effect of the blast wave has been also tackled in an experimental study [Gebel et al. 2013]. Results displayed on Fig. 4.1.7 show that, close to the spark ($5\,mm$), droplets are subjected to catastrophic breakup events resulting in an homogeneous mist of very small droplets which promotes the evaporation and thus the ignition. At a larger distance from the spark ($10\,mm$), the droplet are first deformed and can eventually split into 2 or 3 secondary droplets.

4.1.4 Ignition models

The simplest model to initialize an ignition simulation is to superimpose to the gas flow a 1-dimensional spherical laminar flame profile. This method has been used in DNS to study the influence of the turbulence intensity on the burning rate of premixed flames [Fru et al. 2011]. However, it completely skips the first phase of the ignition to focus on the propagation phase. Furthermore, it is a strong assumption to consider that the spark energy deposition will correspond to a spherical flame without any influence on the gas phase.

To better model the ignition phase, the general phenomenology of the spark ignition needs to be understood. The formation of a flame kernel using a spark-plug device results in the formation of a hot plasma between the electrodes [Maly and Vogel 1978]. A plasma is a mixture containing charged species including heavy ions and free electrons. The full simulation of the spark discharge until the kernel formation is still

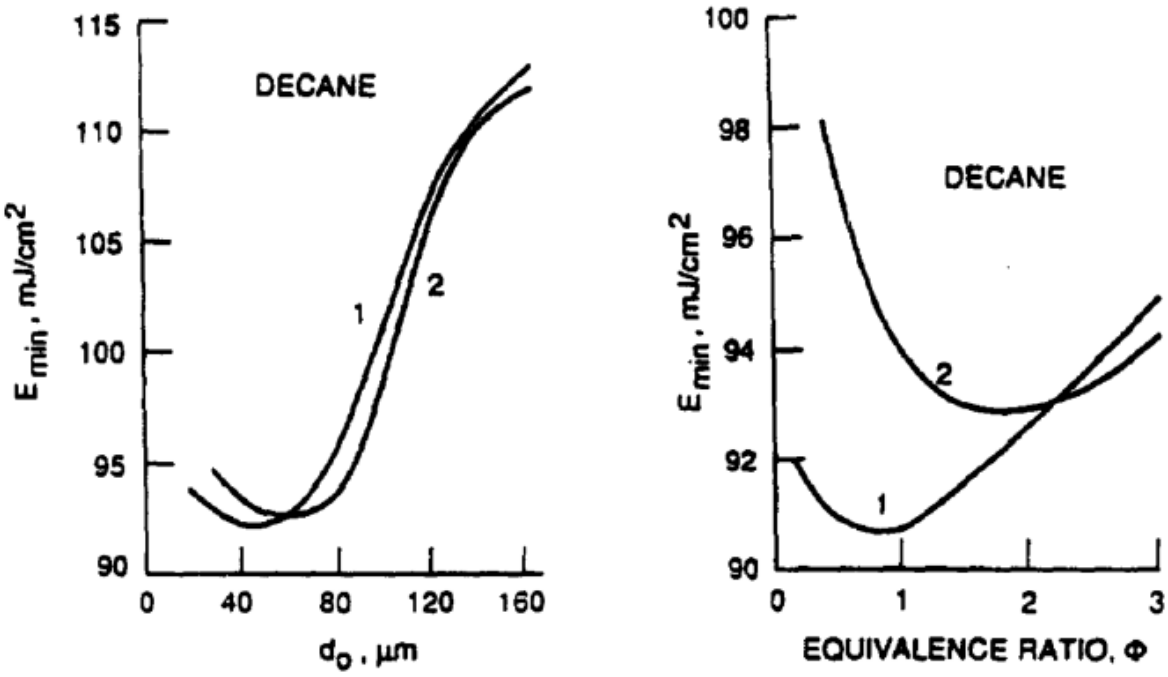

(a) $\phi = 1$ (curve 1) and $\phi = 2$ (curve 2).

(b) $d_0 = 40\,\mu s$ (curve 1) and $d_0 = 80\,\mu s$ (curve 2).

Figure 4.1.5: Dependency of the MIE to the droplet diameter (a) and total equivalence ratio (b) (adapted from [Aggarwal and Nguyen 1990]).

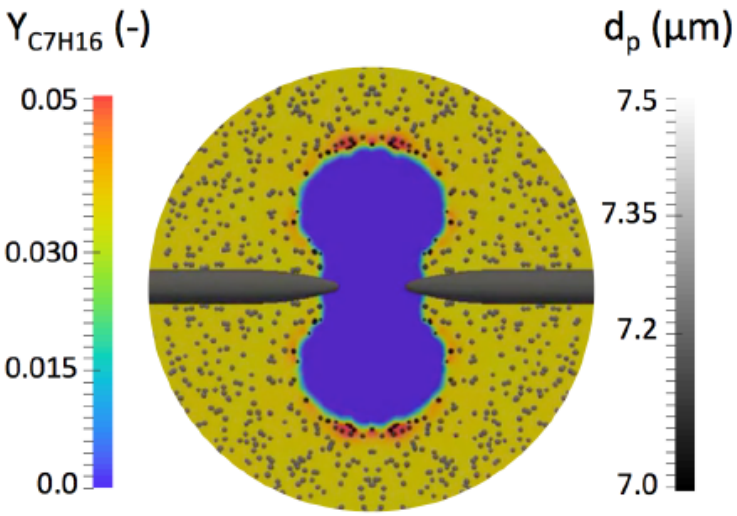

Figure 4.1.6: Ignition of an n-heptane/air mixture at atmospheric conditions ($\phi_g = 0.5$ and $\phi_l = 0.5$). Fuel droplet are uniformly initiated in the domain with a constant initial diameter $d_p = 15\,\mu m$ (extracted from [Collin-Bastiani 2019]).

an open problem, especially the plasma physics is not fully understood and very complex to simulate. Several studies have tried to couple the Navier-Stokes equations with statistical thermodynamic models [Sher et al. 1992, Kravchik et al. 1995]. These studies and experimental measurements have shown that the transition between the spark and the kernel formation can be divided in several steps illustrated Fig. 4.1.8:

- **Breakdown phase** $t_{bd} \approx 1\,ns$**:**
  In the breakdown phase, free electrons move quickly from the cathode towards the anode due to the

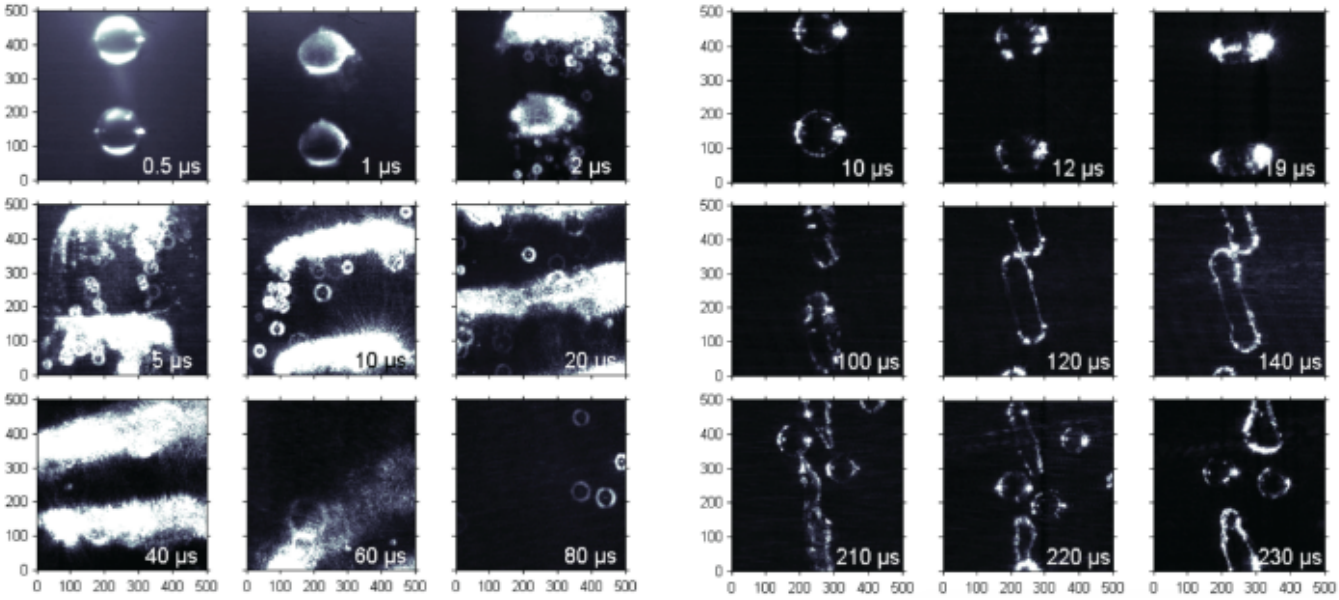

Figure 4.1.7: MIE scattering of Jet A1 droplet breakup at $5\,mm$ (left) and $10\,mm$ (right) below the breakdown focus. Dimensions are given in μm (extracted from [Gebel et al. 2013]).

high voltage applied between the electrodes. This displacement creates a cylindrical streamer of a few micrometers diameter which moves like an ionizing wave. At this stage, the gas temperature remains relatively low ($1000\,K$). The electrons are not in thermal equilibrium with the gas and reach a temperature as high as 60 000 K thanks to the high electric field: this is what it is called a non-equilibrium or low-temperature plasma. This plasma is typical of Nanosecond Repetitively Pulsed (NRP) Discharges applications [Barleon 2022, Cheng 2022] where the applied voltage is switched-off after a few nanoseconds to avoid thermal equilibrium transition. The breakdown corresponds to the moment when the plasma fills the entire inter-electrode gap which becomes conductive. The gas impedance drops as well as the voltage, and the current largely increases. Thus, the electron flux rises in the channel causing a large number of collisions with the species. These interactions heat the gas up to $60000\,K$ leading to a hot equilibrium plasma. At such temperature, all the species are considered dissociated or ionized. The pressure raises up to $100\,bar$ creating a shock wave which controls the kernel front.

f

- **Arc phase** $t_{arc} \approx 1\,\mu s$**:**
  At the arc phase, the power progressively decreases, and the ionized gas starts to cool down towards the adiabatic temperature and recombines to form uncharged species. The kernel flame front detaches from the shock wave since this latter propagates faster than the flame speed. The arc phase is controlled by the diffusion processes.

- **Glow phase** $t_{glow} \approx 1\,ms$**:**
  The last phase of spark ignition is the glow. This phase provides the most important part of the energy due to its long duration. The kernel flame front is driven by the competition between the thermal diffusion and the heat release rate coming from the chemical reactions. A typical toroidal shape (see Fig. 4.1.9) is observed due to recirculating flows [Thiele et al. 2000, Collin-Bastiani et al. 2019].

Because of its complexity, the resolution of the plasma phase in ignition computations is almost impossible and has been performed only in small DNS configurations. These simulations require to solve the Navier-Stokes system of equations with complex transport as well as the coupled charged species transport and electromagnetic equations. Such simulations need a mesh discretization and time-steps much smaller than the regular ones traditionally used to solve classical chemical combustion processes: $\Delta x_{plasma} \approx 1-5\,\mu m$ and $\Delta t_{plasma} \approx 10^{-12} - 10^{-13}\,s$. At the end, the CPU-cost is too large. Thus, several models have been

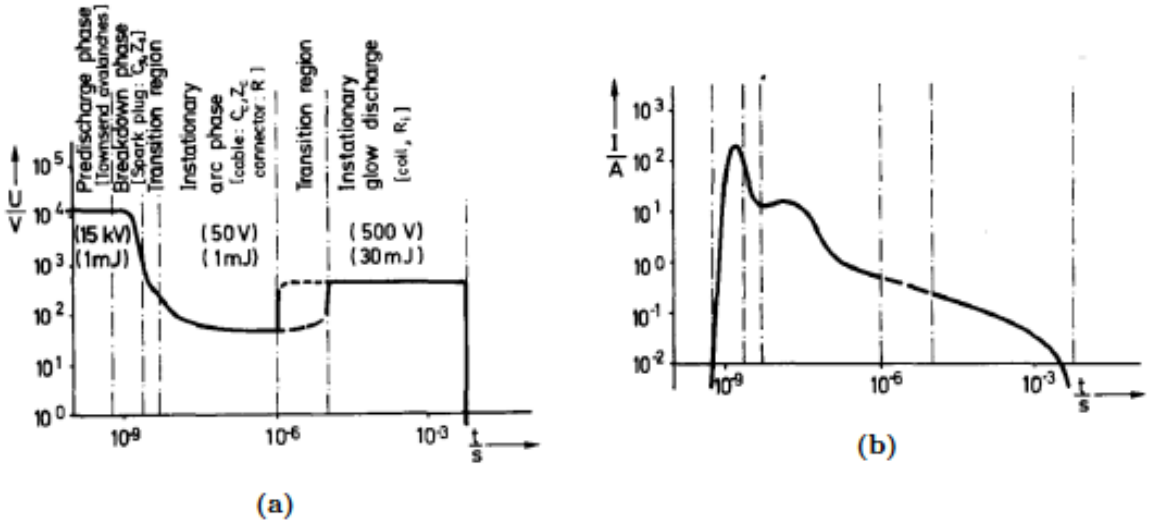

Figure 4.1.8: Diagrams of voltage (a) and current (b) during the ignition illustrating the three phases of ignition (extracted from [Maly and Vogel 1978])

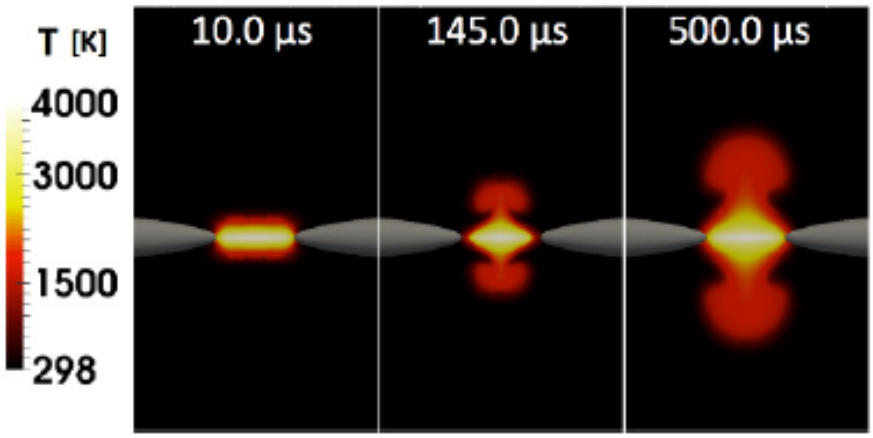

Figure 4.1.9: Spark ignition simulation in pin-pin configuration (extracted from [Collin-Bastiani 2019])

suggested to solve independently the ignition phase and their outputs are integrated to LES or RANS simulations:

- A first approach is to solve, in a reduced domain, the laminar development of the kernel and then interpolate it on the LES mesh [Boudier et al. 1992]. The laminar kernel is interpolated when its laminar stretch becomes lower than the turbulent one.

- The ATKIM model has been developed by Duclos and Colin [2001] and is dedicated to RANS simulations. It uses an electrical circuit model, a description of the arc phase using Lagrangian particles, a tracking of several sparks that can potentially lead to a kernel formation, and a modeling of the electrodes to take into account the thermal losses.

- For RANS two-phase flow simulations, Ouarti et al. [2003] and then Garcia-Rosa [2008] have created a model computing the 1-dimensional development of the kernel based on the flow conditions at the spark location and taking into account the two-phase flow phenomena.

Another solution to mimic the energy deposit of the spark is simply to add a source term to the energy conservation equation. The resulting temperature increase enables to activate the chemical reactions and

ignite the mixture. This approach has been used in several DNS studies [Poinsot 1991, Baum and Poinsot 1995, Chakraborty et al. 2007], and LES simulations [Lacaze et al. 2009, Jones et al. 2011, Esclapez 2015, Collin-Bastiani 2019]. Sloane [1985] has studied the ignition in a laminar flow using an energy source term, or a radical species source term (H, O and OH), or both at the same time. The results indicate that, for the kinetic scheme used, the radical addition effect is negligible compared to the thermal effect. This can be explained because ignition is mainly driven by a thermal balance.

In this PhD, the classical model of Lacaze [2009] is used and presented in Appendix G.5. In this model, the maximum temperature of the energy deposit is limited to $5000\,K$ to avoid numerical and chemical instabilities. To conserve the same energy deposited, the deposit size is increased and follows a Gaussian profile equivalent to the diffusion profile observed after a real spark. Until now, a good agreement has been observed between simulations using this approach and experimental measurements [Enaux 2010], indicating that this strong approximation is accurate enough to study the ignition.

Except for the first instants of the ignition, it has been shown that it is not necessary to consider the high temperatures and the plasma chemistry [Collin-Bastiani et al. 2019]. Fig. 4.1.10 shows the evolution of the temperature at the spark location depending on the use of a plasma chemistry or not in a pin-pin configuration. The results indicate that the temperature increase is almost twice larger without the plasma reactions. Indeed, with the plasma modeling, a part of the deposited energy during the breakdown phase is stored chemically mainly due to the dissociation processes. However, this chemical energy is then progressively converted to heat during the arc phase due to the recombination reactions. Finally, at two microseconds, both temperature profiles merge.

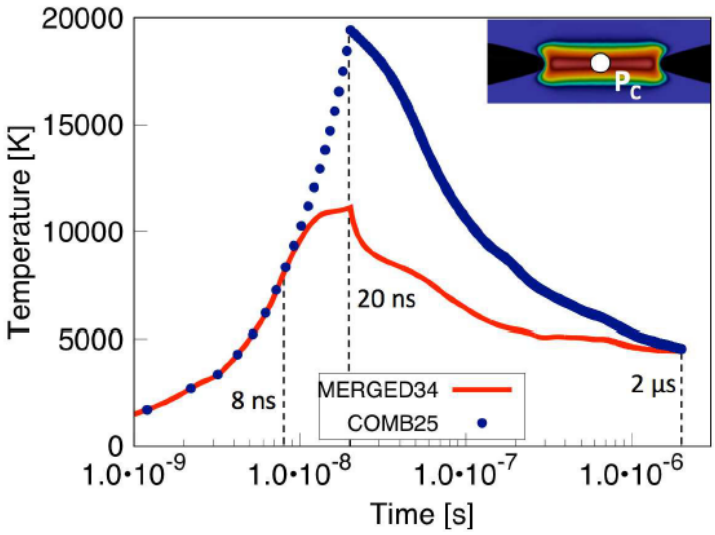

Figure 4.1.10: Evolution of the temperature versus time at the spark position. MERGED34: with the plasma chemistry, COMB25: Only classical combustion chemistry (extracted from [Collin-Bastiani 2019])

On the contrary, Sloane and Ronney [1993] have shown that using too simplified chemical schemes along with simplified thermodynamic and transport properties makes any correct evaluation of the MIE impossible. The global chemistries are not accurate enough to recover the unsteady kernel development and formation. They observed that the MIE predicted with the global chemistry was one order magnitude lower than the value given with the detailed chemistry or experimentally measured. The authors explained these differences by the missing endothermic reactions of radical formations or fuel pyrolysis at the beginning of the ignition process.

4.2 Propagation towards the injector

Once the stable kernel is formed, the latter must propagate toward the injector and interact with the surrounding media. the transition from laminar to turbulent propagation, the effect of the turbulence,

the kernel extinction mechanisms and the influence of the liquid phase are discussed in the following parts.

4.2.1 Laminar-turbulent transition of the propagating flame

At the beginning of the propagation, the combustion speed is controlled by the stretch resulting from the kernel expansion [Poinsot 1991]. The stretch of a spherical kernel flame front without turbulence writes [Poinsot and Veynante 2012]:

$$\kappa = \frac{2}{R_{ker}} \frac{dR_{ker}}{dt} \tag{4.13}$$

with R_{ker} the kernel radius. At this stage, the kernel development rate strongly depends on the fuel Lewis number Le_F: for $Le_F < 1$ the stretch increases the consumption speed, and inversely for $Le_F > 1$ [Poinsot and Veynante 2012]. In the general case $Le_F > 1$ which indicates that the stretch has a detrimental effect on the kernel development. For the specific case of hydrogen flames $Le_F < 1$ which induces thermo-diffusive instabilities as shown on Fig. 4.2.1. Indeed, when the flame front is convex (on the fresh gases side), the fuel species diffuses towards the flame front faster than the temperature diffuses towards the fresh gases. These reactants are then heated and burnt faster than in the case of a planar laminar flame. Hence, the convex front tends to develop contrary to the concave regions. This unstable phenomenon leads to a flame wrinkling and a transition towards a turbulent flame. The opposite mechanism takes place for heavy fuels: the reactants burn faster in concave regions than convex ones which stabilizes the flame front.

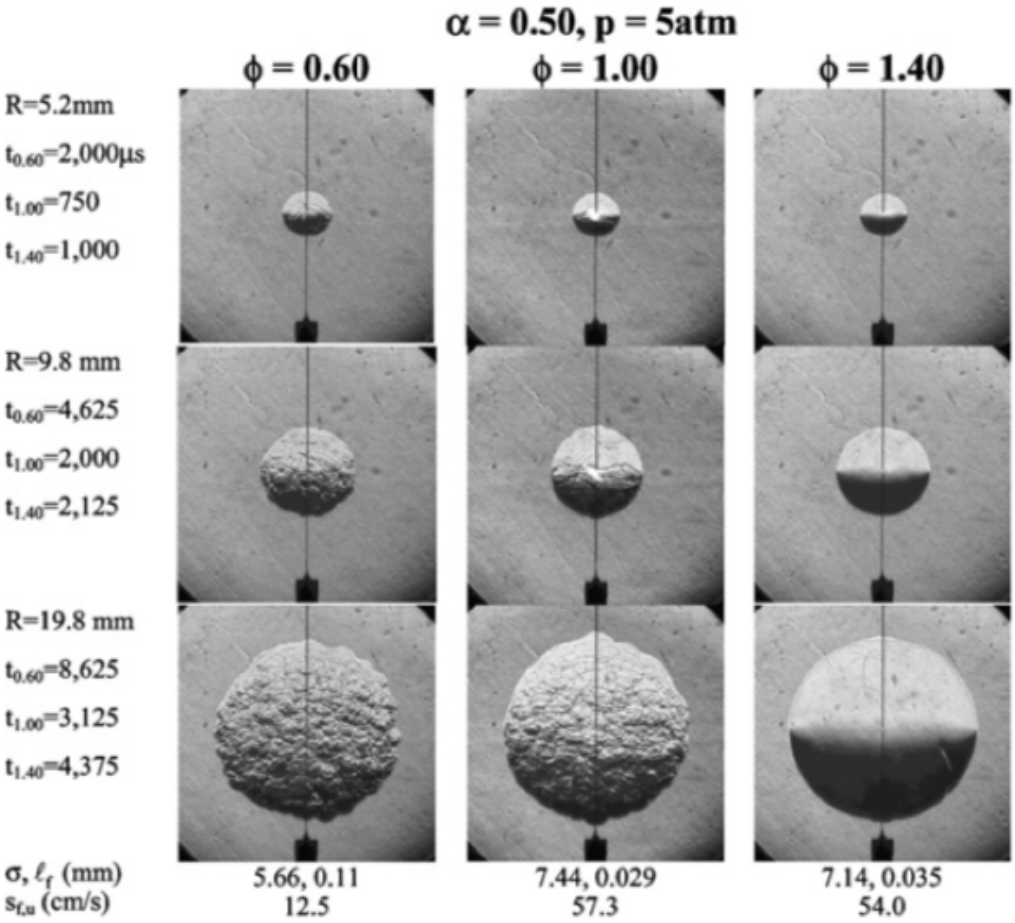

Figure 4.2.1: Schlieren visualizations of the thermo-diffusive instabilities (extracted from [Law et al. 2005])

Initially, the kernel is only sensitive to the turbulence of which the characteristic time is of the order of the elapsed time since the energy deposit $t_{elapsed}$ [Abdel-Gayed et al. 1988]. The turbulent scales larger

than the kernel size only have a global transport effect without affecting the flame front. Then, along with its development, the kernel progressively interacts with larger and more energetic turbulent scales. To account for this effect, Abdel-Gayed et al. [1988] have introduced the effective turbulent velocity concept u'_{eff}. The latter is defined from the integral of the power density spectrum between the cut-off frequency $f_{ker} = 1/t_{elapsed}$ and the Kolmogorov one as shown on Fig. 4.2.2. Experimental measurements of kernel radii from Bradley et al. [2004] have concluded on the effect of the effective turbulence on the kernel development. Fig. 4.2.3 displays the radii as a function of the time: they are very similar at the first instants and diverge at later times. Furthermore, the time corresponding to the curves separation decreases when the turbulent intensity increases. Indeed, the Kolmogorov scale is smaller, thus the integral of the power spectral density is higher, resulting in a larger effective turbulent velocity.

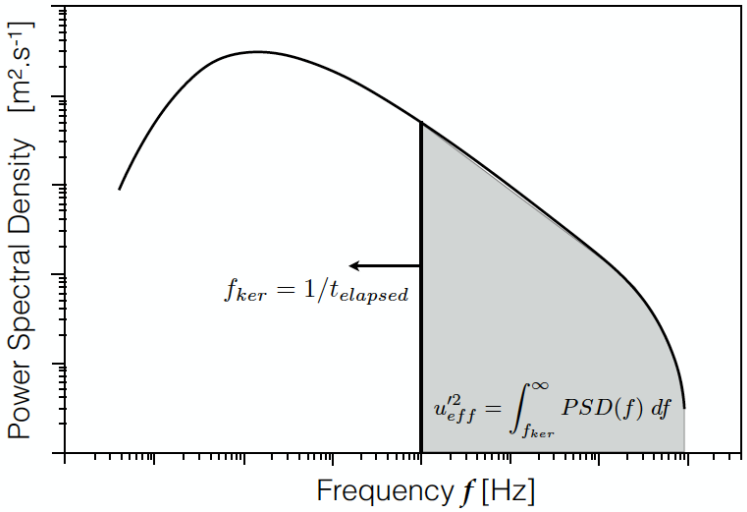

Figure 4.2.2: Power spectral density used to evaluate the effective turbulent velocity (extracted from [Abdel-Gayed et al. 1988])

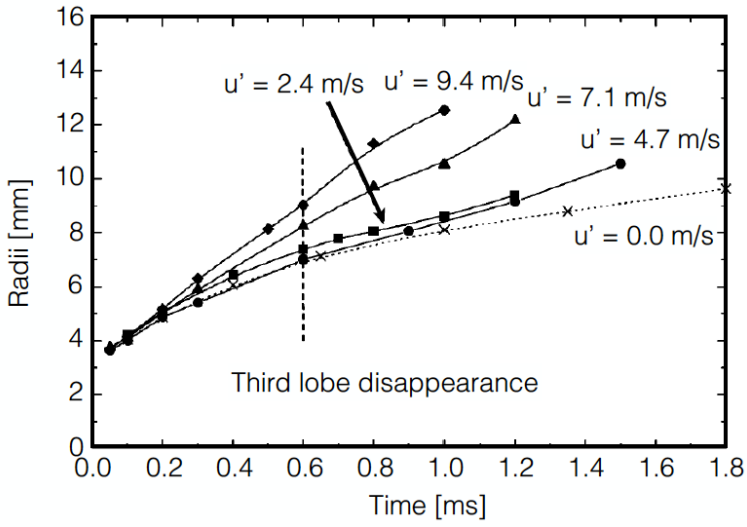

Figure 4.2.3: Kernel radii temporal evolutions for several turbulent intensities (extracted from [Bradley et al. 2004]) (The third lobe disappearance refers to a phenomenon observed in laser ignition experiments)

In non-premixed or partially premixed combustion regimes, the kernel development is strongly correlated to the quantity of flammable mixture in the energy deposit region [Cardin 2013]. In the case of stratified mixtures (the mixture fraction remains either rich or lean at the kernel location), the kernel development is similar to the premixed case. However, the inhomogeneous mixture fraction creates heat release rate variations [Renou et al. 2004]. These variations induce a non negligible wrinkling in low turbulent flows

and drive the kernel towards more stoichiometric regions. For high turbulent flows, this wrinkling becomes negligible compared to the aerodynamic one [Poinsot et al. 1996]. When the kernel reaches the stoichiometric line, the flame front switches to a triple flame structure. Then, the kernel development relies on the capability of the triple flame to propagate [Chakraborty et al. 2007, Chakraborty and Mastorakos 2008].

4.2.2 Effect of turbulence on the kernel propagation

The flame kernel development is similar to a flame front propagation. Hence, the turbulence influence can be analysed using a classical combustion diagram as presented in Chap. 3. When the turbulence starts interacting with the kernel, a flame front wrinkling is observed [Poinsot 1991, Kaminski et al. 2000] which enhances the kernel development. If the turbulence intensity exceeds a critical threshold, the vortexes can enter in the kernel which can lead to its extinction in the extreme case.

In order to understand the effect of the turbulence on the kernel, the simplified configurations of kernel-vortex interactions have first been studied, varying the vortex strength and size. The DNS study of Kolera-Gokula and Echekki [2006] with premixed hydrogen-air mixtures has revealed an increase of the growth rate due to the kernel deformation. Furthermore, two interaction regimes have been highlighted: the breakthrough regime, where the vortexes are strong enough to cross the kernel but without extinction, and the extinction regime. Both regimes go with strong kernel wrinkling, flame-flame interactions, and stretch and curvature effects. In their work, Vasudeo et al. [2010] have built a kernel-vortex interaction diagram presented Fig. 4.2.4 with the following regions:

- **Laminar regime:**
  The vortexes are small or weak. The kernel is little perturbed and the vortexes dissipate with the increase of temperature and viscosity at the flame front.

- **Wrinkling regime:**
  The vortexes size and strength increase, enabling them to deform and enter in the kernel. However the vortexes are quickly dissipated and do not break the kernel structure.

- **Breakthrough regime:**
  If the vortexes intensity keeps increasing, they can cross the kernel and split it in several parts.

- **Global extinction regime:**
  This regime corresponds to the total extinction of the flame kernel.

- **Regeneration after Global Extinction (RGE) regime:**
  Finally, the RGE regime is an extension of the breakthrough regime. If the vortex is large enough compared to the kernel, the splitted parts of the kernel are convected by the global motion and can regenerate separately.

One can note that the ratios given in Fig. 4.2.4 are very high because it corresponds to an hydrogen-air chemistry. For kerosene kernels, similar regimes are expected but with much reduced ratios. Furthermore, [Vasudeo et al. 2010] have shown that the chemical description has an important effect on the kernel-vortex interaction. A simplified global chemistry is not able to reproduce the re-ignition associated to the flame-flame interaction and the kernel reconstruction.

In the more realistic case of the kernel development inside a turbulent flow, the interaction is not fully equivalent to a vortexes superposition of several sizes and strengths. The coupling interactions between the various scales must be taken into consideration. Reddy and Abraham [2013] have realized 2-dimensional DNS of kernel-turbulence interactions with lean methane-air mixtures and have built the interaction diagram of Fig. 4.2.5. Globally, these regimes are close to those observed in the kernel-vortex interactions:

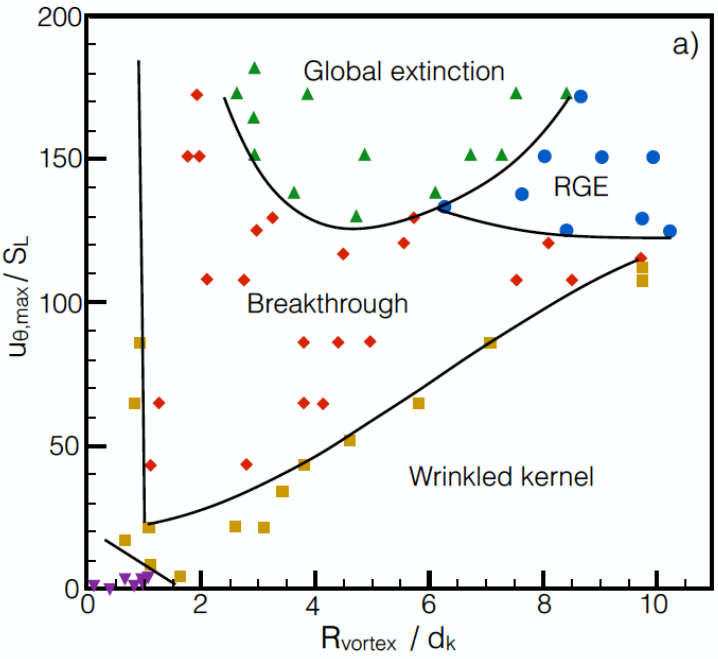

Figure 4.2.4: Kernel-vortex interaction diagram (extracted from [Vasudeo et al. 2010])

- **Laminar regime:**
  In the case of a too weak turbulent intensity, the effect on the kernel is negligible. The kernel development is similar with a flow at rest.

- **Wrinkling regime:**
  In the case where the velocity fluctuations are of the same order of magnitude than the flame speed, the turbulence has a wrinkling effect on the kernel flame front. The wrinkling regime is optimal for the kernel development and the maximum growth rates are observed. Turbulence enhances the combustion processes due to the increase of the flame surface [Poinsot 1991, Gashi et al. 2005, Jenkins et al. 2006, Fru et al. 2011, Reddy and Abraham 2013].

- **Breakup regime:**
  The breakup regime corresponds to excessive u'/S_L ratios. As well as the kernel-vortex or flame-vortex interactions, the eddies cause local extinctions and can split the kernel in several parts which may lead to its global extinction.

- **Convection regime:**
  In this additional regime, the turbulent integral scale is larger than the kernel size. With these conditions, the kernel is subject to a convection effect rather than a deformation. A recent study of Turquand d'Auzay et al. [2019] shows that the turbulent convection can also cause an ignition failure with long energy deposit if the kernel moves away from the deposit center. Furthermore, the kernel can also be convected in cooler regions which increases the thermal losses, or towards low flammability regions.

The effect of turbulence in non-premixed configuration is difficult to evaluate because of the coupling between the velocity fluctuation and the mixture fraction fluctuation. Chakraborty et al. [2007] have shown in a turbulent mixing layer DNS study that the high turbulent velocities increase the mixture fraction gradients which slows down the triple flame propagation [Ko and Chung 1999].

Finally, most of the DNS studies are limited to 2-dimensional configurations due to the high computational cost. Several studies [Thevénin et al. 2002, Gashi et al. 2005] have shown that the the maximal

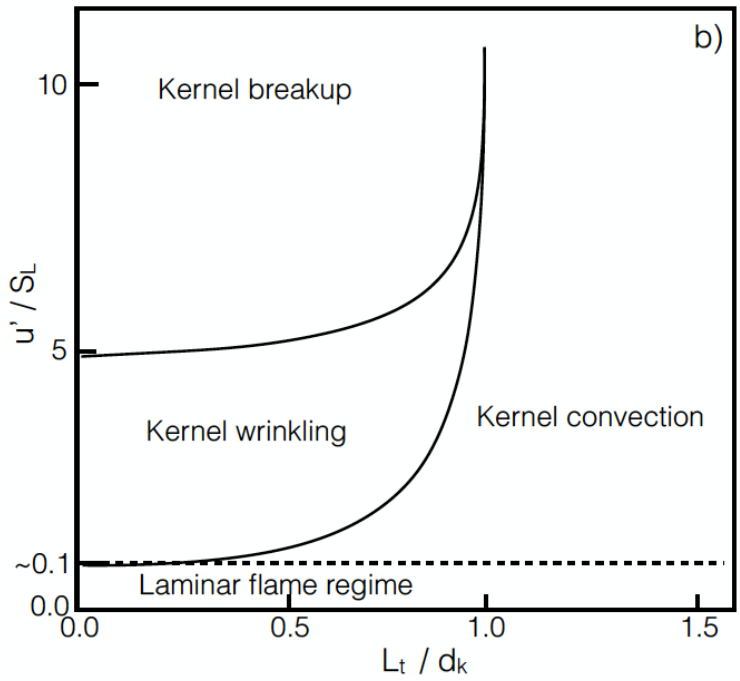

Figure 4.2.5: Kernel-turbulence interaction diagram (extracted from [Reddy and Abraham 2013])

stretch is higher in 3-dimensional cases, and the curvature distribution is shifted to lower values.

4.2.3 Extinction mechanisms

The kernel extinction mechanisms have been studied relatively recently in experimental set-ups using advanced optical diagnostic methods [Trunk et al. 2013, Kerl et al. 2013, Peterson et al. 2015]. These techniques have brought a new knowledge on kernel development and enable to validate results coming from the numerical simulations. Two main mechanisms can lead to a kernel extinction: 1) a modification of the global kernel structure by the large scales of the turbulence, 2) a modification of the flame front structure with vortexes with a size of the order of the flame thickness.

In their 2-dimensional DNS study of kernel development in a turbulent flow, Poinsot [1991] has shown that the turbulent flow can remove gas pockets from the kernel. Due to their small size, these pockets face larger thermal losses than the heat release production, and thus extinct. As a consequence, from the kernel point of view, this mechanism removes a non negligible part of the heat, making it more sensitive to the heat release rate or diffusion variations due to the turbulence. Hence, the kernel development is slowed down or, in the worst case, it extinguishes which corresponds to the kernel break-up regime detailed in the previous section. Such mechanism has been also observed in 3-dimensional DNS for several turbulence intensities and methane-air equivalence ratios [Fru et al. 2011]. The kernel temporal evolution and the interaction with the turbulence are presented on Fig. 4.2.6 and show the gas pockets detached from the main kernel.

If the pockets are large enough, they can continue to burn independently and contribute to the ignition process as shown with the RGE regime Vasudeo et al. [2010].

The second extinction mechanism results from the interaction between the kernel flame front and the turbulence. A 3-dimensional DNS study from Jenkins and Cant [2002] has shown that the deformation of the flame front by the vortexes induces a stretch and a curvature which harms the kernel development because of a larger tangential diffusion. Klein et al. [2006] have observed in DNS negative displacement speeds characteristic of local extinctions [Gran et al. 1996, Chen and Im 1998, Kolera-Gokula and Echekki 2006], and have highlighted a correlation between these negative speeds and high positive curvatures. Furthermore, studies from Jenkins and Cant [2002], Reddy and Abraham [2013] show the curvature distribution

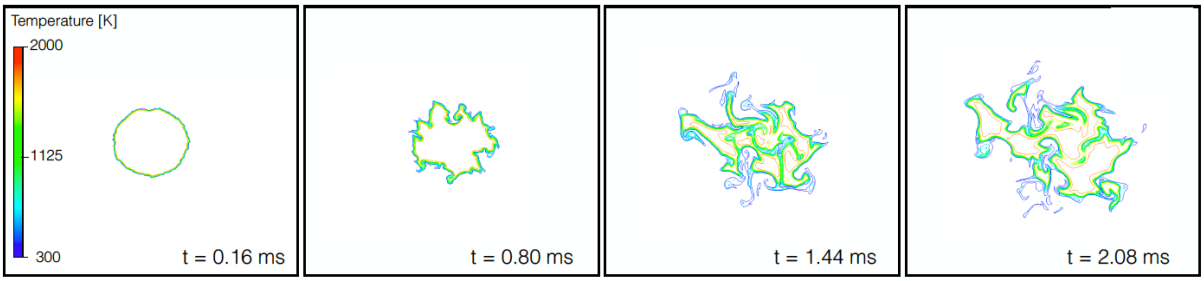

Figure 4.2.6: Temporal evolutions of temperature iso-contours in a decreasing HIT (extracted from [Fru et al. 2011])

spreads when the turbulent intensity increases.

The mixture composition influence has been less studied as it requires complex experimental set-ups [Renou et al. 2004, Ahmed et al. 2007]. These studies have shown that the shape and wrinkling of the kernel are also modified by the fuel distribution. DNS studies have evaluated the influence of the mixture fraction and especially its gradient on the kernel growth [Chakraborty and Mastorakos 2006, Neophytou et al. 2010]. Hence, Esclapez [2015] adds an additional quenching regime, corresponding to the mixture inhomogeneities, to the main kernel extinction mechanisms observed in non-premixed combustion. These mechanisms are presented in Fig. 4.2.7

4.2.4 Flame growth in spray mists

The kernel propagation in spray flows is often characterized by an initial non-flammable mixture since the fuel is mainly liquid. Wandel et al. [2009] have shown that different scenarii may happen depending on the initial energy given by the spark:

- With too low energy, droplet evaporation is not sufficient to reach the lean flammability limit. Then, the energy is directly diffused so that ignition never starts. It is referred as the short extinction mode in [De Oliveira et al. 2019].

- With higher energy, a small flammable zone is created and a flame kernel is formed. However, the heat release rate is not high enough to compensate both thermal diffusion and droplet evaporation. Thus, the flame kernel is not able to propagate in the spray mist. It is referred as the long extinction mode in [De Oliveira et al. 2019].

- Finally, with an important initial energy deposition, a large kernel is generated and releases enough energy to evaporate droplets in front of the flame kernel and allows a sustainable propagation.

Neophytou et al. [2010] have also investigated the growth of a flame kernel in a turbulent droplet-laden mixing layer with DNS. The mixture was globally rich $\phi_{tot} = 2$ leading to the creation of a triple flame following spark ignition. However, the measured propagation speed have been found to be lower than the laminar flame speed of the equivalent stoichiometric gaseous flame. They conclude that the flame propagation is mostly due to the turbulent motion of the flow.

The kernel extinction regime due to mixture inhomogeneities presented in [Esclapez 2015] for gaseous mixture remains possible for two-phase flows. Indeed, droplet preferential segregation effects already presented earlier can induce mixture inhomogeneities after evaporation which is detrimental for the kernel propagation. More generally, all the effects presented in Sec. 3.5 are also observed for the kernel propagation.

Finally, according to Mastorakos [2017], the regions of highest ignition probability in a combustion chamber are those close to stoichiometry and with a weak local turbulence. This would correspond to quiescent recirculation zones in typical aeronautical burners.

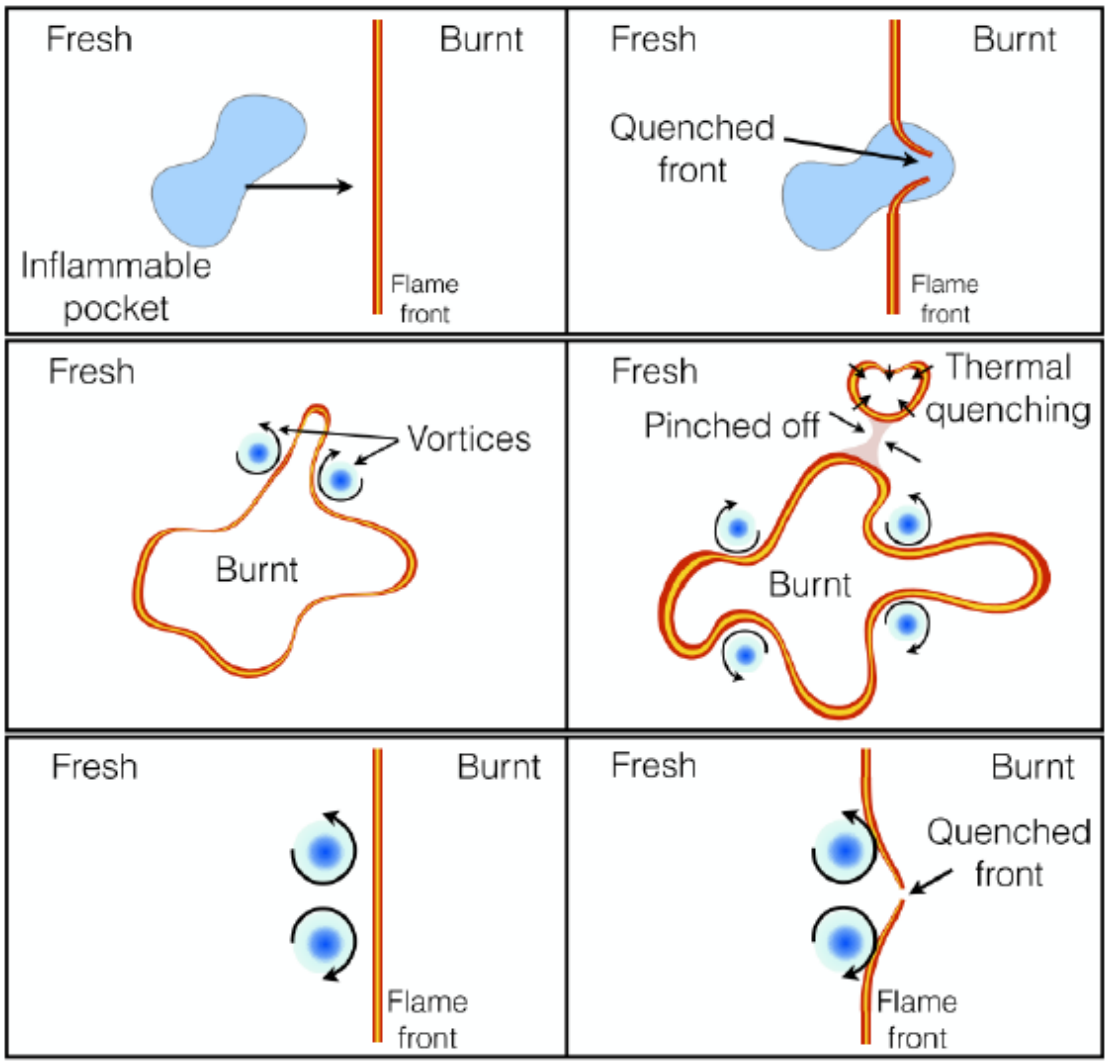

Figure 4.2.7: Summary of the three main flame kernel quenching mechanisms in non-premixed flows (extracted from [Esclapez 2015]).

Part II

Chemical and gaseous aspects

Everything negative - pressure, challenges - is all an opportunity for me to rise.
Kobe Bryant, 1978-2020

Chapter 5

Influence of low pressure and low temperature conditions on canonical cases

Contents

High altitude conditions have a detrimental influence on the engine relight, reducing the ignition probability. The effect of low pressure ($P = 0.3\,bar$) and low temperature ($T = 233\,K$) is however not well understood. Therefore, in this chapter, the impact of high altitude conditions is evaluated from a macroscopic point of view. A review of temperature and pressure influences on combustion processes is first given in Sec. 5.1. Then, the effects of low pressure and low temperature conditions in canonical configurations are described in Sec. 5.2. Finally, the impact of the fuel surrogate model and chemical model in these same configurations is investigated in Sec. 5.3.

5.1 Literature review on pressure and temperature influences

Measurements of macroscopic quantities at different pressure and temperature conditions enable to evaluate the impact of pressure and temperature on laminar flame speed [Poinsot and Veynante 2012]:

$$S_L(P, T_f) = S_L(P_0, T_{f,0}) \times \left(\frac{P}{P_0}\right)^{\alpha_P} \times \left(\frac{T_f}{T_{f,0}}\right)^{\alpha_T} \tag{5.1}$$

where T_f is the fresh gas temperature and the subscript *0* refers to a reference operating point.

Table 5.1.1 provides experimental values for the pressure and temperature power exponents for methane-air combustion depending on the equivalence ratio for a given range of pressure ($1 \leq P \leq 10\,bar$) and a given range of temperature ($300 \leq T_f \leq 400\,K$) [Gu et al. 2000].

The positive exponent α_T indicates that in the range of pressure and temperature considered by Gu et al. [2000], the laminar flame speed increases when the fresh gas temperature increases. On the contrary, the

Fuel	$S_L(P_0, T_{f,0})$ $[m.s^{-1}]$	α_T	α_P
Methane $\phi = 0.8$	0.256	2.105	-0.504
Methane $\phi = 1$	0.360	1.612	-0.374
Methane $\phi = 1.2$	0.314	2.0	-0.438

Table 5.1.1: Example of pressure and temperature exponent coefficients (α_P and α_T respectively) for methane/air combustion (extracted from Gu et al. [2000])

negative exponent α_P suggests that the laminar flame speed increases when pressure decreases. Similar values are generally observed for other fuels and pressure/temperature ranges but with different exponent coefficients. A more detailed analysis of the macroscopic effects of low pressure and low temperature will be presented in Sec. 5.2 for kerosene-air.

Temperature and pressure not only affect global flame quantities but also notably influence the chemical kinetics and the decomposition pathways, as discussed hereafter.

5.1.1 Temperature effects

Temperature plays a major role in the chemical reactions, as it is directly used to compute the reaction rates within the Arrhenius relations:

$$k_j(T) = A_j T^{\beta_j} \exp\left(\frac{-E_{a,j}}{\mathcal{R}T}\right) \quad j = 1, N_r \tag{5.2}$$

where T is the temperature, A_j, β_j, and $E_{a,j}$ are respectively the pre-exponential constant, the temperature exponent, and the activation energy of reaction j. $\mathcal{R}$ is the universal gas constant ($\mathcal{R} = 8.31446 J.K^{-1}.mol^{-1}$).

A minimum kinetic energy is required for the colliding species to result in a reaction, which corresponds to the activation energy $E_{a,j}$ and can be represented with the diagrams on Fig. 2.1.2. The ratio $E_{a,j}/R = T_{a,j}$ can be seen as an activation temperature. The pre-exponential constant A_j quantifies the reaction reactivity compared to other reactions. Finally, the temperature exponent β_j is a correction enabling to cover a wider temperature range [Laidler 1984].

Temperature also significantly influences the chemical pathways. Indeed, there are two main distinct oxidation processes for heavy hydrocarbon decomposition depending on the temperature [Wang et al. 2018, Felden 2017]:

- **High and intermediate temperature oxidation chemistry:** $T > 750K$
  At high temperature, the fuel decomposition is mainly driven by thermal homolysis reactions which correspond to the spontaneous decomposition of the fuel species into smaller radical alkyls:

  $$F \rightarrow R_1 + R_2 \tag{R1}$$

  These reactions require high activation energies to break the fuel species. The other decomposition mechanism corresponds to the attack of highly radical species (mainly O, OH, and H) on the fuel hydrocarbon [Battin–Leclerc et al. 2000, Warnatz 2000]:

  $$F + R_1 \rightarrow R_3 + P \tag{R2}$$

  The produced radicals then decompose into smaller ones, or enable further fuel decomposition. Finally, they recombine to form the product species CO_2 and H_2O.

- **Low temperature oxidation chemistry (LTC):** $T < 750K$
  For temperatures lower than $T = 750K$, the available kinetic energy is lower than the activation energy required to split the chemical bonds and break the fuel molecule. However, the fuel species can still be decomposed by radical alkyls with the mechanism presented Eq. (R2). Then, the fuel radicals R_3 formed by this reaction mainly react with oxygen to form peroxyalkyls as in Eq. (R3), which can isomerize and be subject again to an oxygen addition reaction. These paths allow

the formation of oxygenated compounds that will also lead to the formation of reactive radicals [Battin–Leclerc et al. 2000].

$$R_3 + O_2 \rightarrow ROO \tag{R3}$$

These mechanisms are often referred to as "cool flames" in the literature, and can impact the combustion processes [Stagni et al. 2018].

The competition of these oxidation mechanisms leads to the so-called Negative Temperature Coefficient (NTC) region ($650\,K < T < 850\,K$). Fig. 5.1.1 shows the generic decomposition pathways at low and high temperatures. When the temperature increases, the path labelled (1) on Fig. 5.1.1 decreases in favour of the high temperature path labelled (2). During this transition, the reaction rates are reduced because the high temperature path produces H_2O_2 species with reactions Eq. (R4) and (R5).

$$\mathrm{F} + \mathrm{HO_2} \rightarrow \mathrm{H_2O_2} + \mathrm{R} \tag{R4}$$

$$2\,\mathrm{HO_2} \rightarrow \mathrm{H_2O_2} + \mathrm{O_2} \tag{R5}$$

Indeed, this species is a "degenerate chain branching" which is stable in the NTC region. If the temperature keeps increasing, the homolysis reaction Eq. (R6) produces OH radical species, which increases the reactivity and enables the chemical runaway:

$$\mathrm{H_2O_2} \rightarrow 2\,\mathrm{OH} \tag{R6}$$

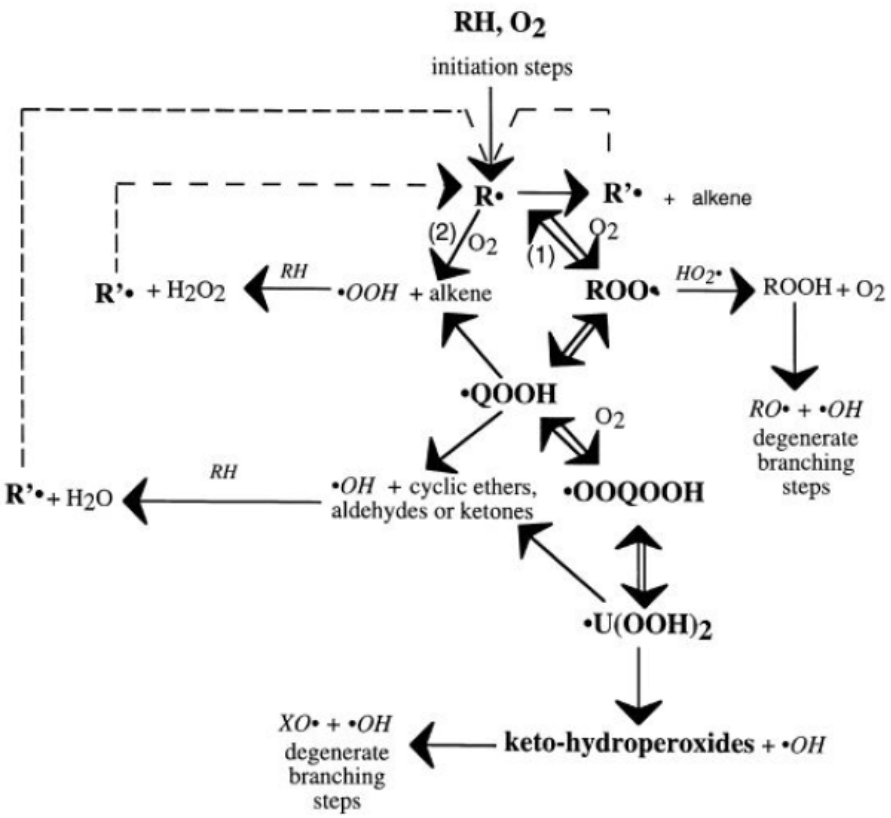

Figure 5.1.1: Simplified schemes for the oxidation of alkanes. (1) Low temperature pathways, (2) high temperature pathways (extracted from Battin–Leclerc et al. [2000])

The resulting effect of the NTC region can be observed on auto-ignition curves for heavy fuels as shown on Fig. 5.1.2. Hence, the low temperature mechanisms and the NTC region need to be taken into account when dealing with low temperature combustion, for example in the study of extinction processes. However, such chemistries require additional species, which increases the computational cost. When

ignition is focused on, the spark results in a high temperature field. Hence low temperature chemistry is often neglected when reducing detailed chemistries to avoid a computational overcost.

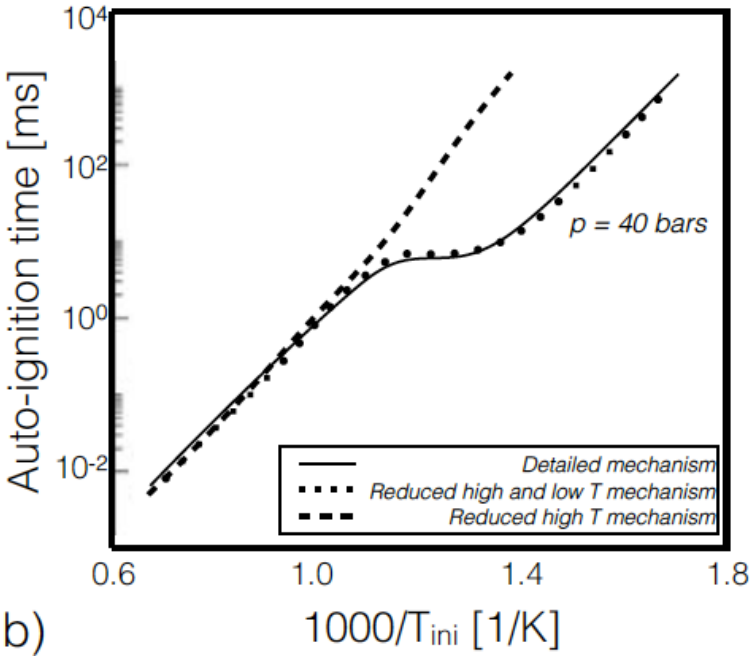

Figure 5.1.2: Auto-ignition time of iso-octane mixture exhibiting the NTC behaviour (extracted from Pepiot-Desjardins [2008])

Note that LTC here refers to combustion processes occurring at temperature in the range $600K - 850K$, which is different from the low temperature conditions encountered at high altitude ($T = 233K$). The low temperature of air at high altitude does not mean that low temperature chemical pathways exist. Indeed, for the ignition of low temperature mixtures, the spark forms, quasi-instantaneously, a high temperature ($T \gg 1000\,K$) region which triggers the chemical reactions via the high temperature pathways. Hence, for such cases, low temperature pathways are negligible.

5.1.2 Pressure effects

Pressure also influences the kinetic chemistry. The vast majority of the reactions are pressure dependent since the production rates are function of the reactant species concentrations which are reduced at low pressure.

Furthermore, several classes of reaction include an additional pressure dependency:

- **Third body reactions:** $A + B + M \leftrightarrow C + M$
  This class of reaction does not include direct pressure dependency in the reaction rate computation. However, it is worth mentioning because these reactions require the collision of 3 species, which is less probable at low pressure conditions. Consequently, in the case of bi-molecular reactions, the reaction rate scales as P^2, whereas for the third body reactions, it scales as P^3. Hence, the third body reactions are predominant at high pressure, and on the contrary reduced at low pressure.

- **Fall-off reactions:** $A + B\,(+M) \leftrightarrow C\,(+M)$
  As presented in Sec. 2.1.3, the fall-off reactions include a pressure dependant correction that enables to change the kinetic order of the reaction as well as the reaction rate. Hence, a fall-off reaction can behave like a third body or a classical reaction depending on the pressure.

- **P-dep reactions:** $A + B \leftrightarrow C$
  The P-dep reactions are classical Arrhenius reactions with a different set of Arrhenius constants

depending on pressure. In this case, the reaction rate is directly dependent on the temperature and the pressure.

Note that the sub-atmospheric and atmospheric pressure conditions considered in this work are generally both considered as low pressures in the literature by opposition to elevated pressures around 10-20 bar that can be encountered in combustion chamber at nominal flight conditions. Therefore, in this work, the fall-off reactions behave like third-body reactions and have a reduced influence.

Low pressures can also modify the chemical pathways. For example, for methane combustion between $P = 0.1\,bar$ and $P = 0.3\,bar$, studies showed that low pressures increase the prompt dissociation of HCO, and that this mechanism must be included in the chemical scheme to reproduce the experimental laminar flame speed [Labbe et al. 2016]. The simulations taking into account this specific dissociation mechanism showed that 20% of the CH_2O decomposition path corresponds to this dissociation [Burrell et al. 2018]. The induced effect is an increased reactivity of the mixture and a laminar flame speed increased by 8% as shown on Fig. 5.1.3.

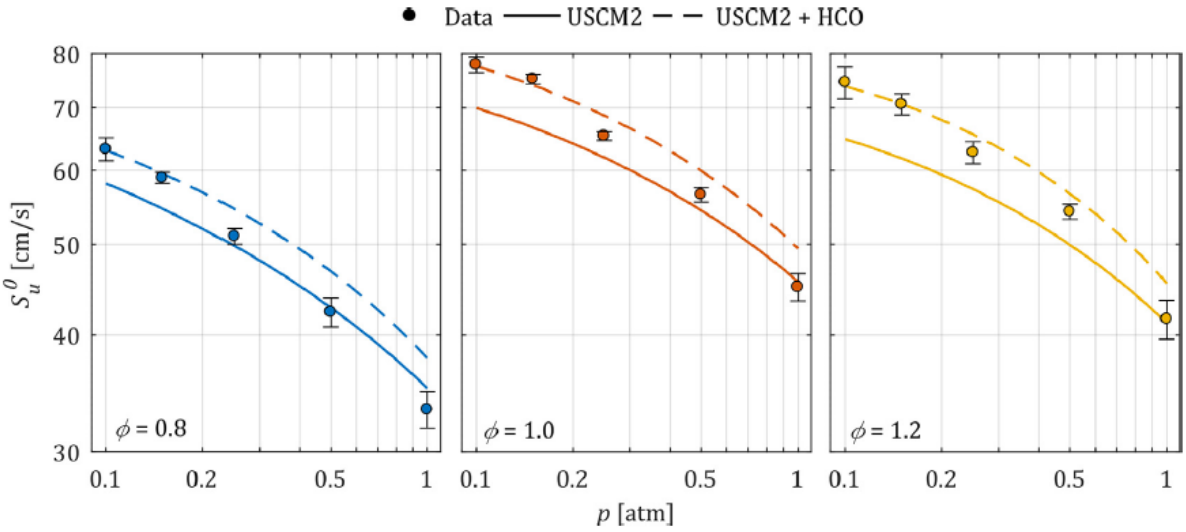

Figure 5.1.3: Experimental (symbols) and numerical (lines) laminar flame speed versus pressure for lean, stoïchiometric and rich methane/air mixtures (Extracted from Burrell et al. [2018])

Another important effect of low pressure is the reduction of the chemical reactivity. Indeed, a study on butane combustion by Li et al. [2018] showed that auto-ignition time increases when pressure decreases. Hence, higher temperatures are reached at ignition as presented on Fig. 5.1.4. However, the laminar flame speed increases due to a larger thermal diffusion.

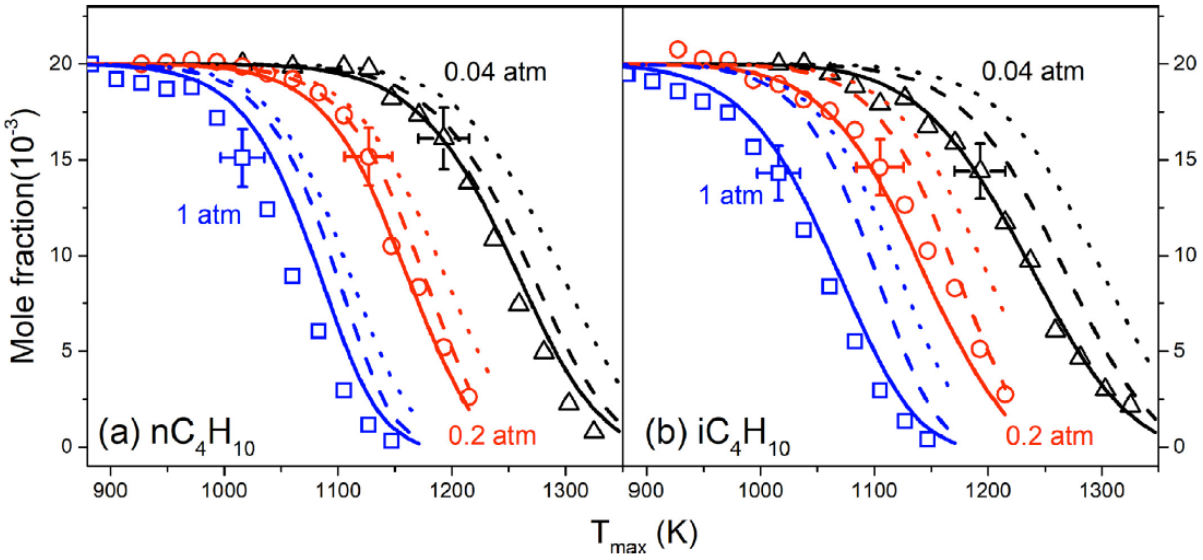

Figure 5.1.4: Comparisons between experimental (symbols) and numerical (lines) butane molar fractions. Solid lines: Li et al. [2018], dotted line: Aramco 2.0 scheme, dashed line: USC Mech II scheme

5.2 Macroscopic effects of low pressure and low temperature

To understand the impact of high altitude conditions on combustion, the effect of the low pressure and low temperature (LPLT) conditions is studied from a macroscopic point of view, considering auto-ignition delay time, laminar flame speed, heat release, adiabatic temperature and flame power.

For this study, detailed chemical mechanisms are directly used within the opensource chemical software CANTERA [Goodwin et al. 2018] that enables to study chemical systems with accurate transport and thermo-chemical properties. However, only 0-dimensional and 1-dimensional canonical configurations (presented Sec. 3.3) can be computed due to the large number of species and reactions involved.

Four specific conditions are studied:

- **PTatmo**, corresponding to the reference atmospheric condition at:
  $T = 300\,K$, $P = 1\,bar$ and $\rho = 1.22\,kg/m^{-3}$
- **LP**, corresponding to the low pressure condition to study the isolated effect of low pressure at:
  $T = 300\,K$, $P = 0.3\,bar$ and $\rho = 0.37\,kg/m^{-3}$
- **LT** corresponding to the low temperature condition to study the isolated effect of low temperature at:
  $T = 233\,K$, $P = 1\,bar$ and $\rho = 1.57\,kg/m^{-3}$
- **LPLT** corresponding to the low pressure and low temperature condition representative of high altitude at:
  $T = 233\,K$, $P = 0.3\,bar$ and $\rho = 0.47\,kg/m^{-3}$

For this part, the detailed kerosene-air chemistry developed by the CRECK modeling group [Ranzi et al. 2012; 2014; 2015] and the tri-component surrogate fuel modeling are used. Detailed information are given in Sec. 2.3.3.

5.2.1 Effects on auto-ignition delay time

The effect of low pressure is firstly studied for 0-dimensional constant pressure reactors using CANTERA. The reaction rate effect can then be isolated because transport properties are not taken into account due to the homogeneity of the mixture. Furthermore, the high temperature auto-ignition is relatively similar to an ignition triggered by energy deposition.

Figure 5.2.1 shows that ignition delay times are increased at low pressure for the whole range of temperature and stoïchiometric mixtures (same results has been observed of rich and lean mixture but not shown). Similar behaviors are observed for rich and lean mixtures. This result shows the slowing down effect of low pressures on the reaction rate which is due to the decrease in density via the perfect gas law $P = \rho \mathcal{R} T$ and thus the species concentrations at low pressure. Indeed, Eq. (5.3) highlights the direct relation between the reaction rate of progress and the species concentrations:

$$\mathcal{Q}_j = K_{f,j} \prod_{k=1}^{N_{spec}} [X_k]^{\nu'_{k,j}} - K_{r,j} \prod_{k=1}^{N_{spec}} [X_k]^{\nu''_{k,j}} \tag{5.3}$$

where $K_{f,j}$ and $K_{r,j}$ are the forward and reverse rates of reaction j, $[X_k]$ is the molar concentration of species k, and $\nu'_{k,j}$ and $\nu''_{k,j}$ are respectively the molar stoichiometric coefficients of the reactants and the products.

The gap between the curves seems globally constant for the whole range of initial temperatures studied. Thus, the pressure influence is decorrelated from the temperature. As explained in Sec. 5.1.1, the initial temperature of the reactor is an important parameter determining the ignition time since it is directly involved in the activation of chemical reactions. The NTC range is not studied here because ignition with energy deposition arises at high temperature ($T > 1000\,K$).

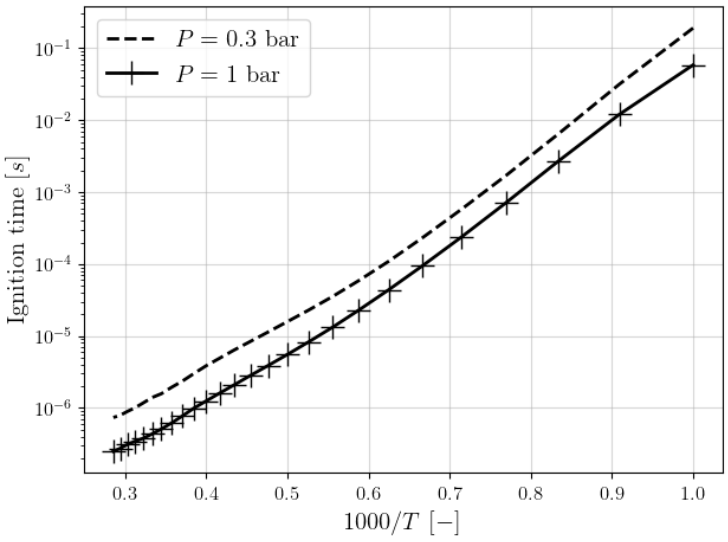

Figure 5.2.1: Auto-ignition delays versus temperature for stoichiometric mixtures and 2 conditions: Patmo (solid line with symbols) and LP (dashed line)

5.2.2 Effects on laminar flame speed

To investigate the impact of the operating conditions on the laminar flame speed, 1-dimensional premixed flames are computed using CANTERA and a multi-component transport formulation for species diffusion [Ern and Giovangigli 1994]. This configuration enables to reproduce the effects of high altitude conditions on the propagating combustion mode encountered during the flame kernel development. The laminar flame speed depends on two main effects: the thermal diffusion and the global reaction rate ($S_L \propto (D_{th} R_r)^{0.5}$) [Poinsot and Veynante 2012]. An increase of the first parameter leads to a faster heating of the fresh gases before they reach the flame front, and an increase of the second one will enhance the combustion processes releasing more heat. In both cases the laminar flame speed increases.

Figure 5.2.2 shows that the laminar flame speed increases at low pressure but decreases at low temperature. This opposite behavior can be directly explained by a transport effect with the modification of density which thereafter modifies the thermal diffusion (see Eq. (5.4)). Indeed, assuming constant ther-

mal conductivity λ and constant heat capacity C_p of the gas[1], the low temperature condition increases the density, leading to a lower diffusion coefficient and therefore a lower laminar flame speed. On the contrary, the low pressure condition reduces the gaseous density, increasing the laminar flame speed.

$$D_{th} = \frac{\lambda}{\rho C_p} \tag{5.4}$$

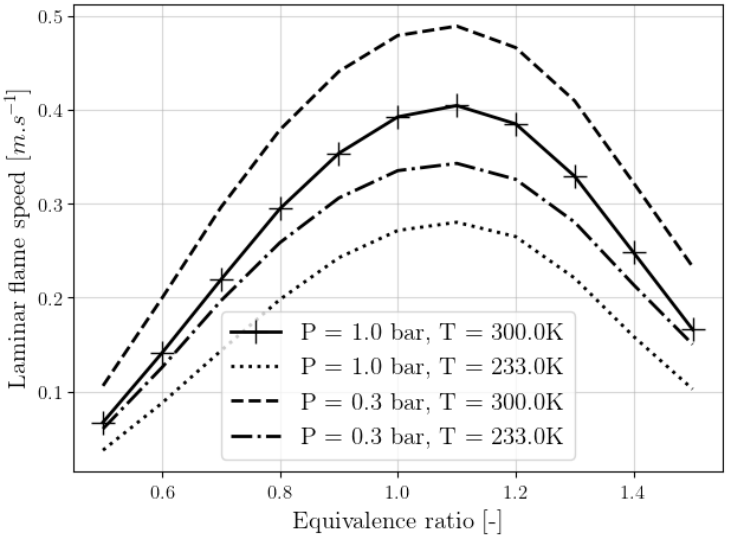

Figure 5.2.2: Laminar flame speed versus equivalence ratio. PTatmo: solid line with symbols, LT: dotted line, LP: dashed line, LPLT: dash-dotted line

However, the transport effect only partly explains the laminar flame speed variation. Considering only the transport effect, a general expression can be derived for the laminar flame speed. Starting with perfect gas law, thermal diffusion definition Eq. (5.4), and a presumed laminar flame speed expression based only on transport effect Eq. (5.5):

$$S_L = C \times \sqrt{D_{th}} \tag{5.5}$$

The following expression can be obtained:

$$S_L^{cond} = S_L^{ref} \times \sqrt{\frac{P^{ref}}{P^{cond}} \frac{T^{cond}}{T^{ref}}} \tag{5.6}$$

with $cond$ and ref indices referring to the conditions of interest and the reference conditions respectively.

Applying this expression[2] to **LP**, **LT**, and **LPLT** cases for the equivalence ratio $\phi = 1.1$ gives the following results:

- $S_L^{LP} = 0.73\, m.s^{-1}$ with transport effects only, and $S_L^{LP} = 0.49\, m.s^{-1}$ with CANTERA simulation
- $S_L^{LT} = 0.35\, m.s^{-1}$ with transport effects only, and $S_L^{LT} = 0.29\, m.s^{-1}$ with CANTERA simulation
- $S_L^{LPLT} = 0.64\, m.s^{-1}$ with transport effects only, and $S_L^{LPLT} = 0.34\, m.s^{-1}$ with CANTERA simulation

The laminar flame speed at **LPLT** conditions with transport effect only is almost twice the real value measured with CANTERA. Furthermore, the variation induced by the transport effect only (i.e., increase of the laminar flame speed compared to the case **PTatmo**) is opposed to the real flame speed variation given by CANTERA (i.e., decrease of the laminar flame speed compared to the case **PTatmo**). As

[1]Thermal conductivity and heat capacity depend on the temperature but their variations are negligible compared to the variation of the density

[2]The reference state used is $S_L^{ref} = S_L^{PTatmo} = 0.4\, m.s^{-1}$

explained before, the low pressure condition reduces the reaction rate. Hence, the reaction rate effect is opposed to the transport effect.

In the case of low pressure and atmospheric temperature (**LP**), the transport effect is stronger than the reaction rate one, which leads to a higher flame speed (compared to **PTatmo** curve on Fig. 5.2.2). In the case of low temperature only (**LT**), thermal diffusion is reduced because of a higher density as well as reactivity as shown with the increase of the auto-ignition time at low temperature. Hence, both effects act in the same way to reduce the flame speed. Finally, the laminar flame speed on Fig. 5.2.2 corresponding to high altitude conditions (**LPLT**) is only slightly reduced. The mechanism governing the reaction rate effect is linked to chemistry and is highly non-linear, thus it is very difficult to propose an accurate expression of laminar flame speed for detailed chemistries.

In terms of fresh gases burnt through the flame front (i.e fuel consumption), results are very different. Indeed, the mass flux corresponds to the laminar flame speed weighted by the fresh gas density. Figure 5.2.3 shows that even if the flame speed is greatly reduced at low temperature, the higher density compensates this reduction to finally obtain a mass flux quite close to the **PTatmo** case. On the contrary, low pressure largely reduces the mass flux passing through the flame. When looking at the combined effect with **LPLT** case, it is even worse and the temperature effect seems negligible compared to the pressure effect. Finally, the fuel consumption rate at high altitude conditions is divided by a factor three.

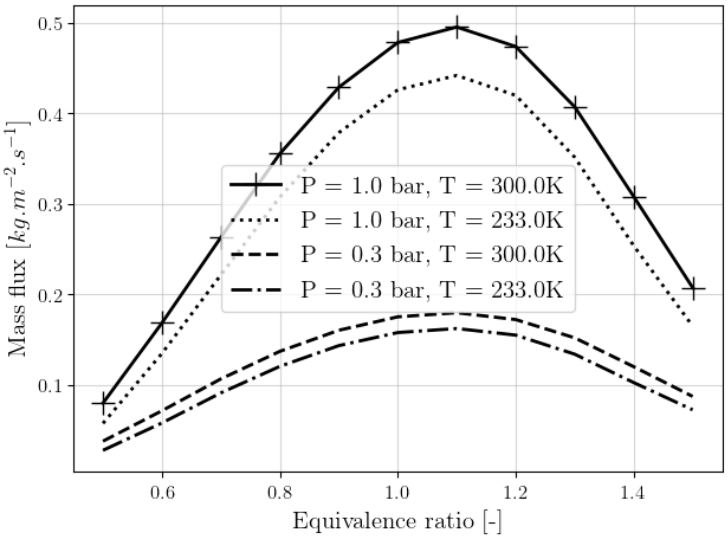

Figure 5.2.3: Mass of fresh gases burnt per flame surface and unit of time versus equivalence ratio. PTatmo: solid line with symbols, LT: dotted line, LP: dashed line, LPLT: dash-dotted line

5.2.3 Effects on laminar flame thickness

The flame thickness can be roughly estimated by the ratio of the thermal diffusion over the laminar flame speed [Poinsot and Veynante 2012]. Thus, like the flame speed, the flame thickness also depends on the thermal diffusion and the reaction rate:

$$\delta = \frac{D_{th}}{S_L} \quad \Rightarrow \quad \delta \propto \sqrt{\frac{D_{th}}{R_r}} \tag{5.7}$$

At low pressure, the thermal diffusion increases whereas the reactivity decreases. Then, both effects act in the same way to increase the flame thickness. On the contrary, at low temperature, thermal diffusion and reactivity are both reduced, thus, both effects compensate. The resulting influence of low temperature is then negligible compared to the pressure one. These predictions are confirmed on Fig. 5.2.4 presenting the thermal thickness (defined using the temperature gradient Eq. (3.22)) of laminar premixed flames versus equivalence ratio.

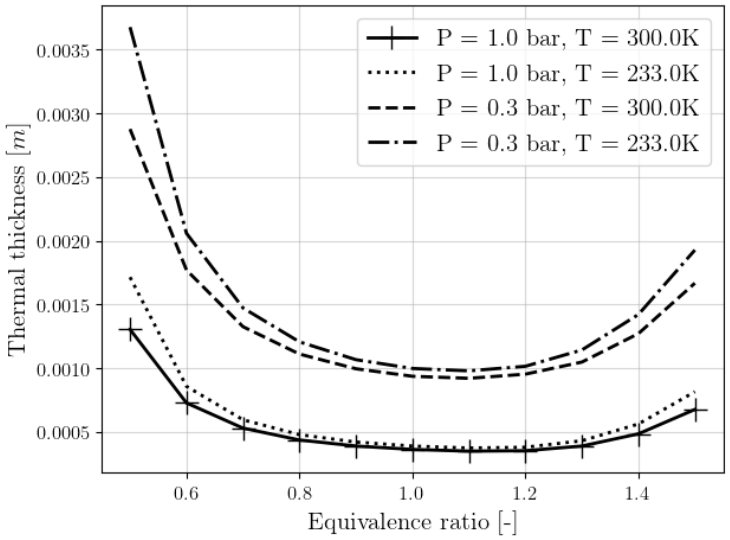

Figure 5.2.4: Thermal thickness versus equivalence ratio. PTatmo: solid line with symbols, LT: dotted line, LP: dashed line, LPLT: dash-dotted line

Close to stoichiometry, the flame thickness at low pressure is more than twice larger than for atmospheric conditions. This larger thickness is numerically favourable because the mesh discretization required to resolve the flame front may be coarser. Hence, the computational cost should be lower for numerical simulations with low pressure conditions. The difference of flame thickness will also modify the interaction with the turbulence. These points will be developed in Chap. 9.

5.2.4 Effects on heat release and flame power

Because the density has an important effect, it is interesting to study the mass heat release hr defined Eq. (5.8) and corresponding to the integrated heat release rate over the domain divided by the fresh gas mass flux. The mass heat release differs from the Lower Heating Value (LHV) because the latter considers only the fuel mass flow rate and a complete combustion at stoichiometric proportions. On the contrary, the mass heat release relies on the air mass flow rate and thus varies depending on the stoichiometric proportions. This quantity allows to characterize the heat released per unit of fresh gases mass burnt, i.e it gives information on the efficiency of the combustion. Figure 5.2.5 shows once again a negligible influence of the temperature. This is not the case for the low pressure conditions as the heat released per unit of mass is lower around stoichiometry. This result indicates that for the same amount of fuel burnt, less thermal energy will be released by the flame. Hence, the combustion at low pressure seems less efficient. It is also observed that the maximum efficiency is obtained for slightly rich flame at low pressure.

$$hr = \frac{\int \dot{\omega}_T(x)\, dx}{\rho_f S_L} \tag{5.8}$$

with $\dot{\omega}_T(x)$ the local heat release rate.

This difference indicates an incomplete combustion process at low pressure. Indeed, Fig. 5.2.6 displays CO and CO_2 mass fractions equilibrium levels in the burnt gases state for a stoichiometric premixed flame at both **PTatmo** and **LPLT** conditions. Results indicate that low pressure conditions shift the thermodynamic equilibrium towards less conversion of CO into CO_2. This phenomenon disappears for rich and lean mixtures because combustion is mainly limited by the oxidant or fuel amount respectively. Yet, reactions of CO conversion into CO_2 are known to be exothermic, which can explain the missing heat release rate. This effect relies only on the initial state (pressure, temperature conditions, and gas composition) and the thermo-chemical properties of the species. Indeed, this result can be also observed with equilibrium computations via a Gibbs minimization of chemical potential [Smith and Missen 1982]

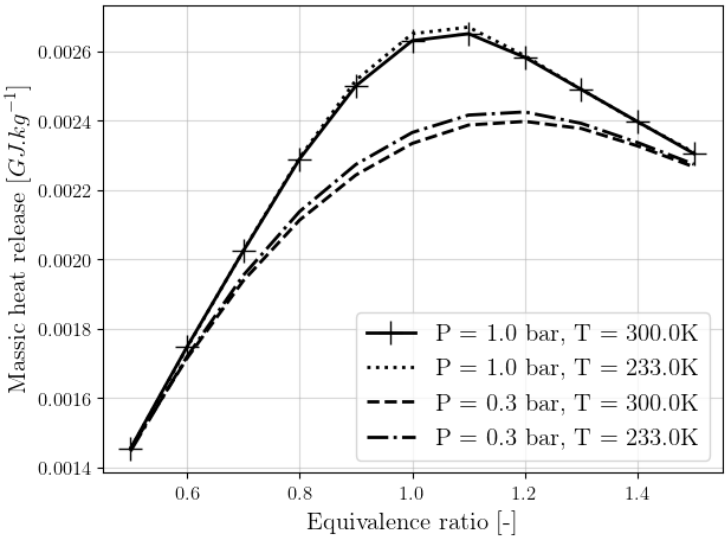

Figure 5.2.5: Mass heat release versus equivalence ratio. PTatmo: line with plus symbols, LT: dotted line, LP: dashed line, LPLT: dash-dotted line

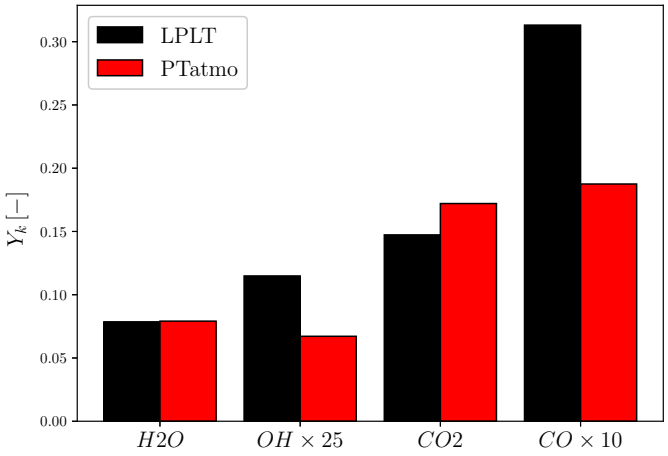

Figure 5.2.6: Final mass fractions of CO, CO_2 in the burnt gases state in a 1-dimensional premixed flame at stoichiometry.

The gap between low and atmospheric pressure curves on Fig. 5.2.5 is reflected on the adiabatic temperature since this latter is computed directly from the enthalpy balance Eq. (5.9):

$$T_{adia} = T_f + \frac{\int \dot{\omega}_T(x)\,dx}{\rho_f C_p S_L} = T_f + \frac{hr}{C_p} \tag{5.9}$$

with T_f the fresh gas temperature.

Hence, Fig. 5.2.7 shows that the low temperature shifts only the curve on the whole range of equivalence ratio. This shift corresponds to the difference of initial temperature T_f as shown in Eq.(5.9). Since low pressure reduces the mass heat release, the adiabatic temperature is also reduced. For the **LPLT** case both effects are taken into account, thus the adiabatic temperature is further reduced.

Finally, since the mass heat release is reduced at low pressure as well as the mass flux that crosses the flame front, it leads to a strong reduction of the flame power corresponding to the integral of the heat

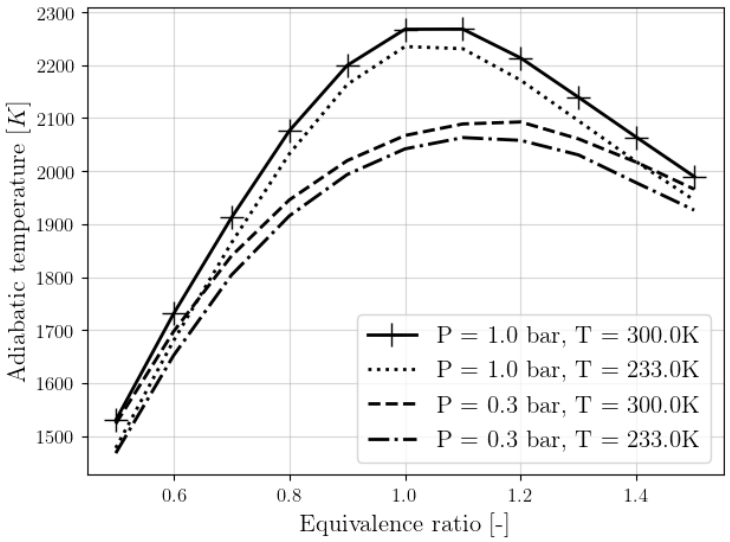

Figure 5.2.7: Adiabatic temperature versus equivalence ratio. PTatmo: line with symbols, LT: dotted line, LP: dashed line, LPLT: dash-dotted line

release rate Eq. (5.10).

$$\mathcal{P}_f = \int \dot{\omega}_T(x)dx = hr \times \rho_f S_L \tag{5.10}$$

Indeed, on Fig. 5.2.8, the flame power is divided by more than three in **LPLT** condition compared to the **PTatmo** case. For the low temperature condition **LT**, the combustion efficiency is the same, thus only the reduced mass flux has an effect, and it is much lower than for low pressures.

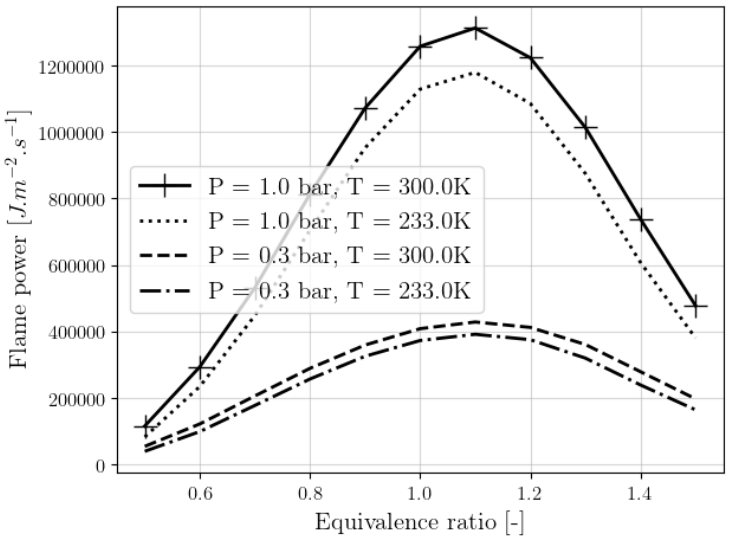

Figure 5.2.8: Flame power per flame surface versus equivalence ratio. PTatmo: line with plus symbols, LT: dotted line, LP: dashed line, LPLT: dash-dotted line

5.3 Effect of fuel modeling

The modeling of the fuel itself is also an important aspect in such a study. Indeed, a complex surrogate formulation provides accurate results but at a larger computational cost. On the other hand, too simple

fuel and/or chemical models are not able to reproduce several macroscopic quantities at the same time. For this purpose, comparisons between a mono-component and a multi-component fuel surrogate formulation is first presented. Then, a globally-fitted two-step chemistry approach is compared to a detailed mechanism with a multi-component fuel surrogate.

5.3.1 Fuel composition effect

The comparison between the three-component Jet-A1 surrogate introduced Sec. 2.3.3 and a pure n-dodecane fuel formulations is presented on Fig. 5.3.1. For this comparison the same CRECK detailed mechanism is used. Since three-component surrogate formulation is mainly composed of dodecane, it is not surprising to observe a very good agreement for both formulations in terms of ignition delay time and laminar flame speed. A small reduction of ignition time and a small increase of laminar flame can be observed when the mono-component surrogate is employed which indicates this mixture is more reactive. Indeed, dodecane is the least stable fuel component and pyrolyses very quickly. On the contrary, the xylene decomposition involved in the three-component surrogate leads mainly to unsaturated species more stable which reduce chemical reactivity.

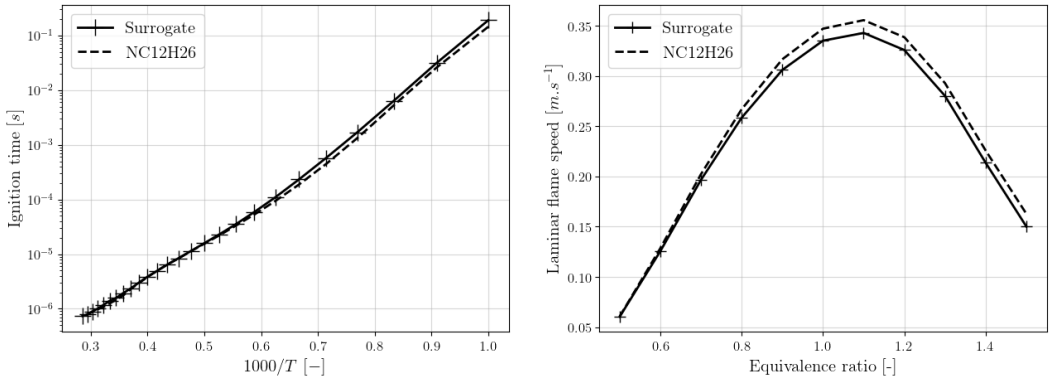

Figure 5.3.1: Comparison of ignition time at $P = 0.3\,bar$ and $\phi = 1$ (left) and laminar flame speed at $P = 0.3\,bar$ and $T = 233\,K$ (right). Solid line: Surrogate formulation with three components, dashed line: mono-component formulation with dodecane as fuel.

Globally the mono-component formulation for kerosene modeling can be used as a first approach in gaseous simulations. Especially, it facilitates chemical reduction compared to the multi-component one since additional species must be taken into account for the decomposition of methyl-cyclohexane and xylene.

5.3.2 Chemical modeling

A comparison between the CRECK detailed chemical mechanism with the three-component surrogate and a BFER globally-fitted two-step chemistry [Franzelli et al. 2010] has been also conducted. The BFER chemistry contains six species and two reactions. This chemistry is used to compute kerosene combustion at a low CPU-cost. Such modeling approaches have already been used to study ignition in combustion chambers at ambient conditions [Eyssartier 2012].

The laminar flame speed as well as the adiabatic temperature are recovered for the whole range of equivalent ratios in atmospheric conditions thanks to corrections of pre-exponential coefficients with equivalence ratio [Franzelli et al. 2010]. In the context of this work, the comparison has been done on a premixed flame at LPLT conditions for a stoichiometric mixture to evaluate the performances of this global scheme at high altitude conditions.

Figure 5.3.2 shows non negligible discrepancies between the BFER chemistry and the detailed mechanism. Indeed, the adiabatic temperature is not well predicted for the BFER scheme, due to a coarse chemical description where most chemical pathways are not taken into account. Hence, CO levels are wrong as if the global mechanism did not take into account the modification of the thermodynamic equilibrium

observed on Fig. 5.2.6 at low pressure.

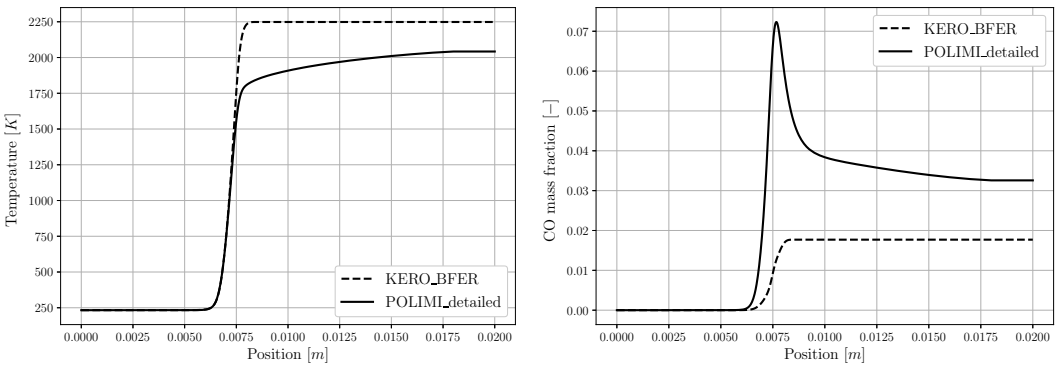

Figure 5.3.2: Temperature (left) and CO mass fraction (right) profiles in a one dimensional premixed flame at $P = 0.3\,bar$, $T = 233\,K$, for a stoichiometric mixture. Solid line: detailed POLIMI (CRECK) mechanism with the three-component Jet-A1 surrogate, dashed line: Global BFER mechanism.

As a conclusion, the use of the two-step globally-fitted BFER chemistry [Franzelli et al. 2010] for the study of low pressure and low temperature effects is not recommended. A more accurate global mechanism could be built adjusting the pre-exponential coefficient for the high altitude conditions.

5.4 Conclusions

To conclude, the low pressure and low temperature conditions encountered at high altitude have several impacts on combustion processes. The main source arises from a reduction of the gaseous density at low pressure (the increase of density due to low temperature is negligible compared to the pressure effect) which induces two main effects:

- **Transport effect:**
  The low pressure along with low density will largely increase the diffusion which enhances the flame propagation.
- **Reactivity effect:**
  The low density also reduces the mixture reactivity. The molecules have a lower probability to collide with low species concentrations. Therefore, chemical reactions are slowed down at low pressures. The low reactivity at high altitude reduces the flame propagation but also the auto-ignition delay.

As a consequence, the laminar flame speed at high altitude is only slightly reduced. On the contrary, the consumption speed is largely reduced at high altitude because it is normalised by the fresh gas density. This quantity is more relevant because it is linked to the flame power with the mass heat release.

The second impact of high altitude conditions is the modification of the equilibrium state at low pressure. This equilibrium effect can be seen as an incomplete combustion. Thus, mass heat release and adiabatic temperature are reduced. This effect is mainly observed around the stoichiometry.

Finally, the third impact of high altitude condition is a further reduction of the adiabatic temperature due to the initial cooler fresh gases.

The strong decrease of the flame power at the **LPLT** condition suggests that the flame kernel may be less robust to extinction especially with additional thermal losses due to turbulence.

In addition to these macroscopic effects, Burrell et al. [2018] shown that pressure and temperature may also modify the chemical pathways at the microscopic level which is the subject of the following chapter.

Concerning the fuel and chemical modelings, large discrepancies have been observed with the comparison of the detailed mechanism and the BFER globally-fitted two-steps chemistry, the latter not being optimized on the low pressure cases. Moreover, the global chemistry approaches do not enable an accurate

chemical description, thus this solution has not been retained for this work. On the contrary, no significant differences have been observed on the macroscopic quantities when using the multi-component Jet-A1 surrogate or its mono-component version with pure n-dodecane as fuel. In the following the three-component formulation will be used to account for the preferential evaporation phenomena encountered in two-phase flow computations.

Chapter 6

Detailed chemical analysis of kerosene chemistry in the context of ignition

Contents

The previous chapter has shown that the high altitude conditions have a strong impact on the combustion processes and modify the macroscopic quantities such as the laminar flame speed, the adiabatic temperature and the flame power. These modifications can be explained by the reduction of the density and a shift of the thermodynamic equilibrium at low pressure. However, modifications of the chemical pathways could also explain the trends observed, as shown in [Burrell et al. 2018]. As a consequence, the microscopic level needs to be looked at by describing the change of chemical pathways caused by the high altitude conditions.

To analyse the impact on chemical pathways, chemical analysis tools have been developed during this work and are presented Sec. 6.1. They are then used Sec. 6.2 to analyse the chemical processes associated with the ignition of a kerosene-air mixture and the influence of temperature/pressure conditions.

6.1 Development of chemical analysis tools

The detailed and reduced chemistries are full of information. In addition to predicting accurately the macroscopic combustion effects, such as the laminar flame speed or the adiabatic temperature, they include all the chemical processes and intermediate mechanisms at the microscopic level. To reach that information and improve our knowledge on these processes, chemical analysis tools have been developed and integrated to ARCANE (Cornell-CERFACS chemical reduction code presented in Chap. 7) in collaboration with Jonathan Wirtz.

For the development and the validations of these tools, the detailed methane chemistry developed by the CRECK modeling group [Ranzi et al. 2012; 2015] and presented Sec. 2.3.2 has been used because it includes fewer chemical pathways than the kerosene one. For each tool presented in the following sections, an application example using this chemistry is presented in Appendix. A. These results enable to better understand the global combustion behavior and low pressure effects, on oxidation mechanisms of the

light species. These mechanisms are important because they are also encountered on the last kerosene combustion phases.

The mathematical methods used to build these tools have been taken from the reference book of Turányi and Tomlin [2014].

6.1.1 Sensitivity analysis

The first tool developed is the sensitivity analysis. The purpose is to determine, in a kinetic mechanism, the chemical reactions or species that have the most influence on macroscopic quantities of interest $\mathcal{Y}_u$ (laminar flame speed, auto-ignition time, maximum of heat release rate, etc.).

To do so, a first reference case is computed with the reaction rates (K_j) as they are given in the kinetic mechanism. It enables to get the reference value for the quantities of interest $\mathcal{Y}_{u,ref}$. Then, for the reaction that is focused on, the corresponding reaction rate is slightly perturbed following Eq. (6.1) and the case is computed once again.

$$K_{pert,j} = K_j \times (1 + \epsilon) \tag{6.1}$$

with $K_{pert,j}$ the new perturbed reaction rate, K_j the original one, and ϵ the perturbation[1]. The variation of the quantities of interest due to this perturbation enables to compute the sensitivity coefficient associated to that reaction. This coefficient is defined as the variation of the targeted quantity due to the linear variation of the reaction rate, based on a logarithmic scale [Turányi and Tomlin 2014]:

$$S_{\mathcal{Y}_{u,j}} = \frac{\partial ln(\mathcal{Y}_u)}{\partial ln(K_j)} = \frac{\mathcal{Y}_{u,pert} - \mathcal{Y}_{u,ref}}{\mathcal{Y}_{u,ref} \times \epsilon} \tag{6.2}$$

This process is iterated for all the reactions to be studied. In the specific case of species sensitivities, the rate perturbation is applied for all the reactions which contain the selected species.

The choice of the perturbation parameter ϵ is important and can lead to different results. A convergence study has been conducted (not shown) indicating that $1.10^{-5} < \epsilon < 1$ to get sensitivities independent from the perturbation ϵ. If the value is too small, the variations of the quantity of interest are the same order as the numerical error. On the contrary, if the perturbation is too large, the strong non-linearity of the kinetic schemes can lead to very different and non-physical results.

This tool indicates the largest sensitivity coefficients and the associated reactions, but it is also possible to compare these coefficients for two different cases. Thus, it is possible to compare two kinetic mechanisms, two combustion processes (ignition, flame propagation, etc.), or two conditions (pressure, temperature, equivalence ratio).

The main drawback of the sensitivity analysis is that it requires the computation of one case for each sensitivity coefficient. Therefore, for the study of very large kinetic mechanisms (more than fifteen thousand reactions for the detailed kerosene mechanisms), the cost of the sensitivity analysis is prohibitive. To ease the study, the reactions to study are pre-selected with a DRGEP method (this method will be presented in detail in Chap. 7) that only requires the reference case to sort reactions by importance, keeping only the relevant reactions for the sensitivity analysis. For example, in the application presented in Appendix. A, using the DRGEP method enables to reduce the number of reactions by three.

6.1.2 Thermochemical analyses

The sensibility analysis is a macroscopic method which enables to analyse the global effect of a reaction but does not indicate when or where this reaction is important. On the contrary, thermochemical analyses enable to understand locally, in a flame or in a reactor, which reactions or species are responsible for a specific phenomenon, such as a heat release rate peak, the production of a pollutant species or the pyrolysis process. In that respect, heat release rate and progress rates monitoring tools have been developed.

[1] Note that the perturbation is not absolute, but relative to the reaction rate magnitude

The first tool called the progress rates analysis is based on the computation of the reaction rate of progress $\mathcal{Q}_j$ presented in Sec. 2.1.2 and reminded here Eq. (6.3):

$$\mathcal{Q}_j = K_{fj} \prod_{k=1}^{N_{spec}} [k]^{\nu'_{kj}} - K_{rj} \prod_{k=1}^{N_{spec}} [k]^{\nu''_{kj}} \tag{6.3}$$

This quantity enables to sort reactions depending on their activations rate. Hence, it shows the most important chemical mechanisms occurring at a specific moment or location. Elsewhere, for reversible reactions, the sign of the progress rate indicates the forward or backward direction of the reaction.

The second tool called the heat release rate analysis is based on the computation of the partial heat releases $\dot{\omega}_{T,j}$ and $\dot{\omega}_{T,k}$ presented in Sec. 2.1.4 and reminded here Eqs. (6.4) and (6.5)[2]:

$$\dot{\omega}_{T,j} = -\sum_{k=1}^{N_{spec}} h_k \times \dot{\omega}_{k,j} = -\sum_{k=1}^{N_{spec}} h_k \times W_k \nu_{k,j} \mathcal{Q}_j \tag{6.4}$$

$$\dot{\omega}_{T,k} = -h_k \times \dot{\omega}_k = -h_k \times \sum_{j=1}^{N_{reac}} \dot{\omega}_{k,j} \tag{6.5}$$

This second tool enables to sort reactions or species depending on their heat release rate contributions. These reactions or species are important in the combustion process because they drive the temperature evolution which in return affects transport and kinetics. However, the heat release rate analysis can miss important reactions with low heat release rate contributions. For this tool, when studying reactions, the reaction rates of progress are also given to ease the analysis with the direction of the reaction.

These tools are used on 1-dimensional flames or 0-dimensional reactors. The cases are sampled in points or instants called samples. Then for each sample the analysis is performed. The number of samples is given by the user depending on the precision required for the analysis. The sample points are defined each n_{sample} points of the case. Hence, the cases are automatically refined at the chemical activity zones (pyrolysis, flame front) as the samples. The analysis results can also be integrated on specific intervals[3]

6.1.3 Graph pathway analyses

The third group of analysis tools implemented in ARCANE enables to study the chemical pathways themselves, i.e the interactions between the different species of the chemical mechanism.

Detailed pathway analysis

The first category of pathway analysis tools deals with detailed processes associated to one or two species. Three tools have been developed:

- **Species to Species (StoS):**
  The StoS analysis gives all the possible species linked to a reference species given by the user. It will indicate all the species leading to the formation of the reference species, but also all its decomposition products or its implications in the formation of other species.

- **Reactions to Species (RtoS):**
  The RtoS analysis is similar to the StoS with the difference that this tool gives all the reactions linked to the species of interest prescribed by the user.

- **Species to Reactions to Species (StoRtoS):**
  Finally, the StoRtoS analysis informs about all the direct reactions interacting between two specific species. When there are several chemical pathways for the transformation to a species into another one, this tool indicates which pathway/reaction is preponderant.

[2] If the species k is not in the reaction j then $\dot{\omega}_{k,j} = 0$.

[3] If 0-dimensional reactors are used, units are $[J.m^{-3}]$ for the heat release, and $[mol.m^{-3}]$ for the progress rates. If 1-dimensional flames are used, units are $[J.m^{-2}.s^{-1}]$ for the heat release, and $[mol.m^{-2}.s^{-1}]$ for the progress rates.

These tools require to quantify the species and reactions interactions. In this work, two different methods, taken and adapted from Turányi and Tomlin [2014], have been used to quantify the interactions:

- **Path Flux Analysis (PFA):**
  The PFA coefficient, in its classical form, corresponds to the normalized partial molar production rate of a species A through a specific reaction j. It writes:

$$PFA_{A,j}^{reac} = \frac{\nu_{A,j} \times \mathcal{Q}_j}{max(P_A, C_A)} \tag{6.6}$$

  with $\nu_{A,j}$ the net stoichiometric coefficient of species A in the reaction j. P_A and C_A are the molar production and consumption terms of species A respectively and are defined as:

$$P_A = \frac{\sum_{j=1}^{N_{reac}} \dot{\omega}_{A,j}}{W_A} = \sum_{j=1}^{N_{reac}} \nu_{A,j}\mathcal{Q}_j \quad \text{for all} \quad \dot{\omega}_{A,j} > 0 \tag{6.7}$$

$$C_A = \frac{-\sum_{j=1}^{N_{reac}} \dot{\omega}_{A,j}}{W_A} = -\sum_{j=1}^{N_{reac}} \nu_{A,j}\mathcal{Q}_j \quad \text{for all} \quad \dot{\omega}_{A,j} < 0 \tag{6.8}$$

  The PFA coefficients are used in the tools RtoS and StoRtoS. For direct species interaction of two species A and B, as in the tool StoS, the PFA coefficients can be generalized by summing the individual components of each reaction including both species. Hence, the species PFA coefficient writes:

$$PFA_{A,B}^{spec} = \frac{\sum_{j=1}^{N_{reac}} \nu_{A,j}\mathcal{Q}_j\delta_B^j}{max(P_A, C_A)} \quad \text{if} \quad sign(\nu_{A,j}) \neq sign(\nu_{B,j}) \tag{6.9}$$

  with δ_B^j equals to 1 if species B is in the reaction j and 0 otherwise. The condition $sign(\nu_{A,j}) \neq sign(\nu_{B,j})$ enables to avoid the case where species A and B are on the same side of the reaction. For example, with the reaction A + B $\rightarrow$ C, $PFA_{A,B}^{spec} = 0$.
  For both cases, the sign of the PFA coefficient indicates the direction of the interaction.

- **Atom Fluxes:**
  Instead of the PFA coefficients, the atom fluxes between two species can be used for the tool StoS. These fluxes[4] are computed as:

$$\mathcal{A}_{A\rightarrow B} = -\sum_{j=1}^{N_{reac}} \frac{n_{\mathcal{A},A}\nu'_{A,j} \times n_{\mathcal{A},B}\nu''_{B,j} \times \mathcal{Q}_j}{N_{\mathcal{A},j}} \quad \text{if} \quad \mathcal{Q}_j > 0 \tag{6.10}$$

$$\mathcal{A}_{A\rightarrow B} = \sum_{j=1}^{N_{reac}} \frac{n_{\mathcal{A},A}\nu'_{B,j} \times n_{\mathcal{A},B}\nu''_{A,j} \times \mathcal{Q}_j}{N_{\mathcal{A},j}} \quad \text{if} \quad \mathcal{Q}_j < 0 \tag{6.11}$$

  with $n_{\mathcal{A},B}$ the number of atoms $\mathcal{A}$ in the species B, and $N_{\mathcal{A},j}$ the total number of atoms $\mathcal{A}$ on either side of the reaction j.

As in the previous section, these methods are based on the sample formalism. Thus, these fluxes can be studied locally at a specific sample, or integrated over a given interval.

Global pathway analysis

The global analysis aims to give an overview of the chemical pathways represented as a graph with the links representing the fluxes between the species. These fluxes can be computed either with the PFA method or the atomic fluxes. The construction of the global graph follows an iterative process as shown in Fig. 6.1.1. At the initial generation a starting species is chosen by the user. Then at each generation, the leaving fluxes of the new species added to the graph are evaluated. For example, generation 1 adds the new species B and C to the global graph, then at generation 2, the leaving fluxes of B and C are added to the graph. This construction process continues, until no new species are added, in the example at generation 3.

[4] Units are $[mol.m^{-3}.s^{-1}]$

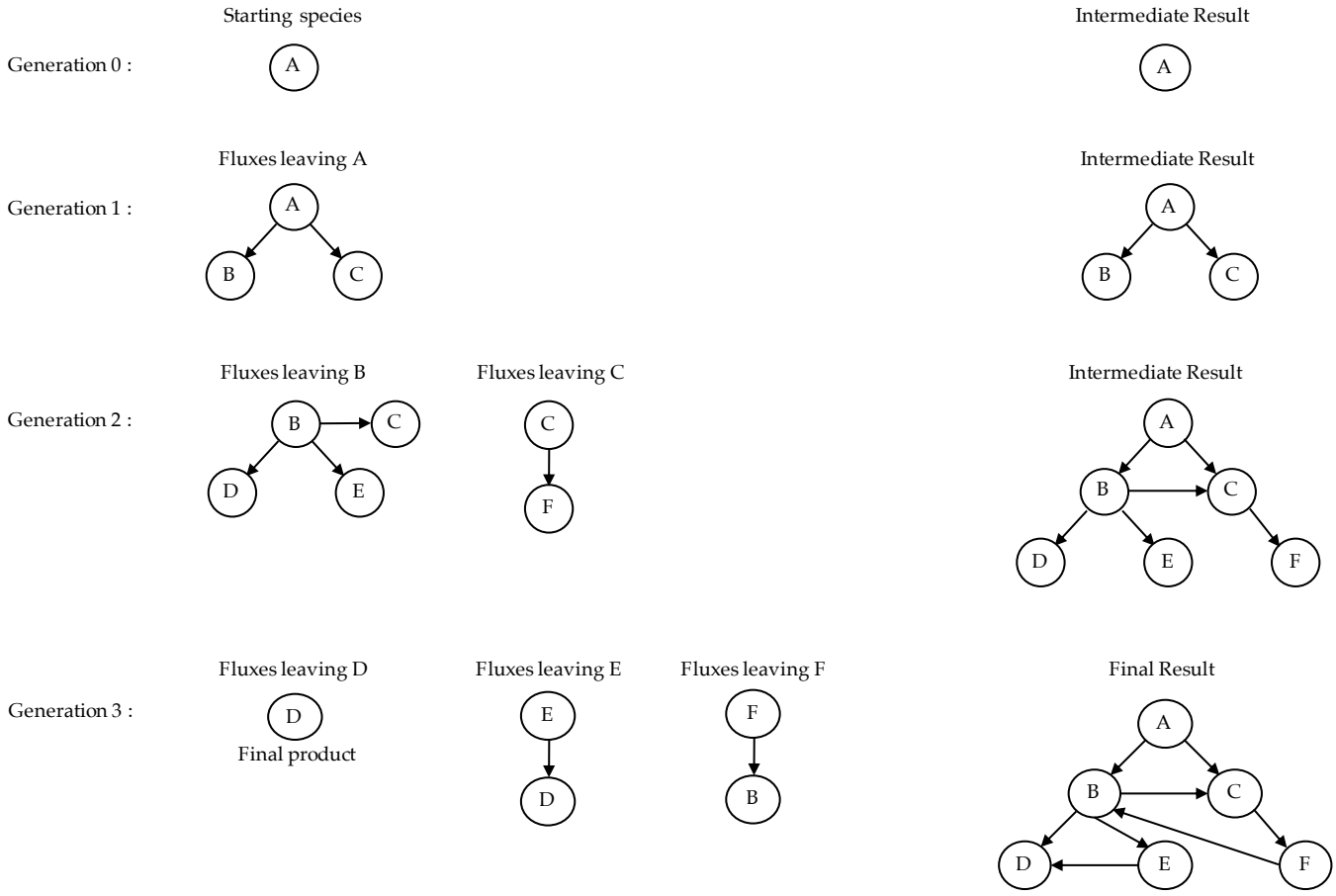

Figure 6.1.1: Iterative construction of the global graph analysis

A consequence of this construction method, based on leaving fluxes, is that the graph cannot give a complete overview of the chemical pathways. Indeed, taking the example of Fig. 6.1.1, it is possible that another species A' has an interaction with species F, but this interaction is not displayed in the present graph. Then, it means that the global graph analysis is highly dependent on the starting species. Furthermore, it means also that the graph displays all the leaving fluxes, but not the incoming ones. Hence, this construction is very well adapted to study decomposition mechanisms. However, for the studies of pathways leading to a specific compound, for example a pollutant, an inverse construction method based on the incoming fluxes is more adapted.

To avoid too complex representations due to the large number of chemical pathways for each species, a flux threshold can be used by the user to display only the major fluxes. It is also possible to perform the analysis on a chosen set of species, which enables to cut the graph in several parts and eases the pathways visualisation.

As for the other tools, the analysis can be done at a specific sample. In this case, the thickness of the arrows is determined by the flux intensity. In the case of an integrated analysis over a given interval and with the atomic fluxes, the coefficients are expressed in percentages of leaving fluxes.

In the following part, the tool StoRtoS will be used with the PFA method, whereas the global graph analysis will be conducted using the atomic fluxes method.

6.2 Kinetic analysis of the ignition of a kerosene-air mixture

The chemical analysis tools presented in Sec. 6.1 are used hereafter to analyse the chemical processes occurring during the ignition of a kerosene-air mixture. The decomposition pathways of the kerosene components are first presented. Then, the influence of the pressure and the temperature on these path-

ways are analysed.

The detailed kerosene-air chemistry developed by the CRECK modeling group [Ranzi et al. 2012; 2014; 2015] and the multi-component surrogate fuel modeling are used. Detailed information are given in Sec. 2.3.3.

6.2.1 Chemical pathways description of the fuel decomposition

In order to analyse the decomposition of the three surrogate components during ignition, a chemical pathway analysis is conducted. The multi-component approach enables to study the pyrolysis step for each component of the fuel surrogate. This study is conducted at low and atmospheric pressure to evaluate the pressure effect on the chemical pathways which will be detailed in Sec. 6.2.2. 0-dimensional constant pressure reactor with a stoichiometric mixture are used with the initial temperature is set to $T_i = 1600\,K$, which corresponds to the temperature observed during the chemical runaway in a forced ignition with energy deposition. The analysis is done with the global graph tool based on the computation of carbon atom fluxes between the different species as presented Sec. 6.1.3.

On Fig. 6.2.1, 6.2.2 and 6.2.3, the carbon fluxes are integrated in time starting from the fuel species. The results are displayed with percentages of leaving fluxes, i.e. for each node all the incoming fluxes are not represented, and equal percentages for two separate nodes do not correspond to the same atom flux. Due to its size, the chemical pathway cannot be represented as a whole. Thus, it has been cut (arbitrarily) into several parts, and only the fuel decomposition will be shown here, the other parts being available in Appendix E. The graphs have been cut at the followings species that are represented with double circles in the figures:

- $nC_{12}H_{26}$ pathway (Fig. 6.2.1):
  C_3H_6, C_3H_5-A, $C_4H_7$1- 4, C_4H_6, nC_5H_{11}, lC_5H_8, and pC_4H_9
- MCYC6 pathway (Fig. 6.2.2):
  C_3H_6, nC_7H_{14}, C_2H_4, C_4H_6, C_2H_5, C_6H_5
- XYLENE pathway (Fig. 6.2.3):
  C_6H_5, CO, C_5H_5, $C_6H_4O_2$.

Furthermore, fluxes lower than 10 percents are not displayed. The red arrows correspond to the atmospheric pressure case, and the black-dashed arrows to low pressure case.

The graphs of kerosene combustion present a very complex structure with a large number of steps and many different paths. Hence the perturbation of individual paths will not have a significant impact at the macroscopic level. This effect is enhanced by the fact that the fuel surrogate chosen is composed of three species that have their own and different decomposition pathways. Thus, it is expected that the modification of a limited number of paths due to low pressures will not significantly impact macroscopic quantities such as laminar flame speed or adiabatic temperature.

Dodecane and methylcyclohexane decomposition pathways presented Fig. 6.2.1 and 6.2.2 have different pyrolysis steps, however, these fuels share common pathways. The main dodecane pyrolysis products are C_3H_5-A, C_4H_6,C_3H_6, and pC_4H_9. While, in the case of methylcyclohexane, the pyrolysis products are C_4H_6,C_3H_6, and C_6H_5. The decomposition seems longer in the case of xylene. Indeed, there are more intermediate species composed of six or more carbon atoms, which may be due to the molecular structure of xylene that presents double chemical bonds, increasing the stability of the cyclic structure. The decomposition products of xylene are mainly C_6H_5, C_5H_5 and $C_6H_4O_2$. The decomposition products of methylcyclohexane are found in the decomposition pathways of dodecane and xylene. Indeed, Fig. 6.2.2 shows two competitive pathways. The first one keeps the cyclic structure and removes successively methyl group and hydrogen atoms to finally obtain C_6H_5 species that has a cyclic aromatic structure. On the other hand, the cyclic structure is broken by the pyrolysis, which leads to a linear alcane structure similar to dodecane and explains the common decomposition species. After the pyrolysis step of fuel species, the pyrolysis products further oxidate into smaller species. Classical C1-C3 oxidation pathways already presented in Sec. 6.1 and in the work of Frouzakis and Boulouchos [2000] are recovered. It is also important to note that the fuel decomposition reactions also produce light species composed of one or two carbon atoms. These species are not represented here because they do not correspond to the main

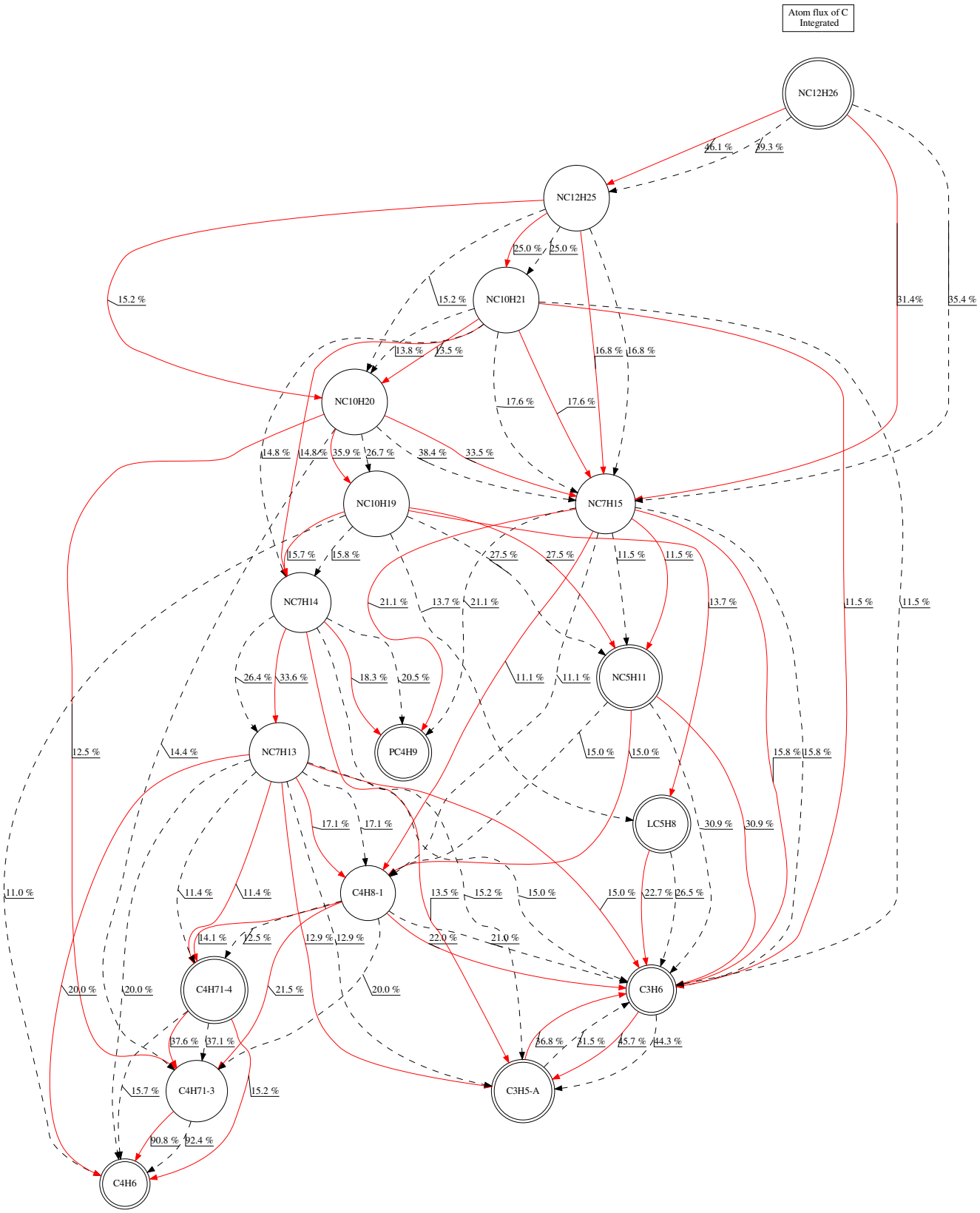

Figure 6.2.1: Integrated carbon flux graph starting with NC12H26 in a 0-dimensional reactor filled with stoichiometric mixture at initial temperature $T_i = 1600\,K$. Red solid line: $P = 1\,bar$, black dashed line: $P = 0.3\,bar$.

carbon fluxes, however, in the mixture and considering molar quantities, they are as represented as the

Figure 6.2.2: Integrated carbon flux graph starting with MCYC6 in a 0-dimensional reactor filled with stoichiometric mixture at initial temperature $T_i = 1600\,K$. Red solid line: $P = 1\,bar$, black dashed line: $P = 0.3\,bar$.

largest species.

6.2.2 Pressure and temperature effects on multi-component fuel decomposition

Comparing the black ($P = 0.3\,bar$) and red arrows ($P = 1\,bar$) on Figs 6.2.1-6.2.3 leads to the following observations regarding the main effects of low pressure conditions on the chemical pathways:

- $nC_{12}H_{26}$ pathway (see Fig. 6.2.1):
  At low pressure, the path towards nC_7H_{15} is increased. This is the result of a pyrolysis reaction that is increased at low pressure (explained in the following paragraphs). Similarly for nC_7H_{14},

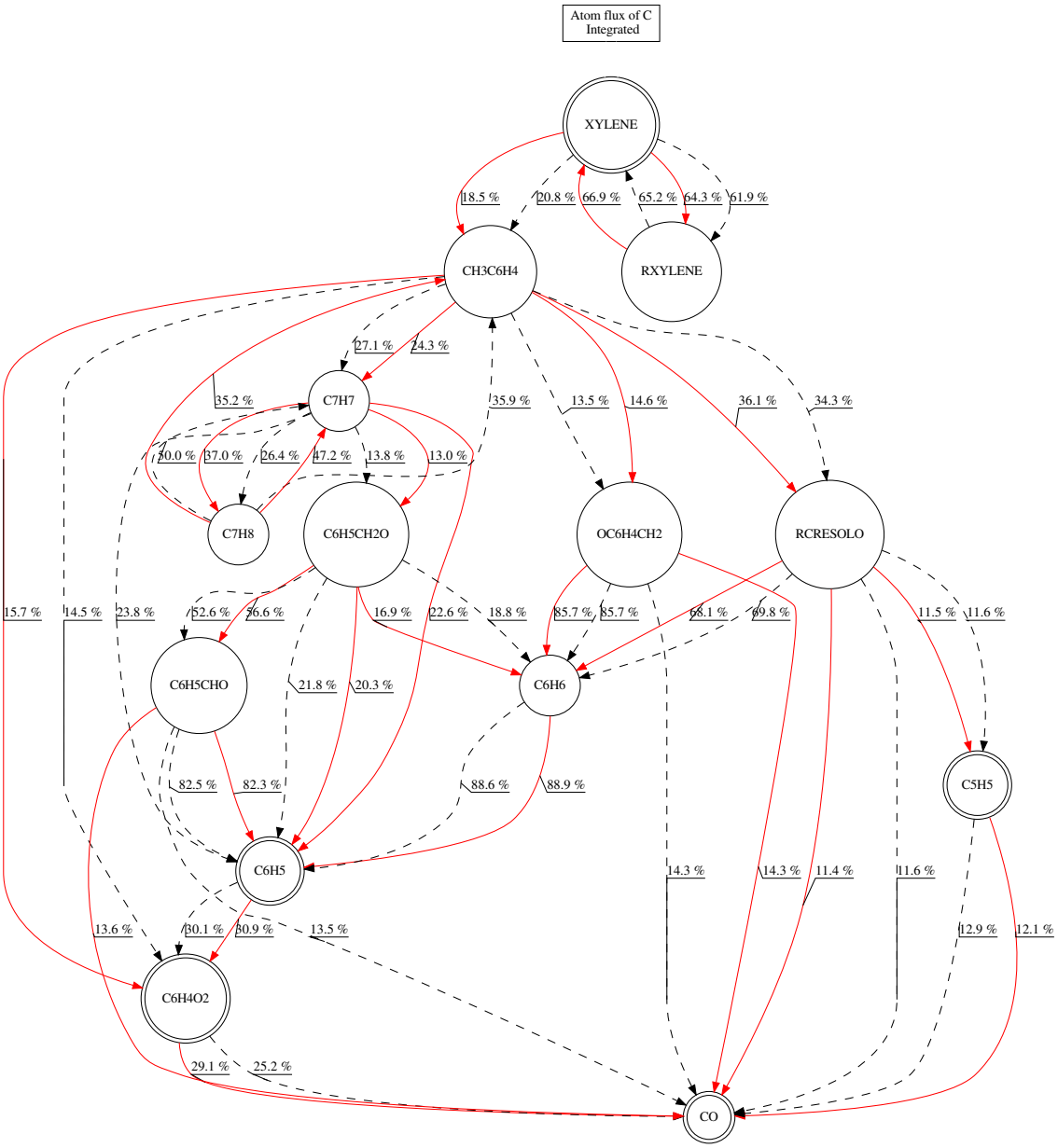

Figure 6.2.3: Integrated carbon flux graph starting with XYLENE in a 0-dimensional reactor filled with stoichiometric mixture at initial temperature $T_i = 1600\,K$. Red solid line: $P = 1\,bar$, black dashed line: $P = 0.3\,bar$.

the pyrolysis path producing pC_4H_9 and C_3H_5-A is increased at low pressure, which reduces the H-abstraction pathways producing nC_7H_{13}.

- MCYC6 pathway (see Fig. 6.2.2):
  At low pressure, the path towards rMCYC6 is reduced and redirected to C_3H_6, iC_4H_8, $CYC\,6\,H_{11}$, and nC_7H_{14} for the same reasons evoked above.

- XYLENE pathway (see Fig. 6.2.3):
  The equilibrium loop between C_7H_7 and C_7H_8 is increased at atmospheric pressure.

- C_4H_6 pathways (see Appendix E):
  The path towards C_3H_3 is increased at low pressure

- C_3H_6 pathways (see Appendix E):
  At low pressure, the decomposition pathway of C_3H_5-A towards C_3H_4-A is more important whereas at atmospheric pressure C_3H_5-A tends to reform C_3H_6.

- nC_5H_{11} pathways (see Appendix E):
  The isomerization reaction of nC_3H_7 into iC_3H_7 is more important at low pressure and lead to the production of C_3H_6. At atmospheric pressure the pathway towards C_2H_4 and CH_3 is more important.
- CH_2CHO pathway (see Appendix E):
  At low pressure, CH_2CHO decomposes into CH_3CO whereas, at atmospheric pressure, there is another path towards CH_2CO. CH_3CO then dissociates into CH_3 and CO whereas another pathways towards HCCO is observed for the decomposition of CH_2CO.
- C_6H_5 pathway (see Appendix E):
  At low pressure, there is a new path towards CYC_5H_4O. This path seems to have more intermediate steps before complete oxidation compared to the atmospheric pathway which produce directly C_2H_2, C_2H and CO.

These modifications of chemical paths at low pressure are very punctual and there is only a small number of significant differences compared to the large amount of pathways. These modifications are often limited to a few number of steps and finally lead to the same sub-products. Hence, except for the fuel species decomposition which concentrates all the atomic fluxes in a limited number of pathways, the influence of low pressure through a pathway modification is diluted and seems negligible. The major part of the pathways are identical. Thus, the macroscopic effects raised in Sec. 5.2 have a low probability to be attributed to a modification of the chemical pathways.

The chemical pathways described in the previous section show that the xylene decomposition leads to unsaturated species that are more stable and thus have different pyrolysis characteristic time scales. Therefore, in the following, time evolution of the fuel component deposition is analysed. Figure 6.2.4 shows that dodecane is the first species to decompose, quickly followed by the methyl-cyclohexane and then the xylene. This order is due to the structure of the species. Indeed, the linear dodecane molecule is easy to break compared to the xylene presenting a double chemical bond making the species more stable. Furthermore, Fig. 6.2.3 shows a strong equilibrium interaction between xylene and its radical form rXYLENE with a missing hydrogen atom. This equilibrium converts a part of xylene instead of decomposing it. Therefore, it slows down the decomposition. A pressure effect is also observed during the fuel decomposition. As expected, the low pressure slows down the decomposition process. However, depending on the initial temperature of the reactor, this phenomenon is not always observed. For example, with $T_i = 2000\,K$ only the xylene is subject to the pressure influence.

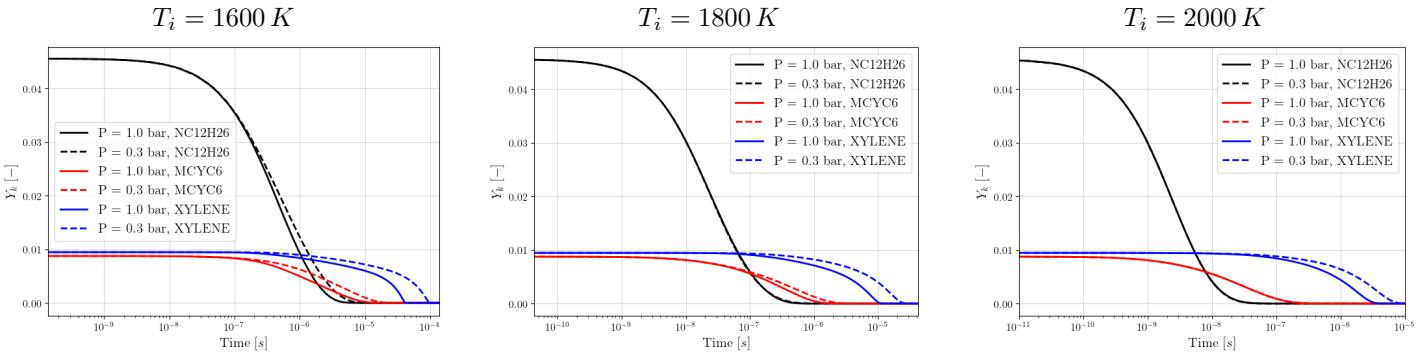

Figure 6.2.4: Evolution of component mass fraction of a stoichiometric 3-component surrogate kerosene in a 0D constant pressure reactor for three intial temperatures: $T_i = 1600\,K, 1800\,K \& 2000\,K$

To analyse the reactions between a fuel component ($nC_{12}H_{26}$) and its main decomposition product $nC_{12}H_{25}$, a StoRtoS analysis is conducted with the PFA method. A 0-dimensional constant pressure reactor is used at $P = 1\,bar$, and the fluxes are integrated over the fuel decomposition time interval. This analysis gives the main reactions that link two species. Hence, in this case, it provides the main decomposition reactions of the fuel species. Figure 6.2.5 indicates that at high initial temperature $T_i = 2000\,K$, the decomposition of dodecane is achieved by pyrolysis reactions R1 and R2 only. The fuel species promptly decomposes in sub-products under the temperature effect. At lower initial temperature $T_i = 1600\,K$, the dodecane still decomposes mainly by pyrolysis reactions. Indeed, no radical species are

available since dodecane is the first fuel to decompose. However, once the pyrolysis decomposition has started, radical attack reactions R3 and R4 increase.

$$\mathrm{nC_{12}H_{26}} \rightarrow 0.5\mathrm{C_2H_5} + 0.5\mathrm{nC_{12}H_{25}} + 0.5\mathrm{nC_3H_7} + 0.5\mathrm{nC_7H_{15}} \quad \text{(R1)}$$

$$\mathrm{nC_{12}H_{26}} \rightarrow 0.1\mathrm{nC_{12}H_{25}} + 0.5\mathrm{nC_5H_{11}} + 0.9\mathrm{nC_7H_{15}} + 0.5\mathrm{pC_4H_9} \quad \text{(R2)}$$

$$\mathrm{H} + \mathrm{nC_{12}H_{26}} \rightarrow \mathrm{H_2} + \mathrm{nC_{12}H_{25}} \quad \text{(R3)}$$

$$\mathrm{nC_{12}H_{26}} + \mathrm{OH} \rightarrow \mathrm{H_2O} + \mathrm{nC_{12}H_{25}} \quad \text{(R4)}$$

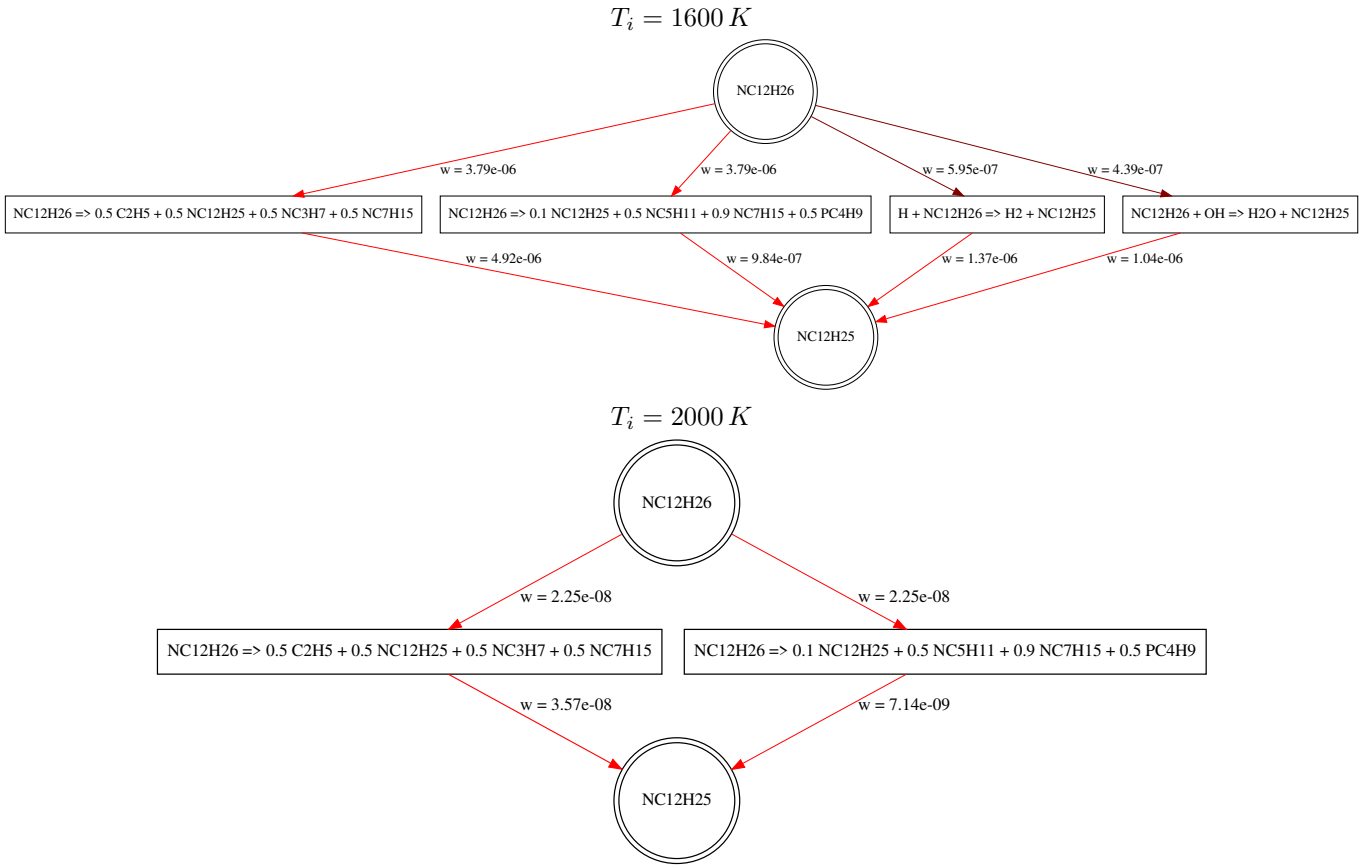

Figure 6.2.5: StoRtoS analysis between $\mathrm{nC_{12}H_{26}}$ and $\mathrm{nC_{12}H_{25}}$ in a 0-dimensional constant pressure reactor at $P = 1\,bar$ and $\phi = 1$.

The rates of the first order pyrolysis reactions R1 and R1 rely only on the fuel concentration. Furthermore, the Arrhenius pre-exponential constants are very high ($A_{R1} = 2 \times 10^{17}$ and $A_{R2} = 2 \times 10^{17}$), which indicates that the reaction activates as soon as the activation energy is reached with a negligible influence of the fuel concentration. Thus, the pressure influence is negligible. On the contrary, for the second order radical attack reaction R3 and R4, the Arrhenius pre-exponential constants are lower ($A_{R3} = 6.6 \times 10^7$ and $A_{R4} = 3.3 \times 10^{10}$), but also with a lower activation energy. Furthermore, the reaction relies also on the radical concentrations. Since these concentrations are reduced at low pressure, it explains why the dodecane decomposition characteristic time is increased. However, this radical attack mechanism is also reduced at low pressure due to the lower concentrations. Hence, it explains the pathways modifications in Fig. 6.2.1 and 6.2.2 with an increase of the pyrolysis paths at low pressure. The same analysis has been conducted for the two other fuel components showing similar results but with different pyrolysis critical temperatures depending on the chemical stability of the molecule.

It is reminded that the chemical pathway analysis Sec. 6.2.1 has been conducted at the initial temperature $T_i = 1600K$. Then, Figs. 6.2.1, 6.2.2, and 6.2.3 represent the chemical decomposition pathways corresponding to the radical attack and pyrolysis pathways.

To conclude, the different evolution curves at low pressure on Fig. 6.2.4 do not correspond to new pathways expressing at low pressure, but rather to different pathways depending on the temperature. These

radical attack pathways are affected by the pressure with a slow down of the chemical processes due to lower species concentrations.

In the case of kernel propagation, it is expected that the radical pathways become dominant. Indeed, contrarily to the ignition phase, the radical species can diffuse from the flame front. In the case of two-phase flow ignition, the droplets evaporate in a very hot environment with $T > 2000\,K$. In that context, the decomposition processes are pyrolysis reactions. Therefore, both mechanisms must be conserved in the chemical reduction (see Chap. 7).

6.2.3 Study of the auto-ignition

In addition to the pressure effect, the temperature influence has been also evaluated on the auto-ignition processes which may be encountered in 3D ignition simulations. The results presented in Appendix A.4 show two distinct pathways for CH_3 oxidation depending on the initial temperature of the mixture which results in a modification of the heat release rate evolution.

6.3 Conclusion

Chemical analysis tools have been developed and integrated to ARCANE in this work based on well-known quantities used in the literature for such analyses (PFA, atomic fluxes, sensitivities, heat release and rate of progresses) [Turányi and Tomlin 2014] . These tools enabled to perform detailed analyses of the chemical processes occurring during the ignition of a kerosene-air mixture. One can note that these tools can be used in several other studies: effect of the blend composition or hydrogen enrichment, analysis of the pathways associated to premixed flame propagation or diffusion flame structures, study of the pollutant formation, etc.

First, it has been observed that the low pressure condition (in the range of high altitude conditions) has a negligible influence on the chemical pathways. Hence, the conclusion of the previous chapter still holds when considering chemistry characteristics: the modifications of the combustion processes at low pressure mainly rely on the reduction of the species concentrations and the shift of the thermodynamic equilibrium. Moreover, the non modification of the chemical pathways in the range of the conditions studied is an advantage for chemical reductions. Indeed, a reduced chemistry designed at low pressure will remain valid at atmospheric conditions. This reduction is presented in the following chapter. However these conclusions only stand for the studied pressure range $P = 0.3{-}1\,bar$. At lower pressures ($P = 0.1\,bar$), modifications of the chemical pathways become non negligible [Burrell et al. 2018]. Similarly, at high pressure ($P > 40\,bar$), additional mechanisms and reactions must be added to recover experimental ignition times [Petersen et al. 1999].

Secondly, the main pathway modifications observed are related to the temperature. The latter can modify the fuel decomposition pathways by activating more or less the pyrolysis reactions or the radical attack ones which are influenced by the pressure. The temperature also changes the core mechanism of methyl transformation (see Appendix A.4), which significantly modifies the heat release rate.

Chapter 7

Chemical reductions

Contents

Correctly describing complex phenomena such as ignition, extinction, pollutant emissions (NOx, CO, soot, etc), real fuel combustion, etc. requires accurate chemical description. The most accurate ones are the so-called detailed chemistries which are composed of several hundreds of species and thousands of reactions. However, the computational cost for 3-dimensional DNS or LES including such detailed chemistries, most of the time, largely exceeds the computing power available today. Fortunately, most flame features and applications can be correctly captured with a reduced number of species and reactions, if taken individually. The philosophy of the reduced chemistries lies on this principle. By carefully selecting the relevant chemical pathways from a detailed mechanism, with respect to a specific application, a smaller mechanism can be extracted, enabling complex 3-dimensional CFD simulations.

In the context of engine ignition, the combustion chamber must be able to ignite at atmospheric conditions but also to re-ignite at high altitude conditions for safety reasons. It has been shown in Chap. 6 that low pressures encountered at high altitude influence the combustion processes. The objective of this chapter is then to derive a reduced kerosene/air chemistry, accurately reproducing the ignition and the flame kernel propagation at atmospheric and low pressure conditions. First, the main reduction methods are described in Sec. 7.1. Then, in Sec. 7.2, the ARCANE reduction code co-developped by Cornell University and CERFACS used to automatically reduce chemistries is introduced. Finally, reduced schemes derived using ARCANE for both atmospheric and low pressure conditions are presented for methane-air chemistry and kerosene-air chemistry in Sec. 7.3 and Sec. 7.4 respectively.

7.1 Reduction methods

An Analytically Reduced Chemistry (ARC) is derived from a detailed chemistry by reducing the number of reactions and transported species using reduction techniques. To be affordable in numerical simulations of complex flames, ARC schemes generally must retain 10 to 35 species. Two different reduction steps can be applied to a detailed chemical scheme:

- **Skeletal reduction:**
  A set of unnecessary species and reactions are discarded or lumped.

- **Analytically Reduced Chemistry (ARC):**
  A time scale analysis is performed on the skeletal mechanism, and the stiffest species are expressed through algebraic relations.

For both reduction steps, pre-determined reference canonical cases are chosen (0-dimensional auto-ignition reactors, 1-dimensional laminar premixed flame, 1-dimensional diffusion flame, etc.). These cases should be representative of the conditions faced by the reduced chemistry during its use. From these cases reference quantities are chosen (Laminar flame speed, auto-ignition delay, adiabatic temperature, etc.) with associated error tolerances. During the reduction processes these quantities are compared between the detailed and reduced schemes to ensure that only unnecessary species and reactions are removed.

One of the main advantages of ARC is the conservation of the detailed chemical mechanism integrity. Indeed, only relevant pathways are conserved, and no rate optimisations nor additional species or reactions are used. Therefore, it enables a better predictability and robustness with respect to a modification of the designed conditions in complex simulations. Furthermore, it facilitates the results interpretations with a fine description of the chemical processes.

7.1.1 Skeletal reduction

The skeletal reduction step first requires to identify species and reactions to discard. A large panel of reduction methods and techniques is available in the literature and readers can refer to [Turányi and Tomlin 2014] for detailed description. In the following part, only the methods used in this work are described.

- **Pathway graphs methods:**
  One way to select the most important reactions or species is to compare rates of competitive reactions [Lepage 2000]. Constructing the decomposition graph with all the chemical pathways enables to select the dominant species and reactions in this decomposition. For the construction of these graphs PFA coefficients Eq. (6.9) or atom fluxes Eqs. (6.10) and (6.11) can be used.

  This method has been successfully used for the reduction of methane [Frouzakis and Boulouchos 2000], kerosene surrogates [Luche et al. 2004] and other liquid fuels [Sun et al. 2010].

  The Direct Relation Graph (DRG) method is part of these graph methods. It identifies the interactions between two species or between a species and a reaction [Lu and Law 2005]. The links between the species as shown on Fig. 7.1.1 corresponds to the contribution of a species B to the production of a species A. Hence, a Direct Interaction Coefficient (DIC) matrix is built and gives the interaction between two species of the chemical mechanism. The interaction coefficients are computed as follow:

$$r_{AB} = \frac{\sum_{j=1}^{N_{react}} |\nu_{A,j}\mathcal{Q}_j\delta_B^j|}{\sum_{j=1}^{N_{react}} |\nu_{A,j}\mathcal{Q}_j|} \tag{7.1}$$

  with $\nu_{A,j}$ the net stoichiometric coefficient of species A in the reaction j, $\mathcal{Q}_j$ the reaction rate of progress of reaction j computed with Eq. (6.3), and δ_B^j equals to 1 if species B is in the reaction j and 0 otherwise. Similar DIC matrices can be constructed for reaction to species interactions, or for the contribution to heat release.

  The DRG method has been improved by Pepiot-Desjardins and Pitsch [2008b] noting that Eq. (7.1) does not distinguish between reactions which create or destroy species A. Then, an alternative definition was proposed:

$$r_{AB} = \frac{\left|\sum_{j=1}^{N_{react}} \nu_{A,j}\mathcal{Q}_j\delta_B^j\right|}{max(P_A, C_A)} \tag{7.2}$$

  with P_A and C_A the molar production and consumption terms of species A respectively that writes:

$$P_A = \frac{\sum_{j=1}^{N_{react}} \max\left(0, \dot{\omega}_{A,j}\right)}{W_A} = \sum_{j=1}^{N_{react}} \max\left(0, \nu_{A,j}\mathcal{Q}_j\right) \tag{7.3}$$

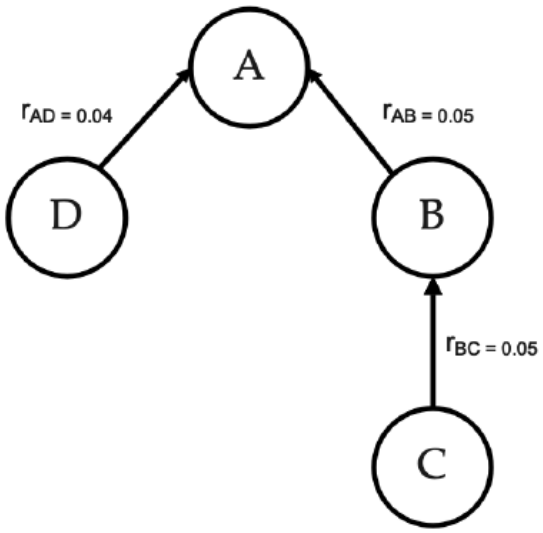

Figure 7.1.1: Visualization of a direct relation graph involving four species (extracted from [Pepiot-Desjardins and Pitsch 2008b])

$$C_A = \frac{-\sum_{j=1}^{N_{react}} \min\left(0, \dot{\omega}_{A,j}\right)}{W_A} = -\sum_{j=1}^{N_{react}} \min\left(0, \nu_{A,j}\mathcal{Q}_j\right) \tag{7.4}$$

The expression of the interaction coefficient Eq. (7.2) becomes very similar to the PFA coefficients but without the sign indicating the direction of the transformation. Secondly, the DRG method was also improved by Pepiot-Desjardins and Pitsch [2008b] considering the contribution of indirectly linked species. This method is then called Direct Relation Graph with Error Propagation (DRGEP). In the DRGEP method, the error propagation coefficient writes:

$$r_{AB,path} = \prod_{i=1}^{n-1} r_{S_i S_{i+1}} \tag{7.5}$$

where n is the distance between species A and B in this specific path (number of species involved in the path), S_i are the intermediate species in the path. Then, in the case of multiple paths, only the maximum value is retained to quantify the link between A and B. In the example of Fig. 7.1.1 the DRG method will discard species D because the link r_{AD} is the weakest. Using the DRGEP method instead, the link $r_{AC} = r_{AB} \times r_{BC}$ is lower than r_{AD}, thus the species C will be discarded first.

The DRGEP method has been implemented first in the former reduction tool YARC [Pepiot-Desjardins 2008] and then in ARCANE [Cazères et al. 2021]. This method will be used for the reduction of methane/air and kerosene/air chemistries in Sec. 7.3 and 7.4.

In addition to this reduction of species and reactions, some species or mechanisms may be required but can be simplified. This is the case of isomers and pyrolysis:

- **Isomers lumping:**
  Another way of expressing the system with a reduced number of variables is to combine or lump a subset of species into a pseudo-species. The choice of the species to lump is based on similar molecular composition or reactive properties. The strategy employed in this work is an adaptation of the one from Pepiot-Desjardins and Pitsch [2008a]. The species with the same thermodynamic and transport data are lumped together and tested. For example, with reactions Eq. (7.6), if the species A_1 and A_2 are isomers, then they can be lumped into A' with the corresponding new reactions Eq. (7.7):

$$\begin{cases} A_1 + B \xrightarrow{k_1} C + D \\ A_2 + E \xrightarrow{k_2} F + G \end{cases} \tag{7.6}$$

$$\begin{cases} A' + B \xrightarrow{k'_1} C + D \\ A' + E \xrightarrow{k'_2} F + G \end{cases} \tag{7.7}$$

The estimation of the kinetic parameters of this lumped species is done by applying the contribution of each species of the lump to the associated Arrhenius-law parameters based on a least square optimisation method.

- **Pyrolysis lumping:**
For heavy fuels, the combustion process can be divided in two main steps. First, the fuel decomposes either by a temperature effect, or by a radical attack, forming a mixture composed of lighter carbonated species (generally a threshold of 3-4 carbon atoms is retained) called pyrolysis products. Then, these light species oxidize to form the final product of combustion. The pyrolysis step is very fast and requires a lot of intermediate species as shown in Chap. 6. Furthermore, whatever the initial fuel species, the pyrolysis products are very similar. Based on these observations, Wang et al. [2018] proposed to decouple the pyrolysis and the oxidation mechanisms for heavy hydrocarbons. This method called HyChem (for Hybrid Chemistry) can be considered as a lumping method. Indeed, the whole pyrolysis step is described by a reduced set of global reactions enabling the direct decomposition of the fuel species into pyrolysis products. In the work of Wang et al. [2018], the coefficients of the pyrolysis reactions are set according to experimental work including shock-tubes and flow-reactors. The HyChem method has been employed by Felden [2017] in combination with a reduced C1-C3 oxydation mechanism to perform LES of turbulent swirled spray kerosene-air flames, showing the capacity of such reduced schemes to accurately reproduce the flame structure. The main drawback of the HyChem method is that it requires experimental data to determine the pyrolysis reaction coefficients. Recently a new reduction method enabling to reduce the pyrolysis chemical phenomenon has been developed [Heberle and Pepiot 2021], enabling to reduce the pyrolysis mechanisms without additional measurement but based on the comparison of target quantities such as laminar flame speed, auto-ignition delay, etc. with the detailed mechanism. Note that this method has been implemented in ARCANE at the end of this PhD work and has not been used in this work but is worth mentioning because it could further improve the reduction of chemical mechanisms for heavy hydrocarbons such as kerosene.

7.1.2 ARC reduction

Definition

Once the skeletal scheme is obtained, it is still possible to continue the reduction by using the Quasi-Steady-State Approximation[1]. Indeed, the skeletal mechanism often contains large timescale disparities. Some species with a very short characteristic timescale are in Quasi Stationary State (QSS). Lu and Law [2006] give the following definition of a QSS species: *"A QSS species typically features a fast destruction time scale, such that its small or moderate creation rate is quickly balanced by the self depleting destruction rate, causing it to remain in low concentration after a transient period. The net production rate of the species is therefore negligible compared with both the creation and the destruction rates, resulting in an algebraic equation for its concentration."* The mathematical description of such species corresponds to:

$$\frac{dc}{dt} = \dot{\omega} \approx 0 \tag{7.8}$$

Thanks to the algebraic expression, a QSS species does not require to be transported in the Navier-Stokes system, which reduces the computational cost. Furthermore, by definition QSS species are the stiffest species (with fast variation of reaction rates), hence, since they are no longer transported, the chemical stiffness is reduced. More details on the development of the QSS algebraic expressions and their implementation are detailed in the thesis of Cazères [2021].

Identification

Before solving the QSS concentration, those species must be identified within the skeletal mechanism.

The **Computational Singular Perturbation** (CSP) method is a technique proposed by Lam [1985] to extract information from a stiff set of equations by analyzing the characteristic timescales of the system.

[1] This method dates back to the early 20's when it was referred to as the Bodenstein method [Turányi and Tóth 1992]

However, the CSP method reduces to an eigenvalue problem which can be very CPU-time consuming. Another method called **Level of Importance** (LOI) can be used to exhibit potential QSS species. The LOI coefficients must take into account several characteristics of the QSS species. First, the species with the shortest overall lifetimes could be potential QSS species. Then, the QSS species definition also requires that the species is present in very small quantities. Indeed, since the QSS species are not transported, species with high concentration converted to QSS will result in an important mass deficit. Finally, a criterion based on the importance of the species is added because a larger error in its concentration is acceptable if the species has a low impact on a desired target. Following these criteria, Løvås et al. [2000] proposed the following expression for the computation of the LOI coefficients:

$$LOI_k = S_{P,k} c_k \tau_k \tag{7.9}$$

with $S_{P,k}$ the sensitivity coefficient of the species k on the parameter P, c_k the concentration of the species k, and τ_k its chemical characteristic time. A generalized interpretation of the species lifetime can be based on the diagonal elements of the Jacobian matrix:

$$\tau_k = |{J_{kk}}^{-1}| \quad \text{with} \quad J_{ij} = \frac{\partial \dot{\omega}_i}{\partial c_j} \tag{7.10}$$

In this work, a modified version of the LOI method is used to identify potential QSS species. The sensitivity coefficient is replaced by the DRGEP coefficient with the same purpose.

7.2 ARCANE code

The reduction methods presented Sec. 7.1 are implemented in the code ARCANE (Analytically Reduced Chemistry: Automatic, Nice and Efficient) co-developped by Cornell University and CERFACS [Cazères et al. 2021]. The main objective is to provide a tool that enables to reduce chemistries fast and with the lowest number of elements possible. Furthermore, ARCANE is written in Python language and exploits the oriented-object philosophy, which makes it very easy to use.

The code can also be used as a user-friendly encapsulation of CANTERA which enables to easily perform 0/1-dimensional computations. In addition, the analysis tools developed during this PhD and presented Chap. 6 have been included to ARCANE. Hence, the code directly enables the post-processing of CANTERA solutions. Chemical analysis from CFD solvers (AVBP or NTMIX) are currently in prospect.

The reduction set-up structure, the reduction algorithms and the improvements brought during this work are detailed in Appendix. B. For complementary information, readers can refer to[Cazères 2021] or to the publication describing ARCANE [Cazères et al. 2021].

7.3 Application to methane-air chemistry reduction

The objective of this reduction is to derive a new generic ARC chemistry for methane-air flames at low and intermediate pressures ($P = 0.3 - 5\,bar$), including ignition . Furthermore, this reduction enabled to develop and test the new reduction methods presented above and included in the tool ARCANE. Two distinct reductions have been performed for different applications, results accuracy and performances. These reductions are labeled S21R158QSS6 and S15R138QSS9. The first one includes chemical pathways and species associated to the auto-ignition delays for $T < 1200\,K$. Such pathways have not been targeted for the second mechanism which explains the reduced number of transported species. For the sake of concision, the description and validation of these two mechanisms can be found in Appendix. C, with detailed information on the set-up, the reductions and the validations

The chemical mechanism S15R138QSS9 has been employed in the context of combustion in porous media [Masset et al. 2022], and in a study aiming to determine and understand the influence of the number of points to discretize a flame front when using an ARC chemistry [Wirtz 2022]. Furthermore, the kinetic scheme is directly included in the AVBP distribution under the name CH4_15_256_9_AP and available for every AVBP user. It is also provided on the CERFACS Chemistry website (`https://chemistry.cerfacs.fr/`) for any willing to test it in Cantera or in any other reactive solvers. In the context of this PhD, this chemistry has been used as an intermediate step of complexity before addressing kerosene/air

chemistry. It has also enabled to develop and test the reduction methods presented in this chapter, to develop numerical methods for chemistry integration (see Chap. 8), and to implement ARCs in the NTMIX solver.

7.4 Application to kerosene-air chemistry reduction

The objective of this section is to derive a kerosene-air reduced chemistry for atmospheric ($T_f = 300\,K$ and $P = 1\ bar$) and high altitude ($T_f = 233\,K$ and $P = 0.3\ bar$) conditions, including flame kernel ignition and propagation processes. Furthermore, the ARC mechanism must be compatible with a multi-component kerosene surrogate modeling at a reasonable cost. The need for such chemistry has been highlighted in Chap. 6 where comparisons between the globally fitted BFER scheme and detailed chemistries have shown that the BFER is not able to reproduce the combustion processes at low pressure.

The reference detailed mechanism and fuel surrogate used for this reduction are presented in Sec. 2.3.3. As a reminder, the detailed chemistry is developed by the CRECK Modeling Group [Ranzi et al. 2012] and is composed of 491 species and 15276 reactions, allowing an accurate description of C1 to C16 carbonated species including high and low temperature chemistry. This chemistry has been validated by comparison with experimental measurements [Ranzi et al. 2014]. It is labelled S491R15276 in the following. The fuel model is a three-components surrogate that represents the behavior of a classical Jet-A1 used in aeronautical engines Humer et al. [2011]. The composition is made up by molar fraction of n-dodecane (60%) representing the paraffin behavior, methylcyclohexane (20%) that stands for the cyclic species, and xylene (20%) representing the aromatics.

7.4.1 Reduction set-up

The main objective is to derive a reduced chemistry able to reproduce ignition phenomena and flame kernel propagation both at atmospheric and at high altitude conditions. The reference cases used for the reduction are then presented in Table 7.4.1.

Cases	Temperature $[K]$	Pressure $[bar]$	Equivalence Ratio $[-]$
0D isobaric reactors	$1600 - 3000$	0.3	$0.6 - 1 - 1.5$
1D premixed flames	233	0.3	$0.6 - 1 - 1.5$

Table 7.4.1: Reference cases for kerosene/air reduction

For all cases, the reference pressure used corresponds to the low pressure condition characteristic of high altitude. The reduction behavior with respect to the atmospheric pressure will be *a posteriori* assessed in the following validation section. 0-dimensional reactors have been used to ensure good prediction of the auto-ignition processes occurring during energy deposition. Two initial temperatures have been used to target a large range of operating points. The initial temperature $T_i = 1600\,K$ corresponds to the temperature observed in energy deposition simulations when the chemical runaway occurs. The initial temperature $T_i = 3000\,K$ is used to keep the high temperature chemical pathways often observed when depositing energy, especially the CO_2 and H_2O dissociation phenomena. Moreover, inclunding premixed flames ensures a good prediction of flame propagation and transport effects. The fresh gas temperature corresponds in this case to high altitude conditions. Finally, the equivalence ratio values range from lean to rich mixtures.

The targets used for the DRGEP step are the fuel components $nC_{12}H_{26}$, $MCYC_6$, XYLENE, and the final products of the global reaction CO_2 and H_2O. For the same reasons as for methane/air reduction, CO mass fraction and integral of heat release rate have also been added to the reduction targets.

The error levels have been monitored during the reduction. Tab. 7.4.2 and 7.4.3 present the quantities of interest and their maximum error levels allowed.

The auto-ignition time is not measured for the 0-dimensional reactor with $T_i = 3000\,K$ because the heat release rate evolution used to define the auto-ignition time does not present a well defined maximum peak as shown on Fig. 7.4.1. The measurement of ignition time on such cases leads to large errors whereas

Quantities	τ_{ig}	HRR dist
Errors 0D $T_i = 1600\,K$	10 %	5 %
Errors 0D $T_i = 3000\,K$	-	5 %

Table 7.4.2: Maximum error levels used during the kerosene/air reduction for the 0-dimensional constant pressure reactor cases

Quantities	S_L	T_{end}	CO_{2end}	H_2O_{end}
Error 1D premixed flames	7.5 %	5 %	5 %	5 %

Table 7.4.3: Maximum error levels used during the kerosene/air reduction for the 1-dimensional premixed flame cases

the heat release rate evolution remains fairly close and acceptable.

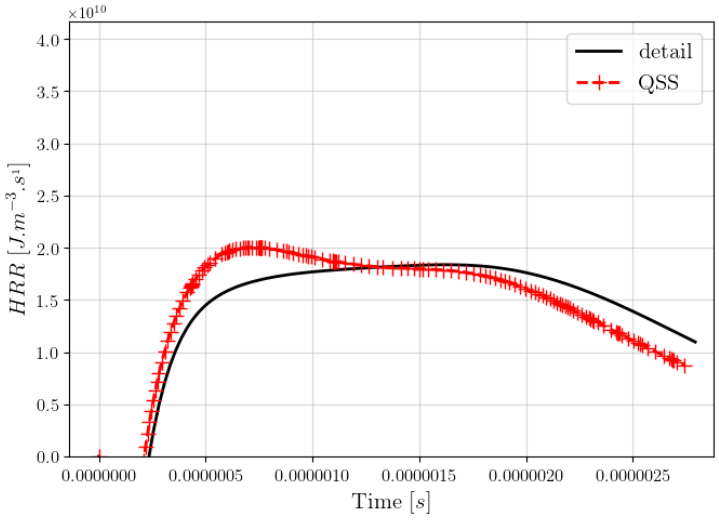

Figure 7.4.1: Evolution of the heat release rate in a 0D reactor at $T_i = 3000K$

Instead, an error based on the distance and the shape difference between the heat release rate profiles is computed (HRR dist). The Dynamic Time Warping matching algorithm [Salvador and Chan 2004] is used here[2]. As shown on Fig. 7.4.2, contrarily to the classical Euclidean matching, this algorithm identifies the curve shape to better evaluate the distance error. The shape error is also used for the initial temperature $T_i = 1600\,K$ because the heat release rate evolution produces several peaks and an endothermic phase as shown in Chap. 6. A simple auto-ignition error is not able to capture these phenomena.

The error factors used for this reduction were: $E_{f,spec} = 0.7$, $E_{f,reac} = 0.56$, $E_{f,lump} = 0.67$ and $E_{f,QSS} = 1$. The non-stop method associated to the layer method were used to get the best reduction performances. These methods are described in Appendix B.

7.4.2 ARC for kerosene-air flames

Reduction result

A first skeletal scheme is obtained and composed of 52 transported species and 310 reversible reactions. It is labeled S52R310 in the following. Then, 22 species are converted to QSS to obtain the ARC mechanism S30R299QSS22:

- Transported species:
  N_2, H_2, H, O_2, O, H_2O, OH, HO_2, CO, CO_2, CH_4, CH_3, CH_2O, C_2H_5, C_2H_4, C_2H_2, C_3H_6,

[2]Python library fastdtw

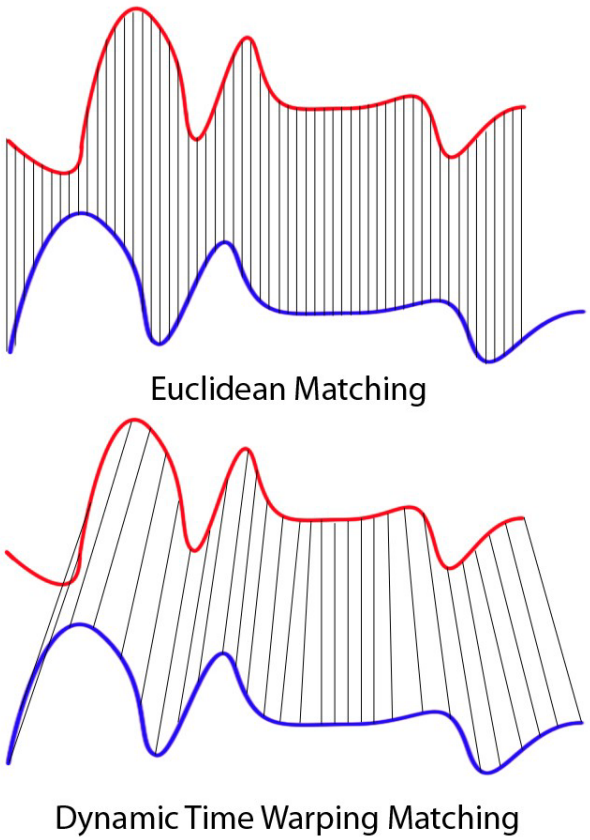

Figure 7.4.2: Comparison Euclidean versus Dynamic Time Warping matching algorithm.

C_3H_4-A, C_4H_8-1, nC_5H_{11}, nC_5H_{10}, nC_7H_{15}, nC_7H_{14}, $MCYC_6$, $nC_{12}H_{26}$, XYLENE, RXYLENE, C_6H_4, $C_3H_7(L_1)$, $CH_3O(L_1)$.

- QSS species:
  $CH_2(S)$, C, CH, HCO, C_2H_6, C_2H_3, C_2H, CH_2CHO, CH_2CO, HCCO, C_3H_5-A, C_3H_3, C_3H_2, pC_4H_9, iC_4H_8, C_4H_7 1-3, C_4H_6, $CH_3C_6H_4$, $nC_{12}H_{25}$, $C_6H_4O_2$, C_6H_2, C_6H_3.

The ARC mechanism S30R299QSS22 with kinetic reactions is available in Appendix D.

A timescale analysis is presented Fig. 7.4.3. These species timescales are computed using Eq. (7.10) and correspond to the minimum value measured on the set of reference cases. For the auto-ignition cases, the stiffest species are the fuel components $nC_{12}H_{26}$ and $MCYC_6$ because they are consumed extremely fast in high temperature conditions through pyrolysis reactions. XYLENE is less stiff because its aromatic structure provides a better stability. The first products of dodecane pyrolysis (nC_5H_{11}, nC_7H_{15}, nC_5H_{10} and nC_7H_{14}) are also long carbonated molecules but also radicals which make them very reactive and stiff too. Finally, classical radicals such as OH and H are also very stiff. In the premixed flame cases, the timescales are much larger because the gaseous temperature increase progressively in the pre-heating zone of the flame. Thus the fuel decomposition, and radical processes are slower. The time steps usually required in explicit solvers based on CFL and FO conditions are of the order of $10^{-8}\,s$ for flame propagation and $10^{-9}\,s$ for ignition. For ignition simulations, the timescale analysis indicates that about ten species are too stiff to be resolved directly with the time-step of the computation. The consequences are developed in the conclusion Sec. 7.4.5.

Chemical pathways analysis

A pathway analysis has been conducted to study the modifications of the chemical pathways due to the reduction. To get this result, the analysis tools developed in Chap. 6 have been used. More specifically, Fig. 7.4.4 shows the decomposition of the three fuel components following the carbon atom conservation.

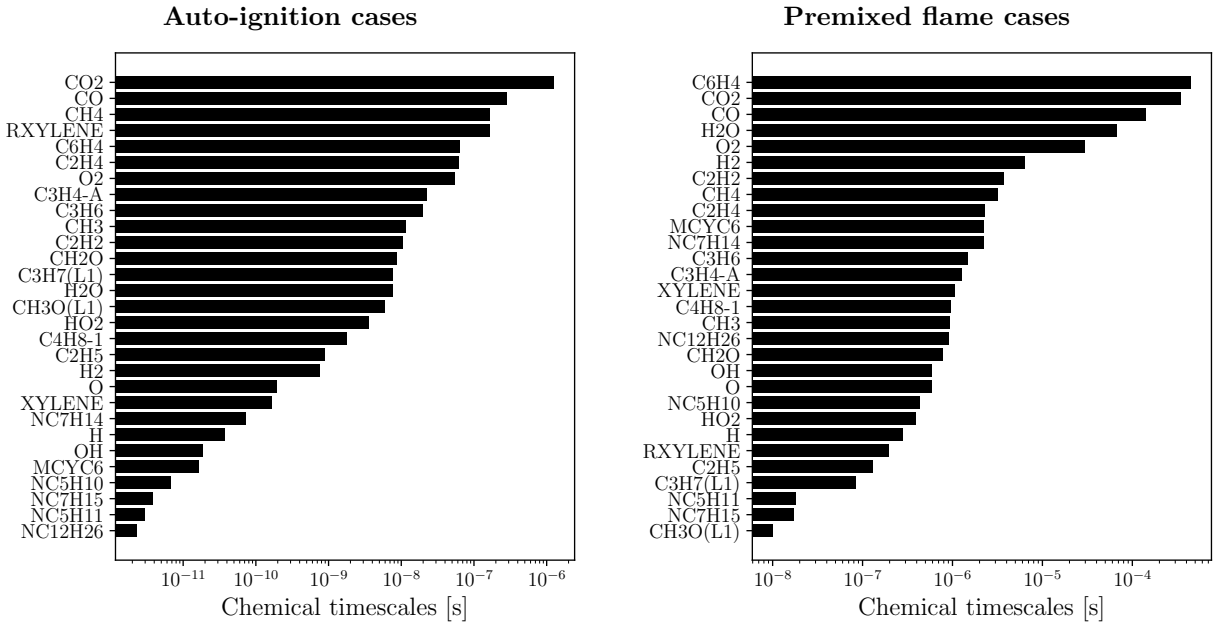

Figure 7.4.3: Evaluation of the species chemical timescales based on the inverse of the Jacobian matrix for S30R299QSS22

These carbon fluxes are integrated on a 0-dimensional constant pressure reactor filled with a stoïchiometric kerosene-air mixture at pressure $P = 0.3\,bar$ and temperature $T_i = 1600\,K$. The fluxes are clipped at 10% to show only the major pathways. The green nodes correspond to species also present in the reduced methane/air chemistry, whereas the red and blue nodes correspond to species specific to the methyl-cyclohexane and xylene decomposition respectively. The remaining black nodes are part of the dodecane decomposition.

This qualitative visualisation shows that methyl species is at the heart of the chemical processes and that a major part of the chemistry refers to the light species oxidation. When compared to the decomposition graphs presented in Sec. 6.2.1, the main pathways conserved during the reduction are those of the dodecane decomposition because it is the main component of the fuel surrogate. There are very few possible pathways for methyl-cyclohexane, and the ones conserved are those that quickly merge in the dodecane decomposition pathways. The same observation applies for xylene. Furthermore, since this latter has a different and more stable structure, the decomposition pathways are isolated until reaching the light species state.

As consequences, if the fuel composition is significantly modified, the reduced chemistry might fail to reproduce the combustion processes with accuracy. Then, the effect of the blend composition with respect to the reduced chemistry is presented in the following validation section.

7.4.3 Validations

Evolution of the quantities of interest

The errors on 0-dimensional and 1-dimensional reference cases are presented on Fig. 7.4.5 for the skeletal scheme S52R310 and the corresponding ARC mechanism S30R299QSS22. On the left picture, while the heat release rate distance error remains acceptable on the whole range of temperature, the auto-ignition error shows large discrepancies at low and high temperatures. In the first case, for initial temperature $T_i < 1300\,K$, the low temperature pathways and the NTC behavior have not been targeted to keep a reduced number of species, which explains the large errors. For high temperature, as already mentioned in Sec. 7.4.1, the auto-ignition being not well defined, this can lead to the detection of non-representative large errors. On the right picture all the errors remain low, except for very lean mixture where the laminar flame speed reaches 14 % errors. This is due to the low value of the flame speed with lean mixture, which increases the relative error.

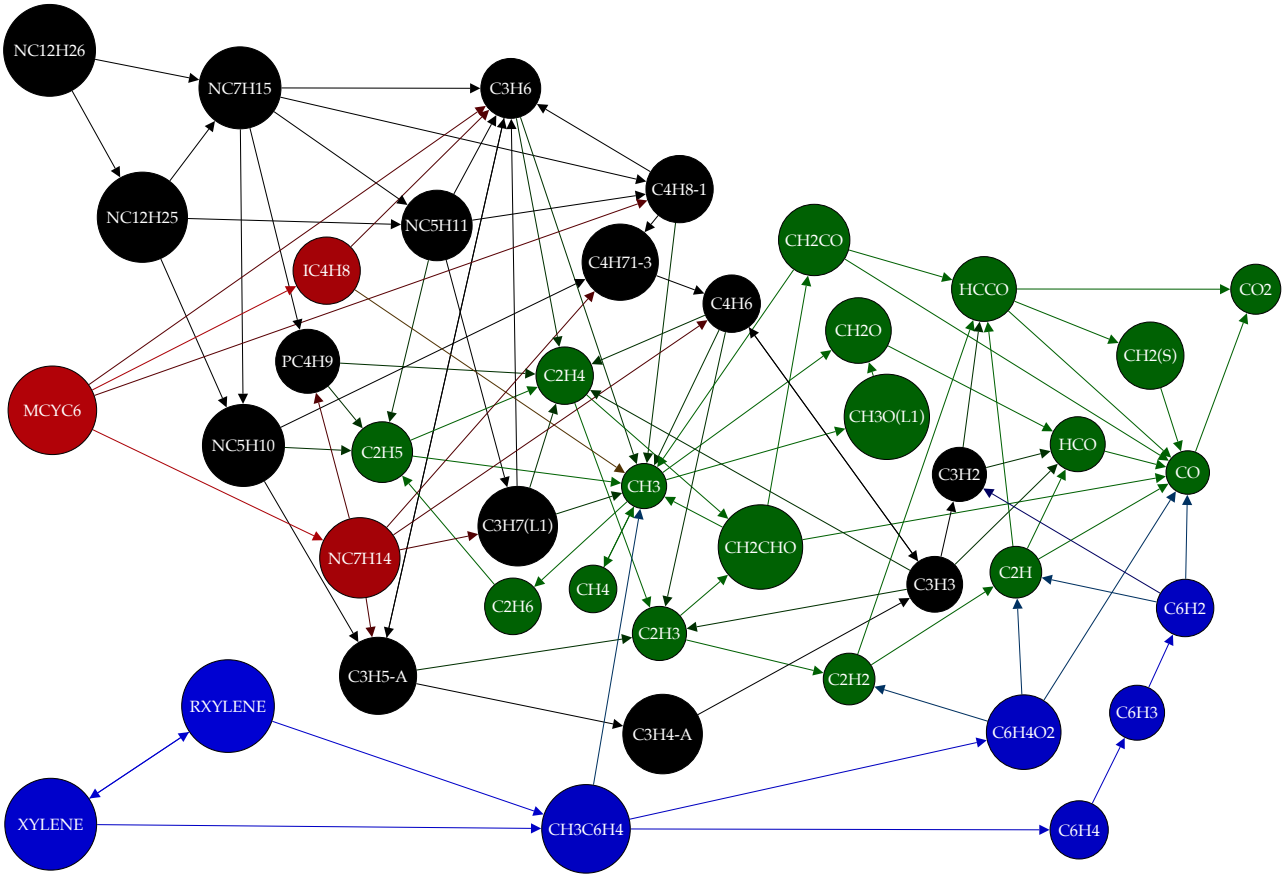

Figure 7.4.4: Visualisation of the fuel decomposition pathways using carbon fluxes with the skeletal S52R310 scheme. Fluxes integrated on a 0-dimensional constant pressure reactor filled with a stoïchiometric kerosene-air mixture at pressure $P = 0.3\,bar$ and temperature $T_i = 1600\,K$

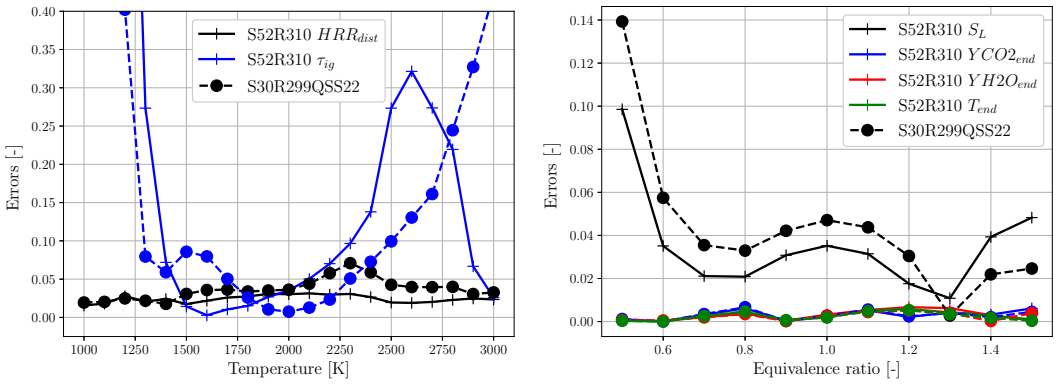

Figure 7.4.5: Errors on 0D constant pressure reactors versus initial temperature at $P = 0.3\,bar$ and $\phi = 1$ (left), and 1D premixed flames versus equivalence ratio at $P = 0.3\,bar$ and $T_f = 233\,K$ (right) for S30R299QSS22 (dots symbols) and S52R310 (plus symbols) schemes.

Detailed profiles of the quantities of interest are presented in the following figures. First, Fig. 7.4.6 presents the evolution of the auto-ignition time depending on the initial temperature and with stoichiometric mixtures for atmospheric ($P = 1\ bar$) and low pressure ($P = 0.3\,bar$). Even if atmospheric pressure was not targeted during the reduction, the profiles show a very good agreement for the high altitude condition too. This result is also generalized to the 1-dimensional profiles in Fig. 7.4.7 to 7.4.10 where both atmospheric ($T_f = 300\,K$ and $P = 1\ bar$) and high altitude ($T_f = 233\,K$ and $P = 0.3\ bar$)

conditions are evaluated. Fig. 7.4.7 shows the evolution of the laminar flame speed, Fig. 7.4.8 the final temperature, Fig. 7.4.9 the final CO and CO_2 mass fraction, because the low pressures have shown to modify the thermodynamic equilibrium in Chap. 5, and Fig. 7.4.10 shows CO and OH maximum concentrations that are important intermediate radical species. For all these quantities, the ARC mechanism S30R299QSS22 demonstrates very good performances.

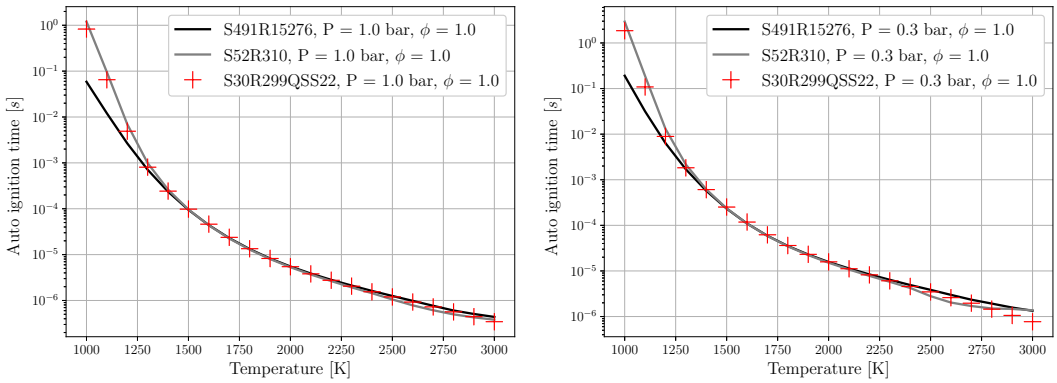

Figure 7.4.6: Auto-ignition time versus initial temperature for S30R299QSS22, S52R310 and S491R15276 schemes in a constant pressure reactor filled with a stoichiometric mixture. Left: $P = 1\,bar$, right: $P = 0.3\,bar$.

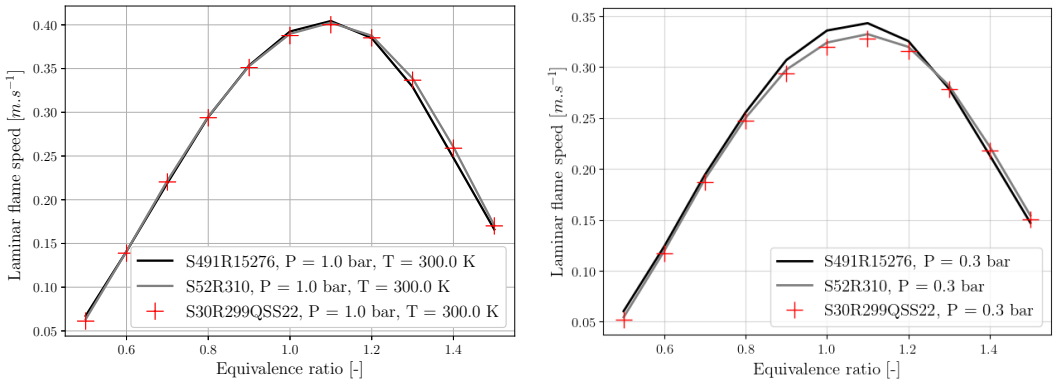

Figure 7.4.7: Laminar flame speed versus equivalence ratio for S30R299QSS22, S52R310 and S491R15276 schemes in 1-dimensional premixed flames. Left: atmospheric conditions ($T_f = 300\,K$ and $P = 1\ bar$), right: high altitude conditions ($T_f = 233\,K$ and $P = 0.3\ bar$).

Fuel blend validity

Section 7.4.2 showed that the reduction mainly keeps the $nC_{12}H_{26}$ decomposition pathways because it is the main fuel component. However, in the context of multi-component droplet ignition, the most volatile fuel will evaporate first, leading to a different fuel mixture composition. The proportion of methylcyclohexane and xylene will be increased as it will be shown in Chap. 12. Fig. 7.4.11 shows the errors on auto-ignition time depending on the fuel blend composition with a stoichiometric mixture and with $T_i = 2000\,K$, which is the typical temperature encountered in two-phase flow ignition.

The results show that the auto-ignition time is well captured for the majority of the blend compositions. As expected, the highest errors are reached for pure methylcyclohexane or xylene compositions with a maximum of 25% differences with the detailed scheme. However, as soon as dodecane is added, the error is reduced. One can note that for multi-component droplet evaporation the presence of pure methylcyclohexane or xylene mixture are highly improbable (see Chap. 12).

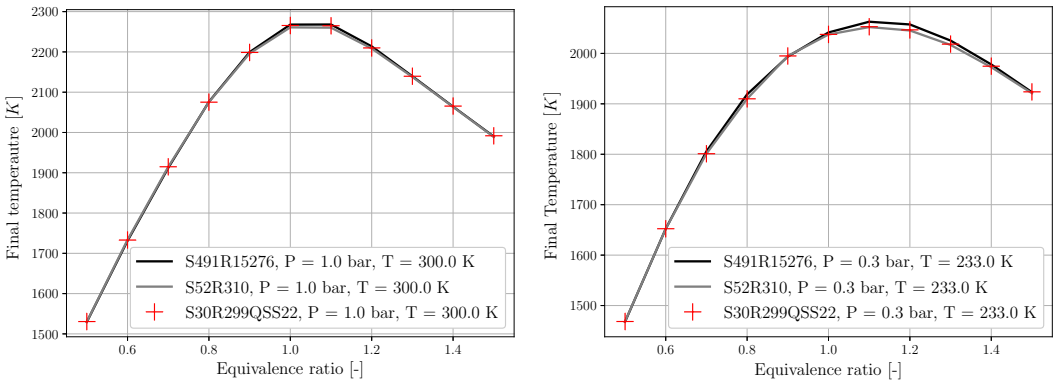

Figure 7.4.8: Final temperature versus equivalence ratio for S30R299QSS22, S52R310 and S491R15276 schemes in 1-dimensional premixed flames. Left: atmospheric conditions ($T_f = 300\,K$ and $P = 1\ bar$), right: high altitude conditions ($T_f = 233\,K$ and $P = 0.3\ bar$).

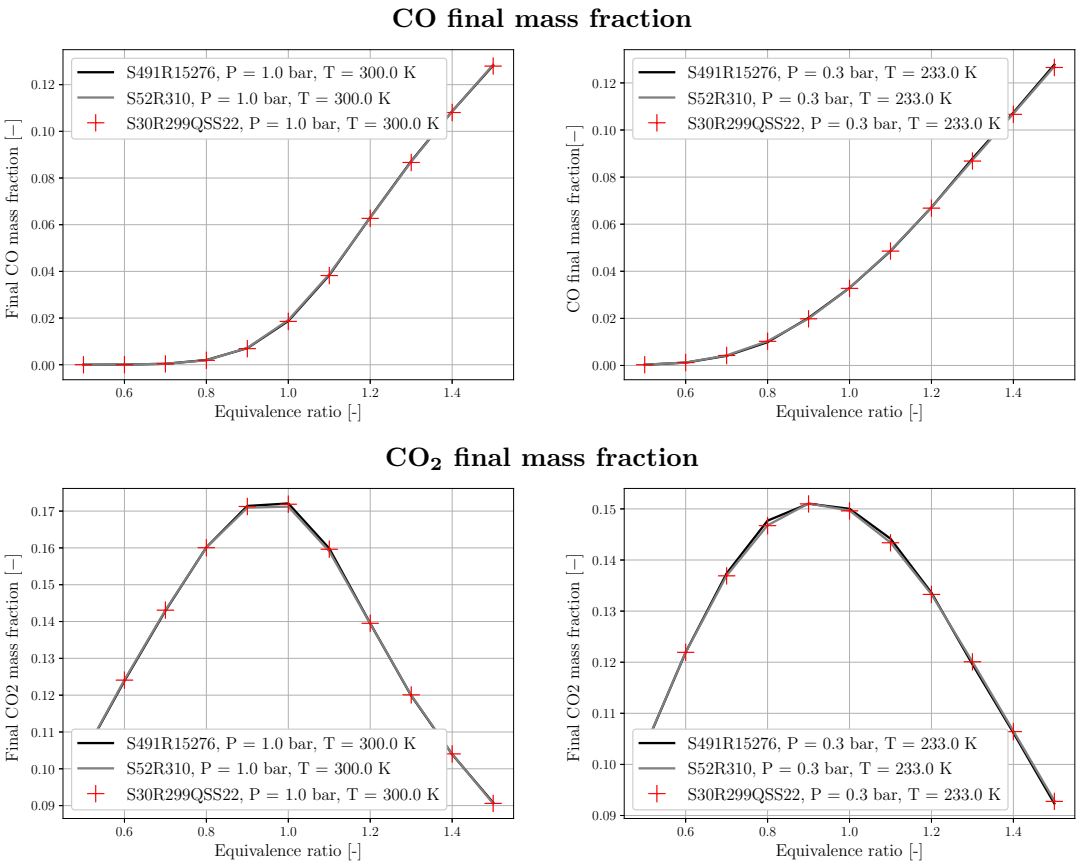

Figure 7.4.9: Final CO and CO_2 mass fractions versus equivalence ratio for S30R299QSS22, S52R310 and S491R15276 schemes in 1-dimensional premixed flames. Left: atmospheric conditions ($T_f = 300\,K$ and $P = 1\ bar$), right: high altitude conditions ($T_f = 233\,K$ and $P = 0.3\ bar$).

The errors on laminar flame speed, due to a modification of the fuel blend, have not been measured because during the kernel propagation, the droplets upstream of the flame front have more time to evaporate. Thus, there is more dodecane in the mixture and fewer blend composition variations.

7.4.4 QSS effect on ignition

The ARC formalism becomes more and more attractive for reacting simulations [Felden et al. 2018a], and it has been used in several configurations [Collin-Bastiani 2019, Felden et al. 2018b]. However, few

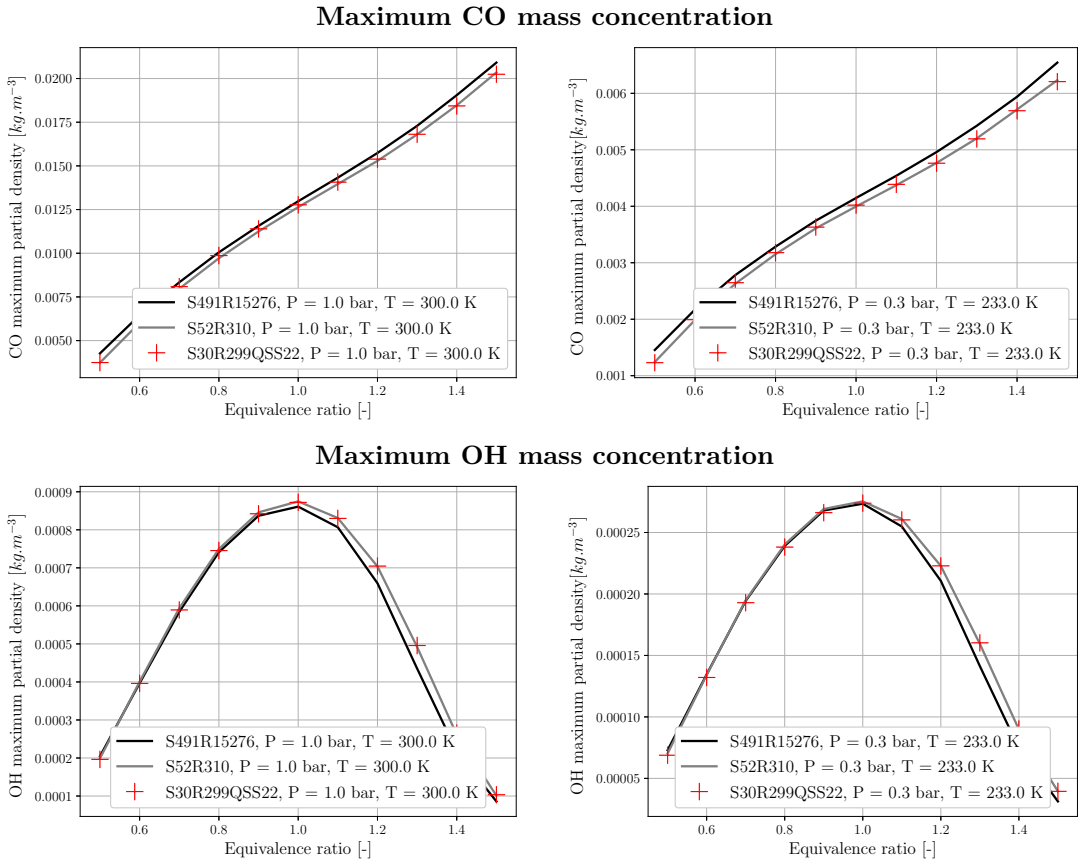

Figure 7.4.10: Maximum CO and OH mass concentrations versus equivalence ratio for S30R299QSS22, S52R310 and S491R15276 schemes in 1-dimensional premixed flames. Left: atmospheric conditions ($T_f = 300\,K$ and $P = 1\ bar$), right: high altitude conditions ($T_f = 233\,K$ and $P = 0.3\ bar$).

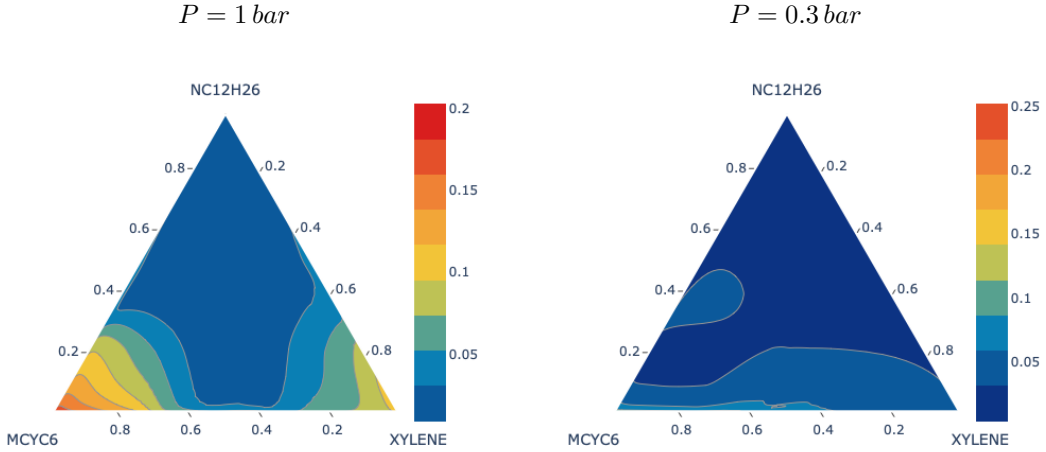

Figure 7.4.11: Errors on auto-ignition time in a constant pressure reactor depending on the fuel blend molar composition for S30R299QSS22 scheme. $T_i = 2000\,K$, $\phi = 1$

studies have provided a direct comparison between skeletal and ARC schemes for ignition studies with thermal chemical runaway. The physics of these phenomena are hard to simulate as it implies many radical species in a transient regime with very short time scales.

To evaluate the influence of the chemical scheme and the QSS species for ignition, a two-dimensional square configuration is considered. The domain size is $1\,cm \times 1\,cm$ and 401 points are used in each

direction to discretize the domain ($\Delta x = 25\,\mu m$). The resulting discretization allows to have around 40 points in the thermal flame thickness, which ensures the spatial resolution required for combustion processes with a detailed chemical mechanism. The domain is initially filled with a gaseous stoichiometric premixed mixture of kerosene-air, at low temperature ($T = 233\,K$), and low pressure ($P = 0.3\,bar$). The ignition and the kernel formation are triggered by an energy deposition in the center of the domain. The temperature increase causes a chemical runaway with auto-ignition processes, which then forms a hot kernel with a spherical propagating flame front.

Two simulations have been performed, the first one with the skeletal chemistry S52R310 is labeled KD1000, the second one with the ARC chemistry S30R299QSS22 is labeled CD50. All the simulations are based on CFL and Fourier conditions for the computation of the time step. This time step reaches the minimum value of $\Delta t = 9.1\,ns$ during the kernel formation. However, due to the stiffness of the chemistry, the computation of the production terms can require lower time steps. In this case, the CFL and Fourier numbers are reduced. Hence, for the case KD1000 the time step had to be divided by 1000 leading to $\Delta t = 9.1 \times 10^{-12}\,s$. Similarly, for the case CD50 the time step had to be divided by 50 leading to $\Delta t = 1.8 \times 10^{-10}\,s$.

The comparison between KD1000 and CD50 on Fig. 7.4.12 shows large differences on the heat release rate profiles at the first instants. The skeletal scheme leads to larger heat release resulting in a faster temperature increase on Fig. 7.4.13. The temporal evolution indicates that the auto-ignition happens at the same time for both chemistries, but differs in the transition phase leading to propagating front. Figure 7.4.12 shows that this transition occurs faster with the skeletal scheme. Indeed, at $t = 60\,\mu s$ the flame front starts to form, and the heat release rate starts to decrease in the kernel center. On the contrary, for the ARC scheme the kernel center remains the most active zone. This difference in the transition phase causes a delay between the two simulations. Hence, at later times, the flame front of case KD1000 precedes the one of case CD50. There is also a slight difference on the maximum value of the heat release rate during the flame propagation, however it is compensated by the larger flame front in the ARC computation which leads then to the same flame speed.

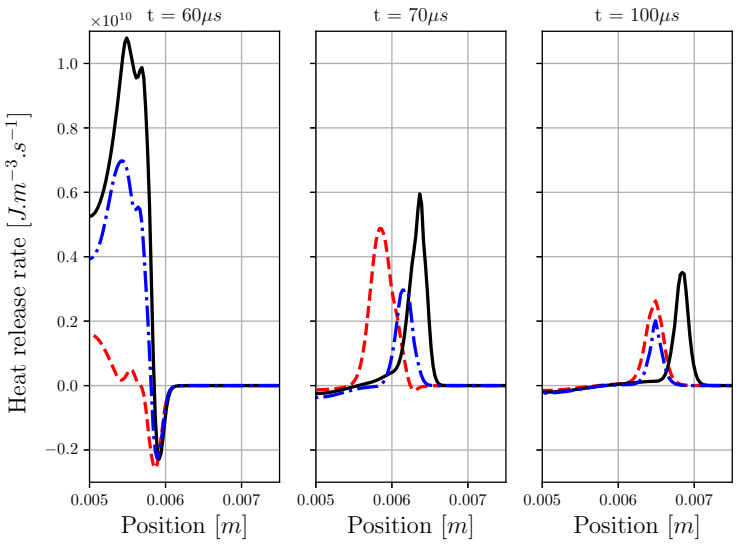

Figure 7.4.12: Heat release rate radial profiles at several instants. Black line: case KD1000 ; red dashed line: case CD50 ; blue dash-dotted line: scheme S31R310QSS21

The time steps used in cases KD1000 and CD50 are different but a simulation of CD50 with a time step divided by 1000 led to the same results and demonstrates that only the QSS species are at the origin of these differences. Indeed, Fig. 7.4.14 shows a higher total production rate in case KD1000 for species that have been put in QSS assumption. These species do not respect this assumption since their production rate is not equal to zero, especially for CH_2CO. Thus, another ARC mechanism has been reduced with the species CH_2CO which is transported. This new scheme is labeled S31R310QSS21 and is represented with the blue dash-dotted curve on Fig. 7.4.12 and 7.4.13. The results show an improved precision with

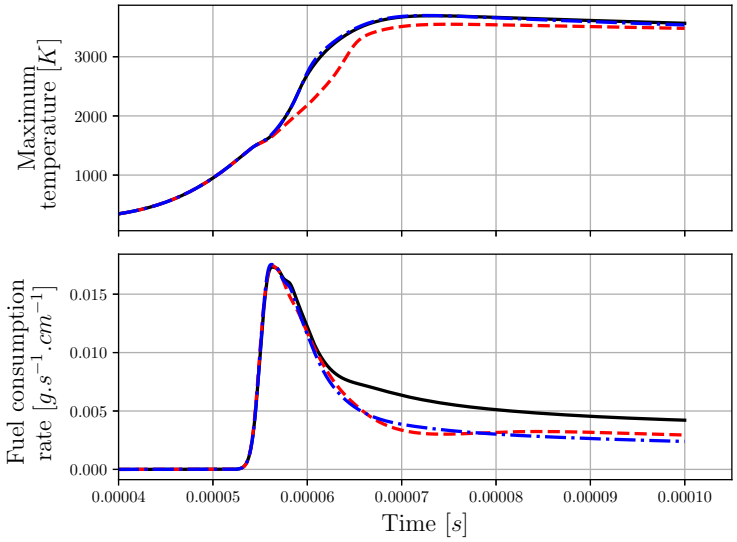

Figure 7.4.13: Temporal evolutions of maximum temperature (top) and fuel consumption rate (bottom). Black line: case KD1000 ; red dashed line: case CD50 ; blue dash-dotted line: scheme S31R310QSS21

this new scheme. Better results could be obtained by transporting the other species presented in Fig. 7.4.14. However, the stiffness of this new scheme is too high. Indeed, the time-steps required are 20 percents smaller. Then, it has been chosen to keep the scheme S30R299QSS22 in the following.

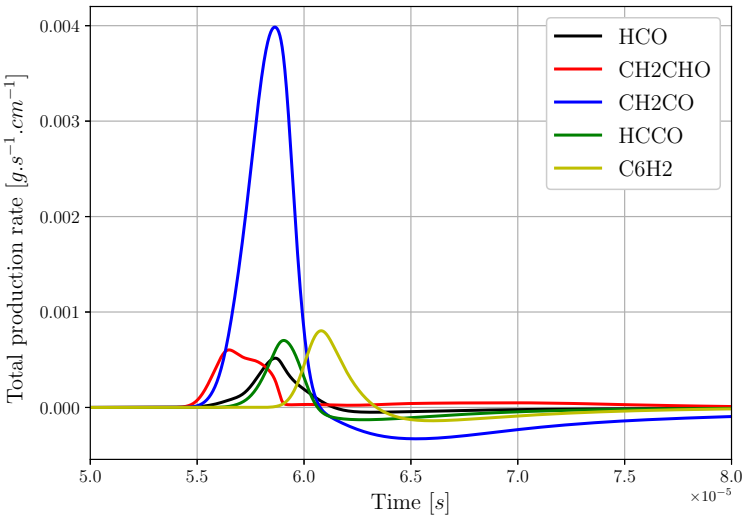

Figure 7.4.14: Evolution of total production rate in case KD1000 for species set in QSS in case CD50

Despite the differences observed on Fig. 7.4.12 between KD1000 and CD50, the temporal evolutions on Fig. 7.4.13 indicate similar behaviors once the flame kernel is formed ($t > 80\,\mu s$). The maximum temperature shows only $50\,K$ difference, and the fuel consumption rates have the same evolution (the offset is due to the larger kernel radius in the KD1000 case). It is reminded that the computations using ARC are far richer in terms of physical information and precision than single or two step chemistries often used in DNS studies [Turquand d'Auzay et al. 2019].

Concerning the performances, the ARC chemistry enables to use time-steps 20 times larger compared to the skeletal mechanism. Furthermore, since the number of transported species is reduced, the total computational time is divided by 40. Hence, the ARC chemistry offers a good cost/precision compromise.

7.4.5 Conclusions

The results in Sec. 7.4.3 demonstrate that the ARC scheme S30R299QSS22 is able to reproduce the ignition processes and kernel flame propagation in atmospheric and high altitude conditions. Furthermore, the reduced chemistry predicts well the auto-ignition times even with a modification of the fuel composition which is important for two-phase ignition with a multi-component evaporation model.

The accuracy could be increased with additional chemical pathways (and fewer QSS species), but it would require to transport more species which would increase the CPU-cost. The number of transported species is large but affordable in terms of CPU and memory cost. However, the issue comes from the small time steps required that are several orders of magnitude lower than the classical ones driven by convective (CFL) and diffusive (FO) effects.

At this stage, the ARC scheme is still too stiff for a 3D simulation, and the time step is limited by chemistry. As shown in Sec. 7.4.2, the stiffest species are part of the dodecane pyrolysis processes. Therefore, the pyrolysis lumping method [Heberle and Pepiot 2021] could be further used to remove these intermediate pyrolysis products and then reduce the CPU-cost. This method not being available in ARCANE during the time of this PhD, another approach based on adapted numerical chemistry integration methods was proposed in this work, as presented in Chap. 8.

The scheme S30R299QSS22 will be used in the following parts of this PhD, especially for the DNS of ignition, the two-phase flow ignitions, and for the academical and industrial applications.

Chapter 8

Numerical methods for the integration of chemistry

Contents

As shown in Chap. 7, the ARC schemes may introduce very short time-scales associated to the short life-time of some intermediate species or to very fast chemical processes. In such case, explicit time-integration methods require small - and even very mall- time-steps to ensure both accuracy and stability which significantly increases the computational cost. In this chapter, new methods are proposed and evaluated to overcome this issue.

The standard explicit chemistry integration is first introduced in Sec. 8.1 to highlight the possible issues. Then, a new approach called exponential integration of chemistry is presented in Sec. 8.2. Both may be combined with an optimized sub-cycling procedure described in Sec. 8.3. Finally in Sec. 8.4 the performances of the new approaches are evaluated in a chemically transient case (ignition) in terms of accuracy and computational cost. These tests have been performed with the DNS solver NTMIX which is presented in Appendix G.

This chapter is adapted from a publication at the European Combustion Meeting [Pestre et al. 2021].

8.1 Standard explicit integration

8.1.1 Problem description

We consider here 0D reactors, i.e., without transport phenomena. The time-evolution of the species concentrations is then only piloted by their production rates:

$$\frac{dc_k}{dt} = \dot{\omega}_k \tag{8.1}$$

with c_k the mass concentration of species k. As explained in Chap. 2, the production rates $\dot{\omega}_k$ are computed from the reaction rates of progress $\mathcal{Q}_j$ and are reminded here:

$$\dot{\omega}_k = \sum_{j=1}^{N_{react}} \dot{\omega}_{kj} = W_k \sum_{j=1}^{N_{react}} \nu_{kj} \mathcal{Q}_j \quad \text{with} \quad \nu_{kj} = \nu''_{kj} - \nu'_{kj} \tag{8.2}$$

$$\mathcal{Q}_j = K_{fj} \prod_{k=1}^{N_{spec}} [k]^{\nu'_{kj}} - K_{rj} \prod_{k=1}^{N_{spec}} [k]^{\nu''_{kj}} \tag{8.3}$$

where K_{fj} and K_{rj} are the forward and backward reaction rates respectively and are computed from the chemical scheme.

The first-order explicit time integration of Eq. (8.1) writes:

$$c_k^{n+1} = c_k^n + \Delta t \times \dot{\omega}_k^n \tag{8.4}$$

with n the current iteration and Δt the time-step.

8.1.2 Stability and stiffness

From Eq. (8.4), it is clear that depending on the chemical source term, a too large time-step may lead to a concentration outside the $[0, c_k^{max}]$ where c_k^{max} is the concentration corresponding to pure species k in the mixture. One could think then that keeping the time-step below $c_k^n / |\dot{\omega}_k^n|$ is sufficient to obtain a correct solution. This is however not the case, due to the fact that each species evolution is embedded in a larger dynamic system made of N species equations. Therefore, even without leading the concentrations outside the authorized range, a too large time-step may lead to an oscillatory behaviour, as illustrated in Fig. 8.1.1. On the left figure the small time-steps allow the species concentration to gradually converge towards the equilibrium target. On the contrary, when the time-steps are too large oscillatory behaviors can be observed as on the right figure. In this case, at the first iteration the concentration is too much decreased. This triggers a too high production at the next iteration which increases again the concentration to a too high level, and so on. In the best scenario, the oscillations attenuate towards the equilibrium. In the worst case, the oscillations persist or even amplify until reaching non-physical concentrations.

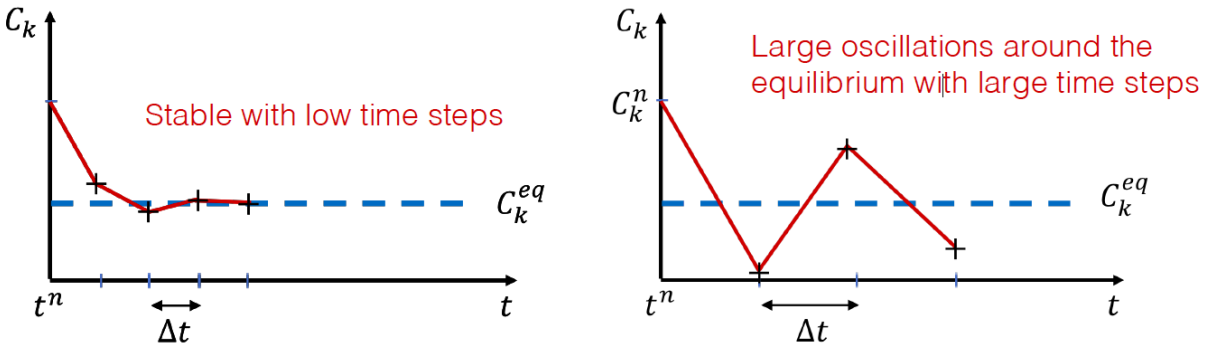

Figure 8.1.1: Examples of temporal evolution of species concentrations depending on the time-step, illustrating stable and unstable behaviors.

To avoid such unstable behaviors, a chemical criterion is often added to the time-step computation. In this work, the following explicit definition is used:

$$\Delta t_{chem,k} = \frac{c_k}{|\dot{\omega}_k|} \times C_{chem,k} \tag{8.5}$$

with $C_{chem,k}$ the chemical number which can depend on the species and the chemical scheme. This definition usually provides larger values than Eq. (7.10) built with the Jacobian matrix. However, Eq. (8.5) is easier to compute and enables to avoid negative species concentrations. Indeed, using $C_{chem,k} = 1$ and

replacing the expression in Eq. (8.4), this chemical time-step corresponds to a complete consumption of the species or a doubling of its concentration.

Typically, chemical stiffness is associated with intermediate radical species as found in ARC. Due to their unfilled electron layer they are very reactive and directly consumed as soon as they are produced. Thus, their concentration is very low while their consumption rate is very high. For example, ARCs for kerosene require a time-step of the order of $10^{-9} - 10^{-11}\,s$ which is lower than CFL and FO conditions. Other sources of stiffness are the very fast pyrolysis processes and spark-ignition where high temperatures are reached.

8.2 Exponential Chemistry integration

Classically stiffness is resolved with implicit time-integration, which stays robust even with large time-steps. However it requires to solve an inverse problem which may turn very costly. At the end, significant computing time is saved only if the time-step is large enough to compensate the extra-cost. This raises then a question about the accuracy of the solution for unsteady cases with time scales smaller than the time-step. Complementary discussions can be found in [Lu and Law 2009, Singer and Pope 2004]. In the context of LES of compressible flows, the time-step piloted by acoustics is of the order of 10^{-7} s to 10^{-8} s with today's mesh size, i.e., between 1 and 3 orders of magnitude larger than the chemical time scale. Therefore the full implicit integration may not always be the best choice, and semi-implicit approaches are a good alternative. This was shown for example in the work of Jaravel [2016], where the most stiff species are semi-implicited as follows:

$$c_k^{n+1} = c_k^n + \frac{\dot{\omega}_k}{1 + \dot{\omega}_k^- \Delta t}\Delta t \quad \text{with} \quad \dot{\omega}_k^- = -\sum_{j=1}^{N_{reac}} \dot{\omega}_{kj} \quad \text{for all} \quad \dot{\omega}_{kj} < 0 \tag{8.6}$$

In an attempt to make this semi-implicit integration even more efficient, another formulation is proposed in this work based on the general analytical form of the solution of Eq. 8.1. Such approach has been already used to solve stiff ODE chemical systems and is refered as "CHEMEQ2" in the literature [Mott and Oran 2001].

8.2.1 Mathematical description

Assuming that species are produced and consumed following first-order differential equation, the chemical problem may be rewritten as in [Blanchard et al. 2022]:

$$\frac{dc_k}{dt} = \dot{\omega}_k = A_k c_k + B_k \tag{8.7}$$

where $A_k c_k$ and B_k are respectively the consumption and production rates:

$$A_k c_k = \sum_{j=1}^{N_{reac}} \dot{\omega}_{kj} \quad \text{for all} \quad \dot{\omega}_{kj} < 0 \tag{8.8}$$

$$B_k = \sum_{j=1}^{N_{reac}} \dot{\omega}_{kj} \quad \text{for all} \quad \dot{\omega}_{kj} > 0 \tag{8.9}$$

Assuming the A_k and B_k coefficients constant, the general form of the solution of Eq. (8.7) is:

$$c_k(t) = \left(c_k(t=0) + \frac{B_k}{A_k}\right)\exp\left(A_k t\right) - \frac{B_k}{A_k} \tag{8.10}$$

In discretized form, Eq. (8.10) leads to the following expression:

$$c_k^{n+1} = \left(c_k^n + \frac{B_k^n}{A_k^n}\right)\exp\left(A_k^n \Delta t\right) - \frac{B_k^n}{A_k^n} \tag{8.11}$$

where A_k^n and B_k^n are the values of A_k and B_k at iteration n and considered constant during the time-step Δt. The production rates are then re-derived to be explicitly injected in the conservation equations:

$$\dot{\omega}_{k,expo}^n = \frac{c_k^{n+1} - c_k^n}{\Delta t} \tag{8.12}$$

In that way, the exponential integration can be seen as a semi-implicit integration with a prediction of the concentration at the iteration $n+1$.

The exponential integration is strictly valid only if all reactions are elementary reactions with unity stoichiometric coefficients for the reactants. More details are available in Appendix F.

8.2.2 Mass conservation

By construction the exponential integration is not mass conservative: $\sum_{k=1}^{N_{spec}} \dot{\omega}_{k,expo} \neq 0$. A demonstration on a simple example is given in Appendix F. One can note that $\dot{\omega}_{\mathrm{H},expo}^n$ approaches $\dot{\omega}_{\mathrm{H}}^n$ when the time-step goes to zero.
The non-conserved mass arises from the assumption that the species concentrations (other than the integrated species) are constant. As a consequence, in the present method A_k and B_k terms are constant while they should vary during the iteration. A better estimation of these terms using higher order expressions (instead of constant values) or iterative approaches may solve this conservative issue.

In this work a brute force correction method is used to ensure the mass conservation. At each iteration, the atomic excess (or deficit) $dn_{\mathcal{A}}\,[mol.m^{-3}]$ of each element is quantified as:

$$dn_{\mathcal{A}} = \sum_{k=1}^{N_{spec}} \frac{c_k^{n+1} - c_k^n}{W_{\mathcal{A}}} n_{\mathcal{A},k} \tag{8.13}$$

with $n_{\mathcal{A},k}$ the number of atoms $\mathcal{A}$ in species k, and $W_{\mathcal{A}}$ the molar mass of $\mathcal{A}$.

This excess or deficit is then added or substracted from the most prominent species containing atoms $\mathcal{A}$. The detailed procedure is given in [Blanchard 2021].

A sub-cycling method can also be applied to reduce the chemical time-step used for exponential integration. This method is presented in Sec.8.3.

8.2.3 Stability and stiffness

Factorizing Eq. (8.11) into Eq. (8.14), and noting that by definition, $A_k < 0$ and $B_k > 0$, it can be seen that the exponential integration is positive, i.e., if the initial concentrations are positive the final concentrations are also positive.

$$c_k^{n+1} = \underbrace{\frac{B_k^n}{A_k^n}}_{<0} \underbrace{\left(\exp\left(A_k^n \Delta t\right) - 1\right)}_{<0} + \underbrace{c_k^n exp(A_k^n \Delta t)}_{>0} \tag{8.14}$$

Moreover, the exponential integration enables a smooth convergence towards equilibrium, reducing the occurrence of spurious oscillations. Note that the exponential form only affects the consumption processes:

$$B_k \to 0 \quad \Leftrightarrow \quad c_k^{n+1} \to c_k^n \times \exp\left(A_k^n \Delta t\right) \tag{8.15}$$

$$A_k \to 0 \quad \Leftrightarrow \quad c_k^{n+1} \to c_k^n + B_k^n \Delta t \tag{8.16}$$

Taking a simple example with the reaction (R4), the consumption and production behaviors are illustrated on Fig. 8.2.1.

$$\mathrm{H} \leftrightarrow \mathrm{I} \tag{R4}$$

The effect of the mass correction is also shown on Fig. 8.2.1 with the green arrows. In this example the mass excess of species H due to the exponential form is compensated by reducing the production of

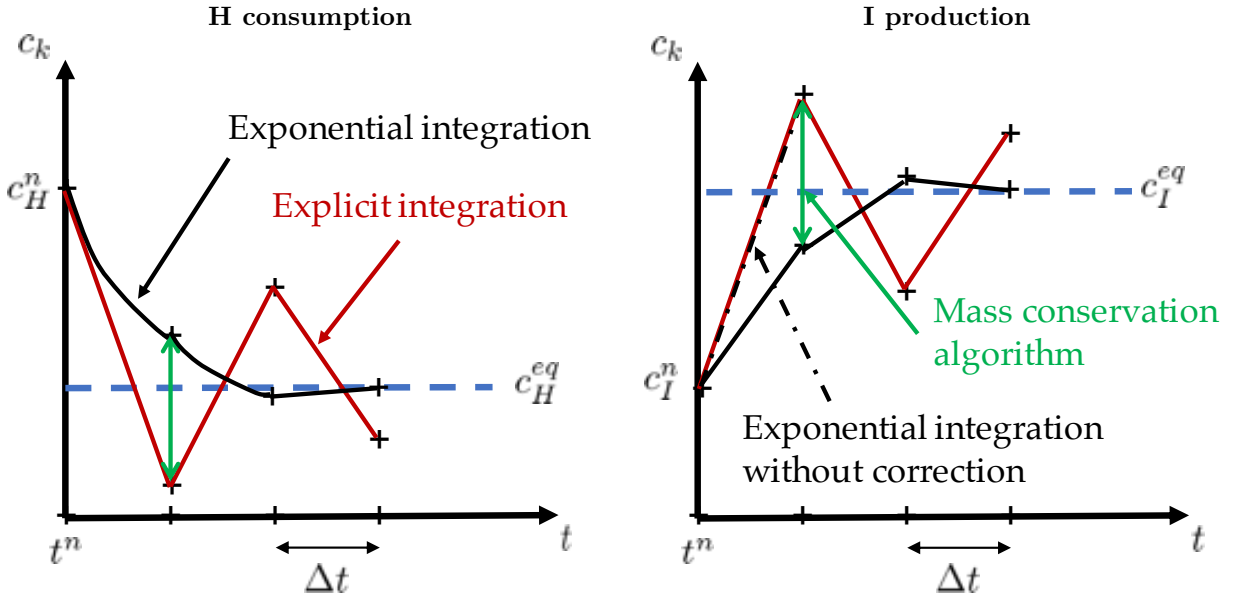

Figure 8.2.1: Theoretical diagram of the temporal evolutions of the species concentrations depending on the chemistry integration.

species I.

When the time-step or the consumption term A_k^n tend to zero, the expression Eq. (8.11) may be replaced by the asymptotic form:

$$c_k^{n+1} = \left(c_k^n + \frac{B_k^n}{A_k^n}\right)(1 + A_k^n \Delta t) - \frac{B_k^n}{A_k^n} \tag{8.17}$$

By re-arranging the terms, one recovers the expression of the standard explicit integration:

$$c_k^{n+1} = c_k^n + c_k^n A_k^n \Delta t + B_k^n \Delta t \tag{8.18}$$

$$\Leftrightarrow \quad c_k^{n+1} = c_k^n + c_k^n \frac{\dot{\omega}_{k<0}^n}{c_k^n} \Delta t + \dot{\omega}_{k>0}^n \Delta t \tag{8.19}$$

$$\Leftrightarrow \quad c_k^{n+1} = c_k^n + \dot{\omega}_k^n \Delta t \tag{8.20}$$

As a consequence, if the time-step is small enough to resolve the chemical processes, the exponential integration is naturally equivalent to the classic explicit integration.
Although the exponential integration increases drastically the robustness, it may not ensure accuracy if the time-step is too large. For transient processes where the short timescales of the chemistry play an important role, like ignition, the increase of the time step should be then considered with care.

The stability properties of the exponential integration are now demonstrated in a simple ignition case. The simulation corresponds to two flame fronts propagating in opposite directions, resulting from a 1-dimensional energy deposit in a premixed mixture. Figure 8.2.2 shows the profile of CH_3O_2H, which is one of the stiffest species. The exponential integration allows to perfectly recover the profile with a CFL time-step $\Delta t_{CFL} = 7\,ns$, while the standard explicit integration requires a time step of $\Delta t_{chem} = 0.032\,ns$ to obtain the same result.

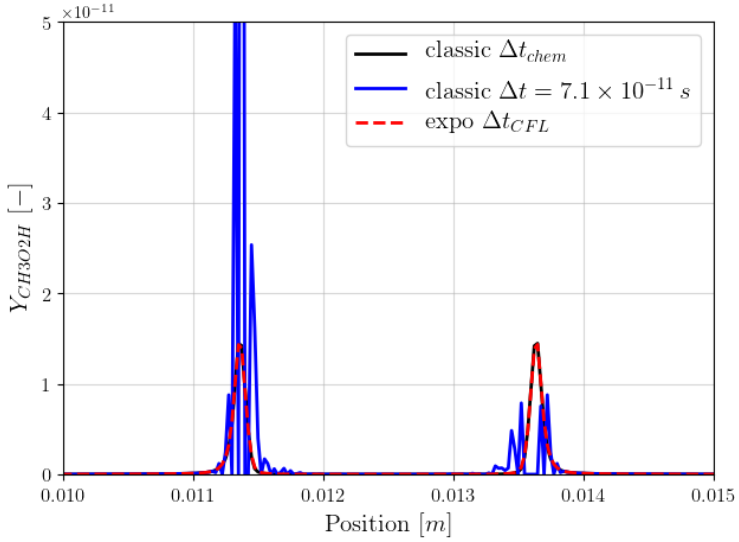

Figure 8.2.2: CH_3O_2H mass fraction profiles in a 1-dimensional ignition simulation of a premixed methane-air mixture at $\phi = 1$.

8.3 Local and Dynamical Sub-Cycling (LDSC) procedure

Another approach to handle chemical stiffness is sub-cycling, which may be also combined with semi-implicit integration. At each iteration, a number of chemical sub-cycles is used to divide the time-step of the current iteration into smaller sub-time-steps only used for the chemistry integration: $\Delta t_{chem-SC} = \Delta t / N_{SC}$. This allows a better precision and stability of the simulation without re-evaluating all the Navier-Stokes equations. For example, Fig. 8.3.1 shows the pressure profiles in a 1-dimensional ignition simulation with various numbers of sub-cycles. The oscillations of the chemical processes create heat release rate fluctuations which in turn produce pressure fluctuations. The increase of the number of sub-cycles up to 100 enables to stabilize the chemical processes and thus remove the pressure fluctuations.

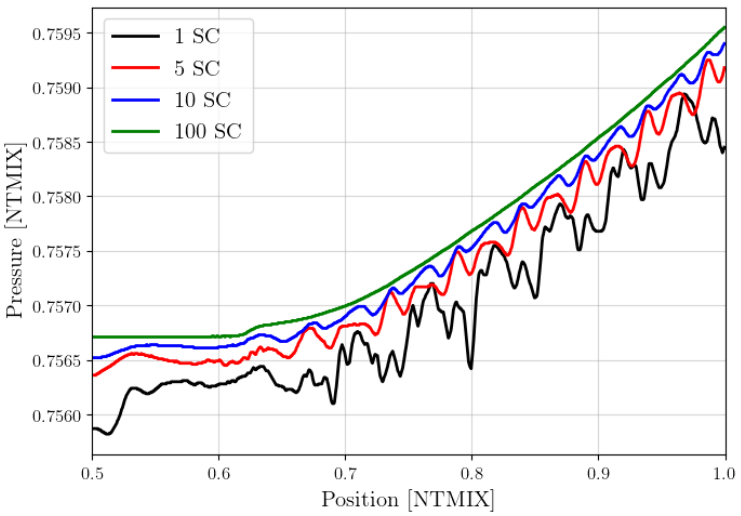

Figure 8.3.1: Pressure profiles in a 1-dimensional ignition simulation of a premixed kerosene-air mixture at $\phi = 1$. Data are non-dimensionized with NTMIX.

Usually, the number of sub-cycles is pre-defined by the user, and is applied in all the domain and during the whole simulation. To limit the over-cost N_{SC} is generally lower than 10 (for 3-dimensional simulations). However, for ARC simulations of kerosene ignition, 10 sub-cycles are not sufficient to get accurate

results and avoid instabilities. In that case, it is interesting to note that since the initial flame kernel is small compared to the domain size, the number of reactive nodes is also small and applying chemical sub-cycles only to these nodes saves a lot of CPU time.

The LDSC procedure requires then to determine for each node and at each iteration the optimum number of sub-cycles. This number is based on the explicit chemical time-step definition Eq. (8.5). This time-step is then clipped at a pre-defined user threshold $\Delta t_{chem,user}$:

$$\Delta t_{chem,k} = \max\left(\frac{c_k}{|\dot{\omega}_k|} \times C_{chem,k}\,,\, \Delta t_{chem,user}\right) \tag{8.21}$$

The value $C_{chem,k} = 0.01$ is advised and corresponds to 1% variation of the species concentration c_k during the time interval $\Delta t_{chem,k}$. These chemical time-steps can be seen as chemical sensors indicating where and how many sub-cycles are needed. The number of sub-cycles is then deduced from the ratio between the chemical time-steps and the current time-step of the simulation:

$$N_{SC} = \min\left[\max\left(\frac{\Delta t}{\Delta t_{chem,k}}\,,\, 1\right),\, M_{SC}\right] \tag{8.22}$$

with M_{SC} a user parameter defining the maximum number of sub-cycles. Both user parameters enable to control the balance cost/accuracy.

Fig. 8.3.2 shows an example of a field of sub-cycle number, obtained with the LDSC method. The simulation corresponds to a 3-dimensional laminar expanding flame kernel resulting from an energy deposit in a kerosene-air premixed mixture. The sub-cycles are activated only at the chemically active nodes corresponding to the flame front.

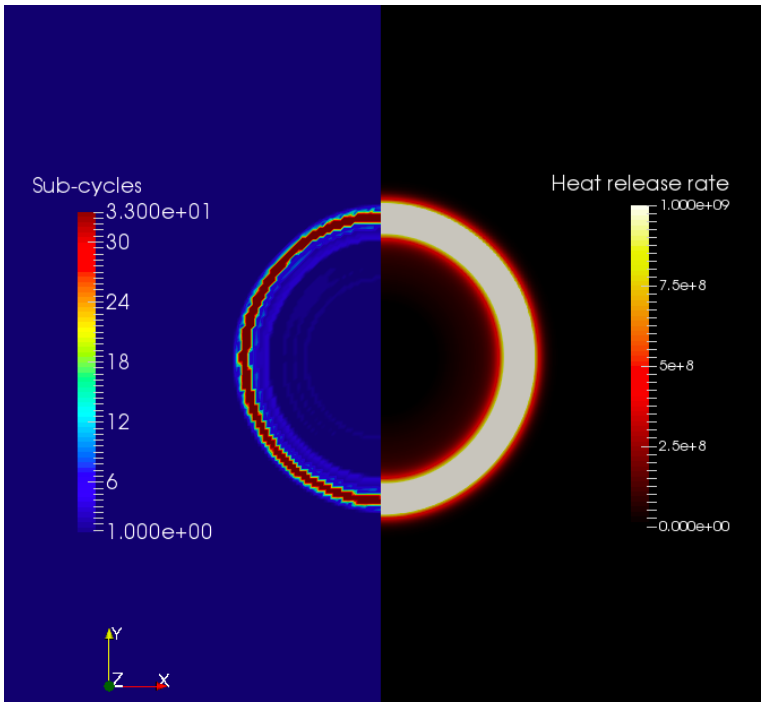

Figure 8.3.2: Field of sub-cycle number obtained using the LDSC procedure. The computation corresponds to a 3D energy deposit in a premixed kerosene-air mixture at $\phi = 1$.

In terms of HPC performance, this non-uniform distribution of sub-cycle number should be associated with a adapted load-balancing. Indeed in the worst case, when all the reactive nodes are located on the same core, all the sub-cycle iterations are computed by this core while the other cores wait and the gain is limited. In reality, the mesh is refined at the flame kernel location so that the kernel spreads over several cores and the computational gain remains favorable. With the current LDSC procedure, the number of local sub-cycles can reach several hundreds at a reasonable cost. Better HPC performances could be

achieved with a more efficient partioning but this is left for future work.

To improve the method, different chemical numbers $C_{chem,k}$ can be used depending on the species production or consumption. In the case of radical production during the first phase of ignition, concentrations are very low. Thus, enabling 10% variation instead of 1% can reduce the number of sub-cycles without modifying the stability.

8.4 Application to ignition and evaluation of the performances

Advantages of using the exponential integration have been demonstrated on laminar and turbulent diffusion flames for methane/oxygen combustion in rocket engine conditions [Blanchard et al. 2022]. In the present work, the application of the exponential integration associated to the LDSC procedure for unsteady ignition processes is evaluated in terms of accuracy and CPU performances.

8.4.1 Set-up

The test case corresponds to ignition in a two-dimensional square domain illustrated on Fig. 8.4.1. The domain size is $1\,cm \times 1\,cm$, discretized with 401 points in each direction ($\Delta x = 25\,\mu m$). The resulting discretization allows to have around 40 points in the thermal flame thickness which ensures the spatial resolution required for combustion processes with a detailed chemical mechanism. The domain is initially filled with a gaseous premixed mixture of kerosene-air at stoichiometry, low temperature ($T = 233\,K$), and low pressure ($P = 0.3\,bar$). The multi-component fuel surrogate presented in Chap. 2 is used, with the chemical scheme S30R299QSS22 presented in Chap. 7. The ignition and the kernel formation are triggered by an energy deposit at the center of the domain. The temperature increase causes chemical runaway with auto-ignition processes, which then form a hot kernel with a spherical propagating flame front. The simulations are done with the DNS solver NTMIX presented in Appendix G.

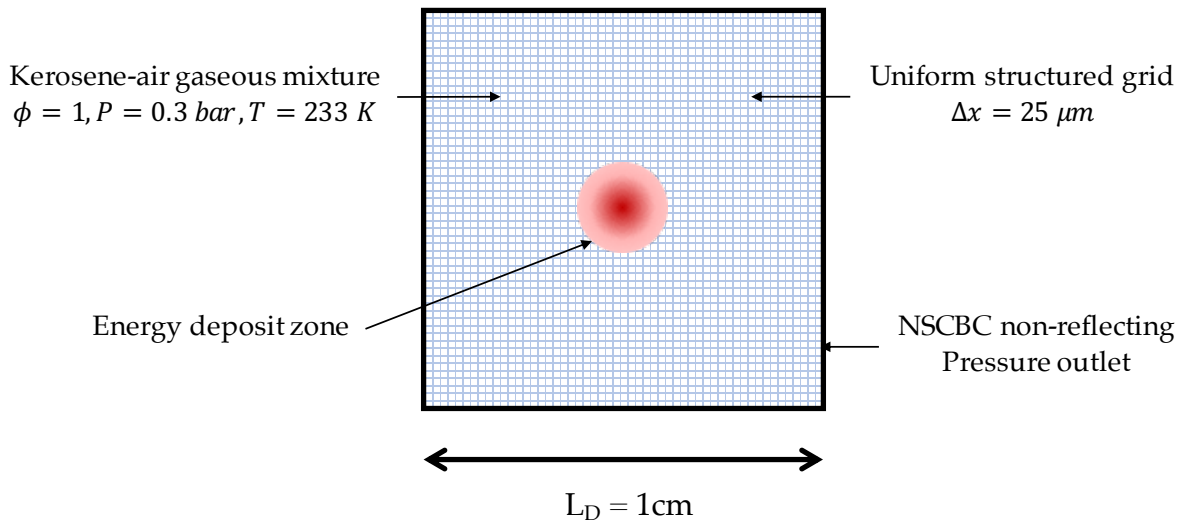

Figure 8.4.1: Numerical set-up for the evaluation of exponential integration and LDSC procedure.

Tab. 8.4.1 summarizes the simulations performed with the corresponding labels and methods used. All the simulations are based on CFL and Fourier conditions for the computation of the time-step. This time-step reaches the minimum value of $\Delta t = 9.1\,ns$ during the kernel formation. However, due to the stiffness of the chemistry, the computation of the production terms require even lower time steps. In this case, the CFL and Fourier numbers are reduced, or the number of sub-cycles is increased. Table 8.4.1 summarizes the reduction factor $\mathcal{F}_{\Delta t}$ and the maximum number of sub-cycles M_{SC}.

Label	Integration Method	M_{SC}	$\mathcal{F}_{\Delta t}$
CD50	Standard explicit	1	0.02
CD10	Standard explicit	1	0.1
C	Standard explicit	1	1
CS10	Standard explicit	10	1
ED10	Exponential	1	0.1
E	Exponential	1	1
ES10	Exponential	10	1

Table 8.4.1: Summary of simulations and methods used

The case **CD50** corresponds to the reference, as smaller time steps gave same results.

8.4.2 Evaluation of the exponential chemistry integration

The comparison between exponential and explicit chemistry integration is presented on Fig. 8.4.2. The results are identical for the cases **CD50** and **ED10**. Thus, the exponential integration allows to use larger time-steps without compromising the precision.

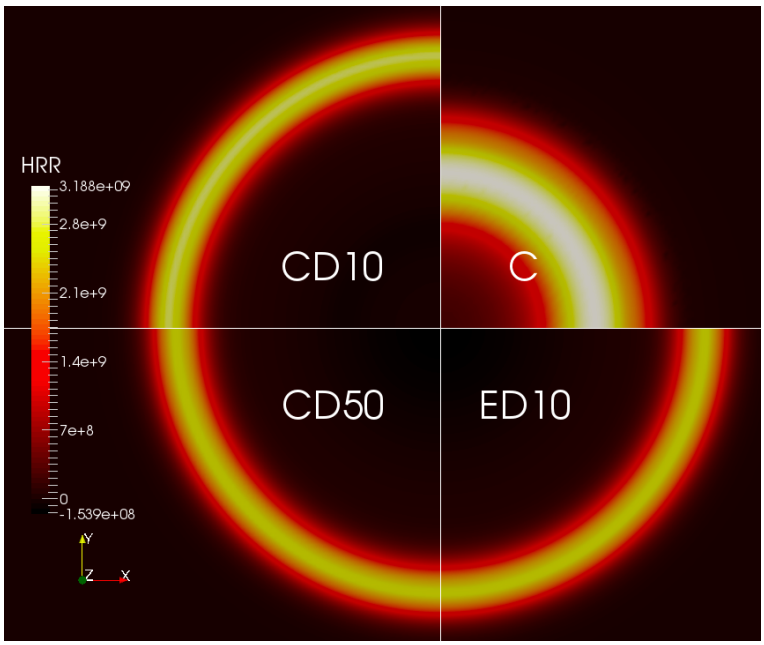

Figure 8.4.2: Comparison of the heat release rate field at the end of the energy deposition for cases **C**, **CD10**, **CD50** and **ED10**

The cases **CD50**, **CD10** and **C** show the effect of the time discretization with explicit chemistry integration. While the **C** case clearly provides a wrong solution, the computation with the time step divided by 10 (**CD10**) shows a reasonably good agreement. However, on Fig. 8.4.3 showing the radial heat release rate profiles, a small shift of the flame front and a slightly higher heat release rate are visible for the case **CD10**. Moreover, no heat release rate is observed at the domain center while endothermic processes take place with the reference case **CD50** indicated by the slightly negative heat release rate values. On the contrary the case **ED10** shows a perfect agreement with **CD50**.
A comparison has been also done between cases **E**, **C** (no time step reduction) and **ED10** on Fig. 8.4.3. The case **E** predicts well the kernel structure while case **C** is far away. However, case **E** exhibits local stability issues, at the center of the domain and at some points in the flame front. This result means that exponential chemistry integration allows well to use larger time steps, but also has a discretization limit for stability.

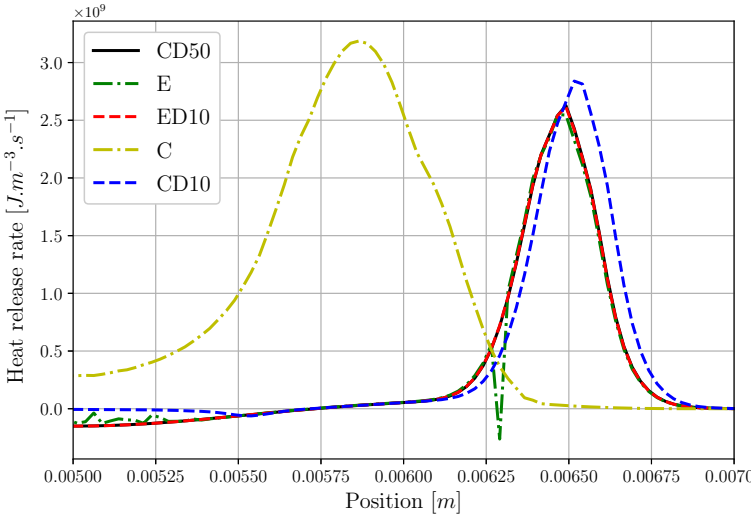

Figure 8.4.3: Comparison of the heat release rate profile at the end of the energy deposition for cases **E**, **ED10**, **C**, **CD10** and **CD50**

8.4.3 Evaluation of the sub-cycling procedure

The effect of sub-cycling can be seen on Fig. 8.4.4. For the exponential integration, the sub-cycling procedure is exactly equivalent to the reduction of the time-step. Indeed, cases **ED10** and **ES10** have the same heat release rate field. Therefore, the LDSC procedure improves the performances because a larger time-step can be used.

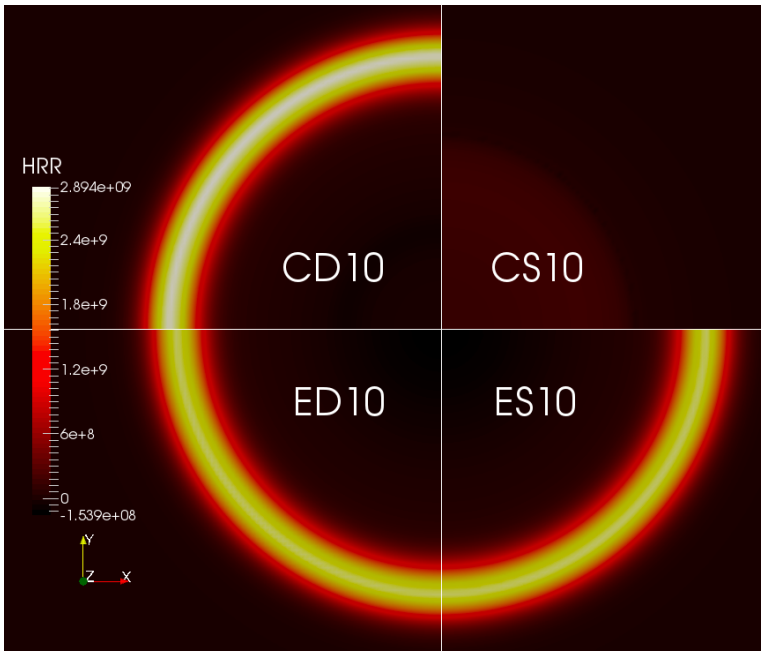

Figure 8.4.4: Comparison of the heat release rate field at the end of the energy deposition for cases **CS10**, **CD10**, **CD10**, **ED10** and **ES10**

For explicit integration this is not the case. On the contrary, it seems that the sub-cycles worsen the heat release rate prediction compared to the **C** case. This phenomenon may be explained by small oscillations of the production rates. Indeed, without sub-cycling, diffusion smooths the solution at each iteration, whereas with sub-cycling, diffusion is computed each 10 chemical sub-cycles. Further studies are needed to validate this assumption. Meanwhile, these results indicate that the sub-cycling procedure

is not adapted to explicit chemistry integration for ignition.

8.4.4 Performances

The exponential integration enables to use time-steps 5 times larger than explicit integration, and the total computational time is divided by 4.48. The sub-cycling procedure enables a further increase of the time-step, which is multiplied by 10. Even if the activation of the sub-cycling method is more expensive, it is compensated by the time-step increase. Then, with the LDSC procedure, the CPU-cost is divided by 4.29. This cost is even more reduced in 3D simulations since the computation of the third direction reduces the relative cost of chemistry.

Finally the exponential method associated to the sub-cycling procedure enables to use time-steps 50 times larger than the standard explicit integration with the same result precision. The performances on 2-dimensional simulations correspond to a CPU-time divided by 19.2. Using these methods, the time-step is no more limited by the chemistry, but only by the CFL and Fourier conditions. The gain still could be increased on coarser meshes by adding more sub-cycles. These methods enable to remove the main over-cost due to the chemistry stiffness in the ARC formalism, and therefore, to perform 3-dimensional DNS of turbulent ignition at a reasonable cost. These simulations are presented in the next Chapter.

Chapter 9

DNS of kerosene-air turbulent ignition

Contents

The effects of low pressure and low temperature conditions have been studied in Chap 5 and 6 in canonical and simplified configurations. To understand the effects of the high altitude conditions in a more realistic 3-dimensional configuration, Direct Numerical Simulations (DNS) of kerosene-air ignition in a turbulent flow have been performed. These computations are based on the ARC chemistry developed in Chap. 7 and the integration methods detailed in Chap. 8. The objective of this study is not to evaluate the combustion / turbulence interation during the ignition process since it has already been studied in the literrature [Fru et al. 2011, Turquand d'Auzay et al. 2019], but rather to analyse the chemical structure of the kernel flame front, to determine the influence of high altitude on the chemistry and to explain the extinction mechanisms that can occur at these conditions.

The numerical set-up of the study is firstly introduced Sec. 9.1. The kernel developments are described in Sec. 9.2 illustrating the influences of pressure, turbulence, and initial energy deposit size. Then, in Sec. 9.3 the chemical structure of the kernels are compared and analysed to characterize the effect of low pressure and the extinction phenomenon. Finally, analytical developments are presented in Sec. 9.4 to determine the kernel temperature evolution equation and to help understand the extinctions occurring at low pressure conditions.

9.1 Numerical set-up

The configuration used for this study is a 3-dimensional cubic domain of 1 centimeter side length meshed with a regular grid. The initial gas phase is a stoichiometric kerosene-air mixture in Homogeneous Isotropic Turbulence (HIT). More information on the turbulent initialization is given in Appendix G.4.

Ignition is triggered with an energy deposition model similar to the one used in [Lacaze 2009]. Hence, the energy source term $\dot{\mathcal{Q}}\,[J.m^{-3}.s^{-1}]$ added to the energy conservation equation follows a Gaussian shape

in both time and space as illustrated on the diagram of Fig. 9.1.1:

$$\dot{\mathcal{Q}} = \frac{\varepsilon_i}{\sqrt{2\pi}^{n+1}\sigma_t\sigma_s^n} \times \exp\left(-\frac{(t-t_0)^2}{2\sigma_t^2}\right) \times \exp\left(-\frac{\sum_{i=1}^{n}(x_i - x_{i,0})^2}{2\sigma_s^2}\right) \tag{9.1}$$

where x_i are the coordinates in direction i, $x_{i,0}$ refers to the center of the deposit volume and n is the number of space dimension. $\varepsilon_i\,[J.m^{-(3-n)}]$ is the amount of energy deposited, t_0 is the time corresponding to the maximum energy deposit, σ_s and σ_t are the characteristic size and duration of the deposit respectively. More details on the turbulent initialization and the energy deposition model are given in Appendix G.5.

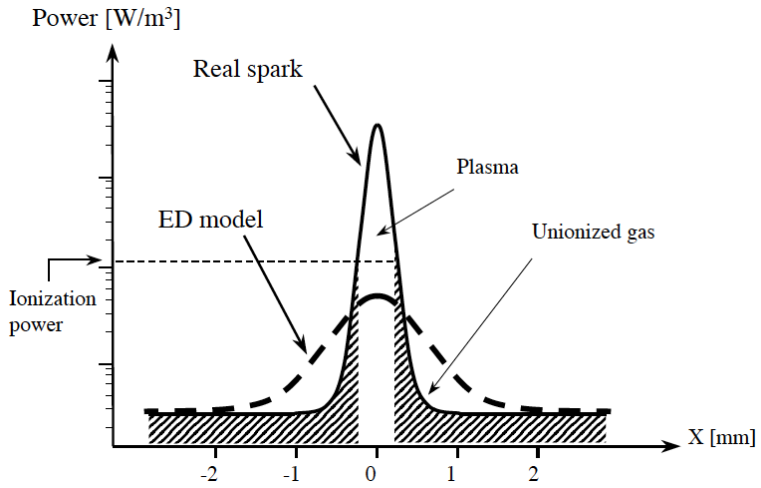

Figure 9.1.1: Sketch of power distribution for real spark and for the ED model (extracted from [Lacaze et al. 2009])

The DNS was performed with the NTMIX solver, using exponential chemistry integration and the LDSC procedure. The kerosene-air chemistry is described with the ARC scheme S30R299QSS22 for the multi-component surrogate fuel presented Chap. 2.

Four simulations have been performed to study the effects of high altitude, turbulence, and energy deposit. Model parameters and corresponding labels are summarized in Tab. 9.1.1 to 9.1.4.

Labels	**Pressure** $[bar]$	**Temperature** $[K]$	**Density** $[kg.m^{-3}]$
PTatmo	1	300	1.22
LPLT	0.3	233	0.47
LPLT-LAM	0.3	233	0.47
LPLT-LED	0.3	233	0.47

Table 9.1.1: Thermodynamic conditions of the four cases.

PTatmo and **LPLT** labels refer respectively to the ground and high altitude conditions. The corresponding density is computed using the perfect gas law.

Labels	$\varepsilon_i\,[mJ]$	$\Delta_s\,[mm]$	$2\Delta_t\,[\mu s]$
PTatmo	9.06	5	100
LPLT	3.5	5	100
LPLT-LAM	3.5	5	100
LPLT-LED	12	7.5	100

Table 9.1.2: Parameters of the energy deposit model for the four cases.

The energy deposited ε_i in the **LPLT** case is chosen so as to reach a maximum temperature of $3000\,K$ without chemical reactions. Using the same energy amount in the **PTatmo** case results in a lower gas temperature following Eq. (G.32), due to the higher density. Therefore it was decided to keep the same deposited energy normalized by the density, which leads to a higher input energy in the **PTatmo** case. The **LPLT-LED** case is equivalent to the **LPLT** case but has a larger energy deposit volume and a higher deposited energy to reach the same maximum temperature.

As explained in Appendix G.5, due to the Gaussian shape, the main part of the energy is deposited during shorter time and space intervals than Δ_t and Δ_s, typically during $[33\,\mu s\,;\,67\,\mu s]$, and over a radius $R_{ker} = 1.8\,mm$ ($R_{ker} = 2.7\,mm$ in the case **LPLT-LED**).

Labels	$L_t\,[mm]$	$u'\,[m.s^{-1}]$	$Re_t\,[-]$	$\eta_k\,[\mu m]$	$\tau_{turb}\,[\mu s]$
PTatmo	1.67	2.425	270	25	344
LPLT	1.67	2.425	127	44	344
LPLT-LAM	-	0	0	-	-
LPLT-LED	1.67	2.425	127	44	344

Table 9.1.3: Parameters of the turbulence initialisation

A visualisation of the initial HIT velocity field is provided on fig. 9.1.2. The same flow has been used for all cases, with the same turbulent characteristic size L_t and velocity fluctuations u' (Tab. 9.1.3). Because of the pressure and temperature dependence of the kinematic viscosity, the turbulent Reynolds number Eq. (1.49) of the same flow is higher in atmospheric conditions and the Kolmogorov scale (Eq. (1.54)) is larger.

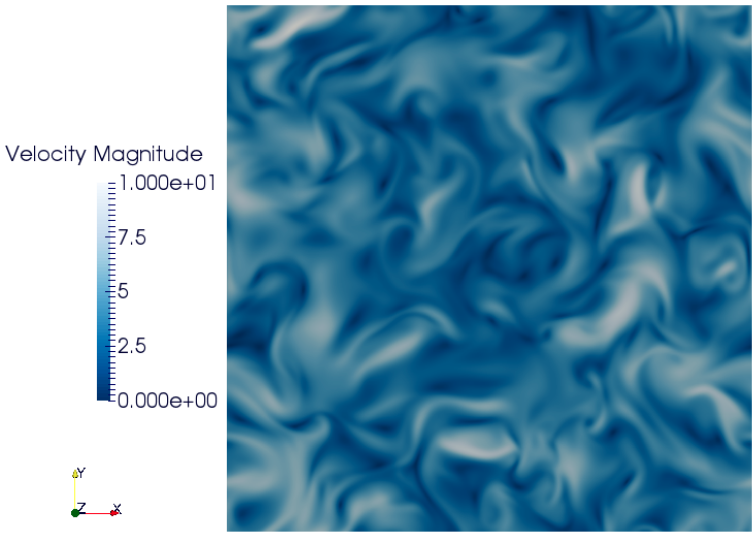

Figure 9.1.2: Turbulent initialization with Passot-Pouquet spectrum before the energy deposit.

The integral length scale is set to ensure at least six turbulent structures in the domain and thus a homogeneous flow (identical turbulent characteristics in all regions of the domain)[Boughanem and A. 1996]. The velocity fluctuation is limited by the CPU-cost of the highest Re_t **PTatmo** case. Indeed, a higher turbulent intensity requires a smaller cell size to ensure at least one point to discretize the Kolmogorov scale η_k.

Labels	$N_p\,[million]$	$\Delta x\,[\mu m]$	$\delta_{th}/\Delta_x[-]$	$\eta_k/\Delta x\,[-]$
PTatmo	64.48	25	16	1
LPLT	14	41.67	24	1.06
LPLT-LAM	14	41.67	24	1.06
LPLT-LED	14	41.67	24	1.06

Table 9.1.4: Parameters of the mesh

Hence, the mesh discretization is determined by the turbulent properties. The flame resolution criterion is less critical since with flame thicknesses of respectively $\delta_{th} = 0.4\,mm$ and $\delta_{th} = 1\,mm$ for atmospheric and high altitude cases, there are at least 16 points in the flame front. The laminar case **LPLT-LAM** discretization is not limited by the turbulence but the same mesh than the other LPLT cases is used for comparison.

Tab. 9.1.5 summarizes the key ratios and orders of magnitude characterizing the interaction of the flame and the turbulence.

Labels	u'/S_L	R_{ker}/L_t	L_t/δ_{th}	δ_{th}/η_k	Da	Ka
PTatmo	6.22	1.20	4.17	16	0.670	24.54
LPLT	7.13	1.20	1.67	22.66	0.234	48.17
LPLT-LED	7.13	1.80	1.67	22.66	0.234	48.17

Table 9.1.5: Key ratios of the flame-turbulence interaction

The modification of the ambient conditions (pressure and temperature) modifies the flame-turbulence interaction. Indeed, at high altitude, the low pressure reduces the flame speed and increases the flame thickness as shown in Chap. 5. Thus, the ratio of velocity fluctuation over laminar flame speed increases at high altitude and the flame thickness becomes almost as large as the turbulent structures. On the one hand, the increased velocity ratio at high altitude promotes turbulent quenching [Reddy and Abraham 2013]. On the other hand, the thicker flame front reduces the influence of the turbulence on the kernel flame. Either way, the different ambient conditions imply a modification of the combustion regime which can be characterized by the Damköhler number defined in Eq. (3.45) and the Karlovitz number defined in Eq. (3.46)[1]. The reduction of the Damköhler at high altitude condition indicates that the combustion processes are slowed down compared to the turbulent ones, thus the turbulence will have a stronger influence on the chemistry through mixing processes. Similarly, the Karlovitz number is increased at high altitude leading to the same conclusion for the small eddies. Finally, a study of flame-turbulence interactions from Peters [1999] (see Fig. 3.4.1) indicates that the **LPLT** cases lie in the thickened interaction zone while the **PTatmo** case lies between the thickened-wrinkled and thickened interaction zone. It means that for **PTatmo** the pre-heat zone may be thickened while the reactive layer is wrinkled. Examples of such flame shapes are shown on Fig. 3.4.2.

Pressure outlet conditions are applied at the boundaries with a relaxation coefficient [Baum et al. 1995] to avoid reflective pressure waves due to the energy deposit.

Finally, it is to be noted that DNS of ignition run with a Fourier time-step. Indeed, at high temperature resulting from the ED and mixture ignition, the thermal diffusion coefficient increases and makes diffusion the limiting process for stability. Furthermore, the low pressure also increases the thermal diffusivity resulting in a lower time-step even if the spatial discretization is larger, leading to the following ranges:

- $\Delta t_{LPLT} \in [2.7\,ns\,;\,11.1ns]$
- $\Delta t_{PTatmo} \in [8.1\,ns\,;\,12.9ns]$

For the resolution of the chemical ignition processes, the user chemical time-step for the LDSC procedure is fixed to $\Delta t_{chem,user} = 0.2\,ns$ which leads to the maximum number of sub-cycles $SC_{max,LPLT} = 55$ and $SC_{max,PTatmo} = 64$.

9.2 Description of the kernel evolutions

Kernel evolutions are presented on Fig. 9.2.1 at the end of the energy deposit ($t = 100\,\mu s$), on Fig. 9.2.2 at $t = 300\,\mu s$, and on Fig. 9.2.3 at the end of the computation (time depends on cases). The kernel is defined using iso-surfaces: the transparent layer (white line in the 2D projections) is the iso-surface of 50 % consumption of the main fuel component $NC_{12}H_{26}$, corresponding to the pyrolysis front and associated to the temperature $T_{pyr} = 900K$; the opaque volume (red line in the 2D projections) is the iso-surface of $T_{oxi} = 1600K$, corresponding to the temperature observed at the maximum heat

[1]The values in Tab. 9.1.5 correspond to the first part of the expression.

release rate in a 1-dimensional laminar premixed flame, hence, defining the oxidation front of the kernel in the propagation regime. Note that during the energy deposit phase, the temperature is driven by the external energy forcing, while in extinction phases, the maximum heat release rate is shifted toward lower temperatures, so that the temperature iso-surface should not be interpreted as a marker of the flame front in these phases.

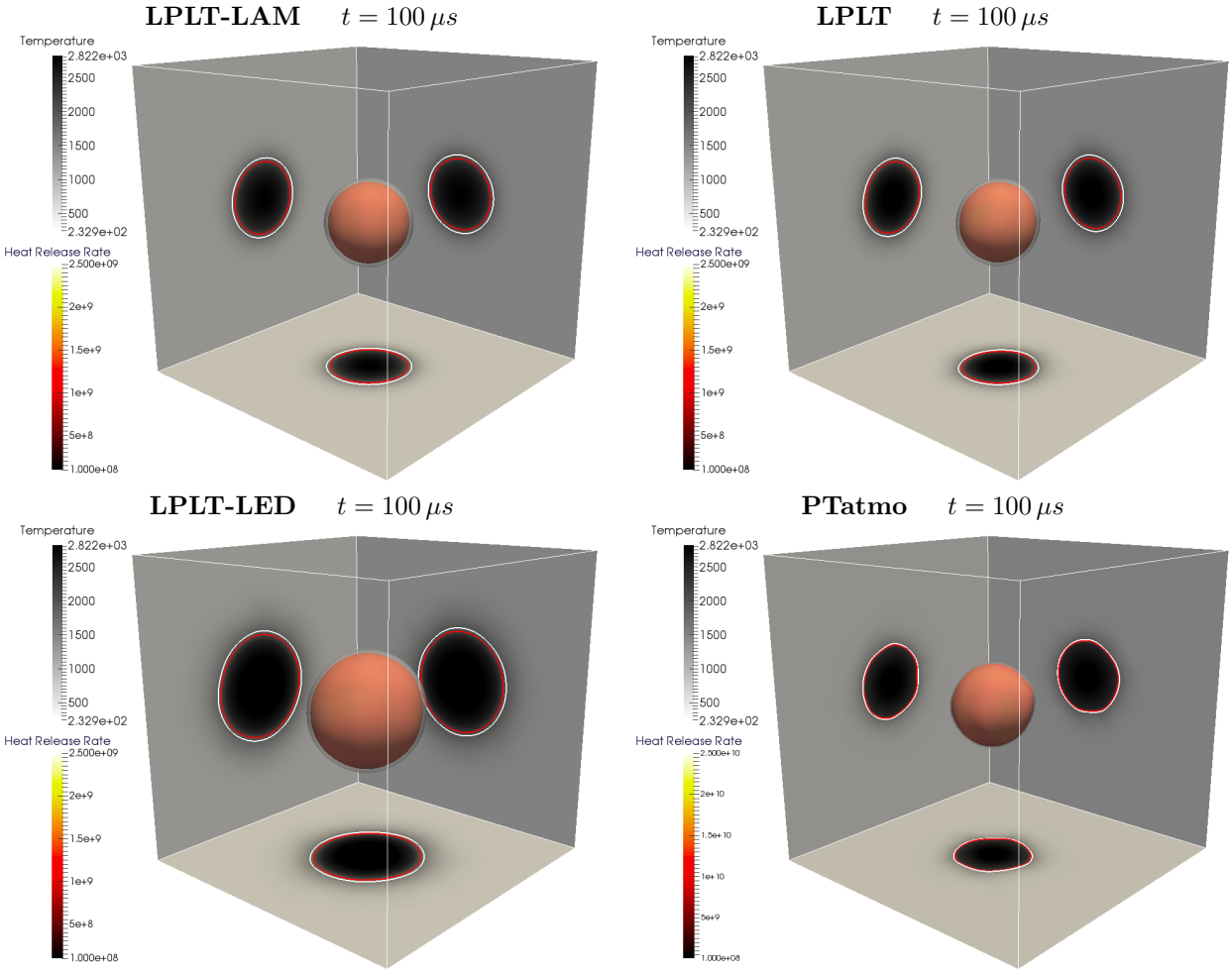

Figure 9.2.1: Kernel visualisations of the 4 cases at $t = 100\,\mu s$ with temperature and fuel consumption iso-surface colored by heat release rate, projected temperature fields.

At the end of the energy deposit (Fig. 9.2.1), few differences are already observed between the cases. The high temperatures resulting from energy deposit increase the mixture viscosity which laminarizes the flow at the spark location. Furthermore, the gas expansion creates a radial velocity that blows the turbulent structures toward the domain sides. This effect is even more pronounced for the **LPLT-LED** case because of the larger energy deposit.

At $t = 300\,\mu s$ (Fig. 9.2.2), the kernels start to develop and to interact with the turbulence. The resulting deformation creates curvature variations which modify the local combustion intensity as evidenced by the higher heat release rate in negative curvature zones.

The final time (Fig. 9.2.3) corresponds to kernel extinction in the cases **LPLT** and **LPLT-LAM**, whereas on the contrary the kernel continues to grow for the cases **LPLT-LED** and **PTatmo**, approaching the limits of the domain. These final snapshots are not directly comparable (different times), but qualitatively show that the conditions are more favorable for ignition in the cases **LPLT-LED** and **PTatmo**. Note that at $t = 500\,\mu s$ the cases **LPLT** and **LPLT-LAM** were already showing signs of extinction (not sown).

Fig. 9.2.4 shows the time evolution of the maximum temperature for the four cases. For all cases, this temperature decreases after the energy deposit. However, the decrease is faster in the low pressure cases

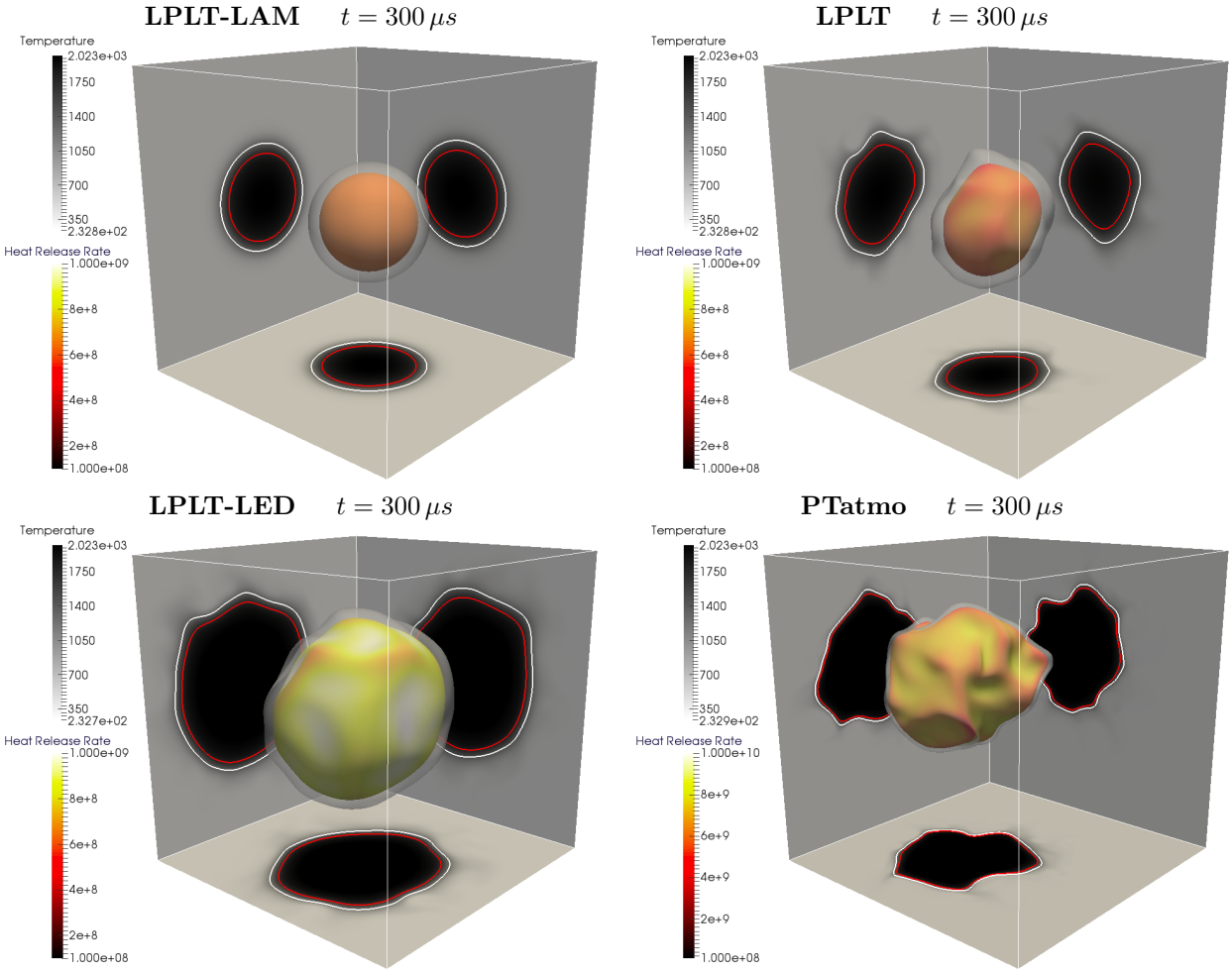

Figure 9.2.2: Kernel visualisations of the 4 cases at $t = 300\,\mu s$ with temperature and fuel consumption iso-surface colored by heat release rate, projected temperature fields.

which may be explained by the higher thermal diffusion and lower heat release rate at low pressure as shown in Chap. 5. The temperature decrease is also lower for the **LPLT-LED** case because the kernel is initially larger. Indeed, the ratio of the surface energy losses over the volume energy production evolves as the inverse of the kernel radius, so that the ratio energy losses over energy production is reduced for larger kernels. This point will be developed in Sec. 9.4. Finally, the turbulence effect on the maximum temperature is negligible because this temperature corresponds to the kernel center which is affected by the turbulence only after a long period. For all cases, the temperature does not stabilize at the end of the computations, either because of extinction in cases **LPLT** and **LPLT-LAM**, or because the temperature is still higher than the adiabatic flame temperatures $T_{adia}^{LPLT} = 2050\,K$, and $T_{adia}^{PTatmo} = 2250\,K$ (see Fig. 5.2.7 from Chap. 5).

Figures 9.2.5 and 9.2.6 show two distinct phases during the kernel formation. The first one is the ignition of the mixture when the temperature reaches $1500 - 1600\,K$. The fuel species in the energy deposit zone are rapidly pyrolysed which creates a consumption peak (the fuel consumption is defined as the sum of the surrogate component consumption rates) and a negative power due to the endothermic pyrolysis reactions. After this short pyrolysis step, the pyrolysis products are then oxidized releasing a large amount of heat. The resulting kernel power is higher in the **PTatmo** case because of the larger density in agreement with the 1-dimensional studies. The larger energy deposit zone of **LPLT-LED** making a larger volume of oxidizing fresh gases also leads to an increased kernel power. At the end of the energy deposit, all kernels transit towards a propagating phase. The released power enables to heat and pyrolyse more fresh gases, but at a reduced rate. While the fuel consumption as well as the kernel power increase in the **PTatmo** case, they decrease at low pressure in this the kernel development phase. Hence, the consumption speed and so the kernel development rate decrease over time. This result is also qualitatively

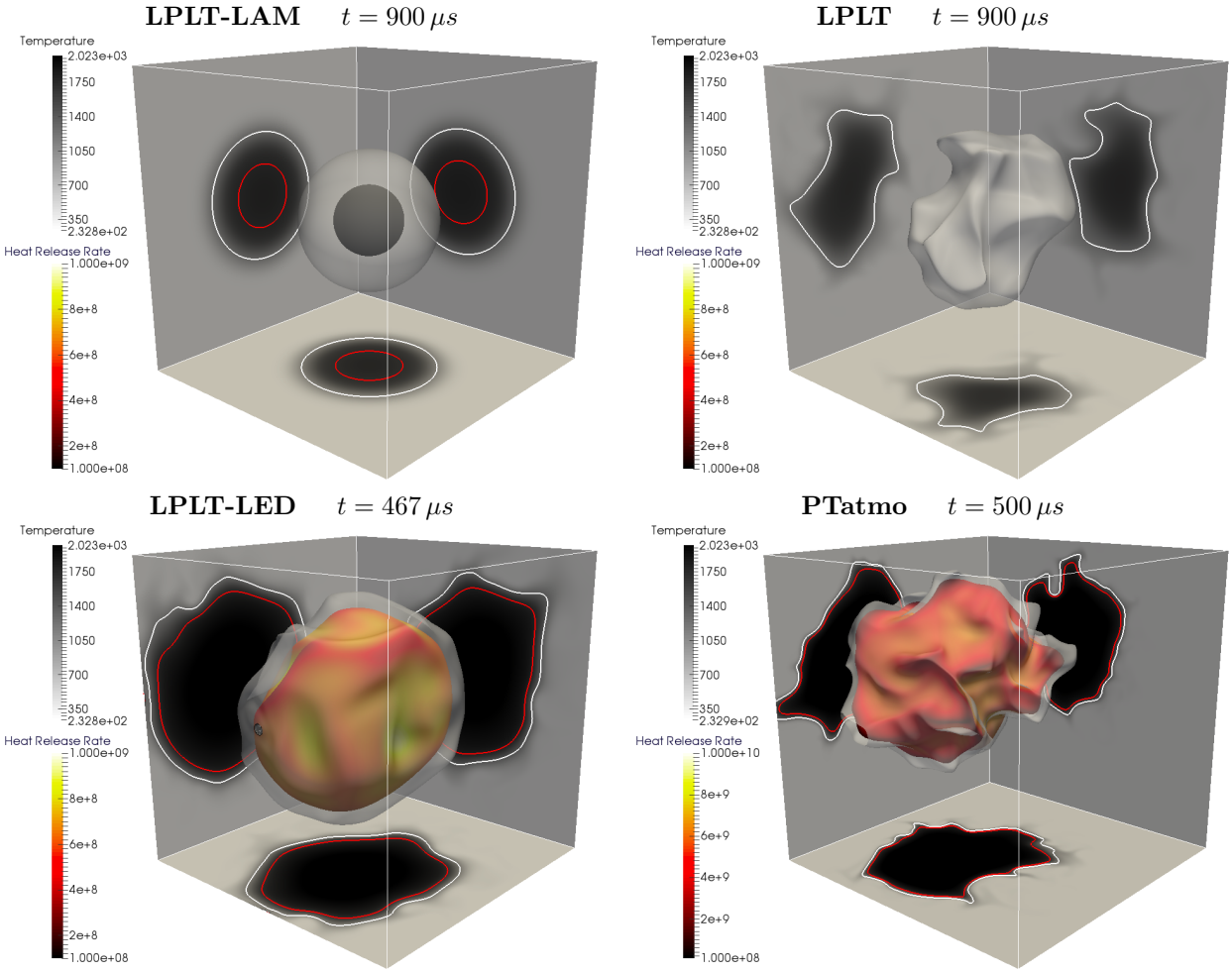

Figure 9.2.3: Kernel visualisations of the 4 cases at final time with temperature and fuel consumption iso-surface colored by heat release rate, projected temperature fields.

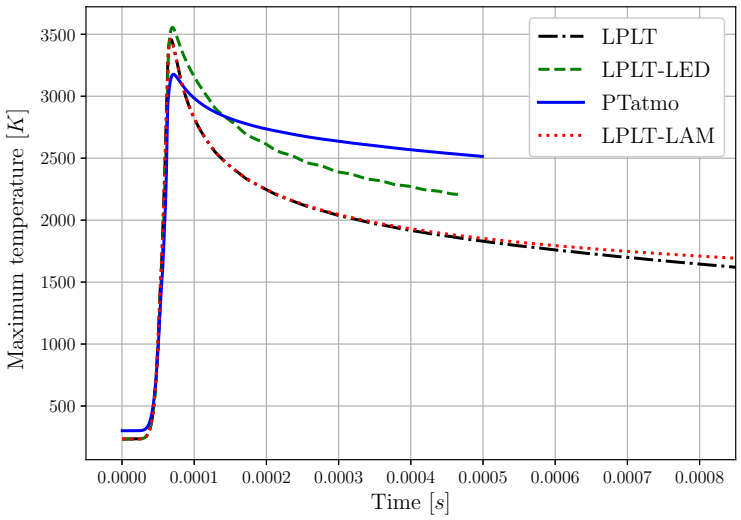

Figure 9.2.4: Temporal evolution of the maximum temperature for the 4 cases.

visible on Figs. 9.2.1 to 9.2.3 where the **LPLT** kernel is much less developed than the **PTatmo** one. As **LPLT** and **LPLT-LAM** kernels seem to quench while the **PTatmo** kernel develops, no conclusions can be drawn for the **LPLT-LED** kernel at this stage.

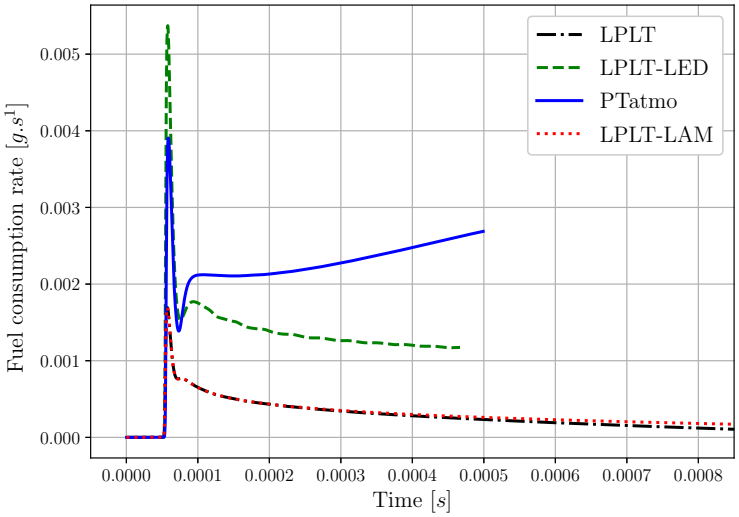

Figure 9.2.5: Temporal evolution of the fuel consumption rate for the 4 cases.

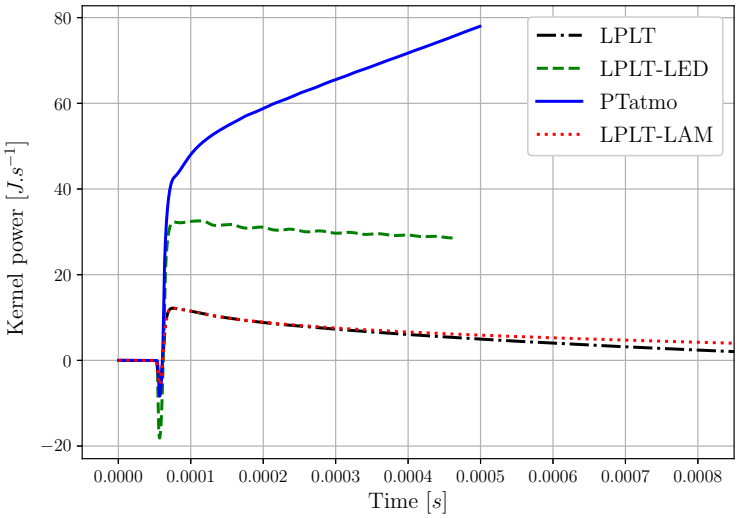

Figure 9.2.6: Temporal evolution of the kernel power released by combustion processes for the 4 cases.

The local heat release rate displayed on the oxidation volumes of Fig. 9.2.1 to 9.2.3 indicates the combustion intensity. The comparison of **LPLT-LED** with **PTatmo** shows one order magnitude difference, directly attributed to the reduced reaction rates at low pressure. The comparison between **LPLT-LED** and **LPLT** during the propagation phase also indicates a difference in combustion intensity, probably due to mean kernel curvature differences. Indeed, for spherical kernel the mean curvature scales as $2/R_{ker}$ and associated with $Le_F > 1$ typically observed with kerosene fuels, the resulting stretch reduces the consumption speed and thus the heat release rate [Bush and Fendell 1970, Clavin 1985, Williams 1985]. This slightly higher combustion intensity and lower temperature decrease in the **LPLT-LED** case enable to avoid the kernel extinction (at least during the simulated time).

The evolution of kernel volumes and surfaces on Fig. 9.2.7 indicate that the development rate is roughly constant for the **PTatmo** case, whereas it decreases in the low pressure cases which is in agreement with the evolutions of fuel consumption and kernel powers. Figure 9.2.2 and 9.2.3 clearly show a reduction of the oxidation volume for the cases **LPLT** and **LPLT-LAM**. The maximum size is observed at $t = 300\,\mu s$ and $t = 400\,\mu s$ respectively. After these times, extinction starts. For this specific set-up, the extinction does not originate from the turbulence since it happens also in the laminar case. However, the turbulence accelerates the extinction process by removing more heat from the kernel through convection. This effect is visible on Fig. 9.2.3 where the oxidation volume has totally disappeared.

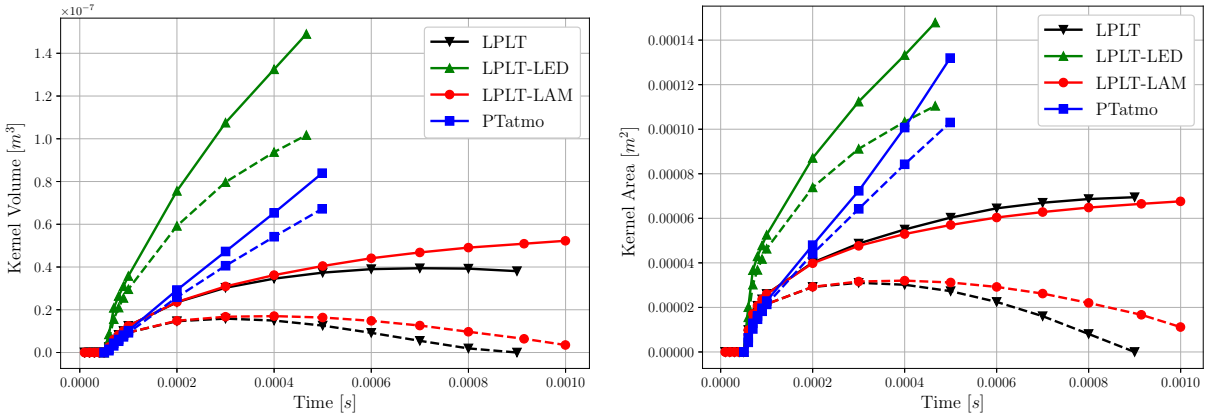

Figure 9.2.7: Temporal evolution of the kernel volumes (left) and kernel surface areas (right) for the four cases. Solid line: pyrolysis front; dashed line: oxidation front.

The deformation rate Ξ is evaluated as the ratio of the turbulent kernel surface area A^t_{ker} over the laminar one, which is reconstructed from the kernel volume V_{ker} assuming a spherical shape:

$$\Xi = \frac{A^t_{ker}}{4\pi(3V_{ker}/(4\pi))^{2/3}} \tag{9.2}$$

Hence, it gives a quantification of the impact of turbulence on the kernel.

Fig. 9.2.8 shows the evolution of the deformation rates depending on the kernel volume. The **PTatmo** case shows the highest deformation as qualitatively evidenced on Fig. 9.2.3. This was expected from the turbulent Reynolds number given in Tab. 9.1.3 which is highest at atmospheric conditions. More precisely, it appears that the main responsible for the stronger kernel deformation is the higher ratio L_t/δ_{th} given in Tab. 9.1.5, while the slightly smaller ratio u'/S_L should have an opposite effect [Turquand d'Auzay et al. 2019], but found here negligible. In the case **LPLT**, the turbulence acts on the kernel even after it stops growing as reflected on Fig. 9.2.3 with a vertical increase of the deformation rate.

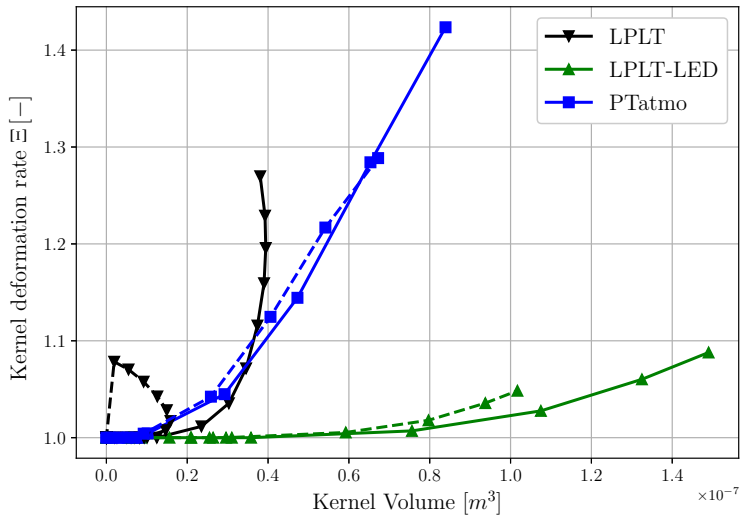

Figure 9.2.8: Deformation rate Ξ versus kernel volume fro the 3 turbulent cases. Solid line: pyrolysis front; dashed line: oxidation front

Kernel snapshots (Fig. 9.2.3) and deformation rates (Fig. 9.2.8) show different behaviors of the pyrolysis and oxidation fronts especially at low pressure and during extinction. To better characterize these

differences, an inter-front length is defined as follows:

$$\Delta_{ff} = R_{ker}^{pyr} - R_{ker}^{oxi} = \left(\frac{3V_{ker}^{pyr}}{4\pi}\right)^{1/3} - \left(\frac{3V_{ker}^{oxi}}{4\pi}\right)^{1/3} \tag{9.3}$$

Results are displayed on Fig. 9.2.9. For the cases without extinction (**PTatmo** and **LPLT-LED**), this distance remains small and lower than the thermal flame thickness (see Fig. 5.2.4). However, this length increases linearly until the end of the computations, which means that the pyrolysis front is propagating faster than the oxidation front, and that the flame front is still not established. For a not quenching kernel, the inter-front length is expected to converge towards a value lower than flame thickness of a turbulent propagating flame. For the quenching cases (**LPLT** and **LPLT-LAM**), the inter-front distance growth rate is higher from the beginning. More precisely, this is attributed to slower propagation of the oxidation front compared to the non-quenching cases (see Fig 9.2.7) while the pyrolysis front is not so much affected. When the maximum oxidation volume is reached and starts to decrease, the inter-front length diverges because the pyrolysis front, which requires lower temperatures than oxidation, continues to propagate. However, pyrolysis as an endothermic process promotes the kernel extinction. As already seen, turbulence amplifies the inter-front distance by removing more heat from the kernel which accelerates the quenching. However, turbulence is not the origin of this mechanism as it is observed on the **LPLT-LAM** case.

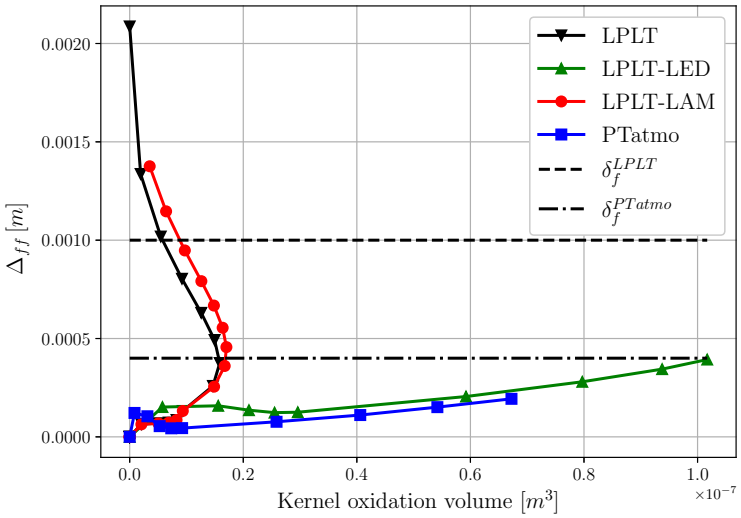

Figure 9.2.9: Inter-front length Δ_{ff} versus kernel oxidation volume for the 4 cases. Dashed and dot-dashed horizontal lines indicate flame thicknesses.

9.3 Analysis of the chemical structure

The various kernel evolutions observed in the 4 cases lead to various chemical structures of the fronts. The cases **PTatmo** and **LPLT-LED** are compared to study the effect of high altitude conditions, while the comparison of **LPLT** and **LPLT-LED** cases shows the modifications of the chemistry associated with kernel extinction at low pressure. All comparisons are done here at $t = 400\,\mu s$ during the propagation phase.

9.3.1 Effects of the low pressure

As observed on 1-dimensional configurations, the low pressure modifies the thermodynamic equilibrium. In both cases **PTatmo** and **LPLT-LED**, Fig. 9.3.1 shows a similar structure in terms of CO-CO_2 chemistry. First CO is produced, reaching a peak after which CO consumption takes over at $T = 1750\,K$ which corresponds to the higher CO_2 increase. Then, at high temperature, the CO_2 mass fraction slightly decreases due to dissociation phenomena which in return produces CO. The CO-CO_2 equilibrium is not the same at low and atmospheric pressure. Less CO_2 is produced at low pressure which leads to a lower

heat release for the same burnt mass of gases. At the same time, before dissociation the CO mass fraction is higher at low pressure.

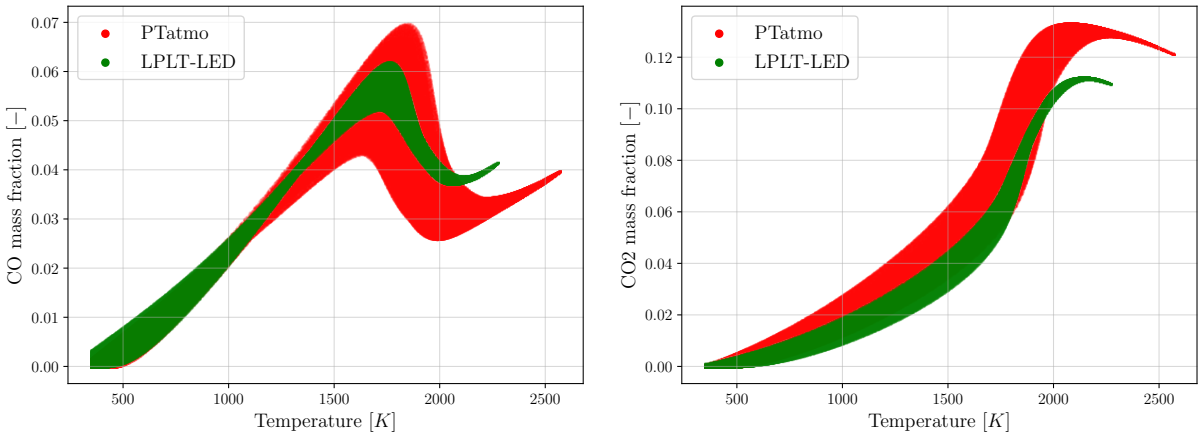

Figure 9.3.1: Scatter plots of CO and CO_2 mass fractions versus temperature at $t = 400\,\mu s$ for cases **PTatmo** and **LPLT-LED**.

Fig. 9.3.2 indicates that H_2 is found in the whole kernel, due to the fast diffusion of this species. Similarly to CO, the mass fraction increases until a peak at $T = 1600\,K$ followed by a consumption-dominant phase which corresponds to the production of H atom. In the atmospheric case, a H production peak is observed around $T = 2000\,K$ followed by a consumption mechanism at higher temperatures, whereas in the low pressure this mechanism is not observed, leading to H accumulation at high temperature and a mass fraction almost twice higher at the maximum temperature.

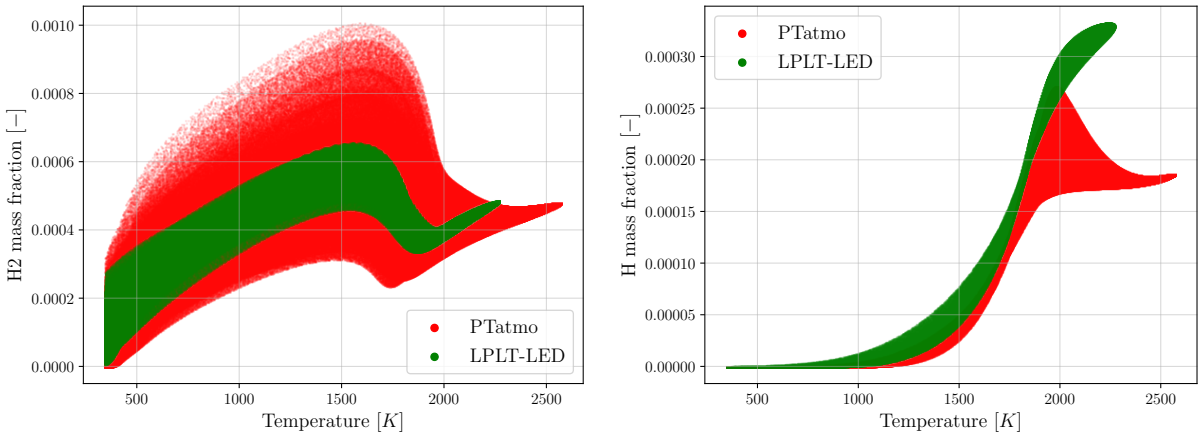

Figure 9.3.2: Scatter plots of H_2 and H mass fractions versus temperature for cases **PTatmo** and **LPLT-LED**.

Similarly to the CO-CO_2 equilibrium, a lower H_2O production is observed at low pressure on Fig. 9.3.3. This lower production can partially explain the H accumulation. The larger H_2O production in the **PTatmo** is associated to a lower OH level. However because the case **PTatmo** reaches higher temperatures, the maximum OH mass fraction is higher.

Finally in the case of the oxygen atom, the Fig. 9.3.4 clearly shows a different behavior for temperature above $T = 1900\,K$. At atmospheric conditions, their consumption occurs which stabilizes the O mass fraction, whereas for low pressure, O continues to increase. This difference matches well with the differences observed on H profiles. It seems that in the **PTatmo** case, both O and H react to form OH, explaining its excess at high temperature although H_2O is produced in larger quantities. On the contrary, for high altitude cases, the OH - H_2O equilibrium is shifted towards less H_2O production. Therefore, OH

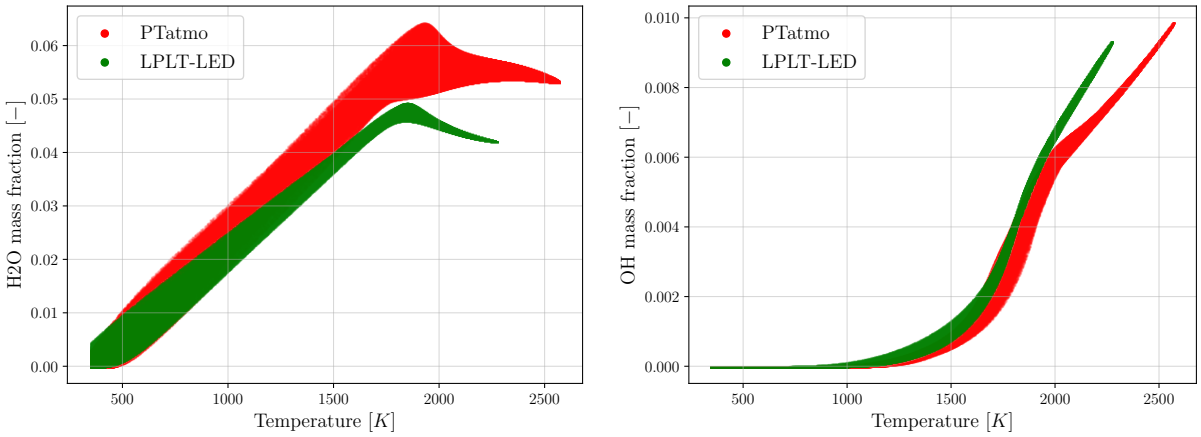

Figure 9.3.3: Scatter plots of H_2O and OH mass fractions versus temperature at $t = 400\,\mu s$ for cases **PTatmo** and **LPLT-LED**.

is not consumed and accumulates until reaching also its equilibrium level. As a consequence, the reaction $H + O \rightarrow OH$ is reduced and O and H atoms accumulate at high temperature (see Figs. 9.3.2 and 9.3.4).

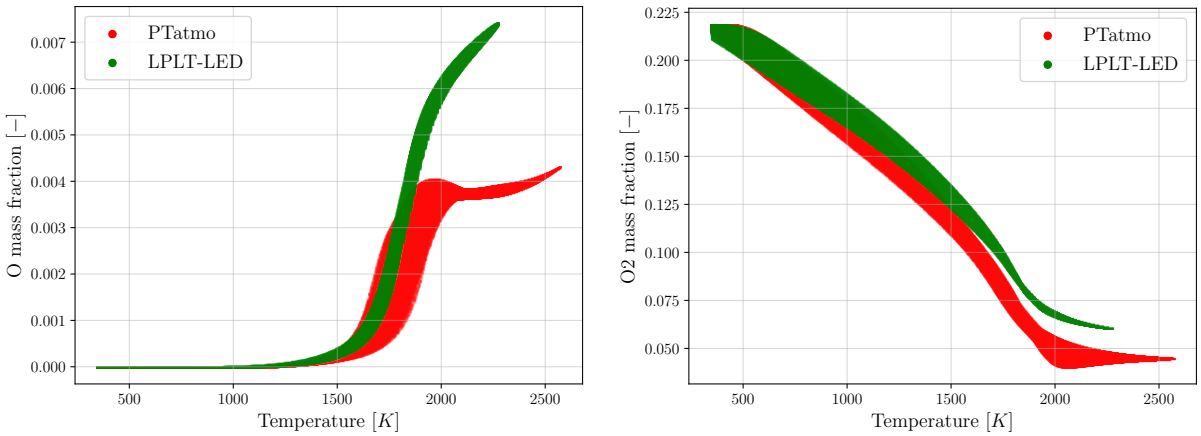

Figure 9.3.4: Scatter plots of O and O_2 mass fractions versus temperature at $t = 400\,\mu s$ for cases **PTatmo** and **LPLT-LED**.

Fig. 9.3.3 also indicates a dissociation phenomenon starting from $T = 1900\,K$ for H_2O. Unlike CO_2 dissociation which arises especially in the **PTatmo** case, the H_2O dissociation is similar in both cases because it starts at lower temperature. Thus, the resulting effect on the kernel temperature is the same in both cases.

Finally, since the combustion is incomplete at low pressure with less oxidized species such as CO_2 and H_2O, it is consistent to observe a lower O_2 consumption on Fig. 9.3.4.

9.3.2 Chemistry around extinction

It can be seen on Fig. 9.3.5 and 9.3.6 comparing the CO - CO_2 - H_2O mass fractions for cases **LPLT** and **LPLT-LED** (with the laminar case **LPLT-LAM** for reference), that maximum values are shifted towards lower temperatures in the extinction case **LPLT**. This is due to the global cooling of the kernel. Indeed, at shorter time (not shown), before extinction starts, there is no such shift and the chemistry is similar to the case **LPLT-LED**.

The dissociation of CO_2 was already reduced at low pressure, but with extinction the dissociation of H_2O

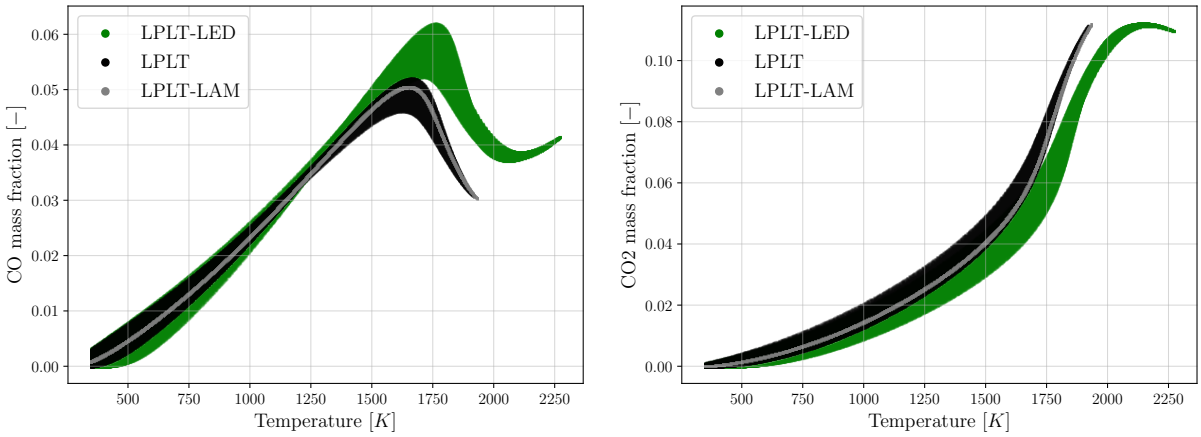

Figure 9.3.5: Scatter plots of CO_2 and CO mass fractions versus temperature at $t = 400\,\mu s$ for cases **LPLT** and **LPLT-LED** (with the laminar case **LPLT-LAM** for reference).

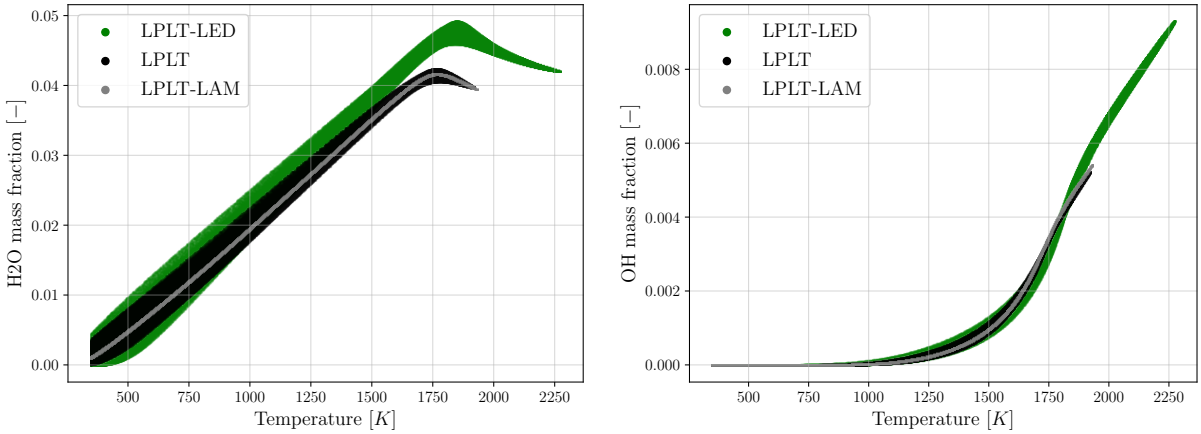

Figure 9.3.6: Scatter plots of H_2O and OH mass fractions versus temperature at $t = 400\,\mu s$ for cases **LPLT** and **LPLT-LED** (with the laminar case **LPLT-LAM** for reference).

becomes also negligible. As a consequence, CO_2 and H_2O mass fractions reach similar final levels even though the H_2O production is reduced during extinction. Hence, the heat release corresponding to these species is the same. However, dissociation is an endothermic process, so that the final chemical energy stored in the kernel is higher in the non-quenching case **LPLT-LED** compared to the quenching cases **LPLT** and **LPLT-LAM**.

Because of the reduced kernel core temperature, the maximum mass fractions of the radical species OH, O, and H are lower in the extinction cases as shown with Fig. 9.3.6 and 9.3.7. These lower concentrations reduce the fuel or intermediate species decomposition which creates a negative feedback loop and promotes the kernel extinction.

Furthermore, because of too low temperature, some intermediate species are no more decomposed and accumulate. This effect is evidenced on Fig. 9.3.8 where the species C_6H_4 requires a critical minimum temperature to be decomposed ($T = 1800\,K$). Such phenomena of incomplete combustion greatly reduce the heat release rate in the kernel and prevent its development as qualitatively shown on Fig. 9.2.2.

9.3.3 Effects of the turbulence

The turbulence effect on the chemical structure of the kernel can be appreciated through Figs. 9.3.5 to 9.3.8 with the comparison of **LPLT** case with **LPLT-LAM**, but also through Figs. 9.3.1 to 9.3.4 because

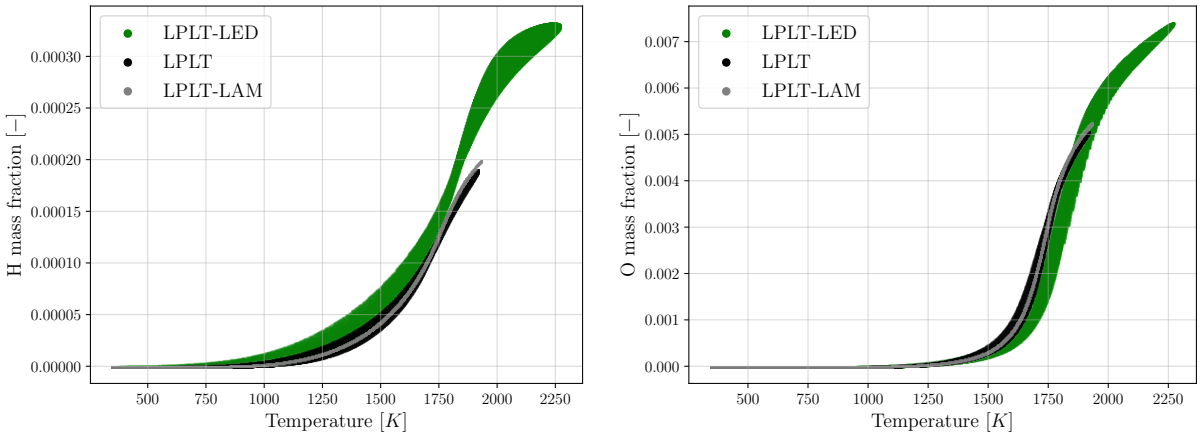

Figure 9.3.7: Scatter plots of H and O mass fractions versus temperature at $t = 400\,\mu s$ for cases **LPLT** and **LPLT-LED** (with the laminar case **LPLT-LAM** for reference).

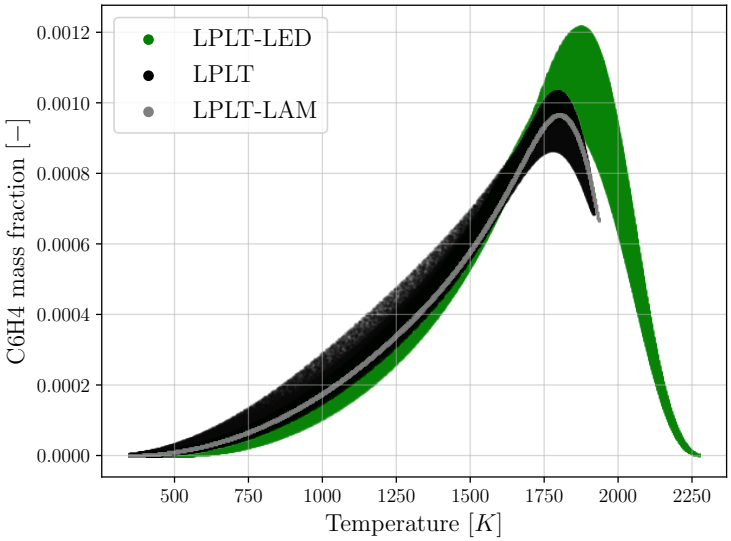

Figure 9.3.8: Scatter plots of C_6H_4 mass fractions versus temperature at $t = 400\,\mu s$ for cases **LPLT** and **LPLT-LED** (with the laminar case **LPLT-LAM** for reference).

the turbulent Reynolds number is higher for the **PTatmo** case. Even if the same velocity fluctuations and the same turbulent scales have been used, the turbulence has a greater influence on the **PTatmo** case for reasons already mentioned in Sec. 9.1. As is usual, the turbulence has a dispersion effect on the species profiles. This is due to turbulent mixing, as well as strain and curvature effects which enhance or reduce the chemical reactivity. For example, on Figs. 9.2.2 and 9.2.3 higher heat release rate values are observed in negative curvature regions. Besides that, Fig. 9.3.9 indicates that the maximum CO mass fractions are overall associated to high heat release rates. This example highlights a correlation between turbulence and the chemical structure of the flame, but dedicated studies requires to draw further conclusions.

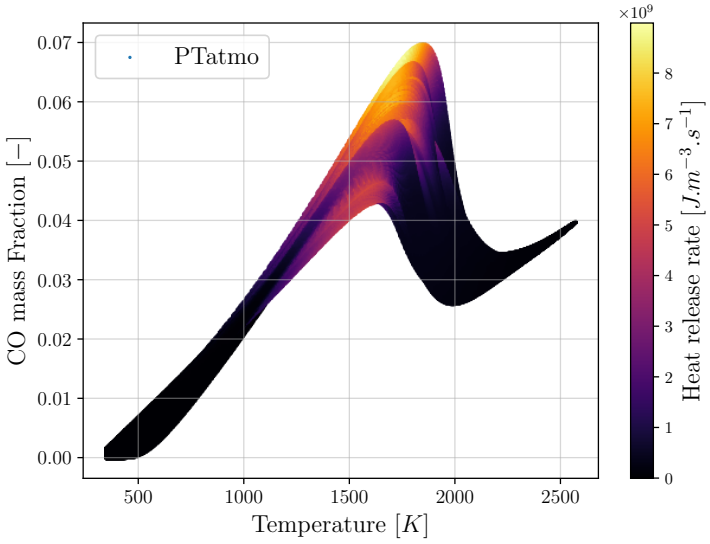

Figure 9.3.9: Scatter plot of CO mass fraction in **PTatmo** case versus temperature and colored by the heat release rate at $t = 400\,\mu s$.

9.4 Analytical study of the kernel extinction

9.4.1 Kernel temperature equation

To understand the extinction of the **LPLT** case, an energy balance on the kernel in a quiescent flow is computed. Starting from the conservation equation of the sensible energy e_s Eq. (9.4) [Poinsot and Veynante 2012] and assuming that species diffusion and volumic forces are negligible:

$$\rho \frac{De_s}{Dt} = \dot{\omega}_T + \nabla.(\lambda \nabla T) + \tau_{ij}\frac{\partial u_j}{\partial x_i} - \frac{\partial u_i P \delta_{ij}}{\partial x_j} \tag{9.4}$$

with $D\,\phi/D\,t$ the total derivative which writes using the continuity equation Eq. (1.1):

$$\rho \frac{D\phi}{Dt} = \rho\left(\frac{\partial \phi}{\partial t} + u_j \frac{\partial \phi}{\partial x_j}\right) = \frac{\partial \rho \phi}{\partial t} + \frac{\partial \rho u_j \phi}{\partial x_j} \tag{9.5}$$

The term τ_{ij} is the viscosity momentum tensor flux defined Eq. (1.3).

Since the DNS are run in a domain with open boundaries, working with the sensible enthalpy h_s is more convenient.

$$e_s = h_s - \frac{P}{\rho} \quad \Leftrightarrow \quad \rho \frac{De_s}{Dt} = \rho \frac{Dh_s}{Dt} - \frac{DP}{Dt} - P\frac{\partial u_j}{\partial x_j} \tag{9.6}$$

Then, Eq. (9.4) becomes:

$$\rho \frac{Dh_s}{Dt} = \dot{\omega}_T + \nabla.(\lambda \nabla T) + \tau_{ij}\frac{\partial u_j}{\partial x_i} + \frac{DP}{Dt} \tag{9.7}$$

Assuming the pressure constant (which is a correct assumption in open boundary domains):

$$\rho \frac{Dh_s}{Dt} = \dot{\omega}_T + \nabla.(\lambda \nabla T) + \tau_{ij}\frac{\partial u_j}{\partial x_i} \tag{9.8}$$

To obtain the temperature evolution equation, the definition of the sensible enthalpy is used:

$$h_s = \sum_{k=1}^{N_{spec}} \int_{T_0}^{T} C_{p,k} dT \times Y_k \quad \Leftrightarrow \quad \rho \frac{Dh_s}{Dt} = \sum_{k=1}^{N_{spec}} \int_{T_0}^{T} C_{p,k} dT \times \rho \frac{DY_k}{Dt} + \rho C_{p,gas} \frac{DT}{Dt} \tag{9.9}$$

Using the simplifying assumption of equal species heat capacities:

$$C_{p,k} \approx C_{p,gas} = C_p \quad \Leftrightarrow \quad \rho \frac{Dh_s}{Dt} = \rho C_p \frac{DT}{Dt} \tag{9.10}$$

Then, Eq. (9.8) becomes:

$$\rho C_p \frac{\partial T}{\partial t} = \underbrace{\dot{\omega}_T}_{\substack{\text{Chemical heat}\\ \text{production term}}} + \underbrace{\nabla.(\lambda \nabla T)}_{\substack{\text{Heat conduction}\\ \text{loss term}}} + \underbrace{\tau_{ij}\frac{\partial u_j}{\partial x_i}}_{\substack{\text{Viscous heating}\\ \text{source term}}} - \underbrace{\rho C_p u_j \frac{\partial T}{\partial x_j}}_{\substack{\text{Heat convection}\\ \text{term}}} \tag{9.11}$$

The mean kernel temperature evolution is obtained by integrating Eq. (9.11) over the kernel volume V_{ker}:

$$\int_{V_{ker}} \rho C_p \frac{\partial T}{\partial t} dV = \int_{V_{ker}} \dot{\omega}_T dV + \oint_{A_{ker}} \lambda \nabla T dS + \int_{V_{ker}} \tau_{ij}\frac{\partial u_j}{\partial x_i} dV - \int_{V_{ker}} \rho C_p u_j \frac{\partial T}{\partial x_j} dV \tag{9.12}$$

The kernel boundary is defined at the maximum heat release rate which corresponds to the iso-surface $T = 1600\,K$. Hence, this boundary corresponds to the maximum temperature gradient which maximises the heat conductive loss term $\oint_{A_{ker}} \lambda \nabla T dS$. Along this kernel boundary, the convection and viscous terms are assumed negligible. Indeed, the gas expansion creates a radial velocity field in the fresh gases side of the kernel flame front, whereas the velocity is at rest ($u = 0$) inside the kernel.
Finally, by using the perfect gas law, the mean kernel temperature $\overline{T_{ker}} = \int_{V_{ker}} T dV / V_{ker}$ evolution writes:

$$\frac{\partial \overline{T_{ker}}}{\partial t} = (\mathcal{P}_{prod} + \mathcal{P}_{loss}) \times \frac{r\overline{T_{ker}}}{P\,C_p\,V_{ker}} \tag{9.13}$$

with $r = \mathcal{R}/W$, $\mathcal{R}$ being the molar gas constant and W the mean molecular weight. The production and loss terms write:

$$\mathcal{P}_{prod} = \int_{V_{ker}} \sum_{k=1}^{N_{spec}} \Delta h^0_{f,k} \dot{\omega}_k \, dV = \int_{V_{ker}} \dot{\omega}_T \, dV \qquad \mathcal{P}_{loss} = \oint_{A_{ker}} \lambda \nabla T \, dS \tag{9.14}$$

If the heat capacities are not considered constant, the expression Eq. (2.29) must be retained for the computation of the production term.

9.4.2 Kernel temperature evolution

From Eq. (9.13) analyses of the production and loss terms are required to determine the kernel temperature evolution.

Based on Eq. (9.14), the production term corresponds to the integral of the heat release rate over the kernel volume. However, in the propagating phase the combustion reactions happen in the flame front at the kernel boundary. Therefore, the production term depends on the gaseous mass flow rate crossing the flame surface multiplied by the mass heat release rate $hr\,[J.kg^{-1}]$:

$$\mathcal{P}_{prod} \propto A_{ker} \times \rho_f \times S_c \times hr \tag{9.15}$$

with ρ_f the fresh gas density and S_c the flow velocity crossing the flame front. hr differs from LHV as the latter is a constant and assumes a complete combustion. On the contrary, hr may vary due to the chemical reactivity (the heat release is not instantaneous after fuel consumption), the thermodynamic equilibrium (as shown in Chap. 5), curvature and turbulent mixing effects encountered in the unsteady kernel formation.

Based on Eq. (9.14), the loss term is direcly proportional to the kernel surface, the gas thermal conductivity, and the temperature gradient:

$$\mathcal{P}_{loss} \propto A_{ker} \times \lambda \times \frac{T_f - \overline{T_{ker}}}{\delta_{th}} \tag{9.16}$$

with T_f the fresh gases temperature, and δ_{th} the thermal flame front thickness.

Therefore, from Eq. (9.13), (9.15) and (9.16), the kernel temperature evolves as the inverse of the equivalent kernel radius (the production and loss terms depend on the kernel surface), which explains the

behavior of the **LPLT** and **LPLT-LED** cases. For large kernels, the temperature variation is less affected by the production and loss terms, so that large kernels are more robust. The kernel evolution towards growth or quenching is given by the ratio of the production term over the loss term. Hence, based on Eq. (9.15) and (9.16), the kernel evolution is independent from its surface.

Equation (9.13) also indicates that the temperature evolves as the inverse of pressure. This reflects that at low pressure there is less mass in the kernel for the same volume, so that the kernel temperature is more sensitive the production and loss terms. However, as shown previously in Sec. 5.2, production and loss terms are also affected by the pressure. Simulations on 1-dimensional premixed flames, done in Chap. 5, have shown on Fig. 5.2.8 that the production term $\mathcal{P}_{prod}$ is directly proportional to the pressure ($\rho_f \times S_c \times hr \propto P$) in a steady state. The loss term is proportional to the maximum temperature gradient, thus, based on the definition of the thermal flame thickness Eq. (3.22), the loss term $\mathcal{P}_{loss}$ is inversely proportional to the thermal flame thickness. Yet, from Fig. 5.2.4, the thermal flame thickness is proportional to $P^{-0.76}$. Hence, by combining all these pressure dependences, the temperature evolution in the kernel is found to be influenced by the pressure as:

$$\frac{\partial \overline{T_{ker}}}{\partial t} \propto P^{-0.24} \tag{9.17}$$

Therefore, at low pressure the evolution rate (extinction or growth) of the kernel remains faster[2].

9.4.3 Kernel extinction mechanism

At the first instants of the kernel formation, $\mathcal{P}_{loss}$ is very large because of the high temperature resulting from the energy deposit. On the contrary $\mathcal{P}_{prod} = 0$ because the chemical kinetic and the associated heat release are not instantaneous. Therefore, the kernel temperature quickly decreases as shown on Fig. 9.2.4. To obtain a propagating kernel, the oxidation reactions must establish and develop so that the ratio $|\mathcal{P}_{prod}|/|\mathcal{P}_{loss}| > 1$.

The possible causes of **LPLT** extinction proposed in this work are: 1) the chemistry is slower at high altitude conditions (see Chap. 5) and 2) the kernel temperature decrease is faster (see Eq. (9.17)). Therefore, the kernel temperature may decrease too fast before oxidation processes and heat release rate are fully established. If the kernel temperature decreases too much it may trigger the extinction mechanisms presented in Sec. 9.3.2 and ultimately lead to quenching as observed in **LPLT** and **LPLT-LAM** cases.

The slower chemistry assumption may be evaluated by looking at the time evolution of the effective mass heat release rate that can be evaluated in the 3D-simulations with Eq. (9.18):

$$hr = \frac{\int_{V_{ker}} \dot{\omega}_T dV}{\dot{m}} \tag{9.18}$$

where $\dot{m} = \dot{m}_F / Y_F^f$ is the mass flow rate crossing the kernel boundary, $\dot{m}_F$ is the fuel consumption rate and Y_F^f the fuel mass fraction in the fresh gases. The time evolution of hr displayed on Fig. 9.4.1 shows that it is not constant and takes more time to converge towards the asymptotic value in the high altitude cases. However, complementary analyses are required to ensure that this heat release rate convergence delay is only attributed to chemical kinetic effects.

Considering the slow chemistry assumption, solutions to enable ignition at high altitude conditions are:

- An increase of the initial kernel size at constant temperature with a higher deposited energy in a larger volume. Following Eq. 9.13 the kernel will be less sensitive to $\mathcal{P}_{loss}$ and the kernel temperature decrease will be slower. For instance, this is the method used with the case **LPLT-LED**.
- An increase of the deposited energy within the same volume. Hence, the resulting kernel temperature will be higher and it will take more time to decrease below the critical value leading to extinction. Moreover, the diffusion of the additional deposited energy will also form a larger kernel.

[2]The Eq. (9.17) stands only for near stoichiometric mixtures

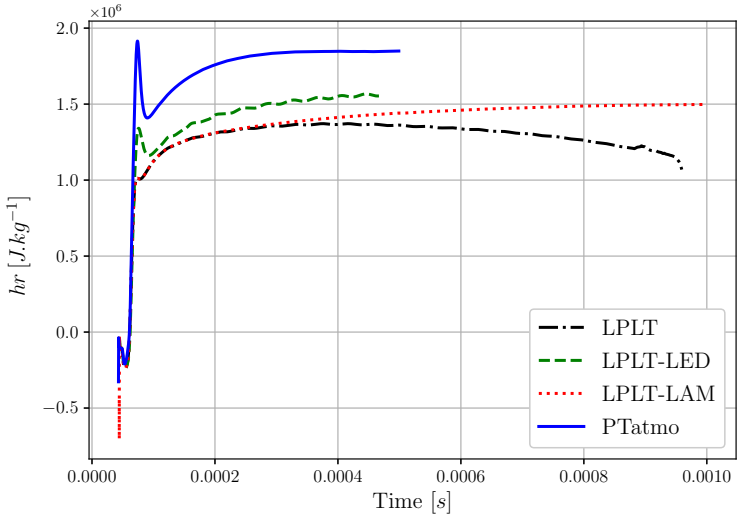

Figure 9.4.1: Temporal evolution of the mass heat release rate for the 4 cases.

Finally, the turbulence also influences the extinction removing more heat from the kernel via convection effects. Therefore, a faster extinction occurs as observed with **LPLT** case compared to **LPLT-LAM** case.

The main conclusions of this study and the key points raised in the first part of this work are summarized in the following conclusion chapter.

Chapter 10

Conclusion

The main objectives of this part was to understand the effects of high altitude conditions (low pressure and low temperature) on the gaseous ignition of a kerosene-air mixture.

To that purpose, these conditions have been first evaluated in Chap. 5 using canonical 0-dimensional and 1-dimensional configurations with CANTERA and a detailed chemistry of the CRECK Modeling Group. This study has shown the macroscopic effect of the high altitude conditions. The main effects are attributed to the reduction of the density. The laminar flame speed as well as the burning rate are reduced and the laminar flame thickness is increased. Due to the lower species concentrations there is a slowing down of the reaction rates which reduces the heat release rate and increases the auto-ignition time. Moreover, around stoichiometry, it has been observed that the mass heat release which can be linked to the combustion efficiency is reduced. This is due to a modification of the thermodynamic equilibrium at low pressure. As a consequence, the adiabatic temperature is also lower. Finally, these modifications lead to a large reduction of the flame power which partially explains the poor re-ignition performances at high altitude.

In order to understand in detail if these effects may be attributed to modifications of the chemical pathways, analysis tools have been developed in Chap. 6 and applied to the test cases. Firstly, based on carbon atom fluxes it was found that the chemical pathways at atmospheric and low pressures have few differences. Then, a detailed analysis of the chemical processes occurring during auto-ignition evidenced a competition of several pathways in the fuel pyrolysis and methyl oxidation phases. These competitive pathways are driven by the gas temperature and strongly affect the heat release rate and temperature evolution.

Since the chemical modifications due to the high altitude conditions are negligible, an ARC chemistry valid in both conditions was developed using ARCANE in Chap. 7. This reduction is based on a three-component surrogate formulation for kerosene-air combustion. It is composed of 30 transported species and 22 QSS which allows to be used in 3-dimensional DNS or LES configurations.

Then, to reduce the CPU-cost due to the ARC chemistry especially in ignition processes, original numerical approaches have been developed in Chap. 8 for the integration of the chemistry in CFD solvers. The exponential chemistry formalism provides a more stable expression to compute species production rates which allows to use larger time steps. A new sub-cycling method has been also developed based on a chemical characteristic time and enabling to apply sub-cycles locally, only when and where it is required. With these methods the time step is less constrained by the chemistry and DNS with accurate chemistry is achievable at reasonable costs.

Finally, DNS of the turbulent kernel ignition at ground and high altitude conditions have been presented in Chap. 9. The kernels developments are highly affected by the pressure and temperature conditions. The high altitude conditions induce a faster temperature decrease as well as a reduced consumption and heat release rates. Hence, the kernels are weaker and more prone to extinction. The results have shown that the initial kernel size must be increased at these conditions to reduce the sensitivity to the thermal losses and ensure the kernel growth. The use of ARC chemistry enables to study the chemical processes during extinction and the modifications due to the pressure conditions. Moreover, an analysis

of the kinetics has shown that chemical processes may take more time to establish in the high altitude cases. Thus, the heat release rate is delayed and the balance production over losses takes more time to establish. As a result, the kernel development is slowed down. Furthermore, if the chemistry is too slow, the kernel temperature decreases below a critical temperature leading to chemical extinction mechanisms and ultimately to the kernel quenching.

To summarize, the major effects of low pressure and low temperature observed in this first part are sketched in Fig. 10.0.1.
In this part, only gaseous processes have been presented. In the next part, two-phase flows effects on ignition in high altitude conditions are addressed.

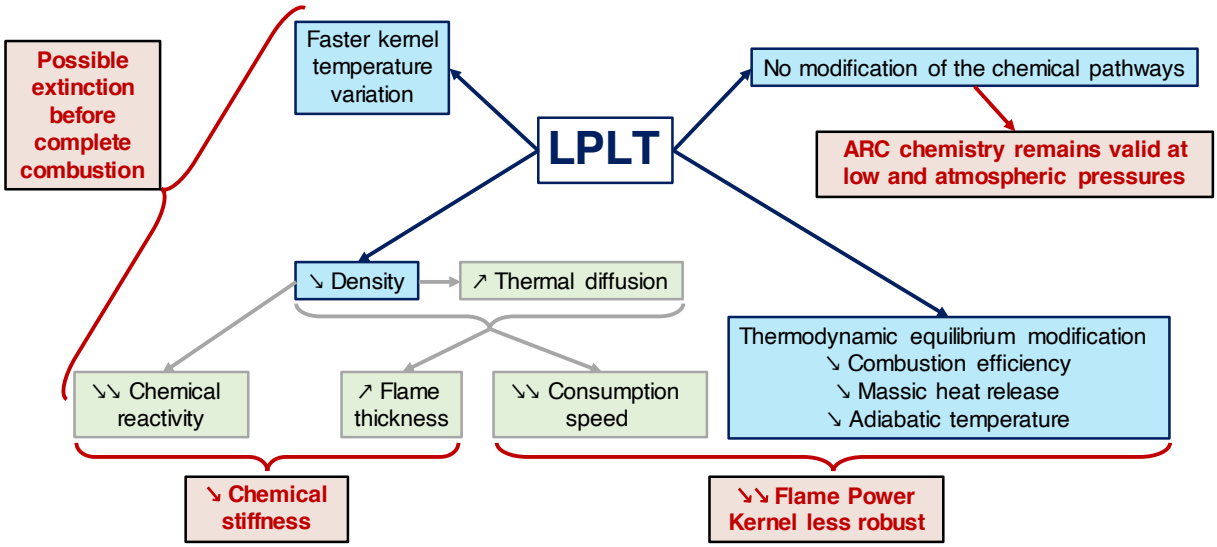

Figure 10.0.1: Summary of the low pressure and low temperature influences on the gaseous kerosene combustion.

Part III

Two-phase flow aspects

Try to figure out what you're most passionate about in life, and what you're good at, and the mixture between those two. And then you should give it your all, all the time. You have to work really hard if you wanna get anywhere, with whatever you do. If you work hard enough you're going to succeed.
Tim Bergling, 1989-2018

Chapter 11

Modeling of the kerosene spray injection

Contents

As presented in chapters 3 and 4, the dispersed liquid phase has a large influence on ignition and more generally on the combustion processes. Hence, the study of two-phase ignition at high altitude conditions requires a modeling of the fuel atomization, taking into account the pressure effect. In this chapter, at first, a literature review on the pressure swirl injectors and on the spray formation in such injectors is presented. Then, a new modeling approach is proposed to predict the characteristic droplet size.

11.1 Literature review on fuel injection

This review mainly focuses on the principles of fuel injection systems in aircraft engines and the formation of fuel sprays. A summary of the ambient conditions and fuel properties effects on the atomization process is also given with a set of correlations.

11.1.1 Injection systems

Pressure swirl

The pressure swirl aeronautical injectors are purely mechanical systems where high pressure fuel is injected through a small hole. The pressure is converted into kinetic energy to obtain a high velocity relative to the air at the exit. The injection is usually swirled to obtain a better stability of the flame and of the atomization processes. In a swirled injector, the high pressure liquid fuel is swirled in the main injector chamber and, under the influence of the centrifugal force, the liquid exits the injector at the nozzle with the shape of a thin hollow cone sheet which then atomizes due to the aerodynamic and hydrodynamic instabilities as shown on Fig. 11.1.1.

This type of injector is referred as "pressure swirl atomizer". The Fig. 11.1.2 shows a sketch of the internal structure of such injector. The picture on the left corresponds to a "simplex" injector with only one fuel channel. However, during the full gas operating regime of the engine, the fuel amount able to flow through the simplex is not sufficient. This is why "dual-orifice" injectors have been developed with two

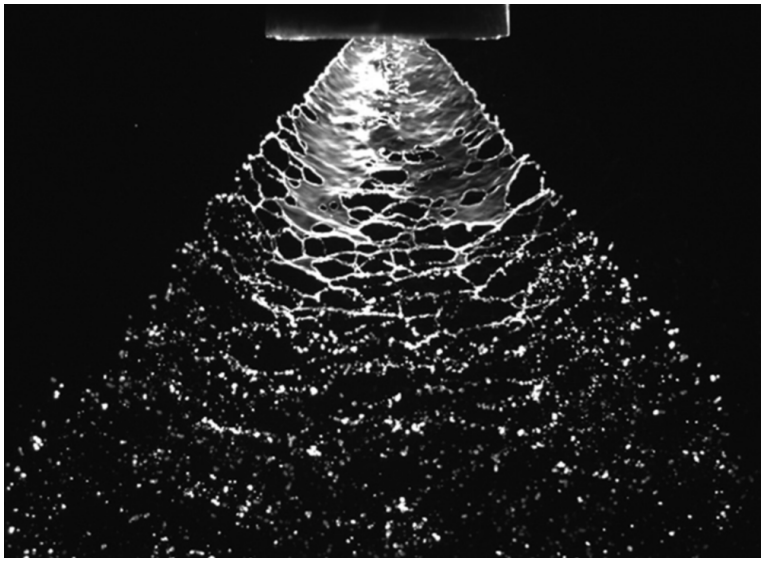

Figure 11.1.1: Photograph illustrating the swirled hollow cone film and the atomization by wavy-sheet disintegration (extracted from [Lefebvre and McDonell 2017]).

fuel channels such as in the right picture. The dual-orifice injectors create two different injection cones with different angles. These hollow cones must not interfere in order to get their maximum efficiencies [Lefebvre and McDonell 2017]. Hence, each fuel circuit can be studied and modeled independently. The ignition phase corresponds to a low power engine operating, thus only the main channel is used for the fuel injection, which is equivalent to a simplex injector.

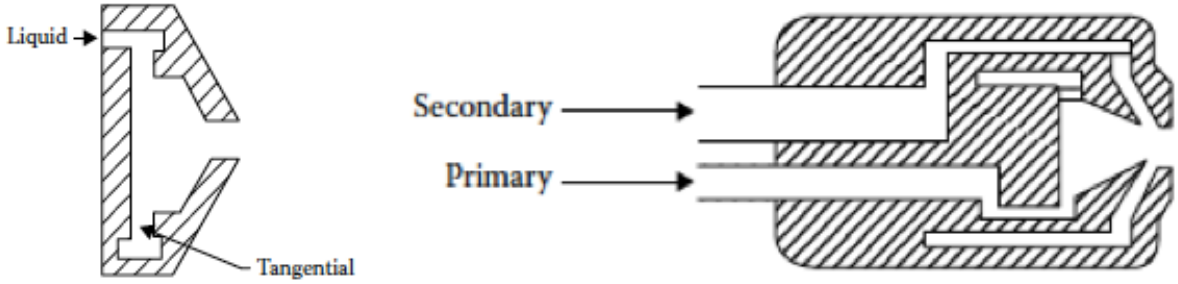

Figure 11.1.2: Pressure swirl injectors. Left: simplex, right: duplex (extracted from [Lefebvre and McDonell 2017]).

As shown on Fig. 11.1.3, a simplex injector is composed of a swirl chamber of characteristic sizes D_s and L_s allowing the rotation of the liquid fuel that comes from several tangential slots of characteristic size D_p and angle ξ (if not tangential). Then, the convergent part, of characteristic angle α and length L_c, allows to accelerate the flow until the nozzle of length and diameter l_0 and d_0 respectively. The rotation of the liquid fuel inside the injector creates a pressure gradient with a depression on the axis which causes in return the apparition of an air-core at the center. This hole is visible on the right picture on Fig. 11.1.3 and is very important as it increases the velocity exit, and helps the formation of the thin film hollow cone characterized by the half angle θ.

Interested readers are referred to [Donjat 2003, Lefebvre and McDonell 2017] for more information on pressure swirl working and modeling.

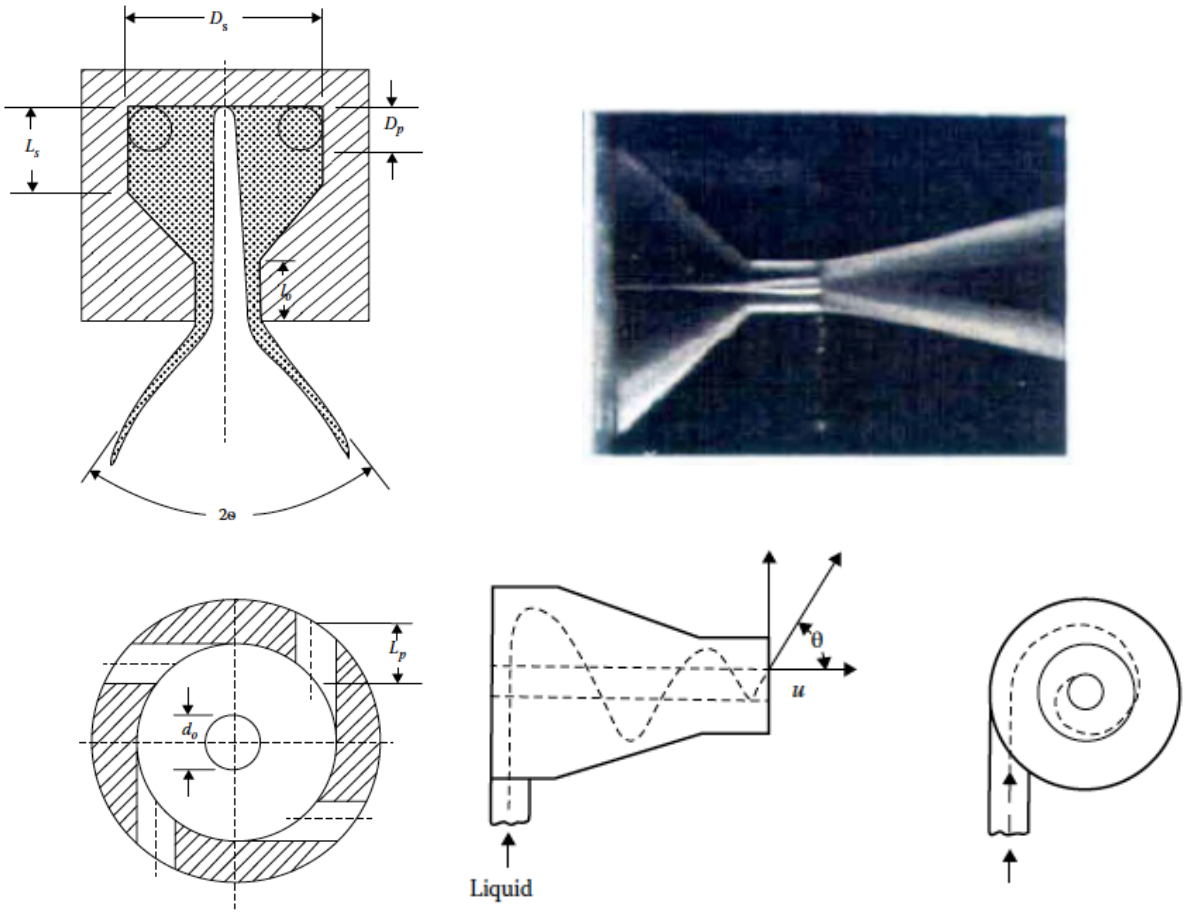

Figure 11.1.3: Sketches of pressure swirl injectors (left and bottom) extracted from [Lefebvre and McDonell 2017], and visualization of the air core (top right) extracted from [Donjat 2003].

Aeronautical injection systems

Based on efficiency and pollutant considerations, the direct use of a pressure swirl in an aeronautical combustion chamber is not optimum. Hence, the pressure swirl injector is often integrated into a global injection system[1] as presented on Fig. 11.1.4. This configuration creates an interaction between the spray created by the pressure swirl and the air coming from secondary channels. This interaction improves the atomization due to secondary break-up.

Depending on the spray angle, a liquid film may form on the injection system walls. This film will be subject to an air-blast atomization as shown in Fig. 11.1.5.

As a conclusion, to have a good representation of the physical behavior happening in the injection system, all these phenomena need to be taken into account through several models as shown on Fig. 11.1.6. In this work, due to the low power engine operating required at ignition, the spray coming from the pressure swirl does not interact with the injection system surfaces. Hence, no film, splash or air-blast modeling are required.

11.1.2 Spray

The liquid spray is formed at the nozzle with the atomization of the hollow cone film. However, as shown on Fig. 11.1.7 there are several steps and many features to be characterized before reaching the fully developed spray with small droplets.

[1] In the following, the term "injector" corresponds to the pressure swirl atomizer while the expression "injection system" represents the injector and the air-stream system.

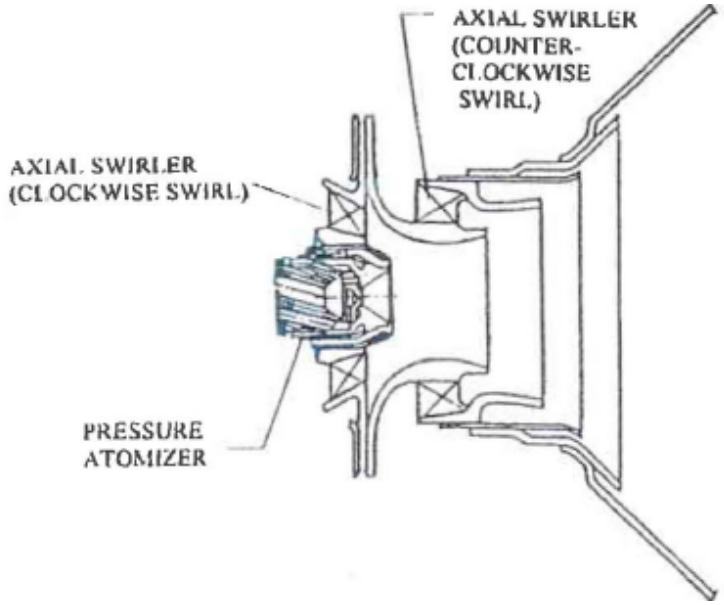

Figure 11.1.4: Sketch of the injection system used in aeronautical engines such as the CFM-56 (extracted from Donjat [2003]).

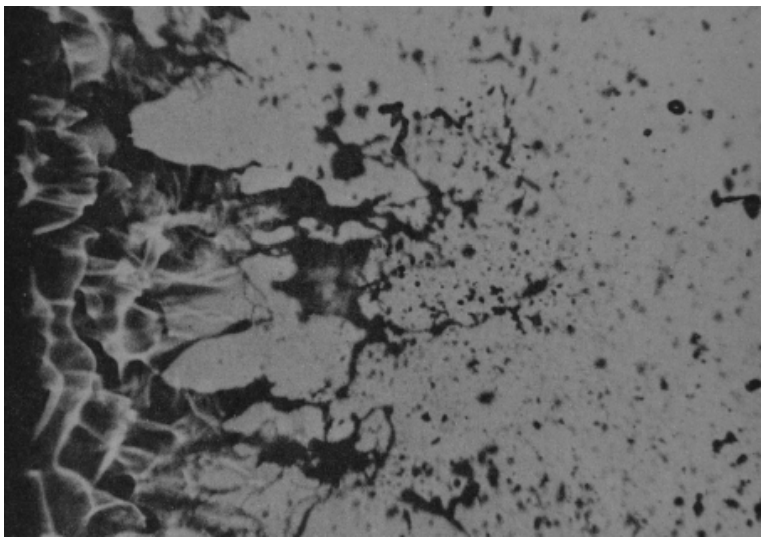

Figure 11.1.5: Photograph illustrating the air-blast atomization mechanism. Airflow is from left to right. (Extracted from Lefebvre and McDonell [2017])

Spray formation

As illustrated on Fig. 11.1.8, the spray topology depends on the injection pressure. The two snapshots on the left show the injection at low mass flow rate. First, the liquid phase takes the form of large droplets due to the dominating surface tension forces over the flow inertia. If the velocity increases, a liquid pencil can form resulting from larger inertial forces. However, destabilization finally happens and creates finer droplets. With the increasing injection pressure, the tangential velocity component and centrifugal forces allow the formation of a cone. However, surface tension forces of the liquid film still dominate and close this cone which leads to the "onion" stage. When the injection pressure is high enough, the surface tension is not able to close it. This is the "tulip" stage. At this step, the atomization is poor with a broad distribution of droplets and large characteristic sizes. Furthermore, when the air core inside the injector is fully developed, the mass flow rate is reduced because the cross section of the liquid exit decreases. Finally, at high injection pressure, the liquid film takes the form of a fully developed hollow cone and

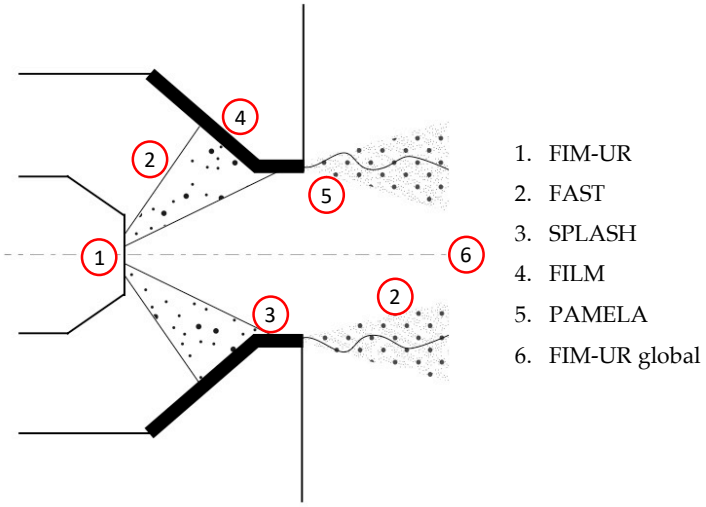

Figure 11.1.6: Sketch of the injection system with the two-phase flow models required in AVBP solver.

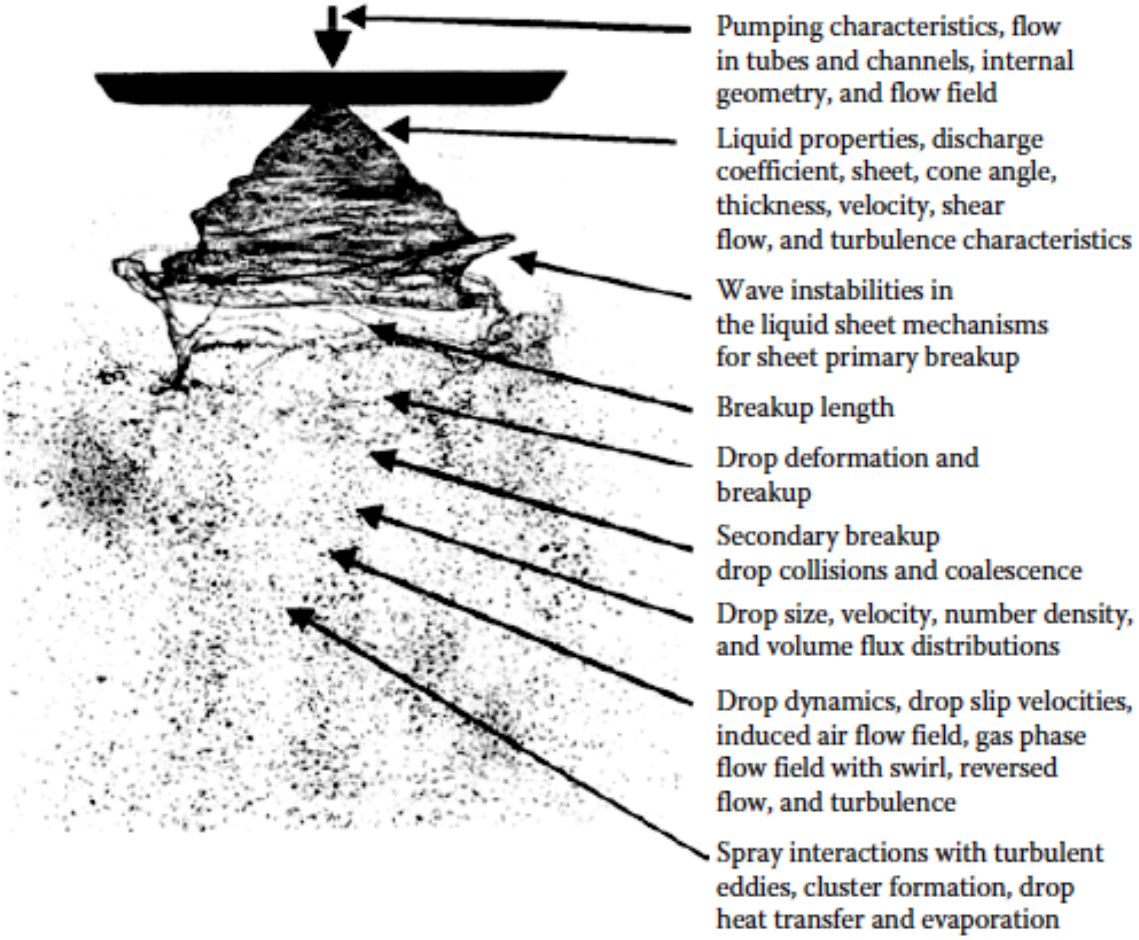

Figure 11.1.7: Spray formation steps and features in a simplex pressure swirl injector (extracted from Lefebvre and McDonell [2017]).

the disintegration length of the liquid film decreases with the rise of the injection pressure [Bayvel and Orzechowski 1993].

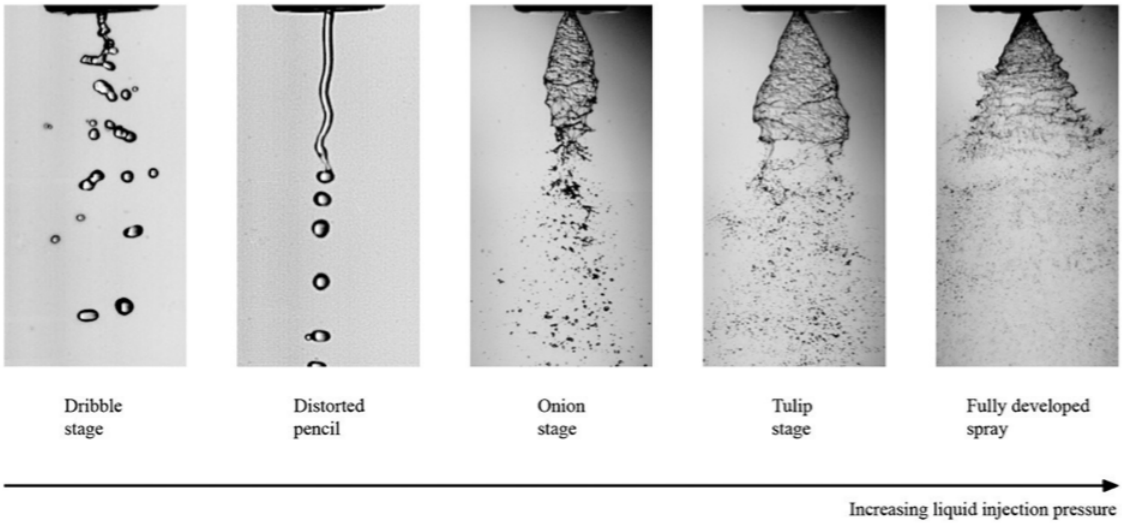

Figure 11.1.8: Photographs illustrating the spray development in a simplex pressure swirl injector (extracted from Lefebvre and McDonell [2017]).

The primary atomization corresponds to the liquid film disintegration into a primary droplets distribution. This disintegration results in the balance between several forces:

- Inertial forces that allow the film penetration in the chamber.
- Centrifugal forces that open the spray cone.
- Friction forces between liquid-air interface that destabilize the liquid film.
- Surface tension forces that reduce the liquid surface area and keep the cohesion of the liquid phase.

A thinning of the liquid film is caused by the extension of the cone in the chamber which makes it unstable. At the liquid-air interface, a strong shear stress generates hydrodynamic instabilities which lead to the formation of interface waves as visible on Fig. 11.1.7 or 11.1.5. Instabilities can also come from a turbulent motion inside the liquid phase. These waves induce a deformation of the liquid film in opposition to the surface tension. At small scale, when the deformation is large enough and the liquid film too thin, the latter breaks to form ligaments which then break in turn into liquid clusters of important sizes (see Fig. 11.1.7). The secondary atomization corresponds to the break-up of these clusters to form smaller droplets. This phenomenon is controlled by the balance between several forces: on the one hand, inertial and aerodynamic forces deform the cluster, and on the other hand, surface tension tries to keep a spherical shape.

In order to characterize the effects of the different forces, several dimensionless numbers are used:

- **Liquid Reynolds Number (Re_l):**

$$Re_l = \frac{\rho_l U_l t_f}{\mu_l} \tag{11.1}$$

  where ρ_l and μ_l are respectively the liquid density and viscosity. U_l is the velocity of the liquid film at the nozzle, and t_f its thickness.
  This Reynolds number allows to characterize the hydrodynamic regime of the film.

- **Weber Number (We):**

$$We = \frac{\rho_l \Delta U^2 L}{\sigma} \tag{11.2}$$

  with ΔU the velocity difference between gas and liquid phase, σ the surface tension, and L a characteristic length scale. This number is very important as it compares the aerodynamic and

surface tension forces. Taking L as the film thickness characterizes the film break-up, whereas taking L as a droplet diameter characterizes the secondary atomization.

- **Ohnesorge Number (Oh):**

$$Oh = \frac{\sqrt{We_{film}}}{Re_l} \tag{11.3}$$

where *film* subscript indicates that $L = t_f$ in the Weber Number definition. This number, which is a combination of the liquid Reynolds number and the liquid film Weber number, compares the influence of the different forces that apply on the film. There is a threshold value $Oh = 2$ where the liquid film breaks into ligaments [Mao 2000].

Droplet size distribution

Most practical atomizers generate droplets in the size range from $1\,\mu m$ to $500\,\mu m$. Due to the heterogeneous nature of the atomization mechanisms (sheet disintegration, ligaments and liquid clusters break-up) originated from fluctuating processes (hydrodynamic instabilities, liquid-air interaction, interfacial waves), the resulting drops vary in size. Therefore, the injected sprays must be characterized with a spectrum/distribution of droplet sizes. Without any fundamental mechanism or model on which to build a theory of droplet size distribution, several functions have been proposed based on empirical considerations to allow a mathematical description of the drop size distribution. The most commonly used are log-normal, Nukiyama-Tanasawa, Rosin-Rammler, modified Rosin-Rammler or upper-limit.

In this work, only the Rosin-Rammler (RR) distribution is used. This distribution, initially developed by Rosin and Rammler [1933] for powders and also referred as the Weibull distribution, writes in its probability density form:

$$RR_{X,q}(d_p) = q \times \frac{{d_p}^{q-1}}{X^q} \times \exp\left(\frac{{d_p}^q}{X^q}\right) \tag{11.4}$$

with $X > 0$ the dimension factor and $q > 0$ the shape factor, two constants to determine so as to represent the experimental spray distribution.
This distribution has been chosen because it is the most widely used and is relatively simple to use while enabling a good representation of the spray.

Any distribution can be characterized by mean diameters computed as [Mugele and Evans 1951] :

$$d_{p,ab} = \left(\frac{\int_0^\infty {d_p}^a \times pdf(d_p) dd_p}{\int_0^\infty {d_p}^b \times pdf(d_p) dd_p}\right)^{\frac{1}{a-b}} \tag{11.5}$$

where $pdf(d_p)$ is the probability density function of the droplet distribution.
In the discrete case, with experimental data measurement for instance, these mean diameters can also be computed as:

$$d_{p,ab} = \left(\frac{\sum N_i {d_{p,i}}^a}{\sum N_i {d_{p,i}}^b}\right)^{\frac{1}{a-b}} \tag{11.6}$$

where $d_{p,i}$ is the middle diameter of the class i and N_i the number of droplets in this class.

The most common mean diameters are:

- **Linear mean $d_{p,10}$:**
  It corresponds to the classical average size of all the drops in the spray.
- **Surface mean $d_{p,20}$:**
  It is the diameter of a droplet whose surface, if multiplied by the number of droplets, equals to the total surface of the sample.
- **Volume mean $d_{p,30}$:**
  It is the diameter of a droplet whose volume, if multiplied by the number of droplets, equals to the total volume of the sample.

- **Sauter mean diameter (SMD) $d_{p,32}$:**
  It corresponds to the diameter of a droplet whose ratio volume to surface area is the same as that of the entire spray. Another interpretation of the SMD is that it is simply the droplet size at the mean of the droplet surface area distribution. Therefore, correlation of processes that depend on surface area (evaporation or combustion) might make more physical sense if expressed using $d_{p,32}$ [Lefebvre and McDonell 2017].

The RR probability density function can also be expressed with the SMD using the following expressions to compute the dimension factor X:

$$X_{vol} = d_{p,32} \times \Gamma(1 - 1/q) \tag{11.7}$$

with $\Gamma(x)$ the standard gamma function.
In this case, the RR corresponds to the volume distribution (distribution of volume or mass per diameter), and 63.2% of the total liquid volume is in droplets of a diameter lower than X_{vol}.

$$X_{num} = d_{p,32} \times \frac{\Gamma(1 + 2/q)}{\Gamma(1 + 3/q)} \tag{11.8}$$

In this case, the RR corresponds to the numerical distribution (distribution of droplet number per diameter), and 63.2% of the droplets have a diameter lower than X_{num}. In the following parts of this work, the numerical distribution is used.

Influencing parameters

The two-phase flow injection depends on a large number of parameters and conditions. The fuel properties, ambient conditions or injector geometries influence the atomization process and the final droplet distribution. A review of the pressure swirl geometrical influences can be found in the PhD of Donjat [2003]. This work focuses on the liquid and air properties that are required for the atomization model developed in Sec. 11.2.3.

Firstly, the liquid properties have a great influence on the flow topology at the injector exit and on the spray formation. As seen above, liquid density, viscosity, and surface tension are needed to compute the dimensionless numbers that characterize the set of applied forces. These influences are listed below [Lefebvre and McDonell 2017, Dorfner et al. 1995, Rizk and Lefebvre 1985, Chen et al. 1992, Ortman and Lefebvre 1985, Chen et al. 1989, Dopazo and Ballester 1994] :

- **Dynamic viscosity μ_l:**
  A viscosity rise increases the friction in the swirl chamber of the injector. As a consequence, the tangential velocity is reduced meaning that less centrifugal force is applied to the liquid film. Thus, the thickness of the liquid film is increased and the hollow cone angle is reduced. The Sauter Mean Diameter (SMD) increases with the viscosity because the latter balances the inertial effect. A larger size distribution of the droplets has been also observed with higher viscosity.

- **Liquid density ρ_l:**
  The density acts in opposite way of viscosity because it increases the flow inertia. Hence, the film thickness and the SMD are reduced, and the cone angle and the velocity coefficient increase with the density.

- **Surface tension σ:**
  The surface tension only has an effect on the atomization. Due to its cohesion effect, the increase of surface tension strongly increases the SMD.

- **Liquid temperature T_l:**
  The liquid temperature also has an indirect influence. Indeed, liquid viscosity and surface tension increase at low temperature whereas density variation with temperature remains small. Thus, a low fuel temperature will reduce the hollow cone angle, and will largely increase the SMD.

Once the liquid phase exits the nozzle, the interaction with the gaseous phase starts. Hence, operating conditions influence the atomizer performances [Jasuja and Lefebvre 2001, Jasuja 1987, Lefebvre and McDonell 2017, Parsons and Jasuja 1986]:

- **Pressure difference $\Delta P = P_{inj} - P$ (equivalent to mass flow rate $\dot{m}_l$):**
  The difference between the injection pressure and the pressure at the exit is linked to the mass flow rate, meaning that an increase in the pressure difference implies an increase in velocity. As a consequence, the film thickness is reduced and the cone angle increases (until a maximum asymptotic value). An augmentation in pressure difference also has a great impact on the atomization process as the SMD is largely reduced.

- **Gas density ρ_g:**
  The gas density only has an influence on the SMD. With the increase in the gas density, air has more inertia and is more able to warp the liquid sheet leading to a better atomization. Hence SMD is reduced with an increase of the gas density.

- **Pressure P:**
  As for the density, the pressure mainly modifies the atomization process. An augmentation in pressure in the chamber independently from the density increases the SMD. It is also observed that the cone angle is reduced with the pressure augmentation.
  The influence of the pressure is contradictory to the observation at low pressure and low temperature. Indeed, in the experimental measurements in Sec. 11.2.2 the SMD evolves inversely to the pressure, which can be explained by the stronger effect of the density. At low pressure, the density is largely reduced and is the dominant effect which causes a poorer atomization.
  The pressure influence should not be confused with the impact of the injection pressure difference. For sub-atmospheric conditions, the ambient pressure chamber changes the injection pressure difference. However, at fixed injection mass flow rate, the ambient pressure has no effect on the pressure difference (ΔP) as the injection pressure is usually adapted to get the target mass flow rate.

- **Temperature T_g:**
  There is no specific temperature effect since the gas temperature is linked to pressure and density with the perfect gases law. Hence, a reduction of the temperature at fixed pressure generally goes with an increase of the density which improves the atomization performances. However, high temperatures can also trigger the evaporation processes (not taken into account for injection in this work).

Correlations

As stated in [Lefebvre and McDonell 2017]: *"Unfortunately, no complete theory has yet been developed to describe the hydrodynamic and aerodynamic processes involved when jet and sheet disintegration occurs under normal atomizing condition, so that only empirical correlations are available for predicting mean drop sizes and drop size distributions"*.

In the following part, only a selection of correlations available in the literature is given. These correlations are built from experiments to describe the spray characteristics issued from a pressure swirl injector. More extended reviews are available in Donjat [2003], Lefebvre and McDonell [2017]:

- **Sauter Mean diameter (SMD)**:
  The SMD is the most important parameter to characterize the spray distribution. Indeed it gives information on the characteristic droplet size which has a large influence on the evaporation and combustion processes as shown respectively in Chap. 12 and 13.

  A first correlation has been proposed by Lefebvre [1998] based on the main influencing parameters:

$$d_{p,32} = 2.25 \times \sigma^{0.25} \times {\mu_l}^{0.25} \times \dot{m}_l^{0.25} \times \Delta P^{-0.25} \times {\rho_g}^{-0.25} \tag{11.9}$$

In a later study, another correlation based on physical mechanisms of droplets formation has been proposed [Wang and Lefebvre 1987]:

$$d_{p,32} = 4.52 \times \left(\frac{\sigma {\mu_l}^2}{\rho_g \Delta P^2}\right)^{0.25} \times (t_f \cos(\theta))^{0.25} + 0.39 \times \left(\frac{\sigma \rho_l}{\rho_g \Delta P}\right)^{0.25} \times (t_f \cos(\theta))^{0.75} \tag{11.10}$$

In the above expression, the first part corresponds to the generation of surface instabilities due to effects of hydrodynamic and aerodynamic forces, while the second part is associated to the conversion of surface protuberances into ligaments and droplets.

Discussions on validity, drawbacks and agreements with simplified inviscid theory or measurements are given in [Lefebvre and McDonell 2017].

- **Flow number (FN)**:
The SMD correlations use the injection pressure difference ΔP which is not always known. It is often more convenient to work with the mass flow rate. This latter is proportional to the pressure difference [Bayvel and Orzechowski 1993], and FN is the coefficient that links those quantities:

$$\dot{m}_l = FN\sqrt{\Delta P\, \rho_l} \tag{11.11}$$

The following correlation has been proposed in [Donjat 2003]:

$$FN = 0.361 \times K^{0.5} \times {d_0}^{1.75} \times {D_s}^{0.25} \tag{11.12}$$

with K the geometrical parameter which writes:

$$K = \frac{N_s A_p}{R_s d_0} = \frac{N_s A_p}{(D_s - D_p - 2\xi) d_0} \tag{11.13}$$

where R_s corresponds to the swirl radius, N_s is the number of fuel slots in the swirl chamber and A_p their areas.

- **Film thickness (t_f)**:
The film thickness is at the origin of primary atomization and has a large influence on the SMD. For instance, a thinner liquid film will result in a finer atomization. The following correlation is proposed by Suyari and Lefebvre [1986]:

$$t_f = 2.7 \left(\frac{d_0 FN^2 \mu_l}{\dot{m}_l}\right)^{0.25} \tag{11.14}$$

- **Half cone angle (θ)**:
On the one hand, the film hollow cone half angle can be determined based on geometrical considerations and inviscid theories. This angle results from the radial over axial velocity components ratio:

$$\tan(\theta) = \frac{u_r}{u_x} \tag{11.15}$$

Then, using mass conservation, the half cone angle can be linked to the film thickness [Rizk 1985]:

$$\cos(\theta) = \frac{1 - X}{1 + X} \tag{11.16}$$

with X the concentration factor which writes:

$$X = \left(\frac{R_a}{R_0}\right)^2 = \frac{(d_0 - 2t)^2}{{d_0}^2} \tag{11.17}$$

where R_a is the air-core radius at the nozzle exit.

On the other hand, the half cone angle can be determined using the following correlation [Donjat 2003]:

$$\theta = 11.21 \times K^{-0.07} \times \left(\frac{\Delta P {d_0}^2 \rho_l}{\mu_l}\right)^{0.04} \tag{11.18}$$

- **Film velocities (u_x, u_r and u_t)**:
  The axial film velocity component can be computed from mass conservation and based on the film thickness and the fuel mass flow rate:

$$u_x = \frac{\dot{m}_l}{\pi\, t_f (d_0 - t_f)\rho_l} \tag{11.19}$$

  If the injector geometry includes a divergent shape at the nozzle exit, as it is the case in this work (the injector geometry is detailed in Sec. 11.2.2), the tangential velocity is assumed equal to zero and the radial component is computed from the angle of the divergent:

$$u_r = u_x \times \tan(\theta) \tag{11.20}$$

$$u_t = 0 \tag{11.21}$$

  If the injector does not include a divergent exit (as in Fig. 11.1.3), the flow is constrained by the injector walls such that the radial velocity is zero:

$$u_r = 0 \tag{11.22}$$

$$u_t = \pm\, u_x \times \tan(\theta) \tag{11.23}$$

  with the sign depending on the clockwise or anti-clockwise flow rotation in the swirl chamber. However, for point injection, the tangential velocity is completely equivalent to the radial velocity when the flow enters in the chamber. Hence, the film velocity becomes identical to the case with a divergent exit.

11.2 Modeling of the fuel injection

The objective of this section is to develop an injection model. Such model must be able to estimate the characteristic SMD diameter of a fuel spray resulting from the primary atomization of the liquid film at the pressure swirl exit. Furthermore, in the context of high altitude conditions of this work, a focus is made on the influence of the low pressure condition. This physically based model is built as much as possible from the study of the internal mechanisms leading to the atomization.

In the following parts, the injection model implemented in AVBP is presented and a new strategy for the injection modelling is introduced. Secondly, the available data used to build this model are presented. Then, the development of the primary atomization model is described with the corresponding equations. Finally, a discussion on the validation and the improvement perspectives is proposed.

11.2.1 Strategies for fuel injection

FIM-UR model

The main methodology used in AVBP to simulate the liquid spray consists in the injection of droplets at the nozzle position following user-defined parameters such as size distribution, liquid mass flow rate and spray angle. [Sanjosé et al. 2011] proposed a method to impose velocity and size profiles at the injector outlet without resolving atomization. This model called FIM-UR (for Fuel Injection Model by Upstream Reconstruction) enables to determine the droplet velocity based on the half cone angle (θ), the fuel mass flow rate ($\dot{m}_l$) and the radius of the pressure swirl exit (R_0). The schematic diagram of the FIM-UR model in shown on Fig. 11.2.1.

In the Lagrangian formalism, the droplets velocities write:

$$u_x = \frac{\dot{m}_l}{\rho_l A_0} = \frac{\dot{m}_l}{\rho_l \pi {R_0}^2 (1 - X)} \tag{11.24}$$

$$u_t(r) = \frac{\dot{m}_l}{\rho_l A_{p,tot}} \frac{r}{R_s^0} = \frac{\dot{m}_l}{\rho_l A_{p,tot}} \frac{2r}{R_0(1 + \sqrt{X})} \tag{11.25}$$

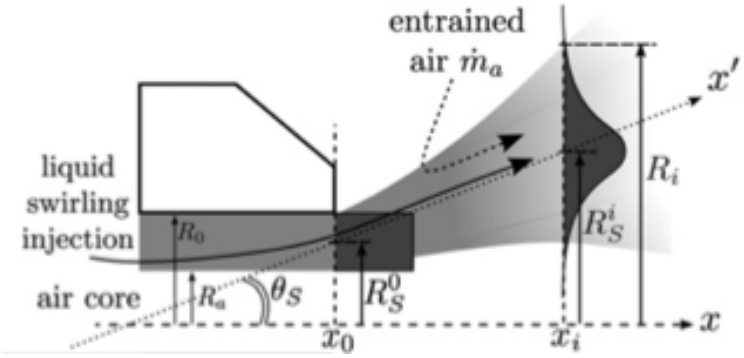

Figure 11.2.1: Schematic diagram of the FIM-UR model.

$$u_r = 0 \tag{11.26}$$

Equation (11.24) is equal to Eq. (11.19) using the definition of Eq. (11.17). Contrarily to Eq. (11.23) which is built from the cone angle, Eq. (11.25) uses the mass conservation of the flow entering tangentially in the swirl chamber. Moreover, the total fuel slot area is not given by the user based on the pressure swirl geometry, but rather re-derived from inviscid flow theories [Taylor 1950] with a correction constant given in [Lefebvre and McDonell 2017]:

$$A_{p,tot} = 20.73 \times {C_D}^2 \pi {R_0}^2 \tag{11.27}$$

where C_D is the discharge coefficient that can also be determined using inviscid theories with the correction from [Giffen and Muraszew 1953]:

$$C_D = 1.17\sqrt{\frac{(1-X)^3}{(1+X)}} \tag{11.28}$$

Finally, the air-core radius R_a required to compute the concentration factor can be obtained re-arranging Eq. (11.16) and (11.17):

$$R_a = \frac{R_0 sin(\theta)}{\sqrt{1+cos(\theta)^2}} \tag{11.29}$$

The FIM-UR model is simple to use however it requires to know a priori the half cone angle θ. The liquid flow modeling in the pressure swirl is over-simplified which can lead to erroneous prediction of the velocity field. For example, the internal swirl geometry as well as liquid properties are not taken into account. In the FIM-UR model, the velocity components are totally derived from the cone angle. As a consequence, for each operating conditions, this angle must be adapted and known (which, in practice, is not always the case) to recover the correct velocity profile. Moreover, the spray distribution parameters (SMD, and shape factor q) are not modeled by FIM-UR and must be given by the user.

In the case where two-phase flow profiles (velocity and SMD) are available, uncertainty quantification tools can be used to determine the optimal FIM-UR parameters (θ and $d_{p,32}$). However, several runs are required, varying the model parameters which may turn very CPU-costly. This methodology has been used in Chap. 14 and in [Wirtz 2022] where only reactive profiles and flame shapes where available.

New approach for fuel injection modeling

The objective is here to model the complete injection process. For this purpose, two sub-models are considered as shown on Fig. 11.2.2. This global injection model may be used directly to inject the droplets, or upstream of the FIM-UR model to get the required parameters θ, R_0, $d_{p,32}$ and q.

The first sub-model aims to represent the pressure-swirl injector. As shown in Donjat [2003], the liquid flow internal structure and the film formed at the nozzle exit are weakly dependant on the ambient condition of the chamber. However, there are important influences of the injector geometrical structure and dimensions, the liquid fuel properties, and the mass flow rate. The model outputs correspond to the

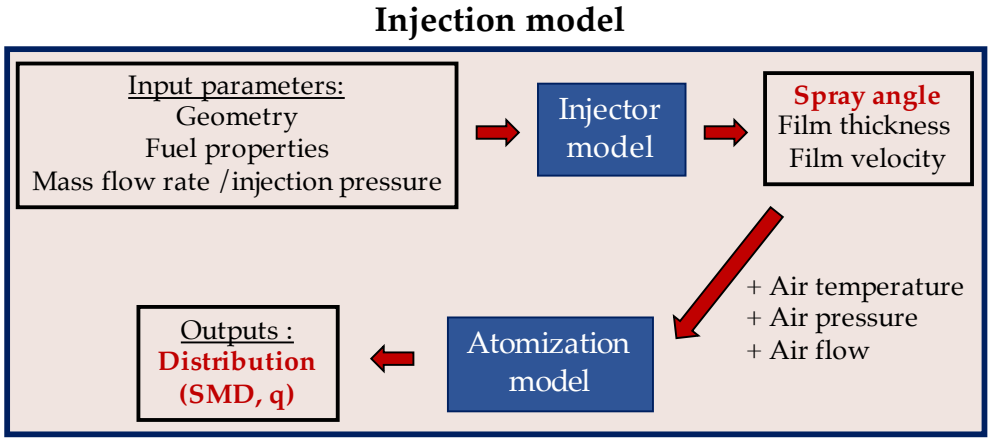

Figure 11.2.2: Schematic diagram of the new injection modeling methodology.

liquid film characteristics: half cone angle, film thickness and film velocity. In this work, the injector sub-model has been provided by Safran Aircraft Engine (SAE). This model is based on a Lamb-Oseen vortex flow and geometrical correlations from the PhD of Donjat [2003].

The second sub-model corresponds to the primary atomization process. As shown in Sec. 11.1.2, the primary atomization is a consequence of the liquid film destabilisation and disintegration when interacting with the air in the chamber. Hence, the primary atomization model requires information about the film characteristics provided by the injector sub-model, and the air-flow conditions interacting with the film: air velocity, pressure, temperature and density. Then, the model outputs are the characteristic droplet size $d_{p,32}$ and distribution shape q resulting from the primary atomization.

11.2.2 Available data

Set-up

The primary atomization sub-model developed in this work is based on measurements (extracted from a SAFRAN private communication) performed on the MERCATO test rig from ONERA [Ouarti 2004]. These measurements are also compared with numerical simulations performed with the solver YALES2 [Moureau et al. 2011a] developed at CORIA and the prediction from the injector sub-model developed at SAE. All these data have been provided by SAE.

The reference injector was provided by SAE, and is sketched with the geometrical characteristics on Fig. 11.2.3. Note that dimensions are not provided for confidentiality reasons.

Several operating points have been tested to evaluate the effect of chamber pressure and liquid mass flow rates. There is no air flow in the injection system and the flow is at rest in the chamber. Hence, the measurements correspond to the primary atomization of the pressure swirl without secondary break-up.

Table 11.2.1 reports the conditions of the experiment in the MERCATO chamber.

Label	$P\,[bar]$	$T_g\,[K]$	$T_l\,[K]$	$\dot{m}_l\,[g/s]$
M1	1	288	273	1.36
M2	1	288	273	1.09
M3	0.45	288	273	1.36
M4	0.45	288	273	1.09

Table 11.2.1: Operating points used for the MERCATO measurements.

Table 11.2.2 reports the conditions used in the YALES2 simulation. The fuel flow rate, fuel temperature and pressure are slightly different, but the differences with the MERCATO experiment are assumed negligible in view of measurements uncertainties.

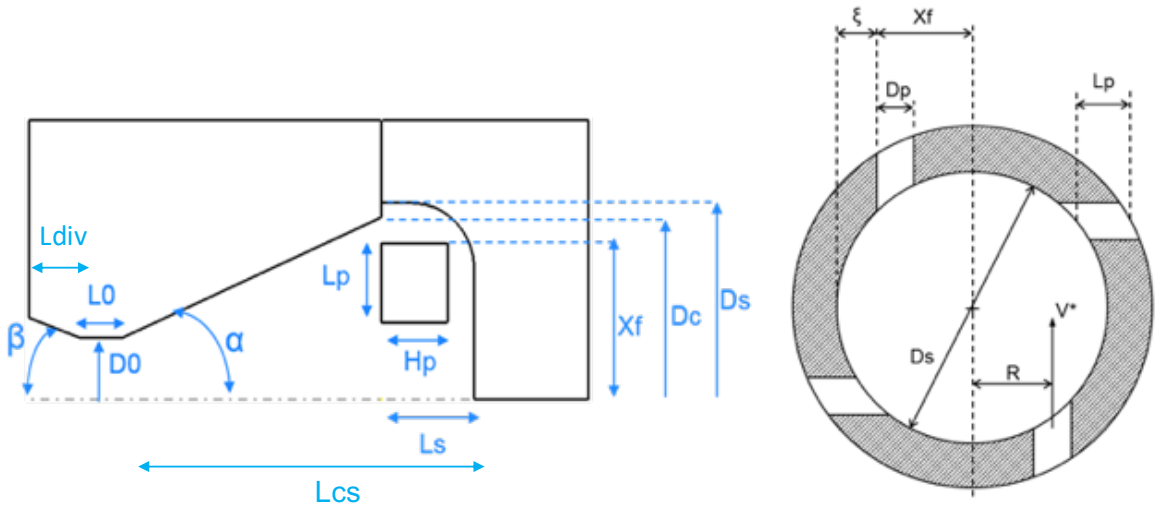

Figure 11.2.3: Schematic diagram of the injector (Courtesy of Safran Aircraft Engine).

Label	$P\,[bar]$	$T_g\,[K]$	$T_l\,[K]$	$\dot{m}_l\,[g/s]$
Y1	1	288	288	1.38
Y2	1	288	288	0.83
Y3	0.43	288	288	0.83

Table 11.2.2: Operating points used for the YALES2 computations.

Finally, Tab. 11.2.3 corresponds to the conditions used in the injector sub-model. This model does not account for chamber pressure and temperature. Thus, only fuel mass flow rate and fuel temperature have been evaluated with the same conditions as MERCATO and YALES2.

Label	$P\,[bar]$	$T_g\,[K]$	$T_l\,[K]$	$\dot{m}_l\,[g/s]$
S1	-	-	288	1.38
S2	-	-	288	0.83
S3	-	-	273	1.36
S4	-	-	273	1.09

Table 11.2.3: Operating points used for the injector sub-model from SAE.

Data

The data are summarized in Tab. 11.2.4. For the experimental study, direct visualizations of the pressure swirl and the measurements of the film thickness were not possible. Only Laser Doppler Anemometry (LDA) measurements at 10 millimeters from the injector nozzle were available. Hence, only velocity magnitude and SMD measurements are given with the corresponding standard deviation to characterize the variability. For the YALES2 simulations, only film thickness has been measured. Finally for the injector sub-model, only film informations (thickness and velocity magnitude) are given. These data are also displayed on Fig. 11.2.4 to qualitatively appreciate the differences and variability.
These results show very large discrepancies depending on the origin of the data. For example, the film thicknesses are three to four times larger for YALES2 computations compared to the injector model predictions, which seems to under-predict the film thickness. Hence, the resulting film velocity is much larger to conserve the same mass flow rate which explains the higher values compared to the MERCATO experiment. This difference may also be due to the downstream location of the measurement in the experimental set-up, whereas the injector model gives values at the nozzle exit. Indeed, the droplet velocity decreases between the nozzle exit and the measurement location because of the interaction with air via the drag force. Finally, the measurement of the SMD indicates an important variability of the results even though the effect of pressure and mass flow rate is clearly visible.

Label	t_f $[\mu m]$	V_f $[m/s]$	σ_v $[m/s]$	$d_{p,32}$ $[\mu m]$	σ_{SMD} $[\mu m]$	Data origin	Symbols
M1	-	10.72	0.73	82	7	MERCATO	(●)
M2	-	7.65	1.14	95	8	MERCATO	(●)
M3	-	13.00	3.47	84	4	MERCATO	(●)
M4	-	8.37	1.42	104	3	MERCATO	(●)
Y1	40	-	-	-	-	YALES2	(▼)
Y2	42	-	-	-	-	YALES2	(▼)
Y3	45	-	-	-	-	YALES2	(▼)
S1	12.5	32.61	-	-	-	Injector model	(■)
S2	14	17.62	-	-	-	Injector model	(■)
S3	13.3	29.95	-	-	-	Injector model	(■)
S4	14.1	22.57	-	-	-	Injector model	(■)

Table 11.2.4: Summary of the data available. σ refers to the standard deviation associated to the velocity or SMD data.

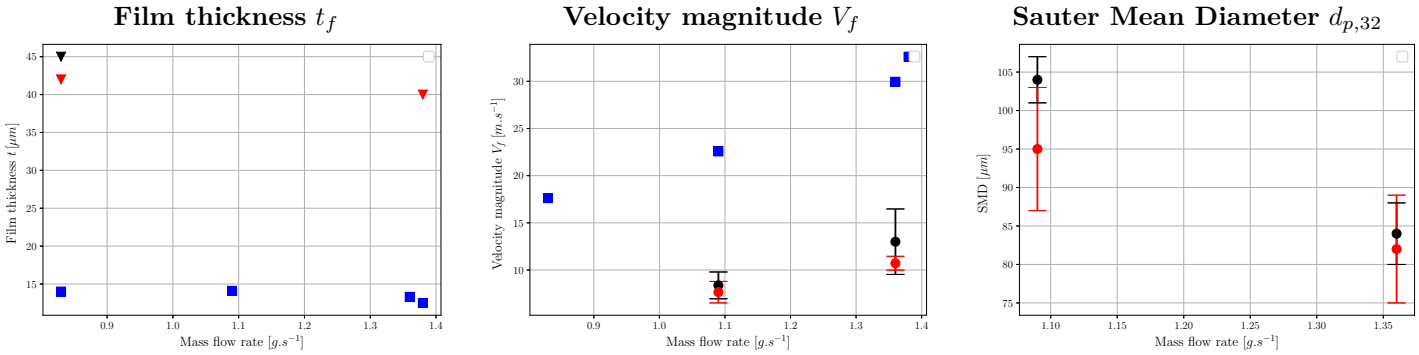

Figure 11.2.4: Summary of the data available. (●) refers to MERCATO measurements, (▼) refers to YALES2 results, (■) refers to the injector model predictions. Black symbols correspond to low pressure and red ones to atmospheric pressure.

Data reconstruction for the experimental measurements

Due to the data inconsistency, it has been decided to focus on the experimental measurements to develop the primary atomization model. Therefore, it is necessary to re-construct the velocity at the injector exit and, from this value, estimate the film thickness using mass conservation. One can note that the velocity at the nozzle exit corresponds to the liquid film velocity, while the velocity in the experiment is the mean droplets velocity. However, the atomization process is assumed to conserve the mean velocity such that the mean droplet velocity reconstructed at the injector exit corresponds to the film velocity.

Starting with the droplet momentum conservation Eq. (1.81) and considering the air flow at rest, the differential equation of the droplet velocity magnitude writes[2]:

$$\frac{d\,V_p(t)}{dt} = -\frac{\rho_g}{\rho_p} C_{\mathcal{D}} \frac{3}{8 r_p} V_p(t)^2 = \mathcal{C} \times V_p(t)^2 \tag{11.30}$$

A first integration leads to the evolution of the velocity depending on the initial velocity at the nozzle exit $V_p(t=0) = V_{p,0}$:

$$V_p(t) = \frac{V_{p,0}}{1 - \mathcal{C} \times V_{p,0} \times t} \tag{11.31}$$

A second integration with the initial condition $x_f(t=0) = 0$ leads to the trajectory equation:

$$x_f(t) = \frac{-\ln\left(1 + V_{p,0}\mathcal{C}t\right)}{\mathcal{C}} \tag{11.32}$$

[2]The drag coefficient $C_{\mathcal{D}}$ is assumed constant for this estimation because the droplet velocity is not expected to vary drastically. This assumption is verified a posteriori and the drag coefficient is corrected to take into account the velocity variation if needed.

Finally, the theoretical velocity at the distance x_f from the injector is obtained combining Eq. (11.31) and (11.32). It provides a direct relation between the initial velocity at the nozzle exit ($V_{p,0}$) and the droplet velocity after traveling a distance x_f ($V_p(x_f)$):

$$V_p(x_f) = \frac{V_{p,0}}{\exp\left(-\mathcal{C} \times x_f\right)} \tag{11.33}$$

The experimental measurement is done at the position $x = 0.01\,m$, however, due to the conical spray shape, the travelled distance is:

$$x_f = \frac{0.01}{\cos\left(\theta\right)} = 0.0126\,m \tag{11.34}$$

with θ the divergent angle of the injector β[3].
Using Eq. (11.33), Fig. 11.2.5 displays the theoretical velocity at the measurement position depending on the pressure/density conditions in the chamber and the droplet size. In the case of the Rosin-Rammler distribution (red curve), the linear mean droplet diameter $d_{p,10}$ is used for the velocity estimation. This characteristic diameter can be computed as:

$$d_{p,10} = X_{num} \times \Gamma(1 + 1/q) \tag{11.35}$$

with q and X_{num} respectively the shape factor and dimension factor of the numerical RR distribution, and Γ the standard gamma function.

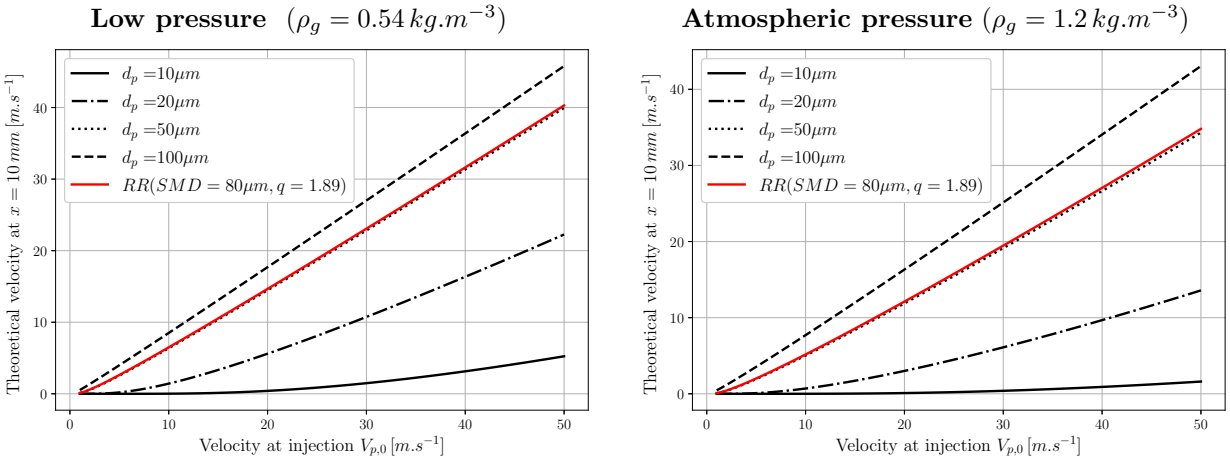

Figure 11.2.5: Theoretical droplet velocity magnitude at measurement position $x = 10\,mm$ ($x_f = 12.6\,mm$) versus initial velocity

Based on the velocities and SMD of Tab. 11.2.4, the Tab. 11.2.5 gives the reconstructed velocities at the nozzle exit ($V_{p,0}$) which corresponds also to the initial liquid film velocity ($V_{f,0}$).

Label	M1	M2	M3	M4
$\dot{m}_l$ $[g/s]$	1.36	1.09	1.36	1.09
P $[bar]$	1	1	0.45	0.45
$V_{f,0}$ $[m/s]$	18.42	12.73	18.01	11.25

Table 11.2.5: Reconstructed velocities at the nozzle exit

These results show the strong effect of the mass flow rate which increases the exit velocity for cases M1 and M3. On the contrary, the effect of the ambient pressure is much lower. The low pressure seems to slightly reduce the velocity, however the pressure influence is of the order of the standard deviations given in Tab. 11.2.4. This result is in agreement with the literature review Sec. 11.1.2 where no pressure influence is considered for the film velocities and thickness. Hence, for the development of the primary atomization model the ambient pressure influence on the film velocity is not considered which is consistent with the modeling strategies presented on Fig. 11.2.2 where the injector model does not use the ambient

[3]Better approximations could be obtained by integrating the spray cone closure due to surface tension forces.

pressure. The velocities retained for the primary atomization model are the average at each mass flow rate:

$$V_{f,0}(\dot{m}_l = 1.36) = 18.2\, m.s^{-1} \tag{11.36}$$

$$V_{f,0}(\dot{m}_l = 1.09) = 12.0\, m.s^{-1} \tag{11.37}$$

Furthermore, these results also demonstrate that the measurement position does not compensate totally the discrepancy with the velocities given by the injector sub-model. Thus, this model requires a correction to match with experimental measurements of the injector.

The last missing parameter for the primary atomization model is the film thickness t_f. This parameter can be estimated based on geometrical consideration defined on Fig. 11.2.6, and mass conservation.

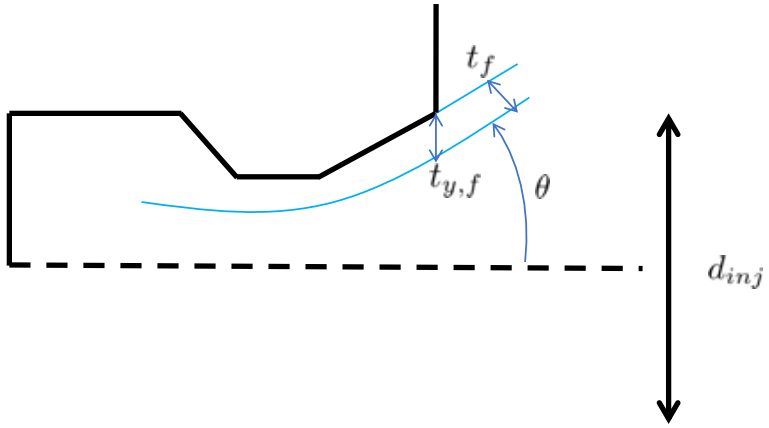

Figure 11.2.6: Schematic diagram for the film thickness reconstruction.

First, the axial velocity component is recovered from the definition of the velocity magnitude and the divergent angle θ and Eq. (11.20):

$$u_x = \frac{V_{f,0}}{\sqrt{1 + \tan(\theta)^2}} \tag{11.38}$$

Then, the film thickness in the vertical direction is obtained from the mass conservation Eq. (11.39) (similar to Eq. (11.19) but adapted to a pressure swirl with a divergent exit) which gives a second order polynomial expression whose physical solution corresponds to Eq. (11.40).

$$\dot{m}_l = \rho_p \times u_x \times A_{exit,film} \quad \text{with} \quad A_{exit,film} = \pi\, t_{y,f}(d_{inj} - t_{y,f}) \tag{11.39}$$

$$t_{y,f} = \frac{d_{inj}}{2} - \frac{1}{2}\sqrt{{d_{inj}}^2 - \frac{4\dot{m}_l}{\rho_p \pi u_x}} \tag{11.40}$$

Finally, the film thickness writes:

$$t_f = \cos(\theta) \times t_{y,f} \tag{11.41}$$

Hence, the thickness values retained for the primary atomization model are:

$$t_f(\dot{m}_l = 1.36) = 20.84\, \mu m \tag{11.42}$$

$$t_f(\dot{m}_l = 1.09) = 25.44\, \mu m \tag{11.43}$$

Using the reconstructed data for initial velocities (i.e., liquid film velocities) and film thicknesses, a primary atomization model is proposed in the following section.

11.2.3 Modeling of the primary atomization

From maximisation entropy formalism to energy conservation principle

Droplet sizes distributions are typically described using one of the following four methods: empirical, maximum entropy formalism (MEF), discrete probability function method, or stochastic method. Among these methods, several studies indicate that the MEF shows good prediction abilities. MEF has been used in many works to study the size and velocity distribution characteristics in all kinds of spray systems [Sellens and Brzustowski 1985, Li and Tankin 1987, Mondal et al. 2004, Nath et al. 2011, Movahednejad et al. 2010, Yan et al. 2015]. Knowing the SMD, MEF is a tool allowing to determine the most suitable of all possible size distributions, under some constraints issued from the current knowledge about the phenomena [Mondal et al. 2004].

The application of the MEF to spray modeling has been pioneered by Sellens and Brzustowski [1985] and Li and Tankin [1987]. In this approach, a control volume is considered, extending from the injector exit to the primary atomization zone. The droplet formation process in the control volume is considered as a transformation from the liquid film to droplets during which mass, momentum and energy are conserved. These conservation laws are used as constraints in the MEF while the most probable size distribution corresponds to the one that maximizes the information entropy (Eq. (11.44)) as defined by Shannon [1948].

$$\mathcal{S}(f) = -\int f(\xi) \times \log_2 f(\xi) d\xi \tag{11.44}$$

where f is the continuous distribution studied.

In this work, the problem is stated in slightly different terms. The distribution shape is fixed: Rosin-Rammler (RR), and the SMD and shape parameter are unknown. However, the framework used in MEF remains valid and the conservation laws still apply.

In this work, the momentum conservation is not used because no droplet velocity distribution is considered: instead it is assumed that all droplets have the same velocity. Then, mass and energy conservation equations write:

$$\dot{m}_l = \dot{m}_{p,tot} \tag{11.45}$$

$$\dot{E}_{c,f} + \dot{E}_{s,f} + \dot{S}_E = \dot{E}_{c,p} + \dot{E}_{s,p} \tag{11.46}$$

with $\dot{m}_l$ the injected mass flow rate and $\dot{m}_{p,tot}$ the mass flow rate of the droplet distribution, $\dot{E}_{c,f}$ and $\dot{E}_{c,p}$ the kinetic energy rate (or power) of the film and droplet distribution respectively, $\dot{E}_{s,f}$ and $\dot{E}_{s,p}$ the surface energy rate (linked to surface tension) of the film and droplet distribution respectively and $\dot{S}_E$ the source term due to the air-flow interaction. This source term can be divided in two contributions, a shear stress effect due to the film deformation induced by the air-flow and a drag effect due to viscous friction. However, the latter has been evaluated smaller than the film kinetic energy rate $\dot{E}_{c,f}$ by four orders of magnitude. Indeed, the film velocity variation due to the drag force is negligible because the film length is very short ($1 - 3\,mm$). Thus, the velocity is considered constant during the primary atomization process and the kinetic energy terms $\dot{E}_{c,f}$ and $\dot{E}_{c,p}$ cancel each out.

The droplet rate distribution required to compute $\dot{m}_{p,tot}$ and $\dot{E}_{s,p}$ is defined as:

$$\dot{f}(d_p) = \mathcal{A} \times RR_{X_{num},q}(d_p) \tag{11.47}$$

where $\mathcal{A}$ is the rate constant corresponding to the number of droplets created per second. Thus, $\dot{f}(d_p)$ is the dimensional droplet distribution which gives the number of droplet of size d_p injected per second. Hence, there are three parameters to determine: $\mathcal{A}$, $d_{p,32}$ (equivalent to X_{num}) and q.

The surface energy E_s of a liquid writes under the general form:

$$E_s = \sigma \times A \tag{11.48}$$

where σ is the liquid surface tension and A the total liquid surface.

The conservation equations finally write:

$$\dot{m}_l = \int_0^\infty \rho_p \mathcal{V}_p \, \dot{f}(d_p) dd_p \tag{11.49}$$

$$\Leftrightarrow \quad \dot{m}_l = \int_0^\infty \rho_p \frac{\pi}{6} {d_p}^3 \, \mathcal{A} \, RR_{X_{num},q}(d_p) \, dd_p \tag{11.50}$$

and

$$\sigma(\dot{A}_{f,ext} + \dot{A}_{f,int}) + \dot{S}_E = \int_0^\infty \sigma \, A_p \, \dot{f}(d_p) \, dd_p \tag{11.51}$$

$$\Leftrightarrow \quad \sigma \, V_{f,0} \, 2\pi(d_{inj} - t_f) + \dot{S}_E = \int_0^\infty \sigma \, \pi \, {d_p}^2 \, \mathcal{A} \, RR_{X_{num},q}(d_p) \, dd_p \tag{11.52}$$

with $\mathcal{V}_p$ and A_p the droplet volume and surface area, and $\dot{A}_f$ the film surface creation rate where *int* and *ext* subscribes refer to the internal and external surfaces of the conical film. $V_{f,0}$ is the liquid film velocity at the nozzle exit computed in Sec. 11.2.2.

The rate constant $\mathcal{A}$ is computed with the mass conservation. The SMD corresponds to the mean diameter whose ratio to surface area is the same as the one of the entire spray. Therefore, its value depends on the surface energy of the droplet distribution and can be computed from the energy conservation. Besides, since the surface energy of the droplet distribution is totally controlled by the SMD, any value of q is valid. Hence, the entropy maximisation principle is used to choose the most probable shape distribution. For the RR distribution, the information entropy writes:

$$\mathcal{S}(q, d_{p,32}) = \gamma \times \left(1 - \frac{1}{q}\right) + \ln\left(\frac{X_{num}}{q}\right) + 1 \tag{11.53}$$

with $\gamma \approx 0.57721$ the Euler–Mascheroni constant.

In the range of SMD studied ($1 - 100\,\mu m$), the value maximising the entropy is $q_{opt} = 1.89$. This value is close to those generally observed in aeronautical applications (see Chap. 14). The influence of this parameter on the combustion processes should be studied to determine if a complementary model is required. Generally speaking, the physical origin of this size dispersion parameter should be investigated.

The general workflow of the model is presented on Fig. 11.2.7. An iterative method based on a least squares algorithm is used. From an initial guess of the SMD, the rate constant is computed with the mass conservation. The error on the energy balance leads to a corrected SMD value. The procedure is iterated until convergence of the SMD which is obtained when the error on the energy balance decreases below a threshold limit.

Closing the energy balance

First the energy balance has been evaluated without the energy source term $\dot{S}_E$,. This corresponds to droplets not interacting with air. In this case, the film surface energy is equal to the droplet distribution surface energy and the maximum theoretical SMD value is obtained.

However, when imposing $\dot{S}_E = 0$ in the energy balance, the model predicts $d_{p,32} \approx 60\,\mu m$ which is much lower than the maximum SMD measured experimentally $d_{p,32}^{max} = 104\,\mu m$. Thus, it demonstrates[4] that there is a missing term in the droplet side of the energy balance. In other words, the film surface energy is not fully converted into droplet surface energy during the primary atomization process, and part goes into another process. This could correspond to droplet oscillation energy or droplet kinetic energy fluctuation (similar to gaseous molecular agitation) resulting from the ligament break-up.

[4] Assuming the validity of the energy conservation between the film and droplet states.

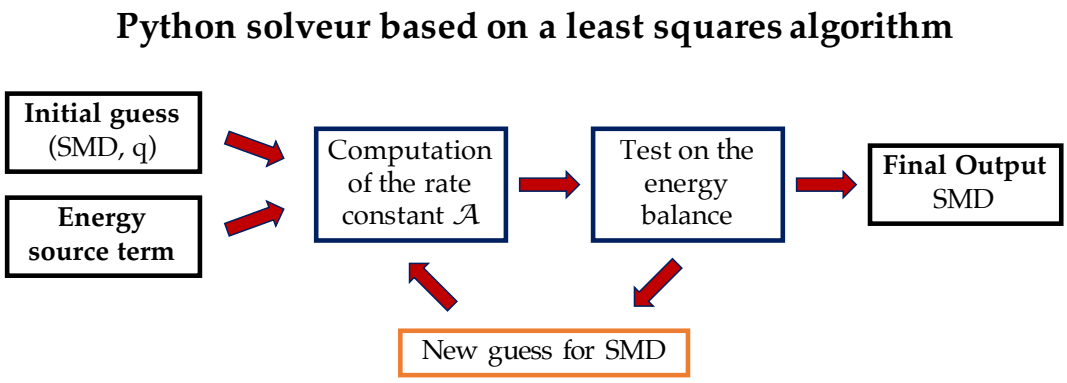

Figure 11.2.7: Workflow of the primary atomization sub-model solver.

Introducing this new contribution $\dot{\mathcal{U}}$ in the energy balance gives:

$$\sigma\, V_{f,0}\, 2\pi(d_{inj} - t_f) + \dot{S}_E = \int_0^{\infty} \sigma\, \pi\, {d_p}^2\, \mathcal{A}\, RR_{X_{num},q}(d_p)\, dd_p + \dot{\mathcal{U}} \tag{11.54}$$

To evaluate this unknown term, the pressure dependence of the SMD is assumed to follow a linear evolution between the measurement points. The following values are obtained depending on the mass flow rate:

$$\dot{\mathcal{U}}(\dot{m}_l = 1.36) = 0.00111 \tag{11.55}$$

$$\dot{\mathcal{U}}(\dot{m}_l = 1.09) = 0.00084 \tag{11.56}$$

Energy source term modeling

The energy source term $\dot{S}_E$ corresponds to a shear effect due to the interaction with air. As shown on Fig. 11.1.7, the liquid film is deformed and waves appear at the surface. This mechanism increases the film surface area and thus the surface energy. As a consequence, the SMD is reduced to get a larger total droplet surface.

The film deformation is described by its wavelength λ_{opt} and its amplitude H_t that are presented on Fig. 11.2.8.

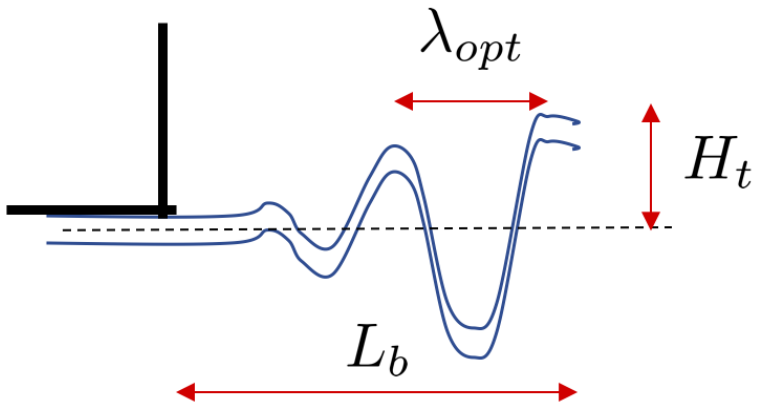

Figure 11.2.8: Film deformation and the associated characteristic quantities.

Following [Lefebvre and McDonell 2017], the film instability follows an exponential growth:

$$H_t = H_0 \times \exp\left(\beta \times \tau_{dis}\right) \tag{11.57}$$

where H_0 is the initial amplitude of the instability, β is the instability growth rate and $\tau_{dis} = L_b/V_{f,0}$ is the film disintegration characteristic time with L_b the break-up length.

The initial amplitude of the instability H_0 is assumed to depend on the film hydrodynamic and geometrical properties: film thickness and turbulence. However, for the studied range of operating conditions, the Reynolds number based on the film thickness is close to unity which indicates a laminar flow. Hence, the film thickness is directly used as the initial amplitude:

$$H_0 = t_f \tag{11.58}$$

The break-up length L_b is estimated using a correlation from Arai and Hashimoto [1985]. However, this correlation has been developed for a planar film sheet, which does not take into account the spray angle. This angle may not be negligible because, with conical film expansion, the latter is being thinned which reduces the break-up length. Based on the correlation of Han et al. [1997][5], a correction to account for the spray angle has been added:

$$L_b = 0.123 \times \sqrt{\frac{t_f}{We}} \times {Re_f}^{0.6} \times \sqrt{\cos(\theta)} \tag{11.59}$$

with $We = \frac{\rho_g {U_r}^2 t_f}{2\sigma}$ the Weber number[6] based on the film thickness t and the relative velocity with the air-flow U_r.

The instability growth rate β has been fitted on available SMD data. It has been observed that the growth rate is not dependent on the fuel mass flow rate, but varies with pressure (or air density). Hence, in this work, a power law has been derived to account for the pressure variation:

$$\beta(P) = \beta(P = 10000\,Pa) \times \left(\frac{P}{10000}\right)^{\alpha} = \beta(P = 10000\,Pa) \times \left(\frac{\rho_g}{1.2}\right)^{\alpha} \tag{11.60}$$

with

$$\beta(P = 10000\,Pa) = 11000\,s^{-1} \qquad \alpha = 0.257 \tag{11.61}$$

From an analysis of the oscillations of a liquid sheet moving in still air, Squire [1953] derived an expression for the optimum wavelength λ_{opt} corresponding to the maximum growth rate:

$$\lambda_{opt} = \frac{4\pi\sigma}{\rho_g U_r^2} \tag{11.62}$$

Then, using the value of H_t and λ_{opt}, a film deformation factor $\mathcal{F}_{def}$ accounting for the increase of the film surface may be determined. This factor is defined as the length of the sinusoid of amplitude H_t and wavelength λ_{opt}, divided by λ_{opt}. The mathematical expression writes:

$$\mathcal{F}_{def} = \frac{2}{\pi} \times E\left(-\left(\frac{H_t \times 2\pi}{\lambda_{opt}}\right)^2\right) \geq 1 \tag{11.63}$$

where $E(m)$ refers to the complete elliptic integral of the second kind:

$$E(m) = \int_0^{\frac{\pi}{2}} \sqrt{1 - m\,sin(\xi)^2}\,d\xi \tag{11.64}$$

Finally, the energy source term resulting from the film deformation writes:

$$\dot{S}_E = \dot{E}_{s,f} \times (\mathcal{F}_{def} - 1) \tag{11.65}$$

11.2.4 Results

Comparison with experiments

The model predictions for the SMD obtained with the liquid and gaseous properties summarized in Tab. 11.2.6, are compared to the experimental measurements on Fig. 11.2.9. Calculations were performed for

$\rho_g^{Pa}\,[kg.m^{-3}]$	$\rho_g^{LP}\,[kg.m^{-3}]$	$\rho_p\,[kg.m^{-3}]$	$\sigma\,[N.m^{-1}]$	$\mu_g\,[kg.m^{-1}.s^{-1}]$	$\nu_p\,[m^2.s^{-1}]$
1.2	0.54	813	0.02487	1.796×10^{-5}	2.405×10^{-4}

Table 11.2.6: Liquid and gaseous properties used in the primary atomization model

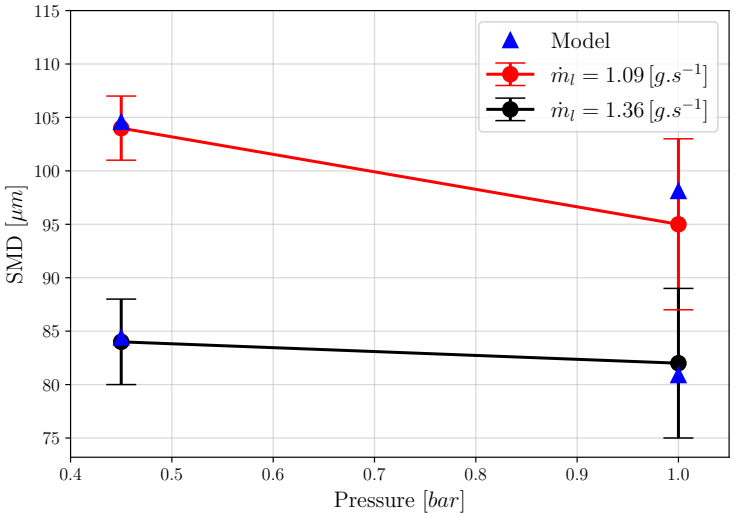

Figure 11.2.9: Summary of SMD data issued from MERCATO experimental measurements (lines) and primary atomization model (symbols), for the two mass flow rates 1.09 $g.s^{-1}$ (red) and 1.36 $g.s^{-1}$ (black).

two mass flow rates, 1.09 $g.s^{-1}$ and 1.36 $g.s^{-1}$.

For the available data, the model seems to correctly predict the SMD. The errors compared to the experimental measurements are given in Tab. 11.2.7 and are lower than the experimental variability measured with the standard deviation.

Label	M1	M2	M3	M4
Error [%]	1.35	3.28	0.49	0.57

Table 11.2.7: Summary of the errors between model predictions and experimental measurements.

Discussion and perspectives

As shown above, the SMD predictions and tendencies with respect to pressure and mass flow rate variations seem well captured by the model. Compared to a simple correlation, this physically-based model enables a better understanding of the mechanism leading to primary atomization: film deformation and break-up length. Hence, considering these mechanisms are well reproduced by the model (which still must be ensured with additional experimental data and validations), a parametric study could then enable to determine the parameter influences and sensitivities on these internal mechanisms and on the global primary atomization.

It should be kept in mind that the above comparison is made with the same data used for the model calibration, therefore limiting the validity. Unfortunately, data on primary atomization is rare. Further validation could still be made by coupling the model to FAST[7] [Senoner 2010], leading to the final spray which is easier to characterize experimentally. Moreover, the atomization model integrates dependencies to surface tension, liquid density and viscosity. Hence, complementary measurements changing the fuel temperature or composition could be evaluated. The origin of the term $\dot{\mathcal{U}}$ should also be characterized based on complementary measurements or using DNS computations of film break-up. The current data

[5]Not retained because it does not account for the liquid viscosity
[6]There is a factor 1/2 compared to the definition given Eq. (11.2)
[7]Secondary break-up model Fast Atomization Stochastic Treatment

indicate that this term is approximately 35% of the initial film energy which is far from negligible.

Finally, the model prediction accuracy (as well as simple correlations) must be placed in the context of two-phase combustion. The influence of the SMD and the shape distribution parameter q may be quantified with respect to two-phase ignition and spray flames. This question started to be addressed in Chap. 13.

Chapter 12

Multi-component droplet evaporation

Contents

High altitude conditions influence the droplet evaporation: at lower temperature the droplet requires more energy for heating and evaporating, and the boiling temperature is lower at low pressure. Evaporation is a key element of the two-phase ignition and combustion as it determines the amount of flammable mixture, and thus must be evaluated in high altitude conditions.

For that purpose, the extension of the evaporation model (presented Chap. 1) for multi-component fuel blends is first detailed in Sec. 12.1. Then, a study on the evaporation of isolated droplets is presented Sec. 12.2 to evaluate the influence of low pressure and low temperature along with the preferential evaporation effect in the context of ignition.

12.1 Multi-component evaporation

The use of chemical schemes composed of several fuel species with their own decomposition pathways enables to consider the preferential evaporation effects on two-phase combustion. The mono-component evaporation model presented in Sec. 1.3.4 is extended in Sec. 12.1.1 to account for the droplet composition and the species properties, especially their volatility, and a special treatment to handle the saturation condition is introduced in Sec. 12.1.2. Finally, a review of recent works studying preferential evaporation effects on two-phase flame propagation is presented in Sec. 12.1.3.

12.1.1 Multi-component evaporation model

Extension of the mono-component evaporation model

A review of discrete and continuous approaches to model the multi-component evaporation is available in [Shastry 2022]. A Discrete Multi-Component (DMC) evaporation model has been recently implemented in AVBP [Shastry 2022] and is built on top of the existing Abramzon & Sirignano (AS) evaporation model presented in Chap. 1.

In the multi-component formalism, the liquid mass and molar fractions are introduced to take into account the droplet composition:

$$\sum_{\kappa=1}^{N_{liq}} Y_{\kappa,liq} = 1 \quad \text{and} \quad \sum_{\kappa=1}^{N_{liq}} X_{\kappa,liq} = 1 \tag{12.1}$$

with N_{liq} the number of liquid fuel species in the droplet. $Y_{\kappa,liq}$ and $X_{\kappa,liq}$ are respectively the mass and molar liquid fractions of the fuel species κ.

The gaseous fuel fractions write from the fuel species fractions:

$$Y_F = \sum_{\kappa=1}^{N_{liq}} Y_\kappa \quad \text{and} \quad X_F = \sum_{\kappa=1}^{N_{liq}} X_\kappa \tag{12.2}$$

The mass Spalding transfer number keeps the same expression as in Eq. (1.98) but it can also be written for each individual liquid components:

$$B_M = \frac{Y_{F,\zeta} - Y_{F,\infty}}{1 - Y_{F,\zeta}} = \frac{\sum_{\kappa=1}^{N_{liq}} Y_{\kappa,\zeta} - \sum_{\kappa=1}^{N_{liq}} Y_{\kappa,\infty}}{\sum_{\kappa=1}^{N_{liq}} \varepsilon_\kappa - \sum_{\kappa=1}^{N_{liq}} Y_{\kappa,\zeta}} = \frac{Y_{\kappa,\zeta} - Y_{\kappa,\infty}}{\varepsilon_\kappa - Y_{\kappa,\zeta}} \tag{12.3}$$

where ε_κ is the mass fraction of the component κ in the evaporation flux.

The individual component fuel surface mass fractions $Y_{\kappa,\zeta}$ are computed from the Raoult's law[1] which writes in the multi-component formalism:

$$X_{\kappa,\zeta} = X_{\kappa,liq} \times \frac{P_{sat,\kappa}(T_p)}{P} \quad \Leftrightarrow \quad Y_{\kappa,\zeta} = Y_{\kappa,liq} \times \frac{W_l}{W_{g,\zeta}} \times \frac{P_{sat,\kappa}(T_p)}{P} \tag{12.4}$$

with

$$W_{g,\zeta} = \sum_{\kappa=1}^{N_{liq}} X_\kappa W_\kappa + (1 - \sum_{\kappa=1}^{N_{liq}} X_\kappa) \times W_{g,f@p} \tag{12.5}$$

and

$$W_l = \sum_{\kappa=1}^{N_{liq}} X_{\kappa,liq} W_\kappa \tag{12.6}$$

$W_{g,\zeta}$ corresponds to the mean gaseous molecular weight at the droplet surface, $W_{g,f@p}$ the mean gaseous molecular weight at the droplet position[2], and W_l the mean liquid molecular weight. $P_{sat,\kappa}(T_p)$ is the vapor pressure of the liquid species κ at the droplet temperature T_p. As for the mono-component case, this quantity is tabulated from the Ambrose-Walton corresponding state method [Poling et al. 2001].

Once the fuel mass fractions at the droplet surface are known, B_M and the total evaporation rate can be computed with the same expression as for the mono-component approach which is reminded here:

$$\dot{m}_p = -Sh^* \pi d_p \rho_g D_F \ln(B_M + 1) \tag{12.7}$$

Furthermore, Eq. (12.3) also enables to determine the value of the individual component mass fraction in the evaporation rate ε_κ. Thus, the evaporation rate of each components can be computed:

$$\dot{m}_{p,\kappa} = \varepsilon_\kappa \times \dot{m}_p \quad \text{with} \quad \sum_{\kappa=1}^{N_{liq}} \varepsilon_\kappa = 1 \tag{12.8}$$

The droplet temperature evolution is also computed with the same expression given for the mono-component approach and reminded here:

$$\frac{dT}{dt} = \frac{1}{m_p C_{p,l}} \left(2Nu^* \pi r_p \lambda (T_\infty - T_\zeta) \frac{\ln(B_T + 1)}{B_T} + \dot{m}_p L_v \right) \tag{12.9}$$

[1] The ideal mixture assumption is used.

[2] The state at the droplet position is considered equal to the infinity state

The liquid heat capacity $C_{p,l}$ and the latent heat of evaporation L_v depend on the droplet composition and vary due to the preferential evaporation. These quantities are computed through a mass averaging:

$$C_{p,l} = \sum_{\kappa=1}^{N_{liq}} C_{p,l,\kappa}(T_p) \times Y_{\kappa,liq} \qquad L_v = \sum_{\kappa=1}^{N_{liq}} L_{v,\kappa}(T_p) \times Y_{\kappa,liq} \tag{12.10}$$

Finally, the approximation introduced Eq. (1.92) and (1.93) and based on fixed evaporation Schmidt and Prandtl numbers are no longer used. These numbers are now directly computed from the transport and thermodynamic properties of the gaseous phase:

$$Sc_F = \frac{\mu}{\rho_g D_F} \qquad Pr = \frac{\mu C_p}{\lambda} \tag{12.11}$$

The mixtures properties vary depending on the mixture composition using mixing laws and D_F[3] is computed from the liquid composition with Eq. (12.12):

$$D_F = \sum D_\kappa \frac{X_\kappa}{\sum X_\kappa} \tag{12.12}$$

Thus, preferential evaporation effects on the transport properties are taken into account. The computation is done using the individual species properties D_κ, μ_k, λ_k and $C_{p,k}$ that are derived from polynomial expressions available in [Yaws 2015]. The reference temperature and composition are taken with a $1/3 - 2/3$ law from the surface and infinity states as in Eq. (1.94) and (1.95).

Validations

The multi-component evaporation model described above has been first validated against experiments [Shastry et al. 2020, Shastry 2022]. Wilms [2005] has conducted extensive experimental studies on evaporation of freely falling tri-component droplets. The comparison of the Normalized Diameter (ND) evolution between experimental measurements and AVBP model are reported on Fig. 12.1.1. In this validation case, the initial droplet size is $d_{p,0} = 100\,\mu m$ and the gaseous temperature is set to $T_{g,0} = 300\,K$. The results show a very good agreement between the model prediction and the experimental measurements.

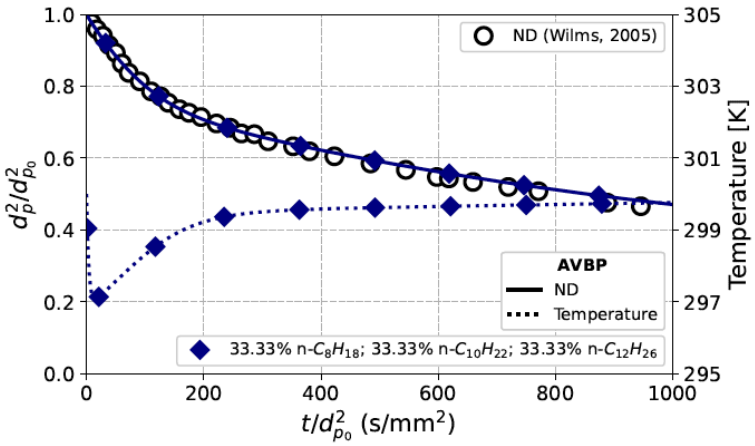

Figure 12.1.1: Validation of the multi-component evaporation model against data from Wilms [2005] (extracted from Shastry [2022]).

Another comparison with a numerical study from Ra and Reitz [2009] has been performed. In this second case, seven species are considered to model a Diesel fuel. The initial droplet size is $d_{p,0} = 100\,\mu m$ and the gaseous temperature is set to $T_{g,0} = 500\,K$. The evolution of the liquid droplet internal composition is presented on Fig. 12.1.2 and very similar results are observed with the AVBP model.

[3]Note that D_F has not a physical meaning since in reality each fuel component diffuses at its own speed. D_F corresponds here to a mathematical tool accounting for the average diffusion of the multi-component fuel.

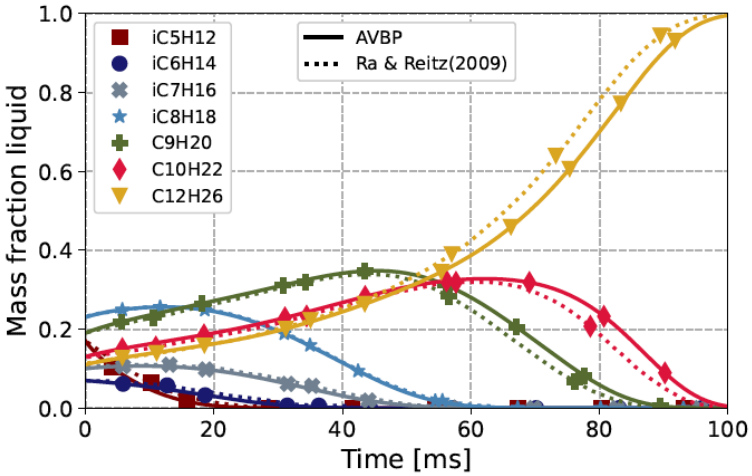

Figure 12.1.2: Validation of the multi-component evaporation model against data from Ra and Reitz [2009] (extracted from Shastry [2022]).

The multi-component evaporation model is developed assuming an infinite liquid heat conduction, but also an infinite liquid species diffusion. As a consequence, the droplet composition is homogeneous. In the case of slow evaporation, as in the above validation cases, the internal diffusion flux is able to compensate the evaporation of the volatile species at the surface. Furthermore, a non quescient gaseous flow around the droplet may create an internal liquid recirculation, leading to a homogeneous droplet composition. Therefore, in these cases, the infinite species diffusion assumption is realistic and provides good results. However, in combustion cases, the evaporation rate is increased due to the high gaseous temperatures around the droplet. Therefore, the internal diffusion flux may not be able to compensate the volatile species depletion at the outer droplet layer. In this case, the species diffusion in the droplet must be taken into account and the droplet cannot be considered homogeneous [Law 1978, Lasheras et al. 1980]. A reduction of the preferential evaporation effect is expected due to the depletion of the volatile species at the droplet surface, or in the most critical cases droplet breakup may occur due to internal boiling. The species diffusion and internal recirculation induced by the surrounding flow should be evaluated in future works.

12.1.2 Saturation

In the above cases of droplet evaporation in ambient conditions, the saturation of the most volatile species has never been reached. In flames, since the evaporation starts in the pre-heat zone, the droplet generally becomes mono-component if and when it reaches the hot burnt gases. In this case, the saturation is not an issue and is treated as in the mono-component case (see Sec. 1.3.4), with a droplet temperature that stabilizes at T_{wb}.

However, in two-phase ignition, the multi-component droplet may be directly in contact with a very hot gaseous mixture ($T > 2500\,K$) due to the energy deposit. In this case, the most volatile species does not have enough time to evaporate and the droplet temperature may exceed the wet-bulb temperature of the most volatile species. For example, using two liquid fuel species, several scenarios are possible[4] The subscript *1* refers to the most volatile fuel and *2* to the second fuel component:

- $T_{wb,1} < T_p < T_{boil,1} < T_{wb,2}$:
  In this case, the saturation pressure of the volatile species is still lower than the ambient pressure ($P > P_{sat,1}$). The droplet temperature can stabilize at an intermediate temperature $T_{wb,1+2}$[5] depending on the physical properties of both species and the gaseous surrounding temperature. Hence, no additional treatments are required for this scenario. This configuration may also be found in spray flames when droplets cross the flame front, and explain why saturation related issues have

[4]The behaviors and corrections presented in the following can be generalized to a droplet composed of more than two species.

[5]Here the subscript *1+2* refers to a state corresponding to the presence of the two fuels (i.e. $T_{wb,1+2} \neq T_{wb,1} + T_{wb,2}$)

not been encountered before.

- $T_{wb,1} < T_{boil,1} < T_p < T_{wb,2}$:
  For higher temperature environments, the heat flux is more important and the droplet temperature may exceed the boiling temperature of the volatile component. In this second case, the saturation pressure of the volatile species becomes higher than the ambient pressure ($P_{sat,2} < P < P_{sat,1}$). This case is not physical because using the Raoult's law leads to $X_{1,\zeta} > X_{1,liq}$ or even may lead to $X_{1,\zeta} > 1$. In this scenario, an additional treatment must be added to avoid this unphysical behavior.

- $T_{wb,2} < T_p$:
  This case is not theoretically possible because the evaporation of the most volatile component (1) induces a greater energy loss compared to the case with only the second component (2).

In this work, the second scenario has been encountered during ignition simulations, for droplets initially located at the center of the energy deposit. In such cases, B_M diverges towards infinity.

To avoid this numerical behavior, a first approach is to consider that the evaporation is limited by the most volatile species. In this batch distillation approach presented on the left picture of Fig. 12.1.3, the droplet temperature follows a step evolution and is limited by the boiling temperature of the most volatile species. In the regime labelled (A), the evaporation is computed with the classical procedure presented in Sec. 12.1.1. In the regime (B), the boiling temperature of the volatile species is reached ($P = P_{sat,1}$). Then, the droplet temperature is kept constant and the evaporation rate is directly computed from the heat flux, as done in the mono-component model with Eq. (1.119) when the wet-bulb temperature is reached. In the regimes (C) and (D) the volatile component is fully evaporated, then the classical mono-component evaporation model applies.

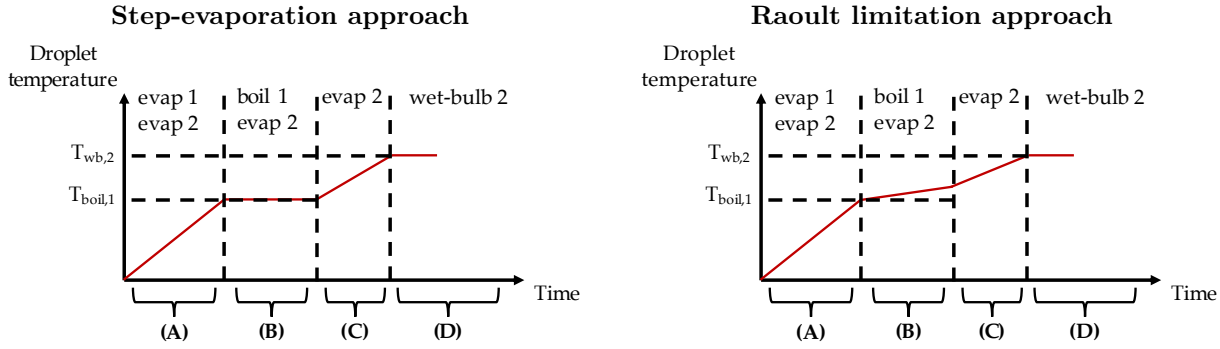

Figure 12.1.3: Droplet temperature evolution depending on the saturation treatment.

However, studies from Law [1978] and Lasheras et al. [1980] show that the droplet temperature can exceed the boiling temperature of the most volatile species. This effect is attributed to the heterogeneity of the droplet during evaporation. Indeed, if the concentration of the volatile component is reduced in the outer droplet layer, the droplet temperature will stabilize at a higher temperature corresponding to the wet-bulb temperature of the second species ($T_{wb,2}$). This temperature can be higher than the boiling temperature of the volatile species ($T_{boil,1}$), especially for large volatility differences. Therefore, a second approach has been used in this work where the droplet temperature is not limited. Instead, the Raoult's law is bounded to the maximum physical value $X_{\kappa,\zeta} = X_{\kappa,liq}$. Hence, in the regime (B) on the right picture of Fig. 12.1.3 corresponding to the saturation of the volatile species, the evaporation rate of this species is maximum while the droplet temperature continues to increase.

This method to account for the multi-component saturation would requires validation against experimental comparison. Furthermore, other phenomena such as internal droplet boiling is not considered. Nevertheless, the multi-component evaporation including the saturation remains more realistic than mono-component evaporation and enables to study the preferential evaporation effects on combustion

as presented in the following section.

12.1.3 Effect of multi-component evaporation on combustion

The effect of preferential evaporation has been recently evaluated in 1-dimensional laminar spray flames. The configuration proposed by Rochette et al. [2019] and presented in Sec. 3.5 has been used by Shastry et al. [2020] with a Jet-A1 3-components surrogate using an ARC mechanism to emphasise the effects of the multi-component description. Several cases have been studied where the gaseous and liquid equivalence ratios, the droplet relative velocity and the droplet size are varied.

In the case of weakly evaporation-controlled flames, i.e., when the gaseous mixture is flammable before reaching the flame, the correlation Eq. (3.52) is adapted to the multi-component formalism and writes now:

$$\phi_{eff} = \sum_{\kappa=1}^{N_{liq}} \left(\frac{\delta_{th}}{\max\left(\delta_{evap,\kappa}, \delta_{th}\right)} \right)^{\frac{2}{3}} \left(\frac{s_{X,\kappa}}{s_{X,F}} \right) \times \phi_l + \phi_g \tag{12.13}$$

with $\delta_{evap,\kappa}$ the evaporation thickness of the component κ, $s_{X,\kappa}$ its molar stoichiometric ratio and $s_{X,F}$ the molar stoichiometric ratio of the fuel blend.

The correlation for the laminar flame speed estimation was validated by comparing it with simulation results presented on Fig. 12.1.4. In the case of evaporation-controlled flames, this correlation does not work anymore.

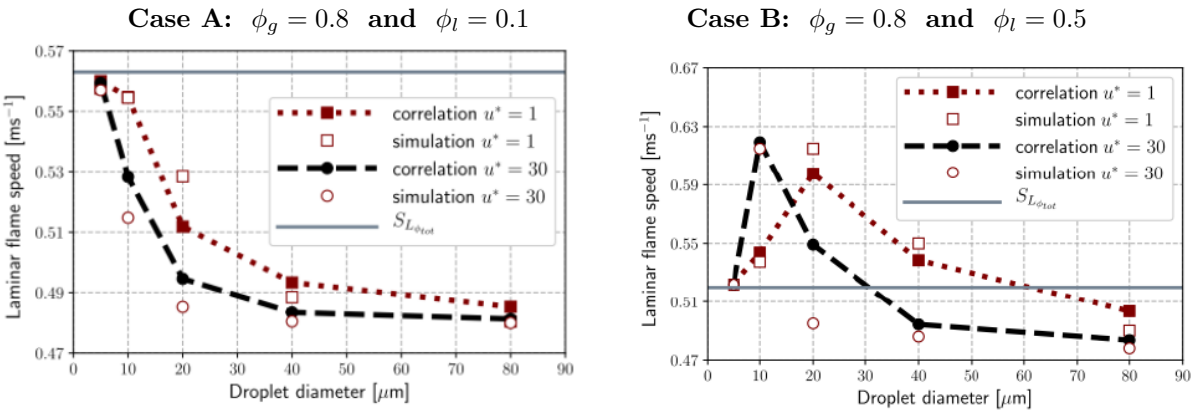

Figure 12.1.4: Comparison of the correlation Eq. (12.13) with simulated flame speed for several droplet sizes and velocities (extracted from Shastry et al. [2020])

This work has been completed in Cazères [2021] where the structure of multi-component spray flames has been studied using the same fuel surrogate as in the present work. The left picture on Fig. 12.1.5 shows the profile of the evaporation rate. The first species to evaporate is methylcyclohexane which is the most volatile species of the blend. Then, it is quickly followed by the xylene. And finally, dodecane is the last species to evaporate. As shown on the right picture, methylcyclohexane is consumed before the flame front while xylene is consumed at the maximum heat release rate. As the evaporation rate peak of these to species lies before or in the flame front, their concentration in the gaseous phase is much higher than in the liquid fuel blend (not shown), which modifies the combustion properties. On the contrary, evaporation and consumption of dodecane happen downstream the flame front, feeding the trailing heat release zone. Because of this slow evaporation, dodecane is not fully contributing to the flame propagation or at a lower level compared to a gaseous flame. However, dodecane is much more reactive than xylene which is a stable species. Therefore, in a propagating flame, dodecane can react before xylene even if this latter evaporates more upstream [Wirtz 2022].

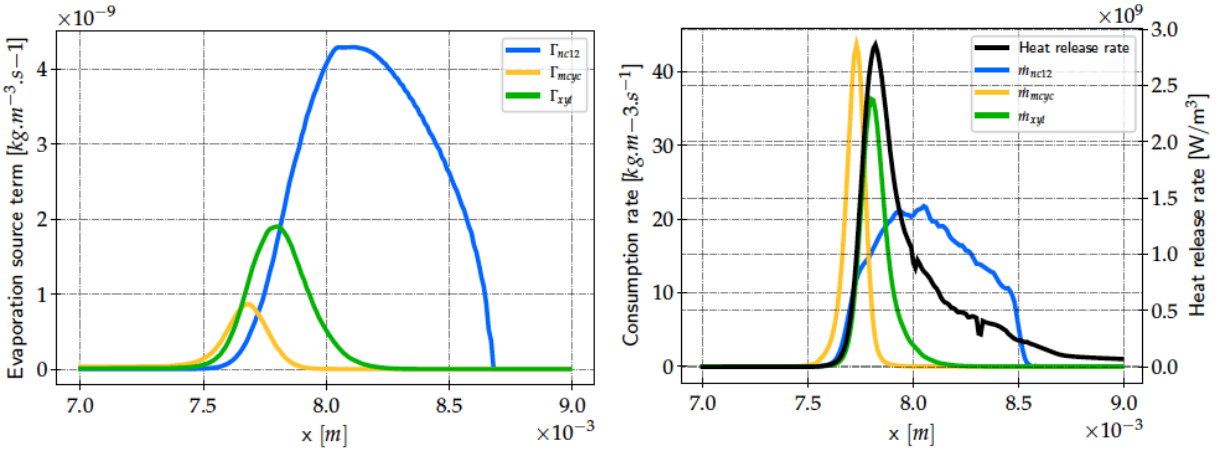

Figure 12.1.5: Evaporation rate profile (left) and fuel species consumption and heat release rate profiles (right) for a 1-dimensional laminar two-phase Jet-A1 multi-component flame (extracted from Cazères [2021]).

12.2 Single droplet evaporation in high altitude conditions

The two-phase ignition phenomenon strongly relies on the presence of flammable mixture at the spark location. Hence, before evaluating the influence of the high altitude conditions on the two-phase ignition, the effect of these conditions on the droplet evaporation process and from a multi-component perspective needs to be investigated.

12.2.1 Numerical set-up

To evaluate the effect of pressure, temperature, and multi-component droplet composition, 0-dimensional simulations of evaporation of an isolated droplet have been performed.

The numerical set-up simply consists in an isolated droplet placed at the center of a cubic, one-cell domain initially filled with still air. Simulations are then 0D, i.e., the gaseous mixture is homogeneous with no convection nor diffusion transport.

Wall iso-thermal boundary conditions have been applied to the cell with a fixed wall temperature $T_w = 2000\,K$. Therefore, the gaseous temperature surrounding the droplet remains fixed at $T_g = 2000\,K$ during the whole evaporation process. Note that this study differs from previous ones in [Cazères 2021, Shastry 2022] because evaporation starts here in a hot environment. This is more representative of the conditions faced by the droplets in the energy deposit volume or in the flame kernel. Note that this temperature does not enable to reach the multi-component saturation condition presented in Sec. 12.1.2[6].

Three conditions have been tested to evaluate the effects of pressure and droplet temperature. These conditions are summarized in Tab. 12.2.1. The case **PTatmo** corresponds to the atmospheric pressure $P = 1\,bar$ and the initial droplet temperature $T_p = 300\,K$. The case **LPTa** corresponds to the low pressure $P = 0.3\,bar$ while keeping the droplet temperature $T_p = 300\,K$. The case **LPLT** corresponds to the low pressure and the low droplet temperature $T_p = 233\,K$. Finally, the case **LPLT-BFER** has the same condition than **LPLT** but the fuel is the KERO-LUCHE surrogate used in the BFER global chemistry [Franzelli et al. 2010]. Thus, for this last case, evaporation is based on the mono-component model presented Sec. 1.3.4.

The cell volume is adjusted so that at the end of evaporation the gaseous mixture is at stoichiometry. For an initial droplet size of $d_{p,0} = 20\,\mu m$, this gives the following cell sizes :

$$\Delta_x(P = 1\,bar) = 326.5\mu m \qquad \Delta_x(P = 0.3\,bar) = 487.9\mu m \tag{12.14}$$

[6]Indeed, the saturation related issues and corrections have been observed and developed for reacting case simulations which are presented in Chap. 13

Label	Pressure $[bar]$	Droplet temperature $[K]$	Gas density $[kg.m^{-3}]$
PTatmo	1.0	300	0.174
LPTa	0.3	300	0.052
LPLT	0.3	233	0.052
LPLT-BFER	0.3	233	0.052

Table 12.2.1: Summary of the studied conditions and corresponding labels

.

Evaporation in a closed volume, as is the case here, leads to a pressure increase. However at $\phi = 1$, the amount of fuel vapor is small compared to the cell volume, and the over-pressure stays negligible ($\Delta P/P \approx 1 - 2\%$).

12.2.2 Results

Droplet temperature

The time evolution of the droplet temperature is presented on Fig. 12.2.1. For all cases, the droplet temperature first increases until reaching an asymptotic value corresponding to the wet-bulb temperature. At this moment, the heat flux from the surrounding gas is exactly balanced with the evaporation endothermic process. As expected, the pressure influences this asymptotic temperature independently from the initial droplet temperature. Low pressure leads to lower wet-bulb temperature, hence promoting evaporation. On the contrary, in the case **LPLT**, the lower initial temperature induces a longer heating time toward the same wet-bulb temperature as the **LPTa** case, which delays the droplet evaporation. Low pressure and low temperature conditions have then opposite influences.

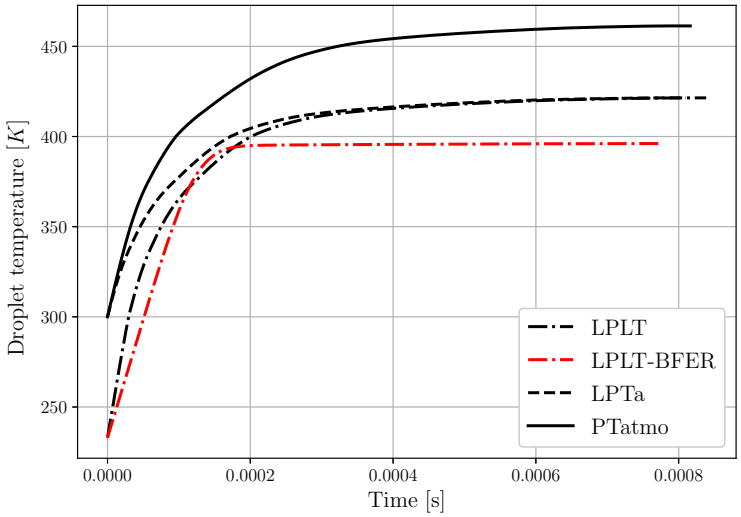

Figure 12.2.1: Evolution of the droplet temperature for an isolated evaporating droplet for the 4 cases of Tab. 12.2.1.

In the mono-component case, the droplet temperature increase is slower. However, the wet-bulb temperature is lower and thus reached faster. Consequently, the evaporation is faster. This behaviors is not attributed to the evaporation model, but to the physical properties of the KERO-LUCHE fuel which are different from those of the multi-component surrogate. The difference between mono-component and multi-component fuels can be appreciated from the shape of the temperature evolution profile, with a smoother transition to the wet-bulb temperature in the cases **LPLT**, **LPTa** and **PTatmo** whereas the case **LPLT-BFER** shows two distinct phases.

In the following, the direct comparison between cases **LPLT** and **LPLT-BFER** is not possible due to the physical fuel properties. However this comparison enables to qualitatively appreciate the effect of the

evaporation model in AVBP.

Droplet diameter

The evolution of the droplet diameter is presented on Fig. 12.2.2. Overall all profiles are very similar. For the case **LPTa**, evaporation is slightly faster compared to **PTatmo** because of the lower wet-bulb temperature at low pressure. For the case **LPLT**, the diameter evolution is initially similar to the case **PTatmo** which confirms that low temperature and low pressure compensate. However, the end of the evaporation is faster in the **PTatmo** case.

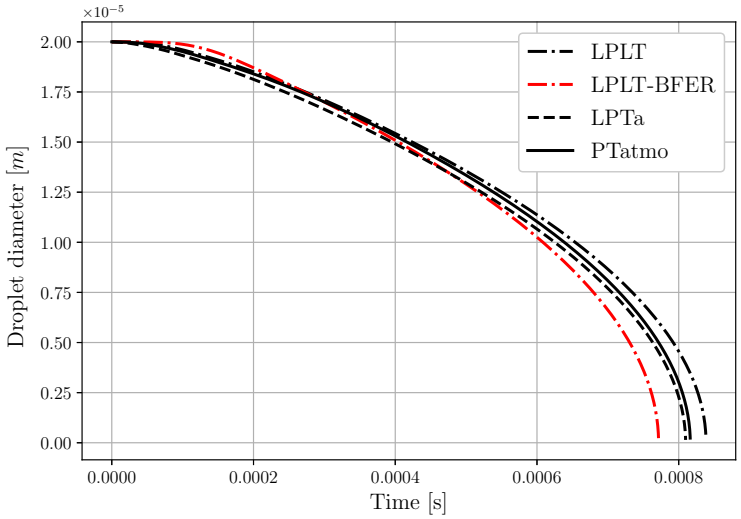

Figure 12.2.2: Evolution of the droplet diameter for an isolated evaporating droplet for the 4 cases of Tab. 12.2.1.

In the mono-component case, the droplet diameter initially takes a longer time to decrease. This is because there is no volatile component that evaporates at low temperature and also because the droplet temperature increase phase is longer. However, once the wet-bulb temperature is reached, the diameter decrease is faster and the case **LPLT-BFER** is the first to fully evaporate.

To summarise, low pressure reduces the evaporation time, however the difference is negligible in terms of total evaporation time. The initial low temperature of the droplet has a larger influence than low pressure but remains very small. In brief, one can note that high altitude conditions have a smaller influence on evaporation than fuel modeling.

Evaporation rates

Thanks to the multi-component formulation, the evaporation rate of each liquid species can be evaluated. Figure 12.2.3 shows on the left the individual component mass fractions in the evaporation flux ε_κ and on the right the resulting species evaporation rates $\dot{m}_{p,\kappa}$.
The first species to evaporate is methylcyclohexane (MCYC6) which is the most volatile, quickly followed by xylene (XYL). However, the mass fraction peak corresponding to these species happens very soon during the heating phase of the droplet and when the total evaporation rate is still low. Thus, even though the evaporation of these species occurs first, their evaporation rate remains low. At their peak, their evaporation rate is two times lower than the one of dodecane (NC12) which is the main component of the surrogate (60% in volume).

In this specific ignition case, the temperature increase is fast, therefore the peak of MCYC6 and XYL evaporation rates occur at the same time. On the contrary, the peak of NC12 evaporation rate appears later as it is the less volatile species.

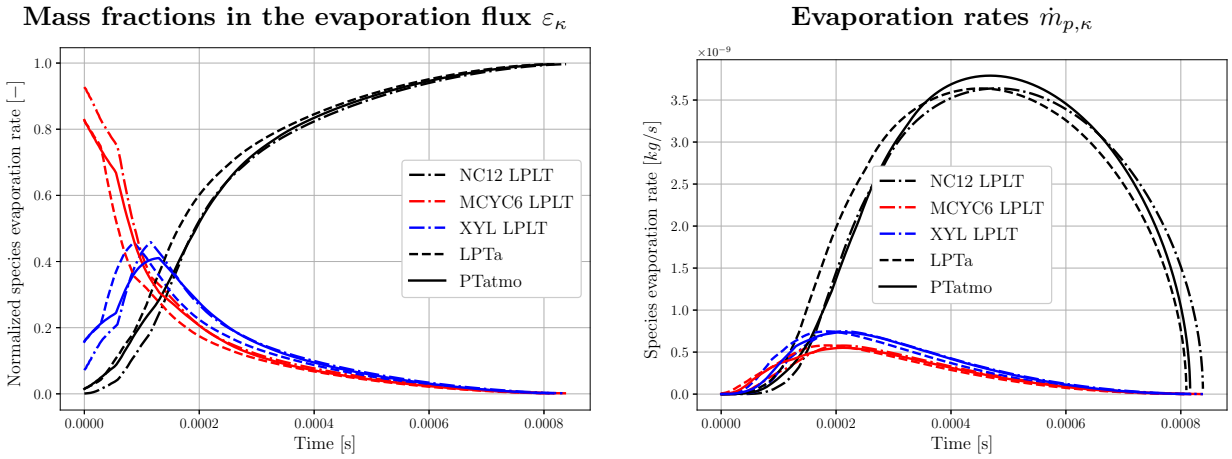

Figure 12.2.3: Evolution of the species evaporation rates for an isolated evaporating droplet for the 3 multi-component cases of Tab. 12.2.1. (–) **PTatmo**, (––)**LPTa** and (– · –)**LPLT**.

The individual component mass fractions in the evaporation flux show that the low droplet initial temperature favours MCYC6 evaporation, however the impact is negligible due to the low total evaporation rate at this moment. In cold gaseous conditions with long residence characteristic time (droplets in recirculation zones for instance), MCYC6 is expected to evaporate first. The comparison of **PTatmo** and **LPTa** cases shows that there is no pressure effect on the preferential evaporation. The low pressure triggers the evaporation sooner but in a same way for all species. To conclude, the effect of both pressure and temperature on preferential evaporation is limited and can be reasonably neglected in ignition.

It is interesting to note that the maximum NC12 evaporation rate is higher in the atmospheric case whereas low pressure is supposed to enhance evaporation. This may be explained with Eq. (12.7) which indicates that the evaporation rate depends on both gaseous density and Spalding number B_M. Both quantities change in opposite ways at low pressure, with a slight advantage for the gas density in the present case. This explains why the droplet diameter decreases faster in the **PTatmo** case compared to **LPLT** whereas the initial evolutions are superimposed. This effect adds to the temperature effect and explains why low pressure finally has a limited influence.

Liquid and Gaseous phase compositions

The multi-component approach also enables to follow the evolution of the droplet composition. Figure 12.2.4 shows that the droplet composition is very similar for all cases, and the pressure and temperature conditions have a limited influence. Since MCYC6 and XYL are the first species to evaporate, the NC12 liquid mass fraction keeps increasing during the whole evaporation process.

Similarly, the pressure and temperature conditions have a limited influence on the gas composition evolution, as shown in Fig. 12.2.5. At the first instants, the gaseous fuel is only composed of the volatile species MCYC6 and XYL. However, the corresponding equivalence ratio is too low to enable the combustion processes. Once the lean flammability limit is reached ($\phi_g = 0.5$), the evaporation of NC12 is already larger than the volatile compounds. At this time, the gaseous fuel is composed of 50% NC12, 25% MCYC6 and 25% XYL (in mass). This particular composition has been tested for the ARC mechanism in Chap. 7 and has shown very good agreement for auto-ignition times.
Since this fuel blend is mainly composed of NC12 and MCYC6 (75% in mass) which share common chemical pathways (see Chap. 7), the chemical behavior should not be drastically changed and the preferential evaporation effect on chemistry should remain limited in the case of ignition. Compared to the reference surrogate composition, the xylene content is increased by 10%. The effect of composition variations on the auto-ignition time is shown on Fig. 12.2.6. Significant increases of auto-ignition times are observed for low NC12 contents only ($Y_{NC12} < 0.4$).

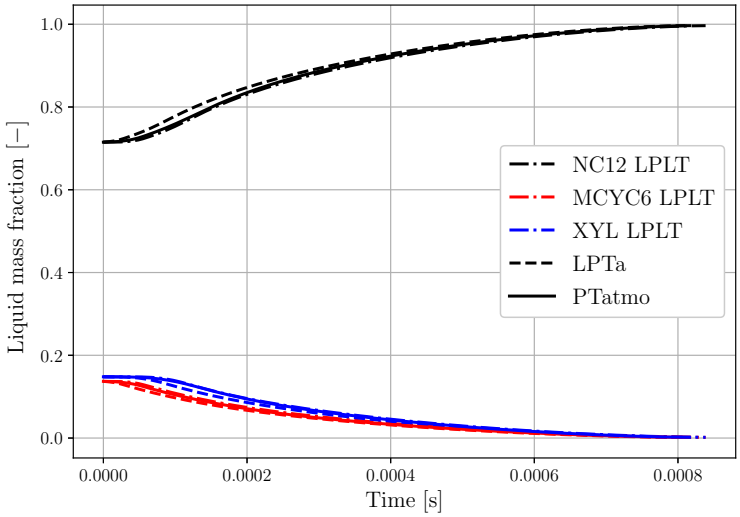

Figure 12.2.4: Evolution of the droplet liquid composition for the 3 multi-component cases of Tab. 12.2.1. (–) **PTatmo**, (––)**LPTa** and (– · –)**LPLT**.

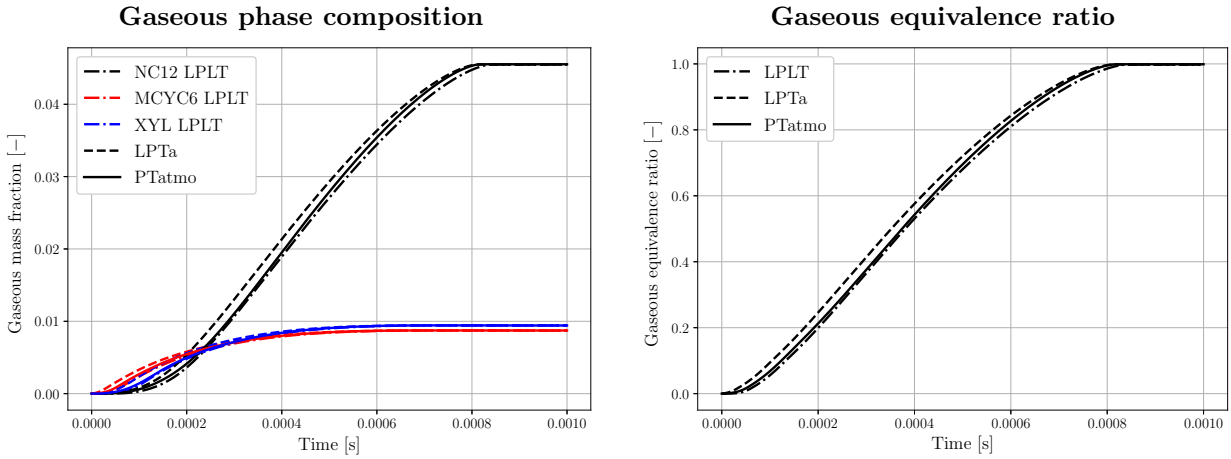

Figure 12.2.5: Evolution of the gaseous phase composition (left) and equivalence ratio (right) for an isolated evaporating droplet for the 3 multi-component cases of Tab. 12.2.1. (–) **PTatmo**, (––)**LPTa** and (– · –)**LPLT**.

12.2.3 Conclusions

The results presented above correspond to an initial droplet size $d_{p,0} = 20\,\mu m$ but the same study was also conducted for other droplet diameters leading to the same observations. The droplet evaporation time depending on the initial droplet size is presented on Fig. 12.2.7 for the conditions **LPLT** and **PTatmo**. For the cases **LPTa** and **LPLT-BFER** the results are only presented for $d_{p,0} = 20\,\mu m$ and $d_{p,0} = 100\,\mu m$.

The results of this chapter show that low pressure slightly reduces the evaporation time by reducing the wet-bulb temperature. On the contrary, low droplet temperature increases the evaporation time due to a longer droplet heating phase. For the conditions studied here which are representative of high altitude, the temperature effect is stronger resulting in a longer evaporation time in the conditions **LPLT** compared to **PTatmo**. However, the influence of low pressure and low temperature is negligible compared to the influence of the initial droplet diameter. Hence, the main effect of high altitude conditions on the two-phase ignition process lies in the formation of larger droplets at fuel injection, as shown in Chap. 11.

Indeed, comparing the droplet evaporation times with the characteristic times observed in the DNS of Chap. 9 (lower than 1 millisecond), indicates that only the droplets with a diameter lower than

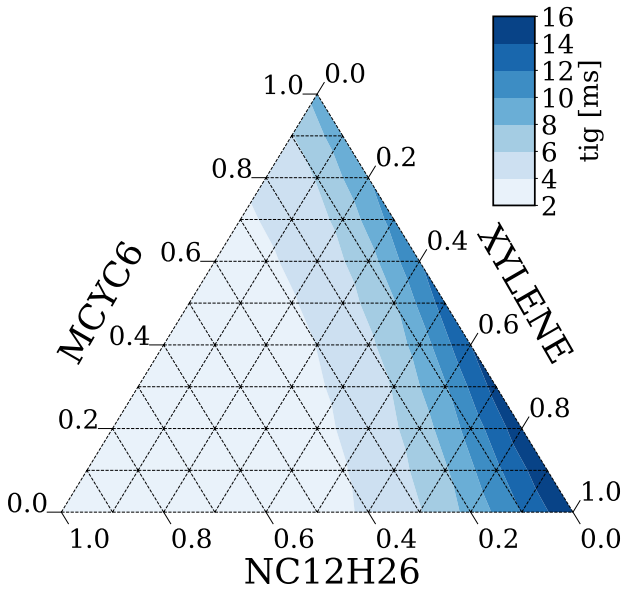

Figure 12.2.6: Auto-ignition time τ_{ig} triangle plots for $T = 1200\,K$, $P = 1\,bar$ and $\phi = 1$ depending on the fuel composition (extracted from [Wirtz 2022]).

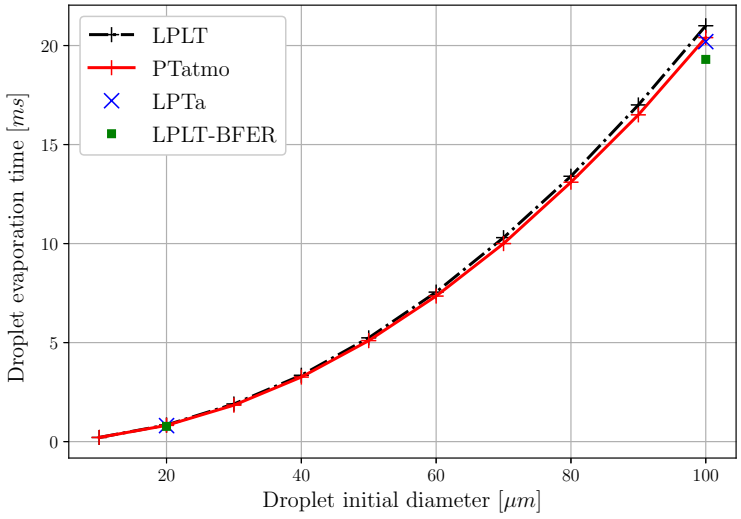

Figure 12.2.7: Evaporation time versus initial droplet diameter for an isolated droplet and $T_g = 2000\,K$ for the 4 cases of Tab. 12.2.1.

$d_{p,0} = 20 - 30\,\mu m$ participate to ignition and kernel formation. For larger droplets, the heating time, and thus the evaporation time are higher than the dissipation time of the energy deposition. Therefore fuel vapor is not sufficiently produced and the combustion reactions can not start. In addition, large droplets remove heat from the gaseous phase which promotes ignition failure.

Finally, the influence of low pressure and low temperature on the preferential evaporation was found also negligible. Furthermore, in high temperature ignition conditions ($T > 2000\,K$), the preferential evaporation effect appears to be less important than in flame propagation. However, it is worth recalling that, when the mixture becomes flammable, the quantity of volatile species is larger than in the liquid fuel blend. This effect on the kernel propagation remains to be determined.

Chapter 13

Two-phase ignition

Contents

In the previous chapters, it has been shown that the high altitude conditions tend to increase the characteristic droplet size at the fuel injection and that the droplet evaporation time is largely driven by the droplet diameter while low pressure and low droplet temperature have a limited influence. In this chapter, the effect of high altitude conditions on the two-phase ignition of a cloud of droplets with a realistic size distribution is evaluated.

The numerical set-up and parameters of this study are firstly presented in Sec. 13.1. Then, in Sec. 13.2, issues related to the numerical stiffness of the two-phase ignition are described with the stabilisation methods used in the present simulations. The results of the two-phase ignition simulations are presented in Sec. 13.3 with a description of the chemical processes, the influence of the droplet size distribution and the effect of pressure and temperature conditions. Finally, results summary and future works perspectives are given in conclusion in Sec. 13.4.

13.1 Numerical set-up

13.1.1 Spherical bomb configuration

To study ignition in the presence of droplets, a simple spherical bomb configuration has been used, illsutrated in Fig. 13.1.1. The domain corresponds to a spherical volume of 5 cm radius in which a droplet cloud is initialized in quescient air. This domain size is chosen so as to enable the kernel development at the center while limiting the computational cost. The ignition is triggered with an energy deposit at the center of the domain as was done in Chap. 9. Hence, this configuration enables to study the heating, evaporation and ignition of the droplets in the hot kernel, and then the kernel radial propagation in the droplet mist. In this case the flow stays laminar, while the influence of turbulence will be tackled in Chap. 14.

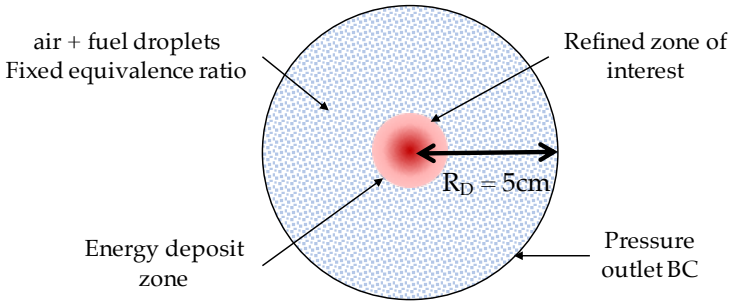

Figure 13.1.1: Configuration for the study of ignition in a spherical bomb.

As shown in Fig. 13.1.2, the grid is composed of tetrahedral elements. The zone of interest corresponds to a spherical volume of 5 mm radius and is discretized with a constant characteristic cell size. Then, the cell size is progressively increased towards the outlet, where a pressure condition is applied with the NSCBC formalism [Poinsot and Lelef 1992].

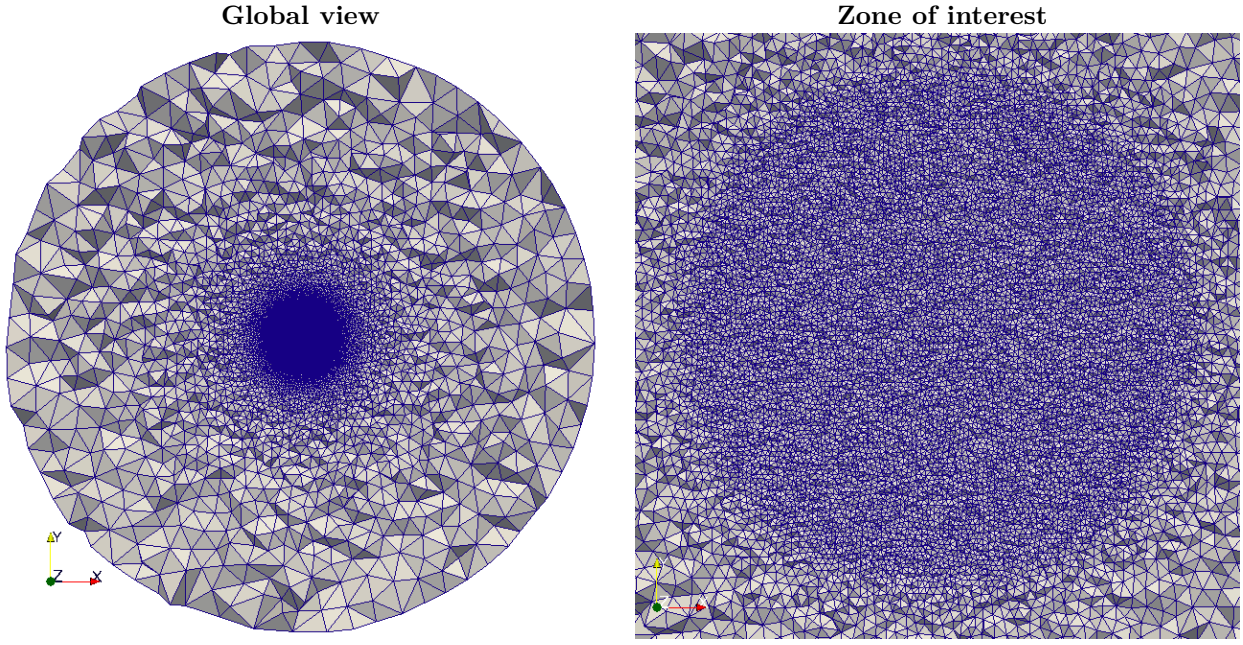

Figure 13.1.2: Visualization of the mesh: whole domain (left); zoom on the zone of interest (right).

Finally, the combustion chemsitry is described with the ARC mechanism S30R299QSS22 developed in Chap. 7 for the Jet-A1 kerosene tri-component surrogate presented in Chap. 2. The droplet evaporation is computed with the discrete multi-component model introduced in Chap. 12.

13.1.2 Cases and parameters

For this study, three cases have been performed, varying the ambient condition and the dispersed phase properties. Tables 13.1.1 and 13.1.2 summarize the properties of the gaseous and liquid phases for the 3 cases, which are all at stoichiometry ($\phi_{tot} = 1$).

PTatmo is the reference case corresponding to atmospheric conditions. The case **LPLT** enables to study the effect of high altitude conditions for the same spray. However because of the lower density, a lower number of droplets is initialized to keep stoichiometry. The resulting droplet initial distributions are presented on Fig. 13.1.3
Finally, the case **LPLT-mono** allows to evaluate the effect of size poly-dispersion. However the same SMD of 60 μm could not be used because this value always failed to ignite with a mono-disperse spray. This indicates the critical role of the small droplets in the poly-disperse sprays of cases **PTatmo** and

Label	Pressure $[bar]$	Temperature $[K]$	Density $[kg.m^{-3}]$
PTatmo	1.0	300	1.16
LPLT	0.3	233	0.45
LPLT-mono	0.3	233	0.45

Table 13.1.1: Summary of the gaseous conditions for the 3 test cases.

Label	Size distribution	SMD $[\mu m]$	Shape $q\,[-]$	Total droplet number
PTatmo	Rosin-Rammler	60	1.8	919
LPLT	Rosin-Rammler	60	1.8	354
LPLT-mono	Mono-dispersed	10	-	38746

Table 13.1.2: Summary of the liquid conditions for the 3 test cases.

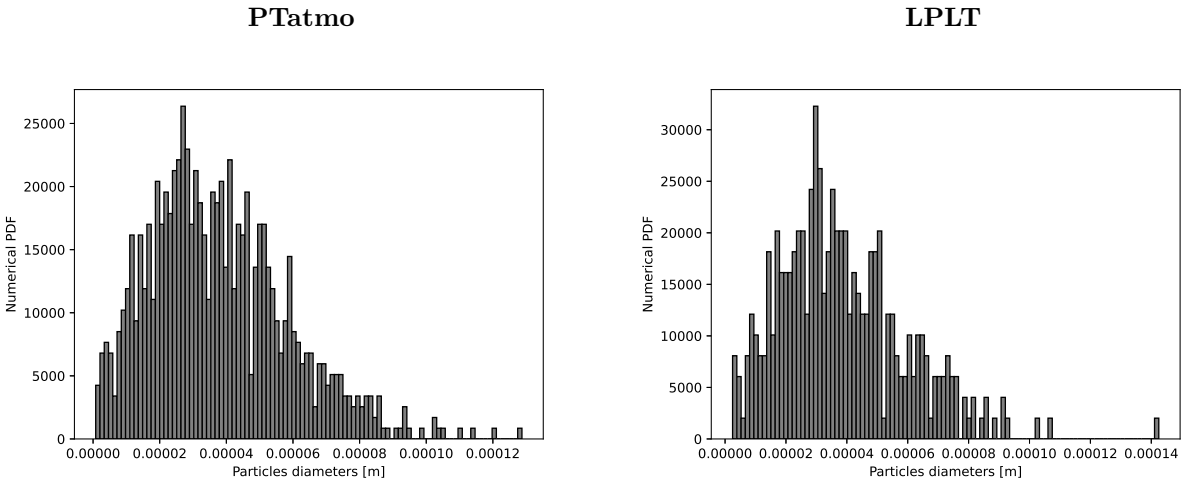

Figure 13.1.3: Initial droplet size distributions for cases **PTatmo** and **LPLT** .

LPLT. To ensure ignition, a constant droplet size $d_p = 10\,\mu m$ was finally chosen for case **LPLT-mono** which corresponds to a characteristic evaporation time of the order of the energy deposition delay.

For all cases, the initial droplet temperature is equal to the gaseous temperature. No fuel vapor is initialized in the the gaseous phase so that the liquid equivalence ratio initially corresponds to the total equivalence ratio.

The discretization of the zone of interest is sufficiently refined to avoid the use of a thickening model[1]. The grid parameters are summarized in Tab. 13.1.3. The mesh visualization on Fig. 13.1.2 corresponds to the cases **LPLT** and **LPLT-mono**.

Label	Grid size $\Delta_x\,[\mu m]$	Number of points in the flame front $[-]$	$N_{cell}\,[million]$
PTatmo	50	8	25.95
LPLT	100	10	4.61
LPLT-mono	100	10	4.61

Table 13.1.3: Mesh parameters

The ignition is triggered with the same energy deposit model used in Chap. 9. However, due to the liquid state of the fuel the input energy, and thus the deposition size, must be largely increased compared to the gaseous case. Otherwise, heat diffuses before the droplets start evaporating and burning (not shown). The parameters of the energy deposit used in these cases are presented in Tab. 13.1.4. The input energy is deliberately large to ensure ignition success and the kernel development. As for the gaseous study in Chap. 9, the input energy is larger in the atmospheric case due to the higher density. Because of

[1] Flame thicknesses are respectively $\delta_{th}^{LPLT} = 1 \times 10^{-3}\,m$ and $\delta_{th}^{PTatmo} = 4 \times 10^{-5}\,m$ (see Chap. 5)

the Gaussian shape, the major part of the energy is deposited in a smaller spherical volume of radius $R_{ED} = 7.2\,mm$. This radius is chosen to avoid a kernel temperature higher than $T_{ED,max} = 3500\,K$[2].

Label	$\varepsilon_i\,[mJ]$	$\Delta_s\,[cm]$	$2\Delta_t\,[\mu s]$
PTatmo	520	2	100
LPLT	200	2	100
LPLT-mono	200	2	100

Table 13.1.4: Parameters of the energy deposition model

All simulations have been performed with the AVBP solver introduced Sec. 1.2. Additional gaseous cases have also been performed with the same conditions as for the DNS of Chap. 9 but with the AVBP solver instead of NTMIX and with the meshes presented in this current section. The results are not presented because they are similar to the previous DNS studies. However these cases enable to validate the grid comparing the results with the DNS studies done with NTMIX.

13.2 Handling numerical stiffness

Two-phase ignition appeared to be a very stiff process as illustrated in the next section. Methods to handle this stiffness are then proposed.

13.2.1 Numerical issues

Figure 13.2.1 illustrates the occurrence of large local heat release rate variations and pressure fluctuations at the droplet locations. This mainly originates from a coupling between the droplet evaporation and the chemical reactions[3].

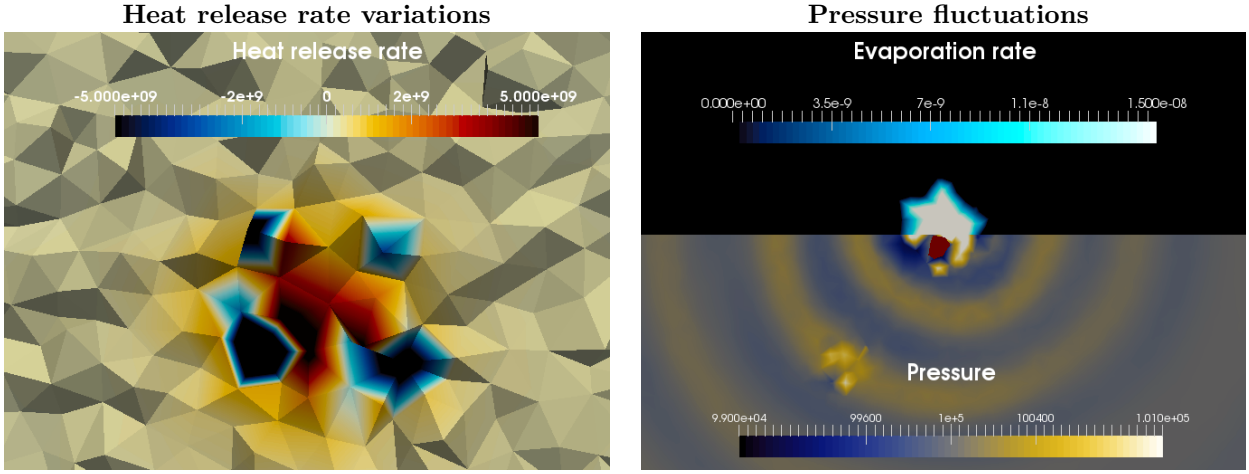

Figure 13.2.1: Illustration of numerical issues on heat release rate and pressure fields.

Simulating two-phase ignition with a Lagrangian formalism leads to a dilemma for the spatial discretization. Indeed, on one side, the ARC mechanism requires small cell sizes of the order of $\Delta_x = 25\,\mu m - 100\,\mu m$ for a correct representation of the chemical processes (there are several radical production/consumption peaks in the flame front). On the other side, the Lagrangian point source approximation leads to too concentrated phase-exchange source terms if the cell size is too small. Looking at the droplet size distribution of Fig. 13.1.3, some droplets reach a diameter around $100\,\mu m$ which is of the same order of magnitude or even higher than the typical cell size. Numerically, this translates in over-pressure in the cell containing the evaporating droplet and isolated fuel point sources of large amplitude.

[2]Higher temperatures would require smaller time steps to solve the diffusion and chemical processes which increases the CPU-cost.

[3]These processes have been evaluated separately without any numerical issue.

Chemsitry adds to the problem, as the large amount of fuel vapor located in one cell directly pyrolyses, creating a strong negative heat release rate at the droplet position. The pyrolysis products then oxidize, creating a positive heat release rate around the droplet. Hence, large variations of the heat release rate are observed as shown on the left picture of Fig. 13.2.1. Contrarily to the gaseous case where the pyrolysis processes happen only at the beginning of the ignition and homogeneously in the whole kernel, for the two-phase configuration, pyrolysis is continuously fed by the droplet evaporation and occurs only at the droplet position. The heat release rate variations then cause temperature and pressure fluctuations that can raise numerical issues.

Pressure fluctuations retrospectively influence the evaporation process by artificially reaching saturation conditions, possibly leading to an unstable behavior.

Note that in the previous study on two-phase ignition of [Collin-Bastiani 2019], none of these issues was observed to be critical. The main reason is that in this study, pre-heated air ($T_g = 416\,K$) was used and the fuel was heptane, which is more volatile than kerosene. Then, part of the fuel was already gaseous at the time of ignition, reducing the influence of droplet evaporation. Moreover, the droplet characteristic size was smaller ($d_{p,32} \approx 30\,\mu m$) and heptane has a much lower endothermic pyrolysis phase. Finally, heptane chemistry required coarser mesh, reducing the impact of the point source approximation.

13.2.2 Numerical methods for two-phase ignition

The above numerical issues arise from the point source approximation, and the ARC chemical stiffness, especially linked to fuel pyrolysis. Hence, several methods have been developed and used to allow the simulation of two-phase ignition.

Point source correction

The first solution to handle numerical issue due to the point source approximation was presented in Sec. 1.3.5 and consists in distributing the evaporation source terms over a larger number of cells around the droplet position. However, for non-structured codes like AVBP, this procedure is very CPU-costly. Indeed, at each iteration and for each particle, the cells close to the particles have to be identified. Typically this method led to an increase of CPU-cost by a factor five, which is not affordable for the present simulations.

An alternative solution proposed in this work is based on the R-parcel approach introduced in Sec. 1.3.5, considering $\mathcal{R}_p < 1$. Hence each numerical particle represents a fraction of a physical one. The "parent" droplet with initial R-parcel parameter $\mathcal{R}_{p,p}$ is burst in N_c child droplets with $\mathcal{R}_{p,c} = \mathcal{R}_{p,p}/N_c$. These child droplets are randomly dispersed around the initial parent droplet position, forming a droplet cluster of radius R_b. Following Eq. (1.133), each child droplet has a reduced evaporation rate, ensuring that the total evaporation rate of the cluster is equal to that of the parent droplet. Since the child droplets are dispersed around the initial parent droplet position, the evaporation source term is automatically spread over several cells around the parent droplet position. The method is illustrated on Fig. 13.2.2.

This method is equivalent to the first solution since the result corresponds to a distribution of the evaporation terms over several cells. However, the identification of the neighbouring cells is much more efficient, as they are linked to the child droplets. The over-cost of the method is only due to the new droplet formation. However, in the case of ignition the droplet bursting procedure is applied to a limited number of droplets, localized in the small region of energy deposit. For example, in the MERCATO application presented in Chap. 14 the total droplet number is increased by maximum 10% resulting in an almost negligible total over-cost (estimated at 3% maximum).

In the following simulations, the method is applied with $N_c = 100$ and a bursting radius $R_b = 2\Delta_x$. Additional studies are required to determine possible generic parameter values depending on the cell size, the droplet diameter, and the droplet number density. Note that there is also a constraint on the bursting radius depending on the gaseous flow. Indeed, all the child droplets must face similar flow conditions to remain clustered during the evaporation time and to avoid dispersion far from the cluster center of mass.

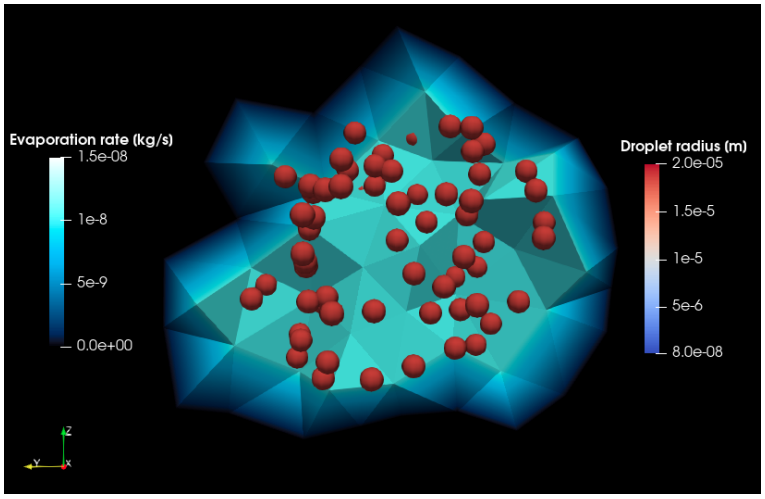

Figure 13.2.2: Visualization of a cluster of child droplets and evaporation rate distribution over several cells using the R-parcel point source correction method. This field is extracted from the **PTatmo** case.

Sub-cycling of chemistry

Chemistry sub-cycling is used, following the LDSC procedure introduced in Sec. 8.3. For this study, the LDSC parameters are : $SC_{max} = 1000$ and $\Delta t_{chem,user} = 0.01\,ns$.

The over-cost with the LDSC method is limited since the sub-cycles are only applied at the droplet clusters where combustion reactions occur. An example of the sub-cycling number field is given on Fig. 13.2.3. Since the grid is refined around the ignition position, it is automatically partitioned on several processors. Thus, the additional sub-cycles and associated over-costs are well balanced between the processors.

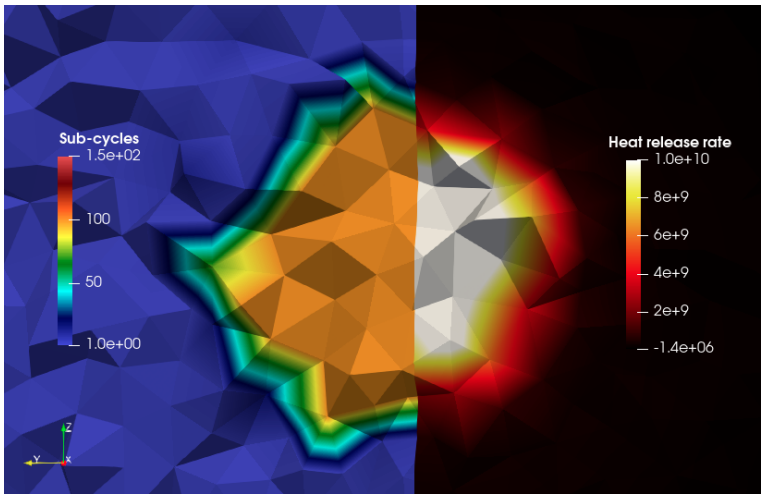

Figure 13.2.3: Sub-cycle number field resulting from the LDSC procedure (left half) and heat release rate (right half). This field is extracted from the **PTatmo** case.

13.2.3 Exponential chemistry integration in the context of two-phase flow

The exponential chemistry presented in Chap. 8 was used in this study and proved to be efficient for the stiff evaporation-combustion coupling.

However, it was found that in some cases it could lead to incorrect chemical evolution. For example, in the case **LPLT-mono**, Fig. 13.2.4 shows a complete conversion of CO into CO_2 between $t = 90\,\mu s$ and

$t = 100\,\mu s$. Since the conversion of CO into CO_2 is an exothermic process, there is also a strong heat release rate resulting in a large increase of the temperature which promotes the kernel development. However, the CO_2 mass fraction level reaches a value around twice higher than the value generally observed in 1-dimensional premixed flame or 0-dimensional constant pressure reactor with similar conditions. After this peak, the CO / CO_2 levels go back to equilibrium through dissociation reactions.

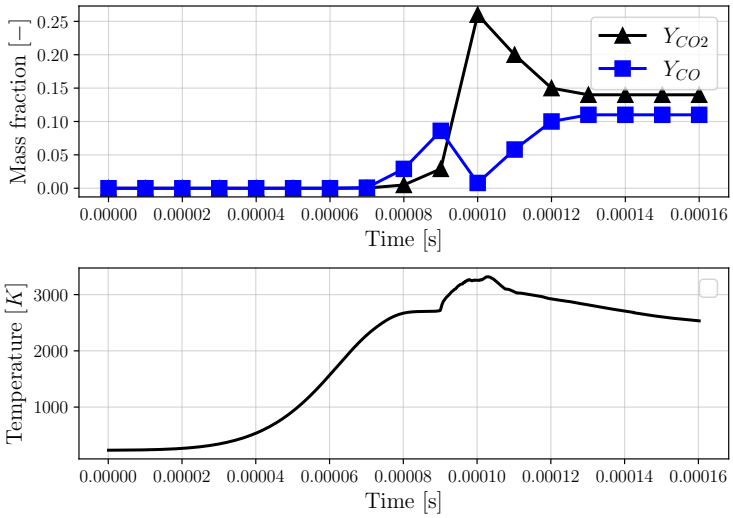

Figure 13.2.4: Evolution of the temperature, CO and CO_2 mass fractions vs time at the center of the domain in the case LPLT-mono.

To evaluate the validity of this chemical trajectory, the gas composition, the temperature and the pressure taken at $t = 90\,\mu s$ have been initialized in the CANTERA 0-dimensional constant pressure reactor and advanced in time. Temperature, CO and CO_2 mass fractions as a function of the time are displayed on Fig. 13.2.5. Contrary to the AVBP simulation with the exponential integration, the CANTERA case does not predict any complete CO consumption. Hence, the CO_2 production is much lower as well as the temperature increase which is about $250K$ instead of $500K$ observed with AVBP.

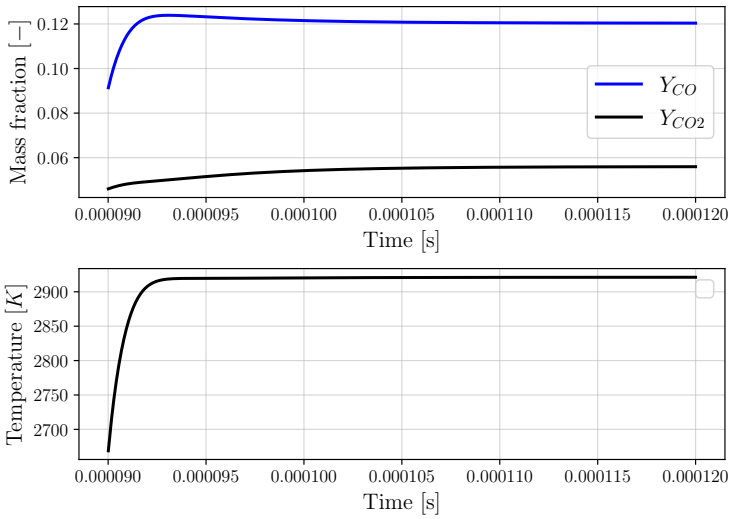

Figure 13.2.5: Time evolution of the temperature, CO and CO_2 mass fractions in a 0-dimensional constant pressure reactor computed with CANTERA. The initial state corresponds to the gaseous state of case LPLT-mono at $t = 90\,\mu s$.

It was found that this wrong CO/CO_2 equilibrium was actually induced by the mass conservation algo-

rithm of the exponential chemistry integration. Indeed, Fig. 13.2.6 shows that if the mass conservation algorithm is disabled, CO is not totally consumed into CO_2. Instead, it accumulates in the kernel as predicted in the CANTERA case[4].

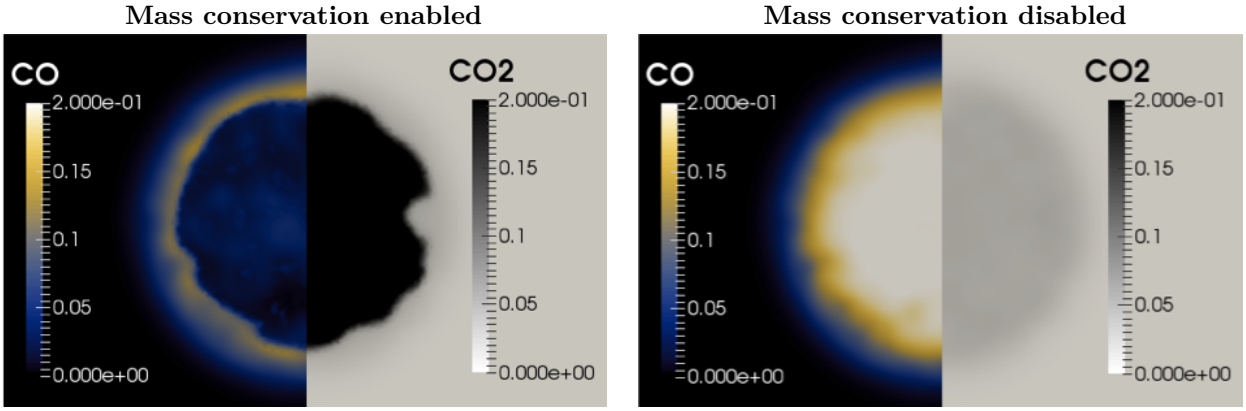

Figure 13.2.6: Effect of the mass conservation algorithm of the exponential chemistry integration on CO/CO_2 equilibrium.

This wrong chemical behavior induced by the mass conservation algorithm is specific to the two-phase ignition. For high temperature droplet combustion, the pyrolysis processes happen continuously until the complete evaporation of the droplet. These processes are very stiff and induce a non-conservative behaviour due to the exponential integration construction. As detailed in Chap. 8, the mass conservation algorithm compensates the non-conservative behaviour by modifying locally the major species. Initially, the major species are pyrolysis products which are also the species linked to the stiff reactions. Hence, the mass conservation algorithm applies the correction to the good species[5]. However, since the pyrolysis reactions continue with the droplet evaporation, there is a critical instant where the major species become the final products such as CO and CO_2. At this moment, the mass conservation compensates the mass excess on CO and CO_2 which causes the chemical system to diverge and leads to the erroneous CO/CO_2 state presented above.

Therefore the mass conservation algorithm must be disabledfor the present simulation of two-phase ignition. To still ensure mass conservation, the atomic balance is verified and compared for both cases between $t = 90\,\mu s$ and $t = 150\,\mu s$ taking into account the gaseous species and the droplet evaporation. The normalized atomic variations $\Delta m^*_{\mathcal{A}}$ computed with Eq. (13.1) are presented in Tab. 13.2.1. These atomic variations are negligible and are of the same order of magnitude for both cases.

$$\Delta m^*_{\mathcal{A}} = \frac{m^{end}_{\mathcal{A},g} + m^{end}_{\mathcal{A},p} - m^{init}_{\mathcal{A},g} - m^{init}_{\mathcal{A},p}}{m^{init}_{\mathcal{A},g} + m^{init}_{\mathcal{A},p}} \tag{13.1}$$

with $m_{\mathcal{A}}$ the mass of element $\mathcal{A}$ in the domain, the subscript $_g$ and $_p$ referring respectively to the gaseous and liquid phase and the index ^{init} and ^{end} referring respectively to the instant $t = 90\,\mu s$ and $t = 150\,\mu s$. This balance is evaluated on the case **LPLT-mono** which is the most critical set-up with the largest initial droplet number.

Mass conservation	$\Delta m^*_{\mathcal{C}}$	$\Delta m^*_{\mathcal{H}}$	$\Delta m^*_{\mathcal{O}}$	$\Delta m^*_{\mathcal{N}}$
Enabled	-8.33×10^{-4}	-9.20×10^{-4}	-3.72×10^{-4}	-3.72×10^{-4}
Disabled	4.68×10^{-3}	5.48×10^{-3}	-3.73×10^{-4}	-3.72×10^{-4}

Table 13.2.1: Atomic balance depending on the activation of the mass conservation algorithm in case **LPLT-mono** and between $t = 90\,\mu s$ and $t = 150\,\mu s$

The overall good atomic conservation, even without the mass conservation algorithm, is explained by the intensive use of chemical sub-cycles with the LDSC procedure. Indeed, it has been shown in Chap.

[4]The CO level is higher in the AVBP case compared to the CANTERA 0-dimensional case because the latter does not take into account the droplet evaporation which progressively increases the equivalence ratio of the mixture

[5]The same explanation holds for gaseous cases

8 that the exponential integration converges towards the standard one which is conservative when the time-step is reduced. In this work the exponential integration associated to the LDSC procedure is still used because it is more stable than standard integration with LDSC as shown in Chap. 8.

13.3 Two-phase ignition

Using the numerical methods presented above, the simulation of two-phase ignition is first performed on the mono-disperse case and presented in Sec. 13.3.1. This set-up is numerically simpler because the droplets are small and quickly evaporate, resulting in a homogeneous gaseous phase.

Then in Sec. 13.3.2, realistic poly-disperse droplet distributions are used to evaluate their effect, and then, the influence of pressure and temperature conditions are presented.

13.3.1 Mono-disperse ignition

Overview

The temporal evolution of maximum temperature and mean heat release rate weighted by the cell volume are displayed on Fig. 13.3.1. These evolutions are similar to the gaseous case. There is a first endothermic ignition phase at $t = 70\,\mu s$ quickly followed by a large increase of heat release rate at $t = 90\,\mu s$ which corresponds to the oxidation processes and leads to the flame front formation. Then, the heat release rate stabilizes at a much lower value corresponding to a flame propagation mode. The kernel maximum temperature also stabilizes around $T_{max} = 2000\,K$ after the end of the energy deposit, which indicates an ignition success.

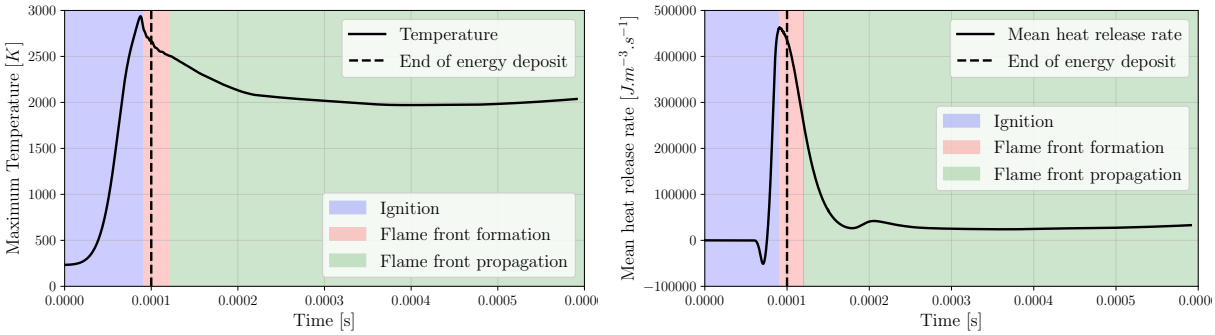

Figure 13.3.1: Temporal evolution of maximum temperature and mean heat release rate for the mono-disperse case **LPLT-mono**.

In the following sections the two-phase combustion mechanisms are detailed for the three ignition phases: (i) until $t = 90\,\mu s$, early ignition, (ii) until $t = 120\,\mu s$, flame front formation, and (iii) until $t = 600\,\mu s$, flame front propagation.

Ignition phase

In this pase,the energy deposit heats the gas, which then heats the droplets through conduction. Evaporation starts when the droplet temperature is high enough, and is therefore strongest at the deposit center where the temperature is highest, as shown on Fig. 13.3.2. Due to the small droplet characteristic size, the droplet density is high and the resulting evaporation rate field projected on the Eulerian grid is quite smooth, with only few empty spots. The gaseous equivalence ratio (computed from the atomic balance of carbon, hydrogen and oxygen) increases accordingly and exceeds stoichiometry at the kernel center where combustion can then start. Note that the equivalence ratio is more sensitive to the liquid phase discrete distribution and does not appear as smooth as evaporation because of diffusion effects towards empty evaporation regions. These regions are highlighted with iso-surfaces on Fig. 13.3.2 (right) delimiting the no-evaporation zones in a region of thickness $8\Delta x$ around the cut-plane. These regions are well correlated with the fluctuations of equivalence ratio.

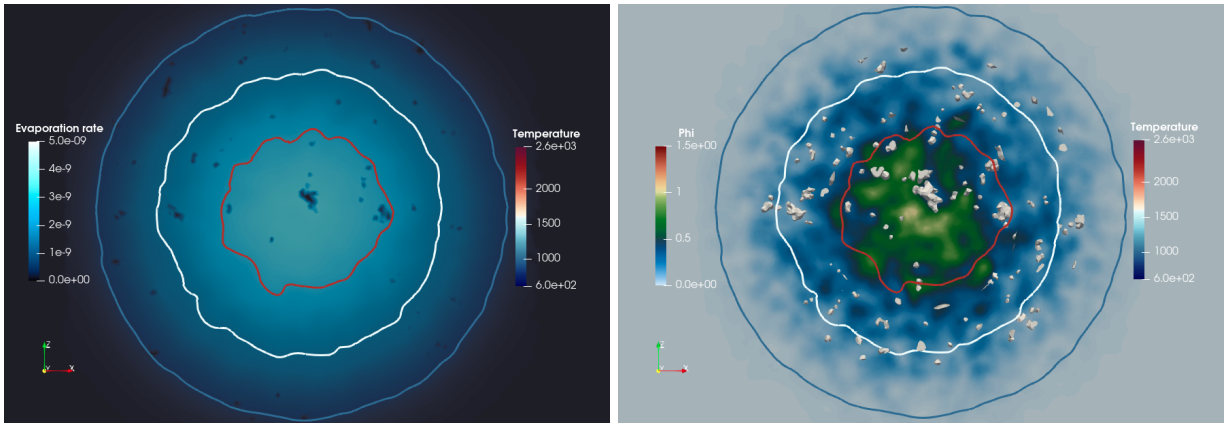

Figure 13.3.2: Evaporation rate (left) and equivalence ratio (right) cut-plane fields with temperature iso-contours of $T = 1000\,K, 1600\,K$ and $2200\,K$, at $t = 80\,\mu s$. The iso-surfaces on the right picture correspond to the no-evaporation zones in a region of thickness $8\Delta x$ around the cut-plane.

Combustion indeed starts at the kernel center as shown on Fig. 13.3.3, in a mixed reactor combustion regime, meaning that the thin propagating flame front has not formed yet. This is confirmed by the pool of reactive radical species such as OH found at the center where $T > 2000\,K$. Interestingly, this flame kernel is bordered by a spherical endothermic zone around $T = 1600\,K$. This endothermic process corresponds to fuel pyrolysis, which occurs everywhere in the reaction zone but is not masked by exothermic combustion only in the lower temperature region. This is well evidenced by the field of nC_7H_{14} species which is the first pyrolysis product of the fuel component MCYC6: although produced everywhere in the reaction zone, nC_7H_{14} only appears at the border where it is not consumed by oxidation reactions.

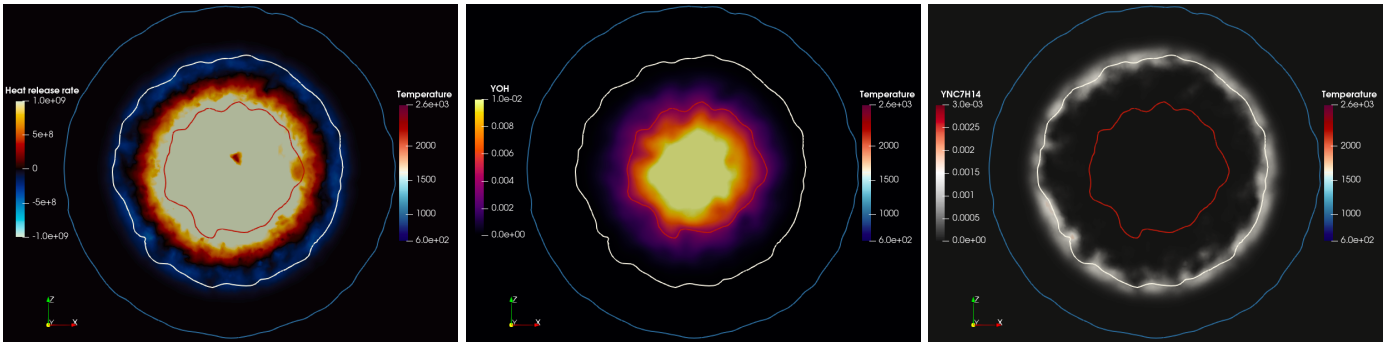

Figure 13.3.3: Heat release rate (left), OH mass fraction (center) and nC_7H_{14} mass fraction (right) cut-plane fields with temperature iso-contours of $T = 1000\,K, 1600\,K$ and $2200\,K$, at $t = 80\,\mu s$.

The fuel components mass fraction fields displayed on Fig. 13.3.4 well illustrate preferential evaporation where MCYC6 being the most volatile species evaporates first as soon as T reaches $1000\,K$. In the hottest center zone where $T > 1600\,K$, this species is immediately pyrolyzed after evaporation and thus disappears. The same mechanism applies to XYLENE but this less volatile species requires a higher temperature to evaporate and is found only above $\sim 1500\,K$. Finally, a negligible quantity of $nC_{12}H_{12}$ is observed in the domain (not shown) because the droplet temperature is still too low at that time to enable its evaporation. Indeed, Fig. 13.3.5 indicates that this species has not started to evaporate at the end of the early ignition phase ($t = 90\,\mu s$). This means that this phase is totally driven by MCYC6 and XYLENE, which is a major difference with gaseous ignition of the same fuel blend where $nC_{12}H_{12}$ would pyrolyse simultaneously with the other components [Stagni et al. 2017].

Combustion in this early ignition phase has not much progressed even at the kernel center. Indeed, Fig. 13.3.6 shows that the production of the main combustion products CO, CO_2 and H_2O are still low and the oxidizer O_2 has been barely consumed.

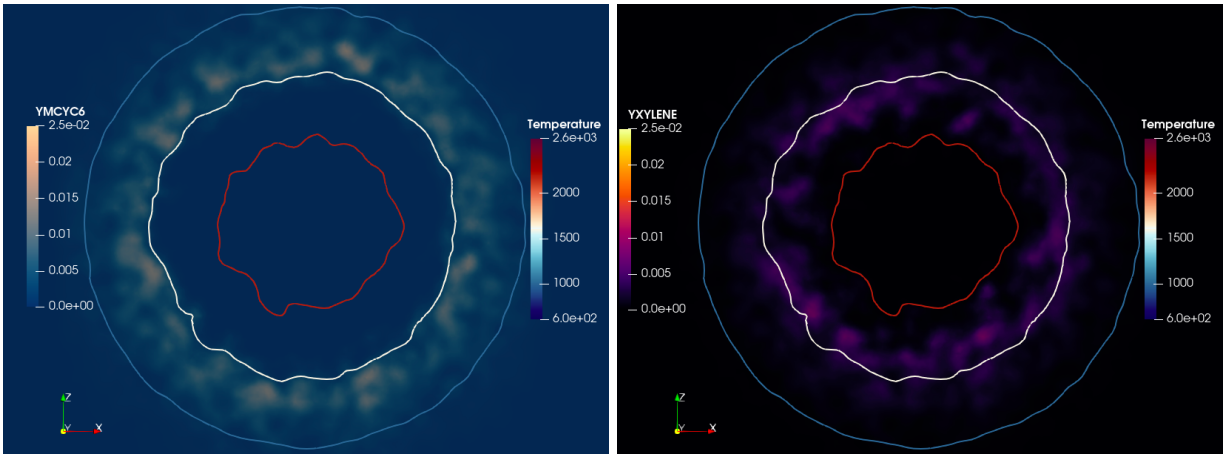

Figure 13.3.4: MCYC6 mass fraction (left) and XYLENE mass fraction (right) cut-plane fields with temperature iso-contours of $T = 1000\,K, 1600\,K$ and $2200\,K$, at $t = 80\,\mu s$.

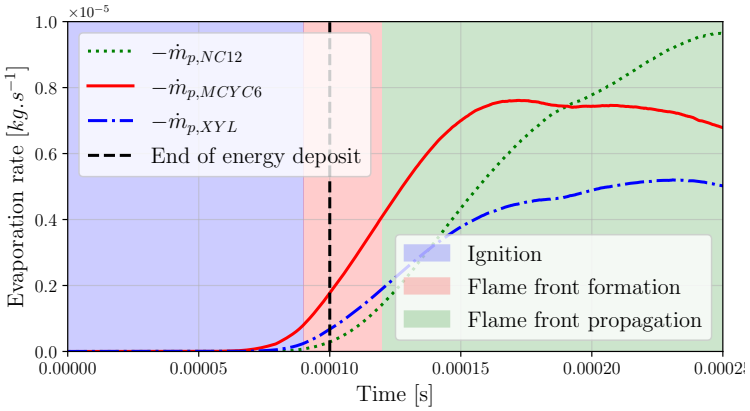

Figure 13.3.5: Temporal evolution of the fuel component evaporation rates during the early ignition phase.

Flame front formation

After the ignition phase at $t = 100\,\mu s$, a propagating flame front has formed as shown on Fig. 13.3.7 with the heat release rate and the radical species OH and CH_2O. The flame front is located around the iso-contour $T = 1600\,K$ which corresponds to the critical temperature for fuel pyrolysis.

Similarly to the previous phase, fuel component vapor is visible along the reaction zone in the low temperature side, but this time $nC_{12}H_{12}$ has started to evaporate and is present, in much less proportion, about ten time smaller than MCYC6 and XYLENE (see Fig. 13.3.8). Hence again at this stage, the flame properties are mainly driven by these two fuel components.

As shown on Fig. 13.3.9 (right), the flame front propagates in a mixture around stoichiometry. The two-phase combustion regime is of the kind of weakly evaporation-controlled where the gaseous mixture has reached flammability before reaching the flame [Rochette et al. 2019]. Therefore, the flame front propagation is not controlled by the droplet evaporation. The weakly controlled evaporation regime is characterized in laminar propagating flames by an evaporation peak located ahead of the flame front in the fresh gases. The situation is different in sparked ignition, where the droplet evaporation is triggered by the energy deposition rather than the flame front. Therefore, the peak evaporation is not located in the fresh gases but remains at the kernel center, until all droplets have evaporated, inducing there large values of the equivalence ratio as shown on Fig.13.3.9

The evaporated fuel components that evaporate inside the volume enclosed by the flame pyrolyze imme-

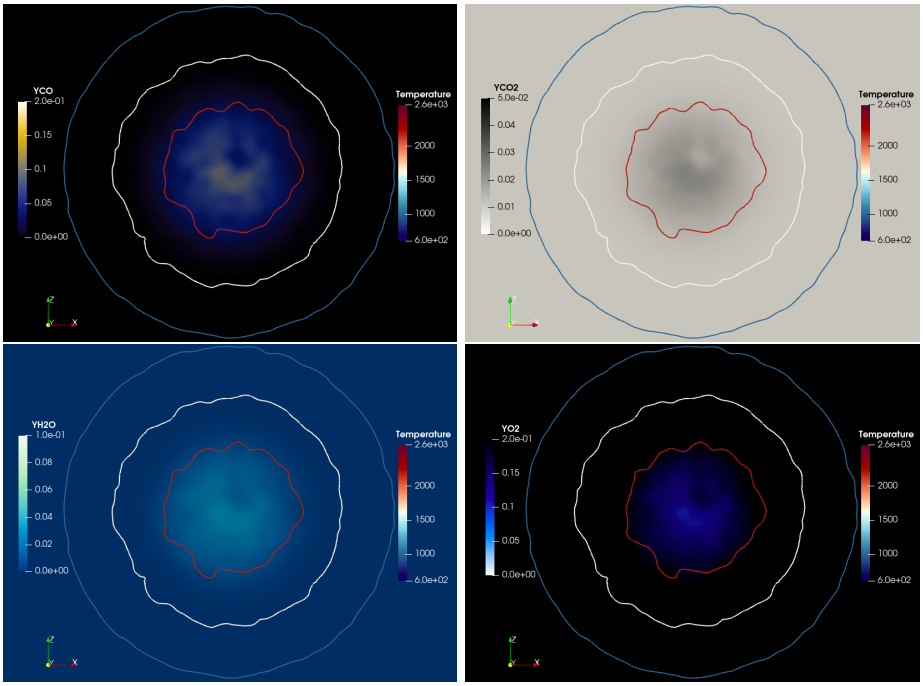

Figure 13.3.6: Final products mass fraction cut-plane fields with temperature iso-contours of $T = 1000\,K, 1600\,K$ and $2200\,K$, at $t = 80\,\mu s$.

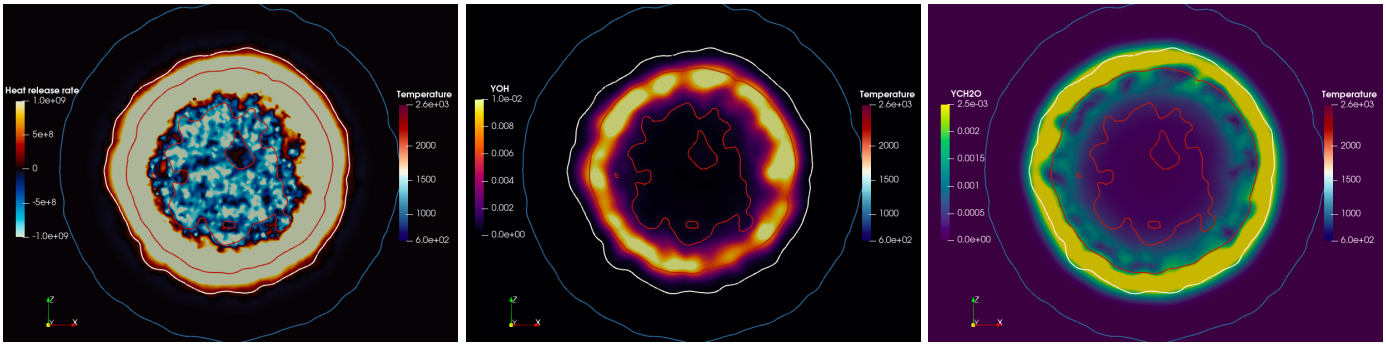

Figure 13.3.7: Heat release rate (left), OH mass fraction (center) and CH_2O mass fraction (right) cut-plane fields with temperature iso-contours of $T = 1000\,K, 1600\,K$ and $2200\,K$, at $t = 100\,\mu s$.

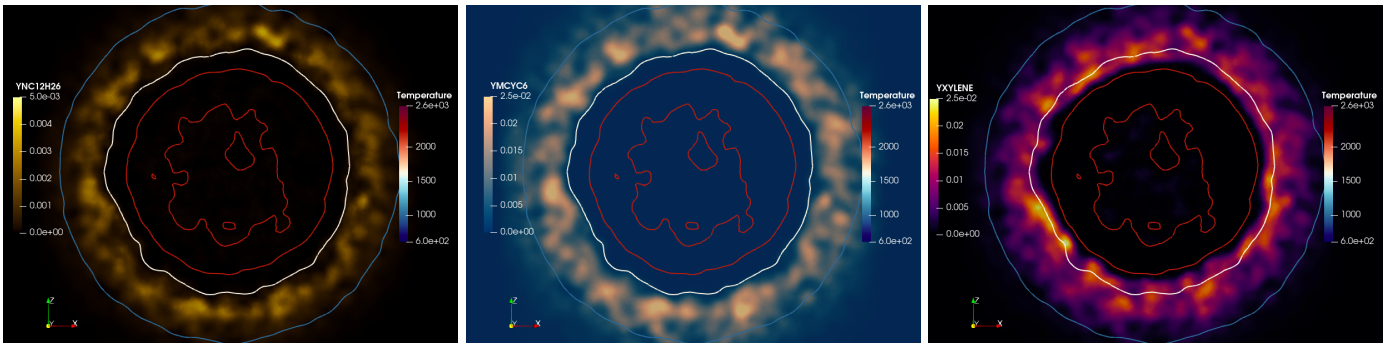

Figure 13.3.8: $nC_{12}H_{12}$ (left), MCYC6 (center) and XYLENE (right) mass fraction cut-plane fields with temperature iso-contours of $T = 1000\,K, 1600\,K$ and $2200\,K$, at $t = 100\,\mu s$.

diately, leading to the formation of light carbonated species such as CH_3 and C_2H_2 (see Fig. 13.3.10). These carbonated species however do not oxidize due to the lack of oxygenated species. Therefore, the temperature is reduced at the kernel center due to both evaporation and pyrolysis. This mechanism

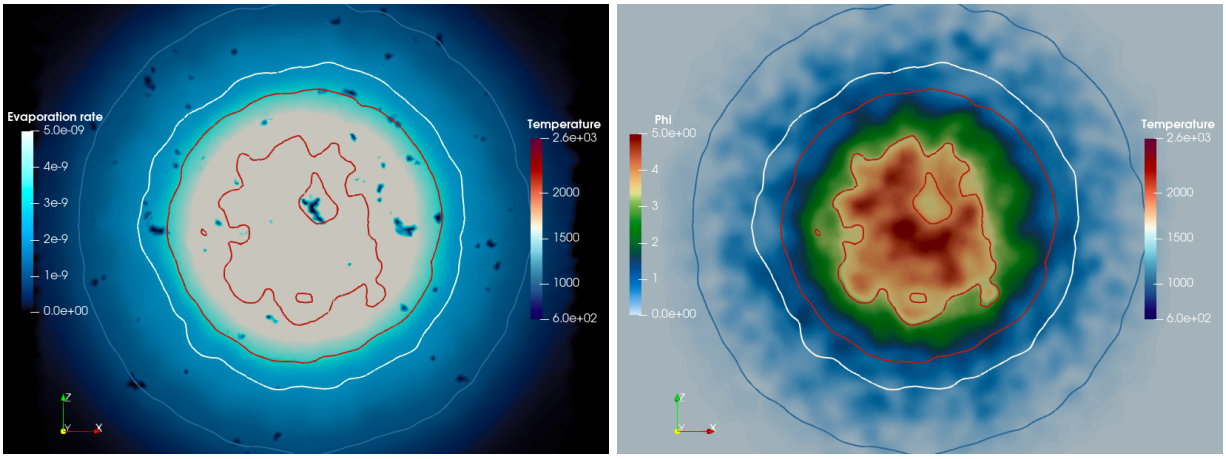

Figure 13.3.9: Evaporation rate (left) and equivalence ratio (right) cut-plane fields with temperature iso-contours of $T = 1000\,K, 1600\,K$ and $2200\,K$, at $t = 100\,\mu s$.

prevents the conversion of chemical energy into thermal energy for the fuel species coming from the remaining evaporating droplets in the kernel. The formation of such rich, not flammable and cooler mixture at the center may be detrimental to the kernel survival and ultimately endanger the ignition process.

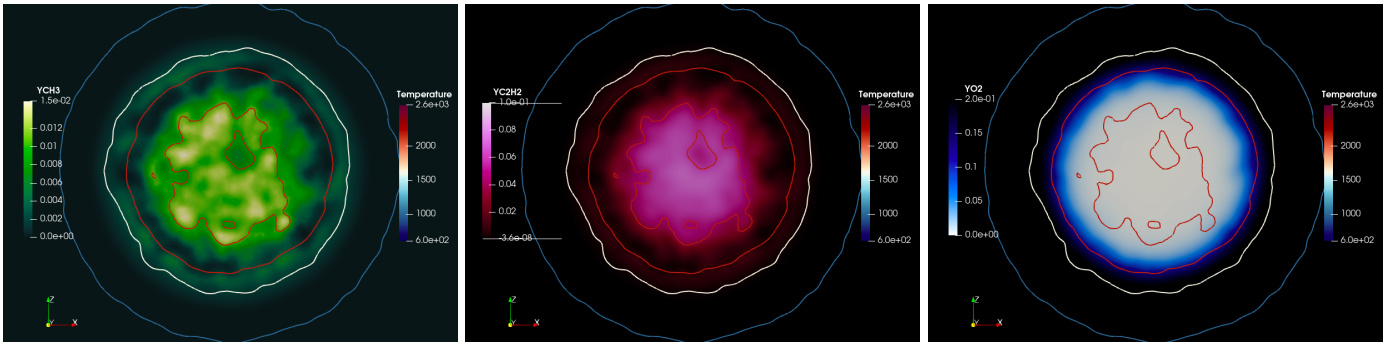

Figure 13.3.10: CH_3 (left), C_2H_2 (center) and O_2 (right) mass fraction cut-plane fields with temperature iso-contours of $T = 1000\,K, 1600\,K$ and $2200\,K$, at $t = 100\,\mu s$.

The number of droplets was initially set to obtain a stoichiometric total equivalence ratio, computed from the mixing with cold air before energy deposit. Since the pressure is constant in the domain, the temperature increase resulting from the energy deposit induces a local decrease of the gas density and an expanding radial flow, which both reduce the oxidizer mass content. Therefore, the two-phase mixture becomes rich and when the droplets start to evaporate, there are fewer oxygen atoms in the gas phase than initially targeted. The resulting total equivalence ratio can be estimated by correcting the initial value with the gas expansion effect as in Eq. (13.2), which gives the maximum value which can be reached:

$$\phi^*_{tot,max} = \phi_{g,0} + \phi_{l,0} \times \frac{\rho_0}{\rho_{min}} \tag{13.2}$$

where $\phi^*_{tot,max}$ is the rescaled total equivalence ratio before ignition, $\phi_{g,0}$ and $\phi_{l,0}$ are respectively the initial gaseous and liquid components of the equivalence ratio and ρ_{min} and ρ_0 are respectively the minimum and initial gaseous densities. In the present case, the theoretical value $\phi^*_{tot,max} = 12.5$ is never reached as it assumes to conserve the same minimum density during the entire evaporation. At the end of the evaporation, the value $\phi_{tot,max} = 8.5$ is observed.

Finally, the main combustion products are presented on Fig. 13.3.11. A large amount of CO is released whereas the CO_2 production is limited which is characteristic of rich combustion processes. Furthermore, a small depletion of H_2O and CO_2 is observed at the kernel center where the equivalence ratio is the highest. The formation of combustion products and the complete consumption of oxidizer at the kernel

center indicate that the combustion is complete at the kernel center. This is also confirmed on Fig. 13.3.7 where there is no exothermic heat release rate or oxidized radicals at the kernel center.

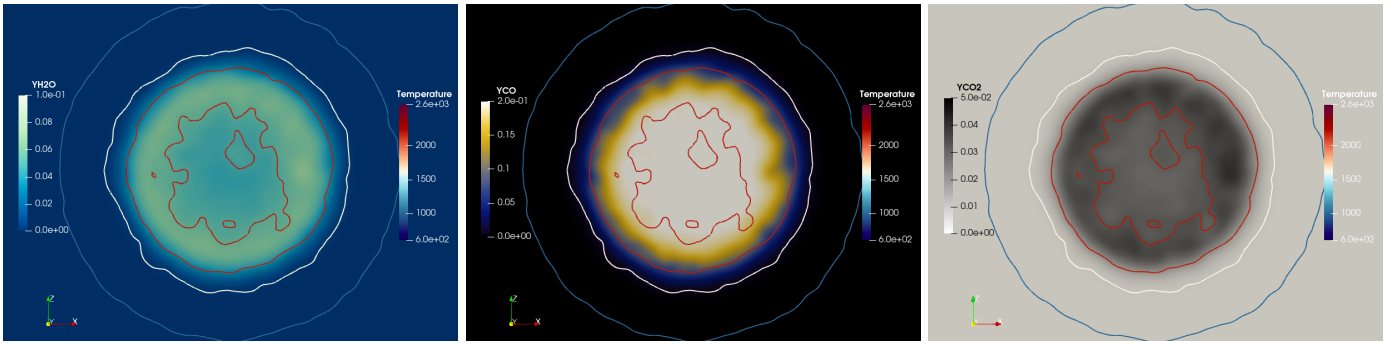

Figure 13.3.11: H_2O (left),CO (center) and CO_2 (right) mass fraction cut-plane fields with temperature iso-contours of $T = 1000\,K, 1600\,K$ and $2200\,K$, at $t = 100\,\mu s$.

Figure 13.3.12 shows the temporal evolution of the smallest droplet radius, which is located at the kernel center. At the end of the flame formation phase ($t = 100\,\mu s$) the droplet radius has been reduced by only 15 percent, which means that evaporation may continue in the next phase. At this time however energy deposition stops and the required heat for evaporation will be now taken from the gas. This may lead to either ignition success or failure, depending on the energy balance of the hot gas.

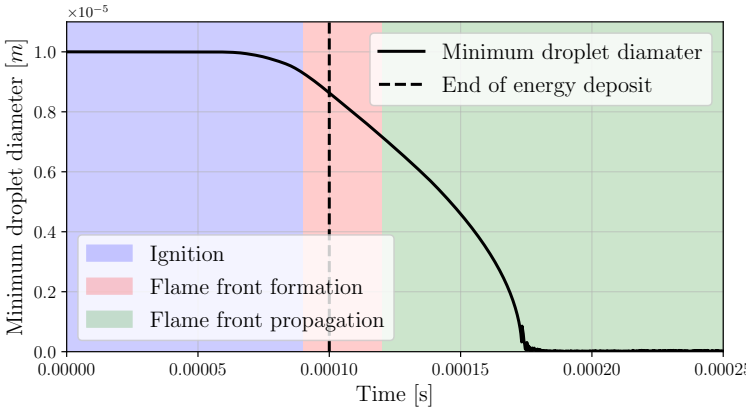

Figure 13.3.12: Temporal evolution of the smallest droplet radius.

Flame front propagation

Jumping to much later time ($t = 500\,\mu s$) a propagating flame is observed, meaning a successful ignition (see Fig. 13.3.13). Because energy deposition has stopped, the hot gas temperature has decreased slightly below 2000K but stabilizes there. As may be seen from Fig. 13.3.12, droplets completed evaporation in the hot gas region at around $t = 175\,\mu s$. Thus at $t = 500\,\mu s$ all endothermic processes have also completed. However, the resulting very high equivalence ratio, up to 5, does not allow oxidation of the pyrolysis products in this hot zone.

Figure 13.3.13 (center) shows that evaporation now only occurs in a spherical zone around the flame front on the cold air side. This means that evaporation is fast enough in the pre-heat zone to feed the propagating flame, which has become therefore purely gaseous. The evaporation zone lies much further from the hot gas than the flame front because evaporation starts at low droplet temperature ($T_p \approx 450 - 500\,K$) compared to the gas temperature at the flame front location ($T = 1600\,K$).

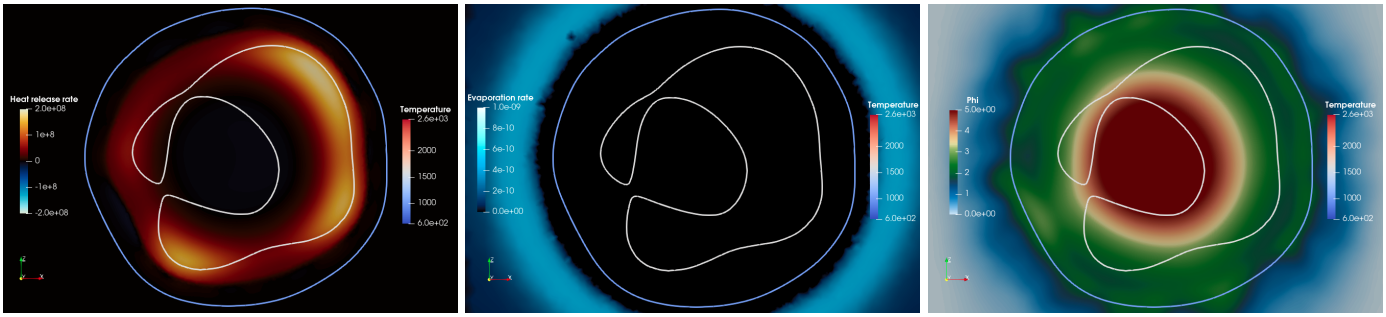

Figure 13.3.13: Heat release rate (left), evaporation rate (center) and equivalence ratio (right) cut-plane fields with temperature iso-contours of $T = 1000\,K, 1600\,K$ and $2200\,K$, at $t = 500\,\mu s$.

Finally, due to the high equivalence ratio resulting from the complete evaporation, the flame evolves in a very rich mixture at the flammability limit ($\phi \approx 2-3$). At this equivalence ratio, the flame is thick and propagates slowly. This reflects on the maximum heat release rate which is one order magnitude lower than it was in the previous phase (see Fig. 13.3.7). This too rich fresh mixture is therefore detrimental for the kernel development and may lead ultimately to extinction. In practice however the turbulent flow may counteract this effect by promoting mixing with fresh air in the pre-heat zone and lowering the too high equivalence ratio.

13.3.2 Ignition in poly-disperse sprays

Effect of droplet number and size

Firstly in the case **LPLT**, pressure, temperature, equivalence ratio, mesh and energy deposit parameters are kept from the previous case. Only a Rosin-Rammler droplet size distribution is introduced with $d_{p,32} = 60\,\mu m$. Hence, droplets much larger compared to the previous case **LPLT-mono** are now present. Furthermore, the droplet total number is also much lower to conserve the same total equivalence ratio: 354 droplets for the case **LPLT** and 38746 for the case **LPLT-mono**. This difference has a large influence on the combustion processes as shown in the following paragraphs.

The major difference with the previous case is the combustion mode. For the case **LPLT-mono** the combustion is homogeneous with the formation of a flame front. On the contrary, for the case **LPLT** the droplets burn individually in the energy deposit zone as shown on Fig. 13.3.14. This is due the inter-droplet distance $\mathcal{I}$ which has much increased with the lower number density. Averaged values can be estimated from the droplet number Eq. (13.3): $\mathcal{I}_{LPLT-mono} = 2.31 \times 10^{-4}\,m$, $\mathcal{I}_{LPLT} = 9.99 \times 10^{-4}\,m$ and $\mathcal{I}_{PTatmo} = 7.52 \times 10^{-4}\,m$.

$$\mathcal{I} = \frac{{V_c}^{1/3}}{{N_{ptcl}}^{1/3} + 1} \tag{13.3}$$

where N_{ptcl} is the number of droplets in the control volume V_c. In this isolated droplet combustion mode, thanks to the kernel high temperature the evaporated fuel burns immediately around the droplets and no continuous fuel vapor field builds up. This combustion mode has been studied in [Chiu and Liu 1977, Chiu et al. 1982] and can be evaluated using the Group number.

A consequence of this combustion mode is that the evaporation and reactive zones are a small fraction of the hot kernel volume. Therefore, the heat release rate is limited as shown on Fig. 13.3.15. Contrary to the mono-disperse case, there are no visible endothermic pyrolysis phase, neither a large heat release rate peak corresponding to the formation of a flame front, but rather a continuous increase of the heat release rate coming from the ignition of new droplets when the kernel expands.

The integral of heat release rate is lower for the poly-disperse case **LPLT**, however, the maximum temperature remains higher. Indeed, as evaporation is also limited due to the lower droplet number, the heat loss due to evaporation is reduced. Moreover, since the droplets are larger, their complete evaporation takes more time. Thus, the liquid mass remains high during the whole simulation (see Fig. 13.3.16).

As a result, the equivalence ratio is much lower than in the mono-disperse case (see Fig. 13.3.17).

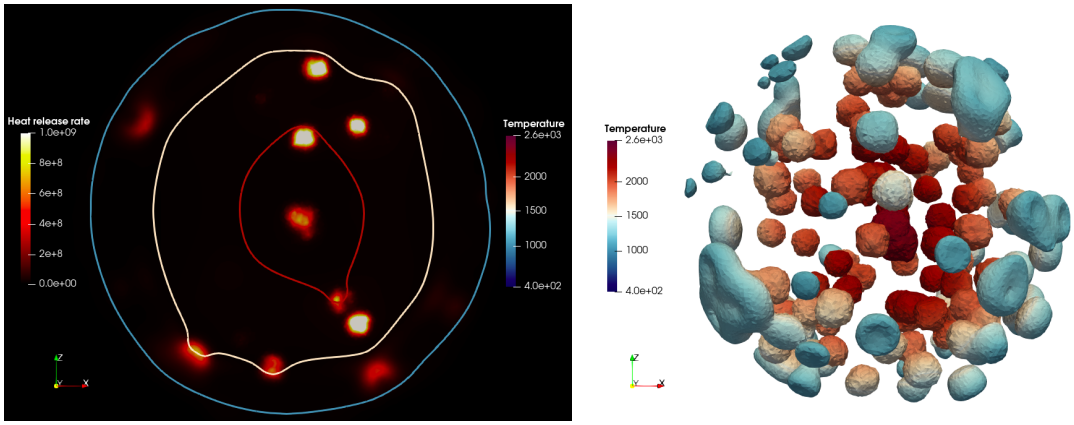

Figure 13.3.14: Heat release rate field with temperature iso-contours (left) and iso-surface of $\dot{\omega}_T = 1 \times 10^8\, J.m^{-3}.s^{-1}$ colored by temperature (right) at $t = 1\, ms$.

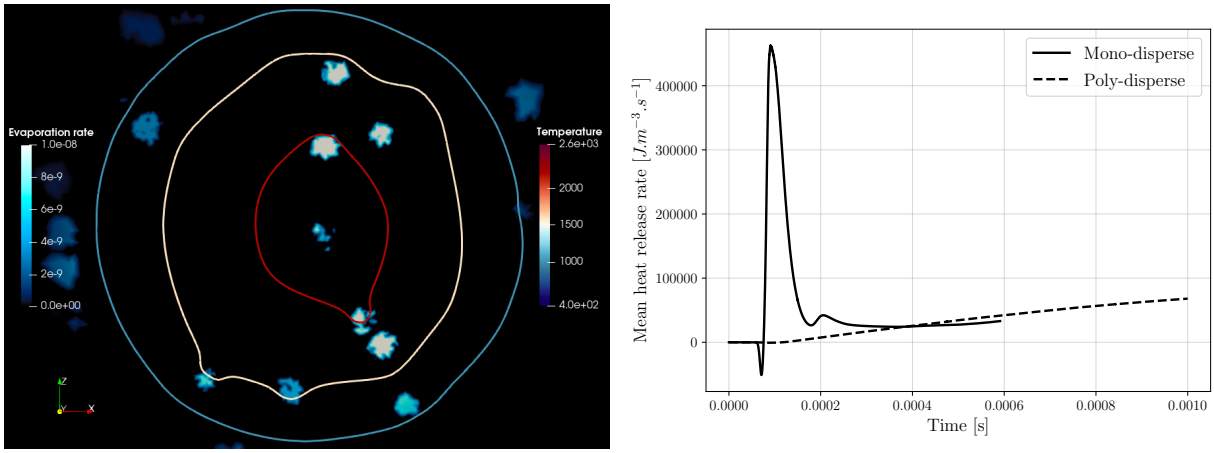

Figure 13.3.15: Evaporation rate field for case **LPLT** (left) and temporal evolution of mean heat release rate for cases **LPLT-mono** and **LPLT** (right).

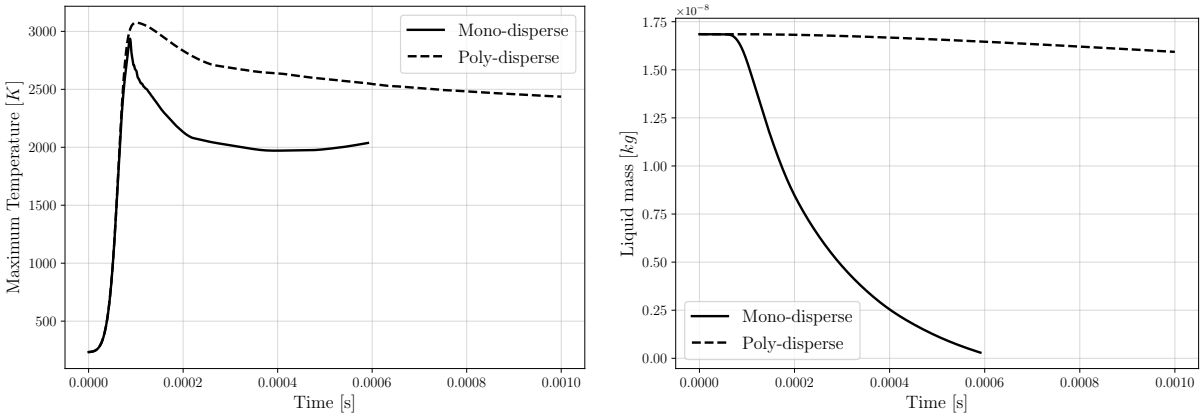

Figure 13.3.16: Temporal evolution of the maximum temperature and the liquid mass in the domain for cases **LPLT-mono** and **LPLT**.

Therefore, for the case **LPLT**, the strong endothermic fuel decomposition without oxidation at the kernel center, as well as the maximum heat release rate reduction due to the rich premixed combustion detailed in Sec. 13.3.1 are not observed.
As for the case **LPLT-mono**, the fuel species pyrolyse in the kernel due to the high temperature as soon as they are evaporated. Therefore fuel vapor is only observed at the external border of the kernel. Even

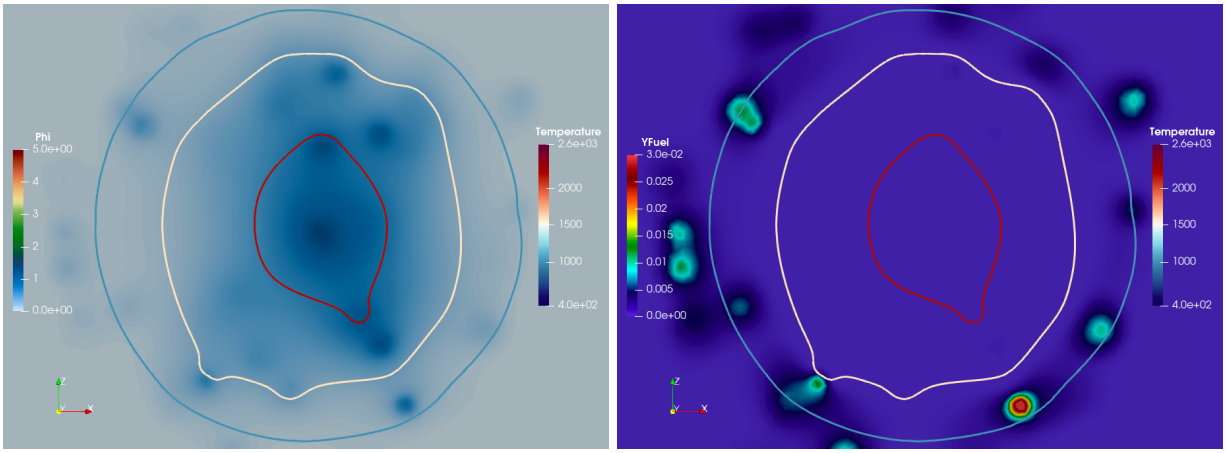

Figure 13.3.17: Equivalence ratio and fuel vapor mass fraction fields (sum of the three surrogate components) for **LPLT** case.

if the temperature is too low for the fuel to directly pyrolyse there, no continuous fuel vapor field forms around the kernel because of the too low droplet number. Therefore, if the released heat from the core kernel is large enough to enable its propagation, there will not be a flame front propagation but only the propagation of a temperature front.

The chemical composition of the kernel is also very different between cases **LPLT-mono** and **LPLT**. For the poly-disperse case the kernel is mainly composed of oxidized radicals such as O and OH as shown on Fig. 13.3.18. On the contrary, the non oxidized radicals arising from the fuel decomposition, for instance CH_3, are localized at the droplet positions. Contrary to the mono-disperse case, these unburnt products including CO which is converted into CO_2 (see Fig. 13.3.19), do not accumulate in the kernel center. These chemical processes are characteristic of lean combustion. Indeed, there is still large amount of oxidizer available for oxidation processes in the kernel.

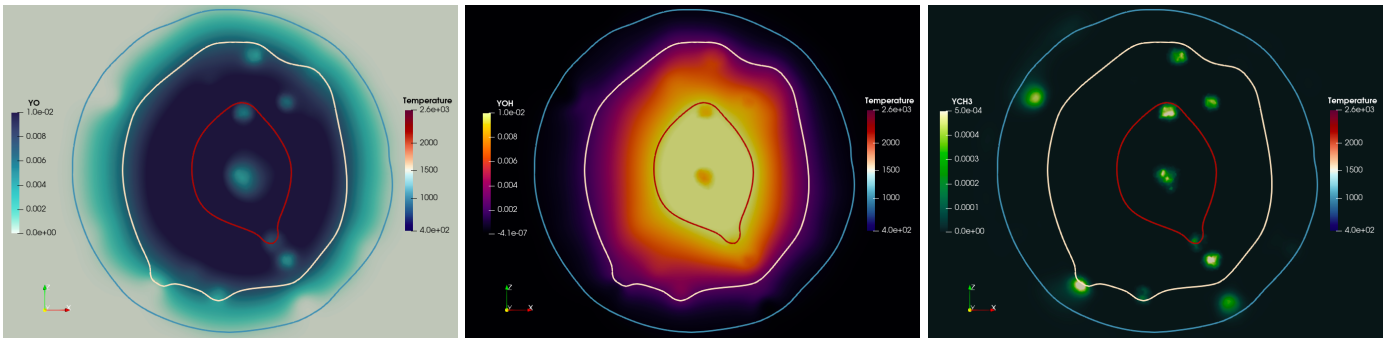

Figure 13.3.18: O, OH and CH_3 mass fraction fields with temperature iso-contours at $t = 1\,ms$ for **LPLT** case.

The isolated droplet combustion mode is characterized by non-premixed combustion regime. Indeed, the fuel vapor issued from the droplet burns with the surrounding oxidizer.

At this stage, the released heat by combustion does not compensate the thermal diffusion losses. Indeed, on Fig. 13.3.16, the maximum temperature continues to decrease. In the case of isolated droplet combustion mode, the kernel power relies on the droplet number and thus on the kernel volume. It differs from the gaseous combustion mode whose power depends on the kernel surface. Therefore, the kernel survival relies on its ability to ignite a sufficient number of droplets whose total heat release compensates the heat losses. As a consequence, the droplet number density and the initial kernel size, which is related to the deposited energy, are two parameters that have a large influence on the outcome of ignition.

Independently from the droplet number, the droplet size also has an influence. Indeed, as shown in Chap.

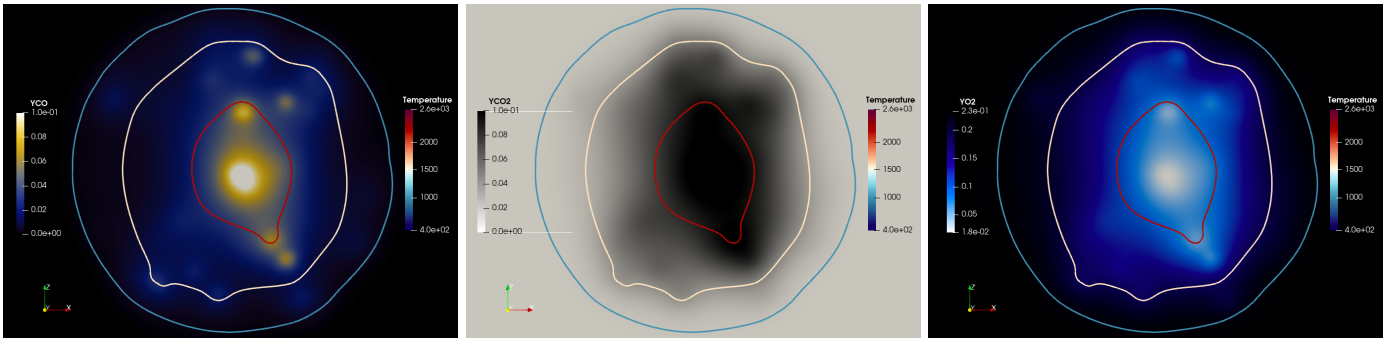

Figure 13.3.19: CO, CO_2 and O_2 mass fraction fields with temperature iso-contours at $t = 1\,ms$ for **LPLT** case.

12, large droplets take more time to heat and to start evaporating. Firstly, as shown on the right picture of Fig. 13.3.15 and on Fig.13.3.20 these large droplets delay the heat release. The droplets ignite later and the total heat release rate increases slowly. Secondly, these droplets are initially seen as heat sinks by the kernel and thus reduce the ignition capabilities.

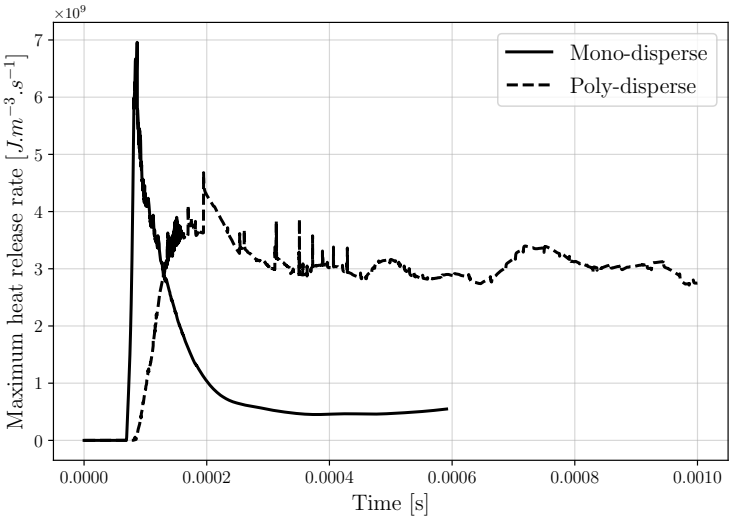

Figure 13.3.20: Temporal evolution of the maximum heat release rate for cases **LPLT** and **LPLT-mono**.

The ignition success or failure cannot be settled at this early time. Indeed, the heat losses are larger than the released heat by combustion, but the temperature is still high enough to trigger droplet evaporation and combustion reactions, and the total heat release is increasing. Moreover, the purpose of this work is to study the kernel formation which is ensured by the large enough energy deposit. Additional studies are required to analyse the kernel propagation and determine the ignition outcome.

Effect of high altitude conditions

The comparison between cases **LPLT** and **PTatmo** enables to evaluate the effect of high altitude conditions. It has been already shown in Chap. 12 that low pressure and low temperature conditions have a limited influence on the droplet evaporation. However the combustion processes are sensitive to these conditions, as well as the droplet size distribution. Concerning the latter, and even though it was shown in Chap. 11 that the characteristic droplet size is higher in low pressure pressure condition, the SMD and distribution shape are identical in both cases for comparison purposes. However, due to the gas density difference, the droplet number and thus the droplet density, are higher in the atmospheric case to keep the same equivalence ratio : 354 droplets for the case **LPLT** and 919 for the case **PTatmo**.

Similarly to the case **LPLT**, an isolated droplet combustion mode is observed on Fig. 13.3.21. The

most reactive regions ($\omega_T > 10^9\, J.m^{-3}.s^{-1}$) are still located around the evaporating droplets. However, contrary to the case **LPLT** and due to the larger droplet density, weak reactive envelopes ($\omega_T = 10^8\, J.m^{-3}.s^{-1}$) are able to merge.

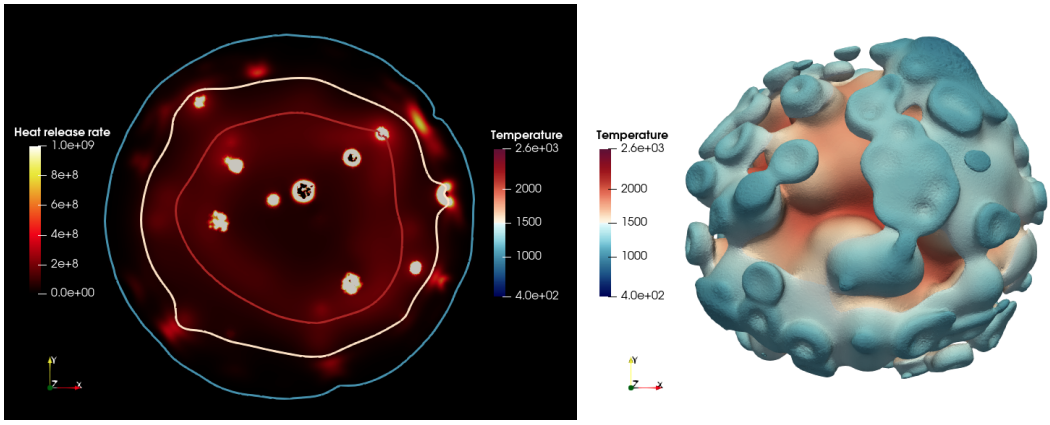

Figure 13.3.21: Heat release rate field with temperature iso-contours (left) and iso-surface of $\dot{\omega}_T = 1 \times 10^8\, J.m^{-3}.s^{-1}$ colored by temperature (right) at $t = 1\, ms$ for the case **PTatmo**.

The chemical processes are identical to those described in the previous section and correspond to the isolated droplet combustion mode. However, in the case **PTatmo**, a weak but non negligible heat release rate is found in the whole kernel center. This reaction zone, not observed in the low pressure case, seems to maintain the high core kernel temperature. Indeed, the iso-volume defined by $T = 2200\, K$ is larger than in the case **LPLT**. This weak reaction zone is due to the increase of the chemical reactivity with the pressure. Indeed, the OH radical concentration presented on Fig.13.3.22 is higher in the case **PTatmo** as well as the production of CO and CO_2.

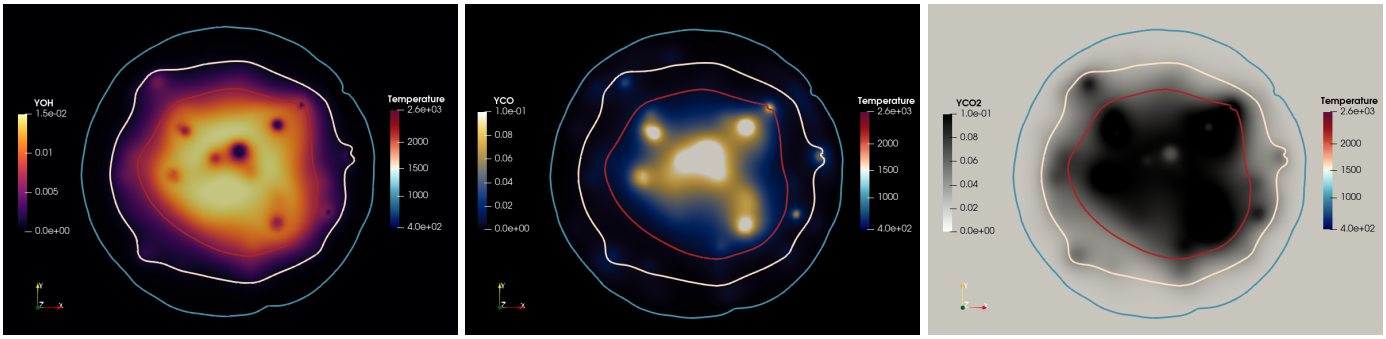

Figure 13.3.22: OH, CO and CO_2 mass fraction fields with temperature iso-contours at $t = 1\, ms$ for the case **PTatmo**.

The differences between the cases **LPLT** and **PTatmo** can also be observed by tracking the temporal evolution of the maximum temperature and heat release rate as presented on Fig. 13.3.23. In the atmospheric case, the initial energy deposit results in a lower maximum temperature because there is more energy lost in the initial pressure wave and the radial flow. However, after the end of the energy deposit, the maximum temperature continues to increase. Hence, the heat release is large enough to directly compensate the thermal losses which is not the case for the low pressure computation. Because of the larger droplet number and the higher reactivity, the mean heat release rate is larger and increases faster in the case **PTatmo**. Therefore, there is enough energy to enable the kernel development and propagation.

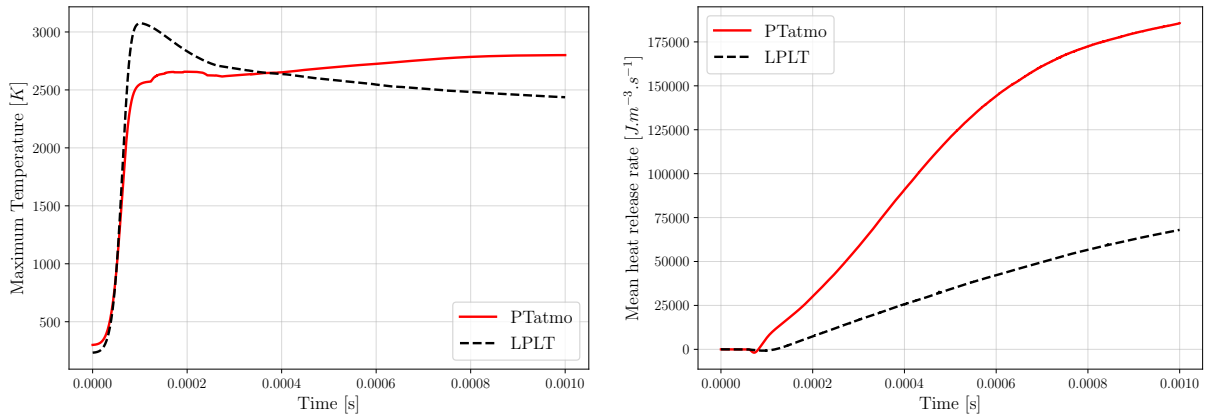

Figure 13.3.23: Temporal evolutions of maximum temperature and mean heat release rate for cases **LPLT** and **PTatmo**.

13.4 Conclusion

13.4.1 Results summary

New numerical methods have been developed to enable the simulation of the ignition of a multi-component kerosene spray with an ARC mechanism. These methods are the exponential chemistry integration, the local and dynamical sub-cycling (LDSC) and the particle bursting method (PBM). This work demonstrates the interest of the PBM with the reduction of the evaporation rate source term stiffness due to the point source approximation. However, the PBM still requires additional developments with a dedicated study to define suitable physical criteria for the control volume size or the number of child particles which are expected to depend on the parent droplet diameters and the mesh discretisation respectively.

In the mono-disperse ignition at low presssure and temperature, with small droplets, the fast evaporation forms a gaseous mixture mainly composed of methyl-cyclohexane and xylene. Hence, a homogeneous gaseous flame front is created and is weakly perturbed by the dispersed phase. An enrichment effect is also observed due to the gaseous density reduction while the liquid fuel quantity remains unchanged. The density reduction results from the temperature increase at the energy deposit center. This effect induces strong endothermic processes due to the droplet evaporation and the fuel decomposition without oxidation. At the end, the droplets are fully evaporated and the flame front becomes fully gaseous. This enrichment effect also leads to an important heat release rate decrease because of the rich premixed combustion processes and could lead to the kernel extinction.

Then, for the poly-disperse case at low pressure and temperature, the combustion mode is totally different. Because of the large droplet size, the total droplet number is largely reduced as well as the droplet density. Hence, the characteristic inter-droplet distance increases and an isolated droplet combustion mode occurs in the hot kernel without forming a continuous flame front. The total heat release rate and evaporation rate are weaker, however, the kernel temperature decreases slowly because there are less endothermic processes resulting from evaporation and pyrolysis. With this combustion mode, the kernel ignition success strongly relies on the number of burning droplets, and thus, the initial kernel size and droplet density.

Finally, the comparison with the atmospheric computation shows that the high altitude conditions are detrimental to ignition because the droplet number density is reduced (at fixed equivalence ratio). Indeed, the gas density is lower and the droplet characteristic size is larger (see Chap. 11). It is reminded that the pressure and droplet temperature conditions have a limited influence on the droplet evaporation time which is mainly driven by the initial droplet size (see Chap. 12). Moreover, like in the gaseous case, a higher chemical reactivity is observed when the pressure increases. Thus, the heat release rate and the kernel development are promoted in atmospheric conditions.

13.4.2 Perspectives

The two-phase ignition computations presented in this chapter have enabled to identify the combustion modes, to describe the chemical processes, and to evaluate the effect of a droplet size distribution and the influence of the high altitude conditions. However, this study should be continued to better evaluate the kernel development phase and determine if the kernel is able to propagate or quenches. Moreover, additional studies on the influence of the shape distribution parameter q and on the fuel pre-evaporation are to be considered.

This simplified configuration can also be used to evaluate the effect of the energy deposit model. Indeed, in the current approach, the droplet-spark interaction is not considered while studies show that the droplets at the spark location can be vaporized or broken into smaller droplets [Gebel et al. 2013]. Therefore, the ignition with a gaseous phase or smaller droplets at the energy deposit center is expected to modify the kernel formation dynamics and to have a non negligible influence on the ignition success.

Finally, the CPU-cost was 6570,2 hCPU for the case **LPLT-mono**[6], 4790.5 hCPU for the case **LPLT** and 31121.3 hCPU for the case **PTatmo**. One can note that the droplet combustion is the stiffest part of the simulation and thus is responsible for the CPU-cost due to the small time-steps and the additional cost induced by the numerical methods: sub-cycles with the LDSC and additional particles with the PBM. Therefore, the modeling of droplet combustion using a MUSTARD like model [Paulhiac 2015] and including ARC mechanisms and multi-component formulations would enable to largely reduce the CPU-cost.

Now that we have stable numerical methods adapted to the two-phase ignition with ARC mechanisms, the fourth part of this manuscript will focus to the ignition of a combustion chamber under low pressure and low temperature conditions.

[6] Extrapolated for a total simulation time of $1\,ms$

Part IV

Applications

Find something you love to do and you'll never have to work a day in your life.
Arthur Szathmary, 1916-2013 (often attributed to Confucius, 551–479 BCE)

Chapter 14

Two-phase ignition in the MERCATO bench

Contents

The previous chapters have presented several aspects of the high altitude ignition using simplified configurations. The final step in this work consists in evaluating the proposed modeling strategy to simulate the high altitude ignition in a burner representative of an aeronautical combustion chamber.
Compared to the previous cases, the characteristic flow patterns observed in combustion chambers (recirculation zones, swirled air streams and fuel injection) add additional interactions with the kernel. Furthermore, the flow is now turbulent at the spark location which may have a non-negligible effect on the kernel formation and development compared to the previous spherical bomb ignition simulations.

The MERCATO academic test bench is first presented in Sec. 14.1 with the available experimental data. Then, the computation is divided in several phases. Firstly, the cold gaseous flow simulation is presented in Sec. 14.2 and the characteristic flow structures are analysed. Secondly, in Sec. 14.3, the liquid fuel is injected in the chamber. Then, ignition simulations are performed and analysed in Sec. 14.4. Finally, conclusions and results discussion are given in Sec. 14.5.

14.1 The MERCATO bench

This first section aims at introducing the MERCATO test bench with a description of the experimental set-up, the previous works, the operating point chosen in this work and the experimental data available.

14.1.1 Configuration

The MERCATO ("Moyen d'Etude et de Recherche en Combustion Aérobie par Techniques Optiques") has been designed to study the detailed phenomena of the two-phase combustion in a configuration in between the fundamental experiment and the industrial application. A picture of the bench located at ONERA Fauga-Mauzac is shown on Fig. 14.1.1.

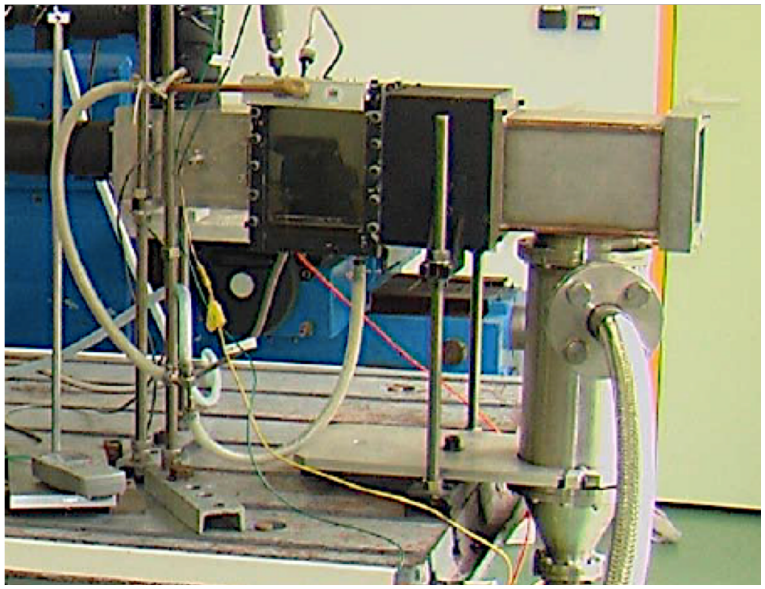

Figure 14.1.1: Photograph of the experimental MERCATO bench (courtesy of ONERA). The flow goes from the left to the right.

The MERCATO bench has been chosen in this work to study ignition because low temperature and low pressure conditions representative of high altitude can be generated. Furthermore, this configuration has recently been used in the context of the JETSCREEN project [Orain 2020] to evaluate the ignition capabilities of several aeronautical fuels at various pressure and temperature conditions including the Jet-A1 used in this work. The available data are presented in the following section. Finally, this bench has previously been studied in several previous theses, both experimentally [Garcia-Rosa 2008, Linassier 2011] and numerically [Lamarque 2007, Sanjose 2009, Senoner 2010, Eyssartier 2012].

The test bench has been built in 2005 following the work of Ouarti [2004]. The MERCATO geometry and dimensions are presented on Fig. 14.1.2. The combustion chamber has a rectangular shape with a square cross-section of 129 x 129 mm and is 500 mm long. The air is injected through the inlet channel into a plenum of 115 mm long. Then, the air enters into the 12 tangential vanes of the injection system which gives a strong swirl motion when entering into the combustion chamber. This air stream can be cooled before entering into the plenum with a liquid nitrogen thermostatic bath which enables to reach $T_a = 233\,K$. The liquid fuel is injected with a pressure swirl located at the center of the injection system (see fig. 14.1.2 right). The liquid fuel forms a film at the injector nozzle which then atomizes due to the interaction with the air stream and the surface tension forces as detailed in Chap. 11. This injector is slightly shifted by 4 mm in the swirler before the backplane of the combustion chamber. However, the spray hollow cone angle is not large enough interact with the injector system walls. In other words, the droplets are directly injected into the combustion chamber. In the following, the reference position will be taken at the tip of the pressure swirl (highlighted with the dashed vertical line $x = 0$ on the right picture of Fig.14.1.2). The flow exits through an exhaust pipe which is added after the combustion chamber (see Fig. 14.1.1 and 14.1.2). Inside the exhaust pipe, there is a co-flow which allows to work under low pressure conditions using the Venturi effect. Finally, the spark plug is located on the top wall at 6 cm from the injector nozzle in the axial direction. More information on the MERCATO bench can be found in Garcia-Rosa [2008].

As explained previously, several operating points have been studied numerically in the past and are summarized in Tab. 14.1.1 and 14.1.2. One can note that the methodology proposed in this work based

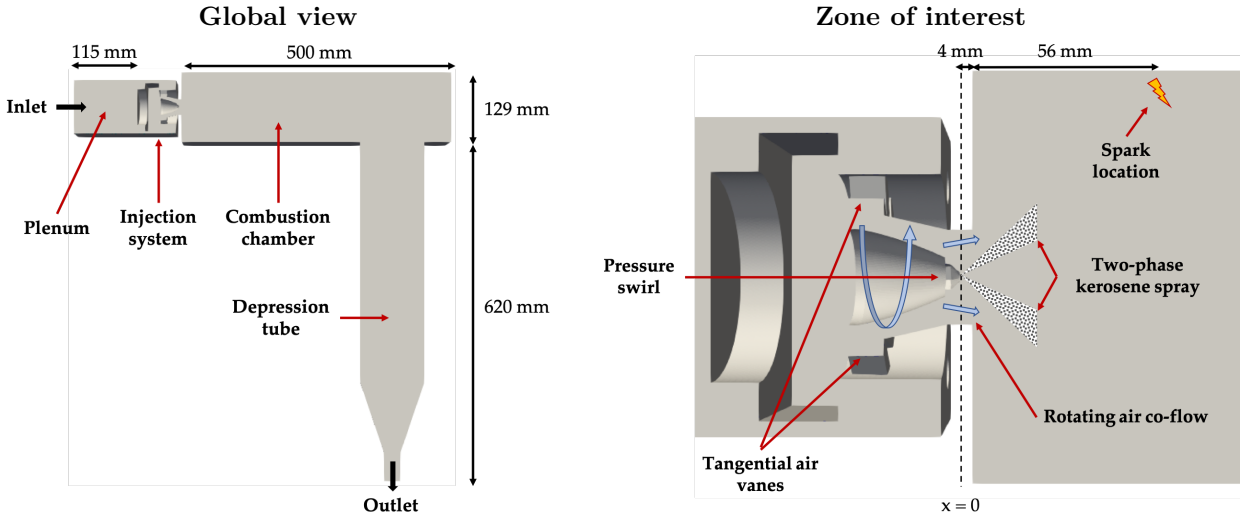

Figure 14.1.2: Representative scheme of the MERCATO chamber.

on the Lagrangian formalism and ARC has never been tested on the MERCATO configuration. This methodology has been used in the work of Collin-Bastiani [2019] in the context of ignition, but on a different configuration (KIAI-spray burner), with heptane instead of kerosene and with pre-heated air ($T_a = 413\,K$). In this work, the objective is to evaluate the methodology for a kerosene fuel which is less volatile, and in low pressure and low temperature conditions that are detrimental for ignition (lower chemical reactivity, no pre-evaporation, larger and less droplets). The operating conditions chosen for this work are presented in the following section.

Test case	$\dot{m}_a\,[g/s]$	$\dot{m}_{fuel}\,[g/s]$	$P\,[bar]$	$T_a\,[K]$	Ref
1	15	1	1	463	[Senoner 2010, Sanjose 2009]
2	15	2	1	493	[Sanjose 2009]
3	26	2.9	1	285	[Lamarque 2007]
4	35.5	2.26	1	293	[Eyssartier 2012]

Table 14.1.1: Summary of the operating points simulated with the MERCATO bench.

Test case	Comments
1	Non reactive computation, Euler-Euler (EE) and Euler-Lagrange (EL) formalism
2	Non reactive computation, EE formalism
3	Stabilized flame, EE formalism, 2-step kerosene BFER
4	Ignition, EE formalism, 2-step kerosene BFER

Table 14.1.2: Comments about MERCATO operating points.

14.1.2 Operating points and experimental data

For this work, the experimental data available in the JETSCREEN project have been used because it includes ignition tests at low pressure and low temperature conditions with Jet-A1 fuel. The operating conditions are summarized in Tab. 14.1.3.

Test case	$\dot{m}_a\,[g/s]$	$\dot{m}_{fuel}\,[g/s]$	$P\,[bar]$	$T_a\,[K]$	$\rho_a\,[kg/m^3]$	$T_{fuel}\,[K]$	$U_{bulk}\,[m/s]$	$FAR\,[-]$
PTatmo	35	2.25	1	293	1.2	293	1.8	0.064
LPLT	19.2	2.8	0.6	233	0.89	293	1.26	0.146

Table 14.1.3: Summary of the MERCATO operating points tested in the JETSCREEN project.

Here, only the **LPLT** operating point is studied. Compared to the atmospheric case the air mass flow rate is largely reduced and leads to a lower bulk velocity, computed with Eq. (14.1), even if the pressure and thus the density are lower. On the contrary, the fuel mass flow rate is increased which leads to a richer mixture in the case **LPLT** as shown with the Fuel-Air Ratio (FAR) computed with Eq. (14.2). The corresponding equivalence ratios are $\phi_{tot,LPLT} = 2.1$, $\phi_{tot,PTatmo} = 0.95$.

$$U_{bulk} = \frac{\dot{m}_a}{\rho_a S_{chamber}} \tag{14.1}$$

with $S_{chamber}$ the transverse surface of the chamber.

$$FAR = \frac{\dot{m}_{fuel}}{\dot{m}_{air}} = \phi_{tot} \times FAR_{st} \tag{14.2}$$

with $FAR_{st} = 0.695$, the FAR corresponding to the stoichiometric proportions for Jet-A1 fuel.

A major issue is the limited experimental data for the **LPLT** operating point[1]:

- **Gaseous cold flow:**
  The velocity profiles have not been measured for the gaseous flow. As a consequence, the flow initialisation which is the first building block of the simulation cannot be validated.

- **Cold two-phase flow:**
  Laser Doppler Anemometry (LDA) and Particle Doppler Analyser (PDA) techniques have been used to determine the droplet spray velocity and characteristic sizes respectively. More information on these experimental optical techniques and their integration on the MERCATO bench are detailed in [Garcia-Rosa 2008]. Each operating point is measured twice which enables to qualitatively estimate the result variability. As shown on the left scheme of Fig. 14.1.3, these measurements are done at the axial position $x = 10\,mm$ in both directions of the transverse plane yz[2]. Along the z-axis the SMD, axial and radial velocities are measured, and along the y-axis SMD, axial and tangential velocities are partially measured.

  The experimental SMD profiles are shown on the right graph of Fig. 14.1.3. Despite the large fluctuations, the effect of low pressure conditions on the atomization is clearly observed with an increase of the SMD in agreement with the trends presented in Chap. 11. All the experimental data have been restricted to the inner positions $z = [-20\,mm; 20\,mm]$ where enough droplets have been detected to consider a statistical convergence of the results. The velocity profiles are directly presented in Sec. 14.3.

- **Ignition:**
  16 and 25 ignition attempts have been performed respectively on the **PTatmo** and **LPLT** cases slightly varying the air and fuel mass flow rates. Each ignition attempt consists in multiple sparks at a frequency of $f_{spark} = 4\,Hz$ until the detection of the ignition with an over-pressure ($\Delta P \approx 0.1 - 0.2\,bar$) and a visual confirmation. A time-interval of 2 to 6 s is observed between the first spark and the ignition detection. Therefore, for each ignition attempt, 8 to 25 sparks are applied. After 10 s, if no ignition is observed, the attempt is considered as a failure. Ignition results are displayed on Fig. 14.1.4 and clearly show that a richer mixture is required at low pressure to ensure the ignition of the chamber. One can note that the conditions presented in Tab. 14.1.3 are slightly richer than the non-ignition limit. The non-ignition limit is defined as the highest equivalence ratio resulting in a failed ignition.

The reduced amount of experimental data may be explained by the low pressure and low temperature conditions. Indeed, as illustrated on Fig. 14.1.5 the larger droplets and the absence of evaporation induce the formation of a liquid film at the wall preventing long-duration measurements. This observation also

[1] Same measurements are given for the case **PTatmo** (in JETSCREEN project) however complementary data can be found in the thesis of Eyssartier [2012] since a similar operating condition has been studied.

[2] Axis direction conventions have been modified from the JETSCREEN experimental data to match the numerical domain: z-axis has been changed by x-axis, x-axis by y-axis and y-axis by z-axis

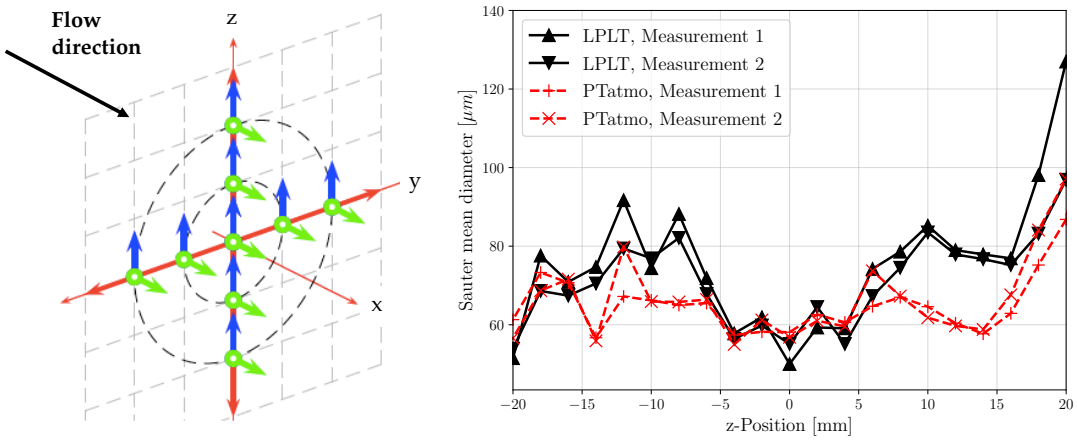

Figure 14.1.3: Left: scheme of LDA/PDA direction measurements. Right: SMD experimental profiles along the z axis for the cases **PTatmo** and **LPLT** (adapted from[Orain 2020]).

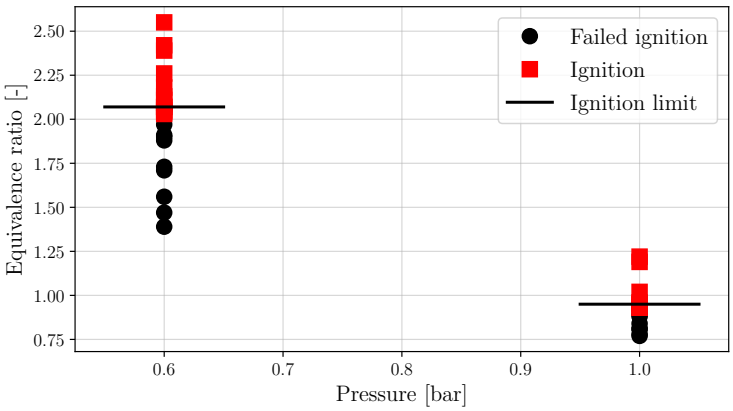

Figure 14.1.4: Ignition results for the cases **PTatmo** and **LPLT** (adapted from [Orain 2020]).

suggests the formation of a liquid film on the ignition device. This effect has not been studied in this work but could largely influence the ignition. Moreover, frost has also been observed due to the cold air.

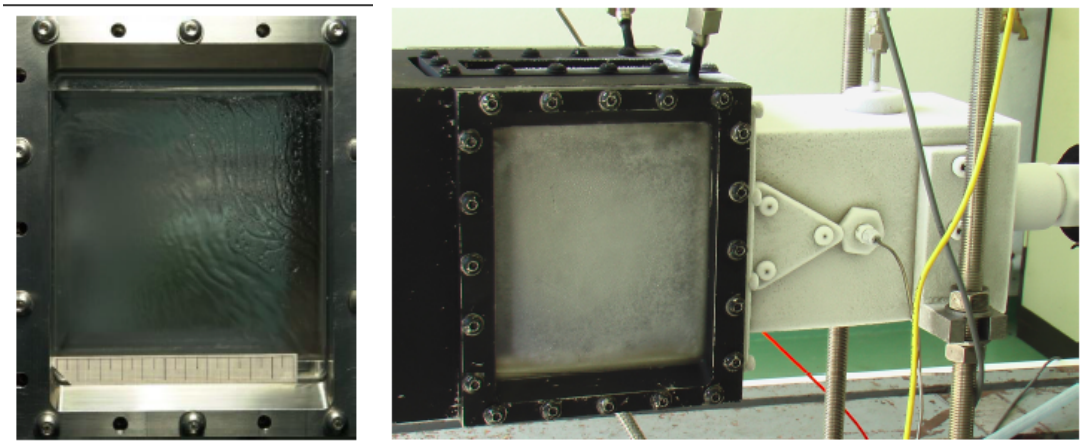

Figure 14.1.5: Photographs of liquid film (left) and frost (right) formation at low pressure and low temperature operating conditions (extracted from [Garcia-Rosa 2008]).

14.2 Gaseous cold flow

Prior to the ignition phase, the gaseous flow and fuel injection must be computed to obtain the characteristic flow structures and the fuel droplet distribution at the spark position. This section aims at introducing the numerical set-up used for the cold flow simulation, and at analysing the resulting flow structures forming in the combustion chamber.

14.2.1 Numerical set-up for cold flow

All simulations have been performed with AVBP [Schönfeld and Rudgyard 1999]. The mesh used for the cold flow simulations[3] is presented on Fig. 14.2.1 with an axial cut. The finest cells have been used in the high velocity regions where the turbulent structures are expected. They correspond to the zone **B** (swirler) and **C** (air stream) which are meshed with a characteristic cell size $\Delta x = 1\,mm$. The mesh characteristic cell sizes for the other zones are given in Tab. 14.2.1 and result in a total of 12 million cells in the domain.

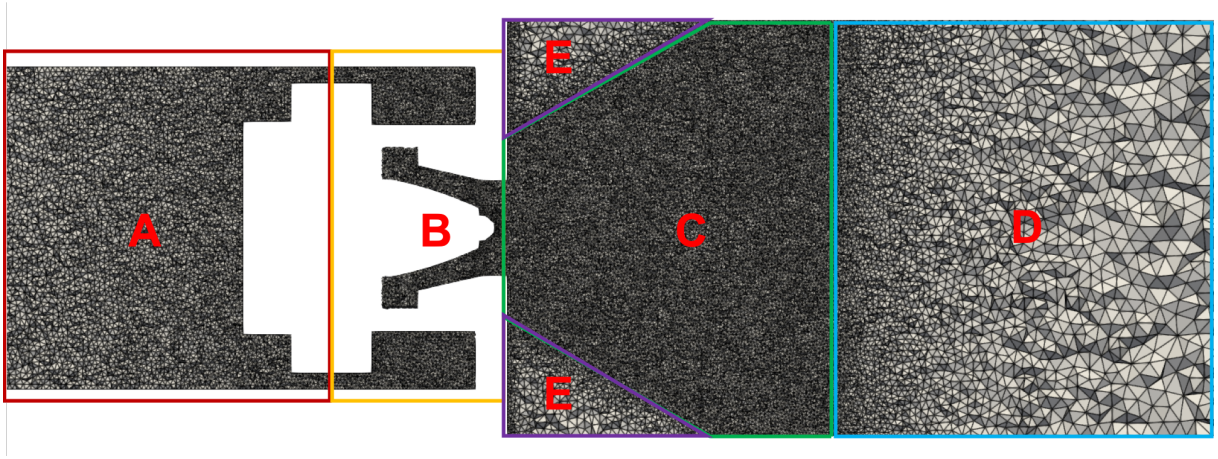

Figure 14.2.1: MERCATO cold flow mesh

Zone	Label	Characteristic cell size $\Delta x\,[mm]$
A	Plenum	1 - 2
B	Swirler	1
C	Air stream / flame	1
D	Post flame	1 - 10
E	Outer Recirculation Zone (ORZ)	1 - 5

Table 14.2.1: Characteristic cell sizes for MERCATO cold flow simulations.

Compared to the previous works of Eyssartier [2012] and Sanjose [2009], the tip-injector geometry has been modified to be more realistic of the real injector shape (see Fig. 14.2.2).
The domain is initially filled with air ($Y_{O_2} = 0.233$ and $Y_{N_2} = 0.767$) at the conditions corresponding to the case **LPLT** in Tab. 14.1.3 ($P = 0.6\,bar$ and $T_a = 233\,K$). The air flow ($\dot{m}_a = 19.2\,g.s^{-1}$) is injected in the plenum and exits the domain through the exhaust pipe (see Fig. 14.1.2) with a pressure outlet condition. Inlet and outlet conditions are based on the NSCBC formalism [Poinsot and Lelef 1992]. The walls are considered adiabatic and no-slip velocity conditions are applied. Finally, the numerical models used in AVBP for the cold flow simulations are summarized in Tab. 14.2.2.

Flow characteristic time-scales are described below:

- **Chamber convective time $\tau_{conv,chamber}$:**
  The chamber convective time is defined as the time taken by the gas to go from the entrance to the

[3]For the ignition simulation the mesh must be refined at the spark location and is presented in Sec. 14.4

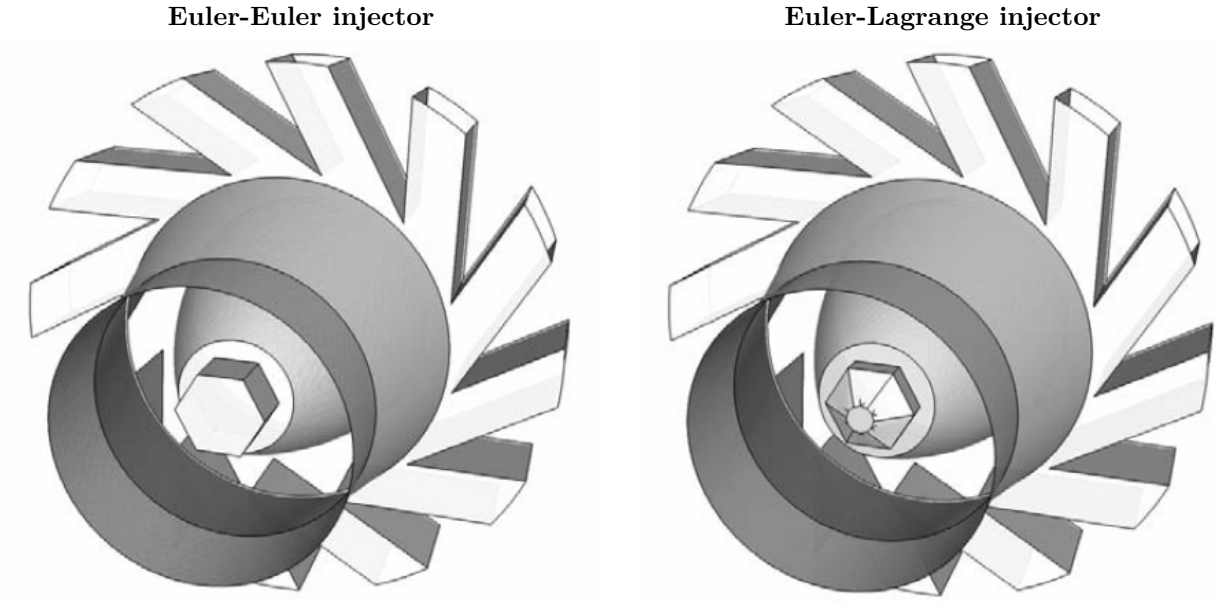

Figure 14.2.2: Injector geometry for Euler-Euler or Euler-Lagrange formalism (extracted from [Sanjose 2009])

Numerical models	
Convective scheme	TTGC [Colin and Rudgyard 2000]
Diffusive scheme	Finite element second order
Artificial viscosity	Colin [Colin 2000] based on ρu ($AV2^{nd} = 0.5$, $AV4^{th} = 0.05$)
LES closure	WALE [Nicoud and Ducros 1999]

Table 14.2.2: Numerical models used for cold flow simulations.

end of the chamber. It is computed based on the bulk velocity :

$$\tau_{conv,chamber} = \frac{L_c}{U_{bulk}} = 397\,ms \tag{14.3}$$

where $L_c = 0.5\,m$ is the chamber length and $U_{bulk} = 1.26\,m.s^{-1}$.

- **Spark convective time $\tau_{conv,spark}$:**
  In the MERCATO configuration, due to the exhaust pipe, the combustion chamber is very long. Thus, the chamber convective time may not be representative of the zone of interest. On the contrary, the spark convective time which corresponds to the time taken by the gas to reach the spark device from the injection is more representative:

$$\tau_{conv,spark} = \frac{x_{spark}}{U_x} = 2.4\,ms \tag{14.4}$$

  with $x_{spark} = 0.06\,m$ the axial position of the spark device and $U_x = 25m.s^{-1}$ the mean axial velocity integrated between $x = 0$ and $x = x_{spark}$.

- **Swirl time τ_{swirl}:**
  The swirl time is defined as the time required for a complete revolution of the flow around the injection axis. Since the swirl is conical and expands in the combustion chamber, the swirl characteristic time increases with the distance to the injector. Two positions has been evaluated: $\tau_{swirl,10}$ corresponding to the base of the swirl at 10 mm from the injector and $\tau_{swirl,60}$ at 60 mm aligned with the spark device.

$$\tau_{swirl,10} = \frac{2\pi R_{swirl}(x = 0.01)}{U_\theta(R_{swirl}, x = 0.01)} = \frac{2\pi \times 0.012}{40} = 1.9\,ms \tag{14.5}$$

$$\tau_{swirl,60} = \frac{2\pi R_{swirl}(x=0.06)}{U_\theta(R_{swirl}, x=0.06)} = \frac{2\pi \times 0.02}{10} = 12.6\,ms \tag{14.6}$$

where $R_{swirl}(x)$ is the swirl radius at the position x and $U_\theta(R,x)$ is the ortho-radial velocity at the radial distance R and the axial position x.

14.2.2 Gaseous flow

From the initialisation, the computation has been converged for 160 ms, then the flow field has been averaged for 170 additional ms. Based on the characteristic flow times presented in the previous section, the averaged results are considered statistically converged, at least in the zone of interest.

Flow visualization

The averaged velocity field is displayed on Fig. 14.2.3 with an axial cut plane at $y = 0$. The axial velocity field highlights the main flow structures in the combustion chamber. The swirled air injection forms three main regions in the combustion chamber: (i) the SWirled Jet (SWJ), (ii) Outer Recirculation Zones (ORZ) also called the Corner Recirculation Zones (CRZ) and (iii) the Inner Recirculation Zone (IRZ) also called Center Toroidal Recirculation Zone (CTRZ). The IRZ can be divided in two main parts. The bottom part, close to the injection vanes, is confined by the SWJ and has a strong recirculating motion. Then, moving away from the injector the tangential velocity decreases which eventually causes a vortex breakup around $x = 85\,mm$ with an opening of the SWJ and an increase of the radial velocity. Firstly this phenomenon induces an expansion of the IRZ which extends until the exhaust pipe, secondly, it closes the ORZ. A radial flow towards the center is also observed in the ORZ at the base-plate which prevents the SWJ to directly open at the injector exit.

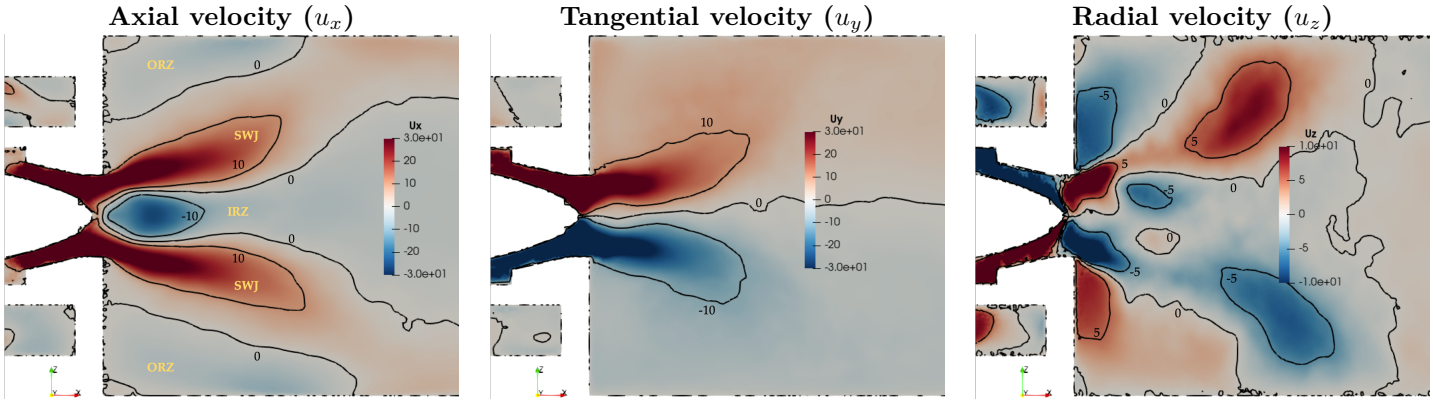

Figure 14.2.3: Time-averaged gaseous velocity fields on the axial cut-plane $y = 0$ in MERCATO.

The strong swirled air motion also enables the formation of a Precessing Vortex Core (PVC) illustrated on Fig. 14.2.4 with the pressure iso-surfaces $P = 59900\,Pa$ colored by the axial velocity. The large velocity fluctuations indicate the formation of strong gradients and vorticity between the SWJ and the bottom part of the IRZ.

The development of the SWJ is also shown on Fig. 14.2.5 with the axial velocity at several transverse cut-planes. The cut-plane at the PVC shows that the SWJ is only located at the center of the chamber and surrounds the bottom part of the IRZ. Both have a symmetry of revolution which is not the case for the ORZ due to the square section of the chamber. This cross structure has been also observed in previous numerical and experimental works [Sanjose 2009, Eyssartier 2012]. At the spark position, the SWJ becomes weaker and starts to expand. One can note that the ORZ completely merges and the spark device is located at the tip of the ORZ. Indeed, moving downstream, and as explained before, the vortex breaks which closes the ORZ and broadens the IRZ.

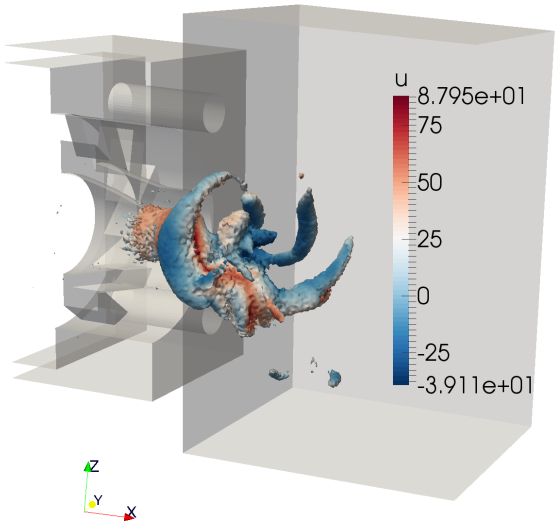

Figure 14.2.4: Formation of the Precessing Vortex Core (PVC) due to the swirled air injection (iso-surface $P = 59900\,Pa$) colored by the axial velocity in MERCATO.

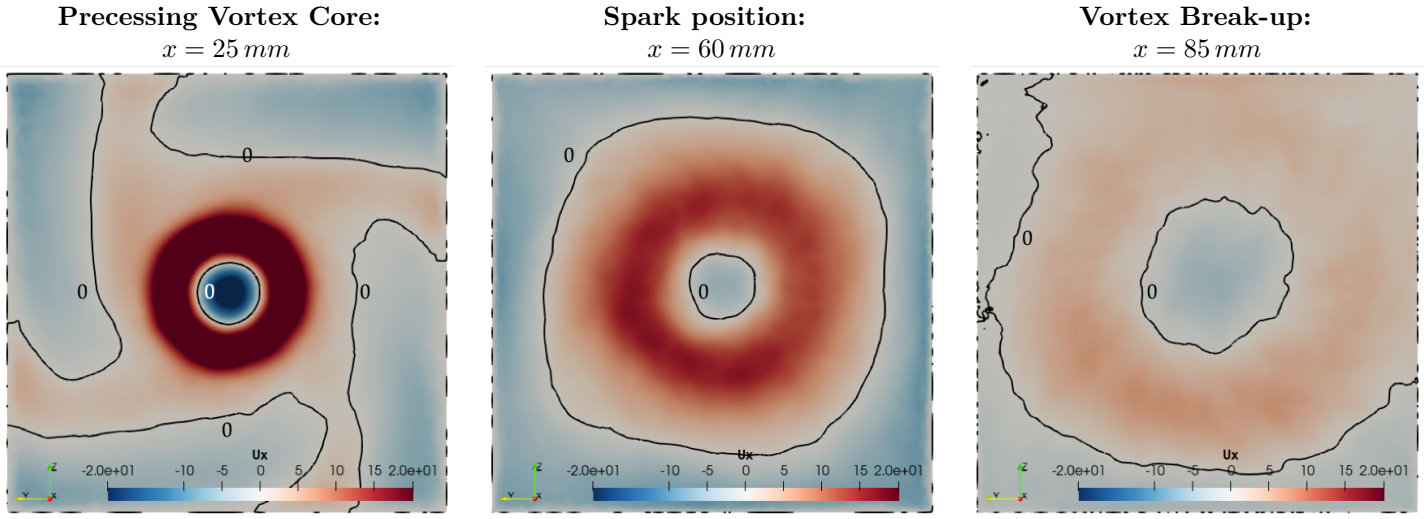

Figure 14.2.5: Time-averaged gaseous axial velocity field (u_x) for three transverse cut-planes in MERCATO.

Finally, the velocity fluctuation fields are displayed on Fig. 14.2.6. As expected, the largest fluctuations are observed in high velocity gradient regions, i.e., in the SWJ and at the bottom part of the IRZ. Therefore, the spark position is located in a relatively low fluctuation region ($U_{rms} < 10\,m.s^{-1}$ with $U_{rms} = \sqrt{{u_{x,rms}}^2 + {u_{y,rms}}^2 + {u_{z,rms}}^2}$) which should promote the kernel formation. However, the fluctuation levels may prevent the flame kernel propagation towards the SWJ.

Influence of the exhaust pipe

One can note that on Fig. 14.2.3 and 14.2.5 the flow field is not centered on the x-axis even after long averaging and convergence periods. As a consequence, a negative radial velocity is observed in the IRZ and the ORZ on the spark device side is shorter.

This asymmetric flow pattern is induced by the exhaust pipe used in the experiment to reproduce the low pressure conditions. Indeed, Fig. 14.2.7 illustrates the time-averaged flow fields with the Line Inte-

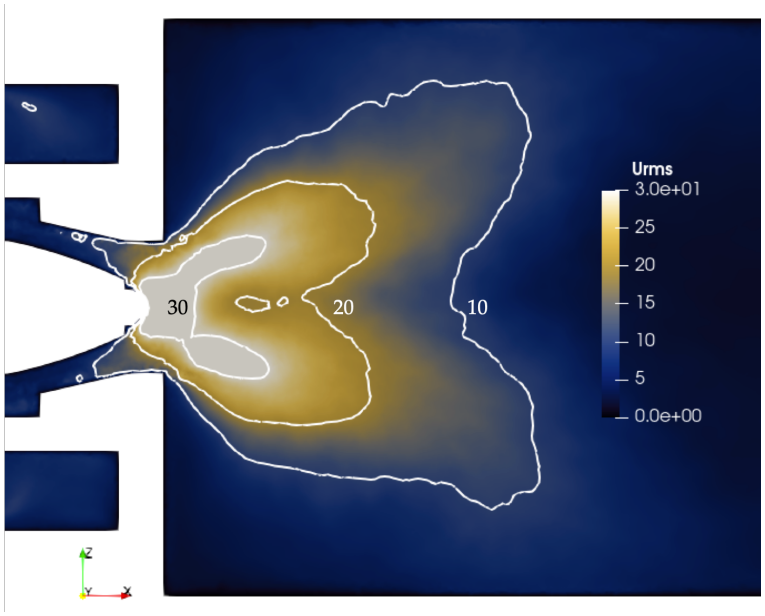

Figure 14.2.6: RMS velocity field on the axial cut-plane $y = 0$ in MERCATO.

gral Convolution (LIC) method which enables to display tangential structures to the velocity field. The formation of several vortices in the upstream part of the combustion chamber is observed due to the aspiration in the exhaust pipe.

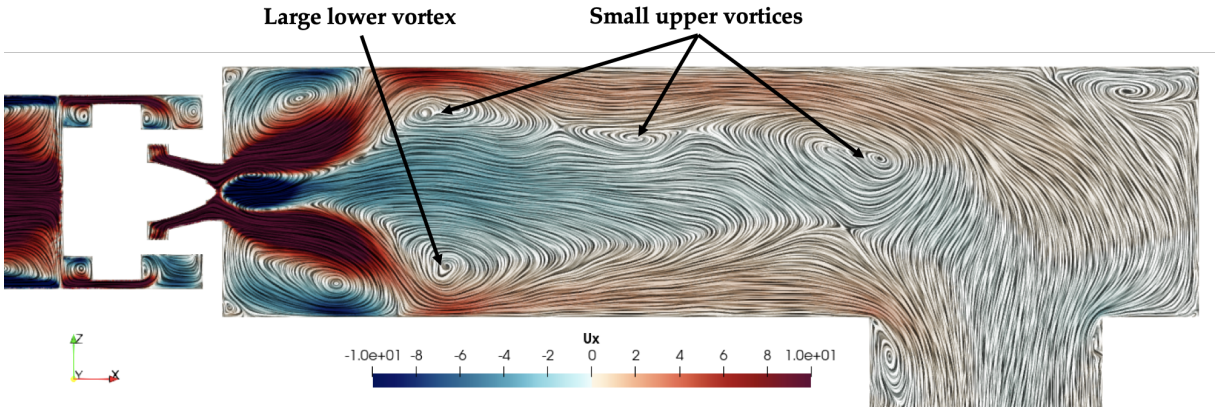

Figure 14.2.7: Averaged flow field visualisation in the axial cut-plane $y = 0$ using Line Integral Convolution (LIC) method colored by the axial velocity.

As it can be seen on Fig. 14.2.8, the symmetry of the flow is recovered when removing the exhaust pipe. Hence, the ORZ edges are located at the same position. However, in the following, the exhaust pipe has been kept for the simulation since it is more representative of the experimental set-up. Indeed, the shorter ORZ at the spark device location may result in a stronger interaction of the kernel with the SWJ at the ignition.

Velocity profiles

Finally, the velocity profiles are given on Fig. 14.2.9 along z-axis for several axial positions. Unfortunately, no experimental data were available for validation. The consequences of the asymmetric flow can be clearly seen on the radial velocity which is completely negative in the IRZ at $x = 30\,mm$ and on the axial velocity at $x = 90\,mm$. These quantitative profiles may be useful to better understand the interactions with the fuel spray at the injection and with the ignition at the spark location. For

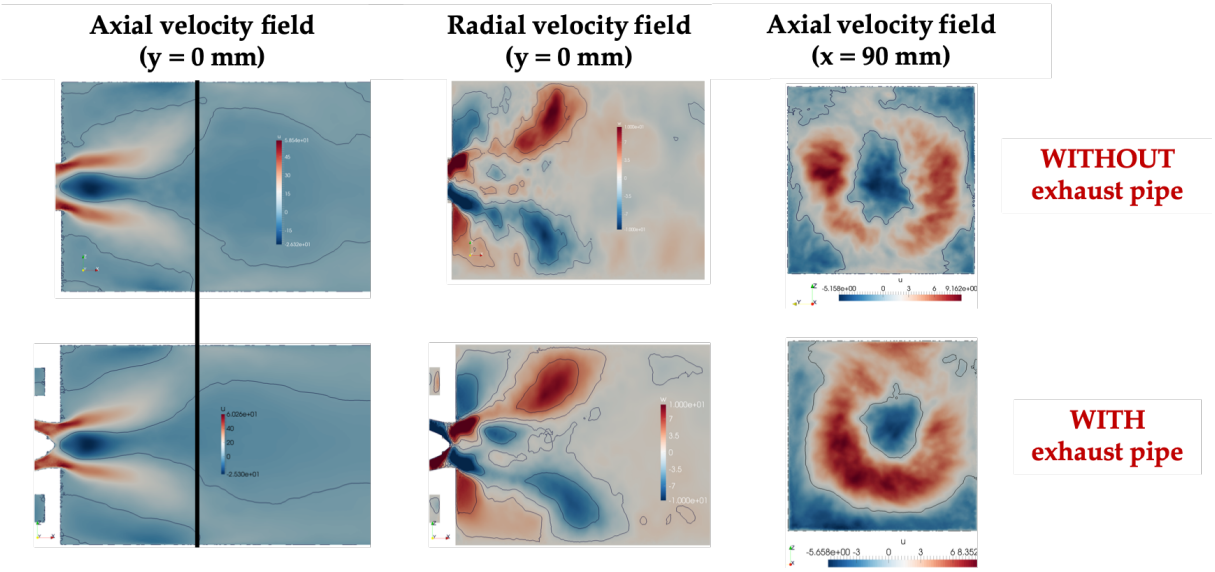

Figure 14.2.8: Qualitative time-averaged velocity fields comparison with and without the exhaust pipe.

instance, the RMS velocity reaches $u_{rms} = 10\, m.s^{-1}$ which is higher than the turbulence levels of the DNS computations in Chap. 9. Therefore, these turbulence levels may cause the kernel extinction if the latter is not able to propagate in the ORZ presenting lower velocity fluctuations.

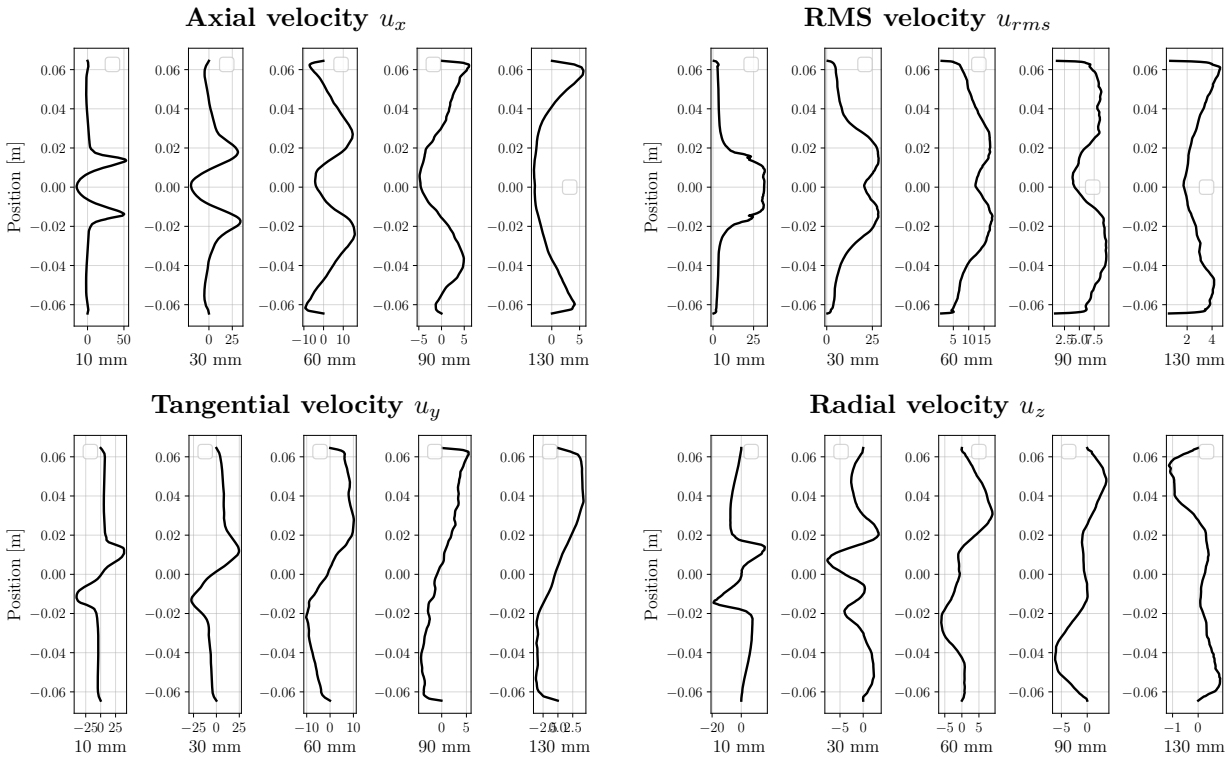

Figure 14.2.9: Time-averaged gaseous velocity profiles $[m.s^{-1}]$ versus z-position ($y = 0$) for several axial positions in MERCATO.

14.3 Two-phase flow

In the following the numerical set-up for the spray injection is first presented. Then, a methodology to determine the optimal injection parameters from experimental data measurements is proposed. Finally, the numerical two-phase flow profiles are analysed and compared to the experimental data.

14.3.1 Numerical set-up for two-phase flow

The liquid injection phase is based on the same mesh as the gaseous cold flow presented in Sec. 14.2.1. Elastic rebound at walls is used for the droplet boundary conditions. A droplet injection patch is applied at the injector nozzle to mimic the fuel spray injection and exit conditions are applied at the outlet.

The liquid fuel injection properties are summarized in Tab. 14.3.1. The liquid density ρ_l corresponds to the fuel blend composition and is computed with the mixing law Eq. (14.7). The liquid density variation with temperature is not considered in this work[4].

$$\rho_{fuel} = \sum_{\kappa=1}^{N_{liq}} X_\kappa \rho_{\kappa,liq} \tag{14.7}$$

with $\rho_{\kappa,liq}$ the liquid density of species κ, and X_κ its molar fraction.

Fuel mass flow rate $\dot{m}_{fuel}\,[g/s]$	**Fuel Temperature** $T_{fuel}\,[K]$	**Fuel density** $\rho_{fuel}\,[kg/m^3]$
2.8	293	784

Table 14.3.1: Fuel injection properties.

Similarly to the gaseous phase, the liquid phase can be characterized with several time-scales:

- **Drag time** $\tau_{p,\mathcal{D}}$**:**
  This time characterizes the droplet velocity response to the drag force and can be computed using Eq. (1.88). In this work, the droplet size ranges from $d_p = 10\,\mu m$ to $d_p = 100\,\mu m$ and the droplet velocity is estimated experimentally at the injection around $u_p \approx 20\,m.s^{-1}$ leading to $0.2\,ms \leq \tau_{p,\mathcal{D}} \leq 10.3\,ms$.
  Combining with the convective gaseous time of Sec. 14.2.1, the Stokes number $St = \tau_{p,\mathcal{D}}/\tau_{g,conv}$ can be computed. Then, considering the convection towards the spark device, $0.08 \leq St \leq 4.3$ is obtained. Therefore, small droplets, with a Stokes number lower than unity, behave like tracers of the flow, whereas the largest ones tend to have a balistic trajectory driven by their own inertia. As a consequence, the distribution at the spark position may differ from the injected one and the smallest droplets may be trapped in the ORZ which could increase their proportion at the spark location. Hence, the carburation time must be long enough to fill the ORZ.

- **Vaporization time** $\tau_{p,vap}$**:**
  Due to the low temperature conditions ($T_a = 233\ K$), the droplets are quickly cooled at the injection and do not evaporate in the combustion chamber. Hence, the vaporisation characteristic time can be considered as infinite and there is no fuel pre-evaporation in the chamber. It is a non negligible difference with the **PTatmo** conditions for which the vaporisation time has been estimated at $\tau_{p,vap}^{PTatmo} \approx 110\,ms$ [Eyssartier 2012] and where the fuel pre-evaporation can promote the ignition.

Finally, the numerical models used for the two-phase flow simulations in AVBP are summarized in Tab. 14.3.2. These models have been detailed in Chap. 1 and 11. The FIM-UR injection model requires to impose the distribution parameters. A Rosin-Rammler (RR) distribution has been chosen because its generic shape enables to represent the spray size distribution. However, the SMD, the shape parameter q and the half-cone injection angle θ are not known a priori. Their determination is the subject of the following section.

[4]The reference species densities are taken at $T = 288\,K$.

Numerical models	
Drag	Schiller and Naumann [Schiller and Naumann 1935]
Evaporation	Abramzon and Sirignano [Abramzon and Sirignano 1989] extended to multi-component [Shastry 2022]
Injection	FIM-UR [Sanjosé et al. 2011]

Table 14.3.2: Numerical models used for two-phase flow simulations.

14.3.2 Optimization of the injection parameters

As explained above, the FIM-UR model requires user parameters such as SMD, shape distribution parameter q and spray half cone angle θ. Unfortunately these parameters are unknown at the **LPLT** operating point. Moreover, neither the injector geometrical dimensions nor the liquid film characteristics (angle, velocity and thickness), which are the input information needed for the the primary atomization model developed in Chap. 11, are known. Therefore, this model cannot be used for this study.

However, droplet velocities, and characteristic moments of the spray distribution measured at $x = 10\,mm$ are available. Based on these data, optimization of the FIM-UR parameters is conducted using the uncertainty quantification tool BATMAN (Bayesian Analysis Tool for modeling and uncertAinty quaNtification) developed at CERFACS [Roy et al. 2018; 2017]. The complete study is presented in Appendix. H and the optimized injection parameters retained in the following are summarized in Tab. 14.3.3.

Injection half angle $\theta\,[°]$	**SMD** $d_{p,32}\,[\mu m]$	**Shape parameter** $q\,[-]$
36	85	1.92

Table 14.3.3: FIM-UR injection parameters obtained from optimimzation.

14.3.3 Two-phase flow profiles

Using the above FIM-UR injection parameters, the two-phase simulation is first converged for 65 ms and then averaged over 120 additional ms. In the following paragraphs, the SMD and two-phase velocity profiles are analysed and compared with experimental data.

SMD profile

The obtained SMD field is shown in Fig. 14.3.1(left) while the profile along z-axis at 10 mm from the injector ($x = 10\,mm$ and $y = 0\,mm$) is displayed on Fig. 14.3.1(right).

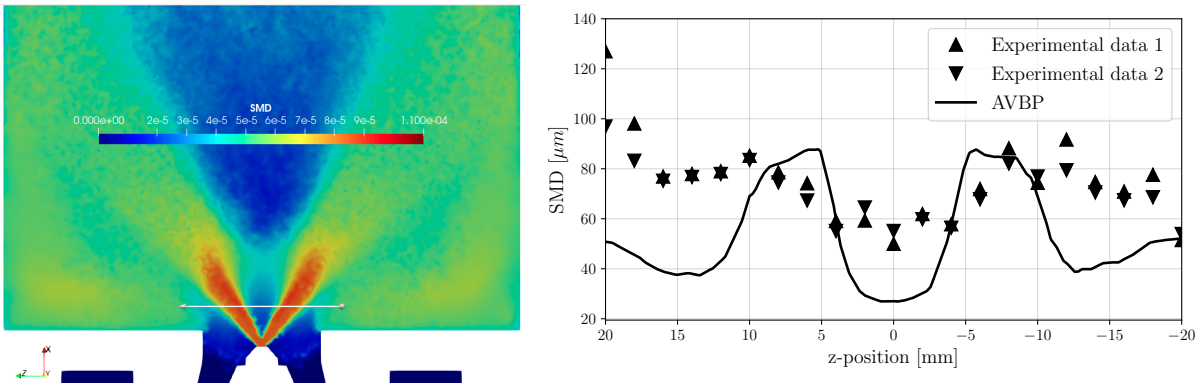

Figure 14.3.1: Time-averaged SMD field in an axial cut-plane (left) and profile along z-axis at $x = 10\,mm$ and $y = 0\,mm$ compared to measurements (right).

The SMD peak value is well retrieved in the simulation, but the injection cone is narrower. As shown in the optimization study (Appendix. H), the peak position does not depend on the injection angle.

Therefore it results from the interaction with the gaseous flow, here the air SWJ. The difference between the simulation and the experiment then means that the gaseous flow also differs. Unfortunately this assumption cannot be verified because no gaseous flow measurement was provided.

The center and lateral zones are filled with much smaller droplets in the simulation. This observation remained even after a much longer convergence time. The cut-plane view clearly indicates that these zones correspond to the ORZ and IRZ. Several assumptions may explain these differences:

- Firstly, the experimental data may be less accurate in these zones of lower droplet number density.
- Secondly, the simulation time may be still too short for statistical convergence in these zones. The simulation could not be run longer because of the CPU-cost. As an alternative, the simulation could start from a homogeneously pre-filled chamber with a given droplet size distribution. However, such methodology raises two questions : how to best initialize the droplet field and how to make sure that this initialiation will not bias the results? In this work, such methodology was not evaluated due to a lack of time, and the possibly incomplete convergence of the two-phase flow in the ORZ and at the spark position must be kept in mind when analysing the ignition and flame kernel propagation.
- Finally, an interaction with the gaseous flow cannot be excluded. Especially, the strong profile decrease before entering the ORZ ($z = \pm 12.5\,mm$) may be explained by unsteady flow re-circulations and is developed in the next paragraph.

Axial droplet velocity

The axial droplet velocity is shown on Fig. 14.3.2. Looking at the profile comparison with experiment, it appears that this velocity component is overall well recovered, in particular in the region $-12\,mm \leq z \leq 12\,mm$.

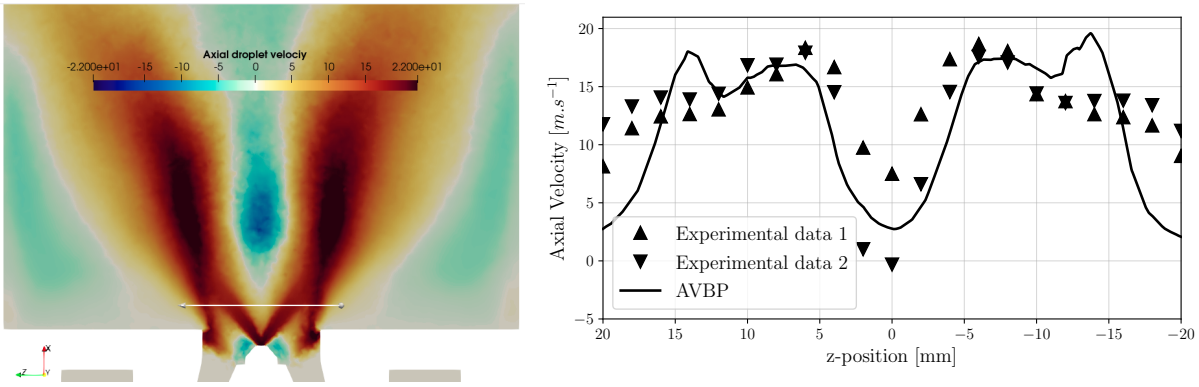

Figure 14.3.2: Time-averaged axial velocity cut-plane field (left) and profile along z-axis at $x = 10\,mm$ and $y = 0\,mm$ compared to measurements (right).

A double peak structure is observed in the simulation which is absent in the experiments. As may be seen in the cut-plane field, the center peaks are associated to the spray injection velocity while the external peaks originate from the interaction of the droplets with the air swirling system. As shown on Fig. 14.3.3, in average the tip of the IRZ remains at the injector exit plane, but intermittently enters in the air swirling system due to the PVC. As a consequence, this back-flow drags the smallest droplets with a small Stokes number backward into the air injection. These droplets are then entrained by the SWJ back into the chamber, forming the external velocity peaks.

These external peaks, only containing small recirculated droplets, explain the SMD decrease observed on Fig. 14.3.1 at $z = \pm 13\,mm$. Since these peaks are not observed in the experimental data (or with a much reduced intensity), the assumption that the numerical gaseous flow field is different from the experiment is reinforced. Finally close to the walls, the axial velocity reduces earlier, from $z \pm 15\,mm$ instead of $z \pm 20\,mm$ in the experiment. The cut-plane field indicates that this transition corresponds to

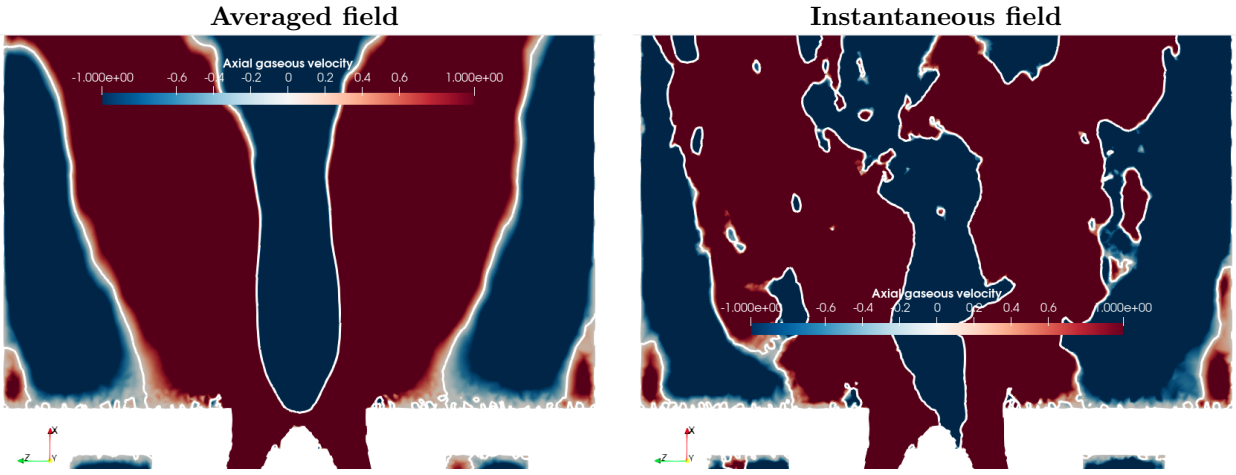

Figure 14.3.3: Time-averaged (left) and instantaneous (right) gaseous axial velocity field on an axial cut-plane. Colors are saturated to highlight negative and positive velocity.

the ORZ limit which is therefore more expanded in the simulation. These flow differences could be explained by an unknown geometry modification of the injection system compared to the previous studies. Especially, Garcia-Rosa [2008] demonstrated that switching from rounded injector edges to right-angled corners largely modifies the flow structure[5].

Radial droplet velocity

Similarly to the axial velocity, the radial velocity shown on Fig. 14.3.4 is in agreement with the measurement in the spray zone $-13\,mm \leq z \leq 13\,mm$. A strong velocity drop, not observed in the experiment, corresponds to droplets entering the ORZ, confirming the wider SWJ in the experiment.

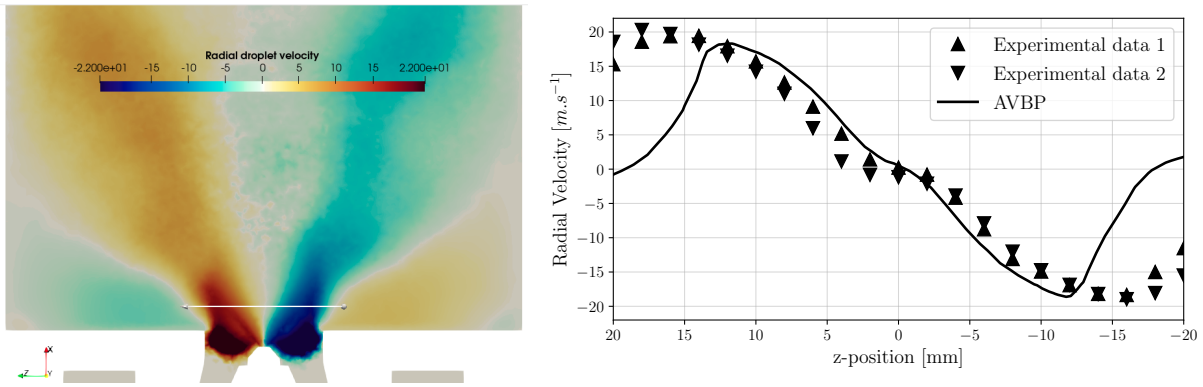

Figure 14.3.4: Time-average radial velocity cut-plane field (left) and profile along z-axis at $x = 10\,mm$ and $y = 0\,mm$ compared with measurements (right). The horizontal line corresponds to the measurement position.

Tangential droplet velocity

Finally, the tangential velocity is presented on Fig. 14.3.5. Since the droplets are not swirled when entering the chamber, they have a negligible tangential velocity at injection. The rotational motion is induced by the interaction with the swirl flow, leading to a gradual radial increase of the tangential velocity. Similarly to the other velocity components, a good agreement with experiment is obtained in

[5]From Garcia-Rosa [2008] the right-angled corners are used (as in this work) because they enable a better SWJ penetration in the chamber which reduces the liquid filming at the wall and improves the measurements.

the spray zone.

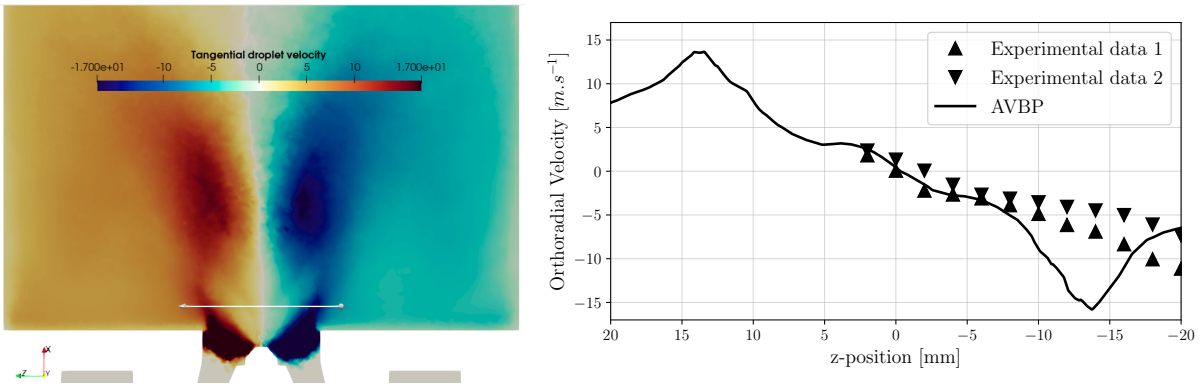

Figure 14.3.5: Time-averaged tangential velocity cut-plane field (left) and profile along z-axis at $x = 10\,mm$ and $y = 0\,mm$ (right) compared to measurements. The horizontal line corresponds to the measurement position.

As shown on the cut-plane of the left picture, the small recirculating droplets in the air swirling system get a strong tangential velocity from the swirling air flow. They are then re-injected in the SWJ zone which results in the large peak in the simulation velocity profile. Here also, this peak is not observed or moved towards the ORZ in the experimental data, which indicates that in the experiment there are no recirculating droplets or that the SWJ is much larger, respectively.

Conclusions

Overall, the numerical two-phase flow matches the experimental data in the spray injection zone which enables to validate the injection parameters. However, in the air SWJ zone, large discrepancies are observed, indicating that the gaseous air flow in the simulation is not in perfect agreement with the experiment at the injection system exit. Especially, the recirculation of small droplets is not observed in the experimental data and the ORZ are less spread towards the injector at the base plate.

Despite these discrepancies which may influence the flame kernel propagation in the ORZ and its attachment to the injector, it is considered that this numerical two-phase flow is suitable to perform ignition simulations, presented in the following section.

14.4 Two-phase ignition

14.4.1 Numerical set-up for ignition

The simulation of ignition requires to adapt the mesh in order to resolve the reactive flow at the spark location and avoid to use a combustion model. To do so, a refined spherical zone is added to the previous mesh (Fig. 14.2.1) and the ORZ are refined as in the air stream / flame zone to correctly account for the possible kernel propagation in the ORZ. The characteristic cell sizes are summarized in Tab. 14.4.1 and the resulting mesh is shown on Fig. 14.4.1. At the spark location, the grid size is $\Delta x = 100\,\mu m$ which enables a complete description of the flame structure (~ 8 points in the flame front). The spark refined zone is 1 cm radius and is located at $x_{spark} = 0.06\,m$, $y_{spark} = 0\,m$ and $z_{spark} = 0.058\,m$ close to the top wall ($z_{top\,wall} = 0.0645\,m$). The resulting mesh is now composed of 42.6 million elements.

In a first approach the walls are adiabatic. Wall heat transfers may have a large influence on the kernel development: either detrimental with cold walls or beneficial with hot walls (depending on the thermal environment of the combustion chamber). However this question was not addressed in the present work due to a lack of time, and dedicated studies on ignition-wall interactions may be investigated in future work.

Zone	Label	Characteristic cell size $\Delta x\,[mm]$
C	Air stream / flame zone	1
E	Outer Recirculation Zone (ORZ)	1
F	Transition zone	0.1 - 1
G	Spark zone	0.1

Table 14.4.1: Characteristic cell sizes for MERCATO reactive simulations.

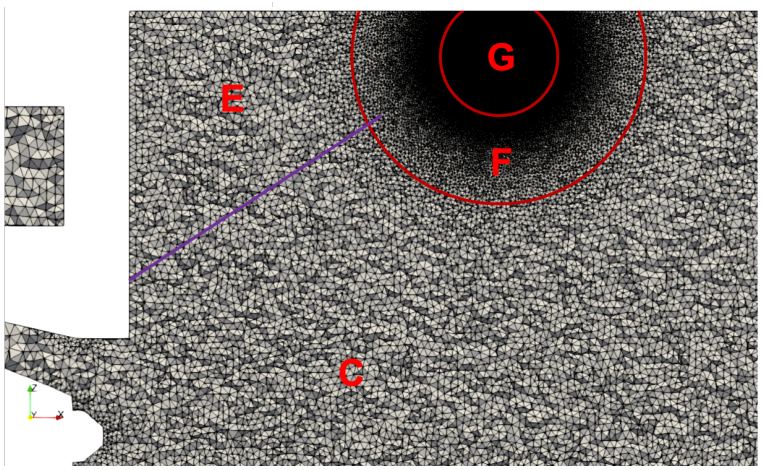

Figure 14.4.1: MERCATO mesh for the simulation of ignition.

The numerical set-up used for ignition with AVBP is identical to the one presented in Chap. 13 for the spherical bomb cases and gathers the different models and modifications developed in this work. The main informations are summarized in Tab. 14.4.2.

Numerical models	
Convective scheme	Lax Wendroff [Lax and Wendroff 1960]
Diffusive scheme	Finite element second order
Artificial viscosity	Colin [Colin 2000] based on ρu and ρY_k ($AV2^{nd} = 0.2$, $AV4^{th} = 0.02$) including the modification on the activation sensor (see Chap. 13)
LES closure	WALE [Nicoud and Ducros 1999]
Chemical scheme	ARC scheme S30R299QSS22 (developed in Chap. 7) tri-component surrogate kerosene - air
Chemistry integration	Exponential integration (presented Chap. 8) without mass conservation algorithm (see Chap. 13) LDSC (developed Chap. 8) ($SC_{max} = 1000$ and $\Delta t_{chem,user} = 0.01\,ns$)
Evaporation	Multicomponent including saturation correction (introduced Chap. 12)
Point source correction	PBM (developed Chap. 13) ($N_c = 100$ and $R_b = 2\Delta x$)

Table 14.4.2: Numerical models used for ignition simulations.

As for the previous computations, the ignition is triggered using the energy deposit model developed in Lacaze [2009] and presented in Sec. 9.1. The model parameters are summarized in Tab. 14.4.3. The deposited energy corresponds to 30 % of the energy measured experimentally in the spark device ($E_{spark,exp} = 580\,mJ$) to account for the thermal losses at the electrodes [Maly and Vogel 1978, Teets and Seel 1988, Collin-Bastiani 2019]. The deposit size is chosen to reach a maximum temperature of $T_{max} = 3500\,K$ resulting in an initial hot gas kernel radius of approximately $R_{ker} = 5.4\,mm$. Lower deposited energies have been also evaluated (from $\varepsilon_i = 50\,mJ$ to $\varepsilon_i = 150\,mJ$), but the resulting kernels were too small to ignite a sufficient number of droplets.

In the experiment, the ignition device sparks at a frequency of 4 Hertz whereas, in the numerical computation, only one spark is simulated. Hence, the stochastic behavior of ignition [Esclapez 2015, Collin-Bastiani 2019] is hardly evaluated and historical effects of previous sparks are not taken into account.

Energy deposit model	
Deposit duration	$2\Delta_t = 100\,\mu s$
Deposit size	$\Delta_s = 1.5\,cm$
Deposited energy	$\varepsilon_i = 175\,mJ$

Table 14.4.3: Parameters of the energy deposit model.

Experimentally the ignition results from one of the multiple sparks corresponding to optimum flow conditions. Therefore, in the simulation, the spark moment must be chosen carefully to maximise the ignition success. This is the subject of the following section.

14.4.2 Flow conditions at spark

The flow conditions at the spark position have been analysed to determine the best moment to trigger the ignition. These conditions are also of interest to understand the subsequent flame kernel dynamics.

Gaseous flow conditions

To increase the ignition probability and promote the kernel propagation, low turbulent intensity is favored to avoid convective heat losses, kernel surface increase which promotes conductive heat losses, and stretch effects which may decrease the heat release rate.

The gaseous velocity profiles already analysed in Sec. 14.2.2 show that the spark position is located at the ORZ tip with a non-negligible axial velocity fluctuation up to $u_{rms} = 10\,m.s^{-1}$. Moreover, a probe at the spark position recorded the three velocity components given on Fig. 14.4.2. The axial velocity component (u_x) is negative in the interval $t = [526.7\,ms\,;\,528.5\,ms]$. Hence, for almost 2 ms, this flow would drive the kernel in the ORZ. The orthoradial velocity (u_y) first has low frequency fluctuations which may induce a global kernel entrainment by the swirling flow. Finally, in the same first phase the radial velocity (u_z) fluctuations are limited to $-5\,m.s^{-1} \leq u_z \leq 5\,m.s^{-1}$ which is favorable for the kernel development. On the contrary in the following time, a strong flow reaching $u_z = 20\,m.s^{-1}$ may be detrimental and drive the kernel towards the wall. This second phase also sees a large orthoradial velocity and more intense axial fluctuations. Hence, it is not suitable for ignition. Therefore, the spark moment has been chosen at $t_{spark} = 526,7\,ms$, i.e., at the beginning of the recorded sequence.

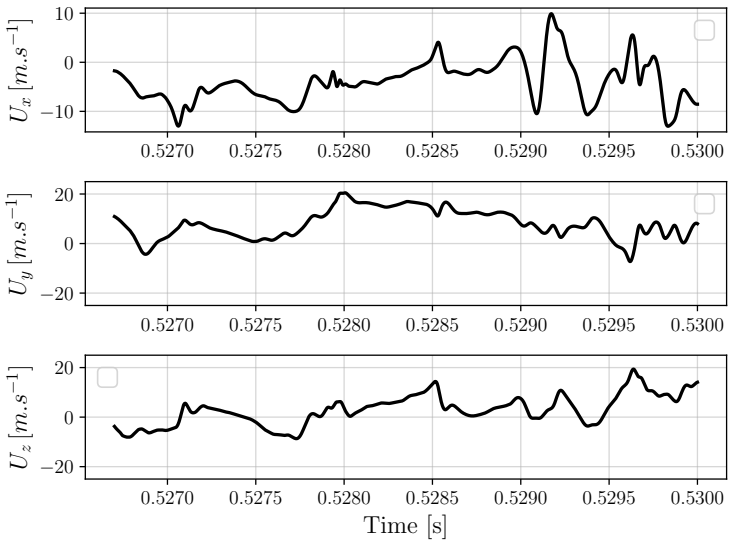

Figure 14.4.2: Temporal evolution of the gaseous velocity components at the spark location.

Two-phase flow conditions

The spark moment has been defined from the optimum gaseous flow, however, the fuel load and the flammability conditions must be also verified. The evolution of the total equivalence ratio during the carburation is shown on Fig. 14.4.3. Large discrepancies can be observed between the injection zone, the spark position and at the exit of the chamber (entrance of the exhaust pipe). The equivalence ratio at the exit ($\phi_{tot,exit} = 1.65 \pm 0.1$) is stabilized but at a lower value than at the injection zone ($\phi_{tot,injection} = 2.1$) which indicates droplet accumulation in the chamber.

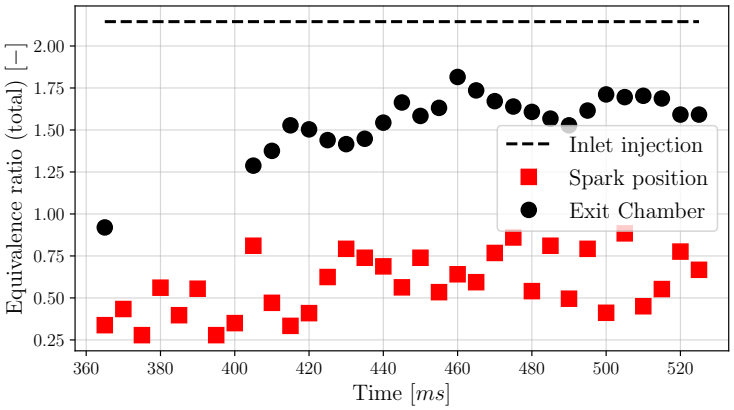

Figure 14.4.3: Time evolution of the total equivalence ratio at injection, spark position and exit of the combustion chamber.

The equivalence ratio at the spark position seems stabilized but with large fluctuations. Contrary to the injection zone, lean conditions close to the lower flammability limit are measured at the spark ($\phi_{tot,spark} = 0.65 \pm 0.2$). This equivalence ratio difference with the injected value is due to the spray dispersion and because the injection is not perfectly aligned with the spark position. Indeed, Fig. 14.4.4 shows that the spark position is located on the side of the spray in the ORZ. The liquid fraction field also illustrates the droplet accumulation zones at the base-plate of the ORZ, reducing the exit chamber equivalence ratio.

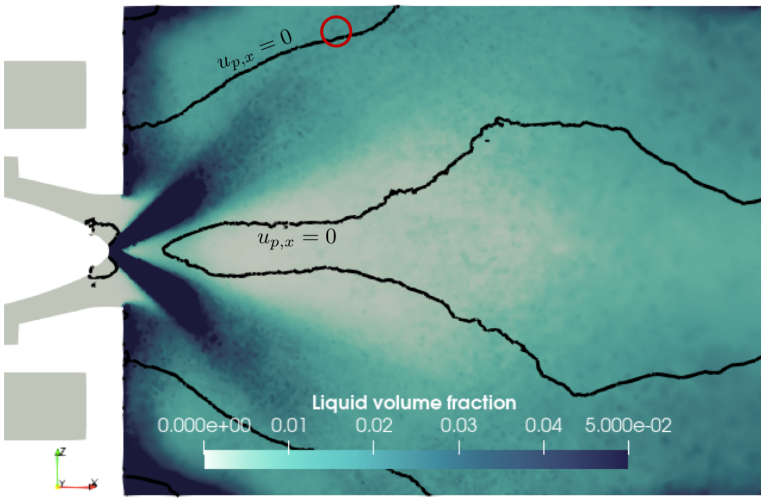

Figure 14.4.4: Liquid volume fraction field α_l with $u_{p,x} = 0$ iso-contours. The red circle indicates the spark position.

The spark position in the ORZ determines the droplet distribution faced during the ignition. Figure 14.4.5 displays the droplet distribution in a cube of 8 mm side length around the spark-plug at $t = t_{spark}$. The red curve corresponds to the RR distribution reconstructed from the measured droplet distribution in

the simulation. By comparison with the injected distribution at the atomizer, the characteristic droplet size is smaller because only the small droplets are more prone to recirculate in the ORZ due to their small Stokes number. As a consequence, the large droplet population is reduced while the small and intermediate ones are increased. The resulting two-phase flow characteristics measured in this control volume at the spark are $N_{droplet} = 518$, $\phi_{tot} = 0.79$ and $d_{p,32} = 57\,\mu m$.

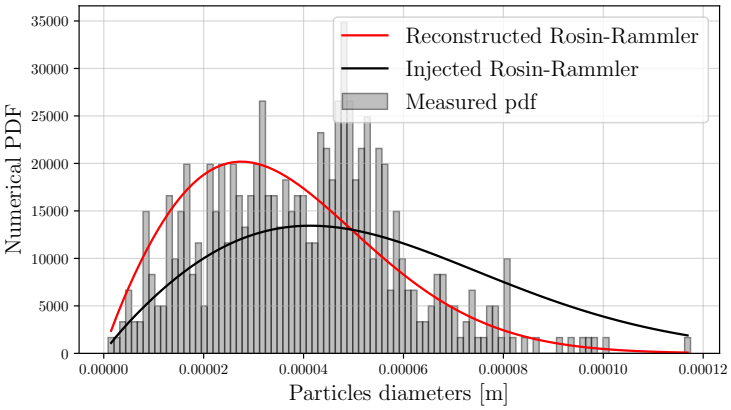

Figure 14.4.5: Droplet distribution measured at the spark and compared to the distribution injected at the atomizer with FIM-UR model.

14.4.3 Ignition results

In the following parts, the kernel formation phase is first described. Then the kernel propagation and extinction are analysed for two initial positions of the energy deposit.

Kernel formation

A hot kernel is well formed at the end of the energy deposit as shown on Fig. 14.4.6. However, only a small part of the droplets has started to react and release heat. At later time, the hot mixture has enabled to heat more droplets and trigger evaporation, increasing the number of reactive zones.

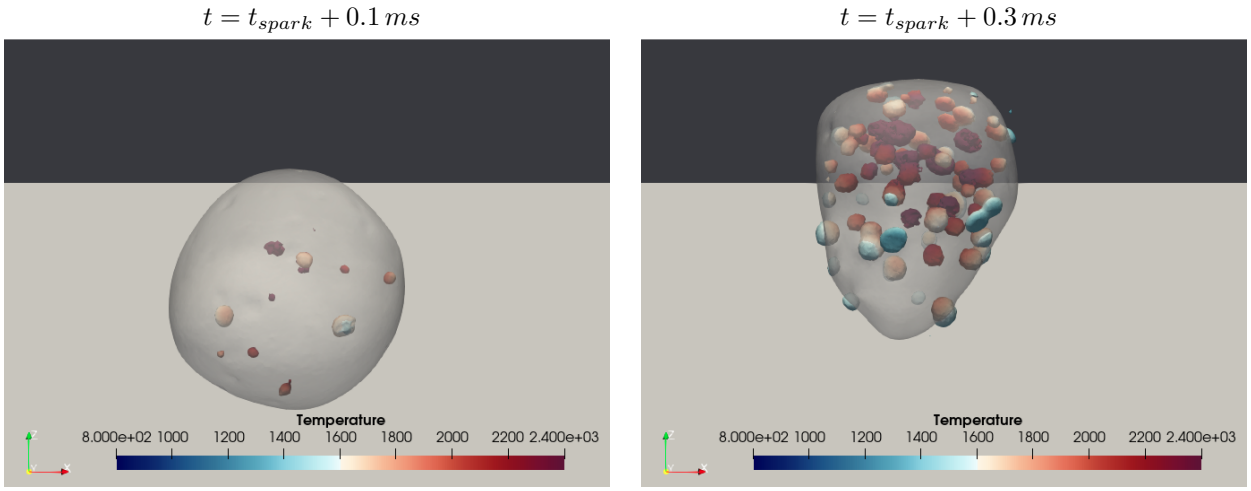

Figure 14.4.6: Hot kernel evolution visualized with transparent iso-surface $T = 1600\,K$. Iso-surface $\dot{\omega}_T = 2 \times 10^8\,J/m^{-3}.s^{-1}$ colored by temperature shows burning droplets. The grey backward surfaces correspond to the chamber walls.

As expected from the flow characteristic properties presented in the previous section (large SMD and

small droplet number density), an isolated droplet combustion regime is observed as it was the case in the poly-disperse spherical bomb ignition cases in Chap. 13. The chemical kernel structure shown on Fig. 14.4.7 is also very similar and will not be detailed again. However, contrary to the spherical bomb ignition, some evaporating droplets are found outside the hot kernel. This is due to the droplet motion different from the gaseous flow. Therefore, some droplets can cross the hot gaseous kernel and heat-up there, allowing their evaporation even after leaving the kernel. Such mechanism is detrimental for ignition because it removes heat from the kernel while the evaporated fuel outside the kernel cannot ignite.

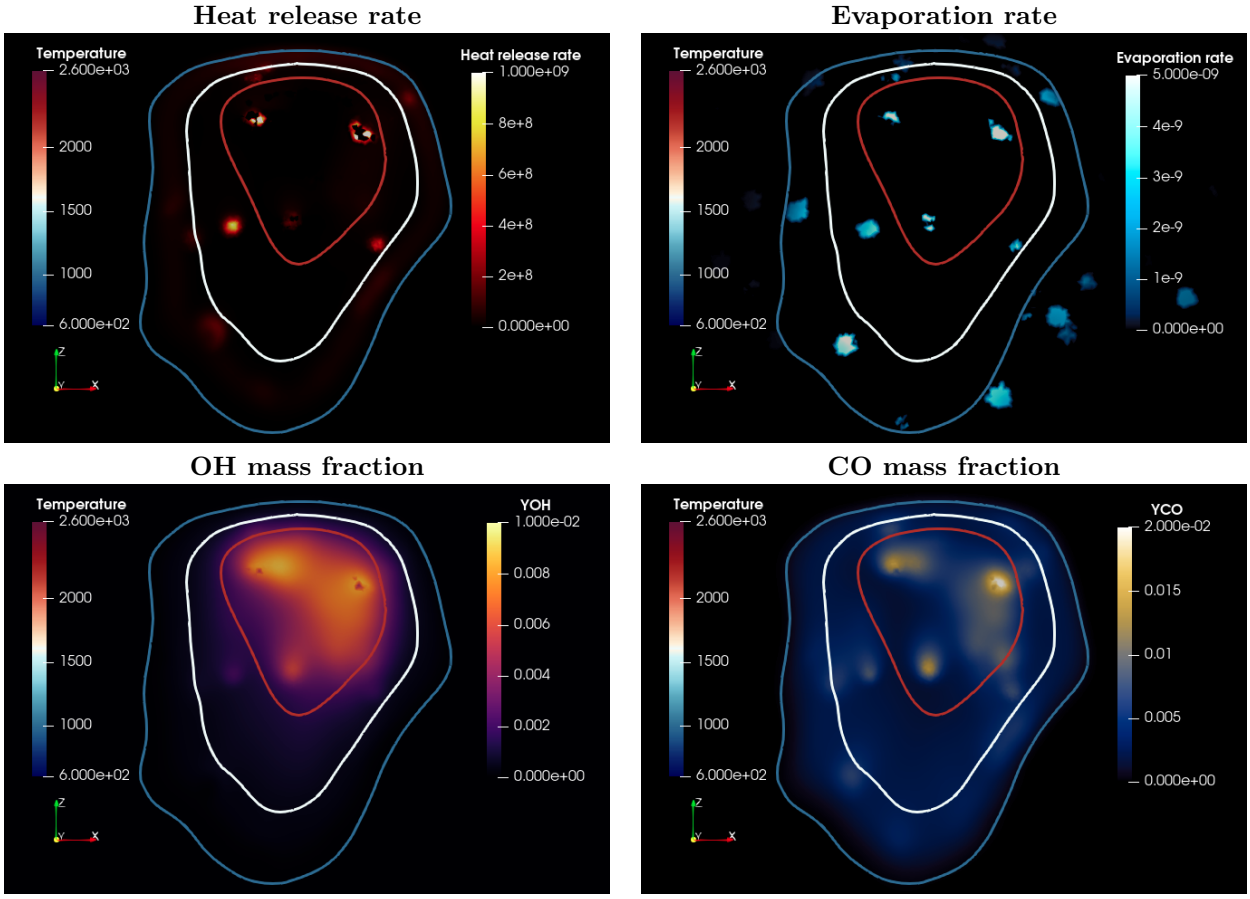

Figure 14.4.7: Cut-plane field with temperature iso-contours $T = 1000\,K$, $T = 1600\,K$ and $T = 2200\,K$ at $t = t_{spark} + 0.3\,ms$.

Now that the hot kernel is successfully formed, its development into a propagating flame is evaluated in the following.

Kernel propagation

The kernel propagation is shown on Fig. 14.4.6 and 14.4.8. The kernel first develops and is pushed towards the top chamber wall[6]. Until $t = t_{spark} + 1\,ms$, the integrated heat release rate increases (not shown) as well as the number of burning droplets.

From $t = t_{spark} + 1\,ms$, a part of the kernel is stretched towards the ORZ due to an upward gaseous flow. This stretch increases the kernel surface and thus the heat losses via conduction whereas the number of burning droplet remains roughly the same (same kernel volume). Furthermore, some droplets do not follow the gaseous hot kernel due to their large Stokes number and continue to burn outside the kernel (right part of the kernel at $t = t_{spark} + 1.3\,ms$). Ultimately, these droplets completely separate from the main kernel and do not participate to its development. Finally, the surrounding mixture cools down the

[6]The visualization window is the same for all pictures to enable an evaluation of the kernel size evolution and displacement.

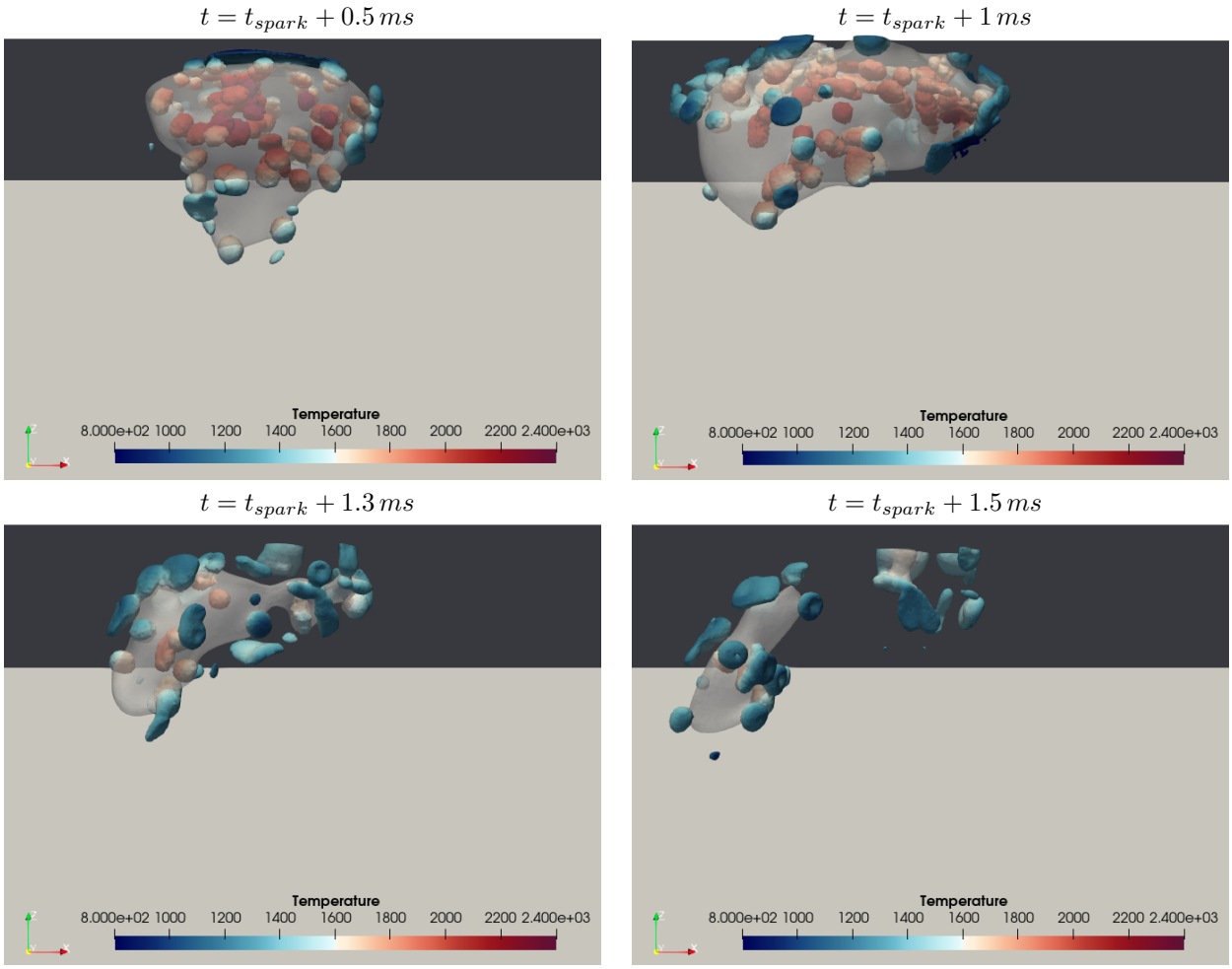

Figure 14.4.8: Hot kernel evolution visualized with transparent iso-surface $T = 1600\,K$. Iso-surface $\dot{\omega}_T = 2 \times 10^8\,J/m^{-3}.s^{-1}$ colored by temperature shows burning droplets. The grey backward surfaces correspond to the chamber walls.

ignited droplets which cannot maintain combustion processes and the kernel completely extinguishes at $t = t_{spark} + 2\,ms$.

The extinction is also attributed to the droplet distribution measured at the spark position, where the major part of the droplet has a diameter between $30\,\mu m$ and $50\,\mu m$. The corresponding characteristic evaporation time ranges from $2\,ms$ to $5\,ms$ (computed in Chap. 12) while the hot kernel is able to survive for only 1 ms before reducing in size (see Fig. 14.4.8). Therefore, there is initially enough energy to compensate the heat losses and start the evaporation, however, due to the large droplets, the evaporation time is too long. As a consequence, the amount of fuel vapor is reduced as well as the heat release rate. Ultimately, the kernel is less robust to the turbulent motion and blows out.

Energy deposit induced flow

As shown above, the kernel is first pushed towards the wall and then stretched by the recirculation of an upward flow. This flow is detrimental to the kernel development because the induced stretch increases the kernel surface (defined with the iso-surface $T = 1600\,K$) and thus the heat diffusion. Such flow must then be avoided. The velocity variation presented at the spark location in Sec. 14.4.2 indicates, on the contrary, a negative radial velocity which should push the kernel away from the wall. Therefore, the flow is modified by the deposited energy at the spark. This is clearly visible on Fig. 14.4.9 showing the radial velocity variations at the spark position with and without the energy deposit, with a strong negative and then positive flow induced by the energy deposit.

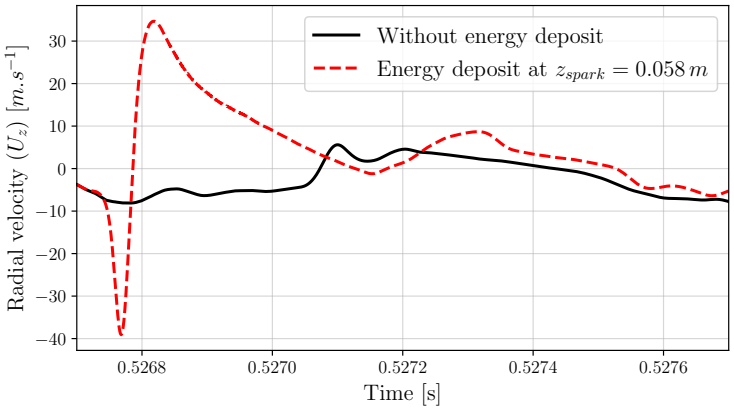

Figure 14.4.9: Influence of the energy deposit on the gaseous radial velocity component evolution at the spark location.

This flow results from the interaction between the wall and the pressure variations due to the energy deposit. As illustrated on the left picture of Fig. 14.4.10 the energy deposit leads to a large depression at the end of the deposit time, inducing a flow towards the kernel center. Due to symmetry, this flow does not lead to kernel motion in the x and y directions. However in the z direction, the disymmetry due to the wall leads to an upward motion towards the wall of the kernel.

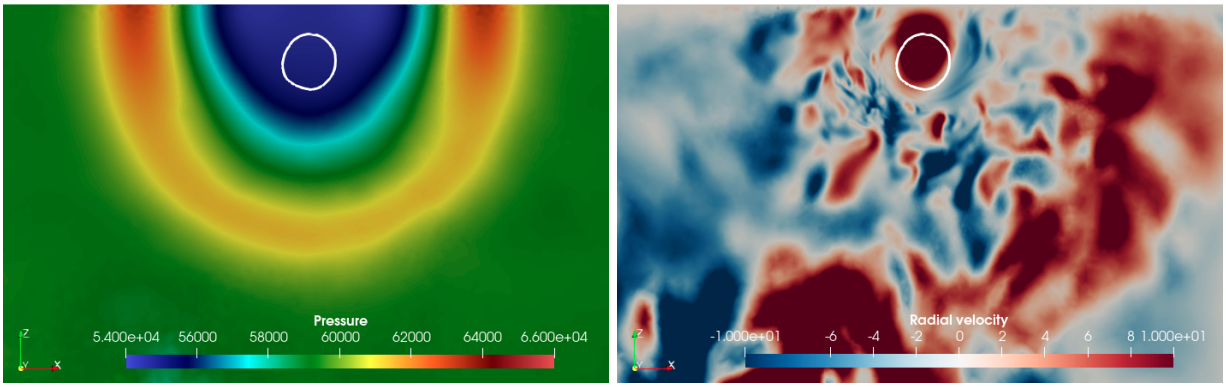

Figure 14.4.10: Pressure (left) and radial velocity field u_z (right) in an axial cut-plane ($y = 0$) at $t = t_{spark} + 100\,\mu s$. The kernel position is displayed with the white iso-contour $T = 1600\,K$.

This issue may be avoided by moving downward the energy deposit by 5 mm. The consequences of this modification can be appreciated on Fig. 14.4.11 where the depression region is divided into two parts with an intermediate zone at the kernel position. As a consequence, the resulting radial velocity field is now downward for the same instant. The corresponding temporal radial velocity variations are displayed on Fig. 14.4.12. In the case $D_{wall} = 11.5\,mm$ ($z_{spark} = 0.053\,m$), the radial velocity variation is reduced and quickly returns to $u_z = 0\,m.s^{-1}$ showing the effect of the wall distance and the interaction with the energy deposit.

In the following part, a second ignition attempt at the new spark position $z_{spark} = 0.053\,m$ is analysed.

Interaction with SWJ

The kernel evolution starting from the lower spark position is displayed on Fig. 14.4.13. Contrary to the previous case, the kernel is not anymore pushed towards the wall. However, it faces stronger velocity fluctuations. At $t = t_{spark} + 0.5\,ms$, the hot kernel is already largely deformed while in the previous

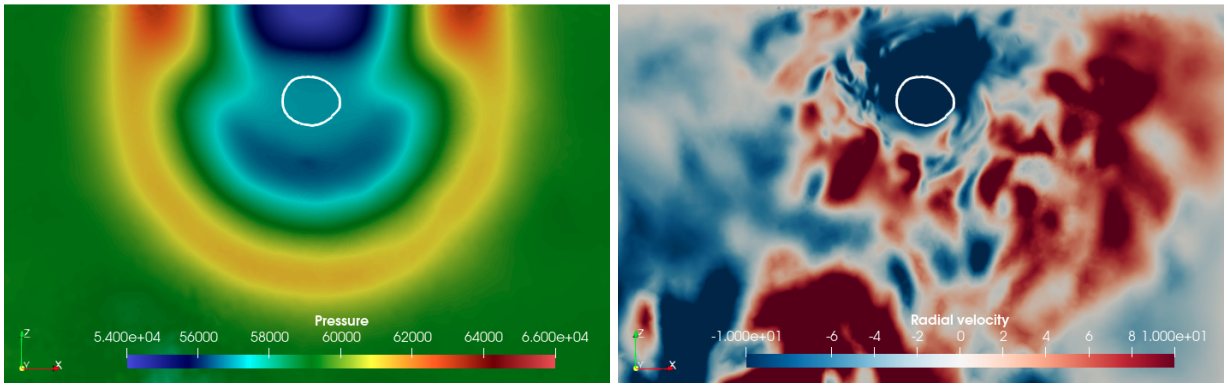

Figure 14.4.11: Pressure (left) and radial velocity field u_z (right) in an axial cut-plane ($y = 0$) at $t = t_{spark} + 100\,\mu s$ and with $z_{spark} = 0.053\,m$. The kernel position is displayed with the white iso-contour $T = 1600\,K$.

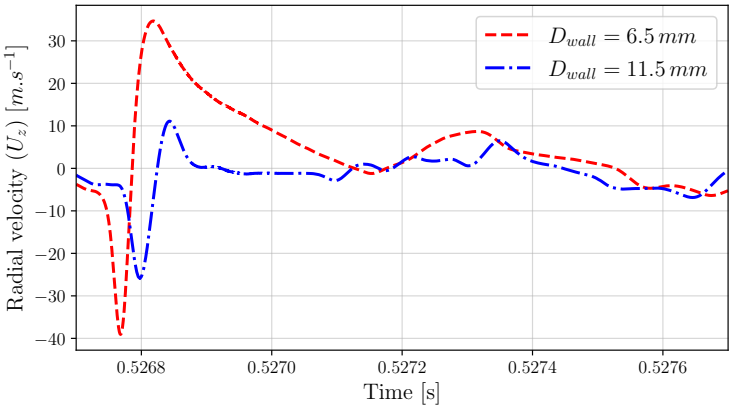

Figure 14.4.12: Effect of the wall distance on the radial velocity evolution at the spark position.

case at the same time, the kernel had kept a relatively spherical shape minimizing heat losses. At $t = t_{spark} + 0.7\,ms$ the kernel is broken into several parts by the turbulent flow which quickly leads to its extinction. At $t = t_{spark} + 0.9\,ms$ there are only isolated droplets burning in the cold mixture and the hot kernel has completely vanished.

The rapid kernel extinction in this second case is due to its proximity with the air SWJ. Indeed, Fig. 14.4.14 shows that the kernel evolves in the transition zone between the SWJ and the ORZ, where large velocity gradients induce the formation of vortices and increase the kernel thermal losses due to convection effects.

Moreover, the spark zone is no more located in the ORZ. As a consequence, the droplet distribution at the spark location is modified with less small droplets. The resulting larger SMD is detrimental to ignition. However, considering the strong and fast kernel deformation by the flow, the liquid phase influence seems here negligible. In other words, it may be possible that the equivalent purely gaseous ignition also fails due to the flow at this spark location, especially at high altitude conditions where the released kernel power is much lower.

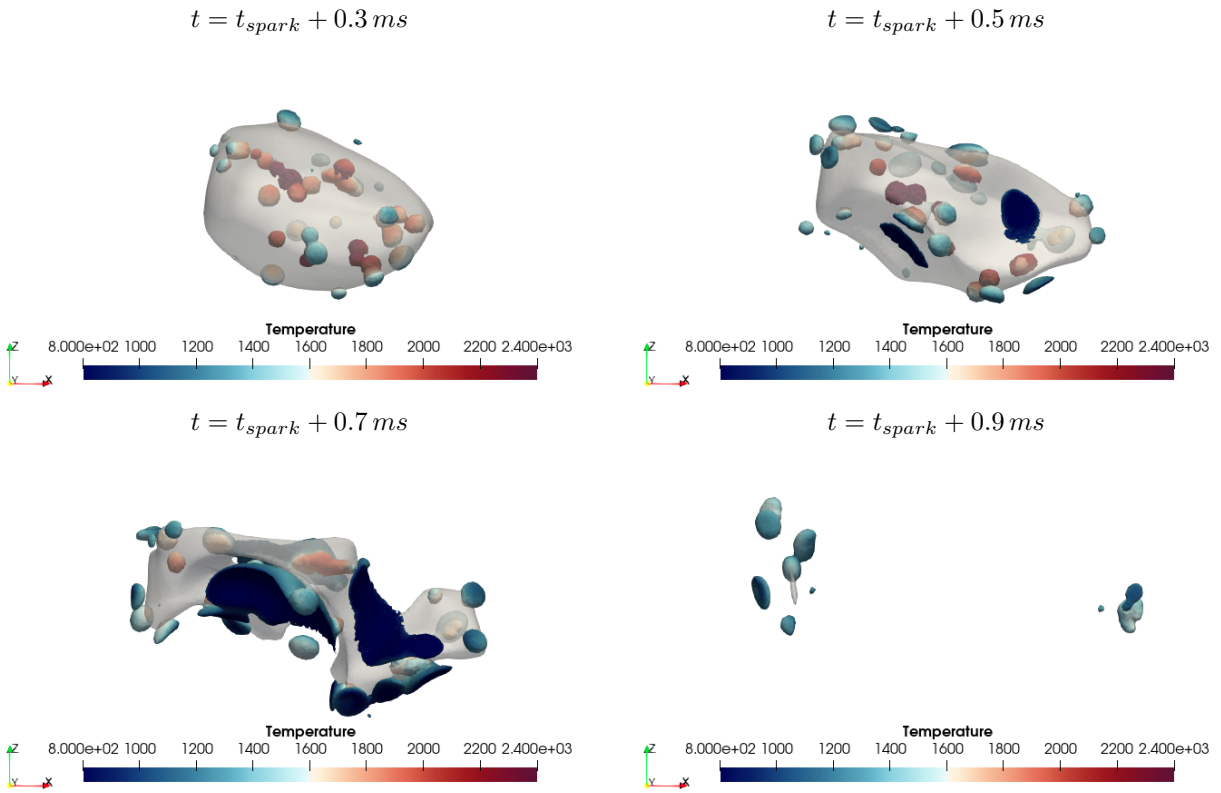

Figure 14.4.13: Kernel evolution visualized with transparent iso-surface $T = 1600\,K$/ Iso-surface $\dot{\omega}_T = 2 \times 10^8\,J/m^{-3}.s^{-1}$ colored by temperature shows burning droplets.

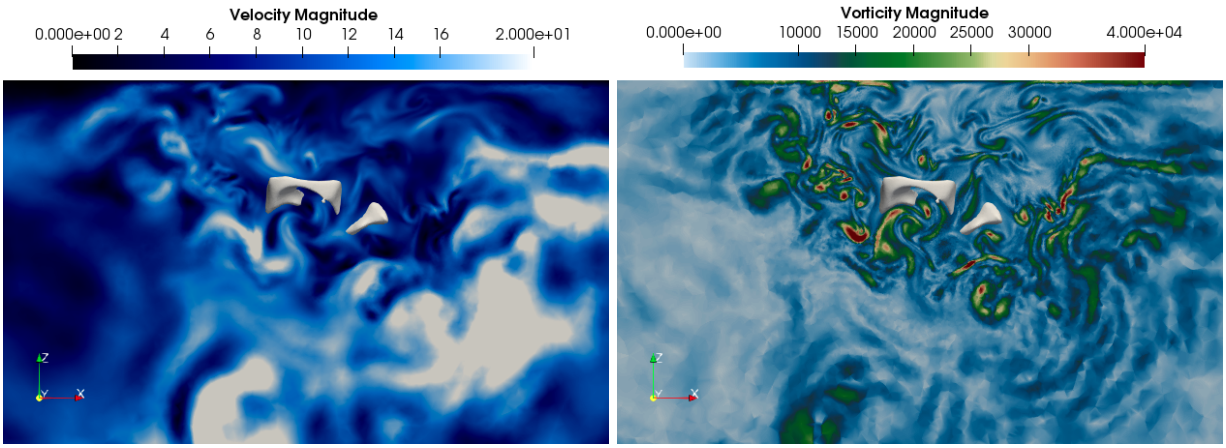

Figure 14.4.14: Velocity (left) and vorticity (right) magnitude in the axial cut-plane ($y = 0$) at $t = t_{spark} + 0.7\,ms$. The hot kernel is represented with the white iso-surface $T = 1600\,K$.

14.5 Conclusions

14.5.1 Results summary and discussion

The main objective of this chapter was to perform ignition simulations in the academic configuration MERCATO with a realistic dispersed phase description and accounting for the high altitude conditions.

The gaseous cold flow simulation has shown first the influence of the exhaust pipe (required in the experimental set-up to create the depression) which breaks the flow symmetry up to the injection position. This gaseous flow could not be validated due to the lack of measurements, however, similar flow patterns have been observed in previous works [Eyssartier 2012]. Then, for the two-phase injection, an uncer-

tainty quantification study has been conducted to determine the optimum injection parameters from the experimental data profiles. Although a good match has been observed in the conical injection region, non-negligible discrepancies have been noticed towards the ORZ. These results suggest a different gaseous flow leading to larger ORZ at the base plate and to small droplets recirculation in the injection system for the simulation. Despite these discrepancies, the flow characteristics at the spark position have been analysed to evaluate the ignition with respect to these conditions. A reduction of the SMD and equivalence ratio have been measured and are attributed to the spark position at ORZ tip.

Finally, ignition simulations have been performed and analysed. Results demonstrate that the numerical methods and models proposed in this work (Multi-component ARC scheme S30R299QSS22, exponential chemistry integration, LDSC, poly-disperse two-phase flow based on Lagrangian formalism, multi-component evaporation and PBM) have been successfully used to simulate the kernel formation.

However, the various ignition attempts did not enable the kernel development towards the injector. On the contrary, extinction scenarios have been observed in all cases. The analysis of these extinctions shows that the dispersed phase has a critical influence due to the evaporation delay but also because of the isolated droplet combustion mode which limits the total heat release. Another well-known mechanism responsible for the kernel extinction is the interaction with the gaseous flow. Especially, the second ignition case presented a complete kernel disruption caused by the turbulent structures. Intermediate computations of ignition in the MERCATO bench under low pressure and low temperature conditions but in purely gaseous phase are then required to determine how much the dispersed phase is responsible for the extinction compared to the gaseous flow influence. In addition, the spark energy deposit model has been found to indirectly influence the kernel propagation via the formation of an induced flow. This flow formation is caused by the wall proximity but also by the deposit duration.

Nevertheless, these results demonstrate once again the detrimental effect of the high altitude conditions on the ignition. For instance, these results can be compared to the ignition successes observed in the work of Eyssartier [2012] at ground pressure and temperature. Indeed, it has been shown that LPLT conditions induce larger droplets and as a consequence a smaller droplet number density which have both a detrimental effect on ignition. Furthermore, the LPLT conditions also modify the chemical combustion processes (less efficient combustion and weaker flame power) and make the kernel more sensitive to the extinction phenomena.

The chosen operating point corresponds to successful ignition in the experiment. Several assumptions may explain why the simulation did not reproduce a successful ignition. Firstly, the stochastic intrinsic behavior of ignition must be taken into account. Indeed, the experimental ignition corresponds to several successive sparks for several seconds while only one spark can be computed. Efforts have been made to determine the optimum spark moment but the evaluated time interval is limited in comparison to the experimental ignition sequence. Secondly, there are large uncertainties on the flow state at the spark moment. In particular, as already discussed, the discrepancies observed on the two-phase flow profiles could strongly influence the ignition process. For future ignition studies, data measurements of gaseous velocity profiles as well as a fine description of the dispersed phase (equivalence ratio and droplet size distribution) at the spark location would enable to remove this assumption. Finally, the ignition failures in the simulation may arise from missing modeling building blocks in the methodology used in this work. For instance, the spark-droplet interaction has not been considered. A droplet located at the center could be instantaneously evaporated and promote the ignition. The shock wave resulting from the spark may also trigger droplet break-up. Finally, historical effects due to multiple sparks are not taken into account. If the spark frequency is too low compared to the convective time and results in a renewing of the mixture, the electrodes surface may remain hot for a longer period inducing droplet pre-heating or evaporation before the following spark. Lastly, at LPLT conditions, the formation of a liquid fuel film at the spark device has been observed experimentally. The influence of such film is not well understood yet. Depending on the location and the liquid amount, the ignition may be promoted via evaporation or prevented if the spark cannot be established. To answer these questions, dedicated experimental versus simulation comparisons, at each step of the kernel ignition and development, are now required.

14.5.2 Industrial configuration

In addition to the MERCATO academic case, the ignition of an industrial configuration representative of an aeronautical combustion chamber has been performed at high altitude conditions ($P = 0.46\,bar$ and $T_{air} = 266\,K$). The configuration is composed of four injection systems (4SI) discretized in 170 millions elements. A cut-plane of the chamber at the injectors position is presented on Fig. 14.5.1 with the normalized velocity field.

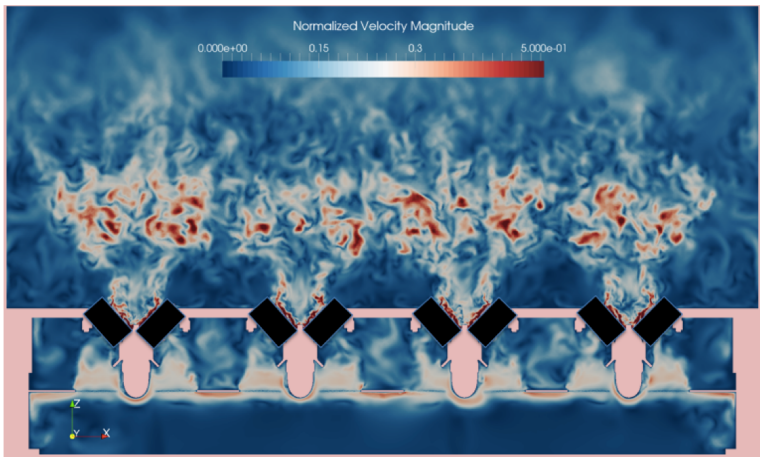

Figure 14.5.1: Normalized velocity field on the injector cut-plane of the 4SI industrial configuration.

The detailed analysis of ignition in this configuration is not given here because kernel formations and extinctions similar to MERCATO have been observed. For instance, the evolution of the heat release rate fields at the spark position is displayed on Fig. 14.5.2. The isolated burning droplet combustion mode is recovered at the kernel formation. However, a thin premixed flame is also surrounding the kernel due to the larger energy deposit zone which enables a fuel pre-evaporation of the droplet on the external kernel layer.

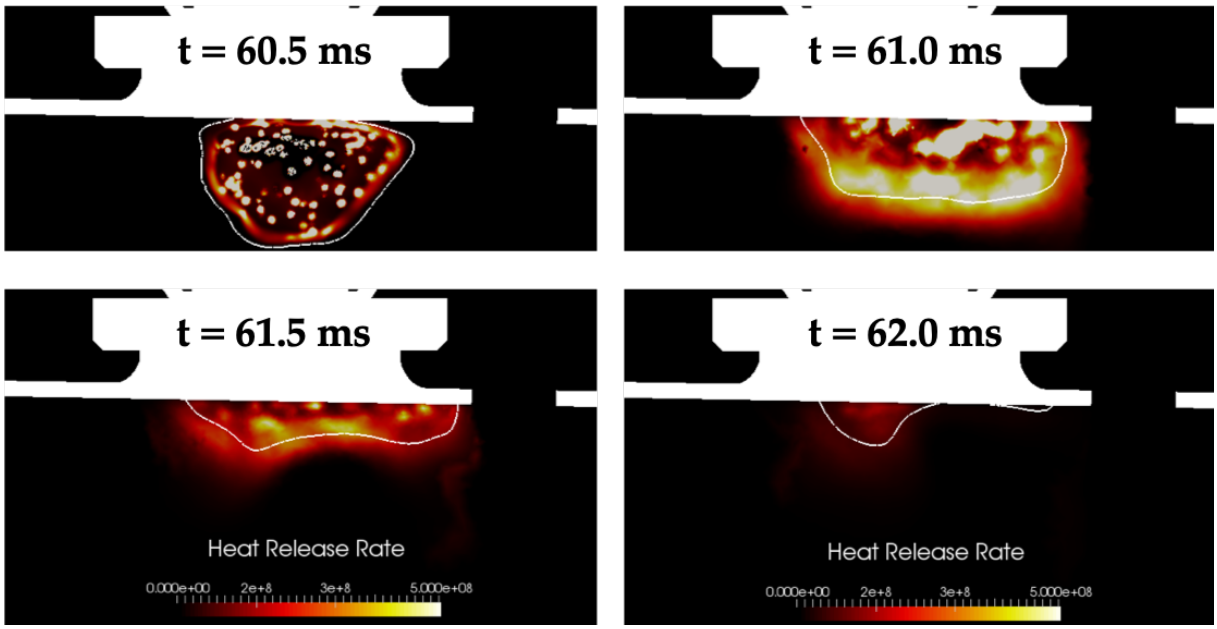

Figure 14.5.2: Evolution of the heat release rate field at the spark position after the energy deposit ($t_{spark} = 60\,ms$).

These results indicate that the methodology used in this work to simulate the ignition can be also applied to study the kernel formation even in complex industrial configurations. Furthermore, once the kernel is

formed, the solution can be interpolated on a coarser mesh to study the kernel propagation at a reduced CPU-cost and using a combustion model. For example, on Fig. 14.5.2 a thickened flame model [Legier et al. 2000, Jaravel 2016] is applied from $t = 61\,ms$.

Finally, for this second configuration as well, kernel extinctions have been observed while ignition have been measured experimentally at this operating point. Therefore, the assumption of a missing modeling building block is reinforced. Current studies are now conducted to better understand the kernel development phase and its propagation towards the injector.

Conclusion

The aim of this work was to study the influence of the high altitude conditions LPLT ($P = 0.3\,bar$ and $T = 233\,K$) on the relight of an aeronautical combustion chamber. Concurrently, a second main objective was to develop new numerical methods enabling the simulation of such ignition phases as accurately as possible. For this purpose, this work has been divided in three main parts. Firstly, the studies of purely gaseous configurations have been conducted to better understand the influence of LPLT conditions on the chemical combustion reactions and on the flame kernel formation and its early development. Secondly, the two-phase flow effects have been integrated to the simulation in order to accurately represent the ignition processes. The evaporation, the two-phase combustion mechanisms, but also the study of the LPLT influence on the fuel injection and the droplet size distribution at the spark have been taken into account. Finally, all the modeling building blocks have been gathered to simulate the ignition phase of an aeronautical engine under realistic high altitude conditions. This PhD work has been performed and funded in the context of the APLAREP project (Augmentation du Plafond d'Allumage - REduction des Particules fines) gathering Safran Group and CERFACS, CORIA and ONERA laboratories. The general conclusions with the main results and the perspectives of this PhD are given in the following sections.

Gaseous ignition and chemical processes

The effects of LPLT conditions have been studied at the macroscopic scale using simplified 0-dimensional reactor and 1-dimensional flame configurations (chap. 5). The reduction of the density at low pressure has a large influence on the combustion processes. Primary, there is a slowing down effect of the chemical reactivity which decreases the heat release rate and the fuel consumption speed. Secondly, the thermodynamic equilibrium is shifted towards less conversion of CO into CO_2 which results in a less efficient combustion and a lower heat release per quantity of fuel burnt. Both effects lead to a lower flame power under LPLT conditions.

At the microscopic scale, the chemical reactions have been analysed showing a negligible effect of LPLT. Indeed, the fuel decomposition chemical pathways are barely modified (chap. 6). Hence, ARC mechanisms working both at low and atmospheric pressures can be derived (chap. 7).

Finally, DNS of gaseous ignition have enabled to better understand the effects of LPLT on the kernel formation and its early development (chap. 9). The macroscopic effects mentioned above have been recovered in the 3D ignitions. In addition, chemical mechanisms linked to the extinction have been observed when the temperature reaches critical thresholds. Furthermore, a faster kernel temperature decrease at low pressure has been demonstrated. Then, since the chemical kinetic is slower at low pressure, the kernel temperature reaches sooner the critical thresholds which triggers the extinction mechanisms. This mechanism explains the ignition failure at LPLT conditions compared to the corresponding atmospheric case.

Two-phase flow related phenomena

The LPLT conditions have also an influence on the two-phase flow related phenomena. Firstly, low pressure and low temperature modify the fuel injection in the combustion chamber (chap. 11). As a result, the spray SMD increases. Moreover, considering the lower fuel temperature, the liquid viscosity and surface tension are also increased which ultimately leads to the formation of larger droplets.

Secondly, isolated droplet evaporations in a hot environment, representative of ignition, have been studied (chap. 12). Results indicate that the low pressure, the low fuel temperature and the mono- or multi-component evaporation modeling have a negligible influence on the evaporation time compared to the droplet size. As a conclusion, the effect of LPLT on the evaporation is indirect and results from the formation of larger droplets at the injection. In addition, this formation of larger droplets implies a reduction of the droplet number density (for the same mass or equivalent ratio). Therefore, the global evaporation rate in the kernel is decreased with LPLT conditions.

Finally, the two-phase ignition simulations have been performed in spherical bomb configurations (chap. 13). These simulations have shown that the liquid phase must be accounted for in the ignition processes. Indeed, as opposed to the gaseous cases, the hot kernel resulting from the spark must first heat and partially evaporate the liquid droplets before the mixture becomes flammable and enables the combustion reactions. Hence, the two-phase ignition requires a larger initial energy to compensate this endothermic phase and the higher heat losses resulting from this longer evaporation delay. Moreover, an isolated droplet combustion regime has been observed because of the small droplet number density obtained with non-uniform droplet size distributions. This combustion regime totally differs from the purely gaseous case and is driven by the localized evaporation and combustion of a small number of droplets in the hot kernel. Hence, the total heat release rate is limited which favours the kernel extinction.

Application to a combustion chamber

Two-phase ignition simulations have been performed in the MERCATO bench to evaluate the effects of LPLT in a combustion chamber configuration (chap. 14). Similarly to the spherical bomb configuration, an isolated droplet combustion regime has been observed. However, all ignition attempts lead to the kernel extinction while ignition successes were observed in the experimental set-up. Based on the simulations results, these extinctions are caused, on the one hand, by the strong kernel deformation induced by the turbulence which increases the surface and thus the thermal losses ; on the other hand, the small number of burning droplets does not enable to compensate the kernel thermal losses. The differences with the experimental results may be explained by several assumptions:

- different mixture states (velocity, equivalence ratio, droplet distribution) at the spark position,
- stochasticity linked to the turbulent flow,
- historical effects linked to the multiple sparks in the experiment,
- spark-droplet interactions not taken into account,
- wrong modeling of the evaporation or the two-phase combustion.

Nevertheless, compared to the previous atmospheric simulations, these computations confirm the detrimental effect of the LPLT conditions on ignition, the critical importance of the droplet size distribution and the presence of pre-evaporated fuel at the spark position.

Numerical modeling

In addition to the previous conclusions, several numerical models have been developed all along the PhD. Firstly, chemical analysis tools have been developed and integrated to ARCANE to study chemical reactive pathways (chap. 6). These tools are now available for other studies, for instance, the analysis of soot formation or NOx production. Then, the reduction methods in ARCANE have been improved and have enabled to derive a new ARC scheme dedicated to Jet-A1 ignition simulations at LPLT or atmospheric conditions(chap. 7).

The analysis of LPLT influences shows a reduction of the chemical stiffness. However, the intrinsic stiffness related to the ignition phenomenon still requires stable methods for the chemistry integration in CFD solvers. In this work, an exponential integration of the chemistry associated to a local and dynamical

sub-cycling (LDSC) procedure have been proposed (chap. 8) showing a large reduction of the stiffness up to time-steps reaching CFL and Fourier conditions without compromising the accuracy.

Then, concerning the two-phase flow simulations, a new approach has been proposed for the development of a phenomenological primary atomization model aiming to predict the characteristic droplet size of a fuel spray exiting a pressure swirl (chap. 11). However, a validation of the model is still required when experimental database are available. For the droplet evaporation, the discrete multi-component model developed in previous works has been extended to high temperature environments encountered in the kernel including the saturation condition (chap. 12). Finally, a particle bursting method (PBM) has been proposed to limit errors linked to the point source approximation inherent to the Lagrangian formalism (chap. 13). This method enables to distribute the evaporation source term on several cells which prevents the apparition of strong local gradients and thus reduces the numerical issues.

Note that these numerical methods (except for the chemical analysis and the primary atomization model) have been successfully used for semi-industrial (MERCATO) and industrial (4SI) computations which now enables complementary two-phase ignition studies in other configurations.

Perspectives

Based on these conclusions, a question remains unsolved: why does the simulation predict kernel extinctions in the application cases while ignitions are clearly observed in the experiments ? Answering this question is the main perspective of this work. Several assumptions have been proposed and must be evaluated. In order to assess the validity of the two-phase ignition modeling, as proposed in this work, experiment versus simulation comparisons are planed in the context of an industrial project led by Safran. Accurate measurements of the mixture state at the spark and a tracking of the early kernel development will enable to remove bias on the initial state before triggering the ignition, to evaluate the modeling accuracy compared to the experimental results and to complete this modeling if necessary.

Secondly, the first computations in the spherical bomb academical configuration have shown that the methodology proposed for the two-phase ignition simulation enables to accurately account for the preferential evaporation effect and the coupling with the chemistry. At this point, these studies need to be further investigated to better understand and analyse the physical phenomena. Especially, this configuration is currently used to quantify the influence of the SMD, the shape distribution and the droplet number density. Similarly, the study of the pre-evaporation influence is planed.

It is also worth mentioning that a liquid film formation on the combustion chamber walls has been observed several times at LPLT conditions. Then, the behavior of the spark device in the presence of such a film or its interaction with a hot kernel needs to be evaluated.

Finally, once the kernel is formed, it must propagate towards the injector. This step has already been studied in other works but not for a multi-component fuel surrogate modeling nor with LPLT conditions. This development and propagation phase cannot be computed with a DNS mesh because of the excessive computational cost, especially in the context of industrial studies. A methodology for the DNS-LES transition using a turbulent combustion model is then also required and must be developed.

Bibliography

Abdel-Gayed, R., Al-Khishali, K., and Bradley, D. (1984). Turbulent burning velocities and flame straining in explosions. *Proceeding of the Royal Society London A*, 391:393–414. 9, 72

Abdel-Gayed, R., Bradley, D., Lawes, M., and Lung, F.-K. (1988). Premixed turbulent burning during explosions. *Proceedings of the Combustion Institute*, 21:497–504. 89, 90

Abdelsamie, A., Fru, G., Oster, T., Dietzsch, F., Janiga, G., and Thévenin, D. (2016). Towards direct numerical simulations of low-Mach number turbulent reacting and two-phase flows using immersed boundaries. *Computers and Fluids*, 131:123–141. 349, 351

Abdelsamie, A., Lartigue, G., Chen, J. H., Ihme, M., Cuenot, B., and Thévenin, D. (2018). Mini-Symposium on Verification and Validation of Combustion DNS. In *17th Int. Conference on Numerical Combustion*. 349

Abramzon, B. and Sirignano, W. A. (1989). Droplet vaporization model for spray combustion calculations. *International Journal of Heat and Mass Transfer*. 38, 249

ACARE (2022). Fly the green deal. Technical report, European Commission. 3

Aggarwal, S. K. (1998). A review of spray ignition phenomena: Present status and future research. *Progress in Energy and Combustion Science*. 82

Aggarwal, S. K. and Nguyen, I. (1990). Ignition Behavior of a Fuel Spray Flowing in a Tube. *Chemical Engineering Communications*. 84, 85

Aggarwal, S. K. and Sirignano, W. A. (1985). Ignition of fuel sprays: Deterministic calculations for idealized droplet arrays. *Symposium (International) on Combustion*. 84

Ahmed, S., Balachandran, R., and Mastorakos, E. (2007). Measurments of ignition probability in turbulent non-premixed counterflow flames. *Proceeding of the Combustion Institute*, 31:1507–1513. 94

Ahmed, S. F. and Mastorakos, E. . (2006). Spark ignition of lifted turbulent jet flames. *Combustion and Flame*, 146:215–231. 82

Akindele, O., Bradley, D., Mak, P., and McMahon, M. (1982). Spark ignition of turbulent gases. *Combustion and Flame*, 47:129–155. 81

Annamalai, K. and Ryan, W. (1992). Interactive processes in gasification and combustion. Part I: Liquid drop arrays and clouds. 9

Arai, T. and Hashimoto, H. (1985). Disintegration of a thin liquid sheet in a cocurrent gas stream. In *Proceedings of the 3rd International Conference on Liquid Atomization and Spray System*. 197

Ballal, D. and Lefebvre, A. (1975). The influence of flow parameters on minimum ignition energy and quenching distance. *Proceeding of Combustion Institute*, 15:1473–1481. 8, 81

Ballal, D. and Lefebvre, A. (1977). Ignition and flame quenching in flowing gaseous mixture. *Proceeding of the Royal Society of London. Series A*, 357:163–181. 8, 81, 83

Ballal, D. R. and Lefebvre, A. H. (1981a). A general model of spark ignition for gaseous and liquid fuel-air mixtures. *Symposium (International) on Combustion*. 83

Ballal, D. R. and Lefebvre, A. H. (1981b). Flame propagation in heterogeneous mixtures of fuel droplets, fuel vapor and air. *Symposium (International) on Combustion*. 75

Barleon, N. (2022). *Detailed modeling and simulations of Nanosecond Repetitively Pulsed Discharges for Plasma-Assisted Combustion*. PhD thesis, INP Toulouse. 86

Battin–Leclerc, F., Glaude, P. A., Warth, V., Fournet, R., Scacchi, G., and Côme, G. M. (2000). Computer tools for modelling the chemical phenomena related to combustion. *Chemical Engineering Science*. 100, 101

Baum, M. (1994). *Etude de l'allumage et de la structure des flammes turbulentes*. PhD thesis, Ecole Centrale Paris. 23, 24, 347, 348

Baum, M. and Poinsot, T. (1995). Effects of Mean Flow on Premixed Flame Ignition. *Combustion Science and Technology*. 88

Baum, M., Poinsot, T., and Thévenin, D. (1995). Accurate boundary conditions for multicomponent reactive flows. *Journal of Computational Physics*. 31, 81, 158, 348

Bayvel, L. and Orzechowski, Z. (1993). *Liquid Atomization*. Taylor & Francis. 181, 186

Beduneau, J.-L. and Kim, B. (2003). Measurements of minimum ignition energy in premixed laminar methane/air flow by using laser induced spark. *Combustion and Flame*, 132:653–665. 9

Bilger, R. (1989). The structure of turbulent nonpremixed flames. *Proceedings of the Combustion Institute*, 22:475–488. 62, 65

Birch, A. D., Brown, D. R., and Dodson, M. G. (1981). Ignition probabilities in turbulent mixing flows. *Symposium (International) on Combustion*. 82

Bird, R., Stewart, W., and Lightfoot, E. (2006). *Transport Phenomena*. John Wiley & Sons, 3rd edition. 38

Blanchard, S. (2021). *Multi-physics large-eddy simulation of methane oxy-combustion in liquid rocket engines*. PhD thesis, Institut National Polytechnique de Toulouse. 146, 289, 345

Blanchard, S., Cazères, Q., and Cuenot, B. (2022). Chemical modeling for methane oxy-combustion in Liquid Rocket Engines. *Acta Astronautica*. 145, 150

Blint, R. (1986). The relationship of the laminar flame width to flame speed. *Combustion Science and Technology*. 65

Boivin, P., Jiménez, C., Sánchez, A. L., and Williams, F. A. (2011). An explicit reduced mechanism for H2-air combustion. *Proceedings of the Combustion Institute*. 352

Boudier, P., Henriot, S., Poinsot, T., and Baritaud, T. (1992). A model for turbulent flame ignition and propagation in spark ignition engines. *Symposium (International) on Combustion*. 87

Boughanem, H. and A., T. (1996). Validation du code de simulation directe ntmix3d pour le calcul des écoulements turbulents réactifs. Technical report. IFP. 157, 354

Boussinesq, J. (1877). Théorie de l'écoulement tourbillant. In *Mémoires Présentés par Divers Savans à l'Académie Royaledes Sciences de l'Institut de France 23*. 30

Bradley, D., Sheppard, C., Suardjaja, I., and Woolley, R. (2004). Fundamentals of highenergy spark ignition with lasers. *Combustion and Flame*, 138:55–77. 7, 90

Bray, K. and Cant, R. (1991). Some applications of kolmogorov's turbulence research in the field of combustion. *Proceedings of the Royal Society of London. Series A: Mathematical and Physical Sciences*, 434:217–240. 72

Bray, K. N. C. and Moss, J. B. (1977). A closure model for the turbulent premixed flame with sequential chemistry. *Combustion and Flame*, 30:125–131. 73

Burrell, R. R., Lee, D. J., and Egolfopoulos, F. N. (2018). Propagation and extinction of subatmospheric counterflow methane flames. *Combustion and Flame*, 195:117–127. 10, 103, 112, 115, 126

Bush, W. and Fendell, F. (1970). Asymptotic analysis of laminar flame propagation for general lewis numbers. *Combustion Science and Technology*, 1:421–428. 66, 162

Cailler, M., Darabiha, N., Veynante, D., and Fiorina, B. (2017). Building-up virtual optimized mechanism for flame modeling. *Proceedings of the Combustion Institute*. 53

Candel, S. and Poinsot, T. (1990). Flame stretch and the balance equation for the flame area. *Combustion Science and Technology*, 70:1–15. 66

Cardin, C. (2013). *Etude expérimentale des phénoménes physico-chimiques de l'allumage dans des écoulements laminaires et turbulents*. PhD thesis, INSA Rouen. 9, 82, 90

Cazères, Q., Pepiot, P., Riber, E., and Cuenot, B. (2021). A fully automatic procedure for the analytical reduction of chemical kinetics mechanisms for Computational Fluid Dynamics applications. *Fuel*. 129, 131

Cazères, Q. (2021). *Analysis and reduction of chemical kinetics for combustion applications*. PhD thesis, Institut National Polytechnique de Toulouse. 49, 50, 56, 57, 130, 131, 206, 207, 299

Chakraborty, N. and Mastorakos, E. (2006). Numerical investigation of edge flame propagation characteristics in turbulent mixing layers. *Physics of Fluids*, 18:1507–1513. 94

Chakraborty, N. and Mastorakos, E. (2008). Direct numerical simulations of localised forced ignition in turbulent mixing layers: the effects of mixture fraction and its gradient. *Flow, Turbulence and Combustion*, 80:155–186. 91

Chakraborty, N., Mastorakos, E., and Cant, R. S. (2007). Effects of turbulence on spark ignition in inhomogeneous mixtures: A direct numerical simulation (DNS) study. In *Combustion Science and Technology*. 88, 91, 92

Champion, M., Deshaies, B., Joulin, G., and Kinoshita, K. (1986). Spherical flame initiation : Theory versus experiments for lean propane-air mixture. *Combustion and Flame*, 65:319–337. 8, 81

Chaussonnet, G., Laroche, T., Lieber, C., Holz, S., Koch, R., and Bauer, H. J. (2020). Investigation of the liquid accumulation characteristics in planar prefilming airblast atomization. In *ICLASS 2018 - 14th International Conference on Liquid Atomization and Spray Systems*. 11

Chen, J. H., Choudhary, A., De Supinski, B., DeVries, M., Hawkes, E. R., Klasky, S., Liao, W. K., Ma, K. L., Mellor-Crummey, J., and Podhorszki, N. (2009). Terascale Direct Numerical Simulations of turbulent combustion using S3D. *Computational Science & Discovery*, 2. 28

Chen, J. H. and Im, H. G. (1998). Correlation of flame speed with stretch in turbulent premixed methane/air flames. In *Symposium (International) on Combustion*. 93

Chen, S. K., Lefebvre, A. H., and Rollbuhler, J. (1989). Influence of liquid viscosity on pressure-swirl atomizer performance. In *American Society of Mechanical Engineers, Heat Transfer Division, (Publication) HTD*. 184

Chen, S. K., Lefebvre, A. H., and Rollbuhler, J. (1992). Factors influencing the effective spray cone angle of pressure-swirl atomizers. *Journal of Engineering for Gas Turbines and Power*. 184

Cheng, L. (2022). *Detailed Numerical Simulation of Multi-Dimensional Plasma Assisted Combustion*. PhD thesis, INP Toulouse. 86

Chiu, H. H., Kim, H. Y., and Croke, E. J. (1982). Internal group combustion of liquid droplets. 19(1):971–980. 227

Chiu, H. H. and Liu, T. M. (1977). Group combustion of liquid droplets. 17(3):127–142. Publisher: Taylor & Francis _eprint: https://doi.org/10.1080/00102207708946823. 227

Chung, S. H. and Law, C. K. (1984). An invariant derivation of flame stretch. *Combustion and Flame*. 66

Clavin, P. (1985). Dynamic behavior of premixed flame fronts in laminar and turbulent flows. *Progress in Energy and Combustion Science*, 11:1–59. 66, 162

Clavin, P. and Joulin, G. (1983). Premixed flames in large scale and high intensity turbulent flow. *Journal Physique Lettres*. 66

Colin, O. (2000). *Simulations aux grandes échelles de la combustion turbulente prémélangée dans les statoréacteurs*. PhD thesis, Toulouse, INPT. 24, 243, 253

Colin, O., Ducros, F., Veynante, D., and Poinsot, T. (2000). A thickened flame model for large eddy simulations of turbulent premixed combustion. *Physics of Fluids*, 12(7):1843–1863. 28, 73

Colin, O. and Rudgyard, M. (2000). Development of High-Order Taylor-Galerkin Schemes for LES. *Journal of Computational Physics*. 24, 243

Collin-Bastiani, F. (2019). *Modeling and Large Eddy Simulation of Two-Phase Ignition in Gas Turbines*. PhD thesis, Institut National Polytechnique de Toulouse. 4, 5, 9, 28, 32, 75, 79, 84, 85, 87, 88, 138, 217, 239, 253

Collin-Bastiani, F., Vermorel, O., Lacour, C., Lecordier, B., and Cuenot, B. (2019). DNS of spark ignition using Analytically Reduced Chemistry including plasma kinetics. *Proceedings of the Combustion Institute*. 86, 88, 356

Cook, A. W. and Riley, J. J. (1994). A subgrid model for equilibrium chemistry in turbulent flows. *Physics of Fluids*, 6:2868–2870. 73

Crowe, C. T., Schwarzkopf, J. D., Sommerfeld, M., and Tsuji, Y. (2011). *Multiphase Flows with Droplets and Particles*. CRC Press, 2nd edition. 32

Cuenot, B. and Poinsot, T. (1994). Effects of curvature and unsteadiness in diffusion flames. implications for turbulent diffusion combustion. *Proceedings of the Combustion Institute*, 25:1383–1390. 71

Dagaut, P. and Gaïl, S. (2007). Kinetics of Gas Turbine Liquid Fuels Combustion: Jet-A1 and Bio-Kerosene. In *Volume 2: Turbo Expo 2007*, pages 93–101, Montreal, Canada. ASMEDC. 55

Damblin, G., Couplet, M., and Iooss, B. (2013). Numerical studies of space filling designs: optimization algorithms and subprojection properties. *Journal of Simulation*. 359

De Oliveira, P. M., Allison, P. M., and Mastorakos, E. (2019). Ignition of uniform droplet-laden weakly turbulent flows following a laser spark. *Combustion and Flame*, 199:387–400. 9, 10, 84, 94

Dehaies, B. and Joulin, G. (1984). On the initiation of a sherical flame kernel. *Combustion Science and Technology*, 37:99–116. 8

Denton, M. J., Tambe, S. B., and Jeng, S. M. (2018). Experimental investigation into the high altitude relight of a three-cup combustor sector. In *Proceedings of the ASME Turbo Expo*. 9

Donea, J. and Huerta, A. (2003). *Finite Element Methods for Flow Problems*. John Wiley & Sons. 24

Donjat, D. (2003). *Etude et modélisation de l'hydrodynamique interne d'un injecteur mécanique de turboréacteur*. PhD thesis, Ecole nationale supérieure de l'aéronautique et de l'espace. 178, 179, 180, 184, 185, 186, 188, 189

Dopazo, C. and Ballester, J. (1994). Discharge coefficient and spray angle measurements for small pressure-swirl nozzles. *Atomization and Sprays*. 184

Dorfner, V., Domnick, J., Durst, F., and Kohler, R. (1995). Viscosity and surface tension effects in pressure swirl atomization. *Atomization and Sprays*. 184

Driscoll, J. F. (2008). Turbulent premixed combustion: Flamelet structure and its effect on turbulent burning velocities. *Progress in Energy and Combustion Science*, 34:91–134. 71, 73

Duclos, J. and Colin, O. (2001). Arc and kernel tracking ignition model for 3d spark-ignition engine calculations. *Comodia 2001*. 87

Echekki, T. and Chen, J. H. (1999). Analysis of the contribution of curvature to premixed flame propagation. *Combustion and Flame*, 118:308–311. 64

EEA, EASA, and EUROCONTROL (2019). European aviation environmental report 2019. Technical report, European Environment Agency, European Union Aviation Safety Agency, Eurocontrol. 3

Enaux, B. (2010). *Simulation aux Grandes Echelles d'un moteur à allumage commandé - Evaluations des variabilités cycliques*. PhD thesis, INSA Rouen. 88

Ern, A. and Giovangigli, V. (1994). *Multicomponent Transport Algorithms*. Springer. Lecture Notes in Physics. 105

Esclapez, L. (2014). LEMCOTEC. Deliverable D3.4.8. Ignition capabilities analysis: LES and analysis of the light-across capability during altitude relight for various injector spacings. Technical report, SNECMA, CERFACS. 11

Esclapez, L. (2015). *Numerical study of ignition and inter-sector flame propagation in gas turbine*. PhD thesis, INP Toulouse. 28, 60, 61, 64, 88, 94, 95, 253

Eyssartier, A. (2012). *LES of two-phase reacting flows: stationary and transient operating conditions*. PhD thesis, INP Toulouse. 31, 111, 238, 239, 240, 242, 244, 248, 261, 262

Favre, A. J. A. (1992). Formulation of the Statistical Equations of Turbulent Flows with Variable Density. In *Studies in Turbulence*. 28

Felden, A. (2017). *Development of Analytically Reduced Chemistries (ARC) and applications in Large Eddy Simulations (LES) of turbulent combustion*. PhD thesis. 47, 54, 56, 100, 130

Felden, A., Esclapez, L., Riber, E., Cuenot, B., and Wang, H. (2018a). Including real fuel chemistry in LES of turbulent spray combustion. *Combustion and Flame*, 193:397–416. 56, 138

Felden, A., Riber, E., and Cuenot, B. (2018b). Impact of direct integration of Analytically Reduced Chemistry in LES of a sooting swirled non-premixed combustor. *Combustion and Flame*, 191:270–286. 138

Fiorina, B. (2012). Habilitation à Diriger des Recherches Benoît Fiorina Partie 2 : rapport scientifique Tabulation de la cinétique chimique pour la modélisation de la combustion turbulente. 52, 62

Fiorina, B., Vicquelin, R., Auzillon, P., Darabiha, N., Gicquel, O., and Veynante, D. (2010). A filtered tabulated chemistry model for LES of premixed combustion. *Combustion and Flame*, 157:465–475. 52, 73

Fornberg, B. (1988). Generation of finite difference formulas on arbitrarily spaced grids. *Mathematics of Computation*. 24

Franzelli, B., Riber, E., Sanjosé, M., and Poinsot, T. (2010). A two-step chemical scheme for kerosene-air premixed flames. *Combustion and Flame*. 51, 111, 112, 207

Frouzakis, C. E. and Boulouchos, K. (2000). Analysis and reduction of the CH4-Air mechanism at lean conditions. *Combustion Science and Technology*. 54, 120, 128, 287

Fru, G., Thévenin, D., and Janiga, G. (2011). Impact of turbulence intensity and equivalence ratio on the burning rate of premixed methane–air flames. *Energies*, 4:878–893. 84, 92, 93, 94, 155

Galmiche, B., Halter, F., and Foucher, F. (2012). Effects of high pressure, high temperature and dilution on laminar burning velocities and markstein lengths of iso-octane/air mixtures. *Combustion and Flame*, 159:3286–3299. 9

Garcia-Rosa, N. (2008). *Phénomènes d'allumage d'un foyer de turbomachine en conditions de haute altitude*. PhD thesis. 87, 238, 240, 241, 251

Garcia-Ybarra, P., Nicoli, C., and Clavin, P. (1984). Soret and dilution effects on premixed flames. *Combustion Science and Technology*. 20

Gardiner Jr., W. C. (2000). *Gas-Phase Combustion Chemistry*. Springer. 44

Gashi, S., Hult, J., Jenkins, K., Chakraborty, N., Cant, S., and Kaminski, C. (2005). Curvature and wrinkling of premixed flame kernels - comparisons of oh plif and dns data. *Proceedings of the Combustion Institute*, 30:809–817. 92

Gebel, G. C., Mosbach, T., Meier, W., Aigner, M., and Le Brun, S. (2013). An experimental investigation of kerosene droplet breakup by laser-induced blast waves. *Journal of Engineering for Gas Turbines and Power*. 84, 86, 233

Gibson, C. (1968). Fine structure of scalar fields mixed by turbulence. i: Zero-gradient points and minimal gradient surfaces. *Physics of Fluids*, 11. 63

Gicquel, O., Darabiha, N., and Thévenin, D. (2000). Laminar premixed hydrogen/air counterflow flame simulations using flame prolongation of ILDM with differential diffusion. *Proceedings of the Combustion Institute*. 52

Giffen, E. and Muraszew, A. (1953). *The Atomisation of Liquid Fuels*. Chapman & Hall. 188

Gilbert, R. G., Luther, K., and Troe, J. (1983). Theory of thermal unimolecular reactions in the fall-off range - 2. weak collision rate constants. *Berichte der Bunsengesellschaft/Physical Chemistry Chemical Physics*. 47

Giovangigli, V. (1999). *Multicomponent Flow Modelling*. Birkhauser. 21

Giovangigli, V. (2015). Multicomponent transport in laminar flames. *Proceedings of the Combustion Institute*. 21

Glassman, I. and Yetter, R. A. (2008). *Combustion Ed. 4*. 81

Goodwin, D. G., Speth, R. L., Moffat, H. K., and Weber, B. W. (2018). Cantera: An object-oriented software toolkit for chemical kinetics, thermodynamics, and transport processes. https://www.cantera.org. Version 2.4.0. 67, 69, 104

Gorbachev, V. M. (1981). A contribution to Semenov's general theory of thermal ignition regarding thermal analysis. *Journal of Thermal Analysis*. 79

Gran, I., Echekki, T., and Chen, J. H. (1996). Negative flame speed in an unsteady 2-d premixed flame: a computational study. *Proceedings of the Combustion Institute*, 26:323–329. 64, 93

Gu, X. J., Haq, M. Z., Lawes, M., and Woolley, R. (2000). Laminar burning velocity and Markstein lengths of methane-air mixtures. *Combustion and Flame*. 99, 100

Hajiw-Riberaud, M. and Alves-Fortunato, M. (2020). JETSCREEN - D2.1 – Report about the detailed chemical composition of the fuels and pseudo-components formula. JETSCREEN project deliverable. 55, 56

Han, Z., Parrish, S., Farrell, P. V., and Reitz, R. D. (1997). Modeling atomization processes of pressure-swirl hollow-cone fuel sprays. *Atomization and Sprays*. 197

Heberle, L. and Pepiot, P. (2021). Automatic identification and lumping of high-temperature fuel decomposition pathways for chemical kinetics mechanism reduction. In *Proceedings of the Combustion Institute*. 130, 142

Herzler, J. and Naumann, C. (2009). Shock-tube study of the ignition of methane/ethane/hydrogen mixtures with hydrogen contents from 0% to 100% at different pressures. *Proceedings of the Combustion Institute*. 68

Hinze, J. (1975). *Turbulence*. Mac Graw-Hill, 2nd edition. 355

Hirschfelder, J. O., Curtiss, C. F., and Bird, R. B. (1969). *Molecular theory of gases and liquids*. John Wiley. 21

Humer, S., Seiser, R., and Seshadri, K. (2011). Experimental investigation of combustion of jet fuels and surrogates in nonpremixed flows. *Journal of Propulsion and Power*, 27(4):847–855. 56, 132

ICAO (2022). 2022 environmental report. Technical report, ICAO. 3

IPCC (2021). *Climate Change 2021: The Physical Science Basis. Contribution of Working Group I to the Sixth Assessment Report of the Intergovernmental Panel on Climate Change. Summary for policymakers*. Cambridge University Press. Masson- Delmotte, V., P. Zhai, A. Pirani, S.L. Connors, C. Péan, S. Berger, N. Caud, Y. Chen, L. Goldfarb, M.I. Gomis, M. Huang, K. Leitzell, E. Lonnoy, J.B.R. Matthews, T.K. Maycock, T. Waterfield, O. Yelekçi, R. Yu, and B. Zhou (eds.). 1, 2

IPCC (2022). *Climate Change 2022: Mitigation of Climate Change. Contribution of Working Group III to the Sixth Assessment Report of the Intergovernmental Panel on Climate Change*, chapter 10. Cambridge University Press. P.R. Shukla, J. Skea, R. Slade, A. Al Khourdajie, R. van Diemen, D. McCollum, M. Pathak, S. Some, P. Vyas, R. Fradera, M. Belkacemi, A. Hasija, G. Lisboa, S. Luz, J. Malley, (eds.). 1

Jaravel, T. (2016). *Prediction of pollutants in gas turbines using Large Eddy Simulation*. PhD thesis, Institut National Polytechnique de Toulouse. 55, 145, 264, 304

Jasuja, A. K. (1987). Spray Performance of a Hybrid Injector Under Varying Air Density Conditions. Turbo Expo: Power for Land, Sea, and Air. 185

Jasuja, A. K. and Lefebvre, A. H. (2001). Influence of ambient air pressure on pressure-swirl atomizer spray characteristics. In *Proceedings of ASME TURBO EXPO*. 185

Jenkins, K., Klein, M., Chakraborty, N., and Cant, R. (2006). Effects of strain rate and curvature on the propagation of spherical kernel in the thin-reaction-zones regime. *Combustion and Flame*, 145:415–434. 92

Jenkins, K. W. and Cant, R. S. (2002). Curvature effects on flame kernels in a turbulent environment. *Proceedings of the Combustion Institute*. 93

Jones, W., Lyra, S., and Navarro-Martinez, S. (2011). Large eddy simulation of a swirl stabilized spray flame. *Proceeding of the Combustion Institute*, 33:2153–2160. 88

Joulin, G. (1985). Point-source initiation of lean spherical flames of light reactants: An asymptotic theory. *Combustion Science and Technology*, 43:99–113. 9, 81

Kaminski, C. F., Hult, J., Aldén, M., Lindenmaier, S., Dreizler, A., Maas, U., and Baum, M. (2000). Spark ignition of turbulent methane/air mixtures revealed by time-resolved planar laser-induced fluorescence and direct numerical simulations. *Proceedings of the Combustion Institute*. 91

Kee, R. J., Coltrin, M. E., Glarborg, P., and Zhu, H. (2017). *Chemically Reacting Flow: Theory, Modeling, and Simulation*. 2nd edition. 69

Kennedy, C. and Carpenter, M. H. (1997). Comparison of several numerical methods for simulation of compressible shear layers. Technical report. 25, 347

Kennedy, C. A. and Gruber, A. (2008). Reduced aliasing formulations of the convective terms within the Navier-Stokes equations for a compressible fluid. *Journal of Computational Physics*. 349

Kerl, J., Lawn, C., and Beyrau, F. (2013). Three-dimensional flame displacement speed and flame front curvature measurements using quad-plane PIV. *Combustion and Flame*. 93

Klein, M., Chakraborty, N., Jenkins, K. W., and Cant, R. S. (2006). Effects of initial radius on the propagation of premixed flame kernels in a turbulent environment. *Physics of Fluids*. 93

Ko, Y., Anderson, R., and Arpaci, V. (1991). Spark ignition of propane-air mixtures near the minimum ignition energy: Part 1. an experimental study. *Combustion and Flame*, 83:75–87. 9

Ko, Y. S. and Chung, S. H. (1999). Propagation of unsteady tribrachial flames in laminar non-premixed jets. *Combustion and Flame*. 92

Kolera-Gokula, H. and Echekki, T. (2006). Direct numerical simulation of premixed flame kernel-vortex interactions in hydrogen-air mixtures. *Combustion and Flame*. 91, 93

Kolmogorov, A. N. (1941). The local structure of turbulence in incompressible viscous fluid for very large reynolds numbers. *Comptes rendus de l'Academie des sciences, USSR*, 30:301–305. 26, 27

Kono, M., Hatori, K., and Iinuma, K. (1984). Investigation on ignition ability of composite sparks in flowing mixtures. *Proceeding of the Combustion Institute*, 20:133–140. 9, 81

Kravchik, T., Sher, E., and Heywood, J. B. (1995). From Spark Ignition to Flame Initiation. *Combustion Science and Technology*. 85

Kuo, K. K. (2005). *Principles of combustion*. John Wiley, 2nd edition. 18, 59

Labbe, N. J., Sivaramakrishnan, R., Goldsmith, C. F., Georgievskii, Y., Miller, J. A., and Klippenstein, S. J. (2016). Weakly Bound Free Radicals in Combustion: Prompt Dissociation of Formyl Radicals and Its Effect on Laminar Flame Speeds. *Journal of Physical Chemistry Letters*. 103

Lacaze, G. (2009). *Simualtion aux grandes échelles de l'allumage de moteurs fusées cryotechniques*. PhD thesis, INP Toulouse. 88, 155, 253, 355

Lacaze, G., Richardson, E., and Poinsot, T. (2009). Large eddy simulation of spark ignition in a turbulent methane jet. *Combustion and Flame*. 88, 156, 356

Laidler, K. J. (1984). The development of the Arrhenius equation. *J. Chem. Educ.*, 61(6):494. 100

Lam, S. H. (1985). *Singular perturbation for stiff equations using numerical methods*. 130

Lamarque, N. (2007). *Schémas numériques et conditions limites pour la simulation aux grandes échelles de la combustion diphasique dans les foyers d' hélicoptère*. PhD thesis, Institut National Polytechnique de Toulouse. 23, 238, 239

Lasheras, J. C., Fernandez-Pello, A. C., and Dryer, F. L. (1980). Experimental Observations on the Disruptive Combustion of Free Droplets of Multicomponent Fuels. *Combustion Science and Technology*. 204, 205

Law, C. K. (1978). Internal boiling and superheating in vaporizing multicomponent droplets. *AIChE Journal*. 204, 205

Law, C. K., Jomaas, G., and Bechtold, J. K. (2005). Cellular instabilities of expanding hydrogen/propane spherical flames at elevated pressures: Theory and experiment. *Proceedings of the Combustion Institute*. 89

Lax, P. and Wendroff, B. (1960). Systems of conservation laws. *Communications on Pure and Applied Mathematics*. 23, 253

Lefebvre, A. (1998). *Gas Turbine Combustion*. Taylor & Francis, 2nd edition. 6, 7, 8, 83, 185

Lefebvre, A. and McDonell, V. G. (2017). *Atomization and Sprays*. CRC Press Taylor & Francis, 2nd edition. 178, 179, 180, 181, 182, 184, 185, 186, 188, 196

Legier, J. P., Poinsot, T., and Veynante, D. (2000). Dynamically thickened flame LES model for premixed and non-premixed turbulent combustion. *Proceedings of the Summer Program, Centre for Turbulence Research*, pages 157–168. 264

Lepage, V. (2000). *Elaboration d'une methode de réduction de schéma détaillés, application aux mécanismes de combustion du gaz naturel et du n-décane*. PhD thesis, Université Paris VI. 128

Lewis, B. and von Elbe, G. (1987). *Combustion, Flames and Explosions of Gases*. Academic Press, 3rd edition. 9, 81

Li, W., Wang, G., Li, Y., Li, T., Zhang, Y., Cao, C., Zou, J., and Law, C. K. (2018). Experimental and kinetic modeling investigation on pyrolysis and combustion of n-butane and i-butane at various pressures. *Combustion and Flame*, 191:126–141. 10, 103, 104

Li, X. and Tankin, R. S. (1987). Droplet Size Distribution: A Derivation of a Nukiyama-Tanasawa Type Distribution Function. *Combustion Science and Technology*. 194

Linassier, G. (2011). *Étude expérimentale et numérique de l'allumage des turboréacteurs en conditions de haute altitude*. PhD thesis. 238

Lindemann, F. A., Arrhenius, S., Langmuir, I., Dhar, N. R., Perrin, J., and McC. Lewis, W. C. (1922). Discussion on "the radiation theory of chemical action". *Trans. Faraday Soc.*, 17:598–606. 47

Løvås, T., Nilsson, D., and Mauss, F. (2000). Automatic reduction procedure for chemical mechanisms applied to premixed methane/air flames. *Proceedings of the Combustion Institute*. 131

Lu, T. and Law, C. K. (2005). A directed relation graph method for mechanism reduction. *Proceedings of the Combustion Institute*. 128

Lu, T. and Law, C. K. (2006). Systematic approach to obtain analytic solutions of quasi steady state species in reduced mechanisms. *Journal of Physical Chemistry A*. 52, 130

Lu, T. and Law, C. K. (2009). Toward accommodating realistic fuel chemistry in large-scale computations. 51, 145

Luche, J. (2003). *Obtention de modèles cinétiques réduits de combustion Application à un mécanisme du kérosène*. PhD thesis, Universite d' Orléans. 55

Luche, J., Reuillon, M., Boettner, J., and Cathonnet, M. (2004). Reduction of large detailed kinetic mechanisms: Application to kerosene/air combustion. *Combustion Science and Technology*, 176(11):1935–1963. 128

Maas, U. and Pope, S. B. (1992). Simplifying chemical kinetics: Intrinsic low-dimensional manifolds in composition space. *Combustion and Flame*. 52

Maly, R. and Vogel, M. (1978). Initiations and propoagation of flame fronts in lean ch4-mixtures by the three modes of the ignition spark. *Proceeding of the Combustion Institute*, 17:821–831. 7, 84, 87, 253

Mao, C.-P. (2000). The Dynamics of a Swirling Liquid Film. In *ICLASS 2000 - 8th International Conference on Liquid Atomization and Spray Systems*. 183

Marchal, T., Deniau, H., Boussuge, J.-F., Cuenot, B., and Mercier, R. (2021). Extension of the Spectral Difference method to combustion. *arXiv preprint arXiv:2112.09636*. 349

Martin, B. (2021). *Méthodes numériques et conditions limites pour la simulation aux grandes échelles du couplage entre plusieurs composants d'une turbomachine*. PhD thesis, INP Toulouse. 350

Martinos, A. D., Zarzalis, N., and Harth, S. R. (2020). Analysis of ignition processes at combustors for aero engines at high altitude conditions with and without effusion cooling. In *Proceedings of the ASME Turbo Expo*. 10

Masset, P.-A., Duchaine, F., Pestre, A., and Laurent, S. (2022). Modelling challenges of volume-averaged combustion in inert porous media. *Combustion and Flame*. Under review. 131

Mastorakos, E. (2009). Ignition of turbulent non-premixed flames. *Progress in Energy and Combustion Science*, 35:57–97. 6

Mastorakos, E. (2017). Forced ignition of turbulent spray flames. *Proceedings of the Combustion Institute*. 82, 94

Mathur, S. and Saxena, S. C. (1966). Viscosity of polar gas mixtures: Wilke's method. *Applied Scientific Research*, 15:404–410. 21

Mathur, S. and Saxena, S. C. (1967). Methods of calculating thermal conductivity of binary mixtures involving polyatomic gases. *Applied Scientific Research*. 22

Mathur, S., Tondon, P. K., and Saxena, S. C. (1967). Thermal conductivity of binary, ternary and quaternary mixtures of rare gases. *Molecular Physics*, 12(6). 22

Miller, R. S., Harstad, K., and Bellan, J. (1998). Evaluation of equilibrium and non-equilibrium evaporation models for many-droplet gas-liquid flow simulations. *International Journal of Multiphase Flow*. 34

Mittinti, D. and Dabora, E. (1984). Plasma jet ignition studies. *Proceeding of the Combustion Institute*, 20:169–177. 8

Mondal, P., Datta, A., and Sarkar, A. (2004). Droplet size and velocity distributions in a spray from a pressure swirl atomizer: Application of maximum entropy formalism. *Proceedings of the Institution of Mechanical Engineers, Part C: Journal of Mechanical Engineering Science*. 194

Mosbach, T., Sadanandan, R., Meier, W., and Eggels, R. (2010). Experimental analysis of altitude relight under realistic conditions using laser and high-speed video techniques. In *Proceedings of the ASME Turbo Expo*. 9

Mott, D. R. and Oran, E. S. (2001). CHEMEQ2: A Solver for the Stiff Ordinary Differential Equations of Chemical Kinetics. Technical report. 145

Moureau, V., Domingo, P., and Vervisch, L. (2011a). Design of a massively parallel CFD code for complex geometries. *Comptes Rendus Mécanique*. 189

Moureau, V., Domingo, P., and Vervisch, L. (2011b). From Large-Eddy Simulation to Direct Numerical Simulation of a lean premixed swirl flame: Filtered laminar flame-PDF modeling. *Combustion and Flame*. 28

Moureau, V., Fiorina, B., and Pitsch, H. (2009). A level set formulation for premixed combustion LES considering the turbulent flame structure. *Combustion and Flame*, 156:801–812. 73

Moureau, V., Lartigue, G., Sommerer, Y., Angelberger, C., Colin, O., and Poinsot, T. (2005). Numerical methods for unsteady compressible multi-component reacting flows on fixed and moving grids. *Journal of Computational Physics*. 24

Movahednejad, E., Ommi, F., and Hosseinalipour, S. M. (2010). Prediction of droplet size and velocity distribution in droplet formation region of liquid spray. *Entropy*. 194

Mugele, R. A. and Evans, H. D. (1951). Droplet Size Distribution in Sprays. *Industrial & Engineering Chemistry*. 183

Narayanaswamy, K. and Pepiot, P. (2018). Simulation-driven formulation of transportation fuel surrogates. *Combustion Theory and Modelling*. 56

Nath, S., Datta, A., Mukhopadhyay, A., Sen, S., and Tharakan, T. J. (2011). Prediction of size and velocity distributions in sprays formed by the breakup of planar liquid sheets using maximumentropy formalism. *Atomization and Sprays*. 194

Neophytou, A. and Mastorakos, E. (2009). Simulations of laminar flame propagation in droplet mists. *Combustion and Flame*. 75

Neophytou, A., Mastorakos, E., and Cant, R. S. (2010). Dns of spark ignition and edge flame propagation in turbulent droplet-laden mixing layers. *Combustion and Flame*, 157:1071–1086. 94

Neophytou, A., Mastorakos, E., and Cant, R. S. (2012). The internal structure of igniting turbulent sprays as revealed by complex chemistry DNS. *Combustion and Flame*. 9

Nicoud, F. and Ducros, F. (1999). Subgrid-scale stress modelling based on the square of the velocity gradient tensor. *Flow, Turbulence and Combustion*, 62:183–200. 30, 243, 253

Nicoud, F., Toda, H. B., Cabrit, O., Bose, S., and Lee, J. (2011). Using singular values to build a subgrid-scale model for large eddy simulations. *Physics of Fluids*, 23. 31

Orain, M. (2020). JETSCREEN - d6.1 - impact of fuel on ignition (experimental and numerical work. 238, 241

Ortman, J. and Lefebvre, A. H. (1985). Fuel distributions from pressure-swirl atomizers. *Journal of Propulsion and Power*. 184

Ouarti, N. (2004). *Modélisation de l'allumage d'un brouillard de carburant dans un foyer de turbomachine*. PhD thesis, Ecole nationale supérieure de l'aéronautique et de l'espace. 189, 238

Ouarti, N., Lavergne, G., and Bissieres, D. (2003). Modeling of the spray ignition for turbojet engine in-flight re-light. *1st International Energy Conversion Engineering Conference (IECEC)*, 27. 87

Parsons, J. A. and Jasuja, A. K. (1986). Effect of Air Pressure Upon Spray Angle/Width Characteristics of Simplex Pressure Swirl Atomizers. In *Turbo Expo: Power for Land, Sea, and Air*. 185

Passot, T. and Pouquet, A. (1987). Numerical Simulation of Compressible Homogeneous Flows in the Turbulent Regime. *Journal of Fluid Mechanics*. 354

Paulhiac, D. (2015). *Modelisation de la combustion d'un spray dans un bruleur aeronautique*. PhD thesis, Institut National Polytechnique de Toulouse. 9, 32, 34, 39, 40, 41, 77, 233

Pepiot-Desjardins, P. (2008). *Automatic strategies to model transportation fuel surrogates*. PhD thesis, Stanford University. 102, 129

Pepiot-Desjardins, P. and Pitsch, H. (2008a). An automatic chemical lumping method for the reduction of large chemical kinetic mechanisms. *Combustion Theory and Modelling*. 129

Pepiot-Desjardins, P. and Pitsch, H. (2008b). An efficient error-propagation-based reduction method for large chemical kinetic mechanisms. *Combustion and Flame*. 52, 128, 129

Pestre, A. (2018). Développement et validation du code de recherche ntmix3d. Internship report. 24, 348

Pestre, A., Cuenot, B., and Riber, E. (2021). Evaluation of numerical methods for explicit chemistry integration and application on DNS of turbulent kerosene ignition at high altitude conditions. In *Proceedings of the European Combustion Meeting 2021*. 143

Peters, N. (1984). Laminar diffusion flamelet models in non-premixed turbulent combustion. *Progress in Energy and Combustion Science*. 52

Peters, N. (1992). Fifteen lectures on laminar and turbulent combustion. 46

Peters, N. (1999). The turbulent burning velocity for large-scale and small-scale turbulence. *Journal of Fluid Mechanics*. 158

Peters, N. (2000). *Turbulent combustion*. Cambridge University Press. 59, 63, 70, 71

Peters, N., Terhoeven, P., Chen, J. H., and Echekki, T. (1998). Statistics of flame displacement speeds from computations of 2d unsteady methane-air flames. *Proceedings of the Combustion Institute*, 27:833–839. 64

Petersen, E. L., Davidson, D. F., and Hanson, R. K. (1999). Kinetics modeling of shock-induced ignition in low-dilution CH4/O2 mixtures at high pressures and intermediate temperatures. *Combustion and Flame*. 126

Peterson, B., Baum, E., Böhm, B., and Dreizler, A. (2015). Early flame propagation in a spark-ignition engine measured with quasi 4D-diagnostics. *Proceedings of the Combustion Institute*, 35(3):3829–3837. 93

Phuoc, T. and White, F. (1999). Laser induced spark ignition of ch4/air mixtures. *Combustion and Flame*, 119:203–216. 7

Phuoc, T. and White, F. (2002). An optical and spectroscopic study of laser-induced sparks to determine available ignition energy. *Proceeding of the Combustion Institute*, 29:1621–1628. 7

Poinsot, T. (1991). Flame ignition in a premixed turbulent flow. annual research briefs. center for turbulent research. 72, 73, 88, 89, 91, 92, 93

Poinsot, T., Hélie, J., Trouvé, A., and Veynante, D. (1996). Turbulent flame propagation in partially premixed combustion. 91

Poinsot, T. and Veynante, D. (2012). *Theoritical and Numerical Combustion*. 3nd edition. 18, 22, 28, 31, 45, 50, 59, 62, 66, 67, 69, 70, 72, 73, 89, 99, 105, 107, 169

Poinsot, T. J. and Lelef, S. K. (1992). Boundary conditions for direct simulations of compressible viscous flows. *Journal of Computational Physics*. 31, 214, 242

Poling, B. E., Prausnitz, J. M., and O'Connell, J. P. (2001). *The Properties of Gases and Liquids* . McGraw-Hill, 5th edition. 35, 202

Pope, S. (2000). *Turbulent Flows*. Cambridge Univ Press. 26

Ra, Y. and Reitz, R. D. (2009). A vaporization model for discrete multi-component fuel sprays. *International Journal of Multiphase Flow*. 203, 204

Rangel, R. H. and Sirignano, W. A. (1989). An evaluation of the point-source approximation in spray calculations. *Numerical Heat Transfer; Part A: Applications*. 40

Ranz, W. E. and Marshall Jr., W. R. (1952). Evaporation from drops - Part II. *Chemical Engineering Progress*. 37

Ranzi, E., Cavallotti, C., Cuoci, A., Frassoldati, A., Pelucchi, M., and Faravelli, T. (2015). New reaction classes in the kinetic modeling of low temperature oxidation of n-alkanes. *Combustion and Flame*, 162(5):1679–1691. 55, 57, 104, 115, 120, 283, 303

Ranzi, E., Frassoldati, A., Grana, R., Cuoci, A., Faravelli, T., Kelley, A. P., and Law, C. K. (2012). Hierarchical and comparative kinetic modeling of laminar flame speeds of hydrocarbon and oxygenated fuels. *Progress in Energy and Combustion Science*, 38(4):468–501. 53, 54, 55, 57, 104, 115, 120, 132, 283, 303

Ranzi, E., Frassoldati, A., Stagni, A., Pelucchi, M., Cuoci, A., and Faravelli, T. (2014). Reduced kinetic schemes of complex reaction systems: Fossil and biomass-derived transportation fuels. *International Journal of Chemical Kinetics*. 55, 57, 104, 120, 132

Rao, K. and Lefebvre, A. (1976). Minimum ignition energies in flowing kerosène-air mixtures. *Combustion and Flame*, 27:1–20. 8

Reaction-Design (2015). Ansys chemkin theory manual 17.0. San Diego. 347

Read, R. W. (2010). *Experimental investigations into high-altitude relight of a gas turbine*. PhD thesis, University of Cambridge. 9

Reddy, H. and Abraham, J. (2013). Influence of turbulence-kernel intereactions on flame development in lean methane/air mixtures under natural gas-fueled engine conditions. *Fuel*, 103:1090–1105. 91, 92, 93, 158

Renou, B., Samson, E., and Boukhalfa, A. (2004). An experimental study of freely propagating turbulent propane-air flames in stratified inhomogeneous mixtures. *Combustion Science and Technology*, 176:1867–1890. 90, 94

Richardson, E. (2007). *Ignition modelling for turbulent non-premixed flows*. PhD thesis, University of Cambridge. 81

Richardson, L. F. (1922). Weather prediction by numerical process Cambridge University Press. *Monthly Weather Review*. 27

Rizk, N. K. (1985). Internal flow characteristics of simplex swirl atomizers. *Journal of Propulsion and Power*. 186

Rizk, N. K. and Lefebvre, A. H. (1985). Influence of liquid properties on the internal flow characteristics of simplex swirl atomizers. In *American Society of Mechanical Engineers (Paper)*. 184

Roberts, W., Driscoll, J., Drake, M., and Goss, L. (1993). Images of the quenching of a flame by a vortex—to quantify regimes of turbulent combustion. *Combustion and Flame*, 94:58–69. 72

Rochette, B., Riber, E., and Cuenot, B. (2019). Effect of non-zero relative velocity on the flame speed of two-phase laminar flames. *Proceedings of the Combustion Institute*. 75, 76, 206, 223

Rosin, P. and Rammler, E. (1933). The laws governing the fineness of powdered coal. *Journal of the Institute of Fuel*. 183

Roy, P., El Moçaïd, N., Ricci, S., Jouhaud, J.-C., Goutal, N., De Lozzo, M., and M.C., R. (2017). Comparison of polynomial chaos and gaussian process surrogates for uncertainty quantification and correlation estimation of spatially distributed open-channel steady flows. *Stochastic Environmental Research and Risk Assessment*. 249

Roy, P., Ricci, S., Dupuis, R., Campet, R., Jouhaud, J.-C., and Fournier, C. (2018). Batman: Statistical analysis for expensive computer codes made easy. *The Journal of Open Source Software*. 249

Rudgyard, M. A. (1993). Cell vertex methods for steady inviscid flow. In *In VKI, Computational Fluid Dynamics*. 23

Sagaut, P. (2006). *Large Eddy Simulation for Incompressible Flows*. Springer, third edition. 30

Salvador, S. and Chan, P. (2004). Toward accurate dynamic time warping in linear time and space. volume 11, pages 70–80. 133

Sanjose, M. (2009). *Evaluation de la méthode Euler-Euler pour la simulation aux grandes échelles des chambres à carburant liquide*. PhD thesis, Institut National Polytechnique de Toulouse. 238, 239, 242, 243, 244

Sanjosé, M., Senoner, J. M., Jaegle, F., Cuenot, B., Moreau, S., and Poinsot, T. (2011). Fuel injection model for Euler-Euler and Euler-Lagrange large-eddy simulations of an evaporating spray inside an aeronautical combustor. *International Journal of Multiphase Flow*. 187, 249

Schiller, L. and Naumann, Z. (1935). *A drag coefficient correlation*. 33, 249

Schönfeld, T. and Rudgyard, M. (1999). Steady and unsteady flow simulations using the hybrid flow solver AVBP. *AIAA journal*. 23, 242, 349

Sellens, R. W. and Brzustowski, T. A. (1985). A prediction of the drop size distribution in a spray from first principles. *Atomisation and Spray Technology*. 194

Semenov, N. (1928). Theories of combustion processes. *Zeitschrift für Physik*. 79

Senoner, J. M. (2010). *Simulations aux grandes échelles de l'écoulement diphasique dans un brûleur aéronautique par une approche Euler-Lagrange*. PhD thesis, INP Toulouse. 32, 198, 238, 239

Shannon, C. E. (1948). A Mathematical Theory of Communication. *Bell System Technical Journal*. 194

Shastry, V. (2022). *Simulation of multicomponent spray combustion in gas turbine engines*. PhD thesis, INP Toulouse. 201, 203, 204, 207, 249

Shastry, V., Cazeres, Q., Rochette, B., Riber, E., and Cuenot, B. (2020). Numerical study of multicomponent spray flame propagation. *Proceedings of the Combustion Institute*. 56, 57, 203, 206

Sher, E., Ben-Ya'Ish, J., and Kravchik, T. (1992). On the birth of spark channels. *Combustion and Flame*. 85

Shy, S., Liu, C., and Shih, W. (2010). Ignitino transition in turbulent premixed combustion. *Combustion and Flame*, 157:341–350. 9, 82

Sierra Sànchez, P. (2012). *Modeling the dispersion and evaporation of sprays in aeronautical combustion chambers*. PhD thesis, INP Toulouse. 35

Singer, M. A. and Pope, S. B. (2004). Exploiting ISAT to solve the reaction-diffusion equation. *Combustion Theory and Modelling*. 145

Sirignano, W. A. (2010). *Fluid Dynamics and Transport of Droplets and Sprays*. Cambridge University Press, 2nd edition. 40

Sloane, T. M. (1985). The effect of selective energy deposition on the homogeneous ignition of methane and its implication for flame Initiation and Combustion Enhancement. *Combustion Science and Technology*. 88

Sloane, T. M. and Ronney, P. D. (1993). A Comparison of Ignition Phenomena Modelled with Detailed and Simplified Kinetics. *Combustion Science and Technology*. 88

Smagorinsky, J. (1963). General circulation experiments wiht the primitive equations I. The basic experiment. *Monthly Weather Review*. 30

Smith, G. P., Golden, D. M., Frenklach, M., Moriarty, N. W., Eiteneer, B., Goldenberg, M., Bowman, C. T., Hanson, R. K., Song, S., Gardiner Jr., W. C., Lissianski, V. V., and Qin, Z. (2000). GRI-Mech 3.0. 54

Smith, M. T., Birch, A. D., Brown, D. R., and Fairweather, M. (1988). Studies of ignition and flame propagation in turbulent jets of natural gas, propane and a gas with a high hydrogen content. *Symposium (International) on Combustion*. 82

Smith, W. R. and Missen, R. W. (1982). *Chemical Reaction Equilibrium Analysis: Theory and Algorithms*. 68, 108

Sontheimer, M., Kronenburg, A., and Stein, O. T. (2021). Grid dependence of evaporation rates in Euler–Lagrange simulations of dilute sprays. *Combustion and Flame*. 40

Spalding, D. B. (1953). The combustion of liquid fuels. *Symposium (International) on Combustion*. 33

Squire, H. B. (1953). Investigation of the instability of a moving liquid film. *British Journal of Applied Physics*. 197

Stagni, A., Brignoli, D., Cinquanta, M., Cuoci, A., Frassoldati, A., Ranzi, E., and Faravelli, T. (2018). The influence of low-temperature chemistry on partially-premixed counterflow n-heptane/air flames. *Combustion and Flame*, 188:440–452. 101

Stagni, A., Esclapez, L., Govindaraju, P., Cuoci, A., Faravelli, T., and Ihme, M. (2017). The role of preferential evaporation on the ignition of multicomponent fuels in a homogeneous spray/air mixture. *Proceedings of the Combustion Institute*, 36(2):2483–2491. 56, 222

Stewart, P. H., Larson, C. W., and Golden, D. M. (1989). Pressure and temperature dependence of reactions proceeding via a bound complex. 2. Application to 2CH3 → C2H5 + H. *Combustion and Flame*. 47

Sun, W., Chen, Z., Gou, X., and Ju, Y. (2010). A path flux analysis method for the reduction of detailed chemical kinetic mechanisms. *Combustion and Flame*. 128

Suyari, M. and Lefebvre, A. H. (1986). Film thickness measurements in a simplex swirl atomizer. *Journal of Propulsion and Power*. 186

Syred, N. and Beér, J. M. (1974). Combustion in swirling flows: A review. *Combustion and Flame*. 4

Taylor, G. I. (1950). The boundary layer in the converging nozzle of a swirl atomizer. *Quarterly Journal of Mechanics and Applied Mathematics*. 188

Teets, R. and Seel, J. (1988). Calorimetry of ignition sparks. *SAE transactions*, 97:371–383. 7, 253

Tennekes, H. and Lumley, J. (1973). A First Course in Turbulence. 26

Thevénin, D., Gicquel, O., De Charentenay, J., Hilbert, R., and Veynante, D. (2002). Two-versus three-dimensional Direct simulations of turbulent methane flame kernels using realistic chemistry. *Proceedings of the Combustion Institute*. 92

Thiele, M., Selle, S., Riedel, U., Warnatz, J., and Maas, U. (2000). Numerical simulation of spark ignition including ionization. *Proceedings of the Combustion Institute*. 86

Trunk, P. J., Boxx, I., Heeger, C., Meier, W., Böhm, B., and Dreizler, A. (2013). Premixed flame propagation in turbulent flow by means of stereoscopic PIV and dual-plane OH-PLIF at sustained kHz repetition rates. *Proceedings of the Combustion Institute*. 93

Turányi, T. and Tomlin, A. S. (2014). *Analysis of Kinetic Reaction Mechanisms*. 116, 118, 126, 128

Turányi, T. and Tóth, J. (1992). Comments to an article of frank-kamenetskii on the quasy-steady-state approximation acta chemica hungarica. 130

Turquand d'Auzay, C., Papapostolou, V., Ahmed, S. F., and Chakraborty, N. (2019). On the minimum ignition energy and its transition in the localised forced ignition of turbulent homogeneous mixtures. *Combustion and Flame*. 82, 92, 141, 155, 163

Vasquez-Espi, C. and Linan, A. (2002). Thermal-diffusive ignition and flame initiation by a local energy source. *Combustion Theory and Modelling*, 6:297–315. 8, 80

Vasudeo, N., Echekki, T., Day, M. S., and Bell, J. B. (2010). The regime diagram for premixed flame kernel-vortex interactions-Revisited. *Physics of Fluids*. 91, 92, 93

Vinot, B. (2020). Simulation numerique directe de la combusiton turbulente. Internship report. 348

Waage, P. and Gulberg, C. M. (1986). Studies concerning affinity. *Journal of Chemical Education*. 44

Wandel, A. P., Chakraborty, N., and Mastorakos, E. (2009). Direct numerical simulations of turbulent flame expansion in fine sprays. *Proceedings of the Combustion Institute*. 84, 94

Wang, H., Xu, R., Wang, K., Bowman, C. T., Hanson, R. K., Davidson, D. F., Brezinsky, K., and Egolfopoulos, F. N. (2018). A physics-based approach to modeling real-fuel combustion chemistry - I. Evidence from experiments, and thermodynamic, chemical kinetic and statistical considerations. *Combustion and Flame*, 193:502–519. 56, 100, 130

Wang, H., You, X., Joshi, A. V., Davis, S. G., Laskin, A., Egolfopoulos, F., and Law, C. K. (2007). USC Mech Version II. High-Temperature Combustion Reaction Model of H2/CO/C1-C4 Compounds. http://ignis.usc.edu/USC_Mech_II.htm. 54

Wang, X. F. and Lefebvre, A. H. (1987). Mean drop sizes from pressure-swirl nozzles. *Journal of Propulsion and Power*. 186

Wang, Z. J., Fidkowski, K., Abgrall, R., Bassi, F., Caraeni, D., Cary, A., Deconinck, H., Hartmann, R., Hillewaert, K., Huynh, H. T., Kroll, N., May, G., Persson, P. O., van Leer, B., and Visbal, M. (2013). High-order CFD methods: Current status and perspective. 349

Warnatz, J. (2000). Hydrocarbon oxidation high-temperature chemistry. In *Pure and Applied Chemistry*. 100

Warnatz, J., Maas, U., and Dibble, R. W. (2006). *Combustion: Physical and chemical fundamentals, modeling and simulation, experiments, pollutant formation*. 53

Weiß, M., Zarzalis, N., and Suntz, R. (2008). Experimental study of Markstein number effects on laminar flamelet velocity in turbulent premixed flames. *Combustion and Flame*. 9

Westbrook, C. K. and Dryer, F. L. (1981). Simplified Reaction Mechanisms for the Oxidation of Hydrocarbon Fuels in Flames. *Combustion Science and Technology*. 51

Wilke, C. R. (1950). A viscosity equation for gas mixtures. *The Journal of Chemical Physics*. 21

Williams, F. A. (1985). *Combustion Theory*. Benjamin Cummings. 21, 66, 162

Wilms, J. (2005). *Evaporation of multicomponent droplets*. PhD thesis, Institut für Thermodynamik der Luft und Raumfahrt, Universität Stuttgart. 203

Wirtz, J. (2022). *Modelling the impact of fuel in aeronautical gas turbines*. PhD thesis, Institut National Polytechnique de Toulouse. 73, 131, 188, 206, 212, 363

Wirtz, J., Riber, E., and Cuenot, B. (2021). Numerical study of alternative fuels burning in a swirl-stabilized combustion chamber. In *Proceedings of the European Combustion Meeting 2021*. 57

Wong, F. C. H. (2001). Chemical Equilibrium Analysis of Combustion Products at Constant Volume. *Combustion*. 67

Wood, A. M., Hwang, W., and Eaton, J. K. (2005). Preferential concentration of particles in homogeneous and isotropic turbulence. *International Journal of Multiphase Flow*. 77

Wörner, M. (2003). A compact introduction to the numerical modeling of multiphase flows. 33

Yamashita, H., Shimada, M., and Takeno, T. (1996). A numerical study on flame stability at the transition point of jet diffusion flames. *Symposium (International) on Combustion*. 61

Yan, K., Ning, Z., Lü, M., and Sun, C. (2015). Study on droplet size and velocity distributions of a pressure swirl atomizer based on the maximum entropy formalism. *Entropy*. 194

Yaws, C. L. (2015). *Transport Properties of Chemicals and Hydrocarbons*. Elsevier, 2nd edition. 203

Zeldovich, Y. B., Barenblatt, G.I.AND Librovitch, B., and Mikaviladze, G. (1980). *Mathematical Theory of combustion and Explosion*. Nauka, Moscow. 8, 80

Ziegler, G. F. W., Wagner, E. P., and Maly, R. R. (1985). Ignition of lean methane-air mixtures by high pressure glow and arc discharges. *Proceeding of the Combustion Institute*, 20:1817–1824. 9

Appendix A

Application of the chemical analysis tools to the oxidation processes of methane-air combustion and kerosene-air auto-ignition.

A.1 Sensitivity analysis

The sensitivity analysis tool has been tested with the methane chemistry developed by the CRECK modeling group [Ranzi et al. 2012; 2015] and presented Sec. 2.3.2. The reference case is a 0-dimensional constant pressure reactor filled with a stoichiometric mixture of methane-air at the initial temperature $T_i = 1000\,K$. For this application, the target quantity used to compute the sensitivities is the auto-ignition time. Atmospheric ($P = 1\,bar$) and low ($P = 0.3\,bar$) pressures have been studied to evaluate the pressure effect on the key reactions influencing the auto-ignition time. Results are displayed on Fig. A.1.1.

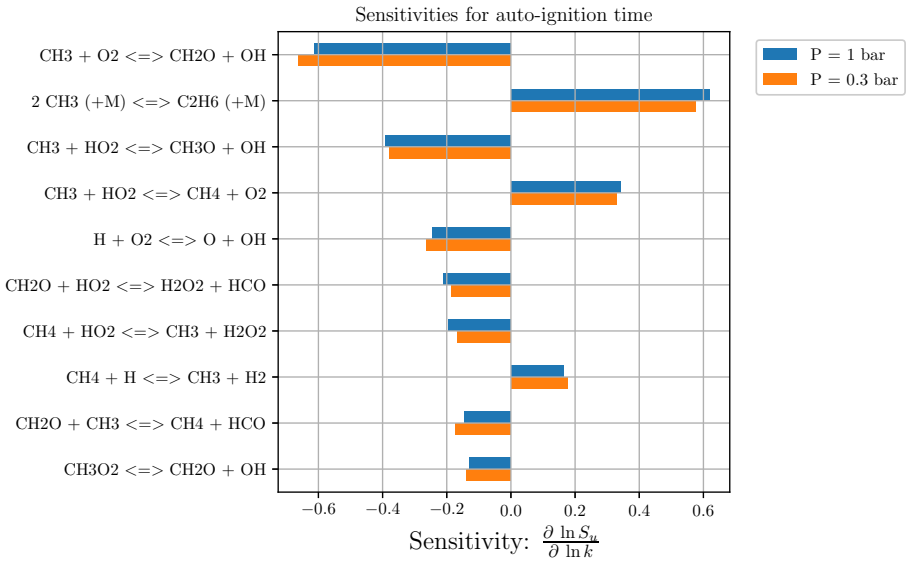

Figure A.1.1: Sensitivity analysis performed on a 0D constant pressure reactor filled with a stoichiometric mixture of methane air at the initial temperature $T_i = 1000\,K$ with respect to the auto-ignition time. Only the ten largest sensitivities are displayed.

Some sensitivity coefficients are positive which indicates that the corresponding reactions increase the auto-ignition time and so are detrimental to the ignition. Indeed, these reactions are recombinations (R1)

and (R2), and a metathesis (R3) that forms a less reactive radical.

$$2\,CH_3\ (+M) \leftrightarrow C_2H_6\ (+M) \quad \text{(R1)}$$
$$CH_3 + HO_2 \leftrightarrow CH_4 + O_2 \quad \text{(R2)}$$
$$CH_4 + H \leftrightarrow CH_3 + H_2 \quad \text{(R3)}$$

The other reactions correspond to a negative sensitivity, thus they reduce the auto-ignition time. The most sensitive reactions are oxidations that produce OH radical enhancing the chemical reactivity (R4), (R5) and (R6).

$$CH_3 + O_2 \leftrightarrow CH_2O + OH \quad \text{(R4)}$$
$$CH_3 + HO_2 \leftrightarrow CH_3O + OH \quad \text{(R5)}$$
$$H + O_2 \leftrightarrow O + OH \quad \text{(R6)}$$

Then, reactions (R7) and (R8) correspond to the decomposition of the key intermediate product CH_2O which then decomposes in HCO, CO and finally CO_2 (see Sec. A.3)

$$CH_2O + HO_2 \leftrightarrow H_2O_2 + HCO \quad \text{(R7)}$$
$$CH_2O + CH_3 \leftrightarrow CH_4 + HCO \quad \text{(R8)}$$

Finally, the reaction (R9) corresponds to the fuel decomposition into methyl, and so reduces the auto-ignition time.

$$CH_4 + HO_2 \leftrightarrow CH_3 + H_2O_2 \quad \text{(R9)}$$

The reactions (R9) and (R10), and generally speaking the large presence of oxygen saturated species (HO_2, H_2O_2, CH_3O_2), is characteristic of low temperature chemical pathways. Here, they are over-represented because the initial reactor temperature $T_i = 1000\,K$ is relatively low.

$$CH_3O_2 \leftrightarrow CH_2O + OH \quad \text{(R10)}$$

Concerning the pressure effect, only negligible differences are observed for all the sensitivities. Thus, it indicates that the low pressure does not change the reactions behavior and the same chemical processes drive the auto-ignition time for both pressures.

A.2 Thermochemical analyses

The thermochemical analyses tools have been tested with the methane chemistry and with the same reference case presented in the previous section. The result will be only presented at the atmospheric pressure because no significant differences have been observed at low pressure and the same conclusions can be drawn. The local analyses have been focused on the sample corresponding to the maximum heat release rate peak. At this instant, the fuel is almost consumed and the temperature increase is maximal, as shown on the right part of Fig. A.2.1 where the dashed line corresponds to the current analysis sample.

At the maximum of heat release rate, the reaction (R6) has the greatest rate of progress as it can be seen on the Fig.A.2.1. This reaction creates two radicals that enhance the chemical reactivity. The reaction (R11) also has a great influence and corresponds to the production of one of the final combustion product H_2O. This analysis also shows the core combustion reaction of methane decomposition. Firstly, the methane is decomposed to produce methyl with radical attack reactions (R3) and (R12). Then methyl is oxidized into CH_2O with reactions (R13) which is decomposed into HCO with the H-abstraction reactions (R14). Finally, HCO dissociates into CO with reaction (R15) which then oxidizes into the main combustion product CO_2 with reaction (R16).

$$H_2 + OH \leftrightarrow H + H_2O \quad \text{(R11)}$$
$$CH_4 + OH \leftrightarrow CH_3 + H_2O \quad \text{(R12)}$$
$$CH_3 + O \leftrightarrow CH_2O + H \quad \text{(R13)}$$
$$CH_2O + H \leftrightarrow HCO + H_2 \quad \text{(R14)}$$
$$HCO + M \leftrightarrow CO + H + M \quad \text{(R15)}$$
$$CO + OH \leftrightarrow CO_2 + H \quad \text{(R16)}$$

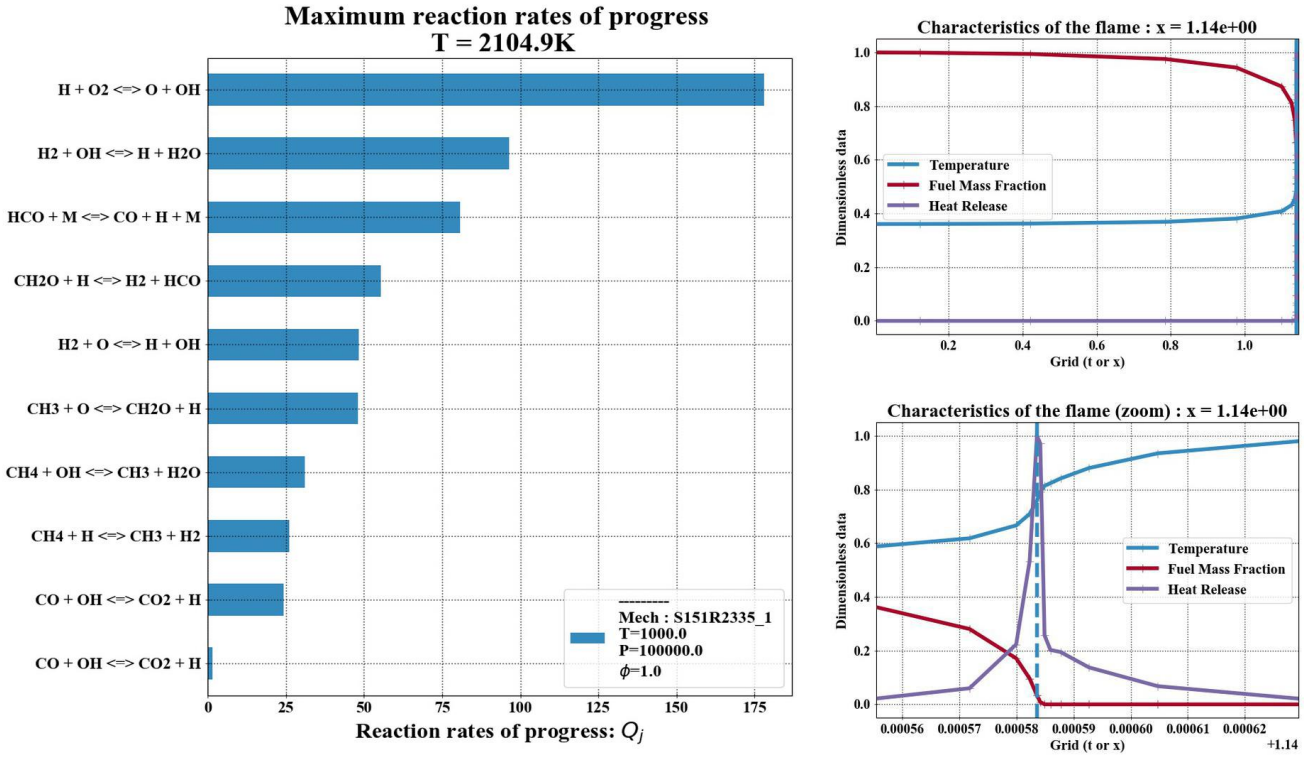

Figure A.2.1: Local progress rate analysis performed on a 0D constant pressure reactor filled with a stoichiometric mixture of methane-air at the initial temperature $T_i = 1000\,K$ and $P = 1\,bar$. Analysis done at the maximum heat release rate. Only the ten largest progress rates are displayed.

With this analysis, reactions are different from the sensitivity analysis, because it is focused on the maximum heat release rate instant, whereas the auto-ignition time and the chemical runaway are driven by reactions occurring before the peak.

The reaction heat release rate analysis Fig. A.2.2 indicates that the reaction (R13) is the largest heat release source. Furthermore, this reaction is not the major one, as seen with the progress rate analysis on Fig. A.2.1. As comparison, the reaction (R13) happens twice more whereas the resulting heat release is more than divided by two. The other important reactions, in terms of heat release rate, are those producing HCO (R14), (R17) and (R18), and CO (R19) and (R20). There is also two large heat release sinks with the reaction (R6) that stores the energy under a chemical form with the radical production, and (R15) which produces CO but through an endothermic dissociation reaction. One can note that, at this instant, the heat release rate associated to CO_2 production is negligible, but largely increases in the post combustion phase (not shown).

$$CH_2 + O_2 \leftrightarrow HCO + OH \quad \text{(R17)}$$
$$CH_2O + OH \leftrightarrow H_2O + HCO \quad \text{(R18)}$$
$$HCCO + OH \leftrightarrow 2\,CO + H_2 \quad \text{(R19)}$$
$$H + HCO \leftrightarrow CO + H_2 \quad \text{(R20)}$$

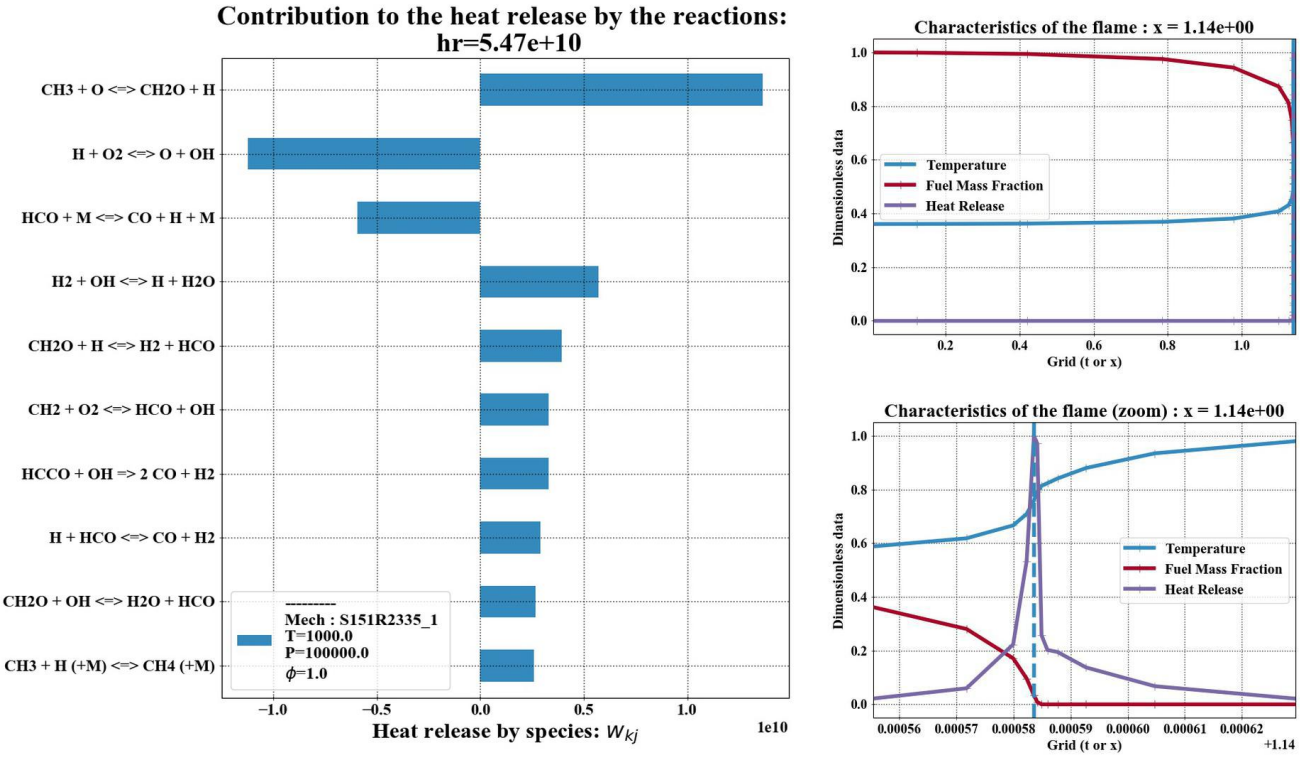

Figure A.2.2: Local heat release rate analysis performed on a 0D constant pressure reactor filled with a stoichiometric mixture of methane-air at the initial temperature $T_i = 1000\,K$ and $P = 1\,bar$. Analysis done at the maximum heat release rate. Only the ten largest heat release rates are displayed.

A.3 Graph pathway analyses

Several application examples are given here. For these examples, the same case will be used. It is a 0-dimensional constant pressure reactor filled with a stoichiometric mixture at $P = 1\,bar$ and $T_i = 1000\,K$.

A.3.1 Complements on atomic flux computation

Let's take an example with the reaction $CH_3 + OH \leftrightarrow CH_2O + H_2$ and the computation of the carbon flux.

In the case of the forward reaction ($\mathcal{Q}_j > 0$), $\mathcal{C}_{CH_3 \to CH_2O} = -\mathcal{Q}_j$ which is negative because the carbon atom is leaving CH_3, and $\mathcal{C}_{CH_2O \to CH_3} = 0$ because CH_2O does not give any carbon atom to CH_3.

In the case of the reverse reaction ($\mathcal{Q}_j < 0$), $\mathcal{C}_{CH_3 \to CH_2O} = 0$ because CH_3 does not give any carbon atom to CH_2O, and $\mathcal{C}_{CH_2O \to CH_3} = \mathcal{Q}_j$ which is also negative because the carbon atom is leaving CH_2O.

In all cases, the atom fluxes are negative because only the leaving fluxes are considered. If the flux goes into the other direction ($\mathcal{C}_{CH_3 \to CH_2O}$ in the reverse case) this flux is considered equal to zero because already taken into account with $\mathcal{C}_{CH_2O \to CH_3}$.

It can be also noted that the case where both species are on the same side of the reaction is already taken into account and lead to a null flux for the corresponding reaction.

A.3.2 Species to Species (StoS)

The first example corresponds to the tool StoS used to study the species CO with the PFA method. The result presented Fig. A.3.1 corresponds to the post-combustion phase after the heat release rate peak. This analysis shows that the main species leading to the production of carbon monoxide are HCO and

HCCO, and its main decomposition product is CO_2. The species O_2, O, OH, and H are involved in the production or decomposition of CO. These species would not be integrated into the analysis with the atomic fluxes method since there is no mass transfer with CO (the oxygen atom always comes from HCO or HCCO). The atomic fluxes method has a greater physical meaning because the atomic flux is a conservative quantity. However, it does not give the full picture of the interaction.

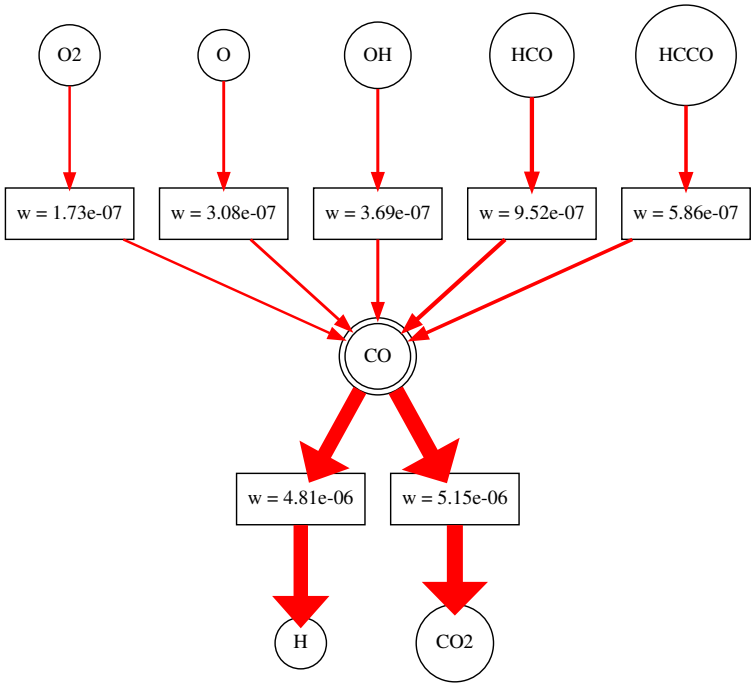

Figure A.3.1: StoS analysis performed on CO with the PFA method. The results are integrated between the maximum heat release rate peak and the end of the peak in a 0D constant pressure reactor of methane-air mixture with $\phi = 1$, $P = 1\,bar$ and $T_i = 1000\,K$.

A.3.3 Reactions to Species (RtoS)

The second example on Fig. A.3.2 corresponds to the tool RtoS used with the species CH_4. This tool enables here to determine the dominant reactions of the fuel decomposition. The tool is used at two different integrated intervals of the same duration. The first one, on the left, is at the pre-ignition phase before the maximum heat release rate. In this case, methane is mainly decomposed with an OH radical attack (only the major interaction is presented). The second one, on the right, corresponds to the maximum of heat release rate. At this time corresponding to the chemical runaway, the concentration of H is increased which allows a secondary decomposition mechanism with the hydrogen radical attack.

A.3.4 Species to Reactions to Species (StoRtoS)

The tool StoRtoS is not presented here but used in Sec. 6.2.2.

A.3.5 Global pathway analysis

The last example is the global graph analysis with the atomic fluxes method. The sample used corresponds to the maximum heat release rate, the starting species is CH_4 and the fluxes are based on the carbon atom. The resulting graph for methane decomposition is presented Fig. A.3.3 with a threshold at 10%. The classical methane decomposition pathways are recovered [Frouzakis and Boulouchos 2000] with the main intermediate species: CH_3, CH_2O, HCO, CO that have already put forward with the thermochemical

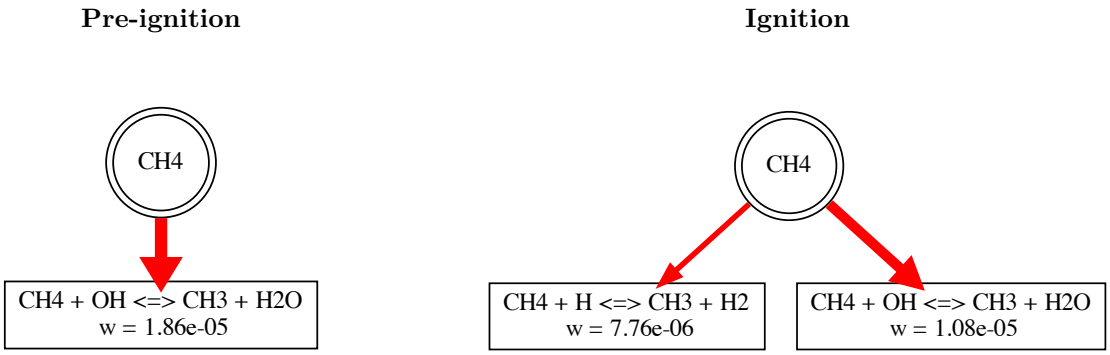

Figure A.3.2: RtoS analysis performed on CH_4 with the PFA method. Both samples used are extracted from a 0D constant pressure reactor of methane-air mixture with $\phi = 1$, $P = 1\,bar$ and $T_i = 1000\,K$.

analyses Sec. A.2. For this sample, the carbon flux between CO and CO_2 is weak because this process arises later after the heat release rate peak.

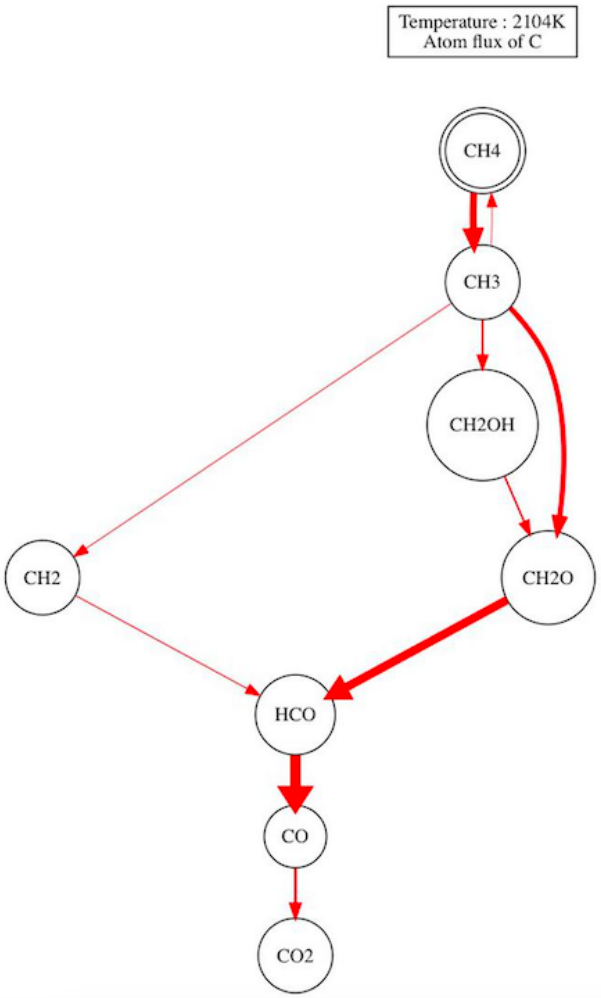

Figure A.3.3: Global pathway analysis of methane decomposition using the carbon fluxes. Analysis done at the maximum heat release rate in 0D constant pressure reactor of methane-air mixture with $\phi = 1$, $P = 1\,bar$ and $T_i = 1000\,K$.

This analysis has been also conducted at low pressure $P = 0.3\,bar$ giving identical results. Thus, the chemical pathways of methane decomposition do not seem sensitive to pressure (at the range studied).

A.4 Study of the kerosene-air auto-ignition

Auto-ignition is relatively close to a forced ignition with energy deposition. Hence, the structural analysis of 0-dimensional constant pressure reactors can bring information to understand the first steps of the flame kernel formation. It has been observed that the heat release rate evolution associated to this process has a non-standard shape, different from the single peak observed in methane ignition for instance or with global chemistries approaches. In the following parts, this evolution is described and chemically analysed.

Global overview

Heat release rate evolutions are plotted Fig. A.4.1 for a stoichiometric mixture at $T_i = 1600\,K$. Two different phases are observed. The first one, on the left (with logarithmic abscissa scale), corresponds to a short but intense endothermic phase. On the other hand, the second one is exothermic, longer and less intense. However, the resulting integral heat release is larger. This second phase presents two distinct peaks separated by a low heat release rate inter-peak step. The effect of pressure is clearly visible. For example, on both phases, as seen with 1-dimensional premixed flames in Chap. 5, the intensity of heat release rate is reduced at low pressure due to lower concentrations. However, the evolution is different between the endothermic phase and the exothermic one. In the first one, the minimum of heat release rate occurs at the same time. On the contrary, the profile is stretched at low pressure during the exothermic phase. The first peak almost disappears, and the inter-peak step is much longer. This behavior is explained by the lower chemical reactivity at low pressure. For the endothermic phase, there is no profile stretching because the heat release rate evolution is mainly due to dodecane decomposition which corresponds mainly to pyrolysis reactions as shown in Sec.6.2.2. Thus, it is not pressure dependent. Hence, the profile stretching effect due to pressure on fuel decomposition is negligible, but the heat release rate amplitude is lower due to the lower concentrations.

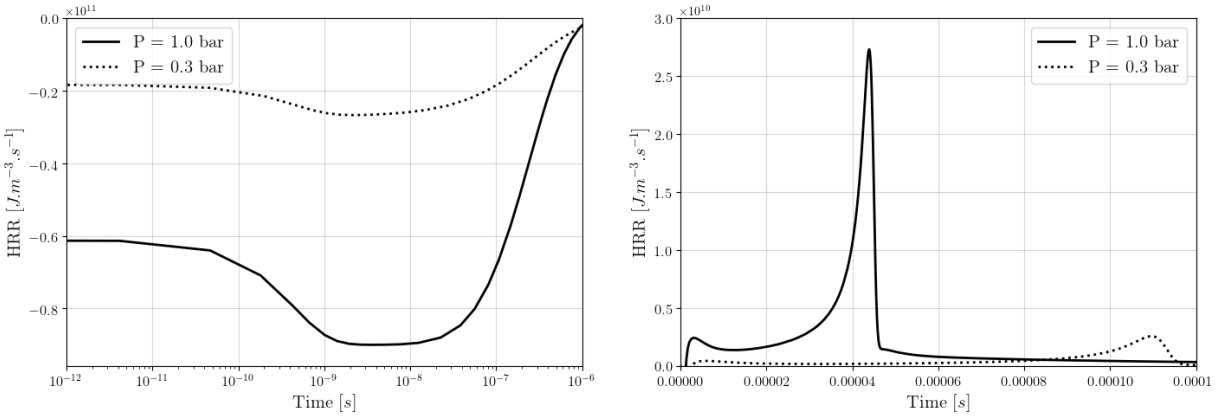

Figure A.4.1: Heat release rate evolution in a constant pressure reactor with stoichiometric mixture and $T_i = 1600\,K$. Left: endothermic phase, right: exothermic phase. Solid line: Patmo, dotted line: LP

This pattern with a first endothermic phase followed by two exothermic peaks seems specific to the auto ignition[1] of heavy fuels since it has not been observed for methane ignition nor in 1-dimensional premixed flame as shown in Fig. A.4.2. In the first case, there is no species to pyrolyse whereas, in the second case, the fuel pyrolysis and oxidation of light species occur at the same location because of diffusion. Therefore, it compensates the heat release rate components.

The consequences of this heat release rate pattern for the kerosene ignition are visible on the temperature evolution Fig. A.4.3. The endothermic phase initially reduces the temperature by about a hundred kelvins. Then the temperature increases slowly at the first heat release rate peak and during the inter-peak step. The large increase in temperature is due to the second peak. After that, the temperature

[1] Double peaks shapes can also be observed in diffusion flames [Blanchard 2021], but this combustion regime has not been studied in this work.

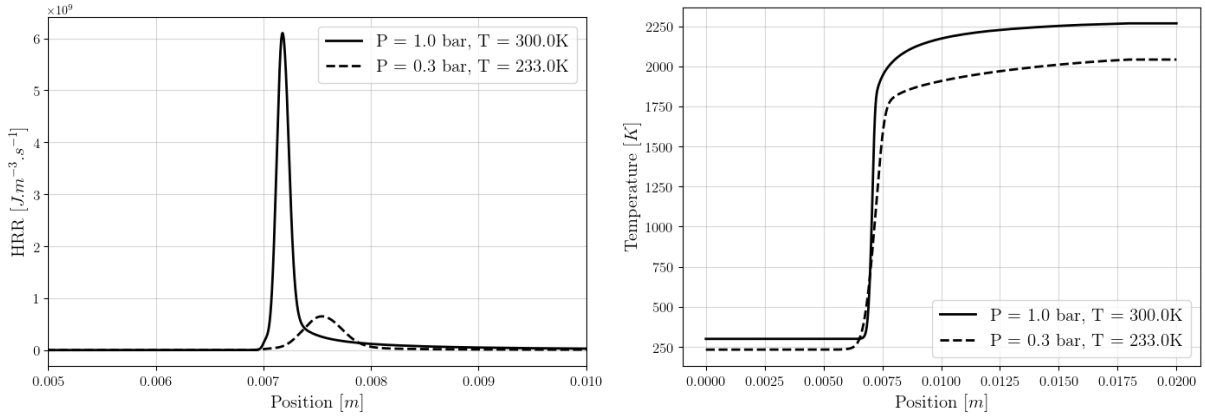

Figure A.4.2: Heat release rate (left) and temperature (right) profiles in a 1D premixed flame with stoichiometric kerosene-air mixture at atmospheric and high altitude conditions.

continues to increase at a slower rate because there is still heat released for a long time after the second peak. The behavior is the same at low pressure, however the temperature increase rate is lower due to the slowing down effect of low pressure. It can be noted that the reduction of the temperature during the endothermic phase is stronger in the low pressure case, even if the endothermic heat release peak is weaker.

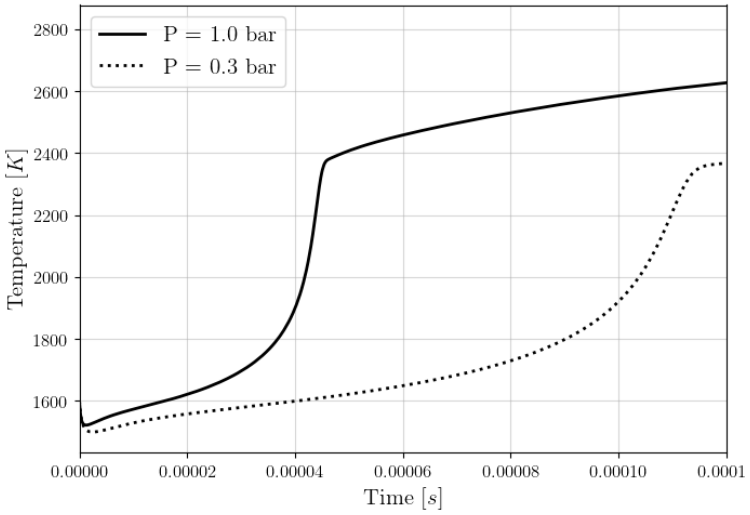

Figure A.4.3: Temperature evolution in a constant pressure reactor with stoichiometric mixture and $T_i = 1600\,K$.

The major difference between auto-ignition reactors and forced ignition with energy deposition is the external energy which is added progressively during the chemical runaway. Thus, the temperature increase also relies on the rate of the energy deposition. Hence, auto-ignition has to be studied also at higher temperatures. Fig. A.4.4 shows heat release rate profiles obtained in auto-ignition reactors with $T_i = 2000\,K$ and $T_i = 2500\,K$. When the initial temperature increases the heat release rate peaks gradually get closer and finally merge for the high temperature operating conditions. This transition seems to indicate two competitive chemical pathways activated by the temperature.

In order to understand the origin of these different peaks, heat release rate and reaction rate of progress studies have been performed. The results have been integrated on the 0-dimensional reactor with $T_i = 1600\,K$ and $P = 0.3\,bar$. The integrated time intervals (expressed in seconds) are the following:

- Endothermic phase: $t = [0; 1 \times 10^{-7}]$
- First peak: $t = [1 \times 10^{-7}; 2 \times 10^{-5}]$

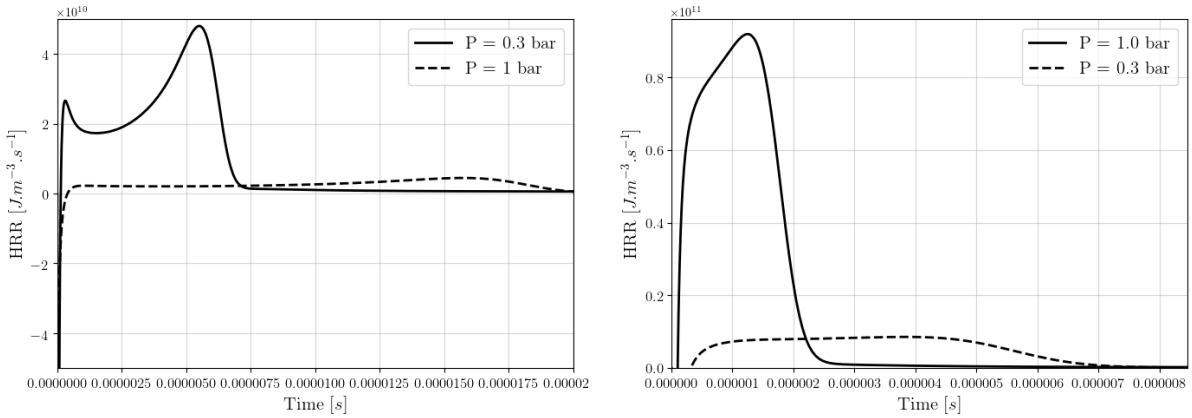

Figure A.4.4: Heat release rate vs time in a constant pressure reactor with stoichiometric mixture. Left: $T_i = 2000\,K$, right: $T_i = 2500\,K$.

- Inter-peak: $t = [2 \times 10^{-5}; 8 \times 10^{-5}]$
- Second peak: $t = [8 \times 10^{-5}; 11.5 \times 10^{-5}]$

Chemical analysis of the ignition phases

Fig. A.4.5 shows that the endothermic step corresponds to the pyrolysis of dodecane and its sub-products. The following species are created: C_2H_5, nC_3H_7, C_2H_4, C_2H_6, C_4H_8-1, and CH_3. The negative heat release rate peak is mainly due to the dodecane pyrolysis reactions that are highly endothermic. The decomposition of the other fuel surrogate species have a negligible influence on this step.

Fig. A.4.6 shows that the first heat release rate peak corresponds to several distinct processes. Firstly, the end of the dodecane, but also the sub-products C_2H_5, nC_3H_7 and pC_4H_9 decomposition to produce mainly C_2H_4, and CH_3. These decompositions are endothermic. Then, the second mechanism is the recombination of methyl into ethane. This chain termination reaction is highly exothermic and compensates the endothermic processes of fuel decomposition. Finally, light species oxidation starts producing radical species such as O, OH, H.

During the inter-peak step (Fig. A.4.7), the chemical activity is reduced and corresponds to light species oxidation with radical production. The classical oxidation pathways observed in methane oxidation are recovered: CH_2O decomposed in HCO that dissociates to produce CO. The released heat comes from the production of HO_2 and CH_2O but it is balanced by endothermic decomposition of C_4H_6 to form C_3H_3 and CH_3, C_2H_5 into C_2H_4, and C_2H_3 into C_2H_2.

The analysis of the second heat release rate peak (Fig. A.4.8) shows also that this step corresponds to the oxidation of light species, however the chemical intensity is one order of magnitude higher compared to the inter-peak step. The main reactions are the oxidation of CH_2O into HCO followed by its dissociation into CO and H. There is also the decomposition of C_2H_2 into HCCO, which then decomposes into CO releasing a lot of heat. These reactions go along with a strong endothermic production of radical species such as O, and OH, and also the exothermic chain termination reaction of H_2O production. The heat release rate analysis indicates that the mean heat release source is the oxidation of CH_3 into CH_2O that also occurs during this step.

A last phase could be added after the second heat release rate peak. Indeed, as seen on Fig. A.4.1 the heat release rate evolution does not fall to zero. On the contrary, a small but non negligible heat release rate is observed during a long time. It indicates that the chemical equilibrium is still not reached. As consequences, the resulting integrated heat release rate corresponds to an additional temperature increase of more than two hundred kelvins for the atmospheric case as seen on Fig. A.4.3. This phase corresponds to the final oxidation of CO into CO_2 (not shown but similar to the examples presented with the methane decomposition in Sec. 6.1.3). One can note that the duration of this phase is very reduced with higher initial temperatures as shown on Fig. A.4.4.

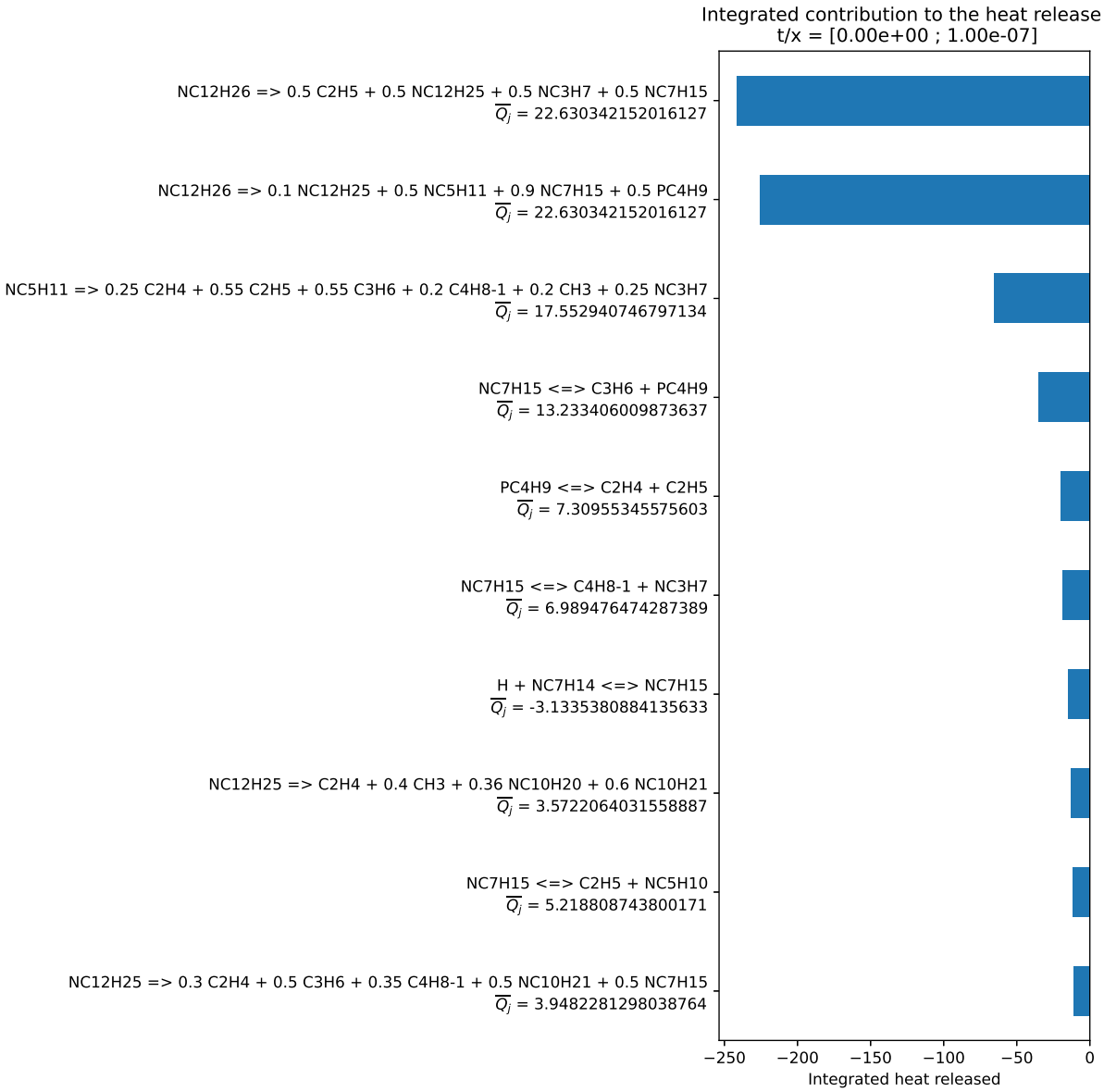

Figure A.4.5: Heat release rate analysis in a constant pressure reactor with stoichiometric mixture, $T_i = 1600\,K$ and $P = 0.3\,bar$. Results are integrated on the endothermic phase.

Origin of the double peaks structure

As presented with Fig. A.4.4, in the case of higher initial temperatures, the inter-peak step disappears and the peaks merge. Based on the previous analysis, it seems that CH_3 production occurring at the first peak directly produces CH_2O as in the second peak. Yet, CH_3 also decomposes into C_2H_6 (shown in the global decomposition graphs in Appendix E). Fig. A.4.9 shows the chemical trajectories of CH_3 and C_2H_6 depending on the temperature. Associated to the reaction rate of progress analysis it is possible to determine which chemical processes are associated to these trajectories.

For the case $T_i = 1600\,K$, CH_3 is first produced in the temperature range $T = [1600K \rightarrow 1500K]$. The temperature decreases, so it corresponds to the endothermic phase with the fuel pyrolysis. Then, as soon as the temperature starts to increase, there is a first consumption step on the same range of temperature $T = [1500K \rightarrow 1600K]$. As seen previously, it corresponds to the first heat release rate peak, and the exothermic reactions are the recombination of methyl into ethane. Indeed, the C_2H_6 trajectory shows a strong increase at the same time/temperature.

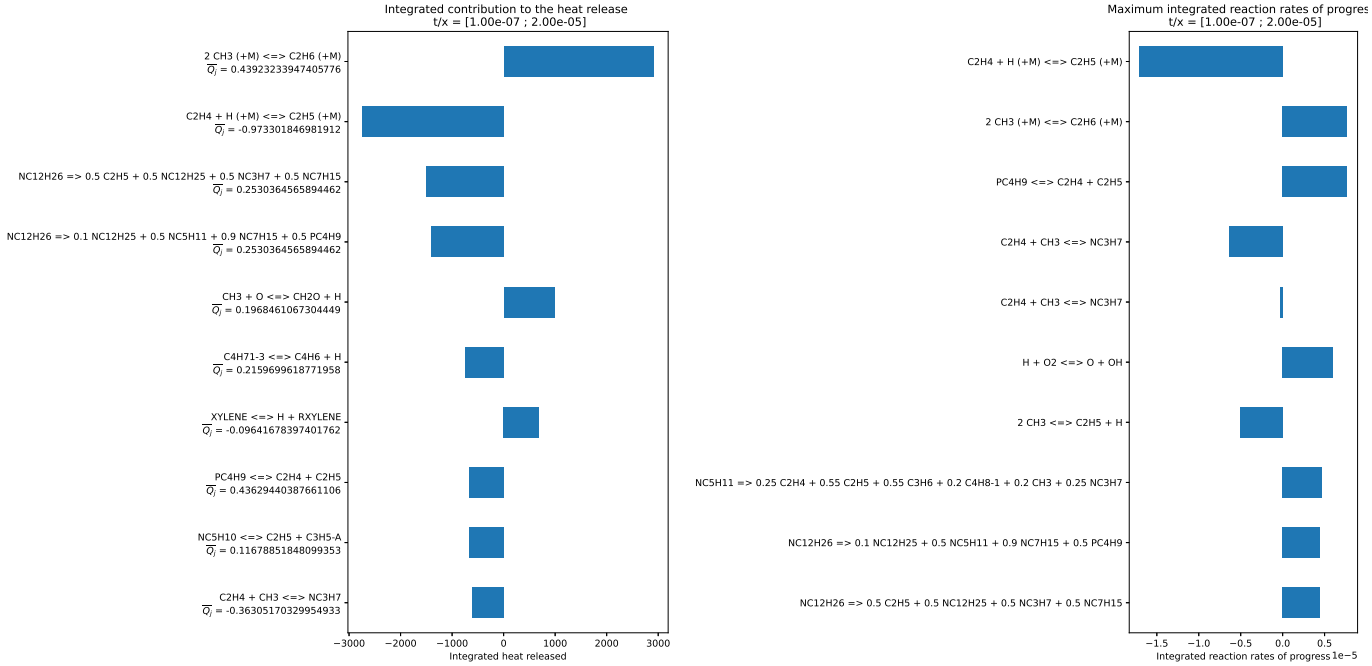

Figure A.4.6: Heat release rate (left) and reaction rate of progress (right) analyses in a constant pressure reactor with stoichiometric mixture, $T_i = 1600\,K$ and $P = 0.3\,bar$. Results are integrated on the first heat release rate peak.

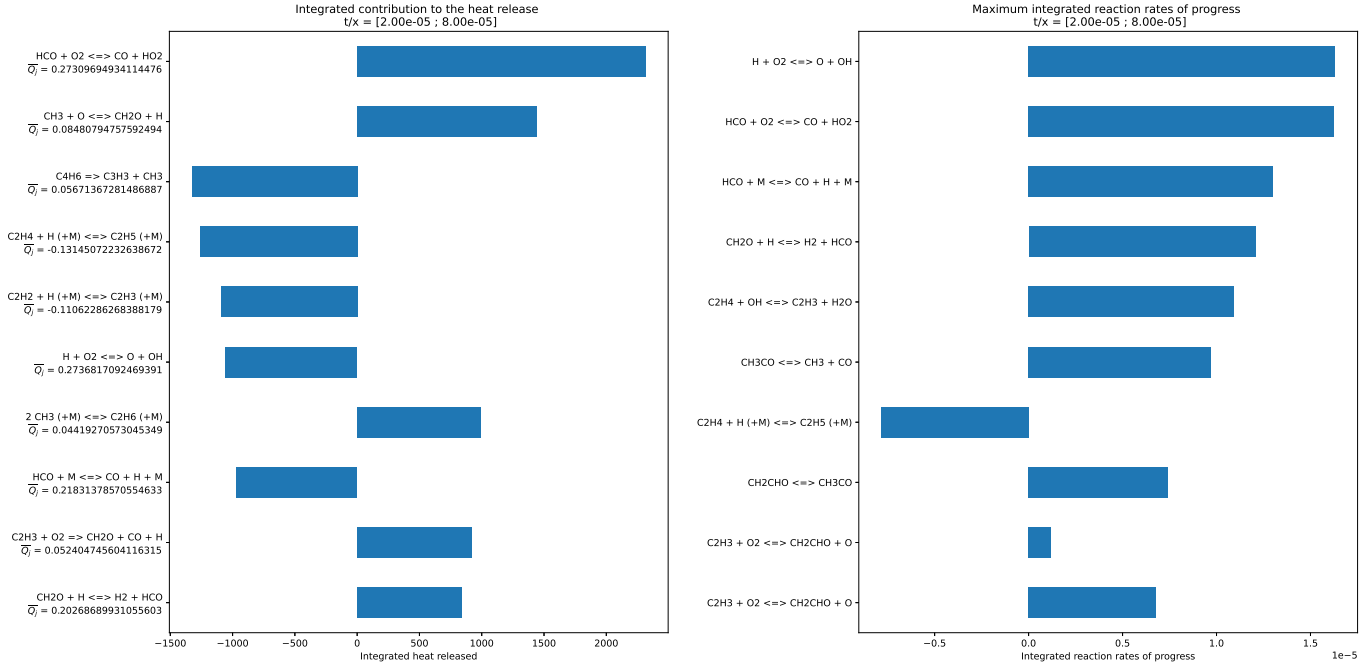

Figure A.4.7: Heat release rate (left) and reaction rate of progress (right) analyses in a constant pressure reactor with stoichiometric mixture, $T_i = 1600\,K$ and $P = 0.3\,bar$. Results are integrated on the inter-peak step.

At the threshold temperature $T_c^{C2H6} = 1600K$ this mechanism stops, the methyl increases again through the dissociation of CH_3CO, and the ethane starts its long decomposition successively into C_2H_5, C_2H_4, C_2H_3, and finally C_2H_2. The temperature range of this step is $T = [1600K \rightarrow 1800K]$ which corresponds to the long inter-peak step with the low temperature increase rate as presented on Fig. A.4.3.

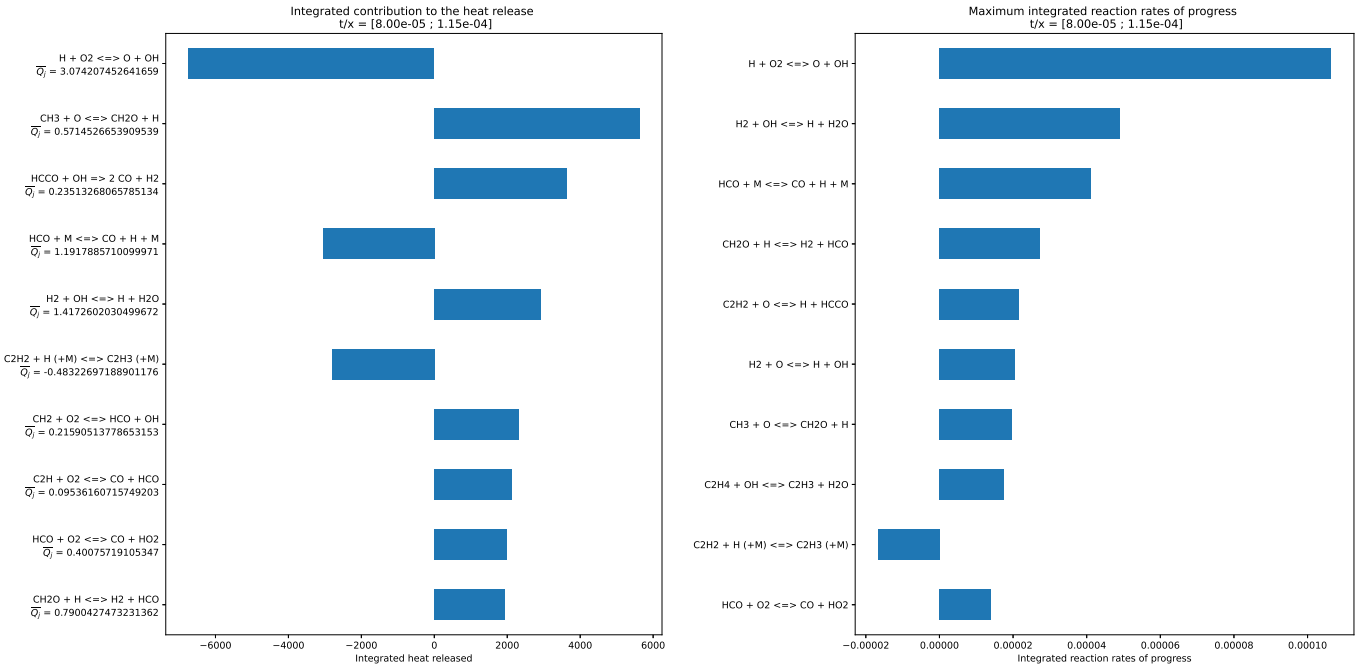

Figure A.4.8: Heat release rate (left) and reaction rate of progress (right) analysis in a constant pressure reactor with stoichiometric mixture, $T_i = 1600\,K$ and $P = 0.3\,bar$. Results are integrated on the second peak.

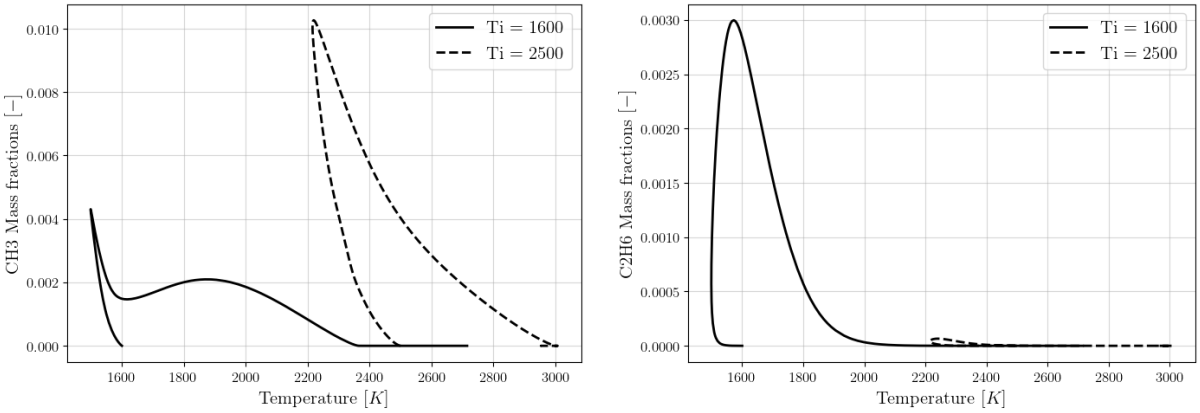

Figure A.4.9: Evolution of methyl (left) and ethane (right) mass fractions versus temperature in a constant pressure reactor with stoichiometric mixture $P = 0.3\,bar$. Solid line: $T_i = 1600\,K$, dashed line: $T_i = 2500\,K$

For temperatures higher than $T_c^{CH2O} = 1800K$, methyl is consumed by an oxidation mechanism that produces CH_2O and releases a lot of heat. It corresponds to the second heat release peak.

In the case of initial temperature $T_i = 2500\,K$, it first starts with the same endothermic pyrolysis process that creates a lot of methyl. However, since the temperature is already higher than T_c^{C2H6}, the methyl does not recombine into ethane. Indeed the ethane trajectory shows a negligible production. Hence there is no first heat release rate peak mechanism and no inter-peak phase. Furthermore, the temperature is also higher than T_c^{CH2O} which means that at the end of the pyrolysis step, methyl is directly consumed with the oxidation reaction that produces CH_2O. Thus, it explains the direct presence of the strong heat release peak on the right picture of Fig. A.4.4 after the endothermic phase.

Both of these competitive chemical pathways are highlighted on Fig. A.4.10 that corresponds to the global graph analysis starting with methyl and following the carbon atom fluxes. Compared to the other

atom fluxes graphs on Fig. 6.2.1, 6.2.2, and 6.2.3 where the pressure effect was negligible, the Fig. A.4.10 showing the initial temperature influence, displays two complete different chemical pathways. The high temperature pathway passing through CH_2O is clearly more efficient compared to the medium temperature one that presents much more intermediate steps and reformation loops with CH_3CO dissociation.

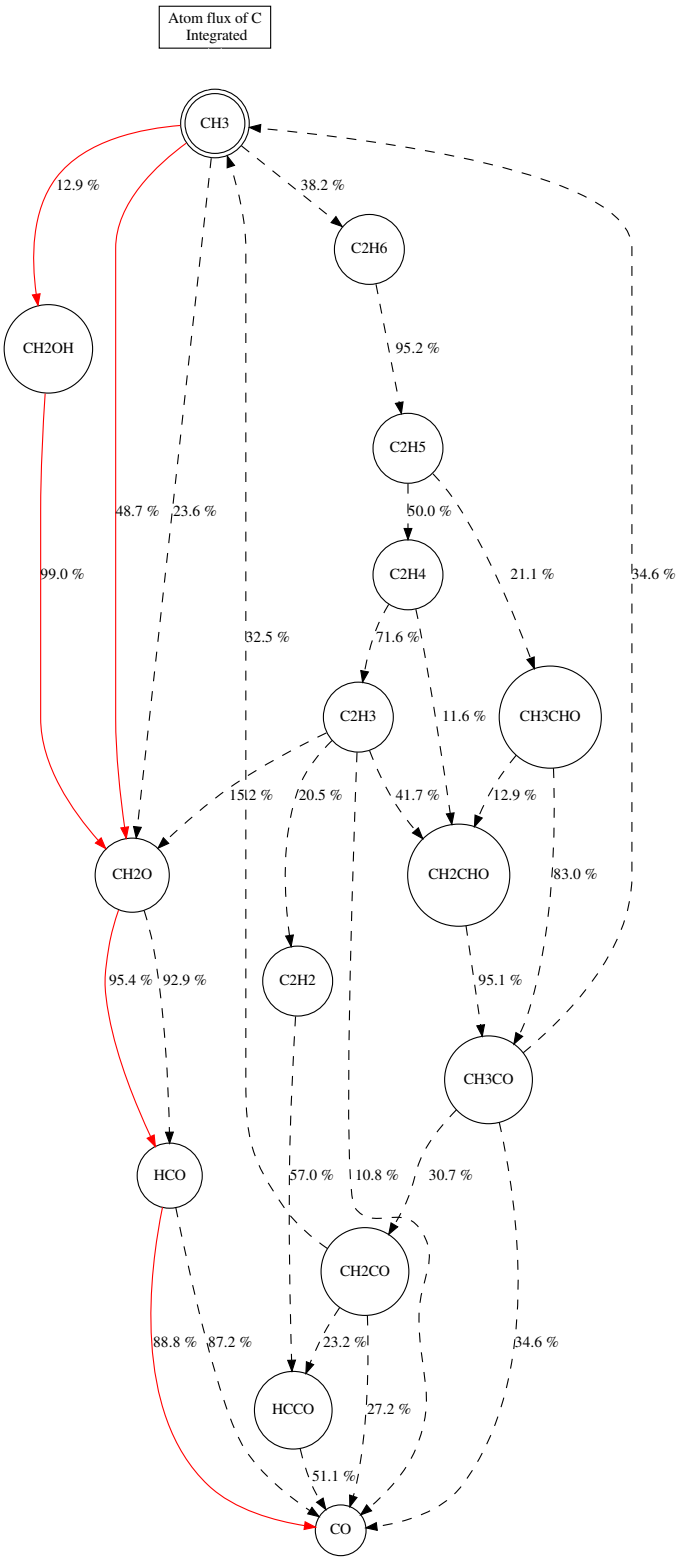

Figure A.4.10: Carbon flux graph starting with CH_3 in a 0-dimensional reactor filled with stoichiometric mixture at $P = 0.3\,bar$. Red solid arrows: $T_i = 2500\,K$, black dashed arrows: $T_i = 1600\,K$.

Appendix B

ARCANE code

B.1 Reduction set-up structure

Independently from the parameters, algorithms or theoretical methods used for the reduction, the ARCANE code always requires the set-up of three main structures by the user. These structures are detailed in this section but concrete examples are given in Sec. 7.3 and 7.4.

B.1.1 Mechanism

The first structure carries all the information about the chemical mechanism to be reduced. Then it includes the transport and the thermodynamic properties, but also all the kinetic reactions.

B.1.2 Cases

The reduction methods presented in the previous section require reference cases to analyse sensibilities and interaction coefficients. Thus, these cases should be representative of the conditions faced by the reduced chemistry during its use. In this work, the mixture ignition to form a flame kernel and its propagation is studied. Therefore, the reference cases are 1-dimensional premixed flames and auto-ignition reactors. These cases are described in Sec. 3.3.

In the ARC formalism, since the rate parameters are not modified and the chemical structure is conserved from the detailed mechanism, the reduced scheme is more robust and can be extrapolated on near conditions from those specified in the reference cases. This property enables to reduce the number of reference cases required in the reduction. For example, only three 1-dimensional premixed flames are usually given to represent the three equivalence ratio behaviors: lean, stoichiometric, and rich. Likewise, for the 0-dimensional reactors, only two initial temperatures are used at each equivalence ratios (6 additional cases). Each reference cases must be used to conserve specific chemical paths during the reduction: lean combustion, high temperature auto-ignition, low temperature mechanisms, etc.

Once the reference cases are defined and computed, the solution is sub-divided in samples (the same procedure is used for the chemical analyses in Chap. 6). Reaction rates, production rates, and species concentrations are extracted from these samples to be used in DRGEP and LOI methods. Hence, interaction and LOI coefficients are evaluated at several times (fuel pyrolysis, light species oxidation) and locations (pre-heat region, core flame front, post flame region) to be representative of the whole combustion process.

B.1.3 Targets

The notion of target derives from the DRGEP methods. As highlighted in Sec. 7.1 with Fig. 7.1.1, the interaction graphs are built from a target species (species A in the example). Several species can be targeted at the same time which leads to the construction of several interaction graphs. The targeted species must be chosen carefully because they have a great influence on the DRGEP species sorting, thus

on the reduction performances. Usually, the target species are the fuel species, the main combustion products (CO_2, CO, H_2O), key intermediate species, or pollutants (for example NOx). The total heat release rate can be also targeted tracking the individual species heat release rate. All the species and reactions linked to the targets are considered important for the reduced chemistry and are removed as a last resort.

B.1.4 Errors

As explained in the previous section, the reduction methods indicate the most probable species and reactions to discard, however they are a priori methods. It means that for each species or reaction to discard, a checking step must be performed to ensure a posteriori that the species or reaction can be removed. In this checking step, the reference cases are computed with the reduced chemistry and compared to the detailed one. The comparisons are based on a set of criteria defined by the user and the associated errors/tolerances enabled. For example, the user can specify 5% errors on the flame speed. If the comparison between reduced and detailed schemes exceeds 5%, the last species or reaction is kept and the reduction stops. Hence, the error level defines the balance between precision and reduction performances. It also ensures that the reduced chemistry is able to recover macroscopic quantities such as laminar flame speed, adiabatic temperature, or ignition times. The error is defined as follow:

$$\epsilon_{\mathcal{Y}} = \left| \frac{\mathcal{Y}_{det} - \mathcal{Y}_{red}}{\mathcal{Y}_{det}} \right| \tag{B.1}$$

with, $\mathcal{Y}$ the quantity of interest and the subscripts $_{det}$ and $_{red}$ corresponding to the detailed and reduced mechanisms respectively.

The most expensive part of the reduction is the cases computation at each checking step, and reducing the number of reference cases can greatly reduce the time needed to derive the chemistry. As explained above, reference cases are not necessary on intermediate ranges. Then, it is possible that the errors are higher on these ranges. However, thanks to the robustness properties through the conservation of the chemical structure, these errors are not expected to diverge. Despite this, it is necessary to check at the end of the reduction if errors are reasonable on the whole range of conditions.

B.2 Reduction algorithms

One of the main ARCANE objectives is to provide an efficient reduction tool. The reduction must be fully automated and able to reduce any detailed chemical mechanism without the need for expert decision. The following sections present the automatic procedure initially developed in ARCANE, but also improved methods developed during this PhD.

B.2.1 Basic algorithm

As explained in the introduction of the reduction methods, the chemical reduction is divided in two general steps: firstly, the generation of the skeletal scheme, and then the ARC chemistry.

The creation of the skeletal scheme is subdivided in three steps: species reduction, reaction reduction, and then a lumping step. Before discarding the species, the DRGEP is computed to sort the species in the decreasing order of importance. The algorithm tries to discard the species one by one following that order. For each species discarded, the user-specified errors are computed until it exceeds a defined tolerance. At the end of this first step, the DRGEP is re-evaluated. Indeed, if some species or reactions are removed, the reaction graph corresponding to the remaining species is modified, thus, the DRGEP coefficients are less and less valid. Then, a new species reduction loop starts with the re-updated DRGEP coefficients. Once no more species can be removed, the same reduction loop is applied to reactions. After the reduction step, the algorithm goes back to the species step and repeats the whole process until no further change is observed. The DRGEP loop of species and reaction is presented on Fig. B.2.1.

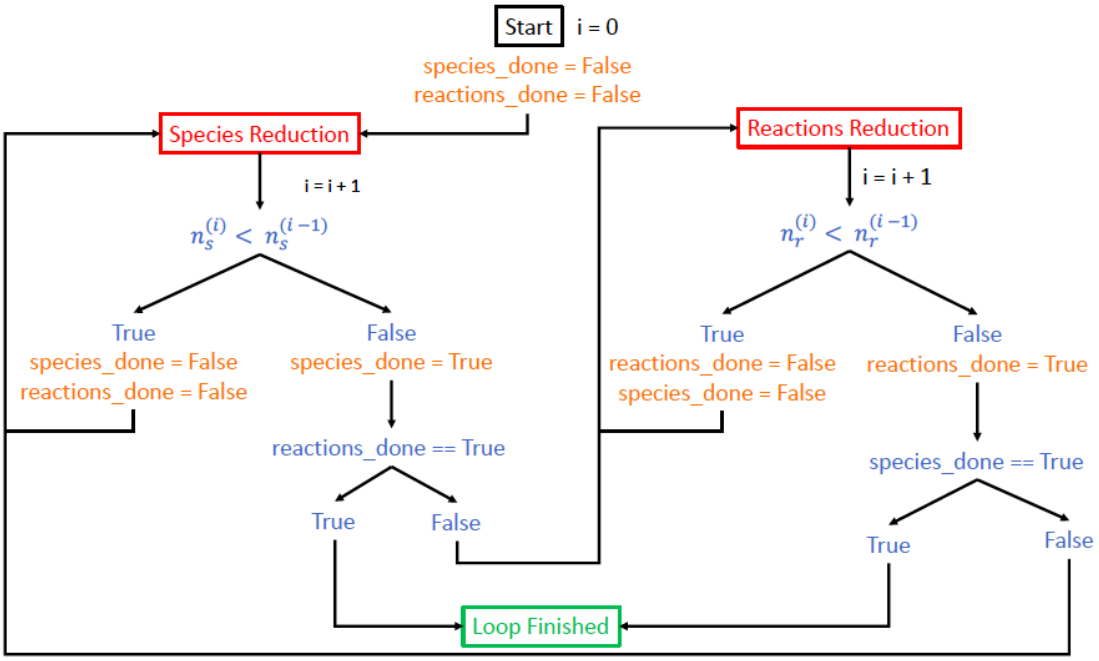

Figure B.2.1: Schematic of the loop between species reduction and reactions reduction steps with $n_S^{(i)}$ and $n_R^{(i)}$ respectively the number of species and reactions in the current mechanism at the i-th iteration (extracted from [Cazères 2021])

The species and reaction loops are followed by the lumping step. For the same reason presented above, the DRGEP loop presented on Fig. B.2.1 is repeated a second time. Once this second loop is finished, the skeletal mechanism is obtained.

The reduction can be extended with the QSSA reduction step. Starting from the skeletal mechanism, the LOI coefficients are computed which enables to sort the remaining species depending on their potential QSS implementation. Similarly to the DRGEP loop, QSS species are progressively added while the errors do not exceed the user threshold. Once this threshold is reached, the QSS reduction is stopped, and the reduced mechanism returned is the final ARC scheme that can be used in CFD solvers.

At the end of the process, the kinetic scheme is written as a dynamic library file that enables to compute reaction rates, production rates, and QSS concentrations from the transported species concentrations, and thermodynamic pressure and temperature conditions. This library file is included to the CFD solver in the form of a compilable subroutine.

B.2.2 Error factors

The error factors enable to modulate the error thresholds imposed by the user depending on the reduction step. For example, if 5% error is allowed on laminar flame speed, and an error factor $E_{f,spec} = 0.8$ is applied on the species reduction step, the resulting error threshold becomes 4% during the species loop but remains 5% for the other steps.

This error modulation method has been added because, it has been observed that each reduction step creates an additional error. Therefore, if the maximal error is reached at the end of the skeletal reduction, no QSS species can be added. Indeed, the additional error will always exceed the user threshold. Hence, using the error factors $E_{f,skel} = 0.8$ and $E_{f,QSS} = 1$, the skeletal scheme will contain more species and reactions, but QSS species could be added resulting in an ARC scheme with less species to transport.

The same phenomenon is observed between species and reactions reduction steps. Due to a size effect (ten times more reactions than species), the removal of one reaction only adds a small error. On the contrary,

a species removal has a larger influence. Therefore, if the same threshold is applied between species and reaction reduction steps, the maximal error allowed will be reached during the reaction reduction step which will prevent further species removal in the following species reduction loops.

Typical values used for error factors in this work are:

$$E_{f,spec} = 0.75 \quad ; \quad E_{f,reac} = 0.6 \quad ; \quad E_{f,lump} = 0.75 \quad ; \quad E_{f,QSS} = 1 \tag{B.2}$$

Non-stop method

Since the DRGEP, lumping, and LOI methods are evaluated a priori, it has been observed that the order provided was globally a good indicator but not optimal. Indeed, species and reactions can be misranked or under-evaluated depending on the chosen targets. The non-stop method simply allows to continue the reduction even when the error exceeds the defined threshold. Hence, it enables to discard additional species ranked further down in the list.

With this method, the species reduction loop is stopped only when all the species have been tested. A lot of important species are tested which increases the cost of the reduction, but it ensures to not miss any species. The non-stop method is not applied at the reactions reduction step. Indeed, large detailed mechanisms are composed of more than a thousand of reactions. The cost would be too high compared to the few advantages to reduce the number of reactions for the CFD solver. This method is also applied for the QSS reduction step.

With this method, the DRGEP order has less influence on the final result of the reduction. Thus, the targets provided by the user to build the DRGEP graph are less important which reinforce the ARCANE accessibility to non-expert users. However, pertinent targets will result in a better initial DRGEP order which reduces the reduction time by removing the unnecessary species first.

Layer method

The layer method has been also developed because of the potential wrong order of the DRGEP. Contrary to the non-stop method which avoids to miss any species to discard, the layer method enables to remove the species in the right order i.e. the species producing less error first. Indeed, if some species (or reactions) are misranked, they can create a large increase of the error, but still below the threshold limit, which can prevent to remove other species in the following. For example, in the case where the threshold error is set to 5% and the current error level of the reduction is 1%. A misranked species adding 3% error will increase the reduction error to 4%. Then, any following species adding an error higher than 1.1% won't be removed, even if their errors are lower than the misranked species.

To avoid such behaviors, the skeletal reduction is sub-divided in several layers/loops (5 in general). For each layer, the error threshold is progressively increased until the user defined value at the last layer. Practically, if the user error tolerance is 5% and 5 layers are used, the reduction algorithm will first start the skeletal reduction with 1% error. Therefore, only the species with the smallest error will be discarded. Once, the skeletal reduction loop is finished, the algorithm starts the second layer with 2% error, and so on until the last layer is reached.

Another interest of this method is that it limits the compensation error between species that can be detrimental to the good behavior of the reduced chemistry outside the ranges specified in the cases. Indeed, if the chemical pathways are completely modified compared to the detailed mechanism after removing a too large number of species / reactions, error compensations can arise. This error compensation mechanism can provide a small error on the measured point, but also a non negligible one for a slight modification of the pressure, temperature or equivalence ratio conditions. Furthermore, the chemical pathways structure is completely lost. On the contrary, if the objective is to get the most reduced chemistry possible for a specific operating condition, the compensation phenomenon becomes desirable and the layer method should not be used.

Performances

The error factors, layers and non-stop methods are used at the same time in the reductions presented Sec. 7.3 and 7.4. The additional CPU-time required compared to the basic algorithm is not negligible. However, 5 to 10 more species have been discarded which results in a significant gain in the CFD computations in terms of CPU-cost but also saved memory.

For this work, ARCANE has been able to run on a Macbook Air (2017). The reduction time especially depends on the initial size of the detailed scheme. Less than one hour for methane chemistries with less than a hundred of species, to several days for kerosene chemistries composed of more than a thousand species. In these large hierarchical mechanisms built to represent a large variety of fuel species, a lot of species are not even in the fuel decomposition pathways. For that reason, and to save time, the first step of the reduction discards several species at the same time. It enables to avoid useless case computations and error computations for each species removed. The greatest CPU-cost comes from the case computations at each reduction steps. This cost is greatly reduced by restarting solutions from the previous reduced mechanism (called parent mechanism). Furthermore, if needed, the case computations can be performed on several cores.

Appendix C

Reduction of methane-air chemistry

The objective of this reduction was to derive a new generic ARC chemistry for methane-air applications and especially for ignition at low and intermediate pressures ($P = 0.3 - 5\,bar$). Furthermore, this reduction enabled to develop and test the new reduction methods presented above and included in the tool ARCANE.

The reduced methane-air chemistry is based on the reference hierarchical mechanism developed by the CRECK Modeling Group [Ranzi et al. 2012; 2015] which is composed of 151 species and 2335 reactions and labeled S151R2335 in the following. This mechanism is designed to reproduce methane-air combustion processes including NOx mechanisms.

Two separate reductions have been performed for different applications, results accuracy and performances, which are detailed in the following section. These reductions will be labeled S21R158QSS6 and S15R138QSS9 in the following. For both schemes NOx mechanism are not retained.

C.1 Reduction set-up

C.1.1 S21R158QSS6

The main objectives were to develop a chemistry able to reproduce ignition phenomena and flame kernel propagation at atmospheric and low pressures. Hence, the reference cases used are presented in Table C.1.1.

Cases	Temperature $[K]$	Pressure $[bar]$	Equivalence Ratio $[-]$
0D isobaric reactors	$1000 - 3000$	1	$0.6 - 1 - 1.5$
1D premixed flames	300	1	$0.6 - 1 - 1.5$

Table C.1.1: Reference cases for S21R158QSS6 reduction

The computation of 0-dimensional reactors have been used to ensure good prediction of the auto-ignition processes occurring during simulations with energy deposition. Two initial temperatures were used to target a large range of operating points. The computation of premixed flames ensures a good prediction of flame propagation and transport effects. The temperature corresponds in this case to the fresh gases one. The reference cases are computed at atmospheric pressure but broader ranges are validated in the validation section. Finally, equivalence ratio values range on the methane-air flammability limits.

The target species used for the DRGEP steps are CH_4, CO_2 and H_2O because they are the fuel and products of the global reaction. CO is also targeted because its production is a main step of methane combustion. Finally, the heat release rate is targeted because it includes several combustion processes and it is a good indicator of combustion dynamic and behavior.

The error levels have been monitored during the reduction on auto-ignition times, laminar flame speeds, maximum heat release rates, final temperatures and final concentrations of H_2O and CO_2. The maximum

error allowed is 10% and is the same for all quantities, however, it is shown in Sec. C.3 that errors are much lower for the final temperature and species concentrations.

For this reduction the error factors used are $E_{f,skel} = 0.5$ and $E_{f,QSS} = 1$. The non-stop method has been activated, but the layer method has not been used since it has been developed later.

C.1.2 S15R138QSS9

For the second reduction, the ARCANE set-up is slightly different. It has been observed with the reduction S21R158QSS6, that a non negligible part of transported species and chemical stiffness was due to low temperature pathways, especially for the prediction of auto-ignition times. Since the main objective of the chemistry was to reproduce ignition phenomena encountered in high energy deposition and high temperatures, the 0-dimensional reactor with $T_i = 1000\,K$ not representative of forced ignition was removed from the reference cases. Except this difference the reference cases are identical to those presented in Table C.1.1. Targets for DRGEP, and error thresholds are also identical to the reduction S21R158QSS6.

The error factors used for this reduction were: $E_{f,spec} = 0.5$, $E_{f,reac} = 0.4$, $E_{f,lump} = 0.5$ and $E_{f,QSS} = 1$. This time, the non-stop method associated to the layer method were used to get the best reduction performances.

C.2 Reduced CH4-air chemistries

C.2.1 S21R158QSS6

A first skeletal scheme is obtained and composed of 27 transported species and 162 reversible reactions. It is labeled S27R162 in the following. Then, 6 species are converted to QSS to obtain the ARC mechanism S21R158QSS6[1]:

- Transported species:
  N_2, H_2, H, O_2, O, H_2O, OH, H_2O_2, HO_2, CO, CO_2, CH_4, CH_3, CH_3O_2H, CH_3O, CH_2O, C_2H_6, C_2H_5, C_2H_4, C_2H_2, $CH_2(L_1)$[2].

- QSS species:
  CH_3O_2, CH_3OH, CH_2OH, HCO, C_2H_3, $C_2H_3O(L_1)$.

The ARC mechanism with kinetic reactions S21R158QSS6 is given in Sec. C.5.1.

A timescale analysis is presented Fig. C.2.1. These species timescales are computed using Eq. (7.10) and correspond to the minimum value measured on the set of reference cases. These timescales are generally lower than the explicit formulation (detailed in Chap. 8) often used in CFD solvers to define a chemical time-step. However, it highlights the global stiffness of a chemical scheme. In the case of S21R158QSS6, the species CH_3O requires very low time steps to be solved and can lead to unstable behavior of the chemistry. Then it is strongly recommended to use a semi-implicit integration of this species [Jaravel 2016] or to use exponential chemistry (presented Chap. 8).

C.2.2 S15R138QSS9

The second skeletal scheme is composed of 24 transported species and 148 reversible reactions. It is labeled S24R148 in the following. Then, 9 species are converted to QSS to obtain the ARC mechanism S15R138QSS9:

[1] The number of reactions is lower because reactions with quadratic coupling (two QSS species on the same side of the reaction) are removed.

[2] (L_1) refers to a lumped species

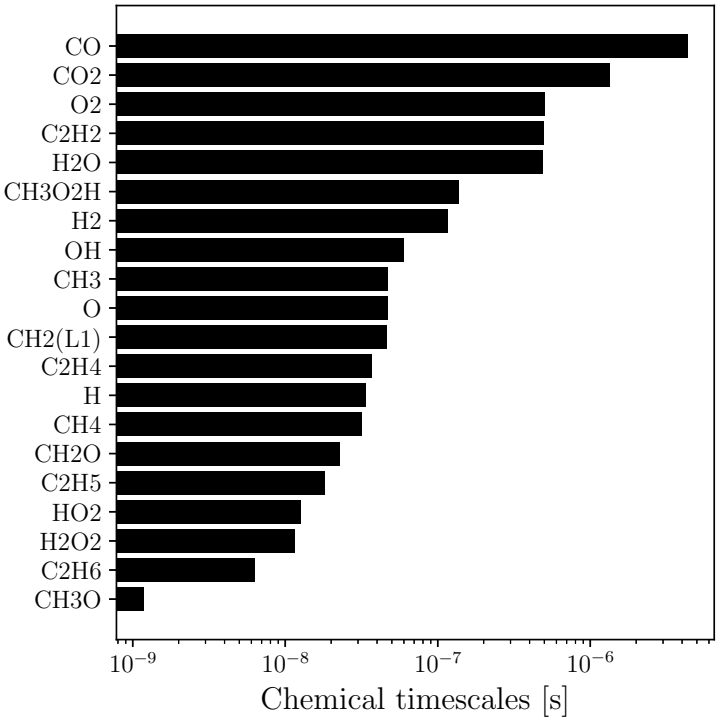

Figure C.2.1: Evaluation of the species chemical timescales based on the inverse of the Jacobian matrix for S21R158QSS6

- Transported species:
  N_2, H_2, H, O_2, O, H_2O, OH, CO, CO_2, CH_4, CH_3, CH_2O, C_2H_6, C_2H_2, $CH_2(L_1)$.

- QSS species:
  CH_3OH, CH_2OH, HCO, C_2H_3, HO_2, CH_3O, C_2H_5, C_2H_4, CH_2CO.

The ARC mechanism with kinetic reactions S15R138QSS9 is given in Sec.C.5.2.

Compare to S21R158QSS6, several species have been converted to QSS while transported before: HO_2, CH_3O, C_2H_5 and C_2H_4. Others corresponding to low temperature pathways have been removed: CH_3O_2, $C_2H_3O(L_1)$, H_2O_2, and CH_3O_2H. And a new species has been added into QSS: CH_2CO. Since the stiff species CH_3O can now be set in QSS, Fig. C.2.2 shows that the time-step required for the stability are larger. The reduced stiffness along with a small number of species to transport enable to use easily this chemistry in CFD solvers.

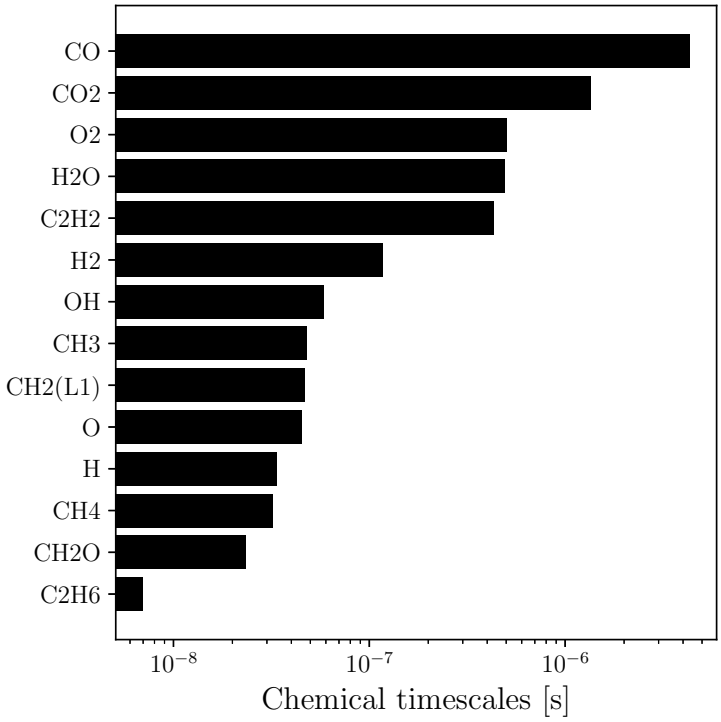

Figure C.2.2: Evaluation of the species chemical timescales based on the inverse of the Jacobian matrix for S15R138QSS9

C.3 Validations

C.3.1 S21R158QSS6

The ARC mechanism S21R158QSS6 and the corresponding skeletal scheme S27R162 have been first validated on 0-dimensional reactors. For that purpose, the relative error to the detailed mechanism, computed with Eq. (C.1), has been measured for the auto-ignition time. The chemical schemes were tested on the whole range of flammability limits while only stoichiometric mixtures were used for the reduction. On Fig. C.3.1 the pressure is $P = 1\,bar$ and the initial temperature are respectively $T_i = 1000\,K$ and $T_i = 3000\,K$ as in the reference cases. Fig. C.3.2 also shows the validation of the reduction for the low pressure condition $P = 0.3\,bar$.

$$\epsilon_{\mathcal{Y}} = \left| \frac{\mathcal{Y}_{det} - \mathcal{Y}_{red}}{\mathcal{Y}_{det}} \right| \tag{C.1}$$

with, $\mathcal{Y}$ the quantity of interest and the subscripts $_{det}$ and $_{red}$ corresponding to the detailed and reduced mechanisms respectively.

The mechanisms have been also validated on 1-dimensional premixed flames on the whole range of equivalence ratio for laminar flame speed, maximum heat release rate, final temperature and final concentrations of CO_2 and H_2O. Fig. C.3.3 shows the error measured on these quantities with a fresh gas temperature $T_f = 300\,K$, for $P = 1\,bar$ and $P = 0.3\,bar$.

C.3.2 S15R138QSS9

Similarly to the reduction S21R158QSS6, errors versus equivalence ratio on 0-dimensional and 1-dimensional cases are respectively presented on Fig. C.3.4 and Fig. C.3.5 for the ARC mechanism S15R138QSS9 and the corresponding skeletal scheme S24R148.

This chemistry has been also validated on extended operating conditions and other cases. On the following figures, the quantities of interest are directly plotted for a better readability. Firstly, Fig. C.3.6

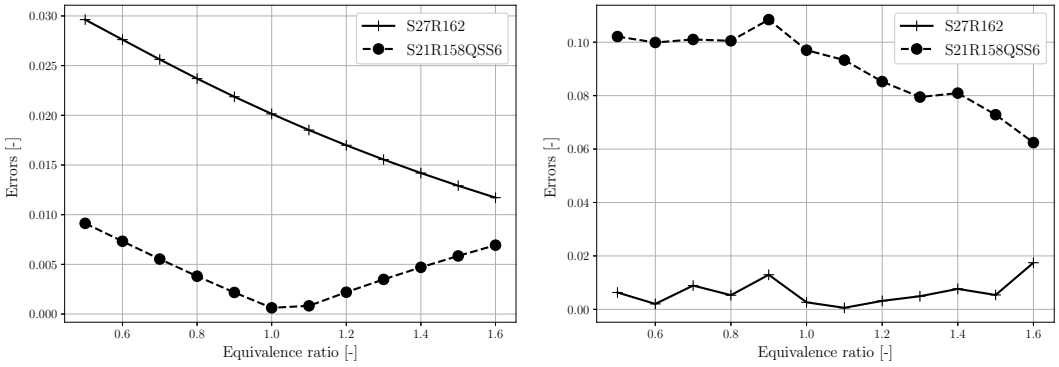

Figure C.3.1: Errors on auto-ignition time versus equivalence ratio for S21R158QSS6 and S27R162 schemes. Left: $P = 1\,bar$ and $T_i = 1000\,K$, right: $P = 1\,bar$ and $T_i = 3000\,K$

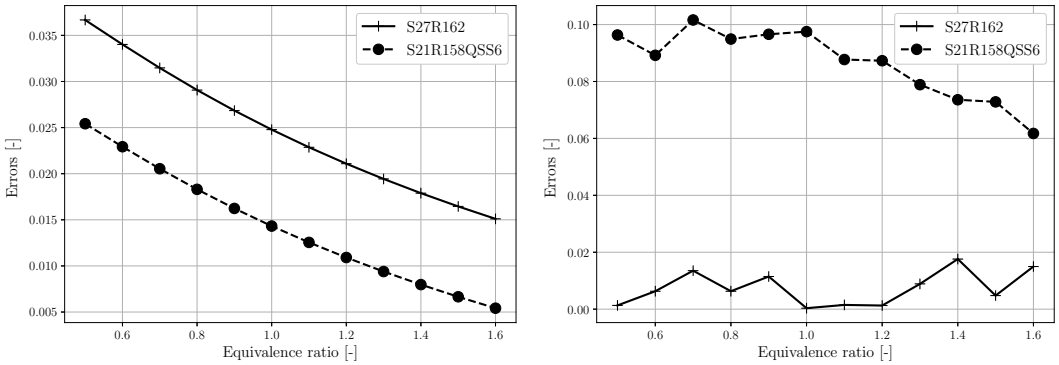

Figure C.3.2: Errors on auto-ignition time versus equivalence ratio for S21R158QSS6 and S27R162 schemes. Left: $P = 0.3\,bar$ and $T_i = 1000\,K$, right: $P = 0.3\,bar$ and $T_i = 3000\,K$

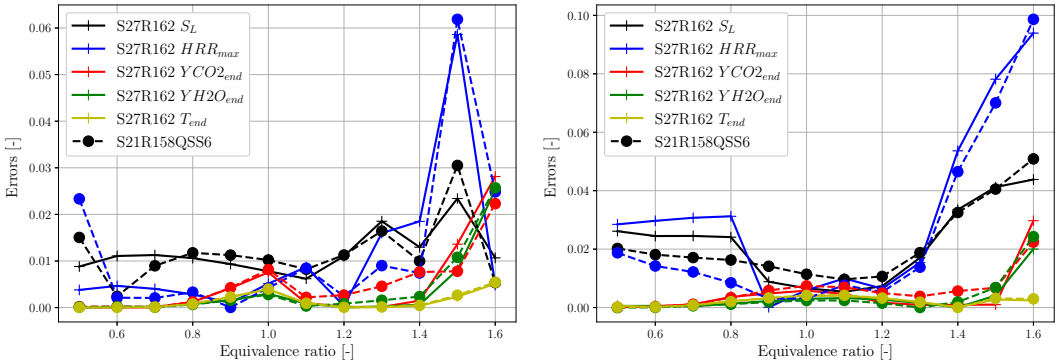

Figure C.3.3: Errors on 1D premixed flames versus equivalence ratio for S21R158QSS6 and S27R162 schemes. Left: $P = 1\,bar$ and $T_f = 300\,K$, right: $P = 0.3\,bar$ and $T_f = 300\,K$

shows the evolution of the auto-ignition time depending on the initial temperature for $P = 1\,bar$ and $P = 0.3\,bar$, and with a stoichiometric mixture. The results show a very good agreement, even for temperatures lower than $T_i = 3000\,K$ used in the reference cases. However, the auto-ignition time is over-predicted by the reduced chemistry when the initial temperature starts to fall below 1500 kelvins. It is reminded that the low temperature chemical pathways have not been targeted for this reduction.

Then, on Fig. C.3.7 to C.3.10, profiles of laminar flame speed, final temperature (burnt gases temperature, $T_b = T_{ad}$[3]), final CO_2 mass fraction, and maximum CO mass concentration are displayed versus equivalence ratio for 1-dimensional premixed flames. These quantities are specifically chosen because

[3]Assuming a complete combustion and that the equilibrium is reached at the exit

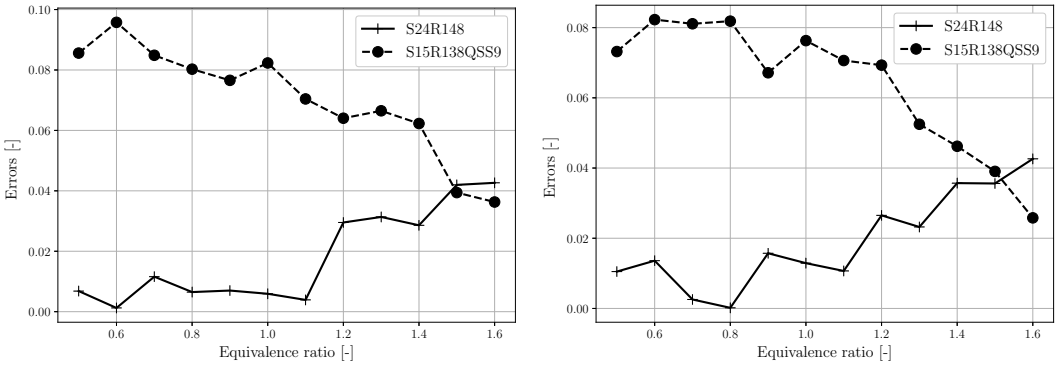

Figure C.3.4: Errors on auto-ignition time versus equivalence ratio for S15R138QSS9 and S24R148 schemes. Left: $P = 1\,bar$ and $T_i = 3000\,K$, right: $P = 0.3\,bar$ and $T_i = 3000\,K$

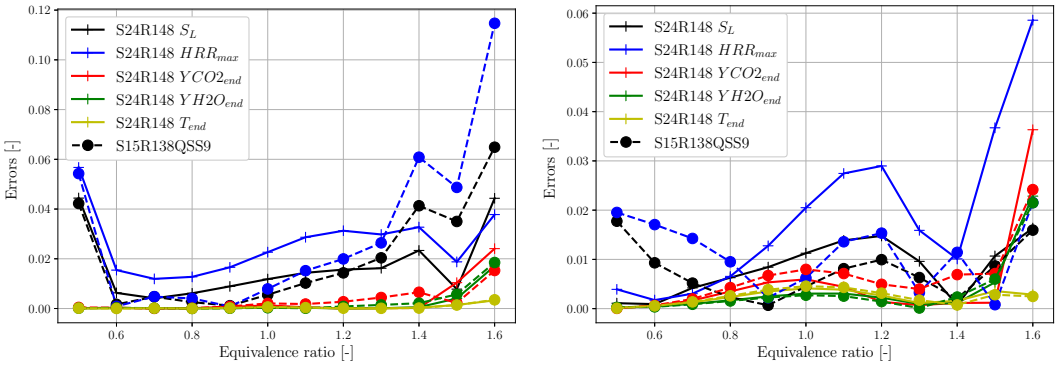

Figure C.3.5: Errors on 1D premixed flames versus equivalence ratio for S15R138QSS9 and S24R148 schemes. Left: $P = 1\,bar$ and $T_f = 300\,K$, right: $P = 0.3\,bar$ and $T_f = 300\,K$

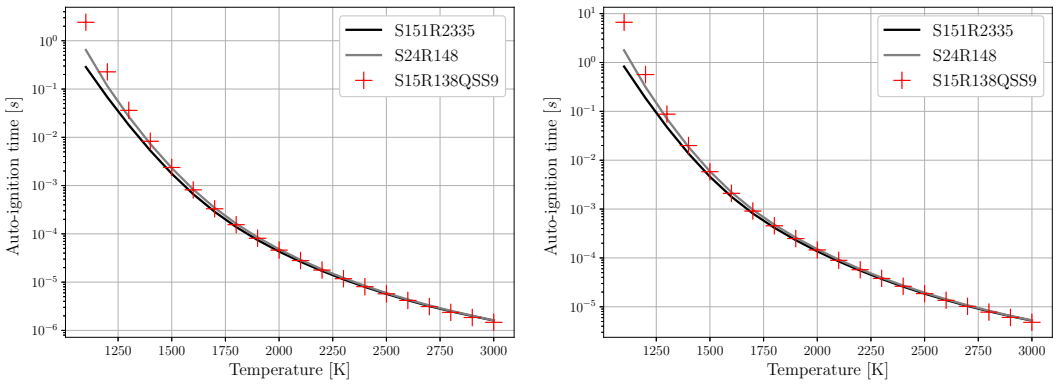

Figure C.3.6: Auto-ignition time versus initial temperature for S15R138QSS9, S24R148 and S151R2335 schemes in a constant pressure reactor filled with a stoichiometric mixture. Left: $P = 1\,bar$, right: $P = 0.3\,bar$

they are not well predicted with global BFER chemistry when changing from the designed operating point (as shown with low pressure in Chap. 5). Hence, Fig. C.3.7 corresponds to the reference case with $T_f = 300\,K$, and $P = 1\,bar$ used during the reduction. Fig. C.3.8 is the equivalent at low pressure $P = 0.3\,bar$. Fig. C.3.9 indicates a validity (at least) up to $P = 5\,bar$ and $T_f = 650\,K$. Next, since the detailed chemical mechanism is designed on a hierarchical construction and methane chemistry includes hydrogen kinetic, a fuel blend of 50% CH_4 and 50% H_2 (molar proportions) has been evaluated with the ARC chemistry. Results on Fig. C.3.10 show a very good agreement with the detailed chemistry which enables to use this chemistry in CH_4/H_2 applications. Fig. C.3.11 displays the laminar flame speed

versus equivalence ratio for several fuel blends showing the limit of this approach for rich pure H_2 mixtures.

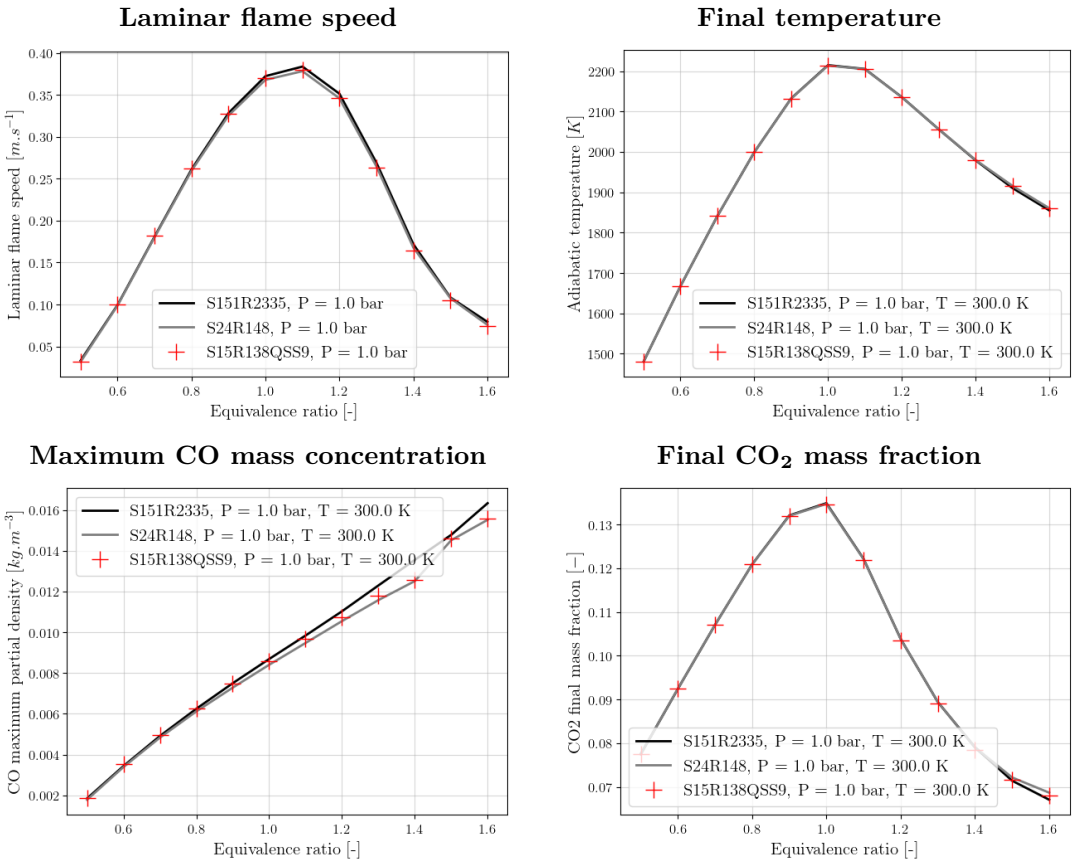

Figure C.3.7: Evolution of the quantities of interest versus equivalence ratio for S15R138QSS9, S24R148 and S151R2335 schemes in 1-dimensional premixed flames. $T_f = 300\,K$, $P = 1\,bar$.

Finally, the chemistry has been also evaluated on CH_4-air 1-dimensional diffusion flames. Fig. C.3.12 shows the evolution of the integral heat release rate, the maximum temperature, and the maximum mass concentrations of CO and CO_2 versus the stoichiometric scalar dissipation rate (computed with Eq. (3.39)) and for $T_f = 300\,K$ and $P = 1\,bar$. The results indicate the ability of the chemical mechanism to accurately reproduce diffusion structures even though no diffusion reference cases were used during the reduction. This phenomena might be explained by the presence of lean, rich, and stoichiometric chemical pathways already targeted with the three reference premixed cases, but the response to stretch was not ensured. A deeper analysis is required to validate this assumption and could be performed using the analysis tools developed in Chap. 6.

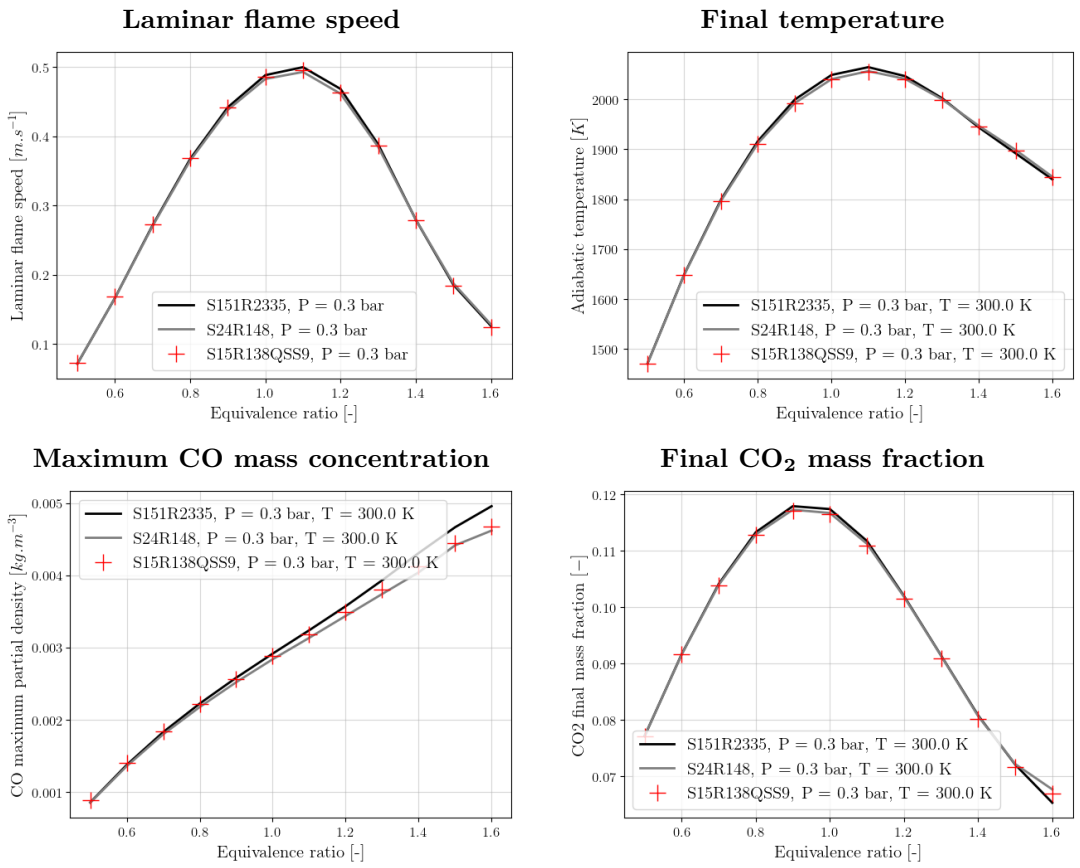

Figure C.3.8: Evolution of the quantities of interest versus equivalence ratio for S15R138QSS9, S24R148 and S151R2335 schemes in 1-dimensional premixed flames. $T_f = 300\,K$, $P = 0.3\,bar$.

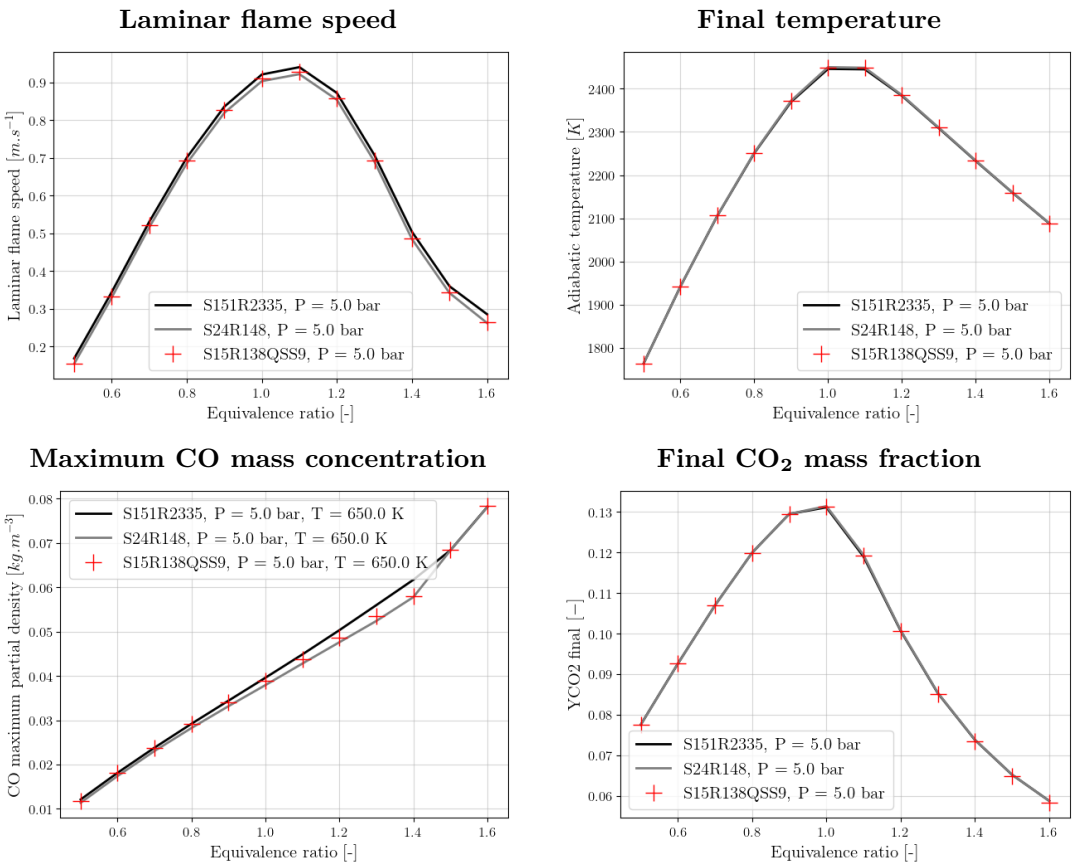

Figure C.3.9: Evolution of the quantities of interest versus equivalence ratio for S15R138QSS9, S24R148 and S151R2335 schemes in 1-dimensional premixed flames. $T_f = 650\,K$, $P = 5\,bar$.

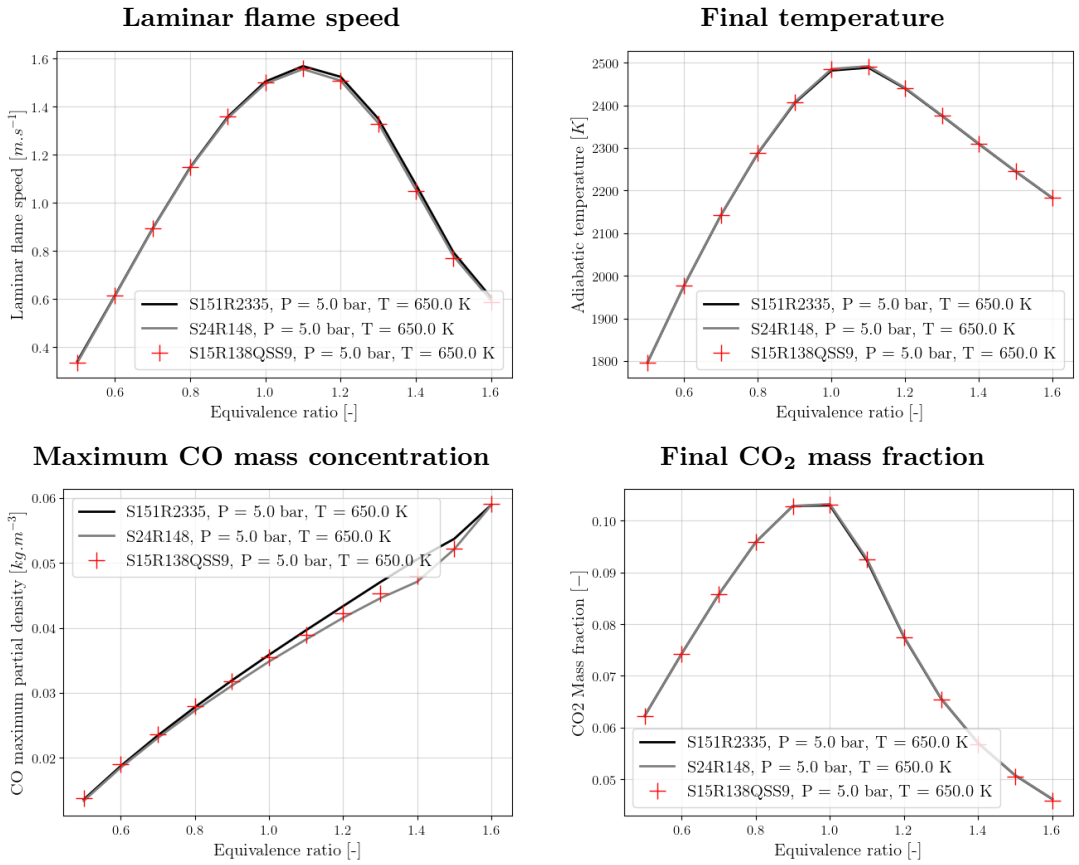

Figure C.3.10: Evolution of the quantities of interest versus equivalence ratio for S15R138QSS9, S24R148 and S151R2335 schemes in 1-dimensional premixed flames with 50% CH_4 + 50% H_2 (molar proportions). $T_f = 650\,K$, $P = 5\,bar$.

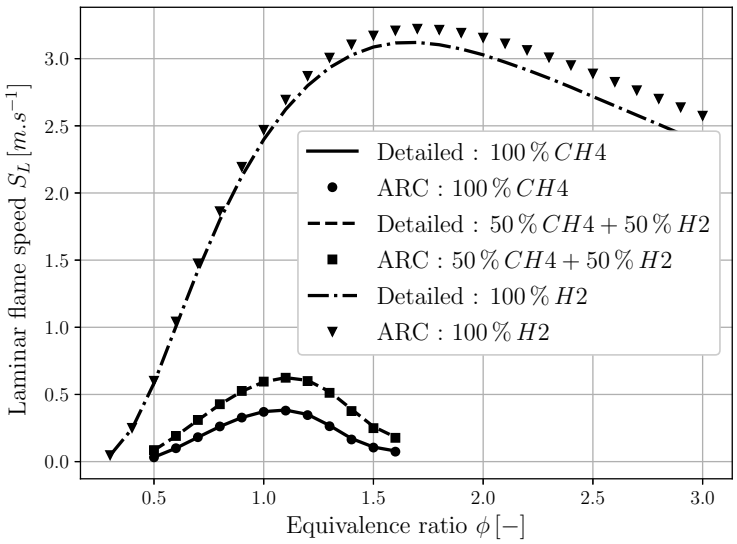

Figure C.3.11: Evolution of the laminar flame speed versus the equivalence ratio for S15R138QSS9 (ARC) and S151R2335 (Detailed) schemes with several CH_4/H_2 fuel blends. $T_f = 300\,K$, $P = 1\,bar$

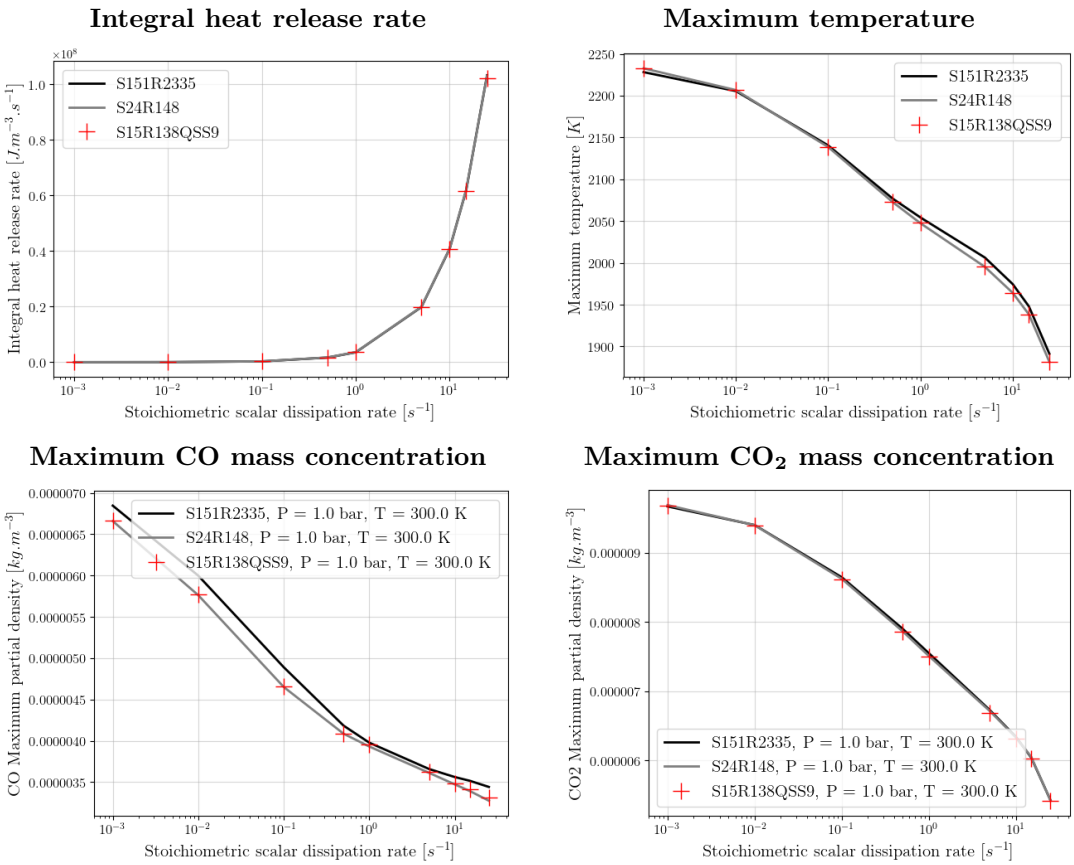

Figure C.3.12: Evolution of the quantities of interest versus stoichiometric scalar dissipation rate for S15R138QSS9, S24R148 and S151R2335 schemes in CH_4-air 1-dimensional diffusion flames. $T_f = 300\,K$, $P = 1\,bar$.

C.4 Conclusions

The previous section demonstrates the validity of S21R158QSS6 and S15R138QSS9 chemistries. However, although both chemistries reproduce accurately the main quantity of interest for combustion, the mechanism S15R138QSS9 is composed of less transported species and is less stiff. Thus, it eases its use in CFD solver and largely reduces the CPU-cost.

In the context of ignition, both schemes have been tested on a 1-dimensional energy deposition simulation with the formation of two opposite propagative flame fronts. Fig. C.4.1 shows that the profiles of heat release rate are perfectly matching for both chemistries. This result indicates that the chemistry S15R138QSS9 is perfectly adapted to the ignition simulations with energy deposition, and that it is not necessarily required to target an error on auto-ignition time at $T_i = 1000\,K$.

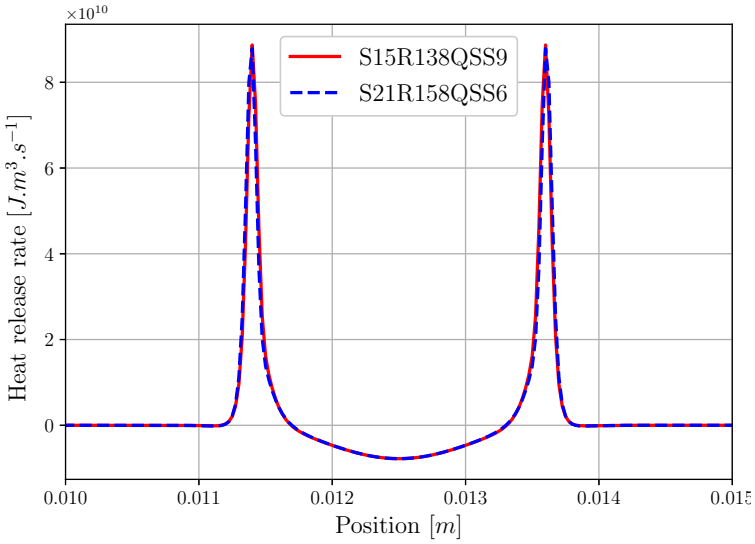

Figure C.4.1: Comparison of the heat release rate profiles between S21R158QSS6 and S15R138QSS9 schemes in a 1D energy deposition configuration.

This is the reason why the mechanism S21R158QSS6 has not been as intensively validated. However, this chemical scheme remains of interest for the specific case of auto-ignition processes with long residence time or for studies of flame-wall interactions which usually require low temperature-like pathways ($T \approx 600 - 1000\,K$).

C.5 Database

C.5.1 S21R158QSS6

Detailed description of the reactions is given in Tab. C.5.1.

Table C.5.1: List of reactions with A the pre-exponential factor in $m^{3(n-1)}/kmol^{n-1}/s$ with n the order of the reaction, b the temperature exponent and E_a the activation energy in $J/kmol$. In the case of fall-off reactions, two sets of Arrhenius coefficients are specified, the first one being the low temperature set and the second one the high temperature set.

No.	Reaction	A	b	E_a
1	H2 + O ⟷ H + OH	5.080000E+01	2.670000E+00	2.632573E+07
2	H2 + OH ⟷ H + H2O	4.380000E+10	0.000000E+00	2.924616E+07
3	H + O2 ⟷ O + OH	1.140000E+11	0.000000E+00	6.395662E+07
4	H + OH + M ⟷ H2O + M	3.500000E+16	-2.000000E+00	0.000000E+00
	Species efficiencies : CH4:2.00E+00 H2O:3.65E+00			
5	H2O + O ⟷ 2 OH	6.700000E+04	1.704000E+00	6.270477E+07
6	H2O2 (+M) ⟷ 2 OH (+M)	2.490000E+21	-2.300000E+00	2.039658E+08
	Troe coefficients : 4.30E-01 1.00E-30 1.00E+30 0.00E+00	2.000000E+12	9.000000E-01	2.039658E+08
	Species efficiencies : CO:2.8E+00 CO2:1.6E+00 H2O:7.7E+00 N2:1.5E+00 O2:1.2E+00			
7	H + H2O2 ⟷ H2O + OH	2.410000E+10	0.000000E+00	1.661048E+07
8	H + H2O2 ⟷ H2 + HO2	2.150000E+07	1.000000E+00	2.510400E+07
9	H2O2 + OH ⟷ H2O + HO2	1.740000E+09	0.000000E+00	1.330512E+06
10	H2O2 + OH ⟷ H2O + HO2	7.590000E+10	0.000000E+00	3.041350E+07
11	H + HO2 ⟷ 2 OH	7.079000E+10	0.000000E+00	1.234280E+06
12	H + HO2 ⟷ H2 + O2	1.140200E+07	1.082700E+00	2.317016E+06
13	HO2 + O ⟷ O2 + OH	3.250000E+10	0.000000E+00	0.000000E+00
14	HO2 + OH ⟷ H2O + O2	7.000000E+09	0.000000E+00	-4.572945E+06
15	HO2 + OH ⟷ H2O + O2	4.500000E+11	0.000000E+00	4.572945E+07
16	2 HO2 ⟷ H2O2 + O2	1.000000E+11	0.000000E+00	4.619504E+07
17	2 HO2 ⟷ H2O2 + O2	1.900000E+08	0.000000E+00	-5.894942E+06
18	H + O2 (+M) ⟷ HO2 (+M)	1.737000E+13	-1.230000E+00	0.000000E+00
	Troe coefficients : 6.70E-01 1.00E-30 1.00E+30 1.00E+30	4.650000E+09	4.400000E-01	0.000000E+00
	Species efficiencies : CH4:2.0E+00 CO:1.9E+00 CO2:3.8E+00 H2O:1.0E+01			
19	CO + O (+M) ⟷ CO2 (+M)	1.173000E+18	-2.790000E+00	1.753514E+07
	Troe coefficients : -	1.362000E+07	0.000000E+00	9.974656E+06
	Species efficiencies : CO:1.8E+00 CO2:3.6E+00 H2O:1.2E+01			
20	CO + OH ⟷ CO2 + H	7.015000E+01	2.053000E+00	-1.488249E+06
21	CO + OH ⟷ CO2 + H	5.757000E+09	-6.640000E-01	1.388251E+06
22	CO + HO2 ⟷ CO2 + OH	1.570000E+02	2.180000E+00	7.506096E+07
23	CH3 + H (+M) ⟷ CH4 (+M)	2.477000E+27	-4.760000E+00	1.020896E+07
	Troe coefficients : 7.83E-01 7.40E+01 2.94E+03 6.96E+03	1.270000E+13	-6.300000E-01	1.602472E+06
	Species efficiencies : CH4:2.0E+00 CO:1.5E+00 CO2:2.0E+00 H2O:6.0E+00			
24	CH4 + H ⟷ CH3 + H2	6.140000E+02	2.500000E+00	4.011201E+07
25	CH4 + O ⟷ CH3 + OH	1.020000E+06	1.500000E+00	3.598240E+07
26	CH4 + OH ⟷ CH3 + H2O	5.830000E+01	2.600000E+00	9.162960E+06
27	CH4 + HO2 ⟷ CH3 + H2O2	1.130000E-02	3.740000E+00	8.790584E+07
28	CH3O2 + CH4 ⟷ CH3 + CH3O2H	9.600000E-04	3.770000E+00	7.451704E+07
29	CH3 + HO2 ⟷ CH4 + O2	1.160000E+02	2.230000E+00	-1.264405E+07
30	CH2(L1) + CH4 ⟷ 2 CH3	1.283027E+04	1.784347E+00	3.639495E+07
31	CH2(L1) + O2 ⟶ CO + H + OH	3.248803E+01	2.224058E+00	-1.899108E+07

No.	Reaction	A	b	E_a
32	CH2(L1) + O2 ⟷ CO + H2O	1.392344E+01	2.224058E+00	-1.899108E+07
33	CH2(L1) + H2 ⟷ CH3 + H	8.122009E+01	2.224058E+00	-1.899108E+07
34	CH2(L1) + OH ⟷ CH2O + H	3.480861E+01	2.224058E+00	-1.899108E+07
35	CH2(L1) + CO2 ⟷ CH2O + CO	1.624402E+01	2.224058E+00	-1.899108E+07
36	CH2(L1) + H (+M) ⟷ CH3 (+M)	1.668978E+22	-3.355653E+00	6.939591E+06
	Troe coefficients : 6.80E-01 7.80E+01 2.00E+03 5.59E+03	1.303889E+14	-1.015653E+00	1.793270E+06
	Species efficiencies : CH4:2.0E+00 CO:1.5E+00 CO2:2.0E+00 H2O:6.0E+00			
37	CH2(L1) + O2 ⟷ HCO + OH	5.528489E+10	-2.156526E-01	8.069271E+06
38	CH2(L1) + O2 ⟶ CO2 + 2 H	1.376907E+10	-2.156526E-01	8.069271E+06
39	CH2(L1) + O ⟶ CO + 2 H	2.607778E+11	-2.156526E-01	1.793270E+06
40	CH3 + O2 (+M) ⟷ CH3O2 (+M)	6.850000E+18	-3.000000E+00	0.000000E+00
	Troe coefficients : 6.00E-01 1.00E+03 7.00E+01 1.70E+03	7.812000E+06	9.000000E-01	0.000000E+00
41	CH3 + O2 ⟷ CH3O + O	7.546000E+09	0.000000E+00	1.184909E+08
42	CH3 + O2 ⟷ CH2O + OH	2.641000E-03	3.283000E+00	3.391132E+07
43	CH3 + O ⟷ CH2O + H	5.540000E+10	5.000000E-02	-5.690240E+05
44	CH3 + OH ⟷ CH2(L1) + H2O	5.282000E+14	-1.518000E+00	7.414048E+06
45	CH3 + OH ⟷ CH2OH + H	4.686000E+07	8.330000E-01	1.492014E+07
46	CH3 + OH ⟷ CH3O + H	1.230000E+06	1.011000E+00	4.999880E+07
47	CH3 + OH ⟷ CH2(L1) + H2O	4.293000E+01	2.568000E+00	1.672680E+07
48	CH3 + HO2 ⟷ CH3O + OH	1.000000E+09	2.690000E-01	-2.876500E+06
49	CH3O2 + O ⟷ CH3O + O2	3.600000E+10	0.000000E+00	0.000000E+00
50	CH3O2 + H ⟷ CH3O + OH	9.600000E+10	0.000000E+00	0.000000E+00
51	CH3O2 + OH ⟷ CH3OH + O2	6.000000E+10	0.000000E+00	0.000000E+00
52	CH3O2 + HO2 ⟷ CH3O2H + O2	2.470000E+08	0.000000E+00	-6.568880E+06
53	CH3 + CH3O2 ⟷ 2 CH3O	5.080000E+09	0.000000E+00	-5.903624E+06
54	CH3O2 + H2 ⟷ CH3O2H + H	1.500000E+11	0.000000E+00	1.089095E+08
55	CH3O2H ⟷ CH3O + OH	6.310000E+14	0.000000E+00	1.769832E+08
56	CH3OH (+M) ⟷ CH3 + OH (+M)	1.500000E+40	-6.995000E+00	4.099994E+08
	Troe coefficients : -4.75E-01 3.56E+04 1.12E+03 9.02E+03	2.084000E+18	-6.150000E-01	3.871899E+08
57	CH3OH (+M) ⟷ CH2(L1) + H2O (+M)	1.430000E+44	-8.227000E+00	4.159611E+08
	Troe coefficients : 2.54E+00 3.29E+03 4.73E+04 4.71E+04	3.121000E+18	-1.017000E+00	3.837230E+08
58	CH3OH + H ⟷ CH3O + H2	1.990000E+02	2.560000E+00	4.309520E+07
59	CH3OH + H ⟷ CH2OH + H2	3.070000E+02	2.550000E+00	2.276096E+07
60	CH3OH + O ⟷ CH2OH + OH	3.880000E+02	2.500000E+00	1.288672E+07
61	CH3OH + OH ⟷ CH3O + H2O	1.500000E-01	3.030000E+00	-3.192392E+06
62	CH3OH + OH ⟷ CH2OH + H2O	3.080000E+01	2.650000E+00	-3.375233E+06
63	CH3OH + O2 ⟷ CH3O + HO2	3.580000E+01	2.270000E+00	1.789267E+08
64	CH2OH + O2 ⟷ CH2O + HO2	1.510000E+12	-1.000000E+00	0.000000E+00
65	CH2OH + O2 ⟷ CH2O + HO2	2.410000E+11	0.000000E+00	2.099113E+07
66	CH2OH + H ⟷ CH2O + H2	6.000000E+09	0.000000E+00	0.000000E+00
67	CH2OH + OH ⟷ CH2O + H2O	2.400000E+10	0.000000E+00	0.000000E+00
68	CH2OH + O ⟷ CH2O + OH	4.200000E+10	0.000000E+00	0.000000E+00
69	CH3O + O2 ⟷ CH2O + HO2	4.380000E-22	9.500000E+00	-2.301618E+07
70	CH3O + H ⟷ CH2O + H2	2.000000E+10	0.000000E+00	0.000000E+00
71	CH3 + CH3O ⟷ CH2O + CH4	1.200000E+10	0.000000E+00	0.000000E+00
72	2 CH3O ⟷ CH2O + CH3OH	6.030000E+10	0.000000E+00	0.000000E+00
73	H + HCO (+M) ⟷ CH2O (+M)	1.350000E+18	-2.570000E+00	5.962200E+06

No.	Reaction	A	b	E_a
	Troe coefficients : 7.82E-01 2.71E+02 2.76E+03 6.57E+03	1.090000E+09	4.800000E-01	-1.087840E+06
	Species efficiencies : CH4:2.0E+00 CO:1.5E+00 CO2:2.0E+00 H2O:6.0E+00			
74	CO + H2 (+M) ⟷ CH2O (+M)	5.070000E+21	-3.420000E+00	3.529120E+08
	Troe coefficients : 9.32E-01 1.97E+02 1.54E+03 1.03E+04	4.300000E+04	1.500000E+00	3.330464E+08
	Species efficiencies : CH4:2.0E+00 CO:1.5E+00 CO2:2.0E+00 H2O:6.0E+00			
75	CH2O + O2 ⟷ HCO + HO2	8.070000E+12	0.000000E+00	2.235093E+08
76	CH2O + O ⟷ HCO + OH	6.260000E+06	1.150000E+00	9.455840E+06
77	CH2O + H ⟷ H2 + HCO	5.740000E+04	1.900000E+00	1.146416E+07
78	CH2O + OH ⟷ H2O + HCO	7.820000E+04	1.630000E+00	-4.414120E+06
79	CH2O + HO2 ⟷ H2O2 + HCO	1.880000E+01	2.700000E+00	4.819968E+07
80	CH2O + CH3 ⟷ CH4 + HCO	3.830000E-02	3.360000E+00	1.804141E+07
81	CH2O + CH3O2 ⟷ CH3O2H + HCO	1.990000E+09	0.000000E+00	4.878544E+07
82	HCO + M ⟷ CO + H + M	5.700000E+08	6.600000E-01	6.221608E+07
	Species efficiencies : CH4:2.00E+00 CO:1.50E+00 CO2:2.00E+00 H2O:6.00E+00			
83	HCO + O2 ⟷ CO + HO2	7.580000E+09	0.000000E+00	1.715440E+06
84	HCO + O ⟷ CO + OH	3.020000E+10	0.000000E+00	0.000000E+00
85	H + HCO ⟷ CO + H2	7.340000E+10	0.000000E+00	0.000000E+00
86	HCO + OH ⟷ CO + H2O	3.011000E+10	0.000000E+00	0.000000E+00
87	CH3 + HCO ⟷ CH4 + CO	2.650000E+10	0.000000E+00	0.000000E+00
88	HCO + O ⟷ CO2 + H	3.000000E+10	0.000000E+00	0.000000E+00
89	HCO + HO2 ⟶ CO2 + H + OH	3.000000E+10	0.000000E+00	0.000000E+00
90	CH2O + H (+M) ⟷ CH2OH (+M)	1.270000E+26	-4.820000E+00	2.732152E+07
	Troe coefficients : 7.19E-01 1.03E+02 1.29E+03 4.16E+03	5.400000E+08	4.540000E-01	1.506240E+07
	Species efficiencies : CH4:2.0E+00 CO:1.5E+00 CO2:2.0E+00 H2O:6.0E+00			
91	CH3O (+M) ⟷ CH2O + H (+M)	1.867000E+22	-3.000000E+00	1.017005E+08
	Troe coefficients : 9.00E-01 2.50E+03 1.30E+03 1.00E+99	6.800000E+13	0.000000E+00	1.094953E+08
	Species efficiencies : CH4:2.0E+00 CO:1.5E+00 CO2:2.0E+00 H2O:6.0E+00			
92	2 CH3 (+M) ⟷ C2H6 (+M)	8.054000E+25	-3.750000E+00	4.107014E+06
	Troe coefficients : 0.00E+00 5.70E+02 1.00E+30 1.00E+30	2.277000E+12	-6.900000E-01	7.317816E+05
	Species efficiencies : CO:2.0E+00 CO2:3.0E+00 H2O:5.0E+00			
93	C2H5 + H (+M) ⟷ C2H6 (+M)	1.990000E+35	-7.080000E+00	2.797004E+07
	Troe coefficients : 8.42E-01 1.25E+02 2.22E+03 6.88E+03	5.210000E+14	-9.900000E-01	6.610720E+06
	Species efficiencies : CH4:2.0E+00 CO:1.5E+00 CO2:2.0E+00 H2O:6.0E+00			
94	C2H6 + O ⟷ C2H5 + OH	3.550000E+03	2.400000E+00	2.439272E+07
95	C2H6 + H ⟷ C2H5 + H2	1.150000E+05	1.900000E+00	3.150552E+07
96	C2H6 + OH ⟷ C2H5 + H2O	1.480000E+04	1.900000E+00	3.974800E+06
97	C2H6 + HO2 ⟷ C2H5 + H2O2	3.460000E-02	3.610000E+00	7.079328E+07
98	C2H6 + CH3 ⟷ C2H5 + CH4	5.550000E-07	4.720000E+00	1.351850E+07
99	C2H4 + H (+M) ⟷ C2H5 (+M)	1.419000E+33	-6.642000E+00	2.413750E+07
	Troe coefficients : -5.69E-01 2.99E+02 -9.15E+03 1.52E+02	9.569000E+05	1.463000E+00	5.669320E+06
	Species efficiencies : CH4:2.0E+00 CO:1.5E+00 CO2:2.0E+00 H2O:6.0E+00			
100	C2H5 + CH3 ⟷ C2H4 + CH4	1.180000E+01	2.450000E+00	-1.222146E+07
101	2 CH3 ⟷ C2H5 + H	3.100000E+11	-3.620000E-01	5.595054E+07
102	C2H5 + O2 ⟷ C2H4 + HO2	1.843000E+04	1.130000E+00	-3.014990E+06
103	C2H3 + H (+M) ⟷ C2H4 (+M)	1.400000E+24	-3.860000E+00	1.389088E+07
	Troe coefficients : 7.82E-01 2.07E+02 2.66E+03 6.10E+03	6.080000E+09	2.700000E-01	1.171520E+06
	Species efficiencies : CH4:2.0E+00 CO:1.5E+00 CO2:2.0E+00 H2O:6.0E+00			

No.	Reaction	A	b	E_a
104	C2H4 + M ⟷ C2H2 + H2 + M	2.610000E+13	0.000000E+00	2.837714E+08
	Species efficiencies : CH4:2.00E+00 CO:1.50E+00 CO2:2.00E+00 H2O:6.00E+00			
105	C2H4 + H ⟷ C2H3 + H2	5.070000E+04	1.930000E+00	5.418280E+07
106	C2H4 + OH ⟷ C2H3 + H2O	2.230000E+01	2.745000E+00	9.269652E+06
107	C2H4 + CH3 ⟷ C2H3 + CH4	9.760000E-01	2.947000E+00	6.337923E+07
108	C2H4 + CH3 ⟷ C2H3 + CH4	8.130000E-08	4.417000E+00	3.696899E+07
109	C2H4 + O ⟷ CH3 + HCO	7.453000E+03	1.880000E+00	7.656720E+05
110	C2H4 + O ⟷ C2H3O(L1) + H	6.098000E+03	1.880000E+00	7.656720E+05
111	CH2(L1) + CH3 ⟷ C2H4 + H	2.320574E+01	2.224058E+00	-1.899108E+07
112	C2H2 + H (+M) ⟷ C2H3 (+M)	6.346000E+25	-4.664000E+00	1.581552E+07
	Troe coefficients : 7.88E-01 -1.02E+04 1.00E-30 0.00E+00	1.710000E+07	1.266000E+00	1.133446E+07
	Species efficiencies : CH4:2.0E+00 CO:1.5E+00 CO2:2.0E+00 H2O:6.0E+00			
113	C2H3 + O2 ⟷ C2H3O(L1) + O	7.100000E+17	-2.650000E+00	2.714998E+07
114	C2H3 + O2 ⟷ C2H3O(L1) + O	2.020000E+07	5.800000E-01	1.606656E+05
115	C2H3 + O2 ⟷ C2H2 + HO2	2.150000E+04	1.190000E+00	1.408753E+07
116	C2H3 + O2 ⟷ C2H2 + HO2	4.600000E-02	2.760000E+00	-2.061875E+06
117	C2H3 + O2 ⟷ CH2O + HCO	2.730000E+32	-7.320000E+00	4.945488E+07
118	C2H3 + O2 ⟷ CH2O + HCO	6.080000E+12	-1.310000E+00	2.701609E+06
119	C2H3 + O2 ⟶ CH2O + CO + H	6.360000E+32	-7.320000E+00	4.945488E+07
120	C2H3 + O2 ⟶ CH2O + CO + H	1.420000E+13	-1.310000E+00	2.701609E+06
121	C2H3 + O2 ⟷ CH3O + CO	1.030000E+08	-3.300000E-01	-3.128795E+06
122	C2H3 + O2 ⟷ CH3O + CO	5.770000E+18	-3.540000E+00	1.996605E+07
123	C2H3 + O2 ⟷ CH3 + CO2	7.250000E+28	-6.700000E+00	4.368096E+07
124	C2H3 + O2 ⟷ CH3 + CO2	5.320000E+10	-1.140000E+00	1.868993E+06
125	C2H3 + H ⟷ C2H2 + H2	9.635250E+10	0.000000E+00	0.000000E+00
126	C2H3 + OH ⟷ C2H2 + H2O	3.011000E+10	0.000000E+00	0.000000E+00
127	C2H2 + O ⟷ CH2(L1) + CO	7.395000E+05	1.280000E+00	1.034285E+07
128	C2H2 + HCO ⟷ C2H3 + CO	1.000000E+04	2.000000E+00	2.510400E+07
129	C2H2 + OH ⟷ CH3 + CO	1.277000E+06	7.300000E-01	1.079054E+07
130	C2H3O(L1) ⟷ CH3 + CO	6.450000E+18	-2.520000E+00	6.877032E+07
131	C2H4 + CH2(L1) ⟷ C2H3 + CH3	4.160000E+21	-3.190000E+00	4.083584E+07
132	C2H4 + CH2(L1) ⟷ C2H3 + CH3	4.920000E+06	1.020000E+00	2.509438E+06
133	O + OH + M ⟷ HO2 + M	1.000000E+10	0.000000E+00	0.000000E+00
134	C2H5 + O2 ⟶ CH2O + CH3O	1.000000E+11	0.000000E+00	1.004160E+08
135	C2H5 + HO2 ⟶ CH2O + CH3 + OH	5.000000E+09	0.000000E+00	0.000000E+00
136	CH3O2 + H ⟷ CH3O2H	5.000000E+10	0.000000E+00	0.000000E+00
137	CH3O2 ⟷ CH2O + OH	1.500000E+13	0.000000E+00	1.966480E+08
138	CH3O2 + OH ⟶ CH3O + HO2	3.000000E+09	0.000000E+00	0.000000E+00
139	CH3O2 + HO2 ⟶ CH2O + H2O + O2	5.000000E+07	0.000000E+00	0.000000E+00
140	CH2(L1) + O ⟷ CO + H2	2.607778E+11	-2.156526E-01	1.793270E+06
141	CH2(L1) + OH ⟷ CH2O + H	1.564667E+11	-2.156526E-01	1.793270E+06
142	CH2(L1) + CO2 ⟷ CH2O + CO	5.737111E+08	-2.156526E-01	5.977271E+06
143	CH2(L1) + O ⟷ CO + 2 H	3.480861E+01	2.224058E+00	-1.899108E+07
144	CH2(L1) + CH4 ⟷ 2 CH3	4.989234E+01	2.224058E+00	-1.899108E+07
145	2 CH3 ⟶ C2H4 + H2	5.000000E+11	0.000000E+00	1.338880E+08
146	2 CH2(L1) ⟶ C2H2 + 2 H	6.258667E+11	-2.156526E-01	1.793270E+06
147	C2H6 ⟷ C2H4 + H2	3.000000E+13	0.000000E+00	3.284440E+08

No.	Reaction	A	b	E_a
148	CH2O + O ⟶ CO2 + 2 H	2.000000E+10	0.000000E+00	2.092000E+07
149	CH2O + OH ⟶ CO2 + H + H2	1.000000E+08	0.000000E+00	0.000000E+00
150	CH3O + CO ⟷ CH3 + CO2	5.000000E+08	0.000000E+00	2.719600E+07
151	C2H4 + O2 ⟶ 2 CH2O	1.000000E+11	0.000000E+00	2.008320E+08
152	C2H4 + O2 ⟶ CH3O + HCO	1.000000E+11	0.000000E+00	1.799120E+08
153	C2H3O(L1) + O2 ⟶ CH2O + CO + OH	9.980684E+14	-2.082250E+00	1.828176E+07
154	CH3 + O + M ⟶ CH3O + M	5.000000E+10	0.000000E+00	0.000000E+00
155	CH3O + OH ⟶ CH2O + H2O	1.500000E+10	0.000000E+00	0.000000E+00
156	CH2OH + CH3 ⟶ CH2O + CH4	1.500000E+10	0.000000E+00	0.000000E+00
157	C2H2 + OH ⟶ C2H3O(L1)	5.000000E+08	0.000000E+00	0.000000E+00
158	C2H4 + O ⟷ C2H3 + OH	1.083000E+04	2.000000E+00	3.674372E+07

C.5.2 S15R138QSS9

Detailed description of the reactions is given in Tab. C.5.2.

Downloadable .cti and validation files are available at https://chemistry.cerfacs.fr

Table C.5.2: List of reactions with A the pre-exponential factor in $m^{3(n-1)}/kmol^{n-1}/s$ with n the order of the reaction, b the temperature exponent and E_a the activation energy in $J/kmol$. In the case of fall-off reactions, two sets of Arrhenius coefficients are specified, the first one being the low temperature set and the second one the high temperature set.

No.	Reaction	A	b	E_a
1	H2 + O ⟷ H + OH	5.080000E+01	2.670000E+00	2.632573E+07
2	H2 + OH ⟷ H + H2O	4.380000E+10	0.000000E+00	2.924616E+07
3	H + O2 ⟷ O + OH	1.140000E+11	0.000000E+00	6.395662E+07
4	H + OH + M ⟷ H2O + M	3.500000E+16	-2.000000E+00	0.000000E+00
	Species efficiencies : CH4:2.00E+00 H2O:3.65E+00			
5	H2O + O ⟷ 2 OH	6.700000E+04	1.704000E+00	6.270477E+07
6	H + HO2 ⟷ 2 OH	7.079000E+10	0.000000E+00	1.234280E+06
7	H + HO2 ⟷ H2 + O2	1.140200E+07	1.082700E+00	2.317016E+06
8	HO2 + O ⟷ O2 + OH	3.250000E+10	0.000000E+00	0.000000E+00
9	HO2 + OH ⟷ H2O + O2	7.000000E+09	0.000000E+00	-4.572945E+06
10	HO2 + OH ⟷ H2O + O2	4.500000E+11	0.000000E+00	4.572945E+07
11	H + O2 (+M) ⟷ HO2 (+M)	1.737000E+13	-1.230000E+00	0.000000E+00
	Troe coefficients : 6.70E-01 1.00E-30 1.00E+30 1.00E+30	4.650000E+09	4.400000E-01	0.000000E+00
	Species efficiencies : CH4:2.0E+00 CO:1.9E+00 CO2:3.8E+00 H2O:1.0E+01			
12	CO + O (+M) ⟷ CO2 (+M)	1.173000E+18	-2.790000E+00	1.753514E+07
	Troe coefficients : -	1.362000E+07	0.000000E+00	9.974656E+06
	Species efficiencies : CO:1.8E+00 CO2:3.6E+00 H2O:1.2E+01			
13	CO + OH ⟷ CO2 + H	7.015000E+01	2.053000E+00	-1.488249E+06
14	CO + OH ⟷ CO2 + H	5.757000E+09	-6.640000E-01	1.388251E+06
15	CH3 + H (+M) ⟷ CH4 (+M)	2.477000E+27	-4.760000E+00	1.020896E+07
	Troe coefficients : 7.83E-01 7.40E+01 2.94E+03 6.96E+03	1.270000E+13	-6.300000E-01	1.602472E+06
	Species efficiencies : CH4:2.0E+00 CO:1.5E+00 CO2:2.0E+00 H2O:6.0E+00			
16	CH4 + H ⟷ CH3 + H2	6.140000E+02	2.500000E+00	4.011201E+07
17	CH4 + O ⟷ CH3 + OH	1.020000E+06	1.500000E+00	3.598240E+07
18	CH4 + OH ⟷ CH3 + H2O	5.830000E+01	2.600000E+00	9.162960E+06
19	CH3 + HO2 ⟷ CH4 + O2	1.160000E+02	2.230000E+00	-1.264405E+07
20	CH2(L1) + CH4 ⟷ 2 CH3	1.326516E+04	1.785451E+00	3.663295E+07
21	CH2(L1) + O2 ⟶ CO + H + OH	1.746412E+02	1.988656E+00	-1.763074E+07
22	CH2(L1) + O2 ⟷ CO + H2O	7.484624E+01	1.988656E+00	-1.763074E+07
23	CH2(L1) + O ⟷ CO + H2	9.355780E+01	1.988656E+00	-1.763074E+07
24	CH2(L1) + O ⟷ H + HCO	9.355780E+01	1.988656E+00	-1.763074E+07
25	CH2(L1) + H2 ⟷ CH3 + H	4.366031E+02	1.988656E+00	-1.763074E+07
26	CH2(L1) + OH ⟷ CH2O + H	1.871156E+02	1.988656E+00	-1.763074E+07
27	CH2(L1) + CO2 ⟷ CH2O + CO	8.732062E+01	1.988656E+00	-1.763074E+07
28	CH2(L1) + H (+M) ⟷ CH3 (+M)	1.725550E+22	-3.354549E+00	7.177589E+06
	Troe coefficients : 6.80E-01 7.80E+01 2.00E+03 5.59E+03	1.348086E+14	-1.014549E+00	2.031268E+06
	Species efficiencies : CH4:2.0E+00 CO:1.5E+00 CO2:2.0E+00 H2O:6.0E+00			
29	CH2(L1) + O2 ⟷ HCO + OH	5.715883E+10	-2.145491E-01	8.307269E+06
30	CH2(L1) + O2 ⟶ CO2 + 2 H	1.423578E+10	-2.145491E-01	8.307269E+06
31	CH2(L1) + O ⟶ CO + 2 H	2.696171E+11	-2.145491E-01	2.031268E+06

No.	Reaction	A	b	E_a
32	CH3 + O2 ⟷ CH3O + O	7.546000E+09	0.000000E+00	1.184909E+08
33	CH3 + O2 ⟷ CH2O + OH	2.641000E-03	3.283000E+00	3.391132E+07
34	CH3 + O ⟷ CH2O + H	5.540000E+10	5.000000E-02	-5.690240E+05
35	CH3 + OH ⟷ CH2(L1) + H2O	5.282000E+14	-1.518000E+00	7.414048E+06
36	CH3 + OH ⟷ CH2OH + H	4.686000E+07	8.330000E-01	1.492014E+07
37	CH3 + OH ⟷ CH3O + H	1.230000E+06	1.011000E+00	4.999880E+07
38	CH3 + OH ⟷ CH2(L1) + H2O	4.293000E+01	2.568000E+00	1.672680E+07
39	CH3 + HO2 ⟷ CH3O + OH	1.000000E+09	2.690000E-01	-2.876500E+06
40	CH3OH (+M) ⟷ CH3 + OH (+M)	1.500000E+40	-6.995000E+00	4.099994E+08
	Troe coefficients : -4.75E-01 3.56E+04 1.12E+03 9.02E+03	2.084000E+18	-6.150000E-01	3.871899E+08
41	CH3OH (+M) ⟷ CH2(L1) + H2O (+M)	1.430000E+44	-8.227000E+00	4.159611E+08
	Troe coefficients : 2.54E+00 3.29E+03 4.73E+04 4.71E+04	3.121000E+18	-1.017000E+00	3.837230E+08
42	CH3OH + H ⟷ CH3O + H2	1.990000E+02	2.560000E+00	4.309520E+07
43	CH3OH + H ⟷ CH2OH + H2	3.070000E+02	2.550000E+00	2.276096E+07
44	CH3OH + O ⟷ CH3O + OH	3.880000E+01	2.500000E+00	1.288672E+07
45	CH3OH + O ⟷ CH2OH + OH	3.880000E+02	2.500000E+00	1.288672E+07
46	CH3OH + OH ⟷ CH3O + H2O	1.500000E-01	3.030000E+00	-3.192392E+06
47	CH3OH + OH ⟷ CH2OH + H2O	3.080000E+01	2.650000E+00	-3.375233E+06
48	CH3 + CH3OH ⟷ CH3O + CH4	3.220000E+00	2.425000E+00	3.589663E+07
49	CH2OH + O2 ⟷ CH2O + HO2	1.510000E+12	-1.000000E+00	0.000000E+00
50	CH2OH + O2 ⟷ CH2O + HO2	2.410000E+11	0.000000E+00	2.099113E+07
51	CH2OH + H ⟷ CH2O + H2	6.000000E+09	0.000000E+00	0.000000E+00
52	CH2OH + OH ⟷ CH2O + H2O	2.400000E+10	0.000000E+00	0.000000E+00
53	CH2OH + O ⟷ CH2O + OH	4.200000E+10	0.000000E+00	0.000000E+00
54	CH3O + O2 ⟷ CH2O + HO2	4.380000E-22	9.500000E+00	-2.301618E+07
55	CH3O + H ⟷ CH2O + H2	2.000000E+10	0.000000E+00	0.000000E+00
56	CH3 + CH3O ⟷ CH2O + CH4	1.200000E+10	0.000000E+00	0.000000E+00
57	H + HCO (+M) ⟷ CH2O (+M)	1.350000E+18	-2.570000E+00	5.962200E+06
	Troe coefficients : 7.82E-01 2.71E+02 2.76E+03 6.57E+03	1.090000E+09	4.800000E-01	-1.087840E+06
	Species efficiencies : CH4:2.0E+00 CO:1.5E+00 CO2:2.0E+00 H2O:6.0E+00			
58	CO + H2 (+M) ⟷ CH2O (+M)	5.070000E+21	-3.420000E+00	3.529120E+08
	Troe coefficients : 9.32E-01 1.97E+02 1.54E+03 1.03E+04	4.300000E+04	1.500000E+00	3.330464E+08
	Species efficiencies : CH4:2.0E+00 CO:1.5E+00 CO2:2.0E+00 H2O:6.0E+00			
59	CH2O + O ⟷ HCO + OH	6.260000E+06	1.150000E+00	9.455840E+06
60	CH2O + H ⟷ H2 + HCO	5.740000E+04	1.900000E+00	1.146416E+07
61	CH2O + OH ⟷ H2O + HCO	7.820000E+04	1.630000E+00	-4.414120E+06
62	CH2O + CH3 ⟷ CH4 + HCO	3.830000E-02	3.360000E+00	1.804141E+07
63	HCO + M ⟷ CO + H + M	5.700000E+08	6.600000E-01	6.221608E+07
	Species efficiencies : CH4:2.00E+00 CO:1.50E+00 CO2:2.00E+00 H2O:6.00E+00			
64	HCO + O2 ⟷ CO + HO2	7.580000E+09	0.000000E+00	1.715440E+06
65	HCO + O ⟷ CO + OH	3.020000E+10	0.000000E+00	0.000000E+00
66	H + HCO ⟷ CO + H2	7.340000E+10	0.000000E+00	0.000000E+00
67	HCO + OH ⟷ CO + H2O	3.011000E+10	0.000000E+00	0.000000E+00
68	CH3 + HCO ⟷ CH4 + CO	2.650000E+10	0.000000E+00	0.000000E+00
69	HCO + O ⟷ CO2 + H	3.000000E+10	0.000000E+00	0.000000E+00
70	CH2O + H (+M) ⟷ CH2OH (+M)	1.270000E+26	-4.820000E+00	2.732152E+07
	Troe coefficients : 7.19E-01 1.03E+02 1.29E+03 4.16E+03	5.400000E+08	4.540000E-01	1.506240E+07

No.	Reaction	A	b	E_a
	Species efficiencies : CH4:2.0E+00 CO:1.5E+00 CO2:2.0E+00 H2O:6.0E+00			
71	CH3O (+M) ⟷ CH2O + H (+M)	1.867000E+22	-3.000000E+00	1.017005E+08
	Troe coefficients : 9.00E-01 2.50E+03 1.30E+03 1.00E+99	6.800000E+13	0.000000E+00	1.094953E+08
	Species efficiencies : CH4:2.0E+00 CO:1.5E+00 CO2:2.0E+00 H2O:6.0E+00			
72	2 CH3 (+M) ⟷ C2H6 (+M)	8.054000E+25	-3.750000E+00	4.107014E+06
	Troe coefficients : 0.00E+00 5.70E+02 1.00E+30 1.00E+30	2.277000E+12	-6.900000E-01	7.317816E+05
	Species efficiencies : CO:2.0E+00 CO2:3.0E+00 H2O:5.0E+00			
73	C2H5 + H (+M) ⟷ C2H6 (+M)	1.990000E+35	-7.080000E+00	2.797004E+07
	Troe coefficients : 8.42E-01 1.25E+02 2.22E+03 6.88E+03	5.210000E+14	-9.900000E-01	6.610720E+06
	Species efficiencies : CH4:2.0E+00 CO:1.5E+00 CO2:2.0E+00 H2O:6.0E+00			
74	C2H6 + O ⟷ C2H5 + OH	3.550000E+03	2.400000E+00	2.439272E+07
75	C2H6 + H ⟷ C2H5 + H2	1.150000E+05	1.900000E+00	3.150552E+07
76	C2H6 + OH ⟷ C2H5 + H2O	1.480000E+04	1.900000E+00	3.974800E+06
77	C2H6 + CH3 ⟷ C2H5 + CH4	5.550000E-07	4.720000E+00	1.351850E+07
78	C2H4 + H (+M) ⟷ C2H5 (+M)	1.419000E+33	-6.642000E+00	2.413750E+07
	Troe coefficients : -5.69E-01 2.99E+02 -9.15E+03 1.52E+02	9.569000E+05	1.463000E+00	5.669320E+06
	Species efficiencies : CH4:2.0E+00 CO:1.5E+00 CO2:2.0E+00 H2O:6.0E+00			
79	C2H5 + CH3 ⟷ C2H4 + CH4	1.180000E+01	2.450000E+00	-1.222146E+07
80	2 CH3 ⟷ C2H5 + H	3.100000E+11	-3.620000E-01	5.595054E+07
81	C2H3 + H (+M) ⟷ C2H4 (+M)	1.400000E+24	-3.860000E+00	1.389088E+07
	Troe coefficients : 7.82E-01 2.07E+02 2.66E+03 6.10E+03	6.080000E+09	2.700000E-01	1.171520E+06
	Species efficiencies : CH4:2.0E+00 CO:1.5E+00 CO2:2.0E+00 H2O:6.0E+00			
82	C2H4 + M ⟷ C2H2 + H2 + M	2.610000E+13	0.000000E+00	2.837714E+08
	Species efficiencies : CH4:2.00E+00 CO:1.50E+00 CO2:2.00E+00 H2O:6.00E+00			
83	C2H4 + H ⟷ C2H3 + H2	5.070000E+04	1.930000E+00	5.418280E+07
84	C2H4 + OH ⟷ C2H3 + H2O	2.230000E+01	2.745000E+00	9.269652E+06
85	C2H4 + CH3 ⟷ C2H3 + CH4	9.760000E-01	2.947000E+00	6.337923E+07
86	C2H4 + CH3 ⟷ C2H3 + CH4	8.130000E-08	4.417000E+00	3.696899E+07
87	C2H4 + O ⟷ CH3 + HCO	7.453000E+03	1.880000E+00	7.656720E+05
88	CH2(L1) + CH3 ⟷ C2H4 + H	1.247437E+02	1.988656E+00	-1.763074E+07
89	C2H2 + H (+M) ⟷ C2H3 (+M)	6.346000E+25	-4.664000E+00	1.581552E+07
	Troe coefficients : 7.88E-01 -1.02E+04 1.00E-30 0.00E+00	1.710000E+07	1.266000E+00	1.133446E+07
	Species efficiencies : CH4:2.0E+00 CO:1.5E+00 CO2:2.0E+00 H2O:6.0E+00			
90	C2H3 + O2 ⟷ C2H2 + HO2	2.150000E+04	1.190000E+00	1.408753E+07
91	C2H3 + O2 ⟷ C2H2 + HO2	4.600000E-02	2.760000E+00	-2.061875E+06
92	C2H3 + O2 ⟷ CH2CO + OH	1.060000E+00	2.390000E+00	2.585712E+07
93	C2H3 + O2 ⟷ CH2CO + OH	5.260000E-04	3.010000E+00	7.434968E+06
94	C2H3 + O2 ⟷ CH2O + HCO	2.730000E+32	-7.320000E+00	4.945488E+07
95	C2H3 + O2 ⟷ CH2O + HCO	6.080000E+12	-1.310000E+00	2.701609E+06
96	C2H3 + O2 ⟶ CH2O + CO + H	6.360000E+32	-7.320000E+00	4.945488E+07
97	C2H3 + O2 ⟶ CH2O + CO + H	1.420000E+13	-1.310000E+00	2.701609E+06
98	C2H3 + O2 ⟷ CH3O + CO	1.030000E+08	-3.300000E-01	-3.128795E+06
99	C2H3 + O2 ⟷ CH3O + CO	5.770000E+18	-3.540000E+00	1.996605E+07
100	C2H3 + O2 ⟷ CH3 + CO2	7.250000E+28	-6.700000E+00	4.368096E+07
101	C2H3 + O2 ⟷ CH3 + CO2	5.320000E+10	-1.140000E+00	1.868993E+06
102	C2H3 + H ⟷ C2H2 + H2	9.635250E+10	0.000000E+00	0.000000E+00
103	C2H3 + OH ⟷ C2H2 + H2O	3.011000E+10	0.000000E+00	0.000000E+00

No.	Reaction	A	b	E_a
104	C2H2 + O ⟷ CH2(L1) + CO	7.395000E+05	1.280000E+00	1.034285E+07
105	C2H2 + HCO ⟷ C2H3 + CO	1.000000E+04	2.000000E+00	2.510400E+07
106	C2H2 + OH ⟷ CH2CO + H	7.528000E+03	1.550000E+00	8.811504E+06
107	C2H2 + OH ⟷ CH3 + CO	1.277000E+06	7.300000E-01	1.079054E+07
108	CH2CO (+M) ⟷ CH2(L1) + CO (+M)	3.000000E+12	0.000000E+00	2.384880E+08
	Troe coefficients : -	3.000000E+13	0.000000E+00	2.970640E+08
	Species efficiencies : CH4:2.0E+00 CO:1.5E+00 CO2:2.0E+00 H2O:6.0E+00			
109	C2H3 + O ⟷ CH2CO + H	3.000000E+10	0.000000E+00	0.000000E+00
110	CH2CO + H ⟷ CH3 + CO	7.770000E+05	1.450000E+00	1.163152E+07
111	CH2CO + OH ⟷ CH2OH + CO	2.000000E+09	0.000000E+00	-4.225840E+06
112	C2H4 + CH2(L1) ⟷ C2H3 + CH3	4.160000E+21	-3.190000E+00	4.083584E+07
113	C2H4 + CH2(L1) ⟷ C2H3 + CH3	4.920000E+06	1.020000E+00	2.509438E+06
114	C2H2 + O ⟶ CH2CO	1.000000E+10	0.000000E+00	6.276000E+07
115	CH2CO + O ⟶ 2 HCO	2.000000E+10	0.000000E+00	9.623200E+06
116	CH2CO + OH ⟶ CH3 + CO2	1.000000E+10	0.000000E+00	0.000000E+00
117	O + OH + M ⟷ HO2 + M	1.000000E+10	0.000000E+00	0.000000E+00
118	C2H5 + O2 ⟶ CH2O + CH3O	1.000000E+11	0.000000E+00	1.004160E+08
119	CH2(L1) + HCO ⟷ CH3 + CO	1.078469E+11	-2.145491E-01	2.031268E+06
120	CH2(L1) + O ⟷ CO + H2	2.696171E+11	-2.145491E-01	2.031268E+06
121	CH2(L1) + OH ⟷ CH2O + H	1.617703E+11	-2.145491E-01	2.031268E+06
122	CH2(L1) + CO2 ⟷ CH2O + CO	5.931577E+08	-2.145491E-01	6.215269E+06
123	CH2(L1) + O ⟷ CO + 2 H	1.871156E+02	1.988656E+00	-1.763074E+07
124	CH2(L1) + CH4 ⟷ 2 CH3	2.681990E+02	1.988656E+00	-1.763074E+07
125	2 CH3 ⟶ C2H4 + H2	5.000000E+11	0.000000E+00	1.338880E+08
126	2 CH2(L1) ⟶ C2H2 + 2 H	6.470811E+11	-2.145491E-01	2.031268E+06
127	C2H6 ⟷ C2H4 + H2	3.000000E+13	0.000000E+00	3.284440E+08
128	CH2O + O ⟶ CO2 + 2 H	2.000000E+10	0.000000E+00	2.092000E+07
129	CH2O + OH ⟶ CO2 + H + H2	1.000000E+08	0.000000E+00	0.000000E+00
130	C2H2 + HO2 ⟶ CH2O + HCO	5.000000E+09	0.000000E+00	6.276000E+07
131	CH3O + CO ⟷ CH3 + CO2	5.000000E+08	0.000000E+00	2.719600E+07
132	C2H2 + O2 ⟶ CH2O + CO	3.000000E+08	0.000000E+00	1.087840E+08
133	C2H4 + O2 ⟶ 2 CH2O	1.000000E+11	0.000000E+00	2.008320E+08
134	C2H2 + O2 ⟶ 2 HCO	3.000000E+08	0.000000E+00	1.129680E+08
135	C2H4 + O2 ⟶ CH3O + HCO	1.000000E+11	0.000000E+00	1.799120E+08
136	CH3 + O + M ⟶ CH3O + M	5.000000E+10	0.000000E+00	0.000000E+00
137	CH2OH + CH3 ⟶ CH2O + CH4	1.500000E+10	0.000000E+00	0.000000E+00
138	C2H4 + O ⟷ C2H3 + OH	1.083000E+04	2.000000E+00	3.674372E+07

Appendix D

Characteristics of S30R299QSS30 mechanism

The reduced ARC mechanism generated by ARCANE comprises 30 transported species, 299 reactions and 22 species in Quasi-Steady State:

- Transported species:
  N_2, H_2, H, O_2, O, H_2O, OH, HO_2, CO, CO_2, CH_4, CH_3, CH_2O, C_2H_5, C_2H_4, C_2H_2, C_3H_6, C_3H_4-A, C_4H_8-1, nC_5H_{11}, nC_5H_{10}, nC_7H_{15}, nC_7H_{14}, $MCYC_6$, $nC_{12}H_{26}$, XYLENE, RXYLENE, C_6H_4, $C_3H_7(L_1)$, $CH_3O(L_1)$.

- QSS species:
  $CH_2(S)$, C, CH, HCO, C_2H_6, C_2H_3, C_2H, CH_2CHO, CH_2CO, HCCO, C_3H_5-A, C_3H_3, C_3H_2, pC_4H_9, iC_4H_8, C_4H_7 1-3, C_4H_6, $CH_3C_6H_4$, $nC_{12}H_{25}$, $C_6H_4O_2$, C_6H_2, C_6H_3.

Detailed description of the reactions is given in Tab. D.0.1.

Table D.0.1: List of reactions with A the pre-exponential factor in $m^{3(n-1)}/kmol^{n-1}/s$ with n the order of the reaction, b the temperature exponent and E_a the activation energy in $J/kmol$. In the case of fall-off reactions, two sets of Arrhenius coefficients are specified, the first one being the low temperature set and the second one the high temperature set.

No.	Reaction	A	b	E_a
1	H2 + O ⟷ H + OH	5.080000E+01	2.670000E+00	2.632573E+07
2	H2 + OH ⟷ H + H2O	4.380000E+10	0.000000E+00	2.924616E+07
3	H + O2 ⟷ O + OH	1.140000E+11	0.000000E+00	6.395662E+07
4	H + OH + M ⟷ H2O + M	3.500000E+16	-2.000000E+00	0.000000E+00
5	H2O + O ⟷ 2 OH	6.700000E+04	1.704000E+00	6.270477E+07
6	H + HO2 ⟷ 2 OH	7.079000E+10	0.000000E+00	1.234280E+06
7	H + HO2 ⟷ H2 + O2	1.140200E+07	1.083000E+00	2.317016E+06
8	HO2 + O ⟷ O2 + OH	3.250000E+10	0.000000E+00	0.000000E+00
9	HO2 + OH ⟷ H2O + O2	7.000000E+09	0.000000E+00	-4.572945E+06
10	HO2 + OH ⟷ H2O + O2	4.500000E+11	0.000000E+00	4.572945E+07
11	H + O2 (+M) ⟷ HO2 (+M)	1.740000E+13	-1.230000E+00	0.000000E+00
	Troe coefficients : 6.70E-01 1.00E-30 1.00E+30 1.00E+30	4.650000E+09	4.400000E-01	0.000000E+00
	Species efficiencies : CO:1.9E+00 CO2:3.8E+00 H2O:1.0E+01			
12	CO + O (+M) ⟷ CO2 (+M)	1.170000E+18	-2.790000E+00	1.753514E+07
	Troe coefficients : -	1.362000E+07	0.000000E+00	9.974656E+06
	Species efficiencies : CO:1.8E+00 CO2:3.6E+00 H2O:1.2E+01			
13	CO + OH ⟷ CO2 + H	7.015000E+01	2.053000E+00	-1.488249E+06
14	CO + OH ⟷ CO2 + H	5.757000E+09	-6.640000E-01	1.388251E+06
15	CH3 + H (+M) ⟷ CH4 (+M)	2.480000E+27	-4.760000E+00	1.020896E+07
	Troe coefficients : 7.83E-01 7.40E+01 2.94E+03 6.96E+03	1.270000E+13	-6.300000E-01	1.602472E+06
	Species efficiencies : CO:1.5E+00 CO2:2.0E+00 H2O:6.0E+00			
16	CH4 + H ⟷ CH3 + H2	6.140000E+02	2.500000E+00	4.011201E+07
17	CH4 + O ⟷ CH3 + OH	1.020000E+06	1.500000E+00	3.598240E+07
18	CH4 + OH ⟷ CH3 + H2O	5.830000E+01	2.600000E+00	9.162960E+06
19	CH3 + HO2 ⟷ CH4 + O2	1.160000E+02	2.230000E+00	-1.264405E+07
20	CH2(S) + O2 ⟶ CO + H + OH	2.800000E+10	0.000000E+00	0.000000E+00
21	CH2(S) + O2 ⟷ CO + H2O	1.200000E+10	0.000000E+00	0.000000E+00
22	CH2(S) + O ⟷ H + HCO	1.500000E+10	0.000000E+00	0.000000E+00
23	CH2(S) + H2 ⟷ CH3 + H	7.000000E+10	0.000000E+00	0.000000E+00
24	CH2(S) + H ⟷ CH + H2	3.000000E+10	0.000000E+00	0.000000E+00
25	CH2(S) + OH ⟷ CH2O + H	3.000000E+10	0.000000E+00	0.000000E+00
26	CH2(S) + CO2 ⟷ CH2O + CO	1.400000E+10	0.000000E+00	0.000000E+00
27	CH + O2 ⟷ HCO + O	3.300000E+10	0.000000E+00	0.000000E+00
28	CH + O ⟷ CO + H	5.700000E+10	0.000000E+00	0.000000E+00
29	CH + H ⟷ C + H2	1.100000E+11	0.000000E+00	0.000000E+00
30	CH + OH ⟷ H + HCO	3.000000E+10	0.000000E+00	0.000000E+00
31	C + OH ⟷ CO + H	5.000000E+10	0.000000E+00	0.000000E+00
32	C + O2 ⟷ CO + O	5.000000E+10	0.000000E+00	0.000000E+00
33	CH3 + O2 ⟷ CH3O(L1) + O	7.546000E+09	0.000000E+00	1.184909E+08
34	CH3 + O2 ⟷ CH2O + OH	2.641000E-03	3.283000E+00	3.391132E+07

No.	Reaction	A	b	E_a
35	CH3 + O ⟷ CH2O + H	5.540000E+10	5.000000E-02	-5.690240E+05
36	CH3 + OH ⟷ CH2(S) + H2O	5.282000E+14	-1.518000E+00	7.414048E+06
37	CH3 + OH ⟷ CH3O(L1) + H	4.686000E+07	8.330000E-01	1.492014E+07
38	CH3 + OH ⟷ CH3O(L1) + H	1.230000E+06	1.011000E+00	4.999880E+07
39	CH3 + HO2 ⟷ CH3O(L1) + OH	1.000000E+09	2.690000E-01	-2.876500E+06
40	CH3O(L1) + O2 ⟷ CH2O + HO2	1.748153E+23	-3.956088E+00	5.987526E+07
41	CH3O(L1) + O2 ⟷ CH2O + HO2	2.790099E+22	-2.956088E+00	8.086639E+07
42	CH3O(L1) + HCO ⟷ 2 CH2O	2.083891E+22	-2.956088E+00	5.987526E+07
43	CH3O(L1) + OH ⟷ CH2O + H2O	2.778522E+21	-2.956088E+00	5.987526E+07
44	CH3O(L1) + O2 ⟷ CH2O + HO2	6.750997E-19	8.476756E+00	-1.937016E+07
45	CH3O(L1) + H ⟷ CH2O + H2	3.082647E+13	-1.023244E+00	3.646026E+06
46	CH3 + CH3O(L1) ⟷ CH2O + CH4	1.849588E+13	-1.023244E+00	3.646026E+06
47	H + HCO (+M) ⟷ CH2O (+M)	1.350000E+18	-2.570000E+00	5.962200E+06
	Troe coefficients : 7.82E-01 2.71E+02 2.76E+03 6.57E+03	1.090000E+09	4.800000E-01	-1.087840E+06
	Species efficiencies : CO:1.5E+00 CO2:2.0E+00 H2O:6.0E+00			
48	CO + H2 (+M) ⟷ CH2O (+M)	5.070000E+21	-3.420000E+00	3.529120E+08
	Troe coefficients : 9.32E-01 1.97E+02 1.54E+03 1.03E+04	4.300000E+04	1.500000E+00	3.330464E+08
	Species efficiencies : CO:1.5E+00 CO2:2.0E+00 H2O:6.0E+00			
49	CH2O + O2 ⟷ HCO + HO2	8.070000E+12	0.000000E+00	2.235093E+08
50	CH2O + O ⟷ HCO + OH	6.260000E+06	1.150000E+00	9.455840E+06
51	CH2O + H ⟷ H2 + HCO	5.740000E+04	1.900000E+00	1.146416E+07
52	CH2O + OH ⟷ H2O + HCO	7.820000E+04	1.630000E+00	-4.414120E+06
53	CH2O + CH3 ⟷ CH4 + HCO	3.830000E-02	3.360000E+00	1.804141E+07
54	HCO + M ⟷ CO + H + M	5.700000E+08	6.600000E-01	6.221608E+07
	Species efficiencies : CO:1.50E+00 CO2:2.00E+00 H2O:6.00E+00			
55	HCO + O2 ⟷ CO + HO2	7.580000E+09	0.000000E+00	1.715440E+06
56	HCO + O ⟷ CO + OH	3.020000E+10	0.000000E+00	0.000000E+00
57	H + HCO ⟷ CO + H2	7.340000E+10	0.000000E+00	0.000000E+00
58	HCO + OH ⟷ CO + H2O	3.011000E+10	0.000000E+00	0.000000E+00
59	CH3 + HCO ⟷ CH4 + CO	2.650000E+10	0.000000E+00	0.000000E+00
60	HCO + O ⟷ CO2 + H	3.000000E+10	0.000000E+00	0.000000E+00
61	HCO + HO2 ⟶ CO2 + H + OH	3.000000E+10	0.000000E+00	0.000000E+00
62	CH2O + H (+M) ⟷ CH3O(L1) (+M)	1.270000E+26	-4.820000E+00	2.732152E+07
	Troe coefficients : 7.19E-01 1.03E+02 1.29E+03 4.16E+03	5.400000E+08	4.540000E-01	1.506240E+07
	Species efficiencies : CO:1.5E+00 CO2:2.0E+00 H2O:6.0E+00			
63	CH3O(L1) (+M) ⟷ CH2O + H (+M)	2.882275E+25	-4.023244E+00	1.053465E+08
	Troe coefficients : 9.00E-01 2.50E+03 1.30E+03 1.00E+99	1.048100E+17	-1.023244E+00	1.131413E+08
	Species efficiencies : CO:1.5E+00 CO2:2.0E+00 H2O:6.0E+00			
64	2 CH3 (+M) ⟷ C2H6 (+M)	8.050000E+25	-3.750000E+00	4.107014E+06
	Troe coefficients : 0.00E+00 5.70E+02 1.00E+30 1.00E+30	2.277000E+12	-6.900000E-01	7.317816E+05
	Species efficiencies : CO:2.0E+00 CO2:3.0E+00 H2O:5.0E+00			
65	C2H5 + H (+M) ⟷ C2H6 (+M)	1.990000E+35	-7.080000E+00	2.797004E+07
	Troe coefficients : 8.42E-01 1.25E+02 2.22E+03 6.88E+03	5.210000E+14	-9.900000E-01	6.610720E+06
	Species efficiencies : CO:1.5E+00 CO2:2.0E+00 H2O:6.0E+00			
66	C2H6 + O ⟷ C2H5 + OH	3.550000E+03	2.400000E+00	2.439272E+07
67	C2H6 + H ⟷ C2H5 + H2	1.150000E+05	1.900000E+00	3.150552E+07
68	C2H6 + OH ⟷ C2H5 + H2O	1.480000E+04	1.900000E+00	3.974800E+06

No.	Reaction	A	b	E_a
69	C2H6 + CH3 ⟷ C2H5 + CH4	5.550000E-07	4.720000E+00	1.351850E+07
70	C2H4 + H (+M) ⟷ C2H5 (+M)	1.420000E+33	-6.642000E+00	2.413750E+07
	Troe coefficients : -5.69E-01 2.99E+02 -9.15E+03 1.52E+02	9.569000E+05	1.463000E+00	5.669320E+06
	Species efficiencies : CO:1.5E+00 CO2:2.0E+00 H2O:6.0E+00			
71	C2H5 + H ⟷ C2H4 + H2	2.000000E+09	0.000000E+00	0.000000E+00
72	2 C2H4 ⟷ C2H3 + C2H5	4.820000E+11	0.000000E+00	2.992815E+08
73	C2H5 + CH3 ⟷ C2H4 + CH4	1.180000E+01	2.450000E+00	-1.222146E+07
74	2 CH3 ⟷ C2H5 + H	3.100000E+11	-3.620000E-01	5.595054E+07
75	C2H5 + O2 ⟷ C2H4 + HO2	1.843000E+04	1.130000E+00	-3.014990E+06
76	C2H4 + M ⟷ C2H2 + H2 + M	2.610000E+13	0.000000E+00	2.837714E+08
	Species efficiencies : CO:1.50E+00 CO2:2.00E+00 H2O:6.00E+00			
77	C2H4 + H ⟷ C2H3 + H2	5.070000E+04	1.930000E+00	5.418280E+07
78	C2H4 + OH ⟷ C2H3 + H2O	2.230000E+01	2.745000E+00	9.269652E+06
79	C2H4 + CH3 ⟷ C2H3 + CH4	9.760000E-01	2.947000E+00	6.337923E+07
80	C2H4 + CH3 ⟷ C2H3 + CH4	8.130000E-08	4.417000E+00	3.696899E+07
81	C2H4 + O ⟷ CH3 + HCO	7.453000E+03	1.880000E+00	7.656720E+05
82	C2H4 + O ⟷ CH2CHO + H	6.098000E+03	1.880000E+00	7.656720E+05
83	CH2(S) + CH3 ⟷ C2H4 + H	2.000000E+10	0.000000E+00	0.000000E+00
84	C2H2 + H (+M) ⟷ C2H3 (+M)	6.350000E+25	-4.664000E+00	1.581552E+07
	Troe coefficients : 7.88E-01 -1.02E+04 1.00E-30 0.00E+00	1.710000E+07	1.266000E+00	1.133446E+07
	Species efficiencies : CO:1.5E+00 CO2:2.0E+00 H2O:6.0E+00			
85	C2H3 + O2 ⟷ CH2CHO + O	7.100000E+17	-2.650000E+00	2.714998E+07
86	C2H3 + O2 ⟷ CH2CHO + O	2.020000E+07	5.800000E-01	1.606656E+05
87	C2H3 + O2 ⟷ C2H2 + HO2	2.150000E+04	1.190000E+00	1.408753E+07
88	C2H3 + O2 ⟷ C2H2 + HO2	4.600000E-02	2.760000E+00	-2.061875E+06
89	C2H3 + O2 ⟷ CH2CO + OH	1.060000E+00	2.390000E+00	2.585712E+07
90	C2H3 + O2 ⟷ CH2CO + OH	5.260000E-04	3.010000E+00	7.434968E+06
91	C2H3 + O2 ⟷ CH2O + HCO	2.730000E+32	-7.320000E+00	4.945488E+07
92	C2H3 + O2 ⟷ CH2O + HCO	6.080000E+12	-1.310000E+00	2.701609E+06
93	C2H3 + O2 ⟶ CH2O + CO + H	6.360000E+32	-7.320000E+00	4.945488E+07
94	C2H3 + O2 ⟶ CH2O + CO + H	1.420000E+13	-1.310000E+00	2.701609E+06
95	C2H3 + O2 ⟷ CH3O(L1) + CO	1.030000E+08	-3.300000E-01	-3.128795E+06
96	C2H3 + O2 ⟷ CH3O(L1) + CO	5.770000E+18	-3.540000E+00	1.996605E+07
97	C2H3 + O2 ⟷ CH3 + CO2	7.250000E+28	-6.700000E+00	4.368096E+07
98	C2H3 + O2 ⟷ CH3 + CO2	5.320000E+10	-1.140000E+00	1.868993E+06
99	C2H3 + H ⟷ C2H2 + H2	9.635300E+10	0.000000E+00	0.000000E+00
100	C2H3 + OH ⟷ C2H2 + H2O	3.011000E+10	0.000000E+00	0.000000E+00
101	C2H2 + O ⟷ H + HCCO	2.958000E+06	1.280000E+00	1.034285E+07
102	C2H2 + HCO ⟷ C2H3 + CO	1.000000E+04	2.000000E+00	2.510400E+07
103	C2H2 + CH2(S) ⟷ C3H3 + H	2.000000E+10	0.000000E+00	0.000000E+00
104	C2H2 + OH ⟷ C2H + H2O	2.632000E+03	2.140000E+00	7.137904E+07
105	C2H2 + OH ⟷ CH2CO + H	7.528000E+03	1.550000E+00	8.811504E+06
106	C2H2 + OH ⟷ CH3 + CO	1.277000E+06	7.300000E-01	1.079054E+07
107	C2H + O2 ⟷ CO + HCO	5.000000E+10	0.000000E+00	6.276000E+06
108	C2H + O ⟷ CH + CO	5.000000E+10	0.000000E+00	0.000000E+00
109	C2H + H2 ⟷ C2H2 + H	4.900000E+02	2.500000E+00	2.343040E+06
110	C2H + OH ⟷ H + HCCO	2.000000E+10	0.000000E+00	0.000000E+00

No.	Reaction	A	b	E_a
111	CH2CHO (+M) ⟷ CH2CO + H (+M)	6.000000E+26	-3.800000E+00	1.816856E+08
	Troe coefficients : 9.85E-01 3.93E+02 9.80E+09 5.00E+09	1.430000E+15	-1.500000E-01	1.907904E+08
112	CH2CHO (+M) ⟷ CH3 + CO (+M)	9.520000E+30	-5.070000E+00	1.727992E+08
	Troe coefficients : 7.13E-17 1.15E+03 4.99E+09 1.79E+09	2.930000E+12	2.900000E-01	1.686152E+08
113	C2H3 + O ⟷ CH2CO + H	3.000000E+10	0.000000E+00	0.000000E+00
114	CH2CO + H ⟷ CH3 + CO	7.770000E+05	1.450000E+00	1.163152E+07
115	CH + CH2O ⟷ CH2CO + H	9.460000E+10	0.000000E+00	-2.154760E+06
116	CH2CO + OH ⟷ CH3O(L1) + CO	2.000000E+09	0.000000E+00	-4.225840E+06
117	HCCO + OH ⟶ 2 CO + H2	1.000000E+11	0.000000E+00	0.000000E+00
118	HCCO + O ⟶ 2 CO + H	8.000000E+10	0.000000E+00	0.000000E+00
119	CH + CO + M ⟷ HCCO + M	7.570000E+16	-1.900000E+00	0.000000E+00
120	H + HCCO ⟷ CH2(S) + CO	1.000000E+11	0.000000E+00	0.000000E+00
121	HCCO + O2 ⟶ 2 CO + OH	1.910000E+08	-2.000000E-02	4.267680E+06
122	HCCO + O2 ⟶ CO + CO2 + H	4.780000E+09	-1.420000E-01	4.811600E+06
123	C3H7(L1) + H ⟷ C2H5 + CH3	2.977004E+12	-7.513269E-01	2.643116E+06
124	C3H7(L1) + OH ⟷ C3H6 + H2O	3.587290E+12	-7.513269E-01	2.643116E+06
125	C3H7(L1) + HO2 ⟶ C2H5 + CH2O + OH	5.572400E+07	5.571560E-01	-4.624073E+06
126	C2H3 + CH3 (+M) ⟷ C3H6 (+M)	4.270000E+52	-1.194000E+01	4.087684E+07
	Troe coefficients : 1.75E-01 1.34E+03 6.00E+04 1.01E+04	2.500000E+10	0.000000E+00	0.000000E+00
127	C2H4 + CH2(S) ⟷ C3H6	2.130000E+55	-1.350000E+01	8.535360E+07
128	C2H4 + CH2(S) ⟷ C3H6	1.300000E+37	-8.770000E+00	2.453414E+07
129	C2H4 + CH2(S) ⟷ C3H5-A + H	4.440000E+32	-6.550000E+00	5.815760E+07
130	C2H4 + CH2(S) ⟷ C3H5-A + H	3.890000E+11	-4.200000E-01	5.178118E+06
131	C2H4 + CH2(S) ⟷ C2H3 + CH3	4.160000E+21	-3.190000E+00	4.083584E+07
132	C2H4 + CH2(S) ⟷ C2H3 + CH3	4.920000E+06	1.020000E+00	2.509438E+06
133	C2H3 + CH3 ⟷ C3H5-A + H	5.300000E+26	-4.570000E+00	6.024960E+07
134	C2H3 + CH3 ⟷ C3H5-A + H	4.480000E+07	6.000000E-01	5.947974E+06
135	C3H6 ⟷ C2H3 + CH3	5.800000E+75	-1.720000E+01	5.606560E+08
136	C3H6 ⟷ C2H3 + CH3	6.700000E+54	-1.180000E+01	4.763066E+08
137	C3H6 ⟷ C3H5-A + H	1.080000E+71	-1.590000E+01	5.224142E+08
138	C3H6 ⟷ C3H5-A + H	6.280000E+42	-8.510000E+00	4.100487E+08
139	C3H6 + H ⟷ C3H5-A + H2	3.644000E+02	2.455000E+00	1.824726E+07
140	C3H6 + O2 ⟷ C3H5-A + HO2	1.200000E+17	-1.670000E+00	1.932677E+08
141	C3H6 + O ⟷ C3H5-A + OH	5.240000E+08	7.000000E-01	2.461866E+07
142	C3H6 + OH ⟷ C3H5-A + H2O	4.460000E+03	2.072000E+00	4.396547E+06
143	C3H6 + CH3 ⟷ C3H5-A + CH4	2.210000E-03	3.500000E+00	2.374420E+07
144	C3H6 + O ⟷ C2H5 + HCO	7.450000E+03	1.880000E+00	7.656720E+05
145	C3H6 + O ⟶ CH2CO + CH3 + H	3.050000E+03	1.880000E+00	7.656720E+05
146	C3H6 + H ⟷ C3H7(L1)	1.040000E+46	-1.150000E+01	6.426206E+07
147	C3H6 + H ⟷ C3H7(L1)	3.780000E+25	-5.570000E+00	2.353542E+07
148	C3H6 + H ⟷ C2H4 + CH3	2.670000E+09	4.700000E-01	2.272372E+07
149	C3H6 + H ⟷ C2H4 + CH3	1.000000E-13	0.000000E+00	0.000000E+00
150	C3H6 + H ⟷ C3H7(L1)	3.260000E+58	-1.494000E+01	8.435362E+07
151	C3H6 + H ⟷ C3H7(L1)	1.060000E+27	-5.630000E+00	2.348647E+07
152	C2H4 + CH3 ⟷ C3H7(L1)	7.670000E+44	-1.117000E+01	9.357934E+07
153	C2H4 + CH3 ⟷ C3H7(L1)	2.600000E+30	-7.460000E+00	5.194854E+07
154	C3H6 + HO2 ⟷ C3H7(L1) + O2	1.310000E+17	-2.580000E+00	7.982235E+07

No.	Reaction	A	b	E_a
155	C3H5-A + H ⟷ C3H4-A + H2	1.232000E+00	3.035000E+00	1.080309E+07
156	C3H5-A + OH ⟷ C3H4-A + H2O	6.000000E+09	0.000000E+00	0.000000E+00
157	C3H5-A + CH3 ⟷ C3H4-A + CH4	3.000000E+09	-3.200000E-01	-5.481040E+05
158	C3H4-A + H ⟷ C3H3 + H2	6.625000E+00	3.095000E+00	2.310405E+07
159	C3H4-A + OH ⟷ C3H3 + H2O	2.000000E+04	2.000000E+00	2.092000E+07
160	C3H4-A + CH3 ⟷ C3H3 + CH4	1.300000E+09	0.000000E+00	3.221680E+07
161	C3H4-A + H ⟷ C3H5-A	4.670000E+48	-1.145000E+01	8.928656E+07
162	C3H4-A + H ⟷ C3H5-A	3.320000E+27	-5.780000E+00	2.892399E+07
163	C3H4-A + H ⟷ C2H2 + CH3	1.260000E+17	-1.830000E+00	6.277255E+07
164	C3H4-A + H ⟷ C2H2 + CH3	1.230000E+01	2.680000E+00	2.650564E+07
165	C3H4-A + O ⟷ C2H4 + CO	2.000000E+04	1.800000E+00	4.184000E+06
166	C3H4-A + O ⟷ C2H2 + CH2O	3.000000E-06	4.610000E+00	-1.775271E+07
167	C3H3 + O ⟷ C2H + CH2O	2.000000E+10	0.000000E+00	0.000000E+00
168	C3H3 + HO2 ⟶ C2H3 + CO + OH	8.000000E+08	0.000000E+00	0.000000E+00
169	C3H3 + H ⟷ C3H2 + H2	2.140000E+02	2.520000E+00	3.118335E+07
170	C3H3 + OH ⟷ C3H2 + H2O	2.000000E+10	0.000000E+00	3.347200E+07
171	C3H3 + OH ⟷ C2H2 + CH2O	2.000000E+09	0.000000E+00	0.000000E+00
172	C3H3 + OH ⟷ C2H4 + CO	1.000000E+10	0.000000E+00	0.000000E+00
173	C3H7(L1) + O2 ⟷ C3H6 + HO2	3.980286E+06	5.571560E-01	1.211193E+07
174	O2 + PC4H9 ⟷ C4H8-1 + HO2	5.000000E+08	0.000000E+00	1.255200E+07
175	H + IC4H8 ⟷ C3H6 + CH3	8.900000E+08	4.700000E-01	2.272372E+07
176	H + IC4H8 ⟷ C3H6 + CH3	1.340000E+03	4.700000E-01	2.272372E+07
177	C3H5-A + CH3 (+M) ⟷ C4H8-1 (+M)	3.910000E+54	-1.281000E+01	2.615000E+07
	Troe coefficients : 1.04E-01 1.61E+03 6.00E+04 6.12E+03	6.000000E+11	-3.200000E-01	-1.097463E+06
	Species efficiencies : CO:1.5E+00 CO2:2.0E+00 H2O:6.0E+00			
178	C4H71-3 + H ⟷ C4H8-1	5.000000E+10	0.000000E+00	2.092000E+07
179	C4H8-1 + OH ⟷ C4H71-3 + H2O	7.769000E+02	2.200000E+00	-1.829161E+06
180	C4H8-1 + O ⟷ C4H71-3 + OH	1.750000E+08	7.000000E-01	2.461866E+07
181	C4H8-1 + O2 ⟷ C4H71-3 + HO2	1.000000E+11	0.000000E+00	1.556030E+08
182	C4H71-3 ⟷ C4H6 + H	8.530000E+07	1.950000E+00	1.986986E+08
183	C4H8-1 + H ⟷ C2H4 + C2H5	9.470000E+13	-1.030000E+00	5.611999E+07
184	C4H8-1 + H ⟷ C2H4 + C2H5	6.020000E+12	-4.900000E-01	3.536317E+07
185	C4H8-1 + H ⟷ C3H6 + CH3	4.570000E+16	-1.540000E+00	3.791122E+07
186	C4H8-1 + H ⟷ C3H6 + CH3	1.210000E+13	-9.900000E-01	5.512420E+07
187	C4H8-1 + H ⟷ PC4H9	1.900000E+28	-6.460000E+00	5.007411E+07
188	C4H8-1 + H ⟷ PC4H9	3.780000E+29	-6.630000E+00	3.039676E+07
189	PC4H9 ⟷ C2H4 + C2H5	7.470000E+43	-9.670000E+00	1.620128E+08
190	PC4H9 ⟷ C3H6 + CH3	2.050000E+42	-9.610000E+00	1.942004E+08
191	C4H8-1 + O ⟷ C3H7(L1) + HCO	7.450000E+03	1.880000E+00	7.656720E+05
192	C4H8-1 + O ⟶ C2H5 + CH2CO + H	3.050000E+03	1.880000E+00	7.656720E+05
193	C4H8-1 ⟷ C4H6 + H2	3.000000E+13	0.000000E+00	2.928800E+08
194	C4H6 + H ⟷ C2H3 + C2H4	6.480000E+29	-4.910000E+00	1.107840E+08
195	C4H6 + OH ⟷ C3H5-A + CH2O	1.370000E+09	0.000000E+00	-4.351360E+06
196	C4H6 + O ⟷ C3H4-A + CH2O	7.260000E+07	8.190000E-01	7.656720E+06
197	C3H4-A + O2 ⟶ CH2CO + CH2O	1.000000E+12	0.000000E+00	1.715440E+08
198	C2H2 + O ⟶ CH2CO	1.000000E+10	0.000000E+00	6.276000E+07
199	CH2CO + O ⟶ 2 HCO	2.000000E+10	0.000000E+00	9.623200E+06

No.	Reaction	A	b	E_a
200	CH2CO + OH ⟶ CH3 + CO2	1.000000E+10	0.000000E+00	0.000000E+00
201	CH2CO + O2 ⟶ CH2O + CO2	1.000000E+11	0.000000E+00	1.548080E+08
202	CH2CO + O2 ⟶ CO + HCO + OH	3.000000E+11	0.000000E+00	1.673600E+08
203	CH2CHO + O2 ⟶ CH2CO + HO2	5.000000E+08	0.000000E+00	1.255200E+07
204	CH2CO ⟶ H + HCCO	1.500000E+14	0.000000E+00	4.284416E+08
205	CH2CO + CH3 ⟷ C3H4-A + OH	1.500000E+08	0.000000E+00	1.351432E+08
206	HCCO + OH ⟷ CO + H + HCO	1.000000E+10	0.000000E+00	0.000000E+00
207	HCCO + O2 ⟷ CO2 + HCO	2.400000E+08	0.000000E+00	-3.573136E+06
208	C2H + O2 ⟷ HCCO + O	2.300000E+10	0.000000E+00	0.000000E+00
209	O + OH + M ⟷ HO2 + M	1.000000E+10	0.000000E+00	0.000000E+00
210	C2H + O2 ⟷ CH + CO2	4.500000E+12	0.000000E+00	1.046000E+08
211	CH + OH ⟷ C + H2O	4.000000E+04	2.000000E+00	1.255200E+07
212	C2H5 + O2 ⟶ CH2O + CH3O(L1)	1.000000E+11	0.000000E+00	1.004160E+08
213	C2H5 + HO2 ⟶ CH2O + CH3 + OH	5.000000E+09	0.000000E+00	0.000000E+00
214	CH2(S) + O ⟷ CO + 2 H	3.000000E+10	0.000000E+00	0.000000E+00
215	C3H2 + OH ⟷ C2H2 + HCO	5.000000E+10	0.000000E+00	0.000000E+00
216	CH + CH3 ⟷ C2H3 + H	3.000000E+10	0.000000E+00	0.000000E+00
217	C + CH3 ⟷ C2H2 + H	5.000000E+10	0.000000E+00	0.000000E+00
218	CH2(S) + CH4 ⟷ 2 CH3	4.300000E+10	0.000000E+00	0.000000E+00
219	2 CH3 ⟶ C2H4 + H2	5.000000E+11	0.000000E+00	1.338880E+08
220	C2H2 + CH ⟷ C3H2 + H	8.400000E+10	0.000000E+00	0.000000E+00
221	C3H3 + CH3 ⟶ C4H6	5.000000E+09	0.000000E+00	1.255200E+07
222	C4H6 ⟶ C3H3 + CH3	5.000000E+16	0.000000E+00	3.765600E+08
223	C3H3 ⟷ C3H2 + H	1.000000E+13	0.000000E+00	4.058480E+08
224	C2H6 ⟷ C2H4 + H2	3.000000E+13	0.000000E+00	3.284440E+08
225	C3H6 ⟷ C3H4-A + H2	1.800000E+13	0.000000E+00	3.263520E+08
226	C2H2 + C2H4 ⟷ C4H6	5.000000E+07	0.000000E+00	1.129680E+08
227	2 C2H4 ⟷ C4H8-1	1.000000E+07	0.000000E+00	1.673600E+08
228	C3H3 + H ⟷ C3H4-A	3.160000E+26	-5.000000E+00	1.971082E+07
229	C4H6 + O ⟶ C3H6 + CO	1.500000E+09	0.000000E+00	0.000000E+00
230	CH2O + O ⟶ CO2 + 2 H	2.000000E+10	0.000000E+00	2.092000E+07
231	C2H2 + HO2 ⟶ CH2O + HCO	5.000000E+09	0.000000E+00	6.276000E+07
232	CH3O(L1) + CO ⟷ CH3 + CO2	7.706617E+11	-1.023244E+00	3.084203E+07
233	C2H4 + O2 ⟶ 2 CH2O	1.000000E+11	0.000000E+00	2.008320E+08
234	C2H4 + O2 ⟶ CH3O(L1) + HCO	1.000000E+11	0.000000E+00	1.799120E+08
235	C4H6 + O2 ⟶ C2H2 + C2H4 + O2	4.000000E+11	0.000000E+00	1.673600E+08
236	CH2CHO + O2 ⟶ CH2O + CO + OH	6.000000E+07	0.000000E+00	0.000000E+00
237	C2H3 + O ⟶ CH2CHO	2.500000E+10	0.000000E+00	0.000000E+00
238	C3H5-A + O ⟶ C2H3 + CH2O	3.250000E+10	0.000000E+00	0.000000E+00
239	CH2CHO + O ⟶ CH2O + HCO	5.000000E+10	0.000000E+00	0.000000E+00
240	C2H3 + HO2 ⟶ CH2CHO + OH	3.000000E+09	0.000000E+00	0.000000E+00
241	CH2CHO + OH ⟶ CH3O(L1) + HCO	1.000000E+10	0.000000E+00	0.000000E+00
242	C2H2 + OH ⟶ CH2CHO	5.000000E+08	0.000000E+00	0.000000E+00
243	C3H5-A + H (+M) ⟷ C3H6 (+M)	1.330000E+54	-1.200000E+01	2.496928E+07
	Troe coefficients : 2.00E-02 1.10E+03 1.10E+04 6.86E+03	1.000000E+11	0.000000E+00	0.000000E+00
	Species efficiencies : CO:1.5E+00 CO2:2.0E+00 H2O:6.0E+00			
244	H2 + HCCO ⟶ CH2CO + H	5.992000E+02	2.000000E+00	3.224140E+07

No.	Reaction	A	b	E_a
245	C2H2 + O ⟶ C2H + OH	4.700000E+03	2.000000E+00	3.371271E+07
246	C2H4 + O ⟶ C2H3 + OH	1.880000E+04	2.000000E+00	3.371271E+07
247	C3H4-A + O ⟶ C3H3 + OH	1.410000E+05	2.000000E+00	3.371271E+07
248	H2O + HCCO ⟶ CH2CO + OH	4.280000E+02	2.000000E+00	5.421564E+07
249	CH2CO + H ⟶ H2 + HCCO	2.400000E+04	2.000000E+00	3.956340E+07
250	CH2CO + O ⟶ HCCO + OH	1.880000E+04	2.000000E+00	3.371271E+07
251	CH2CO + OH ⟶ H2O + HCCO	1.200000E+07	1.000000E+00	9.656044E+06
252	C4H8-1 + H ⟶ C4H71-3 + H2	1.800000E+04	2.000000E+00	1.836726E+07
253	C4H8-1 + CH3 ⟶ C4H71-3 + CH4	1.800000E+02	2.000000E+00	2.359291E+07
254	NC5H11 ⟶ 0.25 C2H4 + 0.55 C2H5 + 0.55 C3H6 + 0.25 C3H7(L1) + 0.2 C4H8-1 + 0.2 CH3	3.300000E+13	0.000000E+00	1.255200E+08
255	NC5H10 ⟷ C2H5 + C3H5-A	2.000000E+16	0.000000E+00	3.117080E+08
256	NC5H10 ⟷ C4H71-3 + CH3	5.000000E+16	0.000000E+00	3.347200E+08
257	NC5H10 ⟷ C2H3 + C3H7(L1)	1.000000E+17	0.000000E+00	4.142160E+08
258	H + NC5H10 ⟷ NC5H11	2.000000E+10	0.000000E+00	1.046000E+07
259	NC5H11 + O2 ⟶ HO2 + NC5H10	7.500000E+08	0.000000E+00	1.255200E+07
260	C2H5 + C4H8-1 ⟷ CH3 + NC5H10	3.000000E+08	0.000000E+00	3.179840E+07
261	C4H71-3 ⟷ C2H3 + C2H4	1.500000E+13	0.000000E+00	2.092000E+08
262	NC7H14 ⟶ 0.5 C2H5 + 0.5 C3H7(L1) + 0.5 C4H6 + 0.5 C4H71-3 + 0.5 CH3	3.000000E+15	0.000000E+00	3.054320E+08
263	H + NC7H14 ⟷ NC7H15	2.500000E+10	0.000000E+00	1.046000E+07
264	NC7H15 ⟷ C2H4 + NC5H11	6.200000E+12	0.000000E+00	1.255200E+08
265	NC7H15 ⟷ C3H6 + PC4H9	1.420000E+13	0.000000E+00	1.255200E+08
266	NC7H15 ⟷ C3H7(L1) + C4H8-1	7.500000E+12	0.000000E+00	1.255200E+08
267	NC7H15 ⟷ C2H5 + NC5H10	5.600000E+12	0.000000E+00	1.255200E+08
268	NC7H15 + O2 ⟶ HO2 + NC7H14	7.500000E+08	0.000000E+00	1.255200E+07
269	NC12H26 ⟶ 0.5 C2H5 + 0.5 C3H7(L1) + 0.5 NC12H25 + 0.5 NC7H15	2.000000E+17	0.000000E+00	3.409960E+08
270	NC12H26 ⟶ 0.1 NC12H25 + 0.5 NC5H11 + 0.9 NC7H15 + 0.5 PC4H9	2.000000E+17	0.000000E+00	3.409960E+08
271	NC12H25 ⟶ 0.35 C2H4 + 0.75 NC5H10 + 0.25 NC5H11 + 0.15 NC7H14 + 0.75 NC7H15	7.000000E+12	0.000000E+00	1.255200E+08
272	MCYC6 ⟶ 0.7 C3H6 + 0.25 C4H8-1 + 0.45 IC4H8 + 0.3 NC7H14	6.000000E+16	0.000000E+00	3.430880E+08
273	H + NC12H26 ⟶ H2 + NC12H25	6.600000E+04	2.000000E+00	1.673600E+07
274	CH3 + NC12H26 ⟶ CH4 + NC12H25	6.600000E+02	2.000000E+00	2.092000E+07
275	C2H5 + NC12H26 ⟶ C2H6 + NC12H25	4.400000E+02	2.000000E+00	2.803280E+07
276	NC12H26 + O ⟶ NC12H25 + OH	5.170000E+04	2.000000E+00	1.046000E+07
277	NC12H26 + OH ⟶ H2O + NC12H25	3.300000E+07	1.000000E+00	2.092000E+05
278	CH3C6H4 + O2 ⟷ C6H4O2 + CH3	3.000000E+10	0.000000E+00	3.765600E+07
279	XYLENE ⟷ H + RXYLENE	9.000000E+15	0.000000E+00	3.732128E+08
280	XYLENE ⟷ CH3 + CH3C6H4	5.000000E+16	0.000000E+00	4.100320E+08
281	C6H4O2 ⟶ C2H2 + C3H2 + CO2	3.500000E+12	0.000000E+00	2.803280E+08
282	O2 + XYLENE ⟷ HO2 + RXYLENE	3.000000E+11	0.000000E+00	1.732176E+08
283	O + RXYLENE ⟶ CH2O + CH3C6H4	8.000000E+10	0.000000E+00	0.000000E+00
284	HO2 + RXYLENE ⟶ CH2O + CH3C6H4 + OH	1.000000E+10	0.000000E+00	3.347200E+06
285	H + XYLENE ⟶ H2 + RXYLENE	2.000000E+11	0.000000E+00	3.315820E+07
286	CH3 + XYLENE ⟶ CH4 + RXYLENE	3.500000E+09	0.000000E+00	3.701166E+07
287	C6H4O2 + H ⟶ C2H + C2H2 + 2 CO + H2	1.050000E+05	2.000000E+00	4.060802E+07
288	C6H4O2 + O ⟶ C2H + C2H2 + 2 CO + OH	8.225000E+04	2.000000E+00	3.273022E+07
289	C6H4O2 + OH ⟶ C2H + C2H2 + 2 CO + H2O	5.250000E+07	1.000000E+00	1.535691E+07
290	O + XYLENE ⟶ OH + RXYLENE	1.410000E+04	2.000000E+00	1.046000E+07
291	OH + XYLENE ⟶ H2O + RXYLENE	9.000000E+06	1.000000E+00	2.092000E+05

No.	Reaction	A	b	E_a
292	H + XYLENE ⟶ 0.5 C2H4 + CH3C6H4 + H2	2.400000E+04	2.000000E+00	4.166118E+07
293	CH3 + XYLENE ⟶ 0.5 C2H4 + CH3C6H4 + CH4	2.400000E+02	2.000000E+00	4.684628E+07
294	O + XYLENE ⟶ 0.5 C2H4 + CH3C6H4 + OH	1.880000E+04	2.000000E+00	3.371271E+07
295	OH + XYLENE ⟶ 0.5 C2H4 + CH3C6H4 + H2O	1.200000E+07	1.000000E+00	1.602518E+07
296	C6H3 + H ⟷ C6H4	1.000000E+10	0.000000E+00	0.000000E+00
297	C6H2 + H ⟷ C6H3	2.000000E+10	0.000000E+00	8.368000E+06
298	C6H2 + OH ⟶ C2H + C3H2 + CO	2.000000E+10	0.000000E+00	0.000000E+00
299	CH3C6H4 ⟷ C6H4 + CH3	8.000000E+41	-7.720000E+00	3.861845E+08

Appendix E

Global graph analysis decomposition of kerosene

The Table. E.0.1 summarizes the several decomposition pathways encountered in the kerosene decomposition.

These pathways, corresponds a 0-dimensional constant pressure reactor filled with a stoichiometric kerosene-air mixture at $\phi = 1$ and $T_i = 1600\,K$. For each graphs two pressures are represented: $P = 1\,bar$ with the red solid arrows and $P = 0.3\,bar$ with the black dashed arrows. The interactions correspond to percentages of leaving carbon atomic fluxes and are integrated over the whole case.

The second column of Table E.0.1 corresponds to the species fully included to the graph and third column corresponds to species where pathways have been clipped for lisibility.

Pathways	Species fully represented	Species clipped
$nC_{12}H_{26}$	See Sec. 6.2.1	See Sec. 6.2.1
$MCYC_6$	See Sec. 6.2.1	See Sec. 6.2.1
XYLENE	See Sec. 6.2.1	See Sec. 6.2.1
C_4H_6	C_4H_6, C_3H_3, C_4H_5, C_2H_3CHO, HCO, C_4H_4, CO, CO_2	CH_3, C_2H_3, C_2H_4, C_4H_3
C_3H_6	C_3H_6, CH_3, CH_4, C_2H_4, C_3H_5-A, CH_3O, CH_2O, C_2H_6, C_2H_3, C_3H_4-A, C_3H_4-P	C_4H_8-1, HCO, C_2H_5, C_3H_3, CH_2CHO
lC_5H_8	lC_5H_8, C_5H_6, C_5H_7, C_5H_5	CO, C_2H_4, C_2H_2, C_3H_6
pC_4H_9	pC_4H_9, C_2H_5	C_2H_4, CH_3
C_4H_71-4	C_4H_71-4, C_4H_71-3	C_2H_4, C_2H_3, C_4H_6
nC_5H_{11}	nC_5H_{11}, nC_3H_7, C_3H_8, iC_3H_7	C_4H_8-1, C_2H_5, C_3H_6, CH_3, C_2H_4
C_6H_5	C_6H_5, $C_6H_4O_2$, C_6H_5O, C_2H, CYC_5H_4O, C_4H_3, C_4H_2, C_3H_2, C_2H_2	CO, C_5H_5, HCCO, C_4H_5 , HCO
CH_2CHO	CH_2CHO, HCCO, CO_2, CO, CH_2(S), CH_2, CH, C_2H_3O1-2, C, CH_3CO, CH_2CO	CH_3

Table E.0.1: Summary of the different pathways of kerosene decomposition in a constant pressure reactor with a stoichiometric mixture initially at $T_i = 1600\,K$.

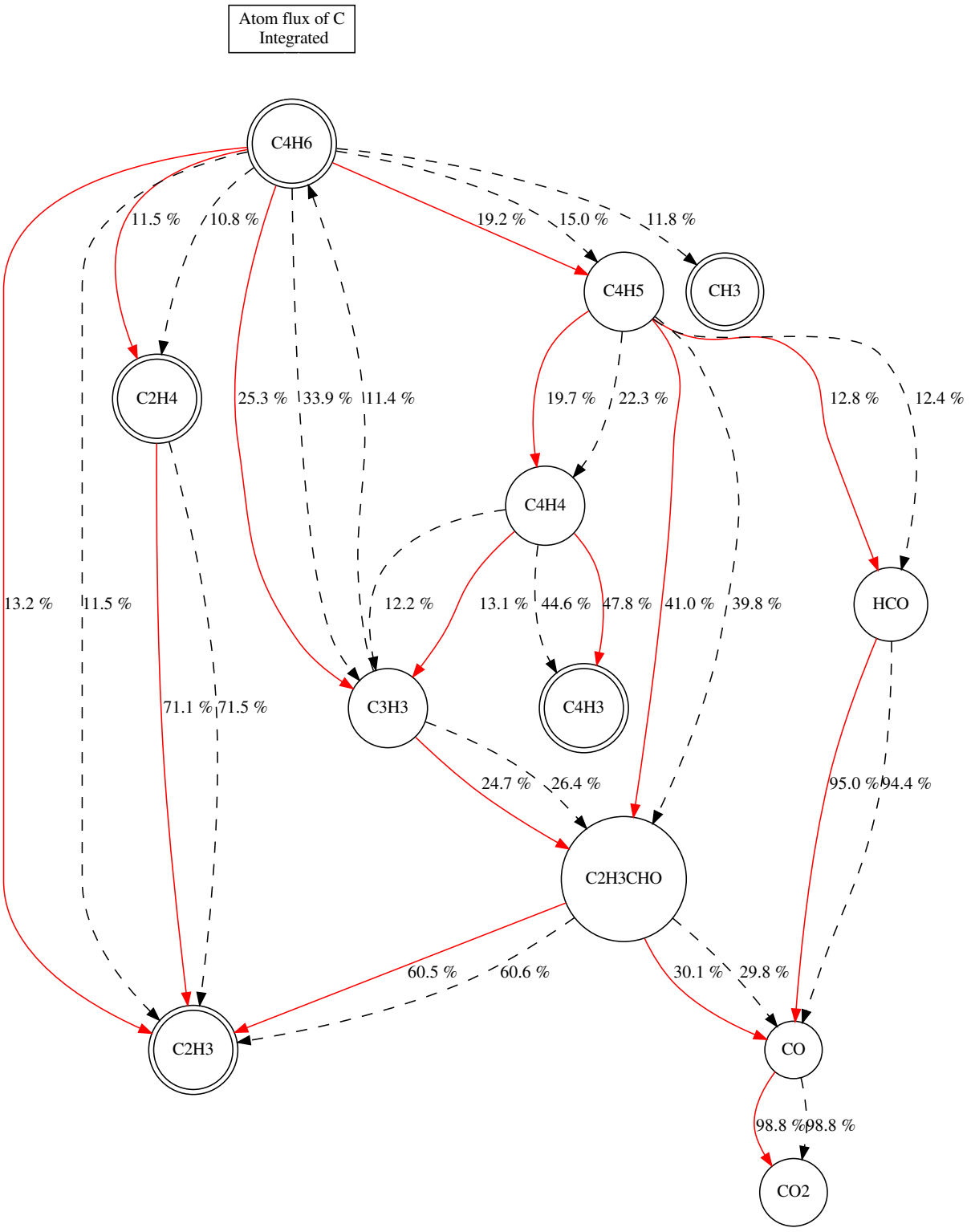

Figure E.0.1: Carbon flux graph starting with C_4H_6 in a zero-dimensional reactor filled with stoichiometric mixture at initial temperature $T_i = 1600\,K$. Red solid line: $P = 1\,bar$, black dashed line: $P = 0.3\,bar$.

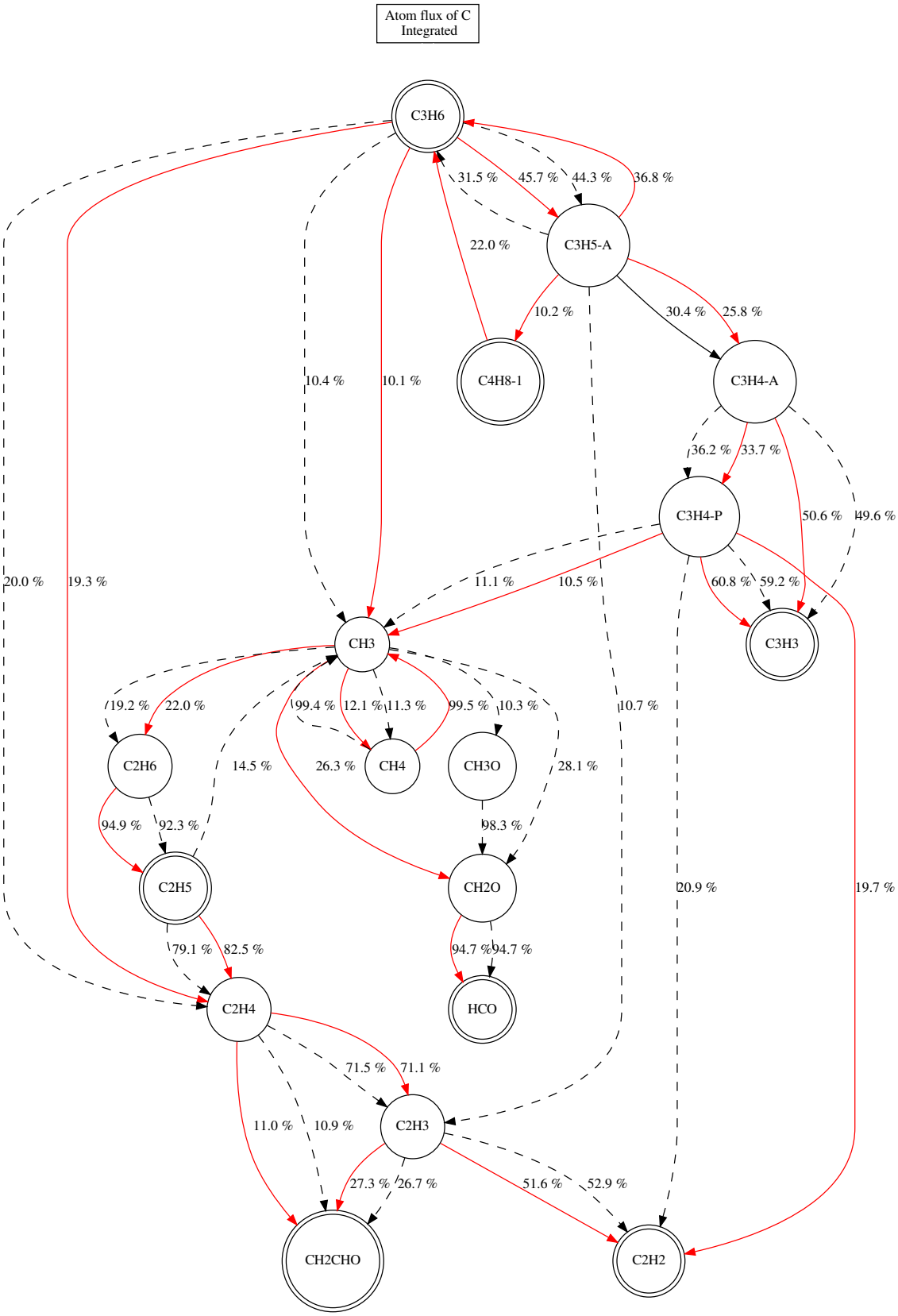

Figure E.0.2: Carbon flux graph starting with C_3H_6 in a zero-dimensional reactor filled with stoichiometric mixture at initial temperature $T_i = 1600\,K$. Red solid line: $P = 1\,bar$, black dashed line: $P = 0.3\,bar$.

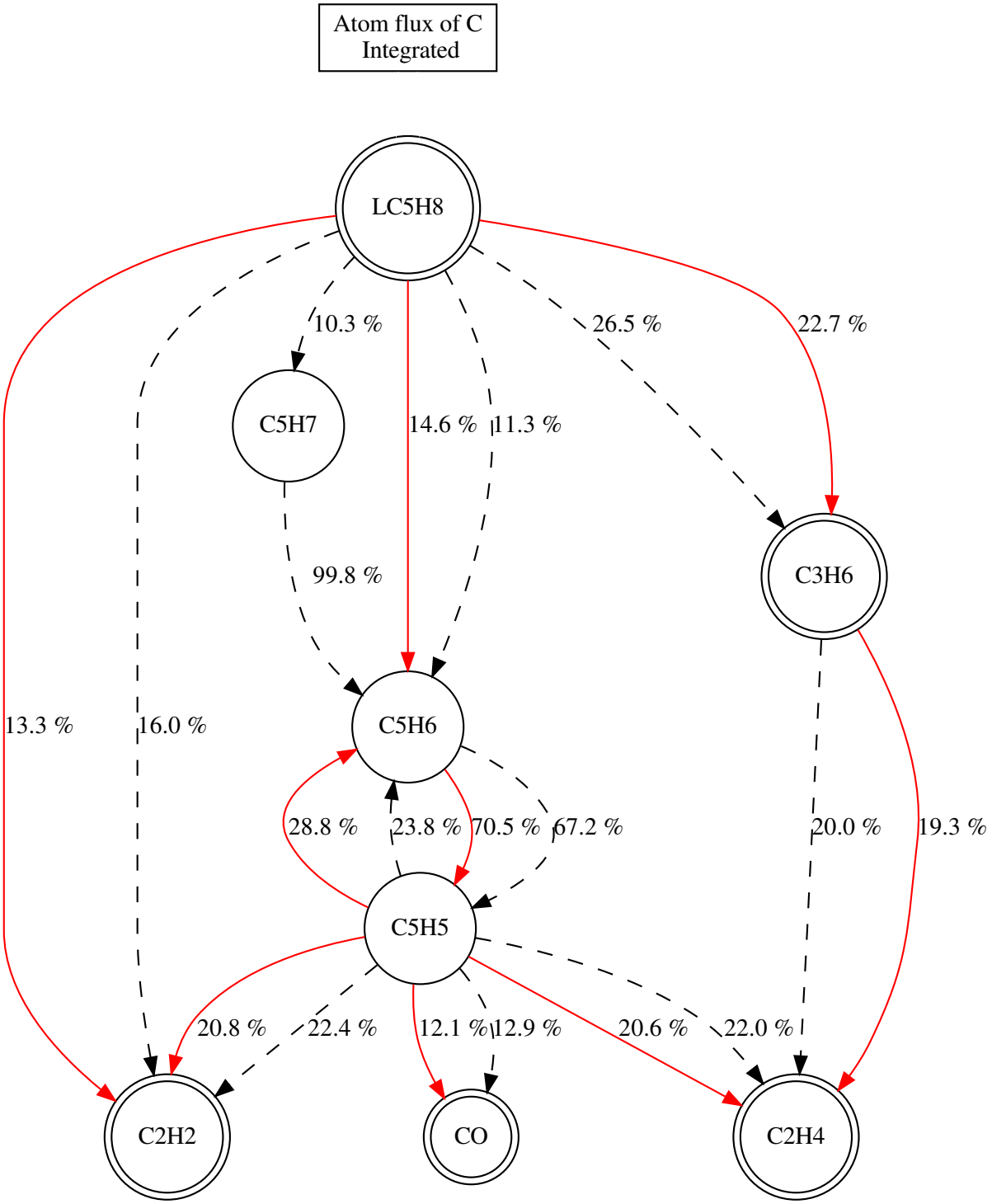

Figure E.0.3: Carbon flux graph starting with lC_5H_8 in a zero-dimensional reactor filled with stoichiometric mixture at initial temperature $T_i = 1600\,K$. Red solid line: $P = 1\,bar$, black dashed line: $P = 0.3\,bar$.

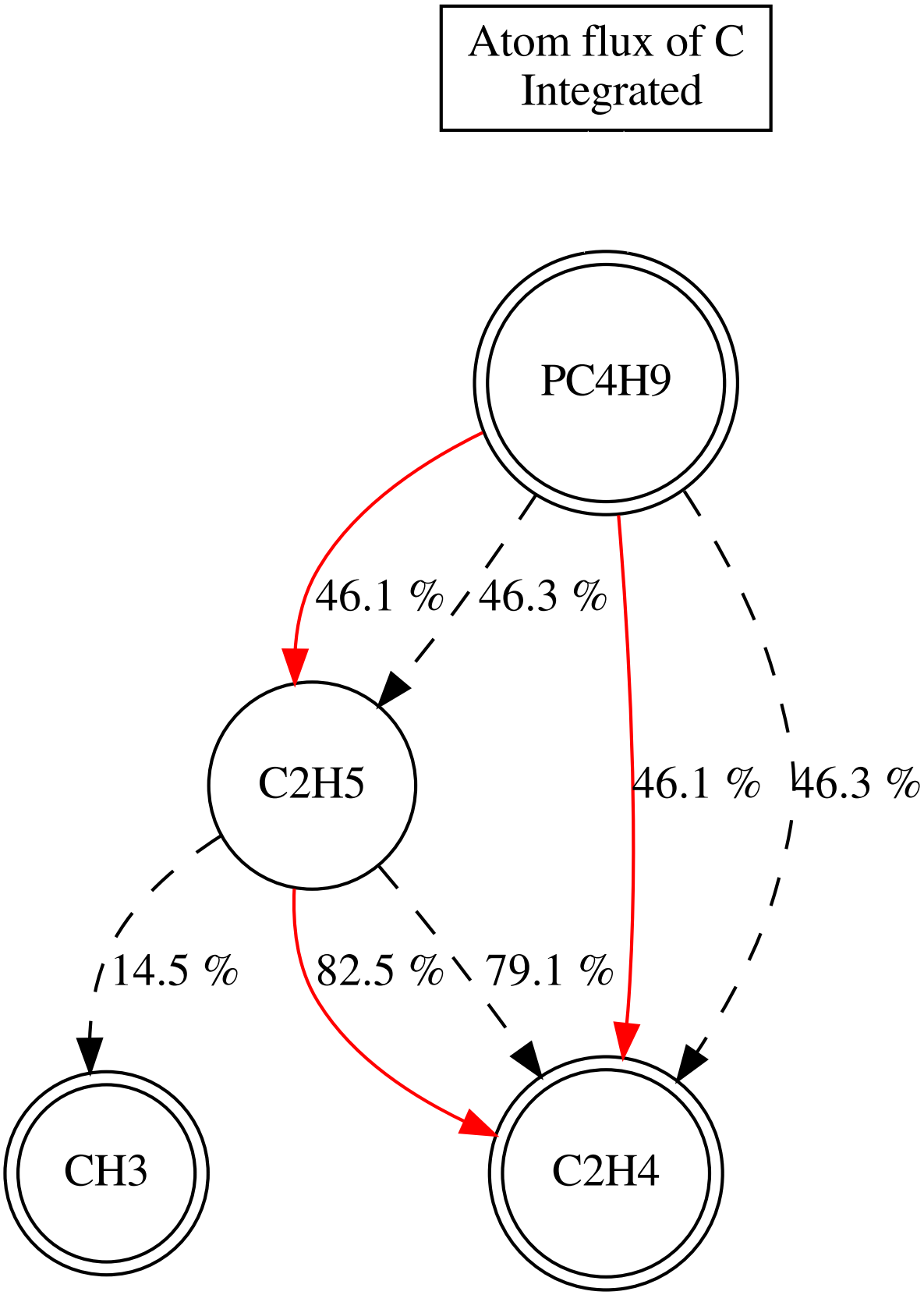

Figure E.0.4: Carbon flux graph starting with pC_4H_9 in a zero-dimensional reactor filled with stoichiometric mixture at initial temperature $T_i = 1600\,K$. Red solid line: $P = 1\,bar$, black dashed line: $P = 0.3\,bar$.

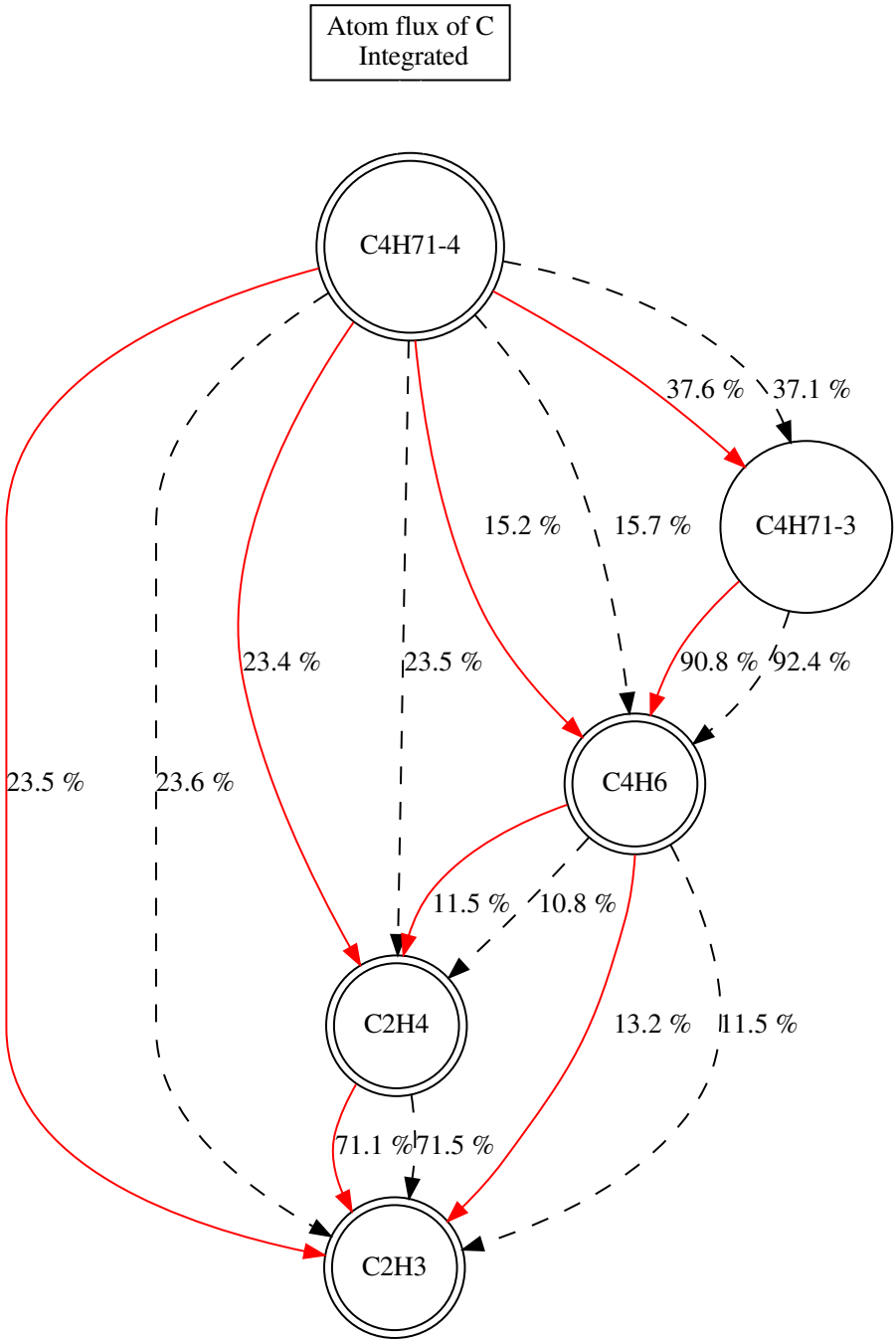

Figure E.0.5: Carbon flux graph starting with $C_4H_7$1-4 in a zero-dimensional reactor filled with stoichiometric mixture at initial temperature $T_i = 1600\,K$. Red solid line: $P = 1\,bar$, black dashed line: $P = 0.3\,bar$.

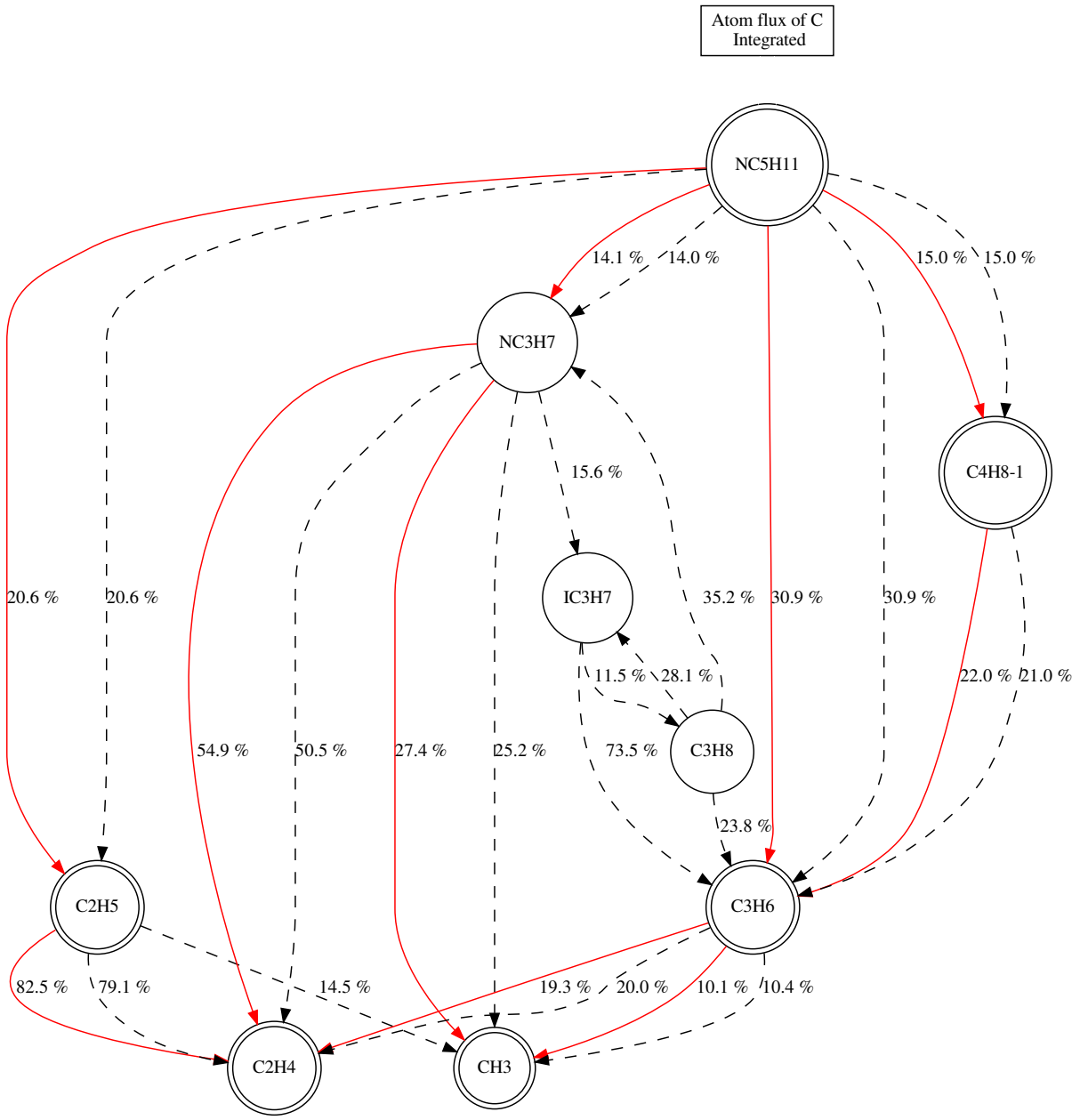

Figure E.0.6: Carbon flux graph starting with nC_5H_{11} in a zero-dimensional reactor filled with stoichiometric mixture at initial temperature $T_i = 1600\,K$. Red solid line: $P = 1\,bar$, black dashed line: $P = 0.3\,bar$.

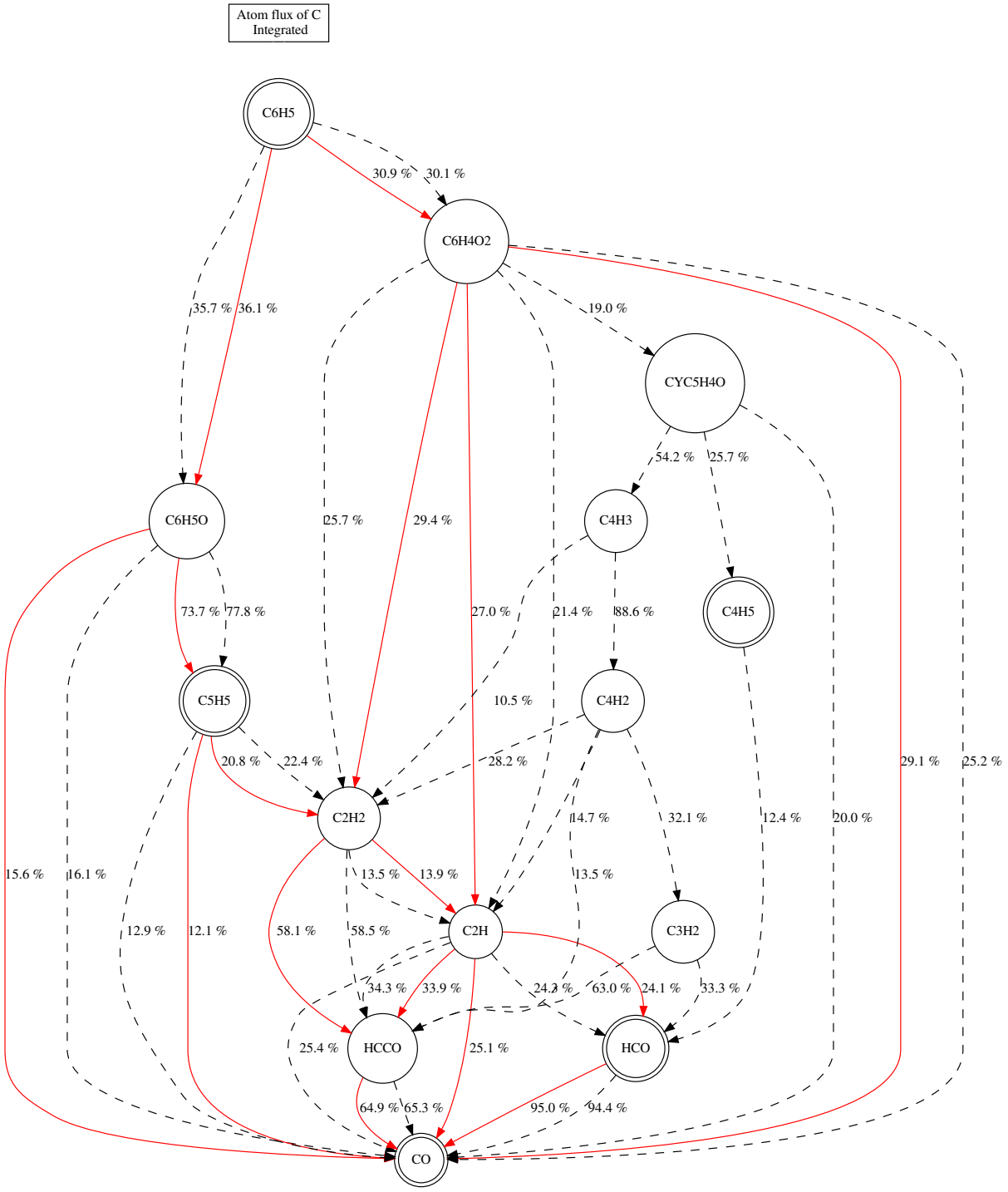

Figure E.0.7: Carbon flux graph starting with C_6H_5 in a zero-dimensional reactor filled with stoichiometric mixture at initial temperature $T_i = 1600\,K$. Red solid line: $P = 1\,bar$, black dashed line: $P = 0.3\,bar$.

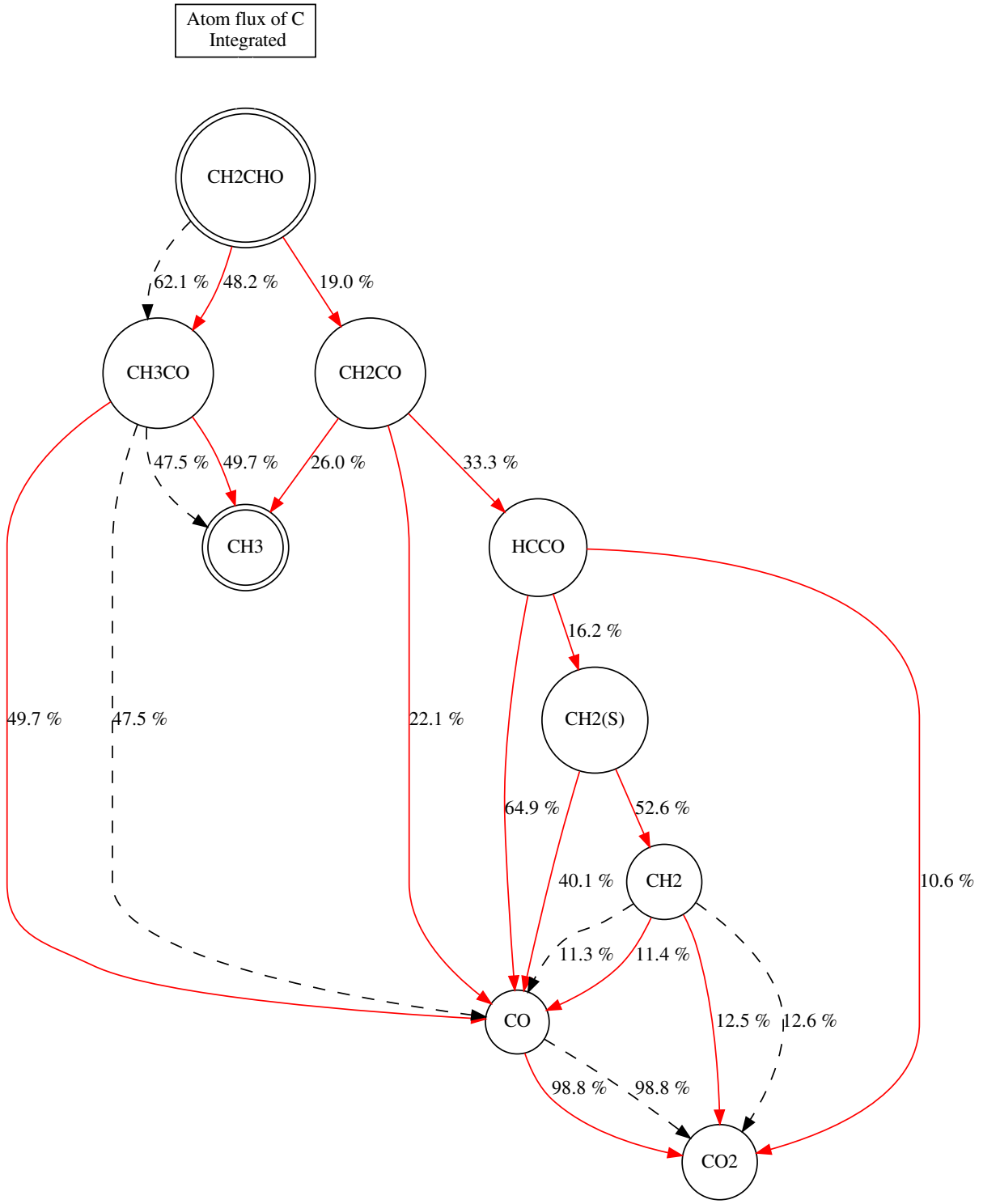

Figure E.0.8: Carbon flux graph starting with CH_2CHO in a zero-dimensional reactor filled with stoichiometric mixture at initial temperature $T_i = 1600\,K$. Red solid line: $P = 1\,bar$, black dashed line: $P = 0.3\,bar$.

Appendix F

Exponential chemistry integration

F.1 Theoretical derivation for first order species

The exponential integration is strictly valid only if all reactions are elementary reactions with unity stoichiometric coefficients for the reactants i.e. for first order species concentration temporal variations which is different than the reaction rate order. For example, the simplified reaction system with (R1) and (R2) is composed of second order reactions as shown with the expression of the reaction progress rates Eq. (F.1) and (F.2).

$$\mathrm{A} + \mathrm{B} \rightarrow \mathrm{C} \tag{R1}$$

$$\mathrm{C} + \mathrm{D} \rightarrow \mathrm{E} \tag{R2}$$

$$\mathcal{Q}_1 = K_1 \times [\mathrm{A}] \times [\mathrm{B}] \tag{F.1}$$

$$\mathcal{Q}_2 = K_2 \times [\mathrm{C}] \times [\mathrm{D}] \tag{F.2}$$

On the contrary, the species temporal variations Eq. (F.3) and (F.4) correspond to first order differential equations. The evolution of species E concentration Eq. (F.5) is a 0-order which is a special case of first-order equations and therefore fits in the framework given.

$$\frac{dc_\mathrm{A}}{dt} = -W_\mathrm{A}\mathcal{Q}_1 = \underbrace{0}_{B_\mathrm{A}} \underbrace{-W_\mathrm{A}K_1[\mathrm{A}][\mathrm{B}]}_{A_\mathrm{A}c_\mathrm{A}} \tag{F.3}$$

$$\frac{dc_\mathrm{C}}{dt} = W_\mathrm{C}(\mathcal{Q}_1 - \mathcal{Q}_2) = \underbrace{W_\mathrm{C}K_1[\mathrm{A}][\mathrm{B}]}_{B_\mathrm{C}} \underbrace{-W_\mathrm{C}K_2[\mathrm{C}][\mathrm{D}]}_{A_\mathrm{C}c_\mathrm{C}} \tag{F.4}$$

$$\frac{dc_\mathrm{E}}{dt} = W_\mathrm{E}\mathcal{Q}_2 = \underbrace{W_\mathrm{E}K_2[\mathrm{C}][\mathrm{D}]}_{B_\mathrm{E}} \underbrace{-0}_{A_\mathrm{E}c_\mathrm{E}} \tag{F.5}$$

A second order differential equation is required for reactions of the form (R3). Indeed, in this case, the evolution of the species F corresponds to Eq. (F.6). However, the analytical solution is more complex [Blanchard 2021] and does not ensure the positivity of the concentrations. In the chemical schemes, such reactions are rare. Therefore, using a first order approximation is supposed to have a limited influence on the results.

$$\mathrm{F} + \mathrm{F} \rightarrow \mathrm{G} \tag{R3}$$

$$\frac{dc_\mathrm{F}}{dt} = -W_\mathrm{F}K_3[\mathrm{F}]^2 \tag{F.6}$$

F.2 Exemple of non-conservativity

In the case of classical explicit chemistry integration, the species production rates are directly computed from the progress rates and the reactions are balanced with the stoichiometric coefficients. Therefore, the species temporal evolution is fully conservative: $\sum_{k=1}^{N_{spec}} \dot{\omega}_k = 0$.

In the case of the exponential chemistry integration, the consumption and production processes are not symmetric due to the exponential term. Indeed, taking the example of reaction (R4) with the species H

purely consumed, and the species I purely produced, the asymptotic developments Eq. (8.15) and (8.16) give:

$$c_{\mathrm{H}}^{n+1} = c_{\mathrm{H}}^{n} \times \exp\left(\frac{\dot{\omega}_{\mathrm{H}}^{n}}{c_{\mathrm{H}}^{n}}\Delta t\right) \tag{F.7}$$

$$c_{\mathrm{I}}^{n+1} = c_{\mathrm{I}}^{n} + \dot{\omega}_{\mathrm{I}}^{n} \times \Delta t \tag{F.8}$$

with

$$\dot{\omega}_{\mathrm{I}}^{n} = -\dot{\omega}_{\mathrm{H}}^{n} \quad \text{and} \quad \sum_{k=1}^{N_{spec}} \dot{\omega}_{k} = 0 \tag{F.9}$$

Yet, after reconstruction of the exponential integration with Eq. (8.12), the production rates write:

$$\dot{\omega}_{\mathrm{I},expo}^{n} = \frac{c_{\mathrm{I}}^{n+1} - c_{\mathrm{I}}^{n}}{\Delta t} = \dot{\omega}_{\mathrm{I}}^{n} \tag{F.10}$$

and

$$\dot{\omega}_{\mathrm{H},expo}^{n} = \frac{c_{\mathrm{H}}^{n+1} - c_{\mathrm{H}}^{n}}{\Delta t} = \frac{c_{\mathrm{H}}^{n}}{\Delta t}\left[\exp\left(\frac{\dot{\omega}_{\mathrm{H}}^{n}}{c_{\mathrm{H}}^{n}}\Delta t\right) - 1\right] \neq \dot{\omega}_{\mathrm{H}}^{n} \tag{F.11}$$

Therefore the exponential integration is not mass conservative: $\sum_{k=1}^{N_{spec}} \dot{\omega}_{k,expo} \neq 0$. One can note that $\dot{\omega}_{\mathrm{H},expo}^{n}$ approaches $\dot{\omega}_{\mathrm{H}}^{n}$ when the time-step goes to zero.

Appendix G

The DNS code NTMIX

The code NTMIX [Baum 1994] is an academical solver designed for very accurate DNS in simplified geometries. This code written in Fortran is relatively light (compared to AVBP), and thus, more accessible for model developments and validations. NTMIX is currently developed and used by the CERFACS and Melbourne University (UoM).

G.1 General features

NTMIX solves the Navier-Stokes compressible equations presented Sec. 1.1 with the reactive multi-species formulation. The energy conservation equation is based on the total chemical energy e_t. The resulting energy conservation equation is slightly different from Eq. (1.26) :

$$\frac{\partial \rho e_t}{\partial t} + \frac{\partial \rho e_t u_j}{\partial x_j} = -\frac{\partial q_j}{\partial x_j} - \frac{\partial u_i P \delta_{ij}}{\partial x_j} + \frac{\partial u_i \tau_{ij}}{\partial x_j} + \dot{\mathcal{Q}} \tag{G.1}$$

with the energy flux due to species and heat diffusion that writes :

$$q_j = -\lambda \frac{\partial T}{\partial x_j} + \rho \sum_{k=1}^{N_{spec}} V_{j,k} Y_k (h_{s,k} + \Delta h^0_{f,k}) \tag{G.2}$$

The thermodynamic and transport properties are managed by a CHEMKIN library [Reaction-Design 2015] based on the species properties given in the chemical scheme. To avoid the high numerical cost required to solve the exact diffusion velocities Eq. (1.28)(linear system of size ${N_{spec}}^2$ for the three directions at each node and each iteration), but conserving the accuracy required, the mixture-averaged transport model presented Sec. 1.1.3 is used.

The chemical kinetic can be either directly computed with CHEMKIN, or using dynamic Fortran library files written by ARCANE.

The conservation equations are numerically solved using centered finite difference schemes of order 6 and 8 presented Sec. 1.2.1. Moreover, the time integration is performed using a three-step Runge-Kutta scheme. The solvers using such high order numerical methods are prone to numerical instabilities due to the dispersion errors of unresolved high frequency phenomena. To avoid that, a high frequency filter of order 6 to 10 [Kennedy and Carpenter 1997] can be applied.

The computational domain is discretized using a cartesian structured grid that enables an easy implementation of the high order numerical schemes with large stencils. However, it limits the use to simplified rectangular cuboid geometries. The solver is based on a vertex formulation where the conservative variables and fluxes are saved and computed at the node. This domain is automatically partitioned using the MPI framework.

Finally, the code is dimensionless[1]. The scaling is done using a reference state at the initialization. The detailed procedure is given in [Baum 1994].

[1] except for CHEMKIN that uses the CGS unit system

G.2 Developments during the PhD

During this PhD a lot of modifications have been brought to the code. Initially, the code was based on compact numerical schemes [Baum 1994]. For multi-processing computations, this approach required overlapping domain regions and was efficient only with a limited number of cores. Due to the recent technological advances in computing power, the need for a massively parallel approach in CFD solvers is required. Hence, the compact schemes have been replaced by classical finite differences schemes using MPI buffers communications. This work has been done before the PhD, but several validation tests and corrections have been required before getting a stable version :

- Tests of the numerical schemes using waves convection and diffusion (See [Pestre 2018])
- Correction of MPI communications for periodic boundary conditions (See [Pestre 2018])
- Corrections on buffer communication system for filtering
- Correction of the decentred numerical schemes at boundary conditions.
- Correction of the NSCBC implementation Baum et al. [1995] (See [Vinot 2020])
- Correction of the HIT initialization. The method is detailed in Chap. 9.
- Improvement of the post-processing tool to be able to read large output files.
- Correction of the restart procedure.
- General cleaning of the code

Furthermore, several features have been added to the code :

- Implementation of an energy deposition model. The method is detailed in Chap. 9.
- Implementation of the ARC formalism enabling to use the reduced chemistries derived with ARCANE.
- Implementation of temporal minimum, maximum, mean quantities evolution outputs.
- Implementation of the Exponential Chemistry formalism. The method is presented Sec. 8.2.
- Implementation of the Local and Dynamical Sub-Cycling (LDSC) procedure. The method is presented Sec. 8.3.
- Implementation of additional Fourier criterion numbers associated to thermal and species diffusion.

Finally, modifications associated to the code performances are currently applied :

- Computation of the diffusion terms :
  Based on Eq. (1.25), (1.29) and (1.31), the species conservation equation requires to compute the diffusion species flux which writes :

$$-\frac{\partial}{\partial x_j}(\rho V_{j,k} Y_k) = -\frac{\partial}{\partial x_j}\left[\rho X_k \frac{W_k}{W}\left(-\frac{D_k}{X_k}\frac{\partial X_k}{\partial x_j} + \frac{1}{W}\sum_{k=1}^{N_{spec}} D_k W_k \frac{\partial X_k}{\partial x_j}\right)\right] \tag{G.3}$$

  Eq. (G.3) corresponds to the conservative formulation. For its computation, a first MPI buffer exchange in needed for X_k. Then, the bracket expression is computed and a second buffer exchange is required to compute the full derivative. Thus, the use the conservative expression requires two buffer exchanges.

On the contrary, using the non-conservative formulation Eq. (G.4) developing the derivatives, only one MPI buffer exchange is required including X_k and $\rho D_k W_k/W$.

$$
\begin{aligned}
-\frac{\partial}{\partial x_j}(\rho V_{j,k} Y_k) = & \frac{\partial}{\partial x_j}\left(\rho D_k \frac{W_k}{W}\right) \times \frac{\partial X_k}{\partial x_j} + \rho D_k \frac{W_k}{W} \times \frac{\partial^2 X_k}{\partial x_j^2} \\
& - \sum_{k=1}^{N_{spec}} \left(\rho D_k \frac{W_k}{W} \frac{\partial X_k}{\partial x_j}\right) \times \frac{\partial Y_k}{\partial x_j} \\
& - Y_k \sum_{k=1}^{N_{spec}} \left[\frac{\partial}{\partial x_j}\left(\rho D_k \frac{W_k}{W}\right) \times \frac{\partial X_k}{\partial x_j} + \rho D_k \frac{W_k}{W} \times \frac{\partial^2 X_k}{\partial x_j^2}\right]
\end{aligned}
\tag{G.4}
$$

It has been observed that the non-conservative formulation was less stable and required lower time-steps due to aliasing errors. Furthermore, there are four derivatives to compute instead of two for the conservative formulation. However, for NTMIX, the buffer communications can still be optimized[2]. Then, it has been measured that, even with a smaller time-step, the non-conservative method enables to reduce the CPU-time by 10%.

Possible area of further improvements would be to reduce the aliasing errors using skew-symmetric formulations that correspond to a linear combination of conservative and non-conservative formulations [Kennedy and Gruber 2008]. It still would require two buffer exchanges but if the time-steps are reduced and the buffer communications optimized, the global CPU-cost could decrease.

- CHEMKIN library :
  The CHEMKIN library used by the code dates from 1995 and could be optimized. This work has been done by Mohsen's research group from Melbourn University (UoM) and is currently merged with our own code version.

In addition to the performance optimizations already mentioned, further developments are considered in NTMIX :

- Input/Output parallelization.
- Development of immersed boundary methods to study more complex geometries.
- Two-phase flow computations.

G.3 Mini-Symposium on Verification and Validation of Combustion DNS

NTMIX has been evaluated and compared to AVBP [Schönfeld and Rudgyard 1999] and JAGUAR which is another high order solver based on spectral difference methods [Marchal et al. 2021]. This evaluation has been performed in the context of the Mini-Symposium on Verification and Validation of Combustion DNS [Abdelsamie et al. 2018] and presented at the 17th International Conference on Numerical Combustion (ICNC 2019), the objective being to compare and validate the solvers and their numerical methods with each other. The main results are presented in this section.

G.3.1 2-dimensional cold flow

The benchmark is based on the periodic Taylor-Green Vortex (TGV) configuration already used in several benchmarks like the International Workshop on High-Order CFD Methods [Wang et al. 2013]. In the 2-dimensional case, the TGV is initialized with the following initial velocity field [Abdelsamie et al. 2016] :

$$
u_x(x, y, t = 0) = U_0 \times sin\left(\frac{2\pi x}{L}\right) \times cos\left(\frac{2\pi y}{L}\right) \tag{G.5}
$$

[2]The buffers used in NTMIX have a fixed size. Then, the second buffer exchange in the conservative formulation sends useless information. A buffer of size $\rho V_{j,k} Y_k$ is expected to largely reduce the communication cost.

$$u_y(x,y,t=0) = -U_0 \times cos\left(\frac{2\pi x}{L}\right) \times sin\left(\frac{2\pi y}{L}\right) \tag{G.6}$$

with L the domain length and U_0 the intensity of the velocity field.

In the 2-dimensional case, the viscous analytical solution corresponds to the attenuation of the vortexes due to the momentum diffusion and writes :

$$u_x(x,y,t) = u_x(x,y,t=0) \times exp\left(\frac{-8\pi^2\nu t}{L^2}\right) \tag{G.7}$$

$$u_y(x,y,t) = u_y(x,y,t=0) \times exp\left(\frac{-8\pi^2\nu t}{L^2}\right) \tag{G.8}$$

with ν the cinematic viscosity of the mixture.

It has been observed that compressible solvers require also the initialization of the pressure field. A constant pressure field is not solution of the momentum conservation equations. Thus, the solver will progressively try to converge towards a physical solution which modifies the velocity fields and then creates errors compared to the analytical solution. To avoid this a more physical pressure field is derived from the velocity field solving the momentum equation with steady state and inviscid assumptions. The resulting pressure field obtained writes :

$$P(x,y,t=0) = \frac{\rho_0 {U_0}^2}{4} \times [cos(4\pi x) + cos(4\pi y)] + P_0 \tag{G.9}$$

with ρ_0 and P_0 respectively the reference pressure and density.

Fig. G.3.1 shows the error profile at the center line for NTMIX, AVBP and JAGUAR. For the three solvers, the error computed with Eq. (G.10) is very small. Moreover, the profiles show the influence of the numerical scheme precision order. AVBP has a third order scheme with TTGC if used on cartesian grids [Martin 2021], while JAGUAR uses a fourth order polynomial reconstruction leading to a global fifth order scheme, and NTMIX has a eight order scheme.

$$\mathcal{E}(x) = \frac{u_{x,th}(x) - u_{x,num}(x)}{max(|u_{x,th}(x)|)} \tag{G.10}$$

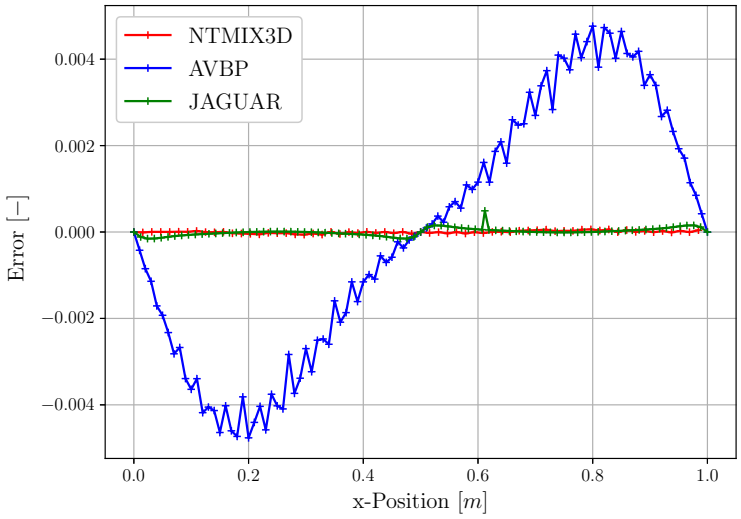

Figure G.3.1: u_x error profile evaluated for several solvers at $y = 0.5L$.

G.3.2 3-dimensional cold flow

The 3-dimensional case is an extension of the 2-dimensional case with a cosine modulation on the third direction :

$$\vec{u}(x, y, z, t = 0) = \vec{u}_{2D}(x, y, z, t = 0) \times cos(2\pi z) \tag{G.11}$$

A representation of the initial z-vorticity component is given on the right picture in Fig. G.3.2.

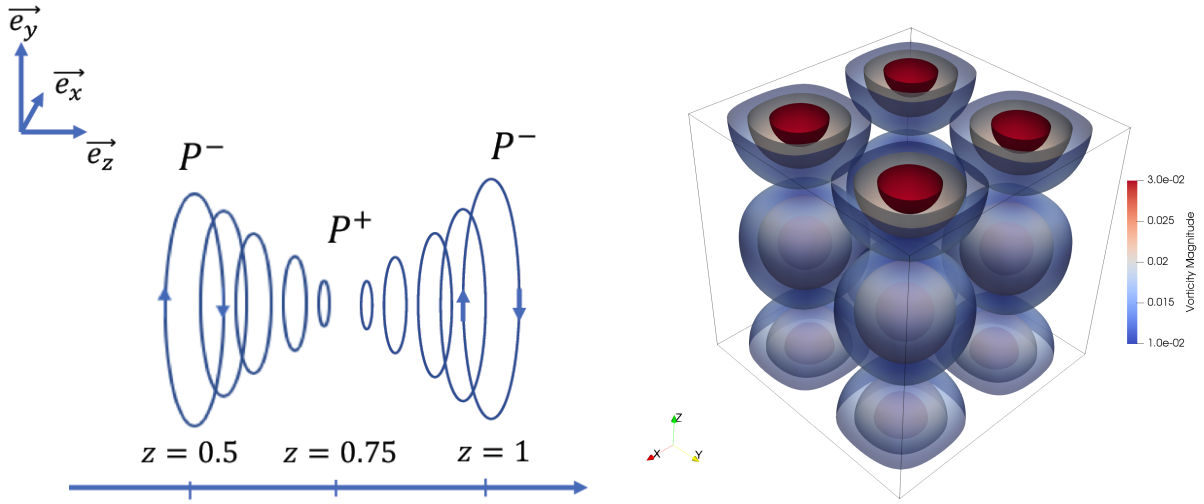

Figure G.3.2: Left : Scheme representation of the vortexes. Right : z-vorticity iso-surfaces at initialization (non-dimensionalized).

Contrarily to the 2-dimensional case, there is no stable physical pressure field compatible with this velocity initialization. Indeed, the pressure field obtained using the two first components of the velocity is given Eq. (G.12) and does not correspond to a pressure gradient equal to zero in the z-direction.

$$P(x, y, z, t = 0) = \underbrace{\frac{\rho_0 {U_0}^2}{4}[cos(4\pi x) + cos(4\pi y)]}_{P_{2D,pert}(x,y,t=0)} \times \underbrace{\frac{1}{2}[cos(4\pi z) + 1]}_{\text{Intensity z-modulation}} + P_0 \tag{G.12}$$

The pressure modulation shown on the left picture of Fig. G.3.2 caused by the variation of the vortexes strengths will create a pressure gradient in the third direction. Therefore, this mechanism induces a flow in the z-direction making the structure unstable. As shown on Fig. G.3.3, the vortexes start to roll-up, then the structure breakdowns and leads to a turbulent-like field, and finally, this turbulence decays because of viscosity.

For this second test-case, the temporal evolution of turbulent kinetic energy $E_{turb} = 1/2 \times (u_x'^2 + u_y'^2 + u_z'^2)$ and dissipation rate ϵ (Eq. (1.53)) have shown similar evolutions between NTMIX, AVBP and JAGUAR.

G.3.3 3-dimensional diffusion

To evaluate the diffusion, hyperbolic tangent profiles of H_2, O_2 and temperature are added to the flow field. These profiles aim to represent a double hydrogen-air diffusion flame front, but chemical reactions are deactivated. The resulting initial fields are presented on Fig. G.3.4.

This case enables to evaluate the computation of the diffusion terms. The comparison of the diffusion profiles on Fig. G.3.5 between NTMIX, AVBP and the reference [Abdelsamie et al. 2016] provides an overall good agreement. However, some discrepancies can be observed due to the transport modeling approach used. Indeed, NTMIX is based on a mixture averaged model while AVBP and the reference use a simplified transport model with fixed species Lewis numbers. Hence, this result shows the importance of the transport model in DNS.

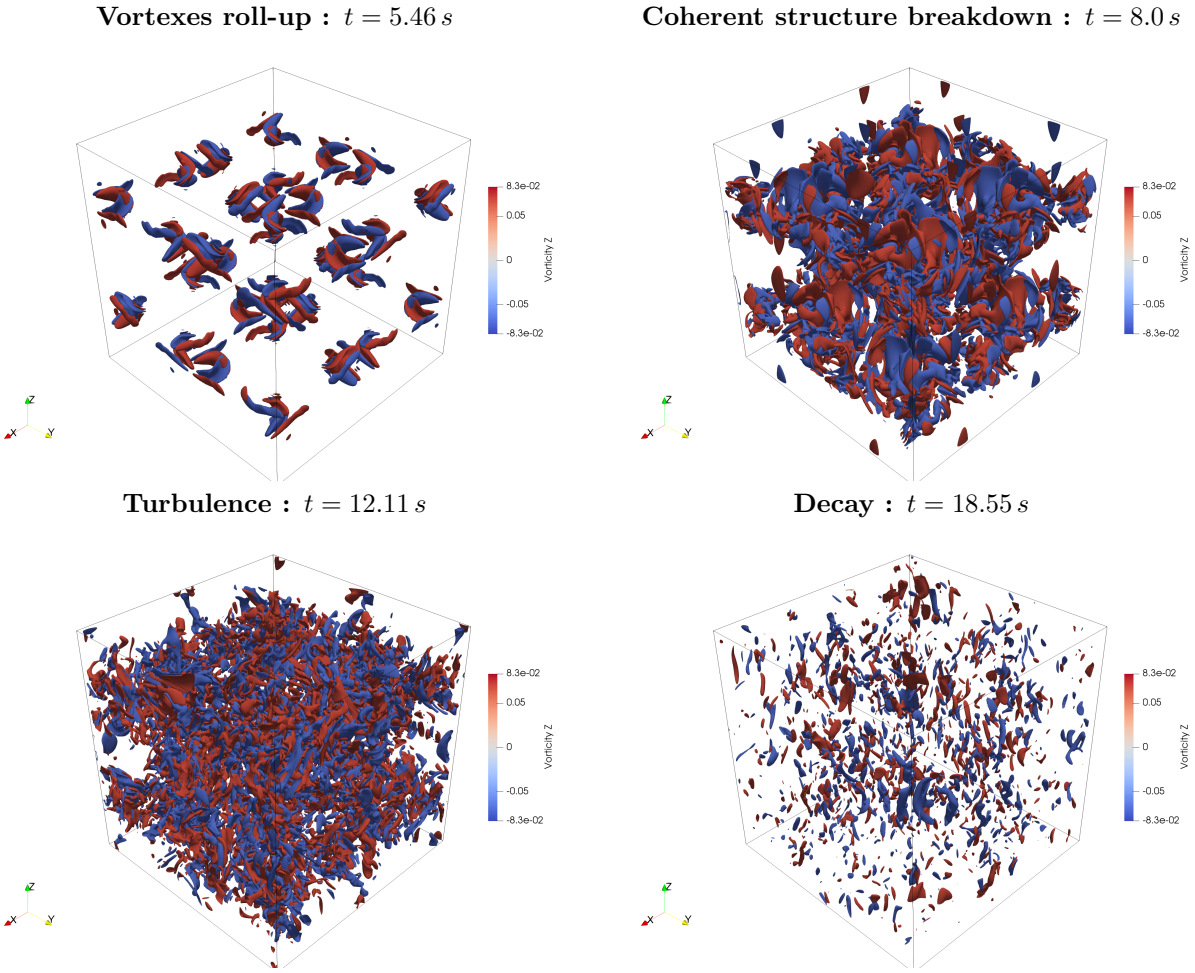

Figure G.3.3: Evolution of the z-vorticity iso-surfaces (non-dimensionalized)

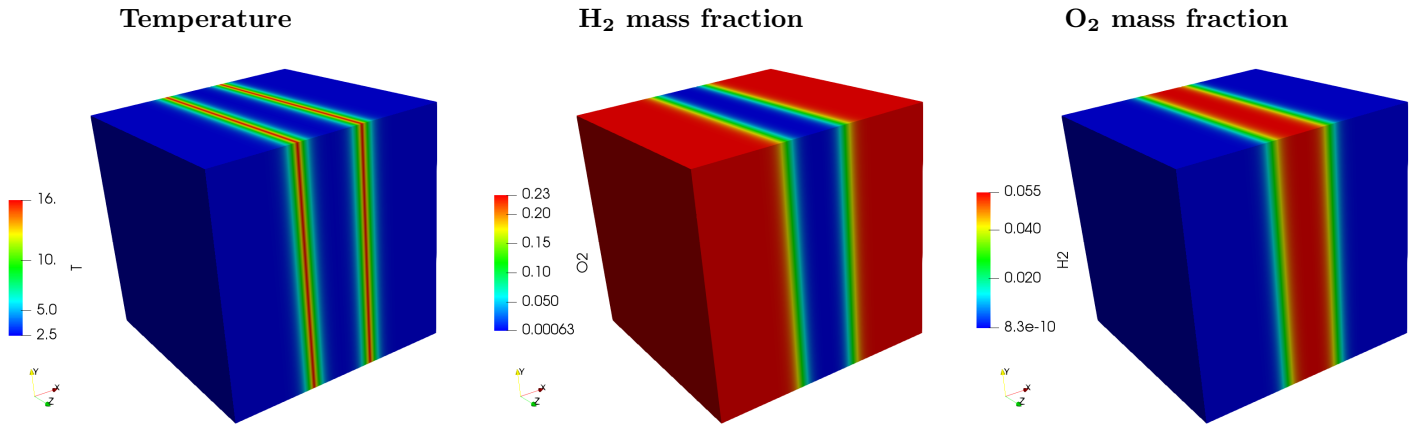

Figure G.3.4: Initialization of temperature (non-dimensionalized), H_2 mass fraction and O_2 mass fraction fields.

G.3.4 3-dimensional reacting DNS

Finally, the last configuration of the benchmark corresponds to the reactive case. The initial set-up is similar to the diffusion case but with the chemical reactions activated and flame profiles extracted from CANTERA. The reaction scheme is the one developed by Boivin et al. [2011].

Fig. G.3.6 shows the temporal evolution of the maximum temperature in the domains for NTMIX,

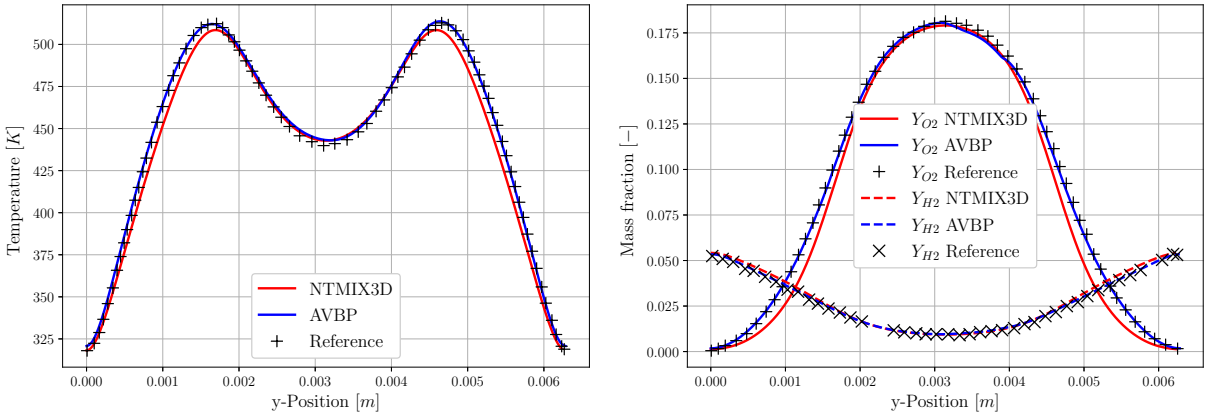

Figure G.3.5: Temperature, H_2 mass fraction and O_2 mass fraction diffusion profiles at $t = 0.5\,ms$, $x = 0.5L$ and $z = 0.5L$.

AVBP and the reference. While NTMIX and AVBP provide similar evolutions, the maximum temperature with the reference simulation is several hundreds kelvins lower. After discussions with the author of the reference simulation, it seems they had forgotten to take into account the pressure increase due to combustion in the energy conservation equation of their incompressible solver. Additional qualitative result visualizations of the end of the computation ($t = 2\,ms$) are displayed on Fig. G.3.7.

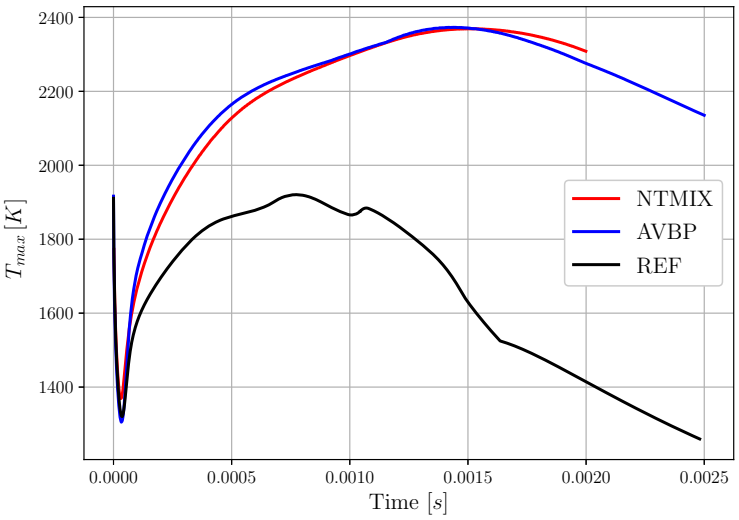

Figure G.3.6: Temporal evolution of the maximum temperature in the domain.

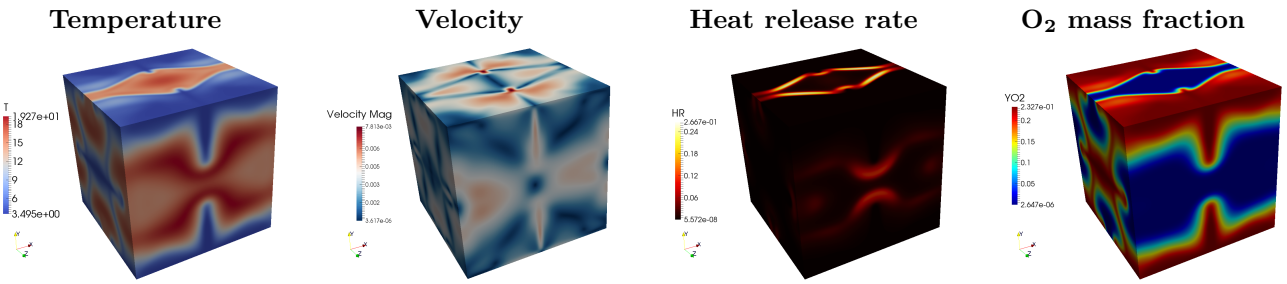

Figure G.3.7: Visualizations of the temperature, velocity magnitude, heat release rate and O_2 mass fraction fields at $t = 2\,ms$ in the reactive test case (non-dimensionalized).

G.4 Initialization of a Homogeneous Isotropic Turbulent (HIT) velocity field

The initial HIT field is generated from a synthetic energy spectrum through inverse Fourier transforms. Key information of the turbulence initialization in NTMIX are summarized in the following, interested readers are referred to [Boughanem and A. 1996] for demonstrations, detailed computations and validations.

The velocity field u_i is linked to the spectral velocities $\hat{u}_i$ through inverse Fourier transforms :

$$u_i(\overrightarrow{x}) = \sum_{\overrightarrow{k}} \hat{u}_i(\overrightarrow{k}) \exp\left(j\overrightarrow{k}.\overrightarrow{x}\right) \qquad i = x, y, z \quad \text{and} \quad j^2 = -1 \tag{G.13}$$

with $\overrightarrow{k}$ the wave vector and $\overrightarrow{x}$ the position vector. The components of the wave vector writes :

$$\overrightarrow{k} = k_x\overrightarrow{e_x} + k_y\overrightarrow{e_y} + k_z\overrightarrow{e_z} \tag{G.14}$$

$$k_x = \frac{2\pi n_x}{L_x} \qquad -\frac{N_x}{2} + 1 \leq n_x \leq \frac{N_x}{2} \tag{G.15}$$

$$k_y = \frac{2\pi n_y}{L_y} \qquad -\frac{N_y}{2} + 1 \leq n_y \leq \frac{N_y}{2} \tag{G.16}$$

$$k_z = \frac{2\pi n_z}{L_z} \qquad -\frac{N_z}{2} + 1 \leq n_z \leq \frac{N_z}{2} \tag{G.17}$$

$$k = \sqrt{\sum {k_i}^2} \neq 0 \tag{G.18}$$

with n_i the mode, L_i the domain length and N_i the number of points for each direction.

The spectral velocity vector writes :

$$\overrightarrow{\hat{u}} = \frac{U_1 k_y k + U_2 k_x k_z}{k\sqrt{{k_x}^2 + {k_y}^2}}\overrightarrow{e_x} + \frac{U_2 k_y k_z - U_1 k_x k}{k\sqrt{{k_x}^2 + {k_y}^2}}\overrightarrow{e_y} - \frac{U_2\sqrt{{k_x}^2 + {k_y}^2}}{k}\overrightarrow{e_z} \tag{G.19}$$

with

$$U_1 = \sqrt{\frac{\mathcal{E}(k)}{2\pi k^2}}\cos(\theta)\exp(j\theta_1) \tag{G.20}$$

$$U_2 = \sqrt{\frac{\mathcal{E}(k)}{2\pi k^2}}\cos(\theta)\exp(j\theta_2) \tag{G.21}$$

where θ, θ_1 and θ_2 are random numbers determining the phase of the spectral velocity.

$\mathcal{E}(k)$ is the discrete Fourier transform of the double cross velocity correlation tensor : $\mathcal{Q}_{i,l}(\overrightarrow{r}) = \overline{u_i(\overrightarrow{x}) \times u_l(\overrightarrow{x} + \overrightarrow{r})}$. With HIT assumptions and for a 3-dimensional flow, the spectral tensor writes directly :

$$\mathcal{E}(k) = \frac{8\pi^3}{L_x L_y L_z}E(k) \tag{G.22}$$

with $E(k)$ being the input energetic spectrum.

The expression Eq. (G.19) is designed to follow the mass conservation in an incompressible flow which is traduced in the spectral space with :

$$\sum k_i \hat{u}_i = 0 \tag{G.23}$$

In this work, a Passot-Pouquet (PP) spectrum [Passot and Pouquet 1987] is used :

$$E(k) = A\left(\frac{k}{k_e}\right)^4 \exp\left(-2\left[\frac{k}{k_e}\right]^2\right) \tag{G.24}$$

where A is the spectrum amplitude :

$$A = \frac{16n\,u'^2}{3k_e}\sqrt{\frac{2}{\pi}} \tag{G.25}$$

with k_e the wave number associated to the most energetic structures.

$$k_e = \frac{4\beta n}{3L_t}\sqrt{\frac{2}{\pi}} \tag{G.26}$$

where $\beta = \pi/2$ in 3-dimensional flows.

The PP spectrum lacks of representativity. Indeed, contrarily to the Von-Karman and Pao (VKP) spectrum Hinze [1975], the major part of the energy is concentrated around k_e, i.e there is no inertial range and no energy at the Kolmogorov scale η_K. However, the PP spectrum remains pertinent for the study of the interaction between turbulent structures and the flame front. Furthermore, the model has the advantage to require only two parameters : the characteristic integral length scale and the velocity fluctuation. Finally, the initial field is converged for a characteristic turbulent time τ_{turb} before the energy deposit using periodic boundary conditions. Hence, it enables a transfer of part of the energy to the Kolmogorov scale and to develop the inertial range. Fig. G.4.1 illustrates the turbulence convergence.

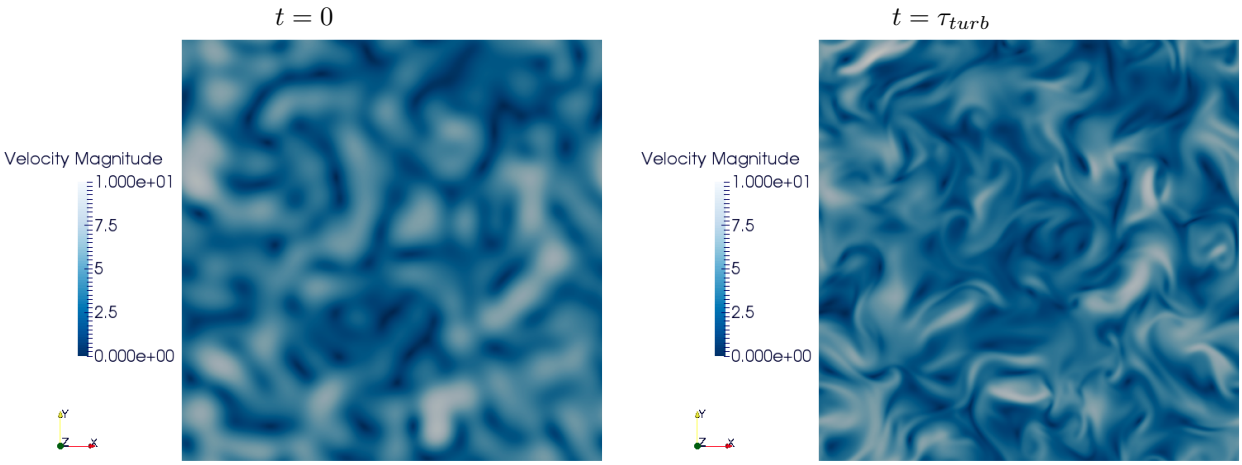

Figure G.4.1: Turbulent initialization with PP spectrum before and after convergence

G.5 Energy deposit model

G.5.1 Energy deposit model in NTMIX

In this work, the ignition is triggered by an energy deposit (ED) at the center of the domain. The resulting temperature increase causes chemical runaway with auto-ignition processes, which then form a hot kernel with a spherical propagating flame front. The deposit model is similar to the one used in [Lacaze 2009]. Hence, the energy source term $\dot{\mathcal{Q}}\,[J.m^{-3}.s^{-1}]$ applied to the energy conservation equation follows a Gaussian shape in both time and space :

$$\dot{\mathcal{Q}} = \frac{\varepsilon_i}{\sqrt{2\pi}^{n+1}\sigma_t\sigma_s^n} \times \exp\left(-\frac{(t-t_0)^2}{2\sigma_t^2}\right) \times \exp\left(-\frac{(x-x_0)^2+(y-y_0)^2+(z-z_0)^2}{2\sigma_s^2}\right) \tag{G.27}$$

where $\varepsilon_i\,[J.m^{-(3-n)}]$ is the amount of energy deposited. x_0, y_0, z_0 are the coordinates of the deposit center, and t_0 is the time corresponding to the maximum energy deposit. n is the dimension of the computation. σ_s and σ_t are the characteristic size and duration of the deposit respectively, and are derived from the Gaussian standard deviation such as the amplitude at a distance $\Delta_{s,t}$ is a ten-thousandth of the amplitude at the deposit center :

$$\Delta_{s,t} = \sigma_{s,t} \times \sqrt{2\ln\left(10^4\right)} \tag{G.28}$$

In NTMIX and AVBP solvers, the maximum temperature is limited to $5000\,K$ to remain in the validity range of classical transport, thermodynamic and chemical kinetic properties. Thus, the deposit size cannot exactly match a real spark. As shown in Fig. G.5.1 the deposit size must be increased in the ED model so that the integral power remains the same as in the real spark. Hence, the ED model enables to avoid using plasma chemistry which is relevant only for the first microseconds of the spark [Collin-Bastiani et al. 2019].

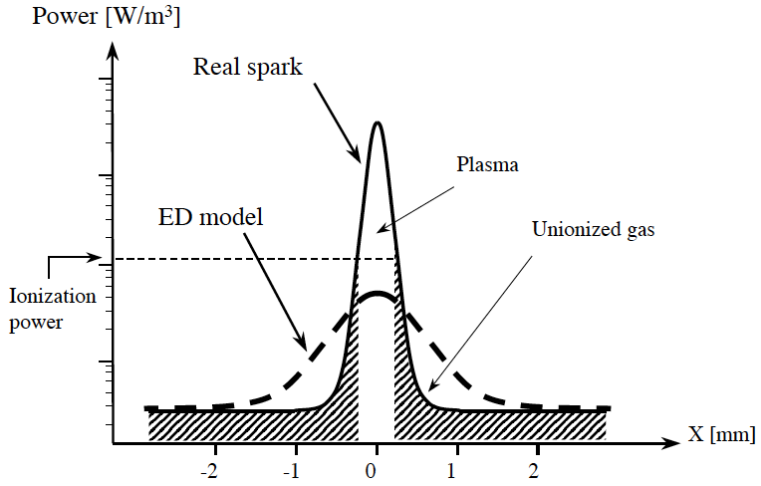

Figure G.5.1: Sketch of power distribution for real spark and for the ED model (extracted from [Lacaze et al. 2009])

Integrating in space and time the Eq. (G.27), the expression of the total energy deposed in a spherical volume of radius R_{ed} during the time interval t_{ed} centered on (x_0, y_0, z_0, t_0) is obtained[3][4] :

$$E_{ed}(R_{ed}, t_{ed}) = \varepsilon_i \times erf\left(\frac{t_{ed}}{2\sigma_t\sqrt{2}}\right) \times \left[erf\left(\frac{R_{ed}}{\sigma_s\sqrt{2}}\right) - \sqrt{\frac{2}{\pi}}\frac{R_{ed}}{\sigma_s}\exp\left(-\frac{{R_{ed}}^2}{2{\sigma_s}^2}\right)\right] \tag{G.29}$$

Choosing $R_{ed} = \Delta_s$ and $t_{ed} = 2\Delta_t$ in Eq. (G.29) gives that 99.96% of the energy ε_i is deposed in the spherical volume of radius Δ_s and in the time interval $[t_0 - \Delta_t\,,\, t_0 + \Delta_t]$. However, due to the Gaussian shape, the major part of the energy is deposed in a smaller volume and time interval.

The Gaussian spherical volume is computed as :

$$V_{Gauss} = \int_0^{2\pi}\int_0^{\pi}\int_0^{+\infty} \exp\left(-\frac{r^2}{2{\sigma_s}^2}\right) r^2 dr\,\sin(\varphi) d\varphi\, d\theta = \left(\sqrt{2\pi}\,\sigma_s\right)^3 = 0.199{\Delta_s}^3 \tag{G.30}$$

with $r = \sqrt{(x-x_0)^2 + (y-y_0)^2 + (z-z_0)^2}$ the distance to the ED center. Then, the equivalent spherical volume of radius R_{eq} corresponds to :

$$R_{eq} = \Delta_s \times \left(\frac{3 \times 0.199}{4\pi}\right)^{\frac{1}{3}} = 0.36\Delta_s \tag{G.31}$$

This radius is a good approximation of the initial hot kernel radius formed at the end of the energy deposit. It is then possible to estimate its mean kernel temperature using the following expression :

$$T_{ker} = T_f + \frac{3\varepsilon_i}{\rho_f C_{p,f} 4\pi {R_{eq}}^3} \tag{G.32}$$

with $_f$ subscript corresponding to the fresh gas state.

[3]This expression stand only for 3D cases

[4]Only if $t_0 > \Delta_t$, else the simulation starts with $\dot{\mathcal{Q}} \neq 0$ and part of the temporal Gaussian is not accounted.

The Eq. (G.32) is a zero-order estimation that enables to calibrate the model parameters ε_i and σ_s. The resulting temperature from the ED model may differ for several reasons. The diffusion is not taken into account and the heat capacity is assumed independent from the temperature. Moreover, the resulting temperature is highly dependant on the ED duration. For example, the left picture on Fig. G.5.2 shows the maximum temperature evolution using two different ED durations. For short ED, the resulting temperature is lower because the energy is deposed at constant density and the temperature increase creates a strong shock wave after the ED. On the contrary, for long ED, the temperature increase is progressive, then, the pressure variation is reduced but a radial flow is established during the ED. Thus, the density decreases during the ED which results in a higher temperature from Eq. (G.32).

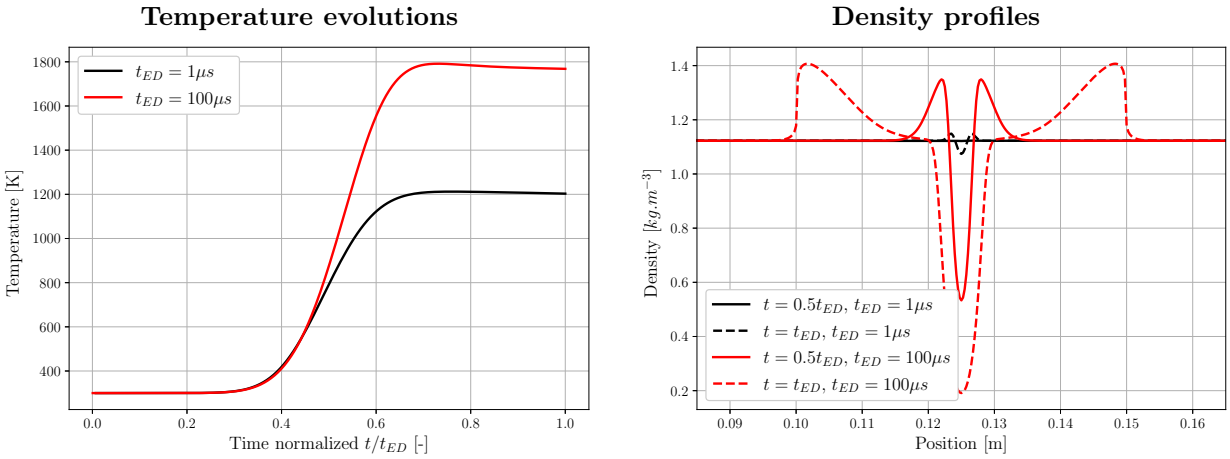

Figure G.5.2: Effect of the energy deposit duration (in air)

Similarly, the practical energy deposit duration is smaller than the user input parameter :

$$t_{eq} = \int_{-\infty}^{+\infty} \exp\left(-\frac{(t-t_0)^2}{2{\sigma_t}^2}\right) dt = \sqrt{2\pi}\,\sigma_t = 0.34\Delta_t \tag{G.33}$$

G.5.2 Energy deposit model in AVBP

The ED model in NTMIX and AVBP differs by the definition given Eq. (G.28). In AVBP, $\Delta_{s,t}$ corresponds to the characteristic diameter of the gaussian distribution (instead of the radius for NTMIX). Moreover, the amplitude at a distance $\Delta_{s,t}/2$ is a hundred (instead of a ten-thousandth for NTMIX) of the amplitude at the deposit center. Therefore Eq. (G.28) becomes:

$$\Delta_{s,t}^{AVBP} = 4\sigma_{s,t}\sqrt{\ln(10)} \tag{G.34}$$

Using this other definition Eqs. (G.29) to (G.33) are no longer valid. 99.52% of the energy ε_i is deposed in the spherical volume of radius $\Delta_s/2$ and during Δ_t. The Gaussian spherical vomule is $V_{Gauss} = 0.07\times{\Delta_s}^3$. The equivalent radius is $R_{eq} = 0.26\times\Delta_s$. Finally, the equivalent energy deposit duration is $t_{eq} = 0.41\times\Delta_t$.

Appendix H

Optimization of the injection parameters

H.1 BATMAN methodology

The objective with BATMAN is to quantify the behavior of several unknown parameters based on a limited number of simulations.

Firstly, a Design of Experiment (DoE) map is built. It corresponds to the sets of parameters that will be computed. In this study, SMD and θ FIM-UR parameters have been chosen. The shape distribution parameter q is not retain as it can be computed from the other moments of the distribution (the methodology is detailed thereafter). A first study (not shown) has enabled to reduce the parameter range to $35° < \theta < 55°$ and $80\,\mu m < d_{p,32} < 125\,\mu m$. Then, ten $(d_{p,32}, \theta)$ couples are defined with a Sobol method [Damblin et al. 2013].

From the results of the ten simulated points, interesting variables are computed and compared to the experiment through an objective function Eq. (H.1) which corresponds to the average distance between experimental and numerical results. Therefore, the smaller $\mathcal{Q}_2$ is, the better $(d_{p,32}, \theta)$ couple is.

$$\mathcal{Q}_2 = \frac{\sum_{i=1}^{N_{pts}} |\mathcal{Y}_{exp}(z_i) - \mathcal{Y}_{num}(z_i)|}{N_{pts}} \tag{H.1}$$

where $\mathcal{Y}$ is the variable of interest, *exp* and *num* subscripts refer respectively to the experimental and numerical data, z_i is the measurement position along z-axis ($y = 0$ and $x = 10\,mm$) and N_{pts} is the total measured number of points.

For each simulated point, the injection is started from the same initial solution[1] to avoid historical effects when switching from one point to the other. Each run is performed 25 milliseconds which is largely enough to converge the flow fields at the measurement position ($x = 10\,mm$).

Finally, BATMAN builds a surrogate model to extrapolate the objective function within the range of targeted parameters which enables to get a surface response giving to optimal parameter couple.

H.2 SMD profiles

The first response surface to be studied is related to the SMD profiles and is shown on Fig. H.2.1. The black points correspond to the simulated points and $\mathcal{Q}_2$ is given in micrometers. This first response surface indicates that the optimal SMD lies in the range $80\,\mu m \leq d_{p,32} \leq 100\,\mu m$ and the half cone angle is lower than 43°.

[1] The initial solution results in 120 milliseconds of fuel injection corresponding to various injection tests before the BATMAN study. Hence, the chamber and ORZ are already filled with droplets.

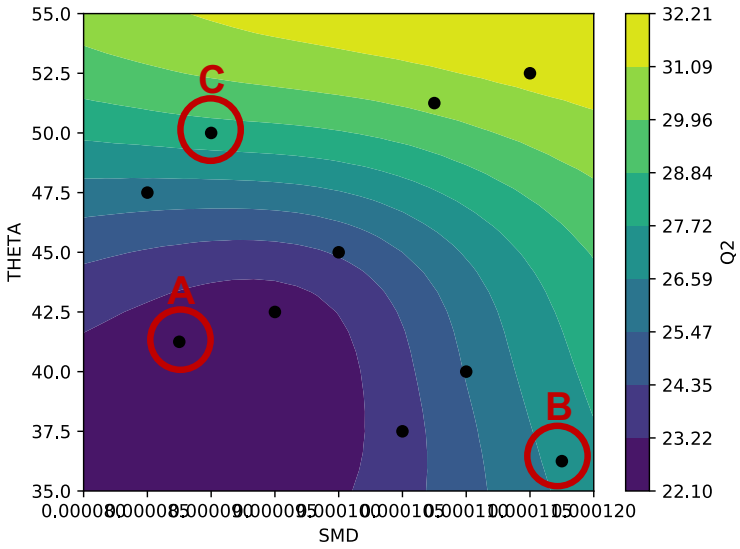

Figure H.2.1: BATMAN response surface associated to the SMD profiles.

To better understand the effect of θ and $d_{p,32}$ parameters, and why $\mathcal{Q}_2$ gives such high values, the experimental and numerical SMD profiles are plotted on Fig. H.2.2 for the three points circled in red on the response surface. On these graphs, the blue and red plus symbols correspond to the experimental data measurements and the black plus symbols are the mean experimental data. Only the mean data are used for the computation of the objective function. The blue line corresponds to the numerical results and orange dots highlight the interpolated position for the objective function.

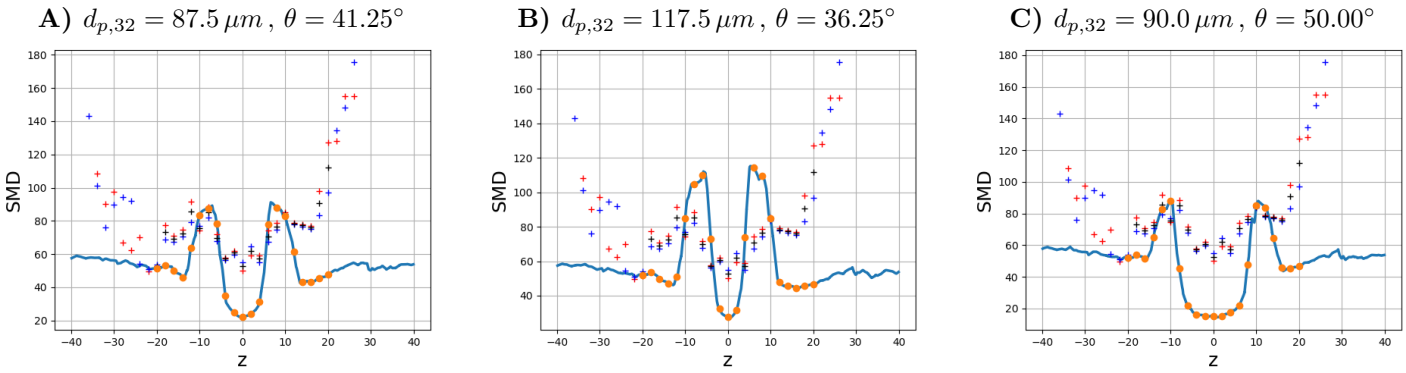

Figure H.2.2: Numerical and experimental SMD profile comparisons on z-axis ($y = 0$ and $x = 10\,mm$). (+) symbols correspond to experimental data, (-) correspond to the numerical solutions and (•) are the numerical solutions at the experimental position.

The first observation, identical for the three cases, is the disability to reproduce the correct SMD levels in the IRZ and ORZ. Indeed, the simulations have much lower SMD values at the center and in the ORZ where only the smallest droplets are able to recirculate. These differences with the experimental data may be due to a not long enough convergence time for the simulation preventing the recirculation zones to be filled with large droplets. Furthermore, it explains the large $\mathcal{Q}_2$ observed in the response surface. However, the simulation of such convergence time is too costly. Therefore, this study focuses on the converged data in the SWJ zone.

The injection angle parameter seems to have a weak influence on the results. Indeed, for $40° \leq \theta \leq 50°$ the peak position is well captured. This result is contradictory with the response surface. Indeed, the latter provides better results for the small angles because the center zone is thinner. As explained above, the points in this zone are not well reproduced by the simulation, thus, if their number is reduced, the objective function $\mathcal{Q}_2$ decreases. In other word, the reduced $\mathcal{Q}_2$ values obtained with small θ angles are

a side effect of the poor numerical representation of the IRZ and must not be taken into account for the choice of the optimal angle. Therefore, the conclusion remains that the injection angle has a weak influence on the SMD profiles.

On the contrary, the injected SMD value has a large influence on the peak amplitude in the SWJ and the peak value corresponds approximately to the injected value. From these results the optimal SMD value is $d_{p,32} = 85\,\mu m$ with an experimental fluctuation of $\pm 10\,\mu m$.

H.3 Velocity profiles

H.3.1 Axial droplet velocity

Response surfaces related to the velocity profiles have also been evaluated and are given on Fig. H.3.1. A large dependency of the angle is observed for the three velocity components. The SMD does not seem to influence the axial velocity, but results indicate that a smaller SMD improves the radial profiles. For the tangential velocity, there is no SMD influence for large angles, whereas for small angles a strange pattern appears and is explained thereafter.

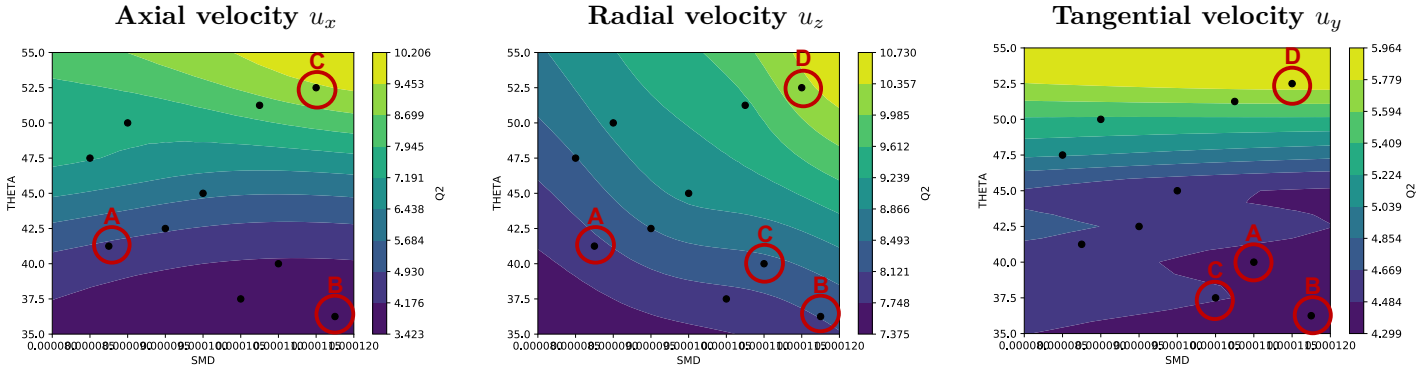

Figure H.3.1: BATMAN response surfaces associated to the velocity profiles.

Similarly to the SMD profiles, several velocity profiles are analysed starting with the axial velocity on Fig. H.3.2. As for the SMD profiles, the injection angle does not have any influence on the peak positions. Indeed, similar peak positions are found varying the angle from 36° to 53°. This result may be due to close-injector measurement position.

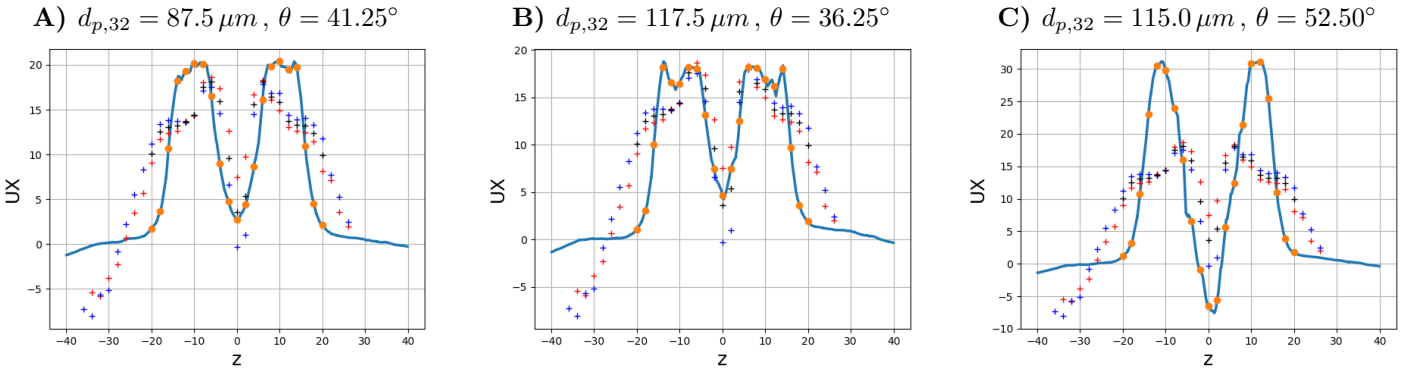

Figure H.3.2: Numerical and experimental axial velocity profile comparisons on z-axis ($y = 0$ and $x = 10\,mm$). (+) symbols correspond to experimental data, (-) correspond to the numerical solutions and (•) are the numerical solutions at the experimental position.

On the contrary, the angle has a large influence on the velocity amplitude and better results are obtained for $\theta \approx 35° - 37°$. This result is linked to the FIM-UR model construction (presented in Chap. 11) that

uses the half cone angle given in input to determine the liquid film thickness and then the velocity profiles. Therefore, in this work, θ is a parameter which enables to fit the spray velocity. A more causality-based construction would be to determine the velocity profile and the half cone angle from the film thickness, as it has been proposed with the injector model in Chap. 11.

Finally, as indicated by the response surface, the SMD does not have any influence on the axial velocity profiles.

H.3.2 Radial droplet velocity

The radial velocity profiles are shown on Fig. H.3.3. The conclusion given for the axial velocity profiles are conserved: the angle does not change the peak position but their intensity. The optimal values are $\theta \approx 35° - 37°$. Contrary to the result given by the response surface, the SMD does not have any influence on the radial velocity profiles.

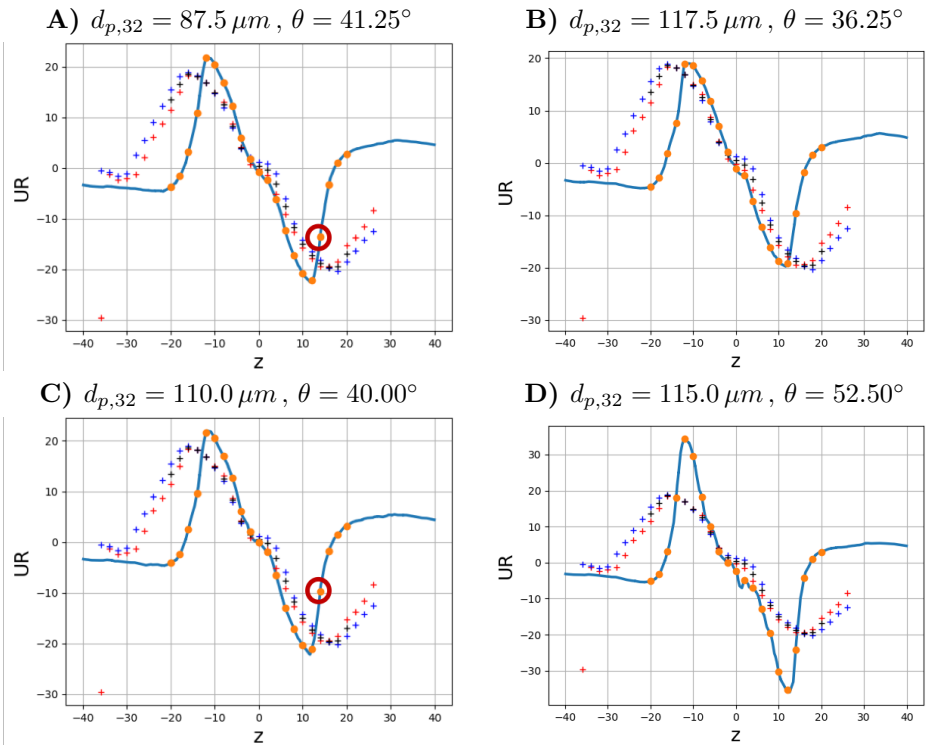

Figure H.3.3: Numerical and experimental radial velocity profile comparisons on z-axis ($y = 0$ and $x = 10\,mm$). (+) symbols correspond to experimental data, (-) correspond to the numerical solutions and (•) are the numerical solutions at the experimental position.

Comparing cases **A)** and **C)** which have almost the same angle but very different SMD, the only difference is due to the point $z = 14\,mm$, circled in red, which is closer from experimental data in case **A)**. Therefore the SMD influence observed on the radial velocity response surface is an artifact of the discretization measurement and is negligible when looking at the velocity profile.

H.3.3 Tangential droplet velocity

Finally, the tangential velocity profiles are given on Fig. H.3.4. These profiles are composed of two peaks more or less significant depending on the input parameters. Once again, the SMD has a negligible influence on the velocity profiles. The half cone angle has an influence on the central peak. This peak is almost not present in the experimental measurement which corresponds to $\theta \approx 35° - 37°$ as for the other velocity components. However, nor the SMD nor θ seem to have an effect on the external peaks. The

origin of these peaks will be detailed in the following section.

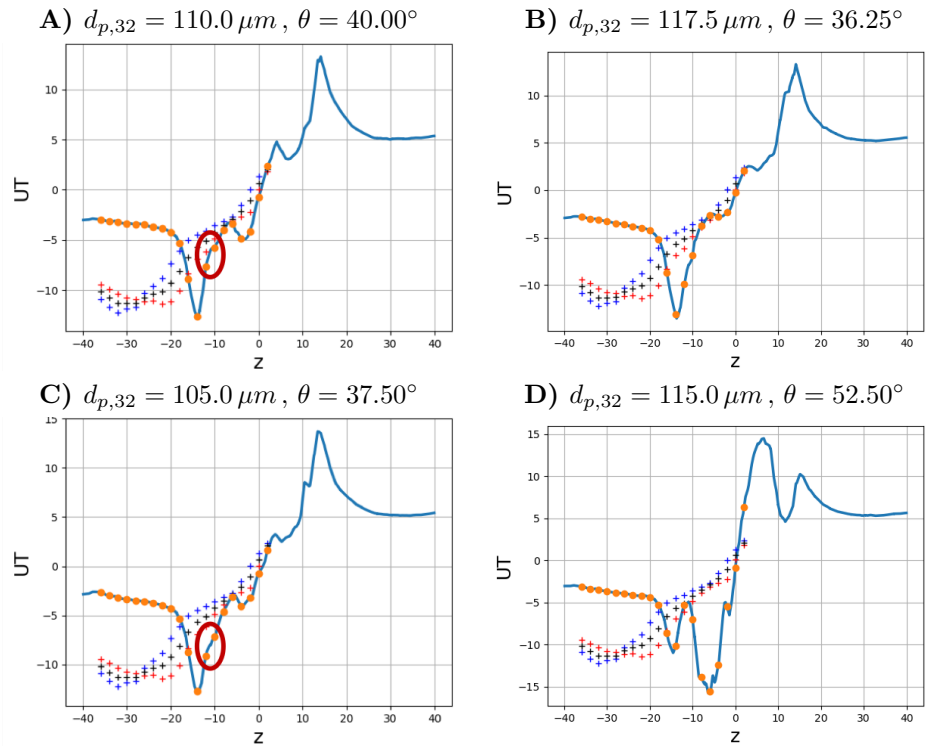

Figure H.3.4: Numerical and experimental tangential velocity profile comparisons on z-axis ($y = 0$ and $x = 10\,mm$). (+) symbols correspond to experimental data,(-) correspond to the numerical solutions and (•) are the numerical solutions at the experimental position.

Similarly to the radial velocity, the strange pattern observed on the tangential velocity response surface, indicating an influence of the SMD, can be associated to a not perfectly converged profile on the external peak. Indeed, on case **C)**, an error is induced (red circled points) whereas the central peak seems better described compared to case **A)** which has a smaller global $\mathcal{Q}_2$ value.

H.4 Conclusions and retained injection parameters

H.4.1 BATMAN methodology

As shown with this study, BATMAN is a tool that can be used to determine the optimal injection parameters based on experimental two-phase flow profiles. This tool has been also used in [Wirtz 2022] to determine the FIM-UR injection parameters, but based on reactive flame spray profiles.

The response surfaces given by the tool indicate the general tendency of the parameters effect with an optimal number of reference runs. However, direct complementary profiles analyses of the BATMAN simulations are required to avoid misleading interpretations. Moreover, the construction of the objective function has a large influence on the response surface results. Especially, the measurements points must be carefully chosen to avoid erroneous conclusions.

H.4.2 Results summary

The main results of the BATMAN study are summarized below:

- As expected, the optimal SMD parameter in FIM-UR is given by the SMD response surface. The optimal value retained in the following is $d_{p,32} = 85\,\mu m$ and corresponds to the injection peak value. From the experimental data, this value may fluctuate about $\pm 10\,\mu m$.

- The SMD has no influence on the two-phase velocity profiles.
- The optimal half cone angle θ is given by the velocity response surfaces. The optimal value retained in the following is $\theta = 36°$
- The angle strongly influences the droplet velocities due to the FIM-UR model construction.
- The angle has no significant influence on the injection peak position.
- Beside the input parameter optimisation, large discrepancies are found between the experimental and numerical profiles and a detailed profile shape analysis is required.

H.4.3 Shape parameter q

One last missing parameter for the FIM-UR model is the shape parameter q of the Rosin-Rammler distribution. Since a unique RR distribution is defined with the couple $(d_{p,32}, q)$, q can be determined from the other moments of the distribution. On one hand, these moments have been measured experimentally and are summarized in Tab. H.4.1. On the other hand, these moments can be numerically computed with Eq. (H.2) depending on q.

$$d_{p,ab} = \left(\frac{\int_0^\infty {d_p}^a \times RR_{X,q}(d_p) dd_p}{\int_0^\infty {d_p}^b \times RR_{X,q}(d_p) dd_p} \right)^{\frac{1}{a-b}} \tag{H.2}$$

with $RR_{X,q}(d_p)$ the Rosin-Rammler probability density function computed with Eq. (11.4) and X the dimension factor computed with Eq. (11.8) to retrieve $d_{p,32}$.

$d_{p,32}$	$d_{p,30}$	$d_{p,31}$	$d_{p,43}$
$72\,\mu m$	$77\,\mu m$	$71\,\mu m$	$99\,\mu m$

Table H.4.1: Characteristic moments of the spray distribution measured experimentally.

Therefore, an optimization has been performed to determine the q value fitting the best the experimental moments. Results are displayed on the left graph of Fig. H.4.1. The dashed lines correspond to the experimental targets while the solid lines correspond to the numerical values depending on q. The error is minimized for the optimal value[2] $q = 1.92$. The resulting distribution is displayed on the right picture with the corresponding numerical and experimental moments. While $d_{p,31}$ is well recovered, $d_{p,30}$ and $d_{p,43}$ are slightly under-estimated. Indeed, the RR distribution is only an approximation of the real droplet distribution which is not an issue considering the experimental data variability.

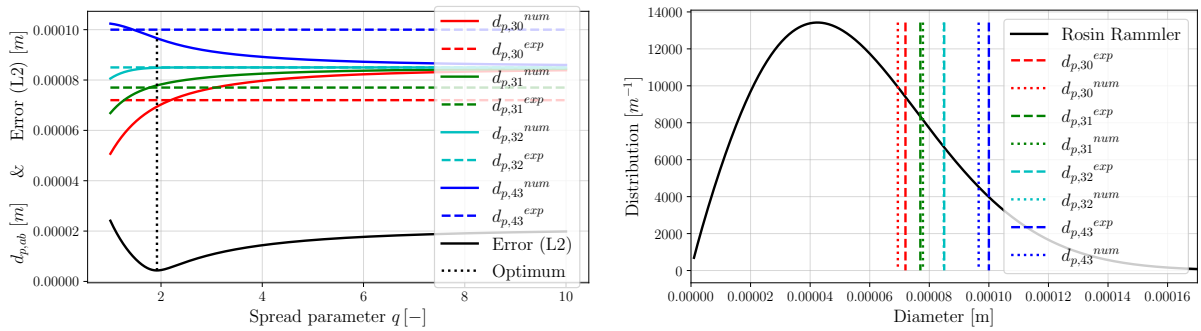

Figure H.4.1: Shape parameter q optimization (left) and resulting Rosin-Rammler distribution (right).

[2]One can note that the optimal value is close to the generic value $q = 1.89$ given by the Maximum Entropy Formalism in Chap. 11.